PROCEEDINGS

30th INTERNATIONAL WORKSHOP ON WATER WAVES AND FLOATING BODIES

EDITORS:
RICHARD PORTER & JUN ZANG

12-15TH APRIL, 2015,
BRISTOL AND BATH, UK

PROCEEDINGS

30th INTERNATIONAL WORKSHOP ON WATER WAVES AND FLOATING BODIES

EDITORS:
RICHARD PORTER & JUN ZANG

12-15TH APRIL, 2015,
THE M-SHED,
BRISTOL, UK

The SS Great Britain in dry dock in Bristol

The SS Great Britain is a museum piece housed in a dry dock on Bristol's floating harbour. Designed by the Victorian engineer Isambard Kingdom Brunel (also responsible for the design of Bristol's Clifton Suspension Bridge, and Temple Meads Train Station), at 98m she held the record for the longest passenger ship in the world from 1845 to 1854. The first ship to combine a screw propeller with an iron hull, the Great Britain was the first iron-hulled steamship to cross the Atlantic in 1845.

When launched in 1843, Great Britain was by far the largest vessel afloat. However, her protracted construction and high cost had left her owners in a difficult financial position, and they were forced out of business in 1846 after the ship was left stranded by a navigational error.

Sold for salvage and repaired, Great Britain carried thousands of immigrants to Australia until converted to sail in 1881. Three years later, she was retired to the Falkland Islands where she was used as a warehouse, quarantine ship and coal hulk until scuttled in 1937.

In 1970 the SS Great Britain was towed back to the Bristol dry dock where she was built. Now listed as part of the National Historic Fleet, she is an award-winning visitor attraction and museum ship in Bristol Harbour, with 150,000-170,000 visitors annually and has become emblematic of the city of Bristol.

Front cover

"The SS 'Great Britain' under steam and sail, saluting a ship of war" by Joseph Walter, 1845.

SPONSORS OF THE 30TH IWWWFB

The organisers of the 30th IWWWFB gratefully acknowledge financial support from the following organisations:

Bureau Veritas

The Office for Naval Research

Lloyds Register

Atkins Global

Wavepower

London Mathematical Society

Hosted by

Scientific Committee

Richard PORTER, University of Bristol, UK
Jun ZANG, University of Bath, UK
Masashi KASHIWAGI, Osaka University, Japan
Bernard MOLIN, École Centrale Marseille & IRPHÉ, France

Local Organizing Committee

Richard PORTER, University of Bristol, UK
Jun ZANG, University of Bath, UK

PREFACE

The International Workshop on Water Waves and Floating Bodies is an annual meeting of engineers and scientists with a particular interest in water waves and their effects on floating and submerged marine structures. The IWWWFB was initiated by Professor D. V. Evans (University of Bristol) and Professor J. N. Newman (MIT) following informal meetings between their research groups in 1984. First intended to promote communications between workers in the UK and the USA, the interest and participation quickly spread to include researchers from many other countries around the world. The workshop places particular emphasis on the participation of younger researchers, on the stimulation of discussions between engineers and scientists, and to the presentation of preliminary basic scientific work before its publication elsewhere. The workshop is an important reference point for organizing and spreading knowledge in this area. In particular, the workshop proceedings are freely accessible through the dedicated internet address www.iwwwfb.org where all contributions from 1986 on can be found.

Over 95 abstracts were submitted to this year's workshop, out of which 64 have been retained for presentation and are included in the proceedings. The contributions cover a wide range of topics related to the interaction between ocean waves and marine structures, while the authors cover all career stages from PhD students to the most senior and distinguished researchers.

This is the sixth year since the establishment of the Tuck Fellowship which, in memory of Prof. Ernie Tuck, supports the participation of one PhD student, or young researcher, each year. Eleven applications for the Tuck Fellowship were received this year and the prize was awarded to Hugh Wolgamot, a Research Fellow in his first year post-PhD at the University of Western Australia, while Tomasz Bobinski, a PhD student at Laboratoire de Physique et Mécanique des Milieux Hétérogènes, UMR CNRS, was selected as the runner-up.

The organisation of a workshop of this size relies on the efforts of many people not immediately visible to the participants. Richard and Jun are particularly grateful to Samantha Dixon and Liz Clark for all their hard work in helping make this event possible.

30TH IWWWFB PROGRAM

30TH INTERNATIONAL WORKSHOP ON WATER WAVES AND FLOATING BODIES

ABSTRACTS

(Abstract submitted to the 30th IWWWFB workshop, Bristol, UK, 2015)

A high-order finite-difference linear seakeeping solver tool for calculation of added resistance in waves *

Mostafa Amini Afshar, Harry B. Bingham, and Robert Read
Department of Mechanical Engineering, Technical University of Denmark
E-mail: maaf@dtu.dk, hbb@dtu.dk, rrea@mek.du.dk

1 Introduction

During recent years a computational strategy has been developed at the Technical University of Denmark for numerical simulation of water wave problems based on the high-order finite-difference method, [2],[4]. These methods exhibit a linear scaling of the computational effort as the number of grid points increases. This understanding is being applied to develop a tool for predicting the added resistance (drift force) of ships in ocean waves. We expect that the optimal scaling properties of this solver will allow us to make a convincing demonstration of convergence of the added resistance calculations based on both near-field and far-field methods. The solver has been written inside a C++ library known as **Overture** [3], which can be used to solve partial differential equations on overlapping grids based on the high-order finite-difference method. The resulting code is able to solve, in the time domain, the linearised potential flow forward-speed hydrodynamic problems; namely the steady, radiation and diffraction problems. The near-field formulation of the wave drift force has also been implemented, and development is under way to include far-field methods. This paper presents validation results based on analytical solutions for exact geometries.

2 Mathematical formulation

A moving Cartesian coordinate system *O-xyz* is adopted, which is in steady translation with the body's forward speed U. The origin of the coordinate system is at the mean free surface position, and z is vertically upward. The body is under the action of incoming waves, and is free to oscillate in 6 degrees of freedom. Assuming a potential flow model, the governing equation is:

$$\nabla^2\phi = \frac{\partial^2\phi}{\partial x^2} + \frac{\partial^2\phi}{\partial y^2} + \frac{\partial^2\phi}{\partial z^2} = 0, \quad \text{where} \quad \phi = -Ux + \phi_b + \phi_u \ \text{ and } \ \phi_u = \phi_0 + \phi_s + \sum_{k=1}^{6}\phi_k.$$

$-Ux + \phi_b$ arises due to the forward speed of the body, and represents the solution of the steady wave resistance problem. For the Neumann-Kelvin linearisation ($\phi_b = 0$), and for the double-body linearisation, the following boundary value problem is solved to obtain the base flow, $\phi_b = \phi_{db}$.

$$\nabla^2\phi_{db} = 0, \quad \frac{\partial\phi_{db}}{\partial n} = \vec{W}\cdot\mathbf{n} \ \text{ on } s_0, \quad \frac{\partial\phi_{db}}{\partial z} = 0 \ \text{ on } z = 0, \quad \nabla\phi_{db} \to 0 \ \text{ in the far field,}$$

where and $\vec{W} = (U, 0, 0)$. Moreover ϕ_0 and ϕ_s are the velocity potentials of the incident waves and the scattered waves respectively, while the body is assumed to be fixed (the diffraction problem). The velocity potentials due to oscillatory motions of the body in the kth direction (the radiation problem) are given by ϕ_k. The decomposed velocity potentials mentioned above are substituted into the non-linear boundary conditions. The linearised conditions are then obtained by Taylor-series expansion around the mean water level $z = 0$ and mean body position s_0 respectively:

$$\frac{\partial\phi_u}{\partial t} = -g\eta_u + U\frac{\partial\phi_u}{\partial x} - \nabla\phi_b\cdot\nabla\phi_u - \frac{1}{2}\nabla\phi_b\cdot\nabla\phi_b + U\frac{\partial\phi_b}{\partial x} - g\eta_b = 0, \tag{1}$$

$$\frac{\partial\eta_u}{\partial t} = \frac{\partial\phi_u}{\partial z} + U\frac{\partial\eta_u}{\partial x} - \nabla\phi_b\cdot\nabla\eta_u + \eta_u\frac{\partial^2\phi_b}{\partial z^2} - \nabla\phi_b\cdot\nabla\eta_b + U\frac{\partial\eta_b}{\partial x} + \eta_b\frac{\partial^2\phi_b}{\partial z^2} = 0. \tag{2}$$

and

$$\frac{\partial\phi_u}{\partial n} = \sum_{k=1}^{6}(\dot{\xi}_k\cdot n_k + \xi_k\cdot m_k), \quad \text{and} \quad \frac{\partial\phi_s}{\partial n} = -\nabla\phi_0(\mathbf{r},t)\cdot\mathbf{n}, \qquad \text{on } z = s_0.$$

*The authors wish to thank the Danish Maritime Fund for supporting this work.

Here, ξ_k is the translation or rotation of the body, and $\dot{\xi}_k$ is the corresponding velocity. The normal vectors n_k and the m terms are defined as follows:

$$(n_1, n_2, n_3) = \mathbf{n}, \qquad (m_1, m_2, m_3) = (\mathbf{n} \cdot \nabla)(\vec{W} - \nabla\phi_b),$$
$$(n_4, n_5, n_6) = (\mathbf{r} \times \mathbf{n}), \qquad (m_4, m_5, m_6) = (\mathbf{n} \cdot \nabla)\Big(\mathbf{r} \times (\vec{W} - \nabla\phi_b)\Big),$$

where $\mathbf{r}$ is the position vector. The above mentioned linear initial boundary value problem is solved in the time domain. Instead of finding the radiation and diffraction impulse response functions, the response of the body is calculated when exposed to a pseudo-impulsive Gaussian forcing given by $\xi_k(t) = \zeta_0(t) = e^{-2\pi^2 s^2 t^2}$, where s is a parameter to control the shape of the pseudo impulse. ζ_0 is the amplitude of the incident waves for the diffraction problem. Having solved for ϕ_u, the first-order force on the body can also be obtained from the linearised Bernoulli equation:

$$p = -\rho \left[\left(\frac{\partial}{\partial t} - \vec{W} \cdot \nabla \right) \phi_u - \vec{W} \cdot \nabla\phi_b + \nabla\phi_b \cdot \nabla\phi_u + \frac{1}{2}\nabla^2\phi_b \right]. \tag{3}$$

The frequency-domain added mass and damping coefficients a_{jk}, b_{jk}, and the wave exciting force coefficient X_j are then obtained by a Fourier transform of the time-domain data. The Froude-Krylov part of the wave excitation force is however, computed from the closed form expression in the frequency domain. Finally the body motion $\hat{\xi}_k$ in the frequency domain is found by solving the equations of motion:

$$\sum_{k=1}^{6} \hat{\xi}_k \left[-\omega^2 (M_{jk} + a_{jk}) + i\omega b_{jk} + c_{jk} \right] = A\, X_j, \qquad j = 1, 2, \ldots, 6 \tag{4}$$

where M_{jk} is the inertial mass, c_{jk} is the hydrostatic coefficient matrix, and A is the incident wave amplitude. The wave drift force is calculated in the frequency domain by considering the second-order pressure terms in the Bernoulli equation. All the terms in these expressions are obtained as described above, via Fourier transform of the corresponding pseudo-impulsive quantities [1].

3 The numerical method

The entire physical domain is descretised by overlapping structured and body-fitted grids using the **Ogen** grid generator. There are three sets of grid points including discretisation, interpolation and hole points. Each grid is mapped to a uniform Cartesian computational grid, where discretisation of the continuous derivatives takes place using fourth-order finite-difference schemes. There are two layers of ghost points generated to handle the derivatives at the boundaries. The continuity equation is descretised by a fourth-order centered scheme. A non-homogeneous Neumann boundary condition is applied at the body to satisfy the body boundary condition. The Dirichlet boundary condition is used to specify the velocity potential at the free surface. The resulting system of equations including the interpolation equations, and the right hand side vector b is constructed as $[A][\phi] = [b]$, and solved by a direct LU factorisation method. The free-surface conditions, (1) and (2) are integrated in time using the fourth-order Runge-Kutta method, and ϕ and η at the free surface are updated at each time step. As the free-surface conditions are in fact a system of hyperbolic equations, a special care is required to set the ghost points while evaluating the convective derivatives at the boundaries. In the region where $\vec{W} \cdot \mathbf{n} < 0$, extrapolation from the internal points is used to populate the ghost layers, which turns the centered scheme at the boundary into an upwind scheme. For the region where $\vec{W} \cdot \mathbf{n} > 0$, a Neumann condition is used to set the ghost points at the boundaries. The dynamic free-surface boundary condition and the known Neumann condition for ϕ on the body boundary can be used to derive a corresponding Neumann condition for η:

$$\nabla\eta \cdot \mathbf{n} \;=\; -\frac{1}{g}\left(\frac{\partial}{\partial t}\left(\nabla\phi \cdot \mathbf{n}\right) - U\,\nabla\left(\frac{\partial\phi}{\partial x}\right) \cdot \mathbf{n} \right) \tag{5}$$

where this expression corresponds to the Neumann-Kelvin linearisation. A similar relation can be obtained for the double-body flow linearisation. The above treatments are necessary for ensuring a stable numerical scheme and for preventing spurious reflections at the boundaries. Moreover in the case of grid stretching, the centered scheme is not suitable for evaluation of the convective derivatives. The unequal weighting of the neighboring points in the convective derivative on a stretched grid will always produce an effective downwinding in some areas of the free-surface, which leads to instability. Two remedies are available: either a centered scheme is used and at the same time a Savitzky-Golay type filter is applied to the solution at each time step, or an upwind-biased scheme is used for evaluation of the convective derivatives.

4 Results

The radiation problem for surge and heave body motion has been solved for a floating cylinder with $Fr = U/\sqrt{ga} = 0.03$, where a is radius of the cylinder. The radiation problem for sway and heave motion has been solved for a submerged sphere with $Fr = 0.40$ with a submergence depth of $h = 2a$. The diffraction problem in the case of the head waves for the submerged hemisphere with $Fr = 0.40$ has also been solved. Just the imaginary part of the complex force is shown here, and $\nu = \omega_e^2/g, \nu_0 = \omega/g$. The numerical results show very good agreement with the analytical solutions from [5] and [6]. The deep-water limit has also been shown in the figure, as the analytical results are for the deep water condition. The wave drift force along the x coordinate and the body motions have been calculated for the case of a floating hemisphere with $Fr = 0$, and results have been compared with those calculated using **WAMIT**. Contributions from both the water line integral and the body surface integral in the near-field method are shown in the figure, and d is the diameter of the hemisphere. The horizontal line in the drift force figure shows the analytical asymptotic value $-\frac{1}{3}$ for the short waves. The results of the developed solver in the figure are shown with the name *OceanWave3D*.

5 Conclusions

A seakeeping solver has been developed based on the high-order finite-difference method applied on overlapping grids. A stable numerical scheme has been achieved either by using a centered scheme and applying a mild filter to the solution, or by using the upwind-biased difference scheme for the convective derivatives in the free-surface boundary conditions. The solver has been validated for exact geometries, and work is under way to validate the code for real ship geometries. The solver is being developed to include more models for the wave drift force calculation, and to run in parallel in order to demonstrate convergence of the added resistance based on both far-field and near-field methods.

References

[1] Amini Afshar, M. *Towards Predicting the Added Resistance of Slow Ships in Waves*. PhD thesis, DTU Mechanical Engineering, 2015.

[2] Bingham, H. B. and H. Zhang. On the accuracy of finite-difference solutions for nonlinear water waves. *Journal of Engineering Mathematics*, 58(1-4):211–228, 2007.

[3] Brown, D. L., W. D. Henshaw, and D. J. Quinlan. Overture: An object-oriented framework for solving partial differential equations on overlapping grids. *Object Oriented Methods for Interoperable Scientific and Engineering Computing, SIAM*, pages 245–255, 1999.

[4] Engsig-Karup, A. P., H. B. Bingham, and O. Lindberg. An efficient flexible-order model for 3d nonlinear water waves. *Journal of computational physics*, 228(6):2100–2118, 2009.

[5] Wu, G. and R. E. Taylor. Radiation and diffraction of water waves by a submerged sphere at forward speed. *Proceedings of the Royal Society of London. A. Mathematical and Physical Sciences*, 417(1853):433–461, 1988.

[6] Wu, G. and R. E. Taylor. The hydrodynamic force on an oscillating ship with low forward speed. *Journal of Fluid Mechanics*, 211:333–353, 1990.

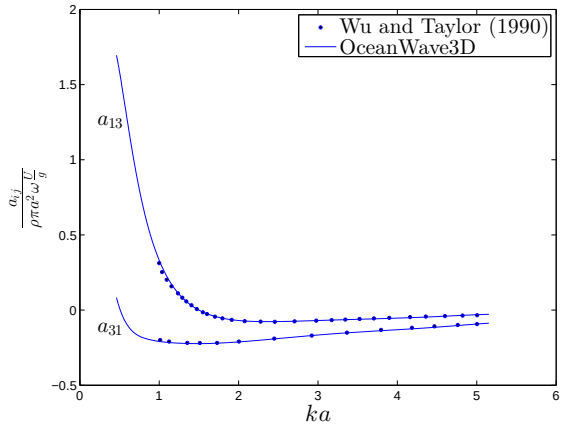

Floating cylinder, a_{13} and a_{31}

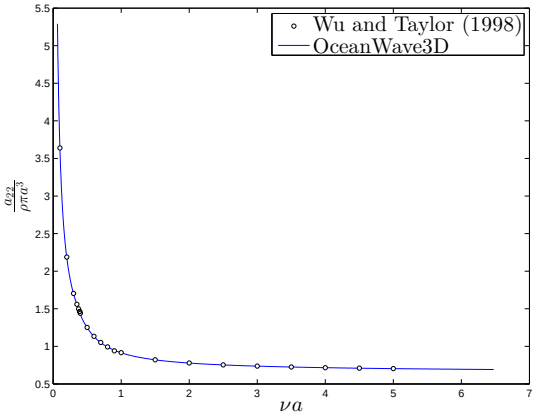

Submerged sphere, a_{22}

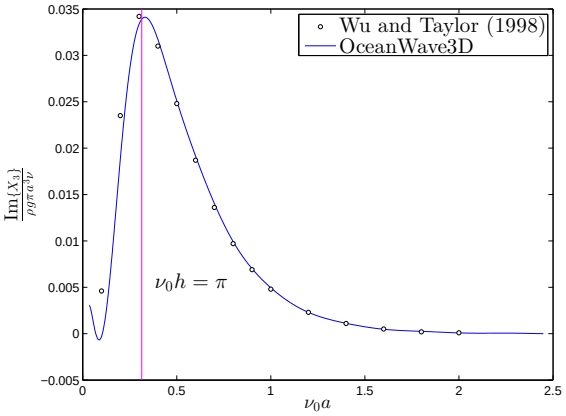

Submerged sphere, heave force imaginary

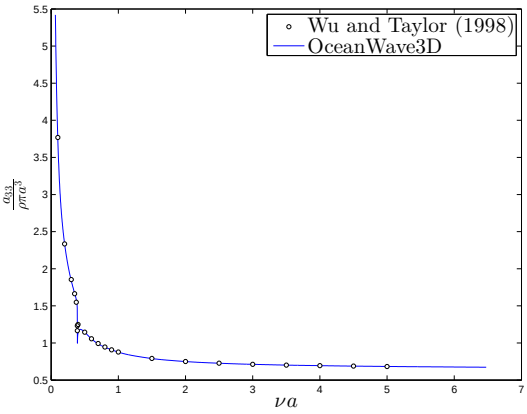

Submerged sphere, a_{33}

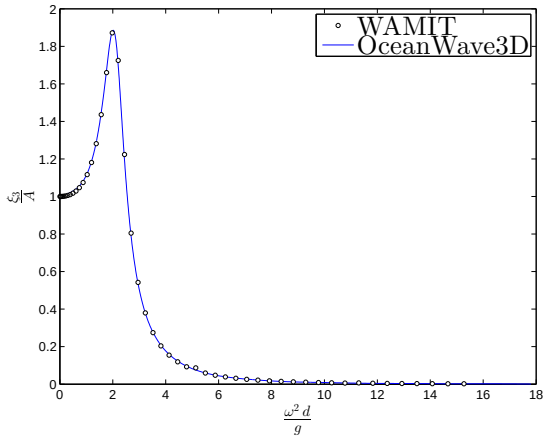

Floating hemisphere, RAO

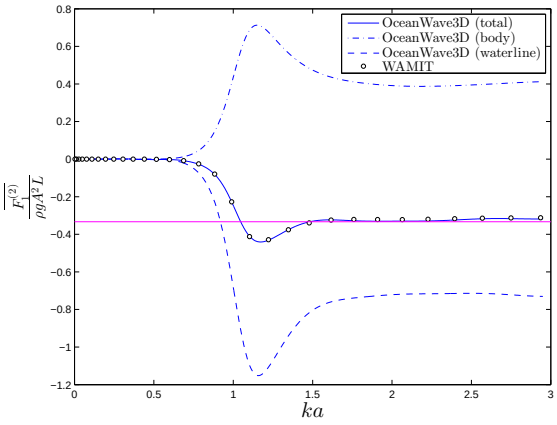

Floating hemisphere, wave drift force

Figure 1: Validation results for various quantities using a floating two-dimensional cylinder, a sumberged sphere, and a floating hemispere.

On the modeling of nonlinear wave-wave and wave-body interactions in a realistic sea state

Wei Bai*, Xingya Feng, Xianglong Chen and Kok Keng Ang
Department of Civil and Environmental Engineering, National University of Singapore, Singapore
E-mail: w.bai@nus.edu.sg

Highlights:

- A time-domain nonlinear potential model is developed to solve wave-body interactions in a realistic sea state.
- Nonlinearity is demonstrated through simulating focused waves and wave diffraction by side-by-side barges subject to an irregular wave field.

1. Introduction

This abstract aims to present a nonlinear potential flow model which generates a realistic sea state and solves wave-body interaction problems. The fully nonlinear potential flow theory (FNPF) remains one of the advanced and efficient methods to model water waves and wave-body interactions. Recently, various numerical models have been developed in order to implement FNPF efficiently. Engsig-Karup *et al.* [1] presented a higher-order finite difference (FD) model, *OceanWave3D*, which was proved very accurate in simulating wave-wave and wave-body interactions by comparisons against experiments. Guerber *et al.* [2] presented a two-dimensional model with a freely or forced moving submerged horizontal cylinder and solved the boundary value problem by a higher-order boundary element method (HOBEM), which was simulated to represent the wave energy converters (WECs). Targeted at improving the computational efficiency, Shao and Faltinsen [3] developed a new 3D FNPF model based on harmonic polynomial cells. The computational domain is discretized by harmonic polynomials such that velocity potential at each field point is interpolated by a set of harmonic polynomials. However, these models focus much on modelling regular wave fields. Ducrozet *et al.* [4] presented a modified higher-order spectral (HOS) nonlinear potential model with a controlled wave maker. The key point in the modified model is wave generation by an additional potential which satisfies the no-flux condition on wave maker and nonlinear free surface conditions. Validation cases of 2D irregular waves and 3D focused waves illustrate high accuracy with comparisons against experimental data.

In this abstract, we present a 3D FNPF model based on HOBEM and focus on modelling irregular wave fields and wave-body interactions in a realistic sea state. One of our concerns is the associated nonlinearity which is yet much discussed in the previous work.

We first simulate a 2D focused wave in a rectangular numerical wave tank (NWT). Of interest is the presence of higher frequency components induced by nonlinear wave-wave interactions, which however cannot be identified in linear models. To improve computational efficiency, we modified the rectangular NWT into a circular tank. In the modified tank, no wave maker is modelled; instead, we impose an irregular wave field as an incoming wave. Only the scattered wave field needs to be solved. To demonstrate its capacity, we simulate a case of two side-by-side barges in a realistic sea state and comparisons with model tests are presented. The nonlinearity in the wave response is investigated.

2. Numerical model

2.1 Rectangular NWT

Following the basic assumptions of FNPF theory, i.e. fluid is incompressible, inviscid and flow irrotational, the velocity potential $\phi(x,y,z,t)$ satisfies the Laplace equation in the domain,

$$\nabla^2\phi = 0\,. \tag{1}$$

On the free water surface S_F, the kinematic and dynamic boundary conditions in the Lagrangian description are

$$\frac{\mathrm{D}\mathbf{X}}{\mathrm{D}t} = \nabla\phi\,, \tag{2}$$

$$\frac{\mathrm{D}\phi}{\mathrm{D}t} = -gz + \frac{1}{2}\nabla\phi\cdot\nabla\phi\,, \tag{3}$$

where D/Dt is the material derivative, $\mathbf{X}$ denotes the position of water particles on the free water surface. On solid walls, non-flux condition is satisfied.

A wave maker is located at one end of the rectangular tank, and a numerical beach is placed at the other end to avoid reflection from the end wall. In order to generate any desired irregular wave field, we need to specify the movement of wave maker (piston type). Given any targeted wave spectrum $S(\omega)$ (discretized into N harmonics), the displacement of wave maker is specified as

$$x_{WM}(t) = \sum_{n=1}^{N} \sqrt{2S_{WM}(\omega_n)\Delta\omega} \cos(k_n x_p - \omega_n t + p_n)\,, \quad (4)$$

$$S_{WM}(\omega_n) = e_0 S(\omega_n)\,, \quad (5)$$

$$e_0 = \frac{4\sinh^2(k_n h)}{2k_n h + \sinh(2k_n h)}\,, \quad (6)$$

where e_0 is a transfer function; ω_n is the wave frequency, k_n the wave number, and p_n the phase offset of the nth component. In addition, h is the water depth and $\Delta\omega$ is the frequency interval. x_p is a reference position, and in the case of focused waves it is the focal point. More details on the irregular wave generation can be found in Frigaard *et al.* [5].

2.2 Circular tank model

While modelling wave-body interaction problems using the above rectangular NWT, the side wall effect becomes significant, unless in a very wide tank which requires huge computational effort. In order to eliminate tank wall effects and improve computational efficiency, we develop a nonlinear decomposition model which solves wave-body interactions in a circular tank. In the decomposition model, the incident wave field is specified explicitly while only the scattered wave is solved instead of computing the original total wave.

The total velocity potential $\phi(x,y,z,t)$ can be separated into an incident wave part and a scattered part, i.e. $\phi = \phi_I + \phi_S$. The free surface is updated from the contributions of incident and scattered velocities. The incident flow potential and velocities are evaluated explicitly in the fluid domain. By substituting the separation of potential and elevation into Eqns. (1), (2) and (3), the decomposition leads to the following boundary value problem (BVP) for the scattered component:

$$\nabla^2 \phi_S = 0\,, \quad (7)$$

with boundary conditions on free surface:

$$\frac{\mathrm{D}\mathbf{X}_S}{\mathrm{D}t} = \nabla\phi - \nabla\phi_I \text{ , on } S_F \quad (8)$$

$$\frac{\mathrm{D}\phi_S}{\mathrm{D}t} = -gz_S + \frac{1}{2}\nabla\phi\cdot\nabla\phi - \frac{1}{2}\nabla\phi_I\cdot\nabla\phi_I \text{ , on } S_F \quad (9)$$

and on body surfaces:

$$\frac{\partial\phi_S}{\partial n} = -\frac{\partial\phi_I}{\partial n} \text{ , on } S_B \quad (10)$$

where the subscripts '*I*' and '*S*' denote the components of incident and scattered waves respectively.

The generation of a realistic sea state is similar to that in the rectangular wave tank, except that there is no wave maker in this circular tank. Once the energy spectrum is chosen, the free surface elevation and the velocity potential can be calculated as a sum of N (N should be large enough to reproduce the desired spectrum) harmonics,

$$z_I(x,t) = \sum_{n=1}^{N} A_n \cos(k_n x - \omega_n t + p_n), \quad A_n = \sqrt{2S(\omega_n)\Delta\omega}, \quad (11)$$

$$\phi_I(x,z,t) = \sum_{n=1}^{N} A_n \frac{\omega_n}{k_n} \frac{\cosh k_n(z+h)}{\sinh k_n h} \sin(k_n x - \omega_n t + p_n)\,, \quad (12)$$

where A_n is the amplitude of the nth wave component. The phase is a random function following the standard uniform distribution, ranging from 0 to 2π. No transfer function is required due to the nature that no wave maker is used in this model.

A higher-order boundary element method (HOBEM) is employed to simulate the wave-body interactions in the time domain. Time integration is performed via the 4th order Runge-Kutta scheme, and free surface conditions are updated based on a Mixed Eulerian -Lagrangian scheme.

3. 2D Focused waves

We employ the rectangular NWT presented in Section 2.1 to simulate 2D focused waves. In our higher-order boundary element simulations, the focused waves (Case D55) are performed in a water depth of 0.7 m, of which the nonlinearity has been validated through comparison with the experimental results in Baldock *et al.* [6]. The wave conditions are designed according to the configuration of Case D (with the input amplitude of 55mm) in Baldock *et al.* [6]. The wave group is comprised of 29 individual wave components and they are subject to a spectrum within a wave period range (0.8 - 1.2s).

The time history of the simulated wave elevation at focal point is compared with the experimental data as shown in Fig. 1 and the linear prediction is also included. A good agreement is achieved between the present numerical result and the experimental data, while the linear prediction is different from them. It is observed that the discrepancy is especially remarkable at the focused crest. This may be due to the contribution of nonlinear interaction between different wave components during the wave propagation. Fig. 2 shows the normalized power spectra derived from the data of the three time histories shown in Fig. 1. The normalized power spectrum of the present numerical result (black solid line) is very close to that of the experimental result (black dot line), though both of them significantly diverge from the spectrum derived from the linear prediction (gray dash line). There is a minor energy leakage towards the lower harmonics, while a large amount of energy is transferred to the higher harmonics. The significant redistribution of the wave energy is clearly identified and again confirms that the energy transferred into higher harmonics mainly results in the crest discrepancy shown in Fig. 1. This may suggest that

the nonlinear wave-wave interaction, which is one of the essential features in the realistic irregular wave field, is also incorporated in the present numerical wave model.

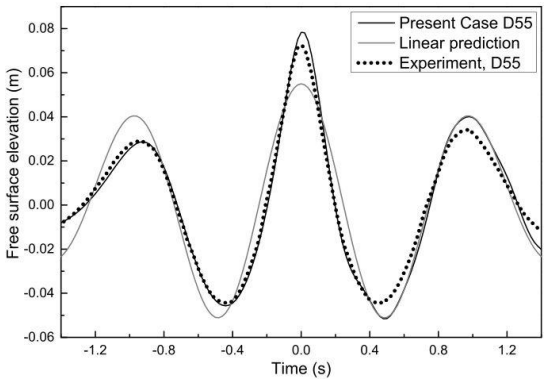

Fig. 1. Comparisons of the time history of wave elevation at the focal point

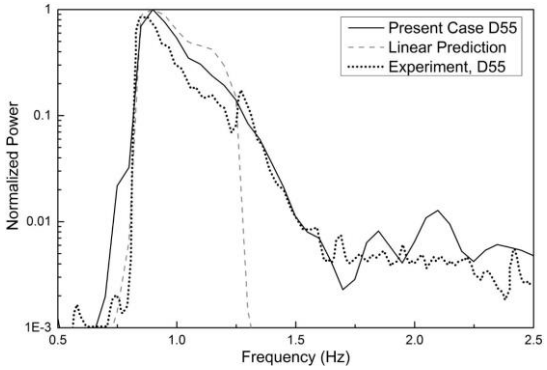

Fig. 2. Normalized power spectra derived from the time histories

4. Twin-barge in irregular waves

The circular tank model presented in Section 2.2 is employed to simulate wave-body interaction problems. The problem of gap resonance has attracted much attention recently due to unrealistic predictions of wave response from linear models. We consider a case of two side-by-side rectangular barges, which has been investigated in Molin *et al*. [7]. The configuration of the side-by-side barges at model scale is as follows: barge length is 2.47 m, width 0.6 m, draft 0.18 m and gap width 0.12 m. The water depth is set as 3 m (the same as in the tests), and the tank radius for the present simulations is either 5 m or four times the incident wave length, whichever is larger. The incident wave heading considered here is 90 degrees, i.e. beam sea. In the experiments in Molin *et al*. [7], the barges are fixed and subject to an irregular sea state with the Pierson-Moskowitz spectrum of a significant wave height H_s = 0.02 m and a peak period T_p = 1 s. In our simulations, we utilize the same PM spectrum, and consider only the beam sea situations. The frequency range is truncated to 3~20 rad/s which covers more than 95% of the energy. The number of wave components is N = 480 which is large enough for the accurate reproduction of the targeted spectrum. With a small time step in the long time simulations, no numerical instability was encountered despite of inclusion of some short-period wave components. A typical time history of output surface elevation in the gap at midship is plotted in Fig. 3, which is normalized by the significant wave amplitude A_s (defined as half the significant wave height here).

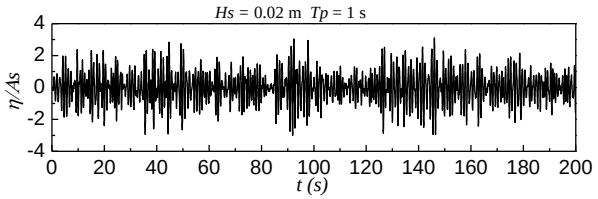

Fig. 3. Time history of elevation in the gap at midship with side-by-side barges in beam sea subject to a PM spectrum

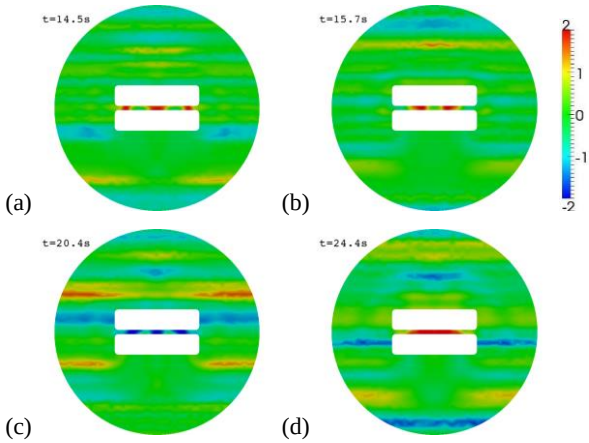

Fig. 4. Contours of free surface elevations near the barges subject to irregular waves at different time instants: (a) t =14.5 s; (b) t = 15.7 s; (c) t = 20.4 s and (d) t = 24.4 s

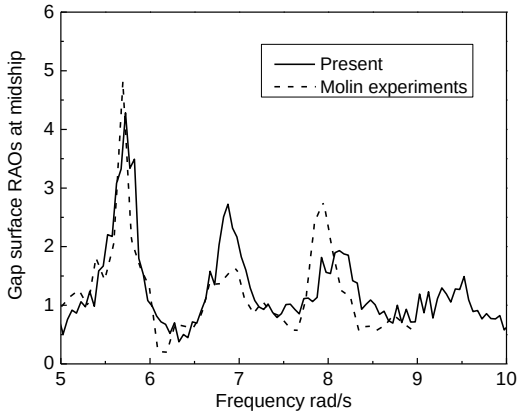

Fig. 5. Free surface RAOs in the gap at midship with barges in beam sea subjected to PM spectrum of H_s = 0.02 m and T_p = 1 s

An overview of the free surface elevations near the barges at some time instants is shown in Fig. 4. Although the surface elevations along the wave propagating direction (unidirectional incident wave) are

mostly random, some peak regions can be clearly recognized within the gap at certain time instants, which indicates the possible trapping or resonant phenomenon. For instance, at t = 14.5 s in Fig. 4(a) we can observe three peak regions distributed along the narrow gap; and at t = 24.4 s the whole surface in the gap tends to be high except at the two openings. This figure implies that in random wave simulations wave in the gap may experience all the possible resonant modes at different time instants in one run if the numerical model is fine enough and the simulation runs for an enough long time.

A close investigation ought to be done by spectral analysis, in order to make a direct comparison against the experimental results in Molin *et al.* [7]. To obtain response RAOs, cross spectral analysis is utilized in processing the recorded time histories of the present simulations. However, with a single set of record of signals, the generated energy spectrum tends to be raw with large errors. To achieve a convergent results from the statistical point of view, we repeat the run for ten times and each run contains 200 s simulating time, with considering the computing resources. The resulting RAOs are predicted by averaging the results in these ten runs. One must bear in mind that in this process information within the small frequency interval of 1/200 Hz might be missing according to the current adopted simulating time and sampling rate.

Fig. 5 shows the response RAOs of the surface elevation in the gap at midship with side-by-side barges in beam sea. It can be seen that our results demonstrate a similar character to that of the experiments, where several peaks are formed at certain frequencies. These peaks are corresponding to the associated wave resonances in the gap. The resonant frequencies are well captured at these peaks in Fig. 5, and the overall agreement of RAO values with the experiments is favorable except at the second and third peaks. Our simulation generates a higher value at the second peak, but a lower one at the third peak than the experiments. It is noticed that the present frequency range near resonances tend to be broader at higher modes, and the peak values are reduced at higher modes compared to that at lower ones, which seem reasonable. A fourth peak is also formed near the frequency 9.5 rad/s, however this mode is even broader and the peak value is much lower compared to the first mode. The simulation in irregular waves, as in the experiments, can successfully capture the possible resonant modes, the accuracy, anyhow, is limited by the fact that the responses are extracted from time recordings at corresponding positions through spectral analysis. This is sensitive in regard to obtaining precise RAOs with a small frequency interval (this is similar to that in the experiments, as commented by Molin *et al.* [7]).

As far as the nonlinearity concerns, we impose an irregular sea state of low significant wave height Hs = 0.002 m as the incident wave. We repeat the case with the same parameters including the random phases of every wave components in the incident wave, except for the significant wave height. A comparison of wave elevation in the gap at midship is presented in Fig. 6 for these two spectra. Both elevations are normalized by significant wave amplitude A_S. The difference between the elevations can be explained by the nonlinearities in the decomposition model, although the incident wave fields are represented by linear wave combinations. This suggests that the present decomposition model is able to capture nonlinear effects despite of adopting a simple irregular wave model as the incident wave.

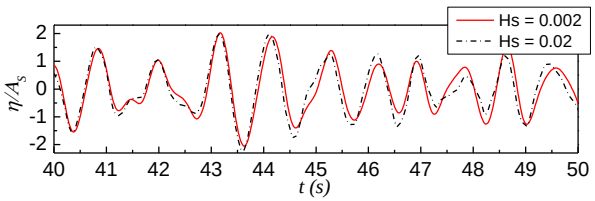

Fig.6. Comparison of wave elevation in the gap at midship for spectra of different significant wave heights

5. Conclusions

We demonstrate the accuracy of a nonlinear potential flow model by simulating focused waves. The nonlinearity in wave-wave interactions explains the discrepancy between linear prediction and experiments. Capability of a nonlinear decomposition model is illustrated by modelling the case of side-by-side barges subject to a realistic sea state. Nonlinearity associated with wave-body interactions is also identifies.

References

[1] Engsig-Karup, A.P. Bingham, H.B., Lindberg. O. 2009. An efficient flexible-order model for 3D nonlinear water waves. *Journal of Computational Physics*, Vol. 228, pp. 2100-2118.

[2] Guerber, E., Benoit, M., Grilli, S.T., Buvat, C. 2012. A fully nonlinear implicit model for wave interactions with submerged structures in forced or free motion. *Engineering Analysis with Boundary Elements*, Vol. 36, pp. 1151-1163.

[3] Shao, Y.L., Faltinsen, O.M. 2014. A harmonic polynomial cell (HPC) method for 3D Laplace equation with application in marine hydrodynamics. *Journal of Computational Physics*, Vol. 274, pp. 312-332.

[4] Ducrozet, G., Bonnefoy, F., Le Touze, D., Ferrant, P. 2012. A modified high-order spectral method for wavemaker modeling in a numerical wave tank. *European Journal of Mechanics B-Fluids*, Vol. 34, pp. 19-34.

[5] Frigaard, P., Hgedal, M., Christensen, M. 1993. Wave generation theory. Hydraulic & Coastal Engineering Laboratory, Department of Civil Engineering, Aalborg University, Aalborg, Denmark.

[6] Baldock, T.E., Swan, C., Taylor, P.H. 1996. A laboratory study of nonlinear surface waves on water. *Philos Trans R Soc Lond Ser A*, Vol. 354, pp. 649–76.

[7] Molin, B., Remy F., Camhi, A., Ledoux, A. 2009, Experimental and Numerical Study of the Gap Resonances in-between Two Rectangular Barges, *Proc. of 13th Cong. of International Maritime Association of Mediterranean IMAM*, (Istanbul).

An extended multi-modal expansion for propagation of waves in a channel of non-uniform width

NICK R. T. BIGGS

Department of Mathematics and Statistics,
School of Mathematics and Physical Sciences,
University of Reading, P. O. Box 220,
Whiteknights, Reading, RG6 7AX, U.K.

(n.r.t.biggs@reading.ac.uk)

Highlights:

- Taking the appropriate limit of the solution of the Helmholtz equation in a wedge geometry suggests a novel set of cross-channel expansion functions, used to model wave propagation in a channel of non-uniform width, which depend on both the local channel width and the slope of the channel walls.
- Numerical results for an extended multi-modal expansion incorporating these novel expansion set will be presented at the Workshop.

1. Introduction

In 2005, Ehrenmark derived in [1] a new dispersion relation for linear surface gravity waves on finite-depth fluid, extending the classical formula $\omega^2/g = k\tanh(kh)$, in which ω is the prescribed angular wave frequency, h is the constant depth, k is the wavenumber and g is the acceleration due to gravity, to the case in which the fluid bed is sloping linearly, with $h' \equiv \text{constant} = \tan\alpha$, say, for α small. He found that

$$\omega^2/g = k\tanh((\alpha\cot\alpha)kh), \tag{1.1}$$

in which the combination $\alpha\cot\alpha \to 1$ in the limit as $h' \to 0$, so recovering the classical result as the bed flattens out. This result comes from a two-term asymptotic expansion, for small α, of an integral form of the standing wave solution on a plane beach, using the method of steepest descent. In [1] this extended dispersion relation is then used within various forms of the mild-slope equation (MSE) to derive numerical solutions which agree well with numerical solutions of the full linear problem, even for relatively steep bed slopes.

Here we follow a similar procedure, but applied to the propagation of linear surface gravity waves along a uniform-depth channel, bounded by vertical walls at $y = \pm h_\pm(x)$, with x and y denoting (horizontal) Cartesian coordinates, which vary with x. If the channel walls vary linearly with x then the domain is wedge-shaped (analogous to Ehrenmark's plane beach geometry); the solution is easily found explicitly in terms of appropriate polar coordinates, with azimuthal dependence proportional to $\cos[\mu_n(\theta-\theta_1)]$ for $n \in \mathbb{N}_0$, where $\mu_n = n\pi/(\theta_2-\theta_1)$ for particular θ_1, θ_2. The appropriate limit of this solution recovers at leading order the uniform width solution, whose cross-channel dependence is proportional to $\cos[\alpha_n(y+h_-)]$ for $n \in \mathbb{N}_0$, where $\alpha_n = n\pi/w$, in which $w(x) = h_-(x) + h_+(x)$ is the channel width. But if the full unapproximated expression for μ_n is retained, the cross-channel eigenvalue α_n is replaced by

$$\bar{\alpha}_n = \alpha_n \left(w' \Big/ \tan^{-1}\left(\frac{w'}{1 - h'_- h'_+} \right) \right).$$

This suggests that a multi-modal approximation in which the solution is expanded in terms of $\cos[\bar{\alpha}_n(y+h_-)]$ may yield accurate results, in the same way as the MSE incorporating (1.1) performs well, and this we investigate here.

2. Statement of problem

We consider the propagation of linear surface gravity waves in a channel of uniform depth h. Cartesian coordinates (x, y, z) are used, z being measured vertically upwards from the undisturbed free-surface. The channel occupies the region $-h_-(x) < y < h_+(x)$, for given continuous functions $h_\pm(x)$, so that we require the solution $\phi(x, y)$ of the boundary-value problem

$$\begin{cases} \phi_{xx} + \phi_{yy} + k^2\phi = 0 & (-h_-(x) < y < h_+(x)) \\ \phi_y \mp h'_\pm \phi_x = 0 & (y = \pm h_\pm(x)) \end{cases} \tag{2.2}$$

together with appropriate radiation conditions. The wavenumber k is the positive root of the dispersion relation $\omega^2 = gk\tanh(kh)$, in which $\omega > 0$ is the prescribed angular wave frequency (harmonic time-dependence proportional to $e^{-i\omega t}$ is implicit throughout) and g is the acceleration due to gravity.

2.1 Multi-modal expansion

In regions of constant width, the solution of (2.2) can be written as

$$\phi(x, y) = \sum_{n=0}^{\infty} (A_n^+ e^{i\gamma_n x} + A_n^- e^{-i\gamma_n x})\phi^{(n)}(h_\pm, y), \quad \phi^{(n)}(h_\pm, y) = \cos[\alpha_n(y + h_-)], \tag{2.3}$$

where $A_n^\pm$ are constants, $w = h_+ + h_-$ is the channel width, $\alpha_n = n\pi/w$, and

$$\gamma_n = \begin{cases} \sqrt{k^2 - \alpha_n^2} & \text{if } k \geq \alpha_n, \\ i\sqrt{\alpha_n^2 - k^2} & \text{if } k < \alpha_n, \end{cases}$$

but in regions where the channel width varies with x a multi-mode expansion of some sort is commonly used to approximate the solution (see [2] for a sophisticated example). The simplest multi-mode expansion assumes that the local modal structure can be approximated by that of a uniform width channel of the same (local) width, so that we write

$$\phi \approx \bar{\phi} = \sum_{n=0}^{M} v_n(x)\phi^{(n)}(h_\pm(x), y) \tag{2.4}$$

for some prescribed $M \in \mathbb{N}_0$, and where now $h_\pm = h_\pm(x)$. Because this approximation cannot hope to exactly satisfy (2.2) we instead require that

$$\int_{-h_-}^{h_+} \left(\bar{\phi}_{xx} + \bar{\phi}_{yy} + k^2\bar{\phi}\right) \phi^{(m)}(h_\pm(x), y)\, \mathrm{d}y = 0, \qquad (m = 0, 1, \ldots, M).$$

This yields a system of differential equations of the form

$$A(x)\mathbf{v}''(x) + 2B(x)\mathbf{v}'(x) + C(x)\mathbf{v}(x) = \mathbf{0},$$

in which $\mathbf{v} = (v_0, \ldots, v_M)^T$, and A, B and C are known matrix-valued functions whose entries are integrals of combinations of the $\phi^{(m)}$ and their derivatives.

2.1.1 Solutions in the wedge geometry, and its limiting form

As an extension of the standard multi-mode expansion, we seek to approximate the local modal structure by that of the solution for a linearly widening or narrowing channel, i.e. for a *wedge*.

Consider the channel close to the point $x = x_0$. For x near x_0, we have $h_\pm(x) \approx h_\pm(x_0) + h'_\pm(x_0)(x - x_0)$, and provided $w'(x_0) \neq 0$ the two straight lines $y = \pm[h_\pm(x_0) + h'_\pm(x_0)(x - x_0)]$ meet at $(x, y) = (\bar{x}, \bar{y})$ where

$$\bar{x} = x_0 - \frac{w(x_0)}{w'(x_0)}, \quad \bar{y} = \frac{h_+(x_0)h'_-(x_0) - h'_+(x_0)h_-(x_0)}{w'(x_0)}.$$

If the channel is locally widening (narrowing) with increasing x then $\bar{x} < x_0$ ($\bar{x} > x_0$). These straight lines form the boundaries of our wedge-shaped domain, and $(\bar{x}, \bar{y})$ is its apex. In terms of polar coordinates (r, θ) defined by $r^2 = (x - \bar{x})^2 + (y - \bar{y})^2$, $\tan\theta = (y - \bar{y})/(x - \bar{x})$, the solution of the Helmholtz equation in the domain $\{(r, \theta) : r > 0,\ \theta_1 < \theta < \theta_2\}$ subject to homogeneous Neumann conditions on $\theta = \theta_1, \theta_2$ for $r > 0$ can be written as

$$\phi = \sum_{n=0}^{\infty} [A_n J_{\mu_n}(kr) + Y_{\mu_n}(kr)] \cos[\mu_n(\theta - \theta_1)], \quad \mu_n = n\pi/(\theta_2 - \theta_1), \tag{2.5}$$

where J_{μ_n} and Y_{μ_n} denote Bessel functions of order μ_n and first and second kind, respectively. Here the boundaries of the wedge are

$$\theta_1 = \tan^{-1}\left(\frac{-h_-(x_0) - \bar{y}}{x_0 - \bar{x}}\right), \quad \theta_2 = \tan^{-1}\left(\frac{h_+(x_0) - \bar{y}}{x_0 - \bar{x}}\right),$$

and we've assumed that the channel is locally widening, so that $\bar{x} < x_0$; a similar expression results if the channel is locally narrowing.

In the limit as the channel walls straighten out, we recover from (2.5) the uniform width solution (2.3). To see this, write $h'_\pm(x_0) = \epsilon\bar{h}'_\pm(x_0)$ and $w'(x_0) = \epsilon\bar{w}'(x_0)$, in which $0 < \epsilon \ll 1$ and $\bar{h}'_\pm(x_0), \bar{w}'(x_0) = O(1)$, and consider the limit $\epsilon \to 0$. Then

$$r = \left[(x - \bar{x})^2 + (y - \bar{y})^2\right]^{1/2} = \frac{w}{\epsilon\bar{w}'} + (x - x_0) + O(\epsilon)$$

and $\mu_n = n\pi/\epsilon\bar{w}' + O(\epsilon)$, in which $w, \bar{w}'$ etc. are all evaluated at $x = x_0$, so that

$$J_{\mu_n}(kr) \sim J_{n\pi/\epsilon\bar{w}'}\left(\frac{n\pi}{\epsilon\bar{w}'} \times \frac{k}{n\pi}[w + \epsilon\bar{w}'(x - x_0)]\right),$$

and similarly for $Y_{\mu_n}(kr)$. If $kw/n\pi < 1$ then use of Debye's asymptotics for Bessel functions of large argument and order (e.g. [3, Eq. (9.3.2)]) shows that

$$J_{\mu_n}(kr) \sim \text{constant} \times \exp(x\sqrt{\alpha_n^2 - k^2}),$$

which agrees with the form of the modes (2.3) which grow as x increases. A similar calculation for $Y_{\mu_n}(kr)$ recovers the modes which decay with increasing x. (If $n = 0$, the standard expansions of J_0 and Y_0 for large argument yields the analogous results.) If instead $kw/n\pi > 1$ then use of [3, Eq. (9.3.3)] gives

$$J_{\mu_n}(kr) \sim \text{constant} \times \cos[(x - x_0)\sqrt{k^2 - \alpha_n^2}]$$

and

$$Y_{\mu_n}(kr) \sim \text{constant} \times \sin[(x - x_0)\sqrt{k^2 - \alpha_n^2}]$$

as $\epsilon \to 0$, which can be combined to give the form of the propagating modes from (2.3). (For simplicity we suppose here that k doesn't coincide with a cut-off frequency α_n.)

More interesting for our purposes is the behaviour of the azimuthal terms in (2.5) in the limit $\epsilon \to 0$. With a bit of rearranging, we have

$$\mu_n = n\pi \Big/ \tan^{-1}\left(\frac{\epsilon\bar{w}'}{1-\epsilon^2\bar{h}'_-\bar{h}'_+}\right) \tag{2.6}$$

$$= \frac{n\pi}{\epsilon\bar{w}'} + O(\epsilon), \tag{2.7}$$

so that, when combining (2.7) with the behaviour

$$\theta - \theta_1 = \frac{\epsilon\bar{w}'}{w}(y + h_-) + O(\epsilon^2)$$

we see that

$$\cos[\mu_n(\theta - \theta_1)] \sim \cos[n\pi(y + h_-)/w]$$

as $\epsilon \to 0$, which agrees with the form of $\phi^{(n)}$ in (2.3). However, retaining the full expression (2.6) yields the approximate cross-channel structure

$$\cos[\mu_n(\theta - \theta_1)] \approx \cos[\bar{\alpha}_n(y + h_-)], \tag{2.8}$$

where

$$\bar{\alpha}_n = \alpha_n\left(\epsilon\bar{w}' \Big/ \tan^{-1}\left(\frac{\epsilon\bar{w}'}{1-\epsilon^2\bar{h}'_-\bar{h}'_+}\right)\right)$$

$$\equiv \alpha_n\left(w' \Big/ \tan^{-1}\left(\frac{w'}{1-h'_-h'_+}\right)\right). \tag{2.9}$$

In (2.9), α_n is recovered if the width w is unchanging with x.

2.1.2 An extended multi-modal expansion

Given (2.9), we propose an extended multi-modal expansion

$$\phi \approx \bar{\phi} = \sum_{n=0}^{M} v_n(x)\bar{\phi}^{(n)}(h_\pm(x), h'_\pm(x), y), \quad \bar{\phi}^{(n)}(h_\pm, h'_\pm, y) = \cos[\bar{\alpha}_n(y + h_-)]. \tag{2.10}$$

Numerical results using this expansion will presented at the Workshop.

References

[1] Ehrenmark, U.T. 2005 An alternative dispersion relation for water waves over an inclined bed. *J. Fluid Mech.* **543**, 249-266.

[2] Felix, S. & Pagneux V. 2001 Sound propagation in rigid bends: a multimodal approach. *J. Acoust. Soc. Am.* **110** (3 Pt 1), 1329-1337.

[3] Abramowitz, M. & Stegun, I. A. 1965 *Handbook of Mathematical Functions*. Dover Publications, New York.

Linearized potential flow analysis of a 40 chamber, oscillating water column wave energy device

Harry B. Bingham and Robert Read

Dept. of Mechanical Engineering, Technical University of Denmark

Email: hbb@mek.dtu.dk, rrea@mek.dtu.dk

This abstract presents an analysis of an attenuator-type Wave Energy Converter (WEC) with 40 Oscillating Water Column (OWC) chambers for the extraction of wave energy. Linearized potential flow calculations are made in the frequency-domain using WAMIT [8]. An equivalent linearized damping coefficient to represent the air turbine Power Take Off (PTO) system is found for each condition by iterating to find the consistent response-damping pair for a given frequency and incident wave amplitude. The absorbed power is estimated based on the pressure in each chamber and the PTO damping coefficient. The calculations are compared to model-scale measurements in a slack-moored condition, and generally good agreement is found. Work is in progress to move the solution to the time-domain and include a more sophisticated PTO model which includes nonlinear and air compressability effects in the turbine.

1 Theory

Evans [2], extended first-order, radiation-diffraction theory to include the response of one or more partially enclosed OWC chambers, together with the usual rigid-body motions. This theory was also discussed by Lee et al [3, 4] and it is implemented in WAMIT as Free-Surface Pressure (FSP) modes. The applied pressure on the water surface in each internal chamber is expressed in a modal decomposition of the form

$$p_0(x,y) = -\rho g \sum_{j=7}^{6+M_p} \xi_j \, n_j(x,y) \tag{1}$$

where n_j gives the spatial form of mode j and M_p is the total number of modes, with ρ the fluid density and g is the gravitational acceleration constant. Here we will only consider one piston-type mode for each OWC chamber, as this is the only mode that contributes to the flux through the turbine, thus M_p is the total number of chambers and $n_j = 1$ on chamber surface j. For the FSP modes, the boundary condition on the internal free surface becomes

$$\partial_z \phi - \frac{\omega^2}{g}\phi = -\frac{\mathrm{i}\omega}{\rho g} p_0 = \mathrm{i}\omega \sum_{j=7}^{6+M_p} \xi_j n_j, \quad \text{on } z = 0 \tag{2}$$

and ξ_j thus represents the pressure head response to a unit amplitude applied pressure on internal free-surface j, with ω the radian frequency of oscillation and ϕ the total velocity potential. This leads to an equation of motion of the same form as the rigid-body modes so that the complete system can be written in the standard non-dimensional form as

$$\sum_{k=1}^{6+M_p} \left[-\bar{\omega}^2 \left(\bar{M}_{jk} + \bar{A}_{jk} - \mathrm{i}\,\bar{B}_{jk} \right) - \frac{1}{\mathrm{i}\bar{\omega}} \bar{B}^0_{jk} + \bar{c}_{jk} \right] \bar{\xi}_k = \bar{X}_j, \qquad j = 1, 2, \ldots, 6 + M_p \tag{3}$$

with $M_{jk}, A_{jk}, B_{jk}, c_{jk}, X_j$ the inertia, added mass, damping, hydrostatic restoring and incident wave exciting force coefficients respectively. All quantities are made non-dimensional with respect to a length scale L, ρ, g, and the incident wave amplitude A; more details can be found in the WAMIT user manual [8]. The air turbine PTO damping coefficient matrix B^0_{jk} is diagonal, and only non-zero

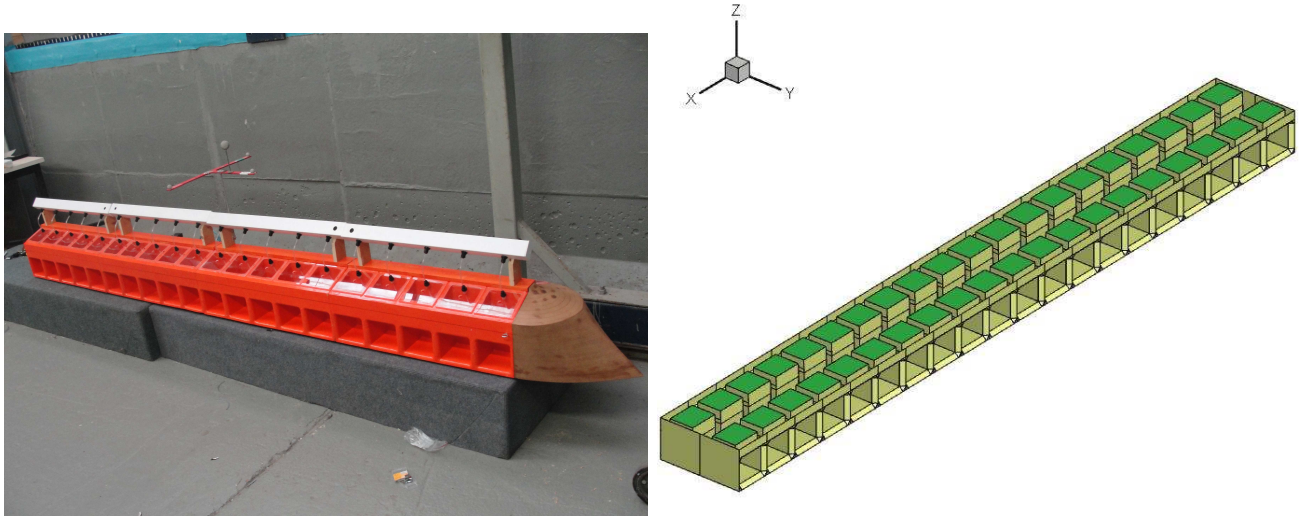

Figure 1: Left: Photo of the scale model ready for testing. A removable bow section is fitted in this picture, but results are presented here only without the bow. Right: The high-order geometry used for the WAMIT calculations. Bright green patches indicate the FSP surfaces.

for the FSP modes with $j > 6$, while all inertia terms associated with the FSP modes are zero. The new terms in the equation are given by

$$\bar{B}^0_{jj} = \frac{\rho\sqrt{gL}}{L^2} B_{j0}, \quad q_j = -\rho g\, B_{j0}\, \xi_j, \quad c_{jj} = -\frac{S_{j0}}{L^2} \tag{4}$$

where a linear relation has been assumed between the volume flux q_j through chamber j and the pressure in that chamber, and S_{j0} is the area of internal free-surface j. Since the structure itself must create the excess pressure in each chamber, there is hydrostatic coupling between the FSP modes and the heave, roll and pitch modes which must also be included in $\bar{c}_{jk}$. The total efficiency of the device can be written as a capture width ratio

$$\overline{W} = \frac{W}{W_{max}} = \sum_{j=7}^{6+M_p} \frac{\bar{B}_{j0}\, \bar{\xi}^*_j \bar{\xi}_j}{\bar{c}_g} \frac{L}{L_c} \tag{5}$$

where $\bar{c}_g = c_g/\sqrt{gL}$, with c_g the wave group velocity, and L_c the length-along-the-wave-crest chosen for normalization. More complete details of this formulation can be found in [1] along with a more complete presentation and discussion of the results shown here.

2 Results

Figure 1 shows a picture of the scale model and the patch boundaries of the high-order geometry used for the WAMIT calculations. This geometry was produced using the MultiSurf surface modeling software [7]. The FSP internal chamber surfaces are indicated by the bright green patches of the numerical model. The model was tested with and without the removable bow section shown in the picture, but here we consider only the data without the bow section. This design is a variant of the I-beam attenuator [6] which was inspired by the Kaimei concept developed in the late 1970s by Masuda and his colleagues in Japan [5]. The target installation area of the device is the Danish North Sea, so the full-scale chambers measure 6 by 5 by 7.5 m in the x, y and z directions respectively, which gives a resonant period of 5.9s. The total device length is $L = 150$m. The model is at scale 1:50 and was tested at the Hydraulic and Maritime Research Center (HMRC) at University College Cork, Ireland in 2013 [9, 10]. The air turbine PTO system was model led by an orifice in each chamber lid of 1.3%

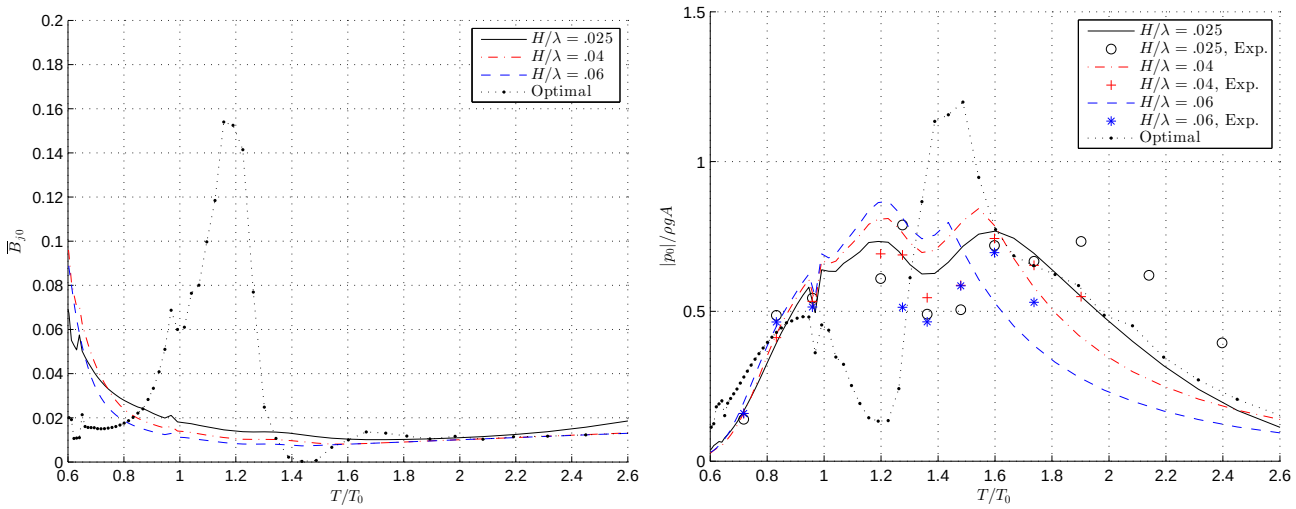

Figure 2: The equivalent linearized damping coefficient (left) and the pressure response (right) in the bow Chamber for the freely floating model.

of the chamber surface area. This is a good model of an impulse turbine, and produces a quadratic relation between the flux and the pressure in the chamber so that $q^2 = B_1|p|$. To find the equivalent linear damping coefficient B_{j0}, we equate the power loss over one cycle of the two relations which gives

$$B_{j0} = \sqrt{\frac{3\pi}{8\rho g|\xi_j|}}B_1. \tag{6}$$

The quadratic damping coefficient B_1 is a constant and has been accurately determined from a simple experiment. Since the equivalent linear damping coefficient is a function of the response amplitude however, we must iterate the solution of (3) and (6) for each incident wave frequency and amplitude. The initial guess is taken to be $\xi_j/A = 0.5$, and the solution generally converges to single precision accuracy in about 10 iterations or less.

The model has been tested at a series of mono-chromatic incident wave conditions corresponding to wave steepness values of $H/\lambda = 0.025, 0.04$ and 0.06, where $H = 2A$ is the wave height and λ is the wave length. The device is slack-moored and free to feather with the incoming waves so that they are always incident from ahead. Symmetry about the $y = 0$ plane is invoked, and the pressure is measured in all chambers along the starboard side of the vessel. The results for the equivalent linear damping coefficients and the pressure in chamber #1 at the bow of the model are shown in Figure 2. We have also computed a numerically optimized linear damping coefficient using the Matlab constrained optimization routine `fmincon`. In all cases, we have constrained the response to ensure that the chamber surface elevation does not exceed 2.5m which is the distance from the mean water level to the submerged chamber opening. The optimized values are also shown in the figure, along with the corresponding experimental measurements. Similar behavior is found for the other chambers. Figure 3 shows the predicted total absorbed power as a capture width ratio with respect to the length $L = 150$m, and also in MW for the full-scale device. The measured and computed chamber pressures and the total mean power absorption are in reasonably good agreement, though somewhat over-predicted near the resonant period and under-predicted in long waves.

We are now working on moving the numerical solution to the time-domain so that a more accurate model of the air turbine PTO system can be included in the calculations. Experimental results are also available in irregular wave conditions, and these will be compared with. Structural loading calculations are also in progress, in order to estimate the construction costs so that a cost of energy prediction can be made. One major advantage for OWC-type devices is the relative simplicity of the structure, with no moving parts in the water, which should allow for relatively inexpensive building materials

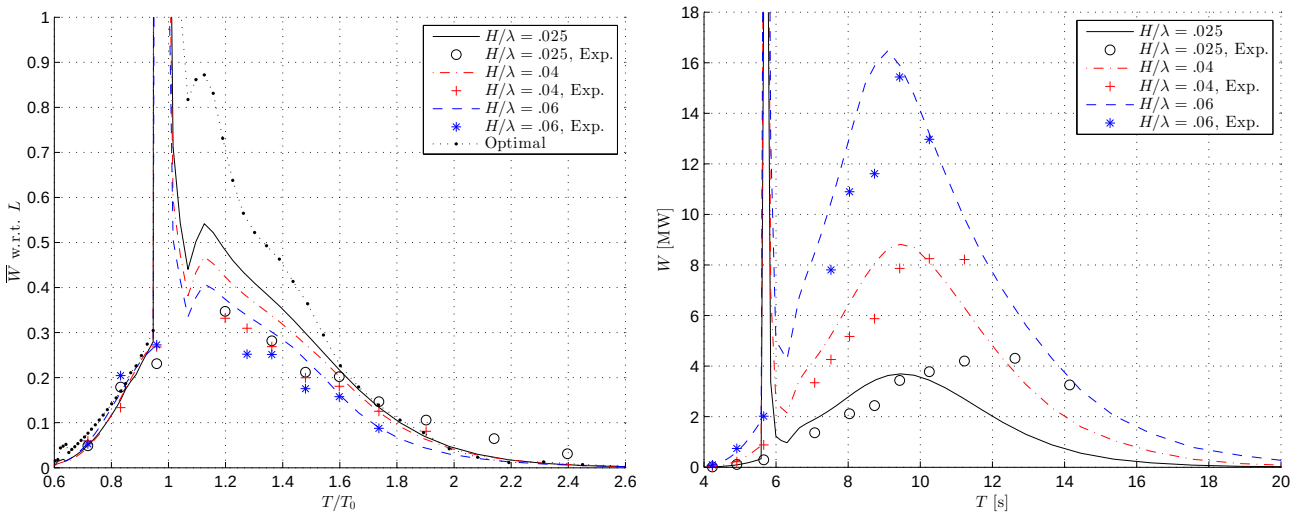

Figure 3: Left: The capture width ratio of the moored 40 chamber model with respect to $L = 150$m. Right: The corresponding full-scale power absorption in mega Watts.

and opportunities for mass production.

References

[1] H. B. Bingham, D. Ducasse, K. Nielsen, and R. Read. Hydrodynamic analysis of Oscillating Water Column, Wave Energy Devices. (Submitted), 2015.

[2] D. V. Evans. Wave-power absoption by systems of oscillating surface pressure distributions. *J. Fluid Mech.*, 114:481–499, 1982.

[3] C.-H. Lee, J. N. Newman, and F. G. Nielsen. Wave interactions with an oscillating water column. In 6^{th}*Intl. Offshore and Polar Engineering Conference*, Los Angeles, USA, 1996. Intl. Offshore and Polar Engineering Conference.

[4] C.-H. Lee and F. G. Nielsen. Analysis of oscillating water column device using a panel method. In 11^{th}*Intl. Wrkshp. Water Waves and Floating Bodies*, Hamburg, Germany, 1996. http://www.iwwwfb.org.

[5] Y. Masuda. Experimental full scale result of wave power machine Kaimei in 1978. In *Proc. 1st Inter. Symp. on Wave Energy Utilization*, Gothenburg, Sweden, 1979.

[6] G. W. Moody. The NEL oscillating water column: Recent developments. In *First Symposium on Wave Energy Utilization, Oct. 1979*, pages 283–296, Gothenburg, Sweden, 1980. Chalmers University of Tech.

[7] MultiSurf. AeroHydro - Relational 3D Modeling for Marine and Industrial Design, 2014. http://aerohydro.com.

[8] J. N. Newman and C.-H. Lee. Wamit; a radiation-diffraction panel program for wave-body interactions, 2014. http://www.wamit.com.

[9] K. Nielsen. Final report: KNSWING attenuator development phase I. Technical report, FP7-MARINET, Marine Renewables Infrastructure Network, 2013.

[10] F. Pors and M. Simonsen. A theoretical and experimental study of an Oscillating Water Column Attenuator. BS thesis, Tech. U. of Denmark, Lyngby, Denmark, 2013.

Experimental demonstration of Epsilon-Near-Zero water waves focusing

T.Bobinski[1], A.Eddi[1], A.Maurel[2], V.Pagneux[3] and P.Petitjeans[1]

[1]Laboratoire de Physique et Mécanique des Milieux Hétérogènes (PMMH), UMR CNRS 7636-ESPCI-UPMC Univ. Paris 6-UPD Univ. Paris 7, 10 rue Vauquelin, 75005 Paris, France
[2]Institut Langevin LOA, UMR CNRS 7587-ESPCI, 5 rue Jussieu, 75005 Paris, France
[3]Laboratoire d'Acoustique de l'Universite du Maine, UMR CNRS 6613, Avenue Olivier Messiaen, 72085 Le Mans, France

Email: tomasz.bobinski@espci.fr

Highlights

We investigate experimentally ϵ-near-zero (ENZ) analogue for water waves in nonlinear regime by tuning bathymetry of the system. We obtain uniform phase at the edge of a semi circular lens, resulting in expected lensing effect. Two-dimensional time space measurements of the surface elevation allow us to separate the linear component and harmonics generated due to nonlinearities. The origin of the harmonics is analyzed in the frame of the competition between free-waves and bound-waves. The results show dominance of free-waves. Surprisingly, we observe a cascade of sub wavelength focal spots with respect to the first harmonic.

1 Introduction

One of the group of newly-designed metamaterials is the so-called ϵ-near-zero materials. In the context of electromagnetic wave, medium filled with such material can be characterized by a very large wavelength. This property makes tailoring phase pattern feasible. Using a semi circular shape at the output of ENZ material, one can obtain extremely well focused wave at the center of such lens. Two-dimensional electromagnetic wave in transverse magnetic polarization can be described by the following equation:

$$\nabla\left(\frac{1}{\epsilon}\nabla H\right)+\frac{\omega^2}{c_0^2}H=0. \tag{1}$$

with H the magnetic field, ω is the frequency, c_0 is the light speed in vacuum and ϵ is the permittivity. As ϵ approaches zero value, refractive index tends to vanish. This allows to achieve constant phase throughout the medium.

In the context of water waves, the ENZ analogy can be analyzed by first considering shallow water approximation:

$$\nabla\left(h\nabla\eta\right)+\frac{\omega^2}{g}\eta=0 \tag{2}$$

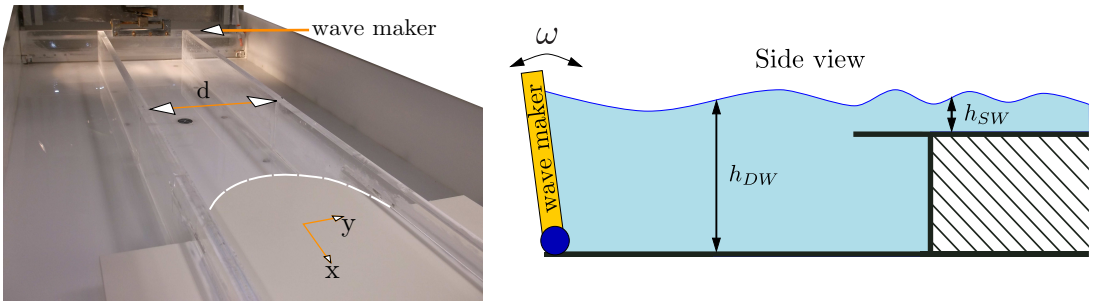

Figure 1: Experimental setup. Position of the lens is marked with white dashed line.

where h denotes the water depth at rest and g stands for the gravitational acceleration. In this regime, wavenumber is given as $k_{\mathrm{SW}} = \omega/\sqrt{gh}$. By comparing Eqs.(1) and (2), one obtains correspondence of permittivity for water waves, i.e. $1/\epsilon \leftrightarrow h$, indicating that the ENZ can be realized in water waves system for h^{-1}-near-zero. By increasing depth, we end up with deep water approximation for which wavenumber is given as $k_{\mathrm{DW}} = \omega^2/g$. Therefore, the efficiency of the h^{-1}-near-zero is given through refractive index defined as $n = k_{\mathrm{SW}}/k_{\mathrm{DW}} = \sqrt{g/\omega^2 h}$.

2 Experimental arrangements

Our system consists of a lens inside a waveguide. The lens is a semi circular edge of diameter $d = 20$cm. The width of the waveguide is adjusted to the size of the lens. The lens is a boundary between two regions with different depths. Depth in a shallow water part (behind the lens) is set to $h_{\mathrm{SW}} = 7$ mm, while in a deep water region it is 67 mm. Waves are generated by a paddle wave maker working within a frequency range $\omega \in [6.28; 13.19]$ s^{-1}, which is shown together with the experimental setup in Fig. 1. We perform time space resolved measurements of the surface elevation using Fourier Transform Profilometry method adapted by our team for water wave measurements [2, 3]. We project fringes by means of a high-resolution projector (1920×1080pix^2). Images are recorded using 4MPix camera with sampling frequency 15Hz. The area of interest is 0.4×0.2 m^2 large and covers deep and shallow water regions.

3 Results and analysis

As expected, in the deep water region wave has a almost constant phase and focuses in shallow water region. As shallow water waves are easily nonlinear, we give the measure of nonlinearity by Ursell number, which in our case is typically of order $U_r = 378$. Hence, we investigate strongly nonlinear case. Temporal spectrum, determined at the center of the lens, indicates the magnitude of second harmonic which is 30% of the fundamental component, while higher-order terms remain significant.

Temporal decomposition of the obtained surface elevation fields allows us to separate the influence of each of harmonics. We suppose that surface elevation η can be expressed as:

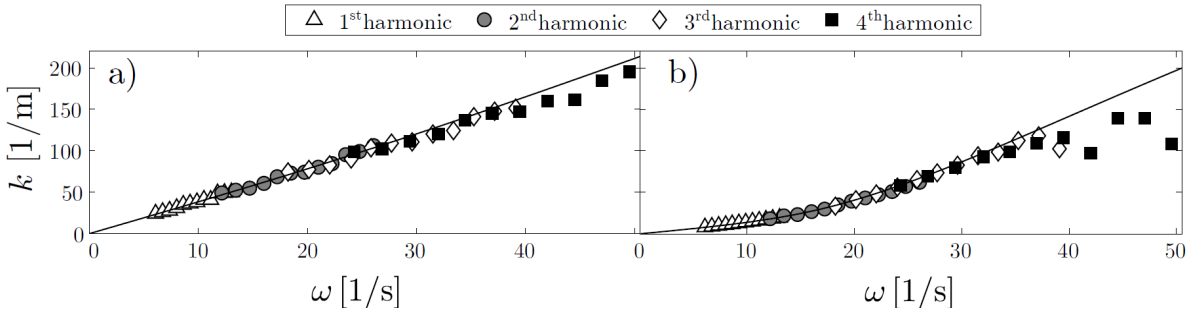

Figure 2: Measured dispersion relation in: a) shallow-water region and b) deep-water region. Solid lines correspond to linear dispersion relation in both regions.

$$\eta(x,y,t) = \sum_{n=0}^{N} \hat{\eta}_n(x,y) \exp\left(\mathrm{i}n\omega t\right) \tag{3}$$

where $\hat{\eta}_n(x,y)$ denote complex field corresponding to the n-th harmonic of the fundamental pulsation ω. We extract $\hat{\eta}_n$ using Fast Fourier Transform.

To describe nature of the harmonics we consider two different types of waves related to nonlinear regime, i.e. bound-waves and free-waves. We can discriminate them because of the difference in dispersion relation. Wavenumber related to free-waves can be described as $k = D(n\omega)$, whereas bound-waves indicate relation $k = nD(n\omega)$. To determine dispersion relation in our experiments we first consider inhomogeneous Helmholtz equation. Neglecting source terms [1], appearing due to nonlinearities, yields the homogeneous problem corresponding to free-waves:

$$\left(\Delta + \mathbf{k}_n^2\right) \hat{\eta}_n\left(x,y\right) = 0 \tag{4}$$

where $\mathbf{k}_n$ is linked to $n\omega$ through the linear dispersion relation. To calculate wavenumber $\mathbf{k}_n$ from a given complex pattern $\hat{\eta}_n(x,y)$, the norm function $|| \left(\Delta + \mathbf{k}_n^2\right) \hat{\eta}_n||$ is minimized in the complex plane $\mathbf{k}_n$ [4]. We determine wavenumbers in the far-field of deep and shallow-water regions separately. By applying described procedure we obtain k for the first and higher harmonics. Measured dispersion relation for all of the components is presented in Fig. 2a),b). In shallow-water part results are in agreement with linear dispersion relation. This confirms that harmonics are dominated by free-waves rather than bound-waves.

Having the nature of harmonics described, we are interested in the quality of the obtained focusing, which is presented in Fig. 3. We show the total field, defined as $I(x,y) = \max\limits_{t\in[0,T]} \eta^2(x,y,t)$, and the intensity fields $I_n\left(x,y\right) = |\hat{\eta}_n\left(x,y\right)|^2$ (normalized by the maximum intensity value of each term $\max I_n$) corresponding to first four harmonics. Surprisingly, each successive $n-$th harmonic is characterized by more and more focused spot. Shape of the focal spot differs among harmonics. The lateral size of the focal spot is decreasing for higher-order terms, meanwhile the horizontal extension remains almost constant. We determine the efficiency of the lens by the following quantities: (i) axial and lateral extension of the focal spot L_x and L_y, (ii) axial position of the maximum intensity X, and (iii) contrast of the focal spot $A_{max}/\overline{A}$. The results indicate that $L_x/\lambda_{\mathrm{SW}}$, with λ_{SW} being

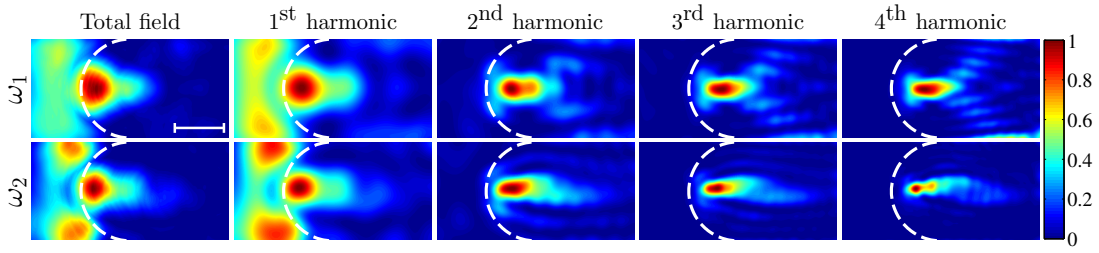

Figure 3: Normalized intensity of the wave field (I/I_{max}) for $\omega_1 = 9.86$ s^{-1} and $\omega_2 = 12.39$ s^{-1}. White dashed line marks the position of the lens. Scale bar in the left top figure corresponds to 0.1 m.

wavelength in shallow water region, varies slowly with the pulsation, while $L_y/\lambda_{\mathrm{SW}}$ follows expected scaling law $\lambda/2$.

4 Conclusions

Characteristic property of the ENZ metamaterials is their incredibly high value of phase velocity, resulting in almost constant phase through a medium. Theoretically, this should allow to perfectly focus waves at a single point. Due to intrinsic properties of water waves one has to face constraints, which do not allow to obtain similar phase velocities. The limitation is governed by the deep-water approximation. Nevertheless, our experiments illustrate that thanks to ENZ analogy it is possible to focus water waves efficiently. With large amplitude of an incident wave we obtained surprising cascade of highly focused nonlinear components.

References

[1] K.A. Belibassakis and G.A. Athanassoulis. A coupled-mode system with application to nonlinear water waves propagating in finite water depth and in variable bathymetry regions. *Coastal Engineering*, 58(4):337–350, April 2011.

[2] P. J. Cobelli, A. Maurel, V. Pagneux, and P. Petitjeans. Global measurement of water waves by fourier transform profilometry. *Experiments in Fluids*, 46(6):1037–1047, June 2009.

[3] A. Maurel, P. Cobelli, V. Pagneux, and P. Petitjeans. Experimental and theoretical inspection of the phase-to-height relation in fourier transform profilometry. *Applied Optics*, 48(2):380–392, 2009.

[4] A. Przadka, B. Cabane, V. Pagneux, A. Maurel, and P. Petitjeans. Fourier transform profilometry for water waves: how to achieve clean water attenuation with diffusive reflection at the water surface? *Experiments in Fluids*, 52(2):519–527, February 2012.

Experimental study of water-oil-boom interaction and failure events

D. Borri[1] **daniele.borri@ntnu.no**
C. Lugni[1,2] **claudio.lugni@cnr.it**
M. Greco[1,2] **marilena.greco@ntnu.no**
O.M. Faltinsen[1] **odd.faltinsen@ntnu.no**

1 **Centre for Autonomous Marine Operations and Systems (AMOS), Department of Marine Technology, NTNU, Trondheim – Norway.**
2 **CNR-INSEAN, Italian Ship Model Basin, Roma – Italy.**

Oil spill caused by maritime accidents can damage valuable ecosystems and have a huge economic impact on fishing and tourism industries. In order to minimize the damage it is important to predict the trajectory of the spilt oil slick and use an effective clean-up strategy. Oil booms represent a valid solution, but their performance has a limitation in sufficiently strong currents and high sea waves. This motivated research efforts in the development of suitable prediction tools useful for the design and for setting the operative limits of these devices. Experiments are instead more difficult to perform. However some relevant studies have been documented along the years, most of them in 2D conditions, with fixed boom and in steady current. For example, Delvigne (1989) studied a scaled boom interacting with different types of oil and identified the failure mechanisms involved. A comprehensive documentation of full- and model-scale tests in 2D and 3D conditions is provided *e.g.* by Grilli *et al.* (2000).

Here a physical investigation is ongoing based on dedicated model tests to be used for gaining further insights on the phenomena involved and as reference data for numerical-tools development. The experimental set-up and some of the results of the analysis are discussed in the following.

Experimental set-up The model tests were performed inside a tank with internal length, height and width, respectively, $L = 3$ m, $H = 0.6$ m and $w = 0.1$ m, at the CNR-INSEAN Sloshing Lab. The experimental set-up is shown in the left of figure 1 and was designed for 2D flow conditions in the tank. However clear 3D features were recorded when instabilities and boom failures occurred. The tank is made of perspex sheets, 1.5 cm thick, and is fixed at the edges to an aluminum

Figure 1: Left: tank mounted on the 6-DOF MISTRAL Hexapode excitation mechanism. Right: boom model and pressure sensors.

frame for structural strengthening. Vertical reinforcements along the front and rear walls were not used in order to have an optimal view of the flow. The boom, in scale 1:6, is shown in the right of the figure. It is realized in rigid expanded polyurethane but geometrically reproducing the different parts of a real boom with an outer floater radius $r_{out} = 4$ cm, a draft $D = 11$cm and a skirt height $h_{skirt} = 8$ cm. It was equipped with seven pressure sensors with sampling frequency 10kHz: two transversally on the edge of the skirt and the others along the centerline of the cylinder, three on the oil side and two on the water side. The tank was filled of water up to 45 cm ($H_w = 0.75H$), so to ensure a ratio H_w/D sufficiently large, and therefore limited bottom effects on the phenomena, and to avoid liquid leakage from the tank (tested without roof). This arrangement was mounted on a 6-DOF motion simulator which prescribes a sway motion with steady-state amplitude of 0.15 m and frequency 0.2 Hz, after a ramp lasting for the first three periods. An accelerometer was used to check the quality of the enforced motion (see left plot of figure 2). These motion parameters were selected in order to realize a slowly-varying current with horizontal speeds of the liquid around 0.2 m/s, which is in the range for boom failure for the chosen geometry and scale (Delvigne 1989). The model was located in the central tank section, where the highest

liquid velocities inside the tank are obtained and failure can occur more easily. In order to reproduce a behavior similar to that of an operative boom, the model is left free in heave by two vertical fishing lines that act as a rail. In particular, each one is fixed at the tank bottom by a spring, it is anchored to a metal plate above the tank and passes through a pipe in the boom. This setting allows also a limited motion in sway and a partial rotation of the boom, mainly due to the deformation of the springs.

A prescribed amount of vegetable oil is released on the right side of the tank relative to the boom and, before starting a test, it is waited until the emulsion has disappeared and calm conditions are achieved. After each test with boom failure, the oil passed on the left side of the tank is collected and brought back to the right side. The oil stuck to the tank wall is removed with a piece of cloth but is then lost, leading to a variation in the oil volume which is however very limited. The oil is a soybean oil with density $\rho_o = 919kg/m^3$ and kinematic viscosity $\nu_o = 56 \cdot 10^{-6} m^2/s$, chosen because of its non toxicity and its properties close to those of a more realistic Bunker B (BB) oil for which entrainment-boom failure typically occurs. One must note that the given density and viscosity refer to nominal values, a more precise evaluation would require a direct measurement of the oil properties. To prevent the oil from passing between the model and the tank walls a felt strip has been attached to the boom sides. Moreover, a thin layer of insulating acetoxy silicone was spread on it to avoid oil absorption.

Video recordings of the experiments were done using two low-speed cameras (with 25 fps) to provide a global view of the test and two high-speed cameras (with 100 fps) to give a detailed view of the flow nearby the boom. The two low-speed cameras have a view overlapping so to allow the reconstruction of the overall tank view by image analysis. Similarly it is done for the two others for a wider view around the boom. Using the images from the enlarged views and glass particles with 1μ diameter as seeding, the liquid velocities were measured with the Particle Tracking Velocimetry (PTV) technique (Miozzi 2004). A dedicated light system was used to properly illuminate the particles. An example of predicted water velocities is given in the right of figure 2 showing a vortical structure shed from the boom bottom.

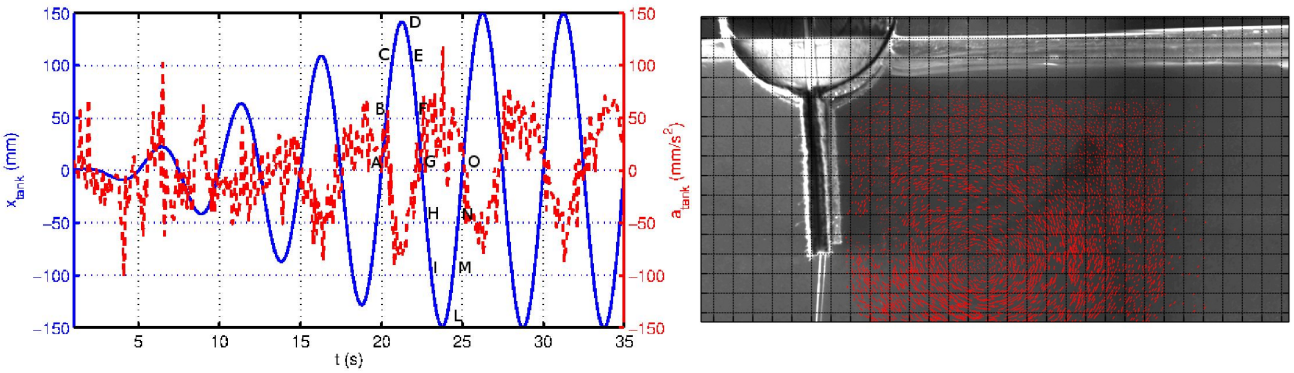

Figure 2: Right: prescribed sway motion (blue line) and measured acceleration (red line) of the tank. Left: enlarged view of the tank with the boom and the local velocities estimated with the PTV technique.

Preliminary standard sloshing tests, *i.e.* without boom and oil, were performed to characterize the flow and verify if velocities in the range of expected critical speed for the failure could be achieved in the central section of the tank. Then five different volumes of oil (V_0) were examined: 0.5, 0.7, 0.8, 0.9 and 1l. In each case the oil was set on the right of the boom and tests until steady-state conditions were performed. The general features of the phenomena are discussed next in terms of the oil case with $V_0 = 1$l.

General features The occurrence of boom failure is a possible consequence of an instability developing under certain conditions at the water-oil interface. The latter seems to be associated with the formation of a headwave (sloped interface leading to and including a thicker oil slick) when there is a combination of sufficiently large slope, thick slick and high local oil-water relative velocity. From a preliminary analysis of the present experimental data, the instability could be affected by the vortex shedding from the boom toward the oil side (see right panel of figure 2). Indeed the vortical structure seems to induce a minimum in the oil slick thickness in the first part of each motion period (*e.g.* from time instant A to about time instant D for the fifth period shown in the left plot of figure 2) contributing in the formation of a headwave close to the boom. However, when the instabilities originate at the oil-water interface the vortex is almost destroyed and can only affect the local inflow velocity in the later evolution. Let us consider a generic period with instability occurrence for $V_0 = 1$l, *e.g.* the fifth period of the tank motion with labelled time instants in the left plot of figure 2. From A to B the oil headwave moves far from the boom. This process continues until D, when the tank position has reached its maximum. At this stage, a thickened area in the oil slick starts to form. After that the oil is pushed towards the boom and instabilities appear at the water-oil interface, in the form of growing waves traveling toward the boom. They

appear both in the mid section of the tank and along the front wall, with clear 3D features. This behavior is qualitatively similar for each period with instability. What happens later depends on the strength of the instability and on the kinematic flow conditions in the specific case. For the amount of oil here considered, the instability occurs the first time at the fourth period (see left plot of figure 3) but it is weak and disappears without consequences. At the fifth period it is able to lead

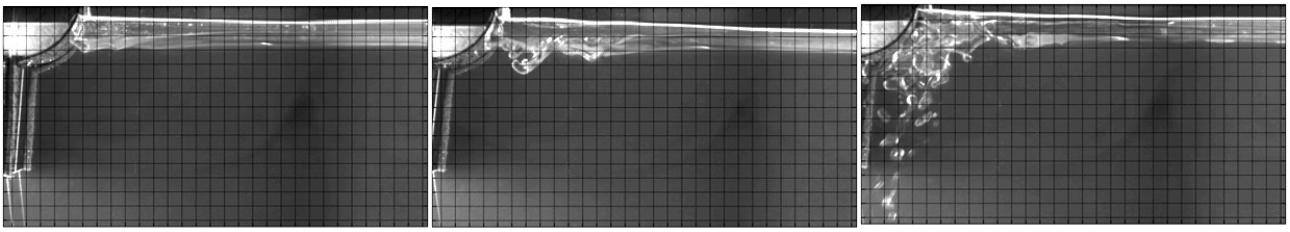

Figure 3: From left to right: enlarged views with instability of water-oil interface during the fourth, fifth and six period of the tank oscillation for the case with $V_0 = 1$l. These instants are near the time G in the corresponding period (see left plot of figure 2 for G definition) and show the maximum amplitude of the instability for the fourth and fifth periods and the onset of boom failure for the sixth period.

to interface breaking with spilling of oil drops into water, but not to a boom failure (see centre plot of figure 3). The latter occurs at the sixth period because of a sufficiently high local speed (see right plot of figure 3) and is an entrainment failure with filaments and droplets of oil detaching from the oil slick and passing beneath the boom. For all three periods the instability starts between the corresponding time instants E and F, soon after the tank has started to move from the oil side toward the boom. The sixth period is in steady-state conditions for the tank motion (see left plot of figure 2), however also in the following periods the flow features close to the boom do not repeat periodically because part of the oil moves to the left side of the tank reducing the amount on the right. Similar conditions occur with the other amounts of oil.

The used experimental set-up allows only a rough estimate of the wavelengths, speed and growth rate of the instabilities. A closer view to these parameters would help in clarifying the nature of the instabilities. From our preliminary investigations they could start as Holmboe waves which become steep in time and may transform in Kelvin-Helmotz instabilities if they are energetic enough. The latter seems to be the responsible for interface breaking with oil drops spilling in water and possible boom failure. The confirmation of this needs a new dedicated experimental study. Available theoretical instability analyses, performed in this context, consider a steady inflow. Interesting works are, for instance, Leibovich (1976) and Smyth and Peltier (1989). The former examines the Kelvin-Helmotz instability at the interfaces of three fluids (water, air and oil) and confirms, among others things, a greater instability for thicker oil. The latter examines possible transition between Kelvin-Helmotz and Holmboe instabilities.

Oil leakage during boom failure When boom failure occurs oil is spelt downstream the boom, *i.e.* at its left side. The amount of this oil is an important parameter when dealing with real booms and their performances in waves and current. In this perspective, the present study is relevant in the case of slowly-varying currents or long waves since the flow inside

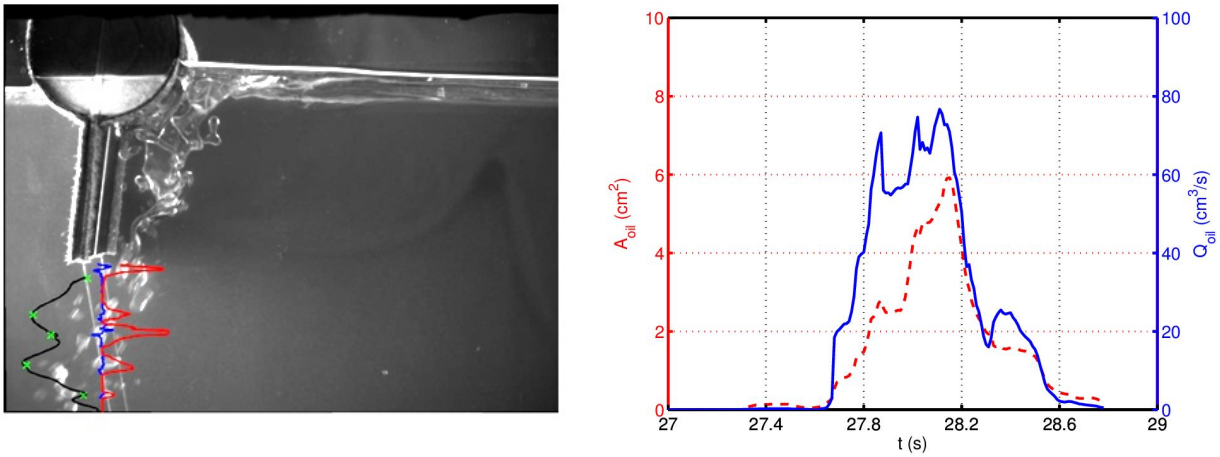

Figure 4: Left: snapshot from the image analysis used to estimate the average speeds and the cross-sectional circular areas of the oil along the selected vertical tank section. Right: time evolution of the total intersection area of the oil (A_{oil}, dashed line) and of the oil flux (Q_{oil}, solid line) for the case with $V_0 = 1$l.

the tank is periodic with a long period. The volume of leaked oil is measured as time integral of the oil flux across a convenient vertical section of the tank near the mean position of the boom (see left plot of figure 4). At this stage the flow has clear 3D features. Therefore as a first approximation, for each oil droplet or filament passing the section, the corresponding intersection segment is assumed as the diameter of a corresponding circular oil cross-section. Left plot of figure 4 provides a snapshot exemplifying the performed analysis. The luminosity (red line) and its gradient (blue line) along the vertical tank section are used to identify and estimate the areas of the circular oil cross-sections. The PTV technique provides the horizontal speed (black line) along the section from which the averaged oil speed (indicated by a green cross) is evaluated for any intersection area. Using the averaged oil speeds and the cross-sectional areas, the oil flux (Q_{oil}) can be estimated in time. An example is provided in the right plot of figure 4 for the case with $V_0 = 1$l (during the sixth period of tank motion), together with the evolution of the total intersection area of the oil (A_{oil}). These curves are obtained by smoothing the original data with a moving average filter that substitutes the instantaneous estimate of the variable with the average among the twenty estimates closest in time. This is done so to minimize the influence of errors associated with the identification process of the oil crossing the vertical section. From the results, both quantities (A_{oil} and Q_{oil}) change quickly in time because of the instability and breaking phenomena of the water-oil interface, leading to rapid passage of the oil below the boom. The boom failure starts around the time instant G of the examined period and lasts for this case about $0.24T$, with T the tank oscillation period. Reducing the initial volume V_0 leads to a delay in the boom failure and shortens the event duration. For example, with $V_0 = 0.9$l the phenomenon lasts 30% less than with $V_0 = 1$l.

The time integration of the oil flux leads to the volume of oil leaked into the left side of the boom (V_l). Table 1 provides this quantity for all V_0 examined and shows a nonlinear behavior, with increasing slope toward largest V_0 and highest value of about 4% of V_0 for $V_0 = 1$l.

Table 1: Volume of leaked oil, V_l, for the different volumes of released oil, V_0.

$V_0(ml)$	1000	900	800	700	500
$V_l(ml)$	36.8	9.9	2.5	0.4	0
$(V_l/V_0) * 100$	3.68	1.1	0.31	0.06	0

The physical investigation is still ongoing. From what discussed also above, some aspects highlighted the need for additional model tests. In particular, clearer views of the water-oil interface would help for a better understanding of the instability nature. It is also important to fully assess the relevance of the vortex shedding by reducing it through proper shaping of the boom and to investigate the instability occurrence in absence of the body. So a second-step experiment has been planned and the results from both activities will be documented at the Workshop.

This research activity is partially funded by the Research Council of Norway through the Centres of Excellence funding scheme AMOS, project number 223254, and partially by the Flagship Project RITMARE - The Italian Research for the Sea - coordinated by the Italian National Research Council and funded by the Italian Ministry of Education, University and Research within the National Research Program 2011-2013.

References

DELVIGNE, G. (1989). Barrier failure by critical accumulation of viscous oil. In *International Oil Spill Conference Proceedings*, pp. 143–148.

GRILLI, S., T. FAKE, AND M. SPAULDING (2000). Numerical Modeling of Oil Containment by a Boom/Barrier System : Phase III. Final Technical Report for DOT Grant. Technical Report DTRS57-95-G-00065, Dept. Ocean Engng., Univ. of Rhode Island.

LEIBOVICH, S. (1976). Oil Slick Instability and the Entrainment Failure of Oil Containment Boom. *Journal of Fluids Engineering 98*, 98103.

MIOZZI, M. (2004). Particle Image Velocimetry using Feature Tracking and Delaunay tesselation. In *12th Int. Symp. Applied Laser Techniques to Fluid Mechanics*, Lisbon, Portugal.

SMYTH, W. D. AND W. R. PELTIER (1989). The Transition between KelvinHelmholtz and Holmboe Instability: An Investigation of the Overreflection Hypothesis. *J. Atmos. Sci. 46*, 36983720.

LAGRANGIAN NUMERICAL WAVE-CURRENT FLUME

E. Buldakov, D. Stagonas, R. Simons

Department of Civil Engineering, UCL, Gower Street, LONDON, WC1E 6BT, UK

SUMMARY

Lagrangian formulation for surface waves with vorticity is used to create a numerical wave-current flume. The numerical flume is then used to reproduce a physical experiment on focused wave groups in sheared currents. The numerical results include evolution of the free surface of focused wave groups in still water and over in-line and opposing currents and flow kinematics under such waves. Numerical results are compared with experiment and demonstrate good agreement.

1 INTRODUCTION

The natural way of modelling strong deformations of a fluid domain is using equations of fluid motion in the Lagrangian form which is solved in a fixed domain of Lagrangian labels. Lagrangian models are capable of efficient modelling of very steep and overturning waves. Advantages of the Lagrangian approach for numerical modelling of steep waves were demonstrated in Buldakov (2013*b*), Buldakov (2013*a*) were a simple fully Lagrangian numerical model was developed and applied for various wave problems.

Another advantage of the Lagrangian formulation is very simple representation of vortical flows. The vorticity in Lagrangian coordinates is constant in time and is specified by initial velocity conditions. This paper exploits this advantage of the Lagrangian formulation. We generalise the previously developed numerical method for free-surface flows with arbitrary sheared currents. Certain practical problems of numerical implementation of the method, such as excessive deformation of physical computational domain, are addressed and successfully solved. The method is then used to create a numerical wave-current flume. The numerical flume is used to reproduce physical experiments on evolution of wave groups over currents. An iterative methodology of generating focused wave groups on currents (Stagonas *et al.*, 2014) is used for both physical and numerical experiments. The results for surface elevation and wave kinematics are obtained and good comparison is achieved between numerical and experimental results.

2 LAGRANGIAN 2D WATER-WAVE FORMULATION WITH VORTICITY

A general Lagrangian formulation for two-dimensional flow of inviscid fluid with a free surface can be found in Buldakov *et al.* (2006). We consider time evolution of Cartesian coordinates of fluid particles $x(a,c,t)$ and $z(a,c,t)$ as functions of Lagrangian labels (a,c). The formulation includes the Lagrangian continuity equation and the Lagrangian form of vorticity conservation

$$\frac{\partial(x,z)}{\partial(a,c)} = J(a,c)\,; \quad \frac{\partial(x_t,x)}{\partial(a,c)} + \frac{\partial(z_t,z)}{\partial(a,c)} = \Omega(a,c)\,, \tag{1}$$

and the dynamic free-surface condition

$$x_{tt}x_a + z_{tt}z_a + g\,z_a\,\big|_{c=0} = 0\,. \tag{2}$$

Functions $J(a,c)$ and $\Omega(a,c)$ are given functions of Lagrangian coordinates. $J(a,c)$ is defined by initial positions of fluid particles associated with labels (a,c). We select $(a,c) = (x_0,z_0)$, which gives $J = 1$. $\Omega(a,c)$ is the vorticity distribution and is defined by the velocity field at $t = 0$. A sheared current can be defined by specifying vorticity depending only on the vertical Lagrangian coordinate c. For our choice of Lagrangian labels the parallel current can be specified as $x = a + V(c)t$; $z = c$, where $V(c) = V(z_0)$ is the current profile. Substitution to the second equation of (1) gives

$$\Omega(a,c) = \Omega(c) = V'(c)\,. \tag{3}$$

Therefore, waves on a sheared current with an undisturbed profile $V(z_0)$ are described by equations (1) with the free surface boundary condition (2) and the vorticity distribution given by (3). A particular problem within a general formulation is defined by initial conditions and boundary conditions on the bottom and side boundaries.

3 LAGRANGIAN NUMERICAL WAVE-CURRENT FLUME

The problem formulated in the previous section is solved numerically using a finite-difference technique. Detailed description of the numerical method can be found in Buldakov (2013*a*) and Buldakov (2013*b*). The numerical method for the formulation with vorticity is mostly identical to the irrotational formulation. Here we only mention differences relevant to the formulation with a sheared current used for construction of a numerical wave-current flume. In the numerical formulation we do not use vorticity distribution directly. We differentiate

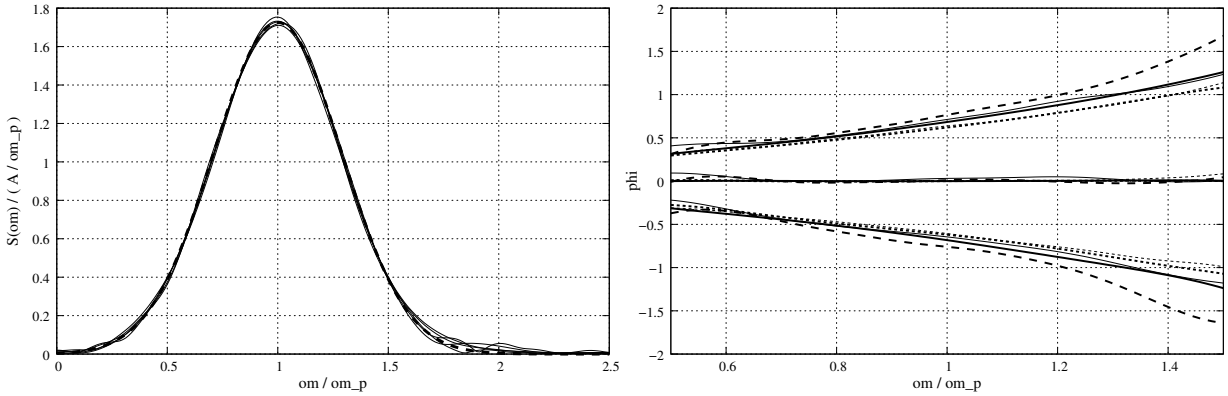

Figure 1: Left: thick dashed – target amplitude spectrum; thin solid – linearised amplitude spectra for all computational and experimental cases at the focus point ($x = 0$). Right: phase spectra at the focus point ($x = 0$) and at positions $x = \pm 0.7h = \pm 0.108\lambda$. Thin – experimental, thick – computational. Solid – no current, dotted – in-line current, dashed – opposing current (computational only). Frequency is scaled by the peak frequency ω_p and amplitude spectral density by the ratio of the linear focus amplitude A to the peak frequency A/ω_p.

the vorticity conservation equation with respect to time to exclude Ω. Vorticity is implicitly defined by the initial condition, when we specify x and z for three initial time steps, which are required to start time marching. The numerical wave-current flume is created by specifying boundary conditions allowing safe inlet and outlet of the current flow into the computational domain, wave generation and absorption of waves reflected from domain boundaries. The two latter requirements are satisfied using re-formulated free-surface boundary condition (2) which includes time-varying pressure gradient and artificial dissipation

$$x_{tt}x_a + z_{tt}z_a + g\,z_a + k(a)\left((x_t - V(c))\,x_a + z_t z_a + g\,z_a\right) = P_x(a,t)\,\big|_{c=0}.$$

The last term in the right-hand side represents the artificial surface dissipation with the space-varying dissipation coefficient k, and the term on the left-hand is the surface pressure gradient. The dissipation coefficient is selected to be zero in the working section of the flume and gradually grows to a large value near the inlet and outlet boundaries. As the result, the free surface at the boundaries remains relatively steady and does not move from its original position. This serves a double purpose. First, reflections from the boundaries are significantly reduced. Second, the boundary conditions at the inlet and outlet boundaries can be specified simply as the undisturbed velocity profile at the inlet ($x_t(a_{in}, c, t) = V(c)$) and as a parallel flow at the outlet ($z_a(a_{out}, c, t) = 0$). The wave in the flume is generated by creating an area in front of one of the wave absorbers where pressure distribution of a prescribed shape is defined. Time-varying amplitude of this pressure disturbance is used as a control input for wave generation. An additional difficulty with numerical realisation of the Lagrangian formulation with a sheared current is sheared deformation of the original domain in physical coordinates which indefinitely increases with time. The shape of the domain eventually becomes impractical as it moves out of an area of interest. Besides, accuracy of computations for strongly deformed computational cells considerably reduces. To avoid these difficulties we perform sheared deformation of the Lagrangian domain to compensate the deformation of the physical domain. Such deformation takes place after several time steps and moves boundaries of the physical domain back to the original vertical lines. After this Lagrangian labels are re-assigned to new values to preserve the rectangular shape of the Lagrangian computational domain with vertical and horizontal lines of the computational grid.

4 NUMERICAL AND EXPERIMENTAL SETUPS

We use the numerical wave-current flume to reproduce results obtained during experimental study of focused wave groups over sheared currents performed in the coastal recirculating flume in the fluids laboratory of the Department of Mechanical Engineering at UCL. The flume has the width of $1.2\,m$ and the distance between two piston wavemakers is about $16\,m$. The depth for all tests was set to $h = 0.5\,m$. A recirculating system with three parallel pumps and vertical inlets $13\,m$ apart is used to create a current. A paddle on the right end of the flume is used as a wave generator and the opposite paddle as an absorber. Blocks of wire mesh of trapesiodal shape are installed on top of the inlet and outlet to condition the flow and create a desired current profile. Surface elevation at selected points along the flume is measured by resistance wave probes and a PIV system is used to measure flow kinematics. Wave groups are generated with 4 constant phase shifts within the

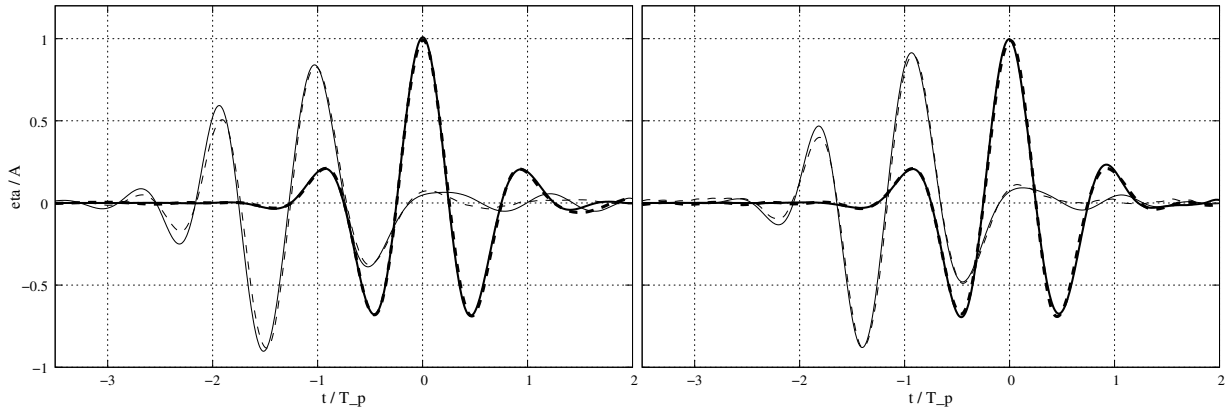

Figure 2: Comparison of computational (solid) and experimental (dashed) time histories of linearised surface at the focus position $x = 0$ (thick) and at position $x = -6.34h = -0.98\lambda$ (thin). Left: no current. Right: in-line current. Time is scaled by the peak period T_p and surface elevation is scaled by the linear focus amplitude A.

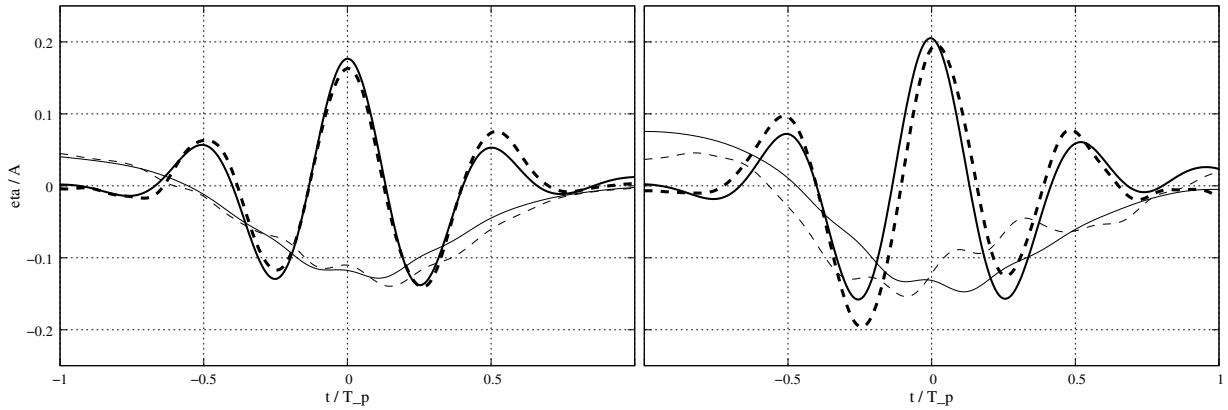

Figure 3: Comparison of computational (solid) and experimental (dashed) time histories of plus (thick) and minus (thin) second-order components at the focus position $x = 0$. Left: no current. Right: in-line current. Time is scaled by the peak period T_p and surface elevation is scaled by the linear focus amplitude A.

same amplitude spectrum. The resulting signals for surface elevations are used to extract linear part of the signal as well as non-linear components including second order subharmonics and second, third and fourth order super-harmonics. An iterative procedure is used to focus the wave group at a prescribed location and time. More details of the experimental setup and the methodology can be found in Stagonas *et al.* (2014). At this stage only tests for waves without current and over in-line currents are completed.

To validate the numerical results we select a moderately non-linear wave group with a Gaussian linear amplitude spectrum. The peak frequency of the spectrum is $f_p = 0.6\,Hz$ for water depth $h = 0.5\,m$. The corresponding linear wave length is $\lambda_p = 6.488\,h$. The linear focus amplitude of the wave is $A = 0.1\,h$. The normalised linear target spectrum is presented on figure 1. The numerical waves were generated in still water and over in-line and opposing currents of maximal velocity $V_0 = 0.09\,C$, where $C = \sqrt{gh}$ is linear shallow water celerity. The profile for computations was created using preliminary ADV measurements of current velocity. The working section of the numerical flume free from wave generator and absorbers is set to about $20\,h$. The origin of the coordinate system is set to the focusing position at the center of the flume with a horizontal axis pointing against the wave propagation direction. The waves in the numerical flume were generated using the same iterative focusing procedure as in the physical flume. Calculations are performed for waves without current as well as for in-line and opposing currents. Calculation results include time histories of surface elevation at the same positions as in physical experiment and flow kinematics at the focus point.

5 RESULTS

Results of numerical tests and their comparison with physical experiment are demonstrated on figures 1-5. Figure 1 demonstrates efficiency of the focusing procedure for all experimental and computational cases. The evolution of phases near the focus point is physically relevant for different current cases and compares well between computations and experiment. The behaviour of the linearised wave at the focus point is identical for

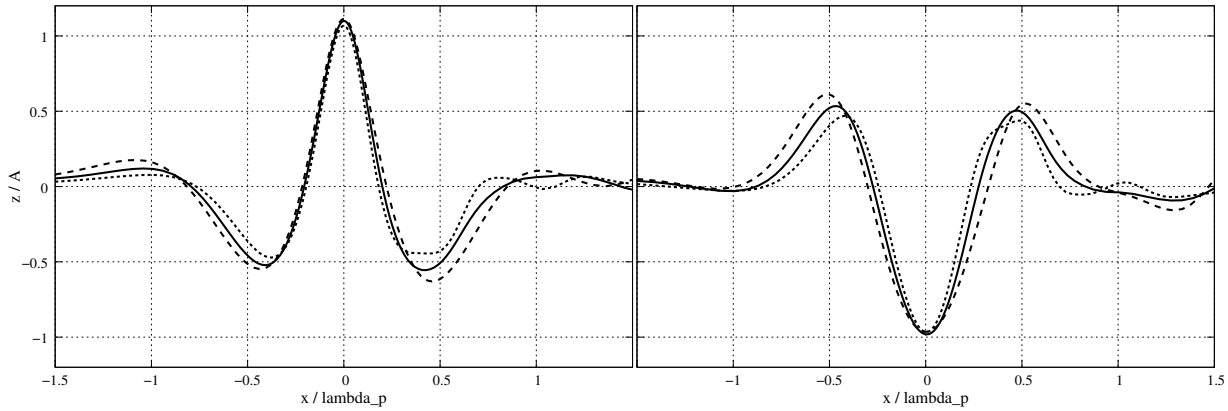

Figure 4: Computational surface profiles at the focus time $t = 0$. Solid – no current; dashed – opposing current; dotted – in-line current. Left: peak focused. Right: trough focused. Vertical coordinate is scaled by the linear focus amplitude A and horizontal coordinate by the peak wave length λ_p.

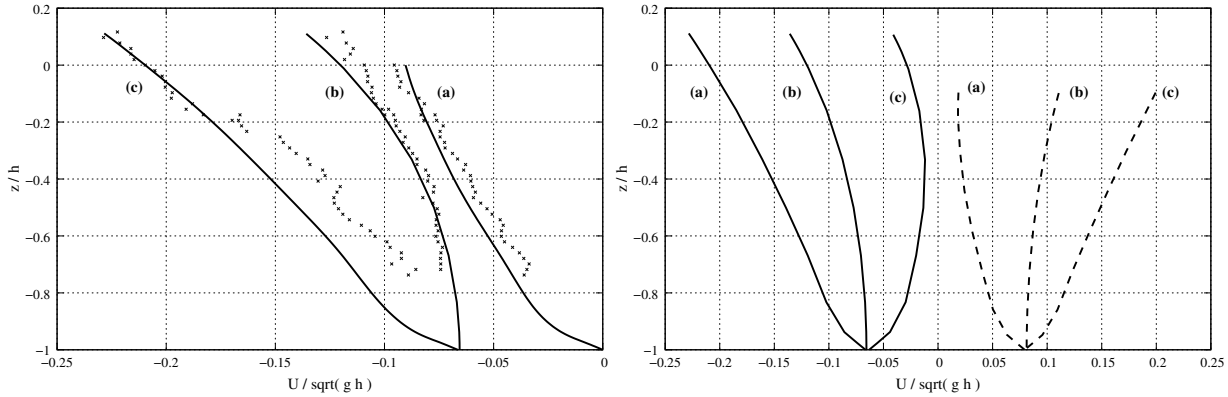

Figure 5: Left: Comparison of computational (lines) and experimental (dots) horizontal velocity profiles for the incoming current (a) and under the crest of the peak focused wave at focus position $x = 0$ and focus time $t = 0$ without current (b) and over in-line current (c). Right: Computational profiles of horizontal velocity under peak (solid) and trough (dashed) focused waves. (a) – in-line current; (b) – no current; (c) – opposing current. Velocity is scaled by the shallow-water celerity $C = \sqrt{gh}$ and vertical coordinate is scaled by depth h.

all cases (figure 2), which is not surprising as this was the aim of the iterative focusing procedure. However, good comparison at the position one wave length before the focusing point demonstrates that the dispersion relation is represented by the numerical model with good accuracy. Figure 3 shows that non-linear terms are also well captured by the numerical model. The calculated wave profiles presented for at focus time for different current direction for peak and trough focused waves are shown on figure 4. Finally, figure 5 demonstrate good agreement with measured wave kinematics. The discrepancy observed for the in-line current case is explained by the defect in the incoming current profile for this experimental run. It is hoped that further analysis of experimental results and generating more experimental cases will allow to remove this discrepancy.

The authors thank EPSRC for supporting this work withing the Supergen Marine Technology Challenge.

References

Buldakov, E. V. 2013*a* Lagrangian modelling of extreme wave groups. In *28th International Workshop on Water Waves and Floating Bodies*. L'Isle sur la Sorgue, France.

Buldakov, E. V. 2013*b* Tsunami generation by paddle motion and its interaction with a beach: Lagrangian modelling and experiment. *Coastal Engineering* **80**, 83–94.

Buldakov, E. V., Eatock Taylor, R. & Taylor, P. H. 2006 New asymptotic description of nonlinear water waves in Lagrangian coordinates. *Journal of Fluid Mechanics* **562**, 431–444.

Stagonas, D., Buldakov, E. & Simons, R. 2014 Focusing unidirectional wave groups on finite water depth with and without currents. In *34th International Conference on Coastal Engineering*. Seoul, Korea.

30th International Workshop on Water Waves and Floating Bodies, Bristol (UK), 12–15 April, 2015

Forced heaving motion of a floating air-filled bag

John Chaplin & Francis Farley
University of Southampton,
Southampton SO17 1BJ, UK

Adi Kurniawan, Deborah Greaves & Martyn Hann
Plymouth University
Plymouth PL4 8AA, UK

Email: *j.r.chaplin@soton.ac.uk*

Highlights

- Measurements of heaving motions of a floating air-filled bag caused by forced oscillations of the internal pressure.
- Partial validation of a linear frequency-domain numerical model.

1. Introduction

A proposed wave energy converter related to that described by Farley (2011) consists of a pressurised axi-symmretic air-filled bag, ballasted to float at about half depth. The bag contracts and expands under the action of wave-induced heaving motion, pumping air into and out of a secondary, rigid, chamber (V2 in figure 1(a)) which acts as an air spring. The system's resonant frequency in heave is determined largely by V2 and the volume of the bag V1. Oscillating air flow between V1 and V2 drives a power take-off.

This paper describes experiments and numerical modelling aimed at understanding the behaviour of this device. Rather than test it in waves, in this initial investigation we chose to replace the power take-off with an oscillating air pump. Forcing air into and out of the bag periodically caused it to heave and radiate waves when floating in water initially at rest. Measurements of the bag's response are compared with the predictions of a linear frequency-domain radiation theory, which uses a finite difference approach to model the harmonic deformations of the bag. Agreement is promising on the whole, providing some insights into the likely performance of the device when operating as a wave energy converter.

2. Experimental arrangements

The experiments were carried out in the wave basin at Plymouth University, measuring 35m x 15.5m, with a water depth of 3m. The overall height of the bag and ballast container (sketched in fig. 1(b)) was about 1.6m. Since the compressibility of air is the same as in the prototype, the volumes of V1 and V2 had to be considerably larger than those implied by the cube of the scale factor (about 1:16), in order for the resonant frequency to be scaled correctly. Accordingly, V1 was augmented by the volume of an additional air chamber which was connected to the top of the bag by a 100mm diameter flexible hose, and to a similar chamber representing V2, as sketched in figure 1(b). Both chambers were mounted on the gantry spanning the tank, and each had a volume of $1m^3$. The duct between them housed an oscillating air pump.

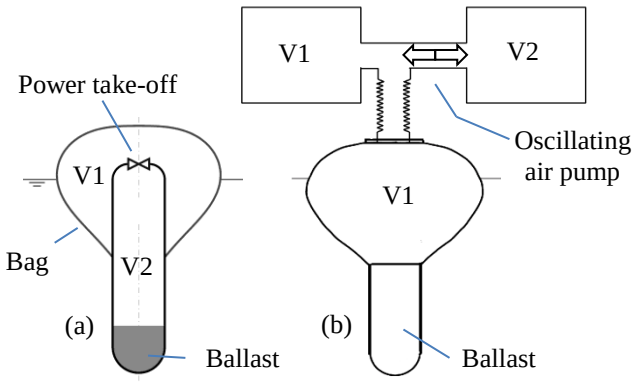

Figure 1 (a) Configuration of (a) the full-scale device and (b) the laboratory model.

The form of construction of the bag, both for the model and envisaged for the full-scale device, is that of a membrane enclosed within an array of longitudinally very stiff tendons distributed around the circumference. This gives it the appearance of a pumpkin, with the membrane bulging out between the tendons, which are intended to carry all of the meridional load. In the model the membrane was unreinforced polyurethane film and the 16 tendons, welded on, were made from 30mm wide polyurethane-coated polyester strips. Ballast was provided by lead shot inside a cylindrical steel container with a hemispherical base, mounted beneath the bag. The device is shown in figure 2, floating in the tank.

The air pump consisted of two pairs of 300mm diameter bellows on either side of diaphragms which were driven by electro-magnetic digital linear actuators. A sketch is shown in figure 3. Other instrumentation included pressure transducers in the bag and on either side of the air pump, and a displacement transducer recording the elevation of the top of the bag. Video cameras recorded the motion of the bag from the side, both above and under water.

Figure 2. Combined under- and above-water images of the bag and ballast container.

Driving the air pump generated an oscillating air flow into and out of the bag, causing it to heave and radiate waves. Measurements were made over a range of frequencies in each of five conditions defined by the initial pressure in the bag and its elevation. As discussed by Kurniawan *et al.* (2015), for a given internal pressure there are in general two elevations at which the bag is in equilibrium in still water.

3. Linear frequency domain numerical model

For the purpose of computing the response of the model device to an oscillating air flow, the shape of a tendon in the vertical plane, together with the outline of the ballast container, can be represented by a series of straight elements of uniform length h between nodes. Nodes and elements are numbered from the bottom of the ballast container to the top of the bag on its axis. (The inlet pipe at the top is omitted.) In still water conditions, the inclination of the nth element from the horizontal is Ψ_n.

Resolving forces in the normal direction at the nth node on the bag (where the radius and the elevation relative to the water surface are R_n and Z_n) leads to

$$\pi R_n\left(P+\rho g H_n Z_n\right)h = T\tan\tfrac{1}{2}\left(\Psi_n-\Psi_{n-1}\right), \qquad (1)$$

assuming that all loads are carried by the tendons. In equation (1) P is the internal pressure, T is the total tension in all tendons, and H_n = 1 when Z_n < 0, otherwise 0. Resolving forces at the node at the bottom where the tendon joins the top of the ballast container (n = 1) provides one boundary condition, namely $T\sin\Psi_1 = W+\pi R^2 P$, where W is the submerged weight of the ballast, while at the top ($n = N$), $\Psi_{N-1} = \pi$ by symmetry. Solutions to equation (1) for the shape of the bag in still water can be found by various means (Kurniawan *et al.*, 2015).

In solving the dynamic case, the time dependent nature of each parameter is represented by a small harmonic perturbation about the mean, i.e. the static solution. Thus the radius of the nth node becomes the real part of $R_n + r_n e^{-i\omega\tau}$ where r_n is a complex amplitude, ω is the frequency and τ is time. Similar adjustments are made to elevations: $Z_n + z_n e^{-i\omega\tau}$; inclinations, $\Psi_n + \psi_n e^{-i\omega\tau}$; the tension, $T + te^{-i\omega\tau}$; the internal pressure, $P + pe^{-i\omega\tau}$, and the internal volume of the bag $V + ve^{-i\omega\tau}$. Also, beneath the water surface all surfaces experience hydrodynamic pressure whose complex amplitude is denoted φ_n.

The solution procedure is first to introduce these perturbations into equation (1), expand the result, discard terms involving products of small quantities, and subtract the static solution in the usual way. It is helpful to define

$$R'_n = R_{n+1}-R_n;\quad Z'_n = Z_{n+1}-Z_n;\quad r'_n = r_{n+1}-r_n;\quad z'_n = z_{n+1}-z_n,\quad n = 1, 2, \ldots N\text{–}1. \qquad (2)$$

The elements of the column matrix $\{r'\} = \{r_1'\ \ r_2'\ \ \ldots\ \ r_{N-2}'\}^{\mathrm{T}}$ and z_1, the complex amplitude of the heaving motion of the ballast, become the primary unknowns. To a first approximation all other parameters can be expressed in terms of these, ultimately rendering the problem in the form of a set of complex linear equations. Besides the geometry of the system in still water, the other independent parameters are the volume swept out by the air pump, and its frequency ω.

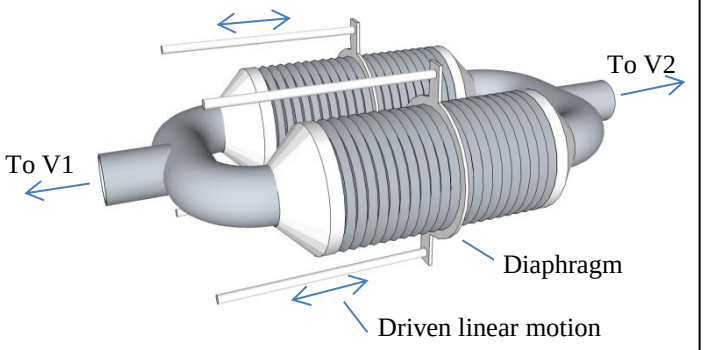

Figure 3. The oscillating air pump.

Hydrodynamic pressures are computed by using an approach for calculating wave radiation by axisymmetric bodies set out by e.g. Fenton (1978) and Isaacson (1982) (both of which contain significant errors). For a given geometry and a given set of normal velocities {υ} at the nodes, the result can always be expressed in the form {φ} = [D]{υ}. In the present case the elements of [D] are computed from the known initial geometry of the device, and those of {υ} can be related to {r'} and z_1 by way of the complex amplitude of the internal pressure, which is assumed to follow the adiabatic law in response to the oscillatory flow of air from the air pump.

4. Measurements and predictions

Slow inflation and deflation

Figure 4 shows a plot (as a continuous grey line) of the measured trajectory traced out by the elevation of the top of the bag against its internal pressure, as the bag is slowly inflated in still water. As described by Kurniawan *et al.* (2015), the pressure initially falls as the bag rises, then increases again as the membrane tightens. The trajectory returns along almost the same path as the air is released again. A dashed line represents a numerical solution of equation (1) for these quasi-static conditions. Better agreement with the measurements than that shown by Kurniawan *et al.* has been achieved here by empirically increasing the length of the tendons in the numerical model from 1.5m (as they were when unstressed in the laboratory model) to 1.65m. Of this 150mm difference, about 35mm can be attributed to stretch in the 16 tendons which, over the range of the test conditions, would have been under a tension of at least 300N each. The remaining difference is tentatively associated with the actual inflated form of the membrane. The bag was constructed from 16 'petals' welded together at the tendons. Since the petals were two-dimensional and less stiff under tension than the tendons, it is inevitable that when the bag was inflated, they would bulge out, stretching in both directions and taking some of the load away from the tendons. With this in mind it seems reasonable to argue that the effective tendon length should be increased to reflect the greater meridional length of the bulging and load-carrying membrane. Accordingly, results presented below were computed for a tendon length of 1.65m. Also, amid some uncertainty (within a range of about 8%) about the effective submerged ballast weight, the calculations used a figure of 3659N to provide a reasonable fit with the measurements.

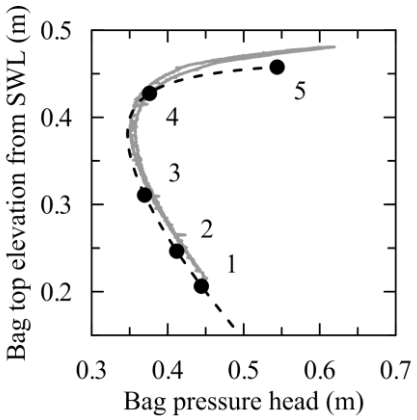

Figure 4. Trajectories of the elevation of the top of the bag when inflated and deflated slowly in still water. The grey line is the measurement, the broken line the prediction, using a tendon length of 1.65m. Initial conditions for dynamic tests are identified 1–5.

Initial conditions for the wave radiation tests and predictions are identified 1–5 in figure 4.

Computed resonant frequencies

Behind the concept of this device lay the idea that the negative stiffness of a body that shrinks as it sinks and expands as it rises in water otherwise at rest would cause it to have a longer resonant period in heave than a rigid body of the same size and shape. This might be an advantage, leading to a reduction in the size of a wave energy converter designed for a given sea-state. Computed resonant periods for compressible and rigid bodies having the shape of defined by the initial conditions in the 5 test cases are plotted in figure 5. For the compressible air-filled bag, predicted periods are more than 15% longer than those for rigid bodies of the same shape, though obviously the frequency response of the bag depends on the stiffness of the air spring, and therefore the volume of air enclosed, and connected to it.

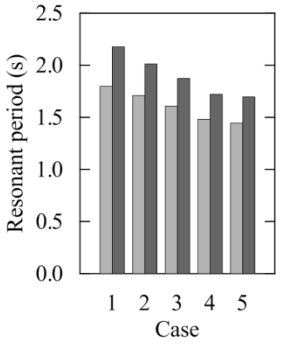

Figure 5. Resonant heave periods of the air-filled bag driven with the air pump (dark grey), and of a rigid body of the same initial shape (light grey).

Response of the device to an oscillating air flow

In these tests the air pump was operated over a range of frequencies in turn, at amplitudes that generated a small heaving motion in the device. Results are plotted below as a function of the period of the driving motion. On the left figure 6 shows, for each case, the amplitude of the vertical motion of the top of the bag, and on the right its phase relative to that of the air pump.

Computed amplitudes and phases agree reasonably well with the measurements for those cases, 5 and 4, in which the bag is strongly inflated and high in the water. The difference between measured and predicted resonant frequencies becomes more pronounced in cases 3, 2 and 1. In the last of these the pressure drop across the membrane would have been negative in the lower part of the bag so that its profile would be concave, but the reason for the disagreement is not clear. Nevertheless, the present numerical model seems to be a good starting point for an investigation into the performance of the device as a wave energy converter.

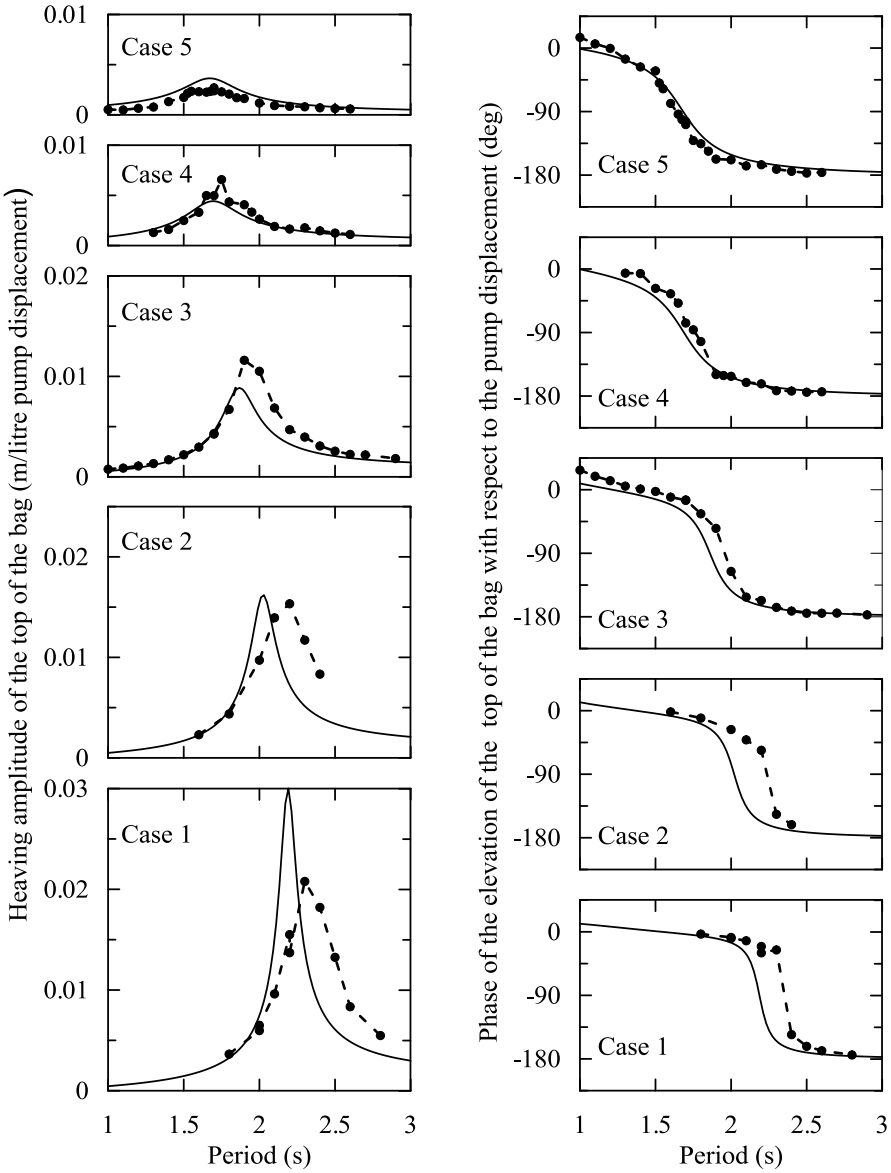

Figure 6. On the left, measured and computed heaving amplitudes of the top of the bag as functions of excitation period for a constant pump displacement of 1 litre. The phase of the motion related to that of the air pump is shown on the right. Measurements are shown as points and broken lines, numerical predictions as continuous lines.

Acknowledgement

This work is supported by the UK EPSRC SuperGen Marine Energy Research Consortium, through grant EP/K012177. We are grateful to Malcolm Cox of Griffon Hoverwork Ltd for supplying model test bags and for useful discussions.

References

Farley, F. J. M. (2011), 'The free floating clam–a new wave energy converter,' in Proceedings of the 9th European Wave and Tidal Energy, Southampton, UK

Fenton, J.D. (1978) 'Wave forces on vertical bodies of revolution', Journal of Fluid Mechanics, **85**, 241-255.

Isaacson, M. de St Q. (1982) 'Fixed and floating axisymmetric structures in waves', Journal of Waterway, Port, Coastal and Ocean Division, Proceedings of the ASCE, **108**, 180-199.

Kurniawan, A., Greaves, D., Hann, M., Chaplin, J.R. & Farley, F.J.M. (2015) 'Static shapes of a floating inflated bag for wave energy conversion'. Abstract submitted for the 30th International Workshop on Water Waves and Floating Bodies, Bristol, UK.

Two-dimensional breaking wave impact on a vertical wall

by

Ioannis K. Chatjigeorgiou[1,2] i.chatzigeorgiou@uea.ac.uk
Alexander A. Korobkin[1] a.korobkin@uea.ac.uk
Mark J. Cooker[1] m.cooker@uea.ac.uk

[1]School of Mathematics, University of East Anglia, Norwich NR4 7TJ, UK
[2]School of Naval Architecture and Marine Engineering, National Technical University of Athens, 9 Heroon Polytechniou Ave, 15773, Athens,Greece

1 Introduction

We investigate the violent slamming of a steep wave onto a vertical wall. The novelty of our work relies on the assumption of a breaking type impact. With reference to the plane impermeable wall of Fig. 1, it is assumed that a thin air pocket is formed adjacent to the wall, between the lower and the upper impacted sections of the wall. The solution process, as outlined in the sequel, could be extended to accommodate an uneven bottom configuration. However, in the present study it is explicitly assumed that the bottom is horizontal.

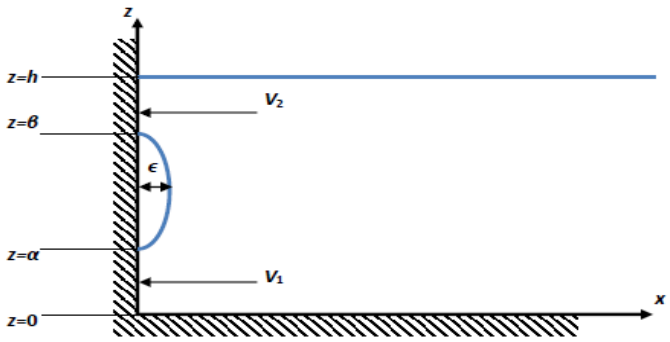

Figure 1 Definition sketch; The curves are free surfaces on which $\phi = 0$.

The boundary conditions at x=0 in the intervals $0 < z < \alpha$ and $\beta < z < h$ are defined by default through the normal components of the velocities of the wave before impact, which are assumed to be the constants V_1 and V_2, respectively. In the general case we assume that $V_1 \neq V_2$. In the intermediate region $\alpha < z < \beta$ the associated boundary condition is governed by the pressure which can be a function of z. The present analysis assumes that the pressure impulse (and accordingly the potential) in the air pocket is zero. Nevertheless the outlined methodology can be extended to accommodate non zero constant potential using the same procedure. It is also assumed that at the time of impact the width of the intermediate section between the wave front and the wall $\varepsilon \to 0$.

2 The mixed boundary value problem

In the realm of potential theory, the mixed boundary value problem in terms of $\phi(x,z)$, which is the sudden change in the velocity potential is:

$$\nabla^2\phi = 0, \qquad (x>0, \quad 0<z<h), \tag{1}$$
$$\partial\phi/\partial z = 0, \qquad (x>0, \quad z=0), \tag{2}$$
$$\phi = 0, \qquad (x>0, \quad z=h), \tag{3}$$
$$\partial\phi/\partial x = V_1, \qquad (x=0, \quad 0<z<\alpha), \tag{4}$$
$$\phi = 0, \qquad (x=0, \quad \alpha<z<\beta), \tag{5}$$
$$\partial\phi/\partial x = V_2, \qquad (x=0, \quad \beta<z<h), \tag{6}$$
$$\phi \to 0, \qquad (x\to\infty, \quad 0<z<h). \tag{7}$$

The form of the solution that satisfies eqs. (1)-(3) and the far-field behaviour (7) is

$$\phi(x,z)=\sum_{n=1}^{\infty}C_n\cos(\lambda_n z)e^{-\lambda_n x} \tag{8}$$

where $\lambda_n=(n-1/2)\pi/h$, $n\in\mathbb{N}$ and C_n are coefficients to be found from the remaining boundary conditions (4)-(6). Note that the present analysis is applied at the instant of the impact and hence C_n are constants, independent of time.

3 Triple trigonometrical series

Introducing eq. (8) into the boundary conditions (4)-(6) we find the following problem that involves triple trigonometrical series

$$\sum_{n=1}^{\infty}\lambda_n C_n\cos(\lambda_n z)=-V_1,\qquad (0<z<\alpha), \tag{9}$$

$$\sum_{n=1}^{\infty}C_n\cos(\lambda_n z)=0,\qquad (\alpha<z<\beta), \tag{10}$$

$$\sum_{n=1}^{\infty}\lambda_n C_n\cos(\lambda_n z)=-V_2,\qquad (\beta<z<h). \tag{11}$$

Most literature on mixed boundary value problems that involve trigonometrical series, concern dual – not triple – relations. Relevant examples are the studies of Tranter [1-3]. For a review of dual trigonometrical series the reader is referred to the classical book of Sneddon [4], which cites nearly all studies prior to the time it was published. Triple trigonometrical series concern more complicated mixed-boundary value problems and relevant examples are the works of Tranter [5] and Kerr et al. [6]. However, in both papers the boundary data in two of the three boundary sets are identically zero.

The required analysis to solve the mixed problem governed by eqs. (9)-(11) is quite complicated and therefore only the basic steps are given in the sequel. After several mathematical manipulations, the triple series of eqs. (9)-(11) are transformed into the following three conditions on new coefficients B_n

$$\sum_{n=1}^{\infty}B_n J_\nu(\mu_n y)=\sqrt{2/(\pi y)}F(\beta y),\qquad (0<y<b), \tag{12}$$

$$\sum_{n=1}^{\infty}\mu_n^{-1}B_n J_\nu(\mu_n y)=\sqrt{2/(\pi y\beta^2)}G(\beta y),\qquad (b<y<1), \tag{13}$$

$$\sum_{n=1}^{\infty}B_n J_\nu(\mu_n y)=0,\qquad (1<y<c). \tag{14}$$

where $B_n=\mu_n^{1/2}\left(\lambda_n C_n+(-1)^{n-1}2V_2/(h\lambda_n)\right)$, $F(\beta y)=-V_1+V_2$, $G(\beta y)=(2V_2/h)\sum_{n=1}^{\infty}(-1)^{n-1}\cos(\mu_n y)/\lambda_n^2$, $\nu=-1/2$, $b=\alpha/\beta$, $\mu_n=\lambda_n\beta$, $c=h/\beta$ $\mu_n=\lambda_n\beta$, $y=z/\beta$. The next step is to reduce the triple trigonometrical series to dual by satisfying the last one (14). This is accomplished assuming an alternative form of the unknown constants B_n according to which

$$B_n=\frac{1}{\mu_n^{1+p/2}J_{\nu+1}^2(\mu_n c)}\sum_{m=0}^{\infty}E_m J_{\nu+2m+1+p/2}(\mu_n),\ -1\le p\le 1. \tag{15}$$

Eq. (15) satisfies eq. (14) as it holds that [7]

$$\sum_{n=1}^{\infty}\frac{J_{\nu+2m+1+p/2}(\mu_n)J_\nu(\mu_n y)}{\mu_n^{1+p/2}J_{\nu+1}^2(\mu_n c)}=0,\qquad y>1. \tag{16}$$

Introducing eq. (15) into eqs. (12) and (13) the problem is reduced to the dual trigonometrical series

$$E_0 a_1(y)+\sum_{m=1}^{\infty}E_m\sum_{n=1}^{\infty}\frac{J_{\nu+2m+1+p/2}(\mu_n)J_\nu(\mu_n y)}{\mu_n^{1+p/2}J_{\nu+1}^2(\mu_n c)}=\sqrt{2/(\pi y)}F(\beta y),\qquad (0<y<b), \tag{17}$$

$$E_0 a_2(y) + \sum_{m=1}^{\infty} E_m \sum_{n=1}^{\infty} \frac{J_{\nu+2m+1+p/2}(\mu_n) J_\nu(\mu_n y)}{\mu_n^{2+p/2} J_{\nu+1}^2(\mu_n c)} = \sqrt{2/(\pi y \beta^2)} G(\beta y), \qquad (b < y < 1), \tag{18}$$

where

$$a_j(y) = \sum_{n=1}^{\infty} \frac{J_{\nu+1+p/2}(\mu_n) J_\nu(\mu_n y)}{\mu_n^{j+p/2} J_{\nu+1}^2(\mu_n c)} \text{ for } j=1,2. \tag{19}$$

The reduced model of eqs. (17) and (18) is processed further using specific expressions that relate the infinite series of Bessel functions which appear in eqs. (17) and (18) and the Sonine-Schafheitlin integral. In particular it can be shown that

$$\int_0^{\infty} u^{1/2} J_{2m}(u) J_{-1/2}(yu)\, du = \sqrt{2/y}\, {}_2F_1(m+1/2, -m+1/2; 1/2; y^2)/\Gamma(2m+1), \tag{20}$$

$$\int_0^{\infty} u^{-1/2} J_{2m}(u) J_{-1/2}(yu)\, du = \sqrt{1/2y} m^{-1}\, {}_2F_1(m, -m; 1/2; y^2)/\Gamma(2m+1)\ , \tag{21}$$

where ${}_2F_1$ is the hypergeometric function with single variable. Finally, after further mathematical manipulations the dual trigonometrical series of eqs. (17) and (18) are reduced to the more compact forms

$$\chi(\psi)\zeta_0/2 + \sum_{m=1}^{\infty} m^{-1} \zeta_m \cos(m\psi) = F^*(\psi), \qquad (0 < \psi < d^*), \tag{22}$$

$$\zeta_0/2 + \sum_{m=1}^{\infty} \zeta_m \cos(m\psi) = G^*(\psi), \qquad (d^* < \psi < \pi). \tag{23}$$

The new unknowns of the problem are now the coefficients ζ_m, whilst the parameters $\psi, \chi(\psi), F^*(\psi), G^*(\psi)$ depend only on the given data of the problem (via expressions omitted for brevity). Dual trigonometrical series of the form of eqs. (22) and (23) have been treated by several authors (see Sneddon [4]). The coefficients ζ_m are

$$\zeta_0 = \frac{2}{\pi}\left[\frac{1}{\sqrt{2}} \int_0^{d^*} h_1(t)dt + \int_{d^*}^{\pi} G^*(t)dt\right] \tag{24}$$

$$\zeta_m = \frac{2}{\pi}\left[\frac{1}{2\sqrt{2}} \int_0^{d^*} h_1(t)\left[P_n \cos(t) + P_{n-1}\cos(t)\right]dt + \int_{d^*}^{\pi} G^*(t)\cos(mt)dt\right],\ m = 1,2,3,\ldots \tag{25}$$

where P_n denotes the Legendre polynomial of degree n and

$$h_1(t) = 2\frac{d}{dt}\int_0^t \frac{\sin(u/2)}{\sqrt{\cos(u)-\cos(t)}}\left[-\frac{dF^*(u)}{du} + \frac{1}{2}\zeta_0 \frac{d\chi(u)}{du} - \frac{2}{\pi}\sum_{m=1}^{\infty}\left(\int_{d^*}^{\pi} G^*(v)\cos(mv)dv\right)\sin(mu)\right]du\,. \tag{26}$$

4 Some results

Although eqs. (24)-(26) appear in a compact set of expressions, the coefficient ζ_0 lies within the definition of the function $h_1(t)$. The right-hand side of eq. (24) depends on ζ_0, so this coefficient can be computed after rearrangement of terms or by an iterative scheme. Once ζ_0 is accurately evaluated, expression (26) is wholly determined and can be used in eq. (25) to compute the other coefficients. Also, the truncation of the infinite series expressions has to be handled sensitively to ensure that eq. (16) is satisfied accurately and at least 200 modes were found necessary to achieve an accuracy of 4 significant digits for the coefficients ζ_m. The rapid decrease in magnitude of ζ_m, with increasing m, is shown in Fig. 2.

In the following we present some results for wave impacts for which we hold fixed h=1m, β=0.8m, $V_2=(gh)^{1/2}\approx$3m/s and vary α and V_1. The solution process indeed converges quite fast, not only for the leading

term ζ_0 but also for the other expansion coefficients ζ_m, $m>0$. Figs. 3 and 4 show the pressure impulse $p=-\rho\phi$ [see eq. (8)] for unit density ρ, along the lower portion of the wall for several α (Fig. 3) and several values of the velocity V_1 (Fig. 4). As expected the pressure impulse is reduced for lower velocities. An interesting result is that the pressure impulse obtains its maximum value at the bottom. Also, for the same velocities the pressure impulse is decreased for longer wetted sections (Fig. 3). Further fluid mechanical consequences of the results will be presented in the talk.

Acknowledgements
The authors are grateful for the EU Marie Curie Intra-European Fellowship project SAFEMILLS "Increasing Safety of Offshore Wind Turbines Operation: Study of the violent wave loads" under grant 622617.

References

[1] Tranter CJ (1959) Dual trigonometrical series, Glasgow Mathematical Journal 4, 49-57.
[2] Tranter CJ (1960) A further note on dual trigonometrical series, Glasgow Mathematical Journal 4, 198-200.
[3] Tranter CJ (1964) An improved method for dual trigonometrical series, Glasgow Mathematical Journal 6, 136-140.
[4] Sneddon IN (1966) Mixed boundary value problems in potential theory. North Holland Publishing Company, Amsterdam.
[5] Tranter CJ (1969) Some triple trigonometrical series, Glasgow Mathematical Journal 10, 121-12 5.
[6] Kerr G, Melrose G, Tweed J (1994) Some triple sine series, Applied Mathematics Letters 7, 33-36.
[7] Cooke JC, Tranter CJ (1959) Dual Fourier-Bessel series, Quarterly Journal of Mechanics and Applied Mathematics, 12(3), 379-386.

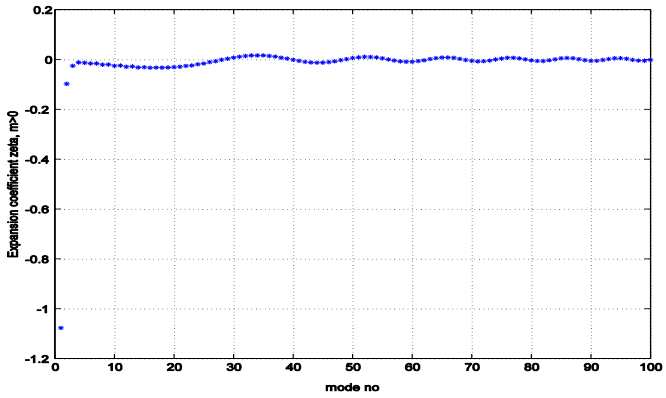

Figure 2 The expansion coefficients ζ_m, $m>0$ for h=1, α=0.1, β=0.8 and V_1=V_2=3 where $\zeta_0=-1.9744$.

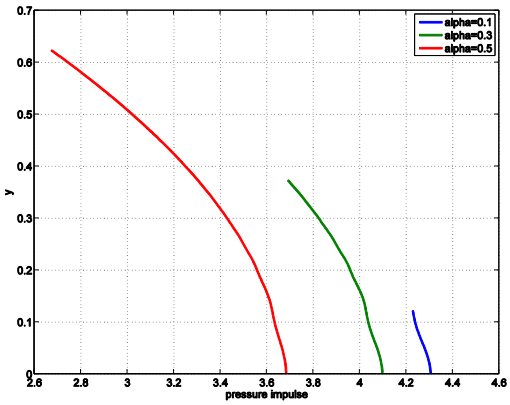

Figure 3 Normalized pressure impulse for equal velocities V_1=V_2=3 and variable α=0.1, 0.3 and 0.5.

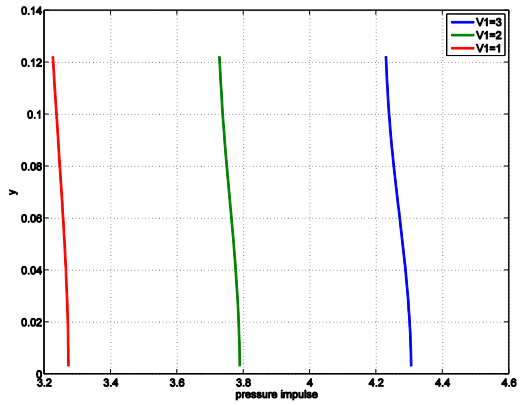

Figure 4 Normalized pressure impulse for α=0.1 and variable velocity V_1=3, 2 and 1.

Added Resistance Simulation of Blunt Ship in Short Wave

by Jikang Chen* and Wenyang Duan
College of Shipbuilding Engineering, Harbin Engineering University, Harbin, China
E-mail: *cjkhrb@sina.com*

Highlights:

- Added resistances of KVLCC2 in short waves are predicted by 2nd order TEBEM and compared with published results by other numerical solutions and experimental results.
- It is found the strength of low-pass filter in numerical treating the free surface elevation plays an important role for accurate predicting the added resistance in short wave.

1. Introduction

The rankine panel method (RPM) for wave-ship interaction has been widely used nowadays. The advantage of RPM is possibility to deal with more complicated free-surface conditions. Nakos (1990), Kring (1994) and Huang (1997) analysed the nonlinear ship motion by a time-domain three dimensional RPM. Kim et al. (2011) compiled a seakeeping analysis program (WISH) for the linear and nonlinear seakeeping analysis and wave loads forecasting by the B-spine RPM. Shao and Faltinsen (2012) proposed a body-fixed formulation to avoid the difficulty which needs to calculate the high order derivatives in the earth coordinate system by HOBEM.

However, a disadvantage of the Rankine panel methods is the necessity of discretization of the free surface surrounding the body, which increases the number of unknowns and also introduces the numerical instability due to the saw-tooth behavior in the time domain numericalsimulations for forward speed problems. Vada and Nakos (1993) and Kim et al (1997) considered that the instability observed in their numerical simulation process were caused by the energy from the external force, which would be accumulated on a wave period with zero group velocity. Buchmann (2000b) pointed out the non-uniformity in the spatially discretized models may cause this phenomenon. However, the reason for the instability has not been fully understood. Several researchers utilized the low-pass filter to suppress the numerical instability. Nakos (1990) and Kring (1994) used five-point filter formulation to suppress the spurious waves for the ship motion RAOs. The seven-point formulation is used by Kim (1997) for the nonlinear interactions of surface waves with bodies without forward speed. He and Kashiwagi (2012) studied the ship steady wave problem using the seven-point formulation. Shao and Faltinsen (2012) utilized a three-point filter to retrain the saw-tooth behavior for the added resistance problem for the fine ship. These numerical experiments had not shown the impacts of the filter for the simulation of blunt ship added resistance problems.

The ship motions are negligible in short waves, and the added resistance is mainly due to wave reflection at the bow. Because the reflection added resistance is very small for fine ship, the strength or frequency of application of the filter causes almost no influence on added resistance of fine ship. However, for large blunt ship, the reflection added resistance in short wave give important contribution in low sea state. It is found application of low-pass filter has sensible influence on the numerical results of added resistance of blunt ship. The strength and frequency of using filter is discussed for KVLCC2 ship.

2. Numerical Method

For forward speed ship motion problems, the velocity potential consists of three components: the steady potential Φ which is computed based on the double-body flow, incident wave potential φ_I and disturbing wave potential φ_d respectively. The potential Φ and φ_d can be obtained by solving each of the following problems :

$$\begin{cases} \nabla^2\Phi = 0 \\ \dfrac{\partial\Phi}{\partial n} = \vec{U}\cdot\vec{n} \quad (on\ S_H) \\ \dfrac{\partial\Phi}{\partial z} = 0 \qquad (on\ S_F) \\ \Phi = 0\left(\sqrt{x^2+y^2+z^2}\to\infty\right) \end{cases} \tag{1a}$$

$$\begin{cases} \nabla^2\varphi_d = 0 \\ \left[\dfrac{\partial}{\partial t} - \left(\vec{U} - \nabla\Phi\right)\cdot\nabla\right]\zeta_d = \zeta_d\dfrac{\partial^2\Phi}{\partial z^2} + \dfrac{\partial\varphi_d}{\partial z} \qquad (on\ S_F) \\ \left[\dfrac{\partial}{\partial t} - \left(\vec{U} - \nabla\Phi\right)\cdot\nabla\right]\varphi_d = \vec{U}\cdot\nabla\Phi - g\zeta_d - \dfrac{1}{2}\left(\nabla\Phi\right)^2 \quad (on\ S_F) \\ \dfrac{\partial\varphi_d}{\partial n} = \sum_{j=1}^{6}\left(\dfrac{\partial\xi_j}{\partial t}n_j + \xi_j m_j\right) - \dfrac{\partial\varphi_I}{\partial n} \qquad (on\ S_H) \\ \varphi_d\big|_{t=0} = 0, \dfrac{\partial\varphi_d}{\partial n}\Big|_{t=0} = 0 \qquad (initial\ condition) \end{cases} \tag{1b}$$

Where $\vec{U}$ is the ship forward speed, ξ_j means the displacement in *j* direction, $\vec{n}$ is the normal vector points out of the fluid domain. The added resistance is calculated by the near-field formulation.

$$
\begin{aligned}
\vec{F}_2 = & \int_{WL} \frac{1}{2}\rho g\left[\zeta-\left(\xi_3+\xi_4 y-\xi_5 x\right)\right]^2\cdot\vec{n}dL-\rho\int_{WL}\left[-\left(\vec{U}-\frac{1}{2}\nabla\Phi\right)\cdot\nabla\Phi\right]\left[\zeta-\left(\xi_3+\xi_4 y-\xi_5 x\right)\right]\cdot\vec{n}_1 dL \\
& -\rho\int_{WL}\vec{\delta}\cdot\nabla\left[-\left(\vec{U}-\frac{1}{2}\nabla\Phi\right)\cdot\nabla\Phi\right]\left[\zeta-\left(\xi_3+\xi_4 y-\xi_5 x\right)\right]\cdot\vec{n}dL-\rho\iint_{S_H} gz\cdot\vec{n}_2 ds \\
& -\rho\iint_{S_H}\frac{1}{2}\nabla\left(\varphi_I+\varphi_d\right)^2\cdot\vec{n}ds-\rho\iint_{S_H}\vec{\delta}\cdot\nabla\left[\frac{\partial\left(\varphi_I+\varphi_d\right)}{\partial t}-\left(\vec{U}-\nabla\Phi\right)\cdot\nabla\left(\varphi_I+\varphi_d\right)\right]\cdot\vec{n}ds \\
& -\rho\iint_{S_H}\left[g\left(\xi_3+\xi_4 y-\xi_5 x\right)+\frac{\partial\left(\varphi_I+\varphi_d\right)}{\partial t}-\left(\vec{U}-\nabla\Phi\right)\cdot\nabla\left(\varphi_I+\varphi_d\right)\right]\cdot\vec{n}_1 ds \\
& -\rho\iint_{S_H}\left[-\left(\vec{U}-\frac{1}{2}\nabla\Phi\right)\cdot\nabla\Phi\right]\cdot\vec{n}_2 ds-\rho\iint_{S_H}\vec{\delta}\cdot\nabla\left[-\left(\vec{U}-\frac{1}{2}\nabla\Phi\right)\cdot\nabla\Phi\right]\cdot\vec{n}_1 ds
\end{aligned}
\tag{2}
$$

Where ζ is the wave elevation, δ is the total displacement of ship motion, *WL* represents the waterline.

TEBEM method (Duan et al. ,2014) is used to solve the boundary value problem. A low-pass filter similar(Shao and Faltinsen, 2012) is applied on the collocation points on the free surface to restrain the instability of wave elevation.

$$
\bar{\zeta}_j = c\zeta_{j-1}+(1-2c)\zeta_j+c\zeta_{j+1} \tag{3}
$$

Where the subscript *j* is mesh number of collocation point. *c* is the strength of low-pass filter, $\bar{\zeta}$ means the wave elevation after smoothing. The filter will affect the solution of velocity potential indirectly through the dynamic free-surface conditions. At each time step the filter is first applied in the azimuthal direction for all points on the free surface panels and then the filter is used in the radial direction for all points on the free surface.

3. Numerical Results and Discussion

To show the role of the strength of low-pass filter on the added resistance in short wave, A typical public blunt ship KVLCC2 ship model in head sea is selected as demonstration.

Calculation condition for KVLCC2 in short wave

Ship motion	Heave and Pitch	Wave length λ / L	0.3
Time-step	0.01T	Simulation time	35T
Free-surface panel	1525	Free-surface size	$5L_{PP}$
Body-surface panel	1212	Damping zone type	O-type grid
Strength of the filter	0.002,0.003,0.004	Damping zone size	$2L_{PP}$
Forward speed	Fr=0.142	Damping zone strength	$\mu_0=15$

Figure 1 and 2 show the panel discretization on the half free surface and body surface, the triangle elements were used on hull surface of the bow and stern part. Fig.3 and 4 show the motion response of the heave and pitch of KVLCC2 model respectively, where the length ratio of wave to ship is from 0.3 to 2.0. The added resistance is shown in Fig.5. The agreement is good between the 2nd TEBEM and the other numerical solution and experiment results. In Fig.6, the contribution of the bow, stern and middle part of KVLCC2 for added resistance at $\lambda / L = 0.3$ is shown. It is found the contribution to the added resistance in short waves is primarily from bow segment, whereas the stern and middle part is quite small. Fig.7 and 8 show the contribution from the waterline and square of velocity integration for the added resistance at the bow part. It can be seen the waterline integration is almost twice of the square of velocity integration but in opposite sign.

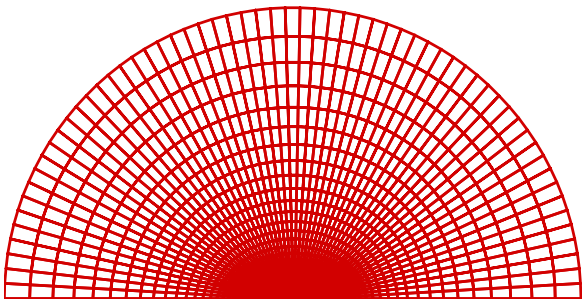

Fig.1 the panel sketch of the free surface

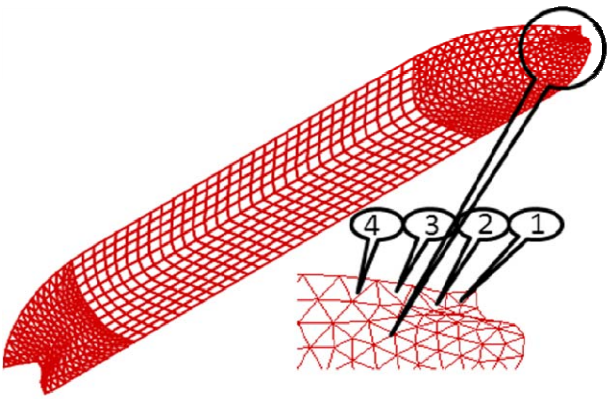

Fig.2 the panel sketch of the body surface

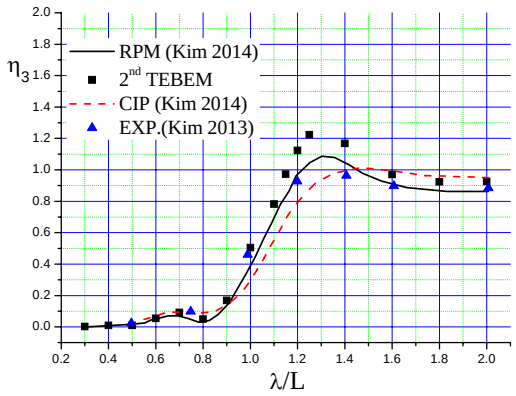

Fig.3 comparison of heave RAOs between experiment and numerical solution

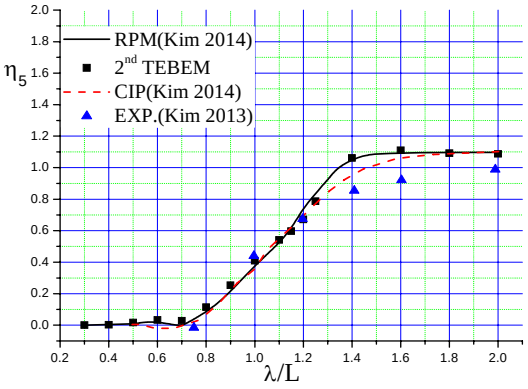

Fig.4 comparison of pitch RAOs between experiment and numerical solution

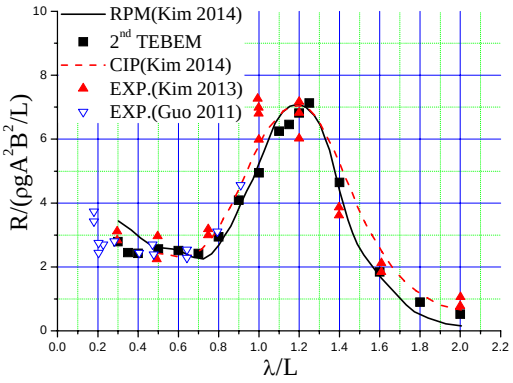

Fig.5 comparison of added resistance between experiment and numerical solution

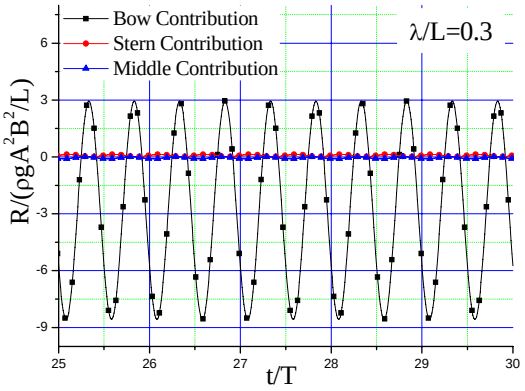

Fig.6 added resistance components from the different parts of the KVLCC2 at $\lambda / L = 0.3$

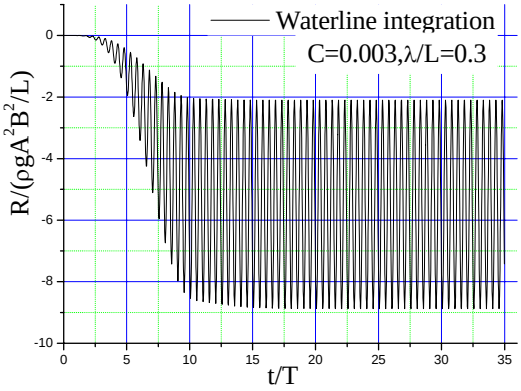

Fig.7 contribution of the waterline integration for added resistance due to the bow part at $\lambda / L = 0.3$

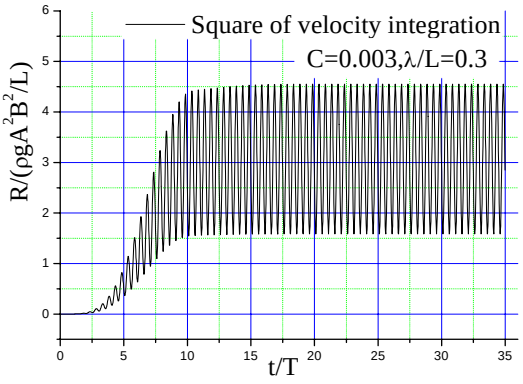

Fig.8contribution of the square of velocity integration for added resistance due to the bow part at $\lambda / L = 0.3$

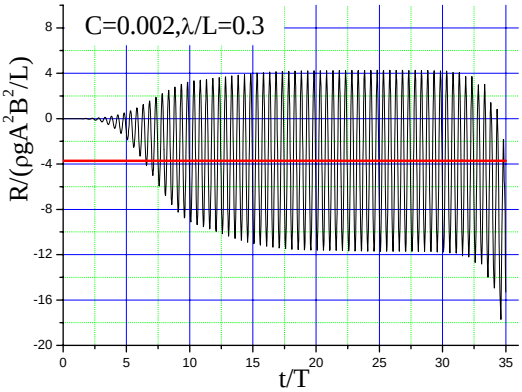

Fig.9 the history of added resistance at $\lambda / L = 0.3, C = 0.002$

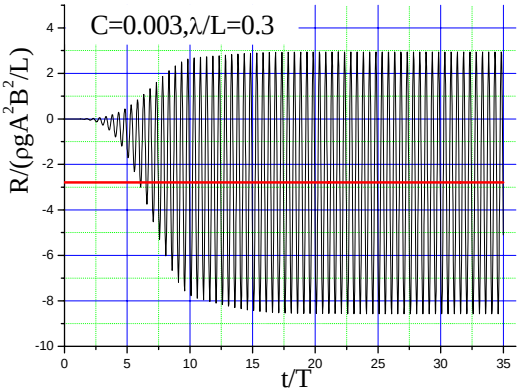

Fig.10 the history of added resistance at $\lambda / L = 0.3, C = 0.003$

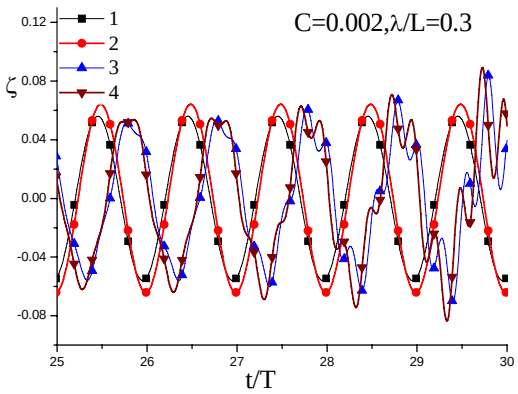

Fig.11 the history of wave elevation at waterline collocation points at $\lambda / L = 0.3, C = 0.002$

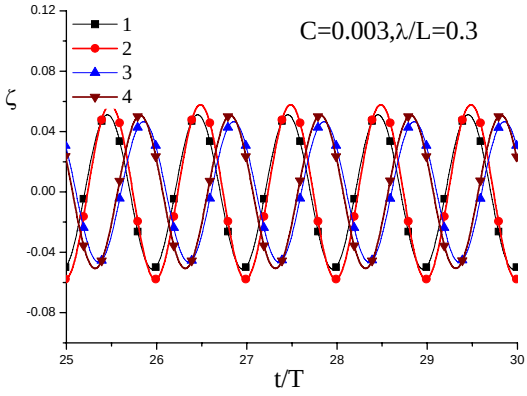

Fig.12 the history of wave elevation at waterline collocation points at $\lambda / L = 0.3, C = 0.003$

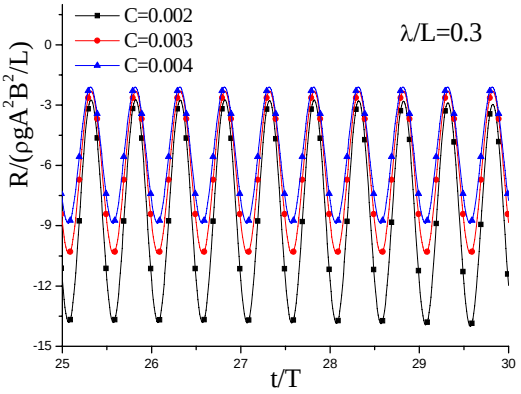

Fig.13 the history of added resistance due to the waterline integration on the bow part surface at $\lambda / L = 0.3$

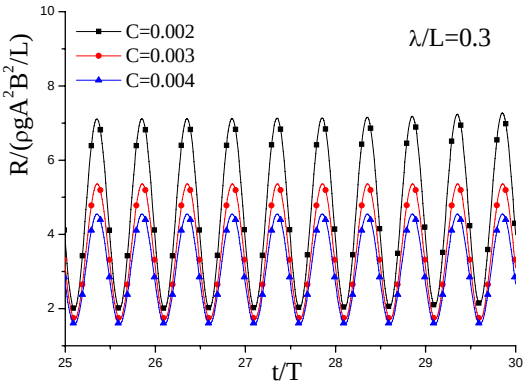

Fig.14 the history of added resistance due to the square of velocity integration on the bow part surface at $\lambda / L = 0.3$

Fig.9 and 10 show the history of the added resistance value with different strength of low-pass filter, the wave elevation around the bow are shown in Fig.11 and 12. It can be seen the history is not stable when the strength of filter is equal to 0.002. Form Fig. 9 and 11, although the added resistance is stable for period $t / T = 20 - 30$, but it is changed after 30 and the wave elevation values has been chaotic for period $t / T = 20 - 30$. So the added resistance is not consistent with local fluid flow as $C = 0.002$. Fig.13 and 14 show the waterline and square of velocity integration vary with different strength of filter, it can be concluded that the strength of filter play a key role for the added resistance prediction in short waves.

References

[1] Nakos D.E., 1990, Ship Wave Patterns and Motions by a Three Dimensional Rankine Panel Method. PhD. Thesis, MIT.

[2] Kring D.C., 1994, Time domain ship motions by a three dimensional Rankine panel method, PhD. Thesis, MIT.

[3] Huang Y.F., 1997, Nonlinear ship motions by a Rankine panel method, PhD. Thesis, MIT.

[4] Song M.J., Kim K.H. and Kim Y.H., 2011, Numerical analysis and validation of weakly nonlinear ship motions and structural loads on a modern containership, Ocean Engineering, 38,77-87.

[5] Shao Y.L and Faltinsen O.M., 2012, Linear seakeeping and added resistance analysis by means of body-fixed coordinate system, J. Mar. Sci. Technol., 17(4), 493-510.

[6] Vada T. and Nakos D., 1993, Time-marching schemes for ship motion simulations. 8th International Workshop on Water Waves and Floating Bodies, Canada (Newfoundland).

[7] Kim Y.H., Kring D.C. and Sclavounos P.D., 1997, Linear and nonlinear interactions of surface waves with bodies by a three dimensional Rankine panel method. Applied Ocean Research, 19, 235-249.

[8] Buchmann B., 2000b, Accuracy and stability of a set of free-surface time-domain boundary element models based on B-splines. Int. J. Numer. Methods Fluids. 33(1), 125-155.

[9] He G.H. and Kashiwagi M., 2012, Time Domain Simulation of Steady Ship Wave Problem by a Higher-Order Boundary Element Method. Proceedings of 22th International Offshore and Polar Engineering Conference. Greese.

[10] Duan W.Y., Chen J.K. and Zhao B.B., 2014, Second order wave loads based on second order TEBEM, 29th International Workshop on Water Waves and Floating Bodies, Japan(Osaka).

[11] Guo B.J. and Stern S., 2011, Evaluation of added resistance of KVLCC2 in short waves. Journal of Hydrodynamics, 23(6), 709-722.

[12] Kim K.H., Yang K.K. and Seo M.G., 2013, Computational analysis of added resistance in short waves, International Research Exchange Meeting of Ship and Ocean Engineering in Osaka.

Particle–In–Cell Numerical Solver for Free Surface Flows with Fluid–Solid Interactions

by Q. Chen[1,*] , J. Zang[1] , D. M. Kelly[2,3], C. J. K. Williams[1] and A. Dimakopoulos[2]

[1]Department of Architecture and Civil Engineering, University of Bath, BA2 7AY, U.K.
[2]H R Wallingford, Wallingford, Oxon, OX10 8BA, U.K.
[3]International Hurricane Research Center, Florida International University, Miami FL 33199, USA
Email: chenqiang913@hotmail.com

Highlights:

• This paper presents a novel numerical approach based on the Particle–In–Cell (PIC) technique for the solution of the incompressible Navier–Stokes equations with emphasis on free surface deformation and two–way fluid–solid interactions. As a hybrid Eulerian–Lagrangian approach, this method has the flexibility of the Smoothed Particle Hydrodynamic (SPH) method as well as the efficiency of an Eulerian method.

• Two–way fluid–solid interaction simulation has been integrated inside the numerical model by adopting the Distributed Lagrangian Multiplier (DLM) technique proposed in Patankar [7].

1 Introduction

In the past few decades Computational Fluid Dynamics (CFD) techniques have been widely used for both academic research and commercial engineering applications. CFD techniques have become more and more popular as computational power has continued to increase. For the solution of the Navier–Stokes equations three principal approaches are typically employed these being: Eulerian methods, Lagrangian methods and hybrid Eulerian-Lagrangian methods. While grid based Eulerian methods perform well in terms of equation discretization, enforcing incompressibility and improving computational efficiency[3], they have drawbacks with regards to integration of the advection term and require more effort in handling the free surface boundary especially when its is subject to extensive deformation. From this point of view, purely Lagrangian techniques such as the SPH method and Moving Particle Semi Implicit (MPS) schemes seem to be more suitable for free surface fluid problems as they can handle large free surface deformation easily (e.g.[1]). In addition Lagrangian methods can integrate the advection term relatively trivially through advecting the discretized fluid elements. However, pure Lagrangian methods tend to be extremely demanding in terms of CPU time as millions of particles may be used for high accuracy (e.g.[1]).

Our work is motivated by the idea of developing a hybrid Eulerian–Lagrangian approach based on the PIC framework which exhibits both the flexibility of the SPH method in terms of ability to simulate complex problems and the computational efficiency of Eulerian methods. The PIC method was originally devised for compressible flows by Francis Harlow [5] in 1955. The idea being that particles, which carry and advect fluid mass and momentum, are seeded on an underlying mesh on which the main process of solving the Navier Stokes equations is undertaken. Information between particles and the grid is transferred via interpolations. The *classic* PIC method (e.g. [5]) suffered from high numerical dissipation due to the direct velocity transfer at each time step. Brackbill and Ruppel [2] suggested incrementing the particle velocity by the change of velocity on the grid, which reduced the dissipation significantly. In a previous work the authors applied the PIC technique to various complicated 2D flow problems including full two–way fluid–solid interactions can be found in [6]. In this paper we will present a 2D validation case and an example case from the 3D version of the PICIN numerical model which is currently under development.

2 Numerical model

The numerical model employs the framework of PIC methodology and solves the incompressible Navier Stokes equations for a Newtonian fluid in both 2 and 3 spatial dimensions. Two–way fluid–solid

interaction model is integrated inside this model using the approach proposed in [7], which forms part of the overall governing equations :

$$\nabla \cdot \vec{u} = 0 \quad \text{in } \Omega, \tag{1}$$

$$\mathbf{D}[\vec{u}] = 0 \quad \text{in } \mathbb{S}, \tag{2}$$

$$\frac{\partial \vec{u}}{\partial t} + (\vec{u} \cdot \nabla)\vec{u} = \vec{f} - \frac{1}{\rho}\nabla p + \nu \nabla^2 \vec{u} \quad \text{in } \mathbb{F}, \tag{3}$$

$$\frac{\partial \vec{u}}{\partial t} + (\vec{u} \cdot \nabla)\vec{u} = \vec{f} - \frac{1}{\rho_S}\nabla p + \nabla \cdot \mathbf{\Pi} \quad \text{in } \mathbb{S}, \tag{4}$$

with boundary conditions:

$$\vec{u} = \vec{u}_\Gamma(t) \quad \text{on } \Gamma(t) \tag{5}$$

and:

$$\vec{u} = \vec{u}_i \text{ and } (\mathbf{\Pi} - p\mathbf{I}) \cdot \hat{\vec{n}} = \vec{T} \quad \text{on } \partial\mathbb{S}(t), \tag{6}$$

where Ω, $\mathbb{F}$ and $\mathbb{S}$ denote the overall computational domain, fluid region and solid region. Γ and $\partial\mathbb{S}$ represent the overall solid boundary and solid region boundary. $\vec{u}$ is the velocity field, p represents the pressure, $\vec{f}$ is the gravity force, ν accounts for the fluid dynamic viscosity coefficient, and ρ and ρ_S are the fluid density and solid density, respectively. $\vec{u}_\Gamma(t)$ and $\vec{u}_i$ represents boundary velocity and $\vec{T}$ is the traction force of the fluid on the solid. As an incompressibility constraint, equation (1) ensures a divergence free velocity field in the whole domain and gives rise to pressure field as a Lagrange Multiplier. Similarly, Equation (2), which represents a rigid body constraint, enforces a deformation free velocity field. Here $\mathbf{\Pi}$ is the extra deformation stress in addition to pressure and it is nothing but distributed Lagrange Multiplier due to rigid body constraint [7]. It is noted that for any vector $\vec{u}$, $\mathbf{D}[\vec{u}] = \left[\nabla\vec{u} + (\nabla\vec{u})^T\right]/2$, which measures the spatial deformation of $\vec{u}$.

The overall solution has been divided into two major steps, i.e. Eulerian step and Lagrangian step. In the Eulerian step, the pressure projection technique of Chorin [4] has been adopted to solve for fluid motion on the MAC grid. A second–order accurate technique has been employed here for the Dirichlet–type free surface boundary condition and the non grid–aligned solid boundary is resolved via a cut–cell approach. In the Lagrangian step the particles, which are initially seeded inside the fluid cells, are advected. They carry with them the updated divergence free velocity field interpolated from the grid. Thus, the advection term of Navier–Stokes equation is integrated with respect to time. We note here that the velocity field will be transferred back to the grid for the next time step computation after the particles are advected. The two–way fluid solid interaction is treated in a manner such that the solid objects are firstly solved as if they were fluid and then a velocity correction inside the solid region is made by taking account of the density difference between solid and fluid. The rigid body restraint is finally enforced by finding a unique solid velocity considering all the momentum contributions from solid region. This technique is straightforward to implement and can treat floating bodies very efficiently. More details of the numerical model can be found in Kelly et al. [6].

3 Case study

3.1 Case 1 : Movement of caisson breakwater

A 2D case of caisson breakwater movement was used for the validation of our 2D numerical model. This case was previously investigated experimentally in Wang et al [9] and numerically in Rogers et al [8] by SPH method. Figure 1 depicts the simulation sketch of a wave paddle generating waves that travel to impact the caisson breakwater which was placed on a fixed foundation and allowed to move horizontally . The generated wave has a period of 1.3s and a height of 0.15m. The caisson was given a density of 1440 kg/m^3 and the numerical fiction force between caisson and the foundation was adopted following the method proposed in [8], where the fiction force was switched from static force and dynamic force based on the relationship between caisson velocity and a threshold velocity which we found had a very sensitive effect on the motion of caisson. Here, following [8], the caisson foundation is considered to be impermeable. The simulation presented here used a cell size of $\Delta x = \Delta z = 0.013m$ with a total number of about 64,000 particles. The CFL number was set at 0.5 to adapt the time step and it took about 1.4hrs for 15 seconds of simulation on an Intel(R) i5-3470 CPU@3.2GHz core.

Figure 2 shows snapshots of our simulation at time instants roughly similar to those presented in [8]. A comparison of results shows that the wave behavior is similar to that observed in [8]. Figure 3 presents comparisons of the caisson displacement and overall horizontal wave force between experimental data and numerical results. It is noted here that the experimental data has some limitations for a comprehensive comparison as reported in [8]. We started to measure the displacement data around the time instant when the caisson was just activated to move backward after a slight forward motion due to seaward water level decline because of the first wave propagation and the wave force was compared from our first relatively stable wave force. It can be seen from Figure 3(a) that the numerical fiction force sensitively influences the motion of caisson though the displacement magnitude is captured by the numerical model. Also, in Figure 3(b), the agreement of impact peak wave force and lowest wave force are acceptable though slight phase difference occurs. Overall, the numerical model quantitatively captures the principal characteristics of caisson movement due to wave actions.

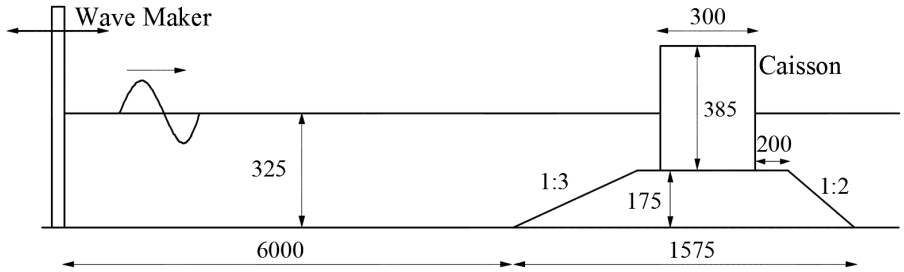

Figure 1: Numerical model set-up for caisson breakwater (Units: mm).

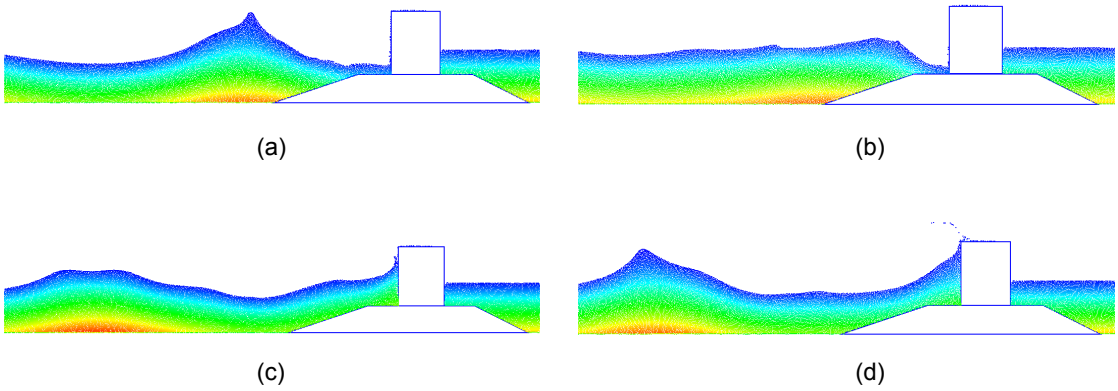

Figure 2: Snapshots of numerical simulation for caisson movement. The colour represents pressure field ranging from min value 0 kPa(blue) to max value 4 kPa (red).

3.2 Case 2 : 3D solid impacting water surface

A falling missile–shaped object impacting water surface case was used to test our 3D version PIC solver. Figure 4 shows snapshots of the numerical simulation – an object falls into water within a tank and causes water surface evolution due to the impact. This is an on-going study using our recently developed 3D version of the PIC solver, we will present more results in the workshop.

Acknowledgments

The authors acknowledge with thanks the financial support of the University of Bath and HR Wallingford.

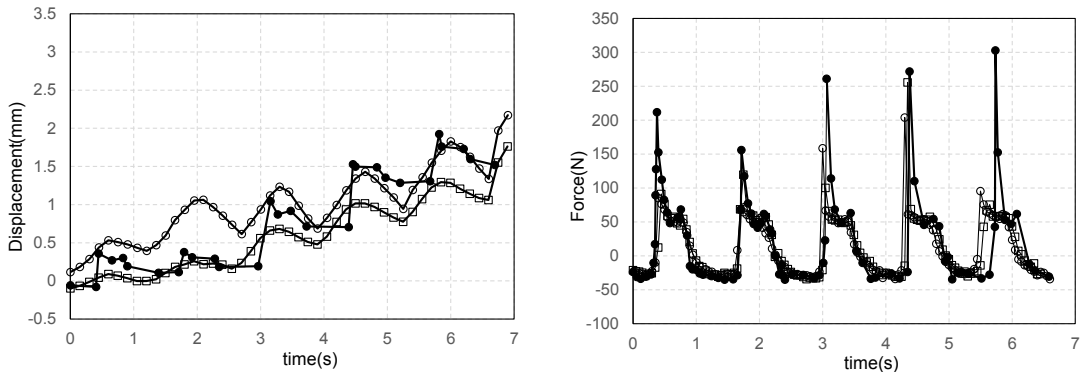

(a) Caisson displacement (b) Wave force

Figure 3: Comparisons between experimental data and numerical results of moving caisson under wave actions. Line with "•": Experimental data; Line with "□":Numerical results, threshold velocity set at 1mm/s; Line with "○":Numerical results, threshold velocity set at 2mm/s .

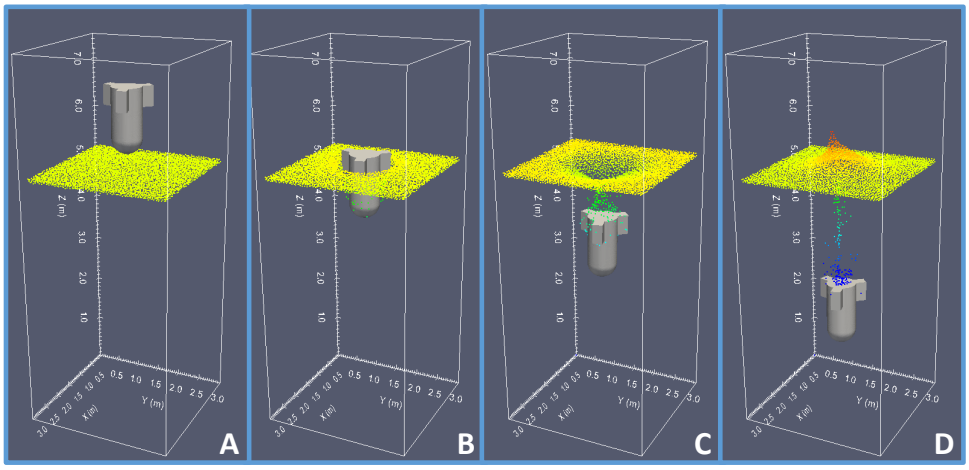

Figure 4: Snapshots of numerical simulation for solid impacting free surface. The colour represents the height of free surface particle position; the warmer colour means the higher position.

References

[1] B. Bouscasse, A. Colagrossi, S. Marrone, and A. Souto-Iglesias. Viscous flow past a circular cylinder below a free surface. In J. M. Smith, editor, *Proceedings of the ASME 2014* 33^{rd} *Int. Conf. on Ocean, Offshore & Arctic Engineering.*, San Fransisco, USA, 2014. OMAE.

[2] J. U. Brackbill and H. M. Ruppel. FLIP: A method for adaptively zoned, Particle-In-Cell calculations of fluid flows in two dimensions. *J. Comp. Phys.*, 65:314–343, 1986.

[3] R. Bridson. *Fluid Simulation for Computer Graphics.* A K Peters, Ltd, 2008.

[4] A. J. Chorin. Numerical solution of the Navier-Stokes equations. *Mathematics of computation*, 22:745–762, 1968.

[5] F. H. Harlow. A machine calculation method for hydrodynamic problems. Technical Report LAMS-1956, Los Alamos Scientific Laboratory, Los Alamos, 1955.

[6] D. M. Kelly, Q. Chen, and J. Zang. PICIN: A particle-in-cell solver for incompressible free surface flows with two-way fluid solid coupling. *Submitted to SIAM Journal*, 2014.

[7] N. A. Patankar. A formulation for fast computations of rigid particulate flows. *Center for Turbulence Research Annual Research Briefs*, 2001:185–196, 2001.

[8] B. D. Rogers, R. A. Dalrymple, and P. K. Stansby. Simulation of caisson breakwater movement using 2-D SPH. *Journal of Hydraulic Research*, 48(S1):135–141, 2010.

[9] Y.-Z. Wang, N.-N. Chen, and L.-H. Chi. Numerical simulation on joint motion process of various modes of caisson breakwater under wave excitation. *Communications in numerical methods in engineering*, 22(6):535–545, 2006.

Dispersion relation and instability onset of Faraday waves

Didier CLAMOND and Jean RAJCHENBACH

Université de Nice – Sophia Antipolis, Parc Valrose, 06108 Nice cedex 2, France.
E-Mail: didier.clamond@gmail.com, jean.rajchenbach@unice.fr

Highlights: Faraday waves; parametric excitation; dispersion relation; stability; bifurcation; wavenumber selection.

1 Introduction

Many studies have been devoted to the phenomenon of Faraday waves, which appear at the free surface of a fluid when the container is submitted to periodical vertical oscillations [3, 9, 12]. The interest of this setup is that it gives rise to the formation of various patterns. According to the forcing amplitude, frequency and fluid viscosity, the free surface can exhibit standing solitary waves [2, 16, 19] or patterns of different symmetry, such as stripes, squares, hexagons, quasicrystalline ordering, or star-shaped waves [4, 5, 6, 15]. These symmetry breaking result from the nonlinear couplings between waves. Thus, the study of Faraday waves constitutes a privileged way to explore complex nonlinear phenomena by the mean of a simple experimental device. Understanding these waves has also applications in hydrodynamics, for instance in sloshing related problems.

Despite noticeable advances in the theoretical understanding of Faraday waves [11, 13, 14, 18] some of their fundamental properties remain into darkness. For instance, the relation of dispersion $\omega(k)$ of parametrically-forced water waves is often erroneously identified with that of free, unforced surface waves; this approximation holding only without forcing and without dissipation. However, the knowledge of the exact dispersion relation is of crucial importance.

The first aim of this work is to establish the actual relation of dispersion of Faraday waves for *nonzero* forcing and dissipation. As shown below, the dispersion relation of free, unforced waves is significantly altered in the case of parametrically–forced excitations: two different wavenumbers correspond then to the same angular frequency. We carry out their stability analysis and we discuss the nature of the bifurcation giving rise to the wavy surface state from the rest state when the forcing is increased. Thus, the threshold of the Faraday instability is established as well as the selected wavenumbers in both cases of short and long waves. At last, it is shown that the transition can be either smooth (supercritical) or discontinuous and hysteretic (subcritical), depending on the thickness of the liquid layer.

2 Mathieu equation

Consider a container partly filled with a Newtonian fluid of depth d, moving up and down in a purely sinusoidal motion of angular frequency Ω and amplitude $\mathcal{A}$, so that the forcing acceleration is $\Omega^2\mathcal{A}\cos(\Omega t)$. In the reference frame moving with the vessel, the fluid experiences a vertical acceleration due to the apparent gravity $G(t) \equiv g - \Omega^2\mathcal{A}\cos(\Omega t)$, g being the gravity acceleration in the laboratory frame of reference and t being the time.

Let be $\boldsymbol{x} = (x_1, x_2)$ and y respectively the horizontal and upward vertical Cartesian coordinates moving with the vessel. Ordinates $y = -d$, $y = 0$ and $y = \eta(\boldsymbol{x}, t)$ respectively correspond to the horizontal impermeable bottom, of the liquid level at rest and of the impermeable free surface. The Fourier transform of the latter is $\zeta(\boldsymbol{k}, t) \equiv \iint_{-\infty}^{\infty} \eta(\boldsymbol{x}, t) \exp(-\mathrm{i}\boldsymbol{k}\cdot\boldsymbol{x})\mathrm{d}^2\boldsymbol{x}$, where $\mathrm{i}^2 = -1$ and $\boldsymbol{k}$ is the wave vector with $k = |\boldsymbol{k}|$.

For parametrically-driven infinitesimal surface waves, ζ is described by a damped Mathieu equation [3, 4]

$$\zeta_{tt} + 2\,\sigma\,\zeta_t + \omega_0^2\,[\,1 - F\cos(\Omega t)\,]\,\zeta = 0, \quad (2.1)$$

where $\sigma = \sigma(k)$ is the viscous attenuation, $\omega_0 = \omega_0(k)$ is the angular frequency of linear waves without damping and without forcing, and $F = F(k)$ is a dimensionless forcing. For pure gravity waves in finite depth, we have

$$\omega_0^2 = gk\,\tanh(kd), \quad F = \Omega^2\,\mathcal{A}\,/\,g. \quad (2.2)$$

In (2.1), the damping coefficient σ originates in the bulk viscous dissipation and in the viscous friction with the bottom in the case of shallow water. For free gravity waves in the limit of

small viscosity, we have [7, 8]

$$\sigma = \nu k^2 \left[2 + \frac{\coth(2kd)}{\sinh(2kd)}\right] + \frac{k\sqrt{k\nu c_0/2}}{\sinh(2kd)} \quad (2.3)$$

where ν is the fluid kinematic viscosity and $c_0 = \sqrt{gd}$. The first term in the right-hand side of (2.3) represents the bulk dissipation, while the second one models the friction with the bottom.

It is well known that systems obeying a (damped) Mathieu equation with excitation angular frequency Ω exhibit a series of resonance conditions for response angular frequencies ω equal to $n\Omega/2$, n being an integer [1]. These solutions are expressed in term of the Mathieu functions together with a dispersion relation involving the so-called *Floquet exponent*. Mathieu functions are transcendent and cannot be expressed in term of simple functions in closed form. In order to understand qualitatively these solution we therefore consider here approximations in the limit of small forcing and dissipation.

Assuming $F \ll 1$ and $\sigma \sim \mathrm{O}(F)$, an approximate dispersion for the sub-harmonic response ($n = 1$) is (with $n = 1$, $\omega = \Omega/2$)

$$\omega_0 \,/\, \omega \;\approx\; 1 \;\pm\; \sqrt{(F/4)^2 - (\sigma/\omega)^2}, \quad (2.4)$$

where ω_0 is related to k via (2.2). One condition to obtain stationary waves is that ω_0 is real, thus defining a threshold $F_\downarrow = 4\sigma/\omega$ with $F > F_\downarrow$ for the forcing in order to obtain time-periodic waves. Interestingly, we note that there are *two* wavenumbers k corresponding to the same wave angular frequency ω (for Ω, F and σ given), whatever the relation $\omega_0 = \omega_0(k)$.

Assuming now $F \ll 1$ and $\sigma \sim \mathrm{O}(F^2)$, an approximate dispersion for the harmonic response ($n = 2$, $\omega = \Omega$) is

$$\omega_0 \,/\, \omega \;\approx\; 1 + \tfrac{1}{12}F^2 \pm \sqrt{\tfrac{1}{64}F^4 - (\sigma/\omega)^2}. \quad (2.5)$$

The condition of reality for ω defines the threshold $F^2 \geqslant 8\sigma/\omega$. Analog approximations for all n can be easily derived.

Despite a limited range of validity, these relations clearly demonstrate that two wavenumbers (i.e., two $\omega_0 \equiv \omega_0^{\pm}$) correspond to the angular frequency $\omega = n\Omega/2$. Equations (2.4) and (2.5) result from a linear approximation, and their validity is restricted to waves of infinitesimal amplitude. However, nonlinearities play a significant role for waves of finite amplitudes, and we will now look closely at the nonlinear effects in an amplitude equation.

3 Amplitude equation

Seeking for an approximation in the form $\eta(x,t) = \mathrm{Re}\{A(t)\}\cos(kx) + \mathrm{O}\big(A^2\big)$, assuming $|kA| \ll 1$ and weak forcing and dissipation (i.e., $F \sim \mathrm{O}(|A|^2)$ and $\sigma \sim \mathrm{O}(|A|^2)$) an equation for the slowly modulated amplitude A can be derived in the form [10, 13]

$$\frac{\mathrm{d}A}{\mathrm{d}t} + (\sigma - \mathrm{i}\omega_0)\,A - \frac{F\Omega}{8\mathrm{i}}\,\mathrm{e}^{\mathrm{i}\Omega t}A^* - \frac{K\Omega k^2}{2\mathrm{i}}\,|A|^2 A = 0, \quad (3.1)$$

a star denoting the complex conjugate. It is obvious that the sign of the nonlinear term in (3.1), via the sign of K, plays a key role in the stability of the solutions.

For pure gravity waves on finite depth, we have [17] (with $s = \mathrm{sech}(2kd)$)

$$K = \frac{2 - 6s - 9s^2 - 5s^3}{16(1+s)(1-s)^2}.$$

Note that K changes sign with the depth: $K > 0$ for short waves, $K < 0$ for long waves and $K = 0$ for $kd \approx 1.058$. Defining $B = A\exp(\frac{\mathrm{i}}{4}\pi - \frac{\mathrm{i}}{2}\Omega t)$, (3.1) yields

$$\frac{\mathrm{d}B}{\mathrm{d}t} = \left(\mathrm{i}\omega_0 + \frac{\Omega}{2\mathrm{i}} - \sigma\right)B + \frac{F\Omega}{8}B^* + \frac{K\Omega k^2}{2\mathrm{i}}|B|^2 B, \quad (3.2)$$

which is a more convenient form for the analysis below.

We focus now on two solutions of (3.2) that are of special interest here: the rest $B = 0$ and the standing wave of constant amplitude. The first one is trivial and we investigate below its stability. The second one is obtained seeking for solutions of the form $B = a\exp(\frac{\mathrm{i}}{4}\pi - \mathrm{i}\delta)$, a and δ being constants, equation (3.2) yielding thus

$$\frac{\omega_0}{\omega} = 1 + K(ka)^2 \pm \sqrt{\frac{F^2}{16} - \frac{\sigma^2}{\omega^2}}, \quad (3.3)$$

with $\omega = \Omega/2$. As $a \to 0$, the approximate dispersion relation (2.4) is recovered. If $F = \sigma = 0$, the dispersion relation of weakly nonlinear, unforced, standing waves in finite depth is recognised too. Therefore, compared to free nonlinear waves, the dispersion relation of parametrically-forced waves is characterised by the shift in angular frequency $\Delta\omega = \pm\sqrt{(F\omega/4)^2 - \sigma^2}$ independent of the wave amplitude a.

In the subsequent discussion, we consider that the relation $K(k)$ is uni-valued and we limit our study to the case $K > 0$ (for $K < 0$ the analysis is similar replacing $\omega_0 - \omega$ by $\omega - \omega_0$).

According to the equation (3.3), we have

$$K(ka)^2 \;=\; \frac{\omega_0}{\omega} \;-\; 1 \mp \sqrt{\left(\frac{F}{4}\right)^2 - \left(\frac{\sigma}{\omega}\right)^2}, \quad (3.4)$$

with the constraint $K(ka)^2$ to be real and positive. The last term in the right-hand side of (3.4) being real, the forcing F must exceed a minimum value $F_\downarrow = 4\sigma/\omega$ to generate at least a stationary nonzero amplitude wave, as already mentioned above. The condition $F > F_\downarrow$ being fulfilled, if we have moreover $F < F_\uparrow$ with

$$F_\uparrow \;\equiv\; 4\,\omega^{-1}\,\sqrt{(\omega_0 - \omega)^2 \,+\, \sigma^2}\,,$$

there are two stationary solutions of nonzero amplitude of the dispersion relation (in addition to the solutions with the opposite phase and to the rest solution $B = 0$).

If $F > F_\uparrow$, the positivity of the right-hand side of (3.4) yields only one nonzero solution of (3.1) (in addition to the solution with the opposite phase and to the rest solution). Thus, disregarding the phase, the flat surface is the unique solution for $F < F_\downarrow$, there are three solutions (one being the rest) in the range $F_\downarrow < F < F_\uparrow$, and two solutions (one being the rest)) in the range $F > F_\uparrow$. An important question to address now is, whether or not, these stationary solutions are stable.

4 Stability analysis

Introducing a small perturbation into the stationary solutions of the amplitude equation (3.2), we look for the eigenvalues of the linearised system of equations obeyed by the perturbation. The stability analysis that we conduct below resembles that carried out in [10] for the parametric pendulum. However, a *major* difference is that the eigenfrequency of a freely-oscillating pendulum is unique, whereas free, unforced, water waves exhibit a continuous spectrum of mode frequencies. Moreover, the sign of the nonlinear terms in the wave equation depend on the depth [17].

First, we study the bifurcation from rest (i.e., the stability of the trivial solution $B = 0$). The linearised equation (3.2) has two eigenvalues λ_1 and λ_2 such that

$$\lambda_j \;=\; -\sigma \;+\; (-1)^j \sqrt{(F\,\omega\,/\,4)^2 - (\omega - \omega_0)^2}\,.$$

If $(F\omega/4)^2 < (\omega - \omega_0)^2 + \sigma^2$, the real parts of both eigenvalues are negative. Therefore, the rest is stable. If $(F\omega/4)^2 > (\omega - \omega_0)^2 + \sigma^2$, the eigenvalue λ_2 is real and positive. Therefore, the rest is unstable and

$$F_\uparrow \;=\; 4\,\sqrt{(1 - \omega_0/\omega)^2 \,+\, (\sigma/\omega)^2} \qquad (4.1)$$

corresponds to the minimal forcing necessary to destabilise the rest state and to generate surface waves.

Second, we analyse the stability of the permanent solutions of finite amplitude $a > 0$ of the amplitude equation (3.2). We consider, for simplicity, small perturbations in the form $B = [a + b(t)]\exp \mathrm{i}(\pi/4 - \delta)$, a, δ and ω_0 being given in (3.3), and b a complex amplitude to be determined such that $|b| \ll a$. To the linear approximation, the eigenvalues of the resulting equation are ($j = 1, 2$)

$$\lambda_j \;=\; -\sigma \;+\; (-1)^j \times$$
$$\sqrt{\sigma^2 - K(2\omega ka)^2\left[1 - \omega_0^\pm/\omega + K(ka)^2\right]}.$$

The criterion for having both eigenvalues real and negative is $1 - \omega_0^\pm/\omega + K(ka)^2 > 0$. This inequality is to be coupled with (3.4). Thus, it appears clearly that, for the case $K > 0$, the two eigenvalues are both negative if $\omega_0 = \omega_0^-$, thence $\omega_0 < \omega$. The corresponding stationary solution is therefore stable. The other stationary solution $\omega_0 = \omega_0^+$, existing in the range $F_\downarrow < F < F_\uparrow$, corresponds to $\lambda_1 < 0$ and $\lambda_2 > 0$ and is therefore unstable.

Note that the neutrally stable limiting case $\lambda_2 = 0$ is obtained for $F = F_\downarrow$ or $ka = 0$ or $K = 0$. The two first cases correspond to the rest (i.e., no waves), while the third one requires a higher-order equation to conclude on the stability. Note also that the opposite conclusions hold for $K < 0$: the stable solution corresponds then to $\omega_0 = \omega_0^+$ (i.e., $\omega_0 > \omega$).

5 Wavenumber selection

We can now determine the wavenumbers selected at the instability onset. The minimal forcing required to destabilise the free surface from rest is given by (4.1), where ω_0 is related

to the wavenumber k by (2.2), the dissipation factor σ being given in (2.3). The first wave to emerge from rest is the one requiring the smaller value of $F_\uparrow$, i.e., this wave corresponds to the wavenumber such that $\partial F_\uparrow/\partial k = 0$, i.e.,

$$\frac{\partial F_\uparrow}{\partial k} = \frac{16\,(\omega_0-\omega)}{\omega^2\,F_\uparrow}\,\frac{\partial\,\omega_0}{\partial k} + \frac{16\,\sigma}{\omega^2\,F_\uparrow}\,\frac{\partial\,\sigma}{\partial k} = 0, \tag{5.1}$$

together with $\omega = \Omega/2$.

In the limiting case of deep water (i.e., $d = \infty$, $\omega_0 = \sqrt{gk}$, $\sigma = 2\nu k^2$, the most unstable wavenumber k given by (5.1) is

$$2\omega_0 = \omega + \sqrt{\omega^2 - 16\sigma^2}.$$

In the opposite limit of long waves (i.e. $kd \ll 1$, $\omega_0 = k\sqrt{gd}$, $\sigma = (gd)^{1/4}\sqrt{k\nu/8d^2}$), the most unstable wavenumber corresponds to

$$\omega_0 = \omega - 16\nu/d^2.$$

In both cases, the first mode emerging from the rest is such that $\omega_0 < \omega$. The same conclusion arises for arbitrary depth and with surface tension under quite general assumptions (to be explained at the conference). We conclude that the critical mode $\omega_0(k)$ selected at the destabilisation threshold $F_\uparrow$ of the rest state fulfils the inequality $\omega_0 < \omega = \Omega/2$ in both cases of short and long waves. However, as we mentioned above, the sign of the nonlinear term in equation (3.1) depends on the depth, K being positive for short waves, and negative for long ones. Therefore, we conclude that the transition from the rest to the wavy state is *subcritical* (i.e., with hysteresis) for long waves, and *supercritical* (i.e., smooth) for short waves.

6 Conclusion

The dispersion relation of Faraday waves is modified compared to that of free, unforced waves: the forcing amplitude and the dissipation play a key role in the relation of dispersion. For a given forcing frequency, there are two corresponding wavenumbers. We have determined the value of the forcing at the instability threshold, in both cases of short and long waves, as well as the selected wavenumbers. We have also studied the nature of the bifurcation at the instability onset, and we have shown that the transition is supercritical for short waves and subcritical for long waves.

References

[1] M. Abramowitz, M. & I. A. Stegun, *Handbook of Mathematical Functions*. Dover, (1965).

[2] H. Arbell & J. Fineberg, Phys. Rev. Lett. **85**, 756 (2000).

[3] T. B. Benjamin & F. Ursell, Proc. R. Soc. Lond. A **225**, 505 (1954)

[4] S. Ciliberto & J.P. Gollub, J. Fluid Mech. **158**, 381 (1985).

[5] B. Christiansen, P. Alstrøm & M. Levinsen, Phys. Rev. Lett.**68**, 2157 (1992).

[6] S. Douady & S. Fauve, Europhys. Lett. **6**, 221 (1988).

[7] S. S. Hough, Proc. Lond. Math. Soc. **28**, 264 (1896).

[8] J. N. Hunt, La Houille Blanche **6**, 685 (1964).

[9] M. Faraday, Phil. Trans. R. Soc. London **52**, 299 (1831).

[10] S. Fauve, in Dynamics of Nonlinear and Disordered Systems, edited by G. Martinez-Meckler and Seligman (World Scientific, Singapore, 1995).

[11] K. Kumar, Proc. R. Soc. Lond. A **452**, 1113 (1996).

[12] J. W. Miles, & D. Henderson, Ann. Rev. Fluid Mech. **22**, 143 (1990).

[13] S. T. Milner, J. Fluid Mech. **225**, 81 (1992).

[14] H. W. Müller, H. Wittmer, C. Wagner, J. Albers & K. Knorr, Phys. Rev. Lett. **78**, pp. 2357 (1997).

[15] J. Rajchenbach, D. Clamond & A. Leroux, Phys. Rev. Lett. **110**, 094502 (2013).

[16] J. Rajchenbach, A. Leroux & D. Clamond, Phys. Rev. Lett. **107**, 024502 (2011).

[17] I. Tadjbakhsh, & J. B. Keller, J. Fluid Mech. **3**, 442 (1960).

[18] K. Kumar, & L. S. Tuckerman, J. Fluid. Mech. **279**, 49 (1994).

[19] J. Wu, R. Keolian & I. Rudnick, Phys. Rev. Lett. **52**, 1421 (1984)

Energy dissipation and spectrum evolution during the breaking of modulated wave trains

F. De Vita[1,2], R. Verzicco[2], A. Iafrati[1],
[1] INSEAN-CNR, Rome, Italy; [2] Univ. di Roma "Tor Vergata"
E-mail: alessandro.iafrati@cnr.it

SUMMARY In this paper the wave breaking induced by modulational instability is investigated numerically. The wave train is composed by a fundamental component with two sideband disturbances and the analysis is performed for those conditions in which the instability leads the limiting steepness to be exceeded. Due to the different speeds characterizing individual waves and the peak of the envelope, the breaking is recurrent and several breaking events are found. The study is focused on the quantification of the initial energy fraction dissipated by the entire breaking process and on the changes operated by the breaking to the initial spectrum.

1. INTRODUCTION

Free surface waves break when the steepness reaches some limiting values. There are several phenomena which can make this happen, e.g. wind-wave and wave-current interactions, shoaling effects, modulation of long waves operated by shorter ones, among others. In typical background deep-water oceanic conditions for dominant waves, however, these processes are two: linear superposition and modulational instability (Babanin *et al.*, 2011).

Due to the complexity of field measurements, detailed experimental studies of the breaking process have been mainly done in laboratory (Perlin *et al.*, 2013). Most of the studies investigate the breaking induced by the dispersive focusing technique, e.g. (Rapp & Melville, 1990; Drazen *et al.*, 2008; Grue *et al.*, 2003) among many others. In this way the breaking occurs at the focusing point as one single event. This is not the case of the wave breaking taking place in open ocean, for which recurrence is observed (Donelan *et al.*, 1972; Lamont-Smith *et al.*, 2003) as a consequence of the interaction of the peak wave component with the group envelope. The generation of such breaking in laboratory is hampered by the quite long distances needed for the development of the modulational instability. Moreover, even if the first breaking event can be generated, the limited lengths of wave tanks do not allow to follow the breaking process up to the end.

The energy dissipation and the spectrum changes associated to the breaking are very important for wave forecasting models operating on large scales (e.g. Xiao *et al.*, 2013). In order to investigate those aspects, in previous studies the breaking generated by modulational instability was simulated numerically (Iafrati *et al.*, 2012; 2013; 2014). The recurrence of the breaking process was observed and the energy amount dissipated by single breaking events was quantified for some conditions. However, not all simulations performed arrived at the end of the breaking processes and thus it wasn't possible to quantify the total energy dissipation and the changes to the pre-breaking spectrum.

In this paper some analyses similar to those discussed in Iafrati *et al.* (2014) are performed. Larger initial steepnesses are considered in order to shorten the transient needed to get to the onset of the breaking. Differently from Iafrati *et al.* (2014), here the open source Gerris code is adopted which has a sharp interface treatment and rather flexible adaptive refinement capabilities, which allow an efficient use of the computational resources. The time histories of the total energy content in water as well as the corresponding evolution of the spectra and of the maximum wave steepness are shown. It is worth remarking that results presented here are based on a two-dimensional assumption. It is hoped that some preliminary results of three-dimensional simulations can be presented at the Workshop.

2. NUMERICAL SETUP

By following what was presented in a previous edition of this Workshop (Landrini *et al.*, 1998), the initial condition is composed by a fundamental wave component with two small side band disturbances, amplitude of which is one tenth of the fundamental component at the beginning of the simulation. The free surface elevation η is thus

$$\eta(x,0) = \frac{\epsilon_0}{k_0}\left[\cos(k_0 x) + 0.1\cos\left(\frac{6}{5}k_0 x\right) + 0.1\cos\left(\frac{4}{5}k_0 x\right)\right]$$

where $k_0 = 2\pi/\lambda_0$ the wave number and $\epsilon_0 = a_0 k_0$ the steepness, a_0 denoting the amplitude of the fundamental component of wavelength λ_0. The initial velocity field in the water domain is taken from linear theory as

$$\begin{aligned} u(x,0) = \epsilon_0 \Bigg[& \sqrt{\frac{g}{k_0}}\exp(k_0 y)\cos(k_0 x) \\ & + 0.1\sqrt{\frac{6}{5}}\sqrt{\frac{g}{k_0}}\exp\left(\frac{6}{5}k_0 y\right)\cos\left(\frac{6}{5}k_0 x\right) \\ & + 0.1\sqrt{\frac{4}{5}}\sqrt{\frac{g}{k_0}}\exp\left(\frac{4}{5}k_0 y\right)\cos\left(\frac{4}{5}k_0 x\right)\Bigg] \\ v(x,0) = \epsilon_0 \Bigg[& \sqrt{\frac{g}{k_0}}\exp(k_0 y)\sin(k_0 x) \\ & + 0.1\sqrt{\frac{6}{5}}\sqrt{\frac{g}{k_0}}\exp\left(\frac{6}{5}k_0 y\right)\sin\left(\frac{6}{5}k_0 x\right) \\ & + 0.1\sqrt{\frac{4}{5}}\sqrt{\frac{g}{k_0}}\exp\left(\frac{4}{5}k_0 y\right)\sin\left(\frac{4}{5}k_0 x\right)\Bigg] \quad , \end{aligned}$$

where $g = 9.81$ m s^{-2} is the gravity acceleration. Simulations are conducted for fundamental wavelength $\lambda_0 = 0.60$ m, which is used as reference value for lengths. Periodic

case	Re	*steepness*
I	10^5	0.18
II	10^5	0.20
III	10^5	0.22
IV	1455664.8	0.18
V	1455664.8	0.20
VI	1455664.8	0.22

Table 1: Simulation conditions

boundary conditions are used at the sides in the horizontal direction. The domain width is $5\lambda_0$ whereas in the vertical direction the domain spans from $y = -0.5\lambda_0$ to $y = 1.5\lambda_0$, $y = 0$ being the still water level.

Simulations are performed by using the open-source Gerris software (http://gfs.sourceforge.net) which solves the incompressible Navier-Stokes equations and has adaptive mesh refinement capabilities by using quad-octree discretization. The solver is based on a projection method and uses a multilevel Poisson solver (Popinet, 2009). The governing equations of the problem are:

$$\frac{d\mathbf{u}}{dt} = \alpha(T)\left\{-\nabla p + \nabla\cdot[\mu(T)(\nabla\mathbf{u} + \nabla\mathbf{u}^T)] + \sigma\kappa\delta_s\mathbf{n}\right\}$$

for the fluid, and:

$$\frac{d}{dt}\int_V T\,dv + \oint_S (T\mathbf{u})\cdot\mathbf{n}\,ds = 0$$

for the interface advection, where $\mathbf{u}$ and p are, respectively, the velocity field and the pressure, $\alpha = 1/\rho$, $\rho(T)$ the local fluid density, $\mu(T)$ the dynamic viscosity, T the Volume-of-fluid variable, κ the interface curvature, σ the surface tension coefficient and δ_s the Dirac distribution which is zero out of the interface.

The fluid properties are related to the VOF variable T as:

$$\rho(T) = \rho_a T + \rho_w(1-T)$$
$$\mu(T) = \mu_a\cdot T + \mu_w(1-T)$$

so that $T = 1$ in air and $T = 0$ in water. The simulations presented here refer to the following parameters: $\mu_a = 1.810\cdot10^{-5}$ N s m^{-2}, $\mu_w = 10^{-3}$ N s m^{-2}, $\rho_a = 1.25$ kg/m^3, $\rho_w = 1000$ kg/m^3 and $\sigma = 0.072$ N/m (subscripts a and w stand for air and water, respectively). Nondimensional parameters of the problem are:

$$Re = \sqrt{g\lambda_0}\frac{\rho_w\lambda_0}{\mu_w} = 1455664.8 \quad (1)$$

$$We = \sqrt{g\lambda_0}\frac{\rho_w\lambda_0}{\sigma_w} = 219.95 \quad (2)$$

where a quantity related to the phase speed, $\sqrt{g\lambda_0}$, is used as reference velocity. As a first step of the study, in order to get confidence with the computational tool and with its adaptive refinement capabilities, simulations were performed using the much lower value of $Re = 10^5$. For this case several simulations were performed and it was found that a maximum resolution of 512 point for wavelength is enough to resolve all the dissipative scales, leading to a grid of 2560x1024 points. In order to limit the computational effort, the adaptive refinement is used. The refinement is based on the gradient of the VOF function and on the vorticity. In a second step, the full Reynolds number was adopted, which required a maximum resolution of 2048 grid point for wavelength for convergence in terms of energy dissipation. The cases studied are summarized in Table 1.

3. NUMERICAL RESULTS

In order to show the dissipation of the wave energy as a result of the breaking process, the time history of the total energy in water, computed as the sum of the kinetic and potential components, is drawn in Fig. 1 for the case with initial steepness $\epsilon_0 = 0.20$. Note that the energy is nondimensionalized by using the square of the reference velocity used for the definition of the Reynolds and Weber numbers, i.e. $g\lambda_0$. The time is made nondimensional by the characteristic time $T_0 = \lambda_0/\sqrt{g\lambda_0}$. Note that, from linear theory, the wave period of the fundamental component is $\sqrt{2\pi} \simeq 2.5$ nondimensional time units.

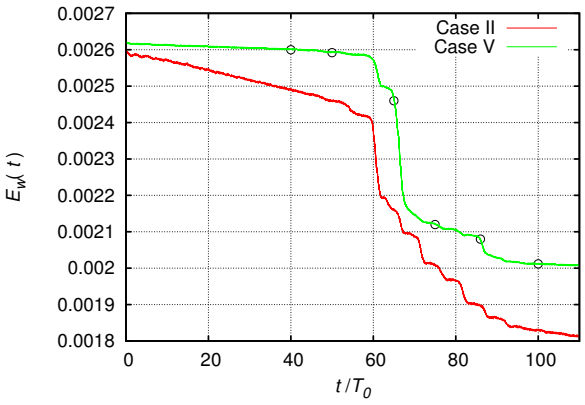

Figure 1: Time history of the total mechanical energy content in water for cases II and V.

From the time histories of the energy it can be seen that, independently of the Reynolds number, there is an initial phase during which the instability develops (see Iafrati *et al.*, 2014). During this stage the energy diminishes only due to the viscous effects associated to the orbital motion. Next, the breaking starts. As already discussed in Iafrati *et al.* (2014), the breaking is recurrent with a period which is twice the period of the fundamental wave component. This is explained as the wave crest propagates with the phase speed c_p whereas the envelop propagates with the group velocity c_g which is half of the phase speed (Lamont-Smith *et al.*, 2003).

The data in Fig. 1 indicate that the energy amount dissipated by the single breaking event can vary substantially. In terms of the total energy dissipated by the breaking process, the simulations at the two Reynolds numbers, although being characterized by a quite different decay in the pre-breaking stage, display a quite similar behavior during the

breaking process, in terms of the total energy fraction dissipated by the breaking and of duration of the process, which is about 20 wave periods in both cases. This is a quite important finding as it indicates that the scale does not play a too relevant role on those aspects, and thus makes the present result applicable to wavelengths much longer than the 0.60 m adopted here.

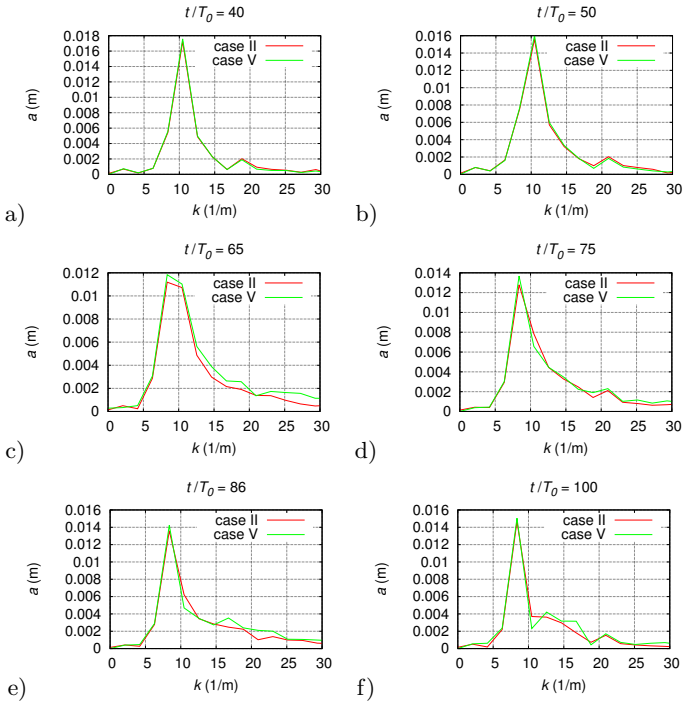

Figure 2: Comparisons of the spectra at different times during the breaking process. The figures refer to the times indicated by circles in Fig. 1. No substantial differences occur between the results at the two Reynolds numbers.

The occurrence of breaking causes a reduction of the higher wavelength components. In order to highlight the phenomenon and to provide a quantitative estimate the spectra at different phases of the breaking process are drawn in Fig. 2. The phenomenon, which was discussed on the basis of experimental data by Tulin and Waseda (1999) and was referred to as downshifting, is clearly shown also by the computational results. By comparing the spectra at the two Reynolds numbers shown in Fig. 2*c* with the corresponding energy contents at the same time shown in Fig. 1, it can be noticed that the spectra are essentially similar although the energy content is quite different. It would seem that the spectrum is mainly related to the time elapsed from the breaking on set rather than the actual energy dissipation, but the point needs a much deeper investigation. Figure 2 indicates that also in terms of the spectra, the results of the simulations at the two different Reynolds display a quite nice overlapping, despite the different dissipation rate in the pre-breaking stage.

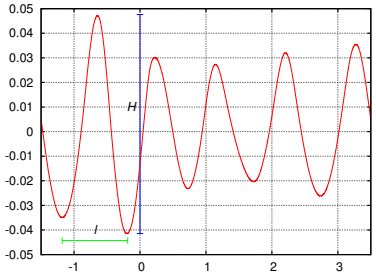

Figure 3: Sketch of the way used to compute the wave height and the wavelength for the calculation of the maximum wave steepness.

Among the many open questions concerning the breaking generated by the modulational instability, an important question is when the breaking ends. As an attempt of answering this question, at each time step the maximum wave steepness is computed. Several definitions exist for that parameter, which depends on how the wavelength and the wave amplitude are defined. In this work the maximum steepness is computed as the maximum of the quantity

$$\epsilon = \frac{H}{2}\frac{2\pi}{l}$$

where H is the vertical distance between the crest and the trough at the right whereas l is the distance between the two troughs next to the crest (see Fig. 3).

In Fig. 4 the time histories of the maximum wave steepness are plotted together with the corresponding energy contents in water. The threshold steepness of 0.32 discussed in Grue and Fructus (2010) and in Iafrati (2009) is also drawn. Although simulations IV and VI are still going, the results indicate that the breaking starts when a limiting steepness is reached and ceases once the steepness drops below the threshold value. Note that once the breaking ceases the energy dissipation rate takes about the same slope of the pre-breaking phase. These conclusions are essentially similar to what was found for a gentle spilling breaking in Iafrati (2011). It is worth noticing that the reduction of the wave steepness shown in Fig. 4 is only partly related to the reduction in the wave amplitude whereas a important role is played by the downshifting phenomenon. This is clearly seen in Fig. 2 where the peak of the spectrum moves from $k = 10.47$ m^{-1} to $k = 8.37$ m^{-1}.

Before closing this section, it is worth providing a few additional considerations on the time histories of the maximum steepness provided in Fig. 4. The maximum steepness oscillates with a period of about 5 nondimensional units, which is twice the wave period. As already discussed, this is a consequence of the interaction between the wave components and the group envelope. A second remark concerns the peak values of the steepness reached during the breaking process for which numerical results predict maximum values exceeding 0.55. In Toffoli *et al.* (2010), the value 0.55 was found to be a limiting steepness for oceanic waves. It is not clear at the moment if the larger values found here are caused by the way in which the maximum steepness is computed during the breaking event when the free surface takes quite complicated shapes. Further studies are needed to clarify this aspect.

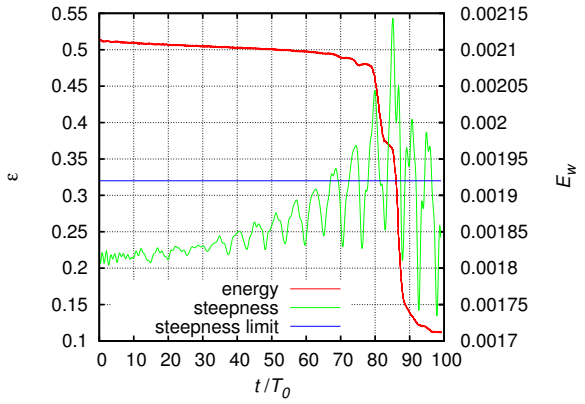

a)

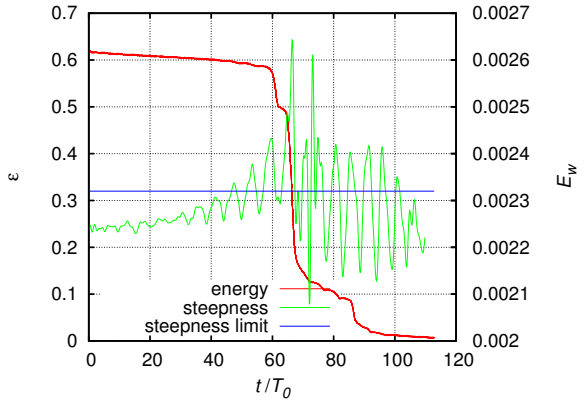

b)

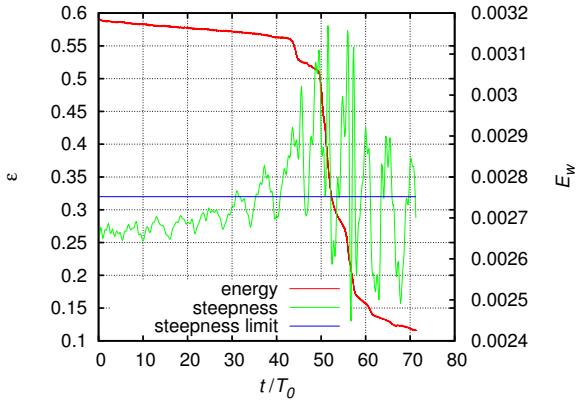

c)

Figure 4: Time histories of the maximum wave steepness and of the total energy content in water for the three different steepnesses: a) case IV ($\epsilon_0 = 0.18$), b) case V ($\epsilon_0 = 0.20$), c) case VI ($\epsilon_0 = 0.22$). The horizontal line indicate the threshold steepness of 0.32.

4. ACKNOWLEDGMENTS

The work has been financially supported by the "Flagship Project RITMARE - The Italian Research for the Sea - coordinated by the Italian National Research Council and funded by the Italian Ministry of Education, University and Research within the National Research Program 2011-2013." Authors express their gratitude to the Gerris team and Dr. S. Popinet not only for making the code available but also for the technical support provided.

5. REFERENCES

M. Perlin, W. Choi, Z. Tian, (2013) Breaking waves in deep and intermediate waters. Annu. Rev. Fluid Mech., 45, pp. 115-145.

A.V. Babanin, T. Waseda, T. Kinoshita, A. Toffoli, (2011) Wave breaking in directional fields. J. Phys. Oceanogr., 41, pp. 145-156.

R.J. Rapp, W.K. Melville, (1990) Laboratory measurements of deep-water breaking waves. Philos. Trans. R. Soc. A, 331, pp. 735-800.

A.D. Drazen, W.K. Melville, L. Lenain, (2008) Inertial scaling of dissipation in unsteady breaking waves, J. Fluid Mech., 611, pp. 307-332.

J. Grue, D. Clamond, M. Huseby, A. Jensen, A. (2003) Kinematics of extreme water waves. Appl. Ocean Res. 25, pp. 355-366.

M. Donelan, M.S. Longuet-Higgins, J.S. Turner, (1972) Periodicity in whitecaps. Nature, 239, pp. 449-451.

T. Lamont-Smith, J. Fuchs, M.P. Tulin, (2003) Radar Investigation of the Structure of Wind Waves. J. Oceanogr., 59, pp. 49-63.

W. Xiao, Y. Liu, G. Wu, D.K.P. Yue, (2013) Rogue wave occurrence and dynamics by direct simulations of nonlinear wave-field evolution. J. Fluid Mech., 720, pp. 357-392.

A. Iafrati, M. Onorato, A. Babanin, (2012) Analysis of wave breaking events generated as a result of a modulational instability. Proc. 29th ONR Symposium on Naval Hydrodynamics, Gothenburg, Sweden.

A. Iafrati, A. Babanin, M. Onorato, (2013) Modulational instability, wave breaking, and formation of large-scale dipoles in the atmosphere. Phys. Rev. Lett., 110, 184504.

A. Iafrati, A. Babanin, M. Onorato, (2014) Modeling of oceanatmosphere interaction phenomena during the breaking of modulated wave trains. J. Comput. Phys., 271, pp. 151-171.

M. Landrini, O. Oshri, T. Waseda, M.P. Tulin, (1998) Long time evolution of gravity wave system. Proc. 13th Int. Workshop Water Waves Floating Bodies, Alphen aan den Rijn, Netherlands.

S. Popinet, (2009) An accurate adaptive solver for surface-tension-driven interfacial flows. J. Comput. Phys., 228, pp. 5838-5866.

M.P. Tulin, T. Waseda, (1999) Laboratory observations of wave group evolution, including breaking effects. J. Fluid Mech., 378, 197-232.

J. Grue, D. Fructus, (2010) Model for fully nonlinear ocean wave simulations derived using Fourier inversion of integral equations in 3D. Advances in Numerical Simulation of Nonlinear Water Waves (ed. Q. W. Ma), in the series of Advances in Coastal and Ocean Engineering. World Scientific.

A. Iafrati, (2011) Energy dissipation mechanisms in wave breaking processes: spilling and highly aerated plunging breaking events. J. Geophys. Res. 116, C07024

A. Toffoli, A. Babanin, M. Onorato, T. Waseda, (2010) Maximum steepness of oceanic waves: Field and laboratory experiments. Geophys. Res. Lett., L05603, doi:10.1029/2009GL041771.

Wave Forces On A Vertical Cylinder With Non-Circular Cross Section

N.B. Dişibüyük[1], A.A. Korobkin[2],

[1] Department of Mathematics, Dokuz Eylul University, Izmir, Turkey
e-mail: bugurcan.ruzgar@deu.edu.tr
[2] School of Mathematics, University of East Anglia, Norwich, UK,
e-mail: a.korobkin@uea.ac.uk

1 Introduction

We consider the linear problem of water waves scattering by a vertical cylinder with non-circular cross section extending from the sea bottom to the free surface in water of finite depth h. We assume a plane wavetrain incident from $x \sim -\infty$ and propagating at an angle α to the positive $x-$direction toward a vertical cylinder whose cross section is described by the equation $r = R + \varepsilon f(\theta)$ with $\varepsilon \ll 1$. The function $f(\theta)$ describes the deviation of the shape of the cylinder from the circular one, $f(\theta) = 0$ corresponds to the circular cylinder with radius R. The problem of wave scattering by a nearly circular cylinder was formulated in [1]. The top view of the problem is shown in Figure 1. The problem of wave diffraction by a vertical cylinder has been solved by a number of researchers for many different shapes. The challenge of the present study is to solve the complex body geometries with less effort. The abstract presents the results which have been obtained for one simple geometry: a cylinder with elliptic cross section.

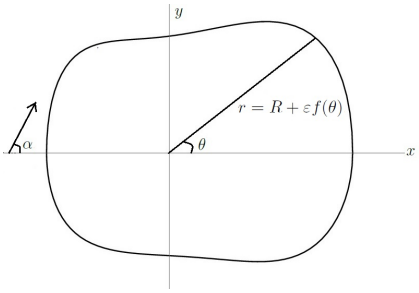

Figure 1: Top view of the problem configuration.

2 Mathematical Formulation of The Problem

The linear boundary problem is formulated with respect to the velocity potential $\Phi(r, \theta, z, t)$

$$\Phi(r, \theta, z, t) = \Re\left\{\frac{gA}{\omega}\frac{\cosh[k(z+h)]}{\cosh(kh)}\phi(r, \theta)e^{-iwt}\right\},$$

where ϕ satisfies the Helmholtz equation $(\nabla^2 + k^2)\phi = 0$ in the flow region, A is the incident wave amplitude, $k = \frac{2\pi}{\lambda}$ is the wave number, λ is the incident wave length, ω is the wave frequency related to the wave number k by the dispersion relation $\omega^2 = gk\tanh(kh)$, where g is the gravitational acceleration. The coordinate system (r, θ, z) is used with the origin at the free surface and the z-axis directed upwards. The axis of the corresponding circular cylinder with $\varepsilon = 0$ coincides with the z-axis.

The boundary condition on the cylinder $r = R + \varepsilon f(\theta)$ is

$$\frac{\partial \phi}{\partial n} = 0 \quad \text{on} \quad r = R + \varepsilon f(\theta), \quad -h < z < 0, \tag{1}$$

where $\vec{n}$ is the unit normal vector on the cylinder. This boundary condition can be written as

$$\frac{\partial\phi}{\partial r}(R+\varepsilon f(\theta),\theta)-\frac{\varepsilon f'(\theta)}{\big[R+\varepsilon f(\theta)\big]^2}\frac{\partial\phi}{\partial\theta}(R+\varepsilon f(\theta),\theta)=0. \tag{2}$$

We approximate the boundary condition (2) up to $\mathcal{O}(\varepsilon^5)$ using the Taylor expansion at $r=R$ and substitute the fifth order asymptotic expansion of the potential ϕ

$$\phi(r,\theta)=\phi_0(r,\theta)+\varepsilon\phi_1(r,\theta)+\varepsilon^2\phi_2(r,\theta)+\varepsilon^3\phi_3(r,\theta)+\varepsilon^4\phi_4(r,\theta)+\mathcal{O}(\varepsilon^5), \tag{3}$$

into the boundary condition (2) with the result

$$\begin{aligned}
&\phi_{0,r}+\varepsilon\left[\phi_{1,r}+f(\theta)\phi_{0,rr}-\frac{f'(\theta)}{R^2}\phi_{0,\theta}\right]\\
&+\varepsilon^2\left[\phi_{2,r}+f(\theta)\phi_{1,rr}-\frac{f'(\theta)}{R^2}\phi_{1,\theta}+\frac{f^2(\theta)}{2}\phi_{0,rrr}+\frac{2f(\theta)f'(\theta)}{R^3}\phi_{0,\theta}-\frac{f(\theta)f'(\theta)}{R^2}\phi_{0,r\theta}\right]\\
&+\varepsilon^3\Bigg[\phi_{3,r}+f(\theta)\phi_{2,rr}-\frac{f'(\theta)}{R^2}\phi_{2,\theta}+\frac{f^2(\theta)}{2}\phi_{1,rrr}+\frac{2f(\theta)f'(\theta)}{a^3}\phi_{1,\theta}-\frac{f(\theta)f'(\theta)}{R^2}\phi_{1,r\theta}\\
&\qquad+\frac{2f^2(\theta)f'(\theta)}{R^3}\phi_{0,r\theta}+\frac{f^3(\theta)}{6}\phi_{0,rrrr}-\frac{3f^2(\theta)f'(\theta)}{R^4}\phi_{0,\theta}-\frac{f^2(\theta)f'(\theta)}{2R^2}\phi_{0,rr\theta}\Bigg]\\
&+\varepsilon^4\Bigg[\phi_{4,r}+f(\theta)\phi_{3,rr}-\frac{f'(\theta)}{R^2}\phi_{3,\theta}+\frac{f^2(\theta)}{2}\phi_{2,rrr}-\frac{f(\theta)f'(\theta)}{a^2}\phi_{2,r\theta}+\frac{2f(\theta)f'(\theta)}{R^3}\phi_{2,\theta}\\
&\quad-\frac{3f^2(\theta)f'(\theta)}{R^4}\phi_{1,\theta}-\frac{f^2(\theta)f'(\theta)}{2a^2}\phi_{1,rr\theta}+\frac{2f^2(\theta)f'(\theta)}{a^3}\phi_{1,r\theta}+\frac{f^3(\theta)}{6}\phi_{1,rrrr}\\
&\quad-\frac{3f^3(\theta)f'(\theta)}{R^4}\phi_{0,r\theta}+\frac{f^3(\theta)f'(\theta)}{a^3}\phi_{0,rr\theta}-\frac{f^3(\theta)f'(\theta)}{6a^2}\phi_{0,rrr\theta}+\frac{f^4(\theta)}{24}\phi_{0,rrrrr}+\frac{4f^3(\theta)f'(\theta)}{R^5}\phi_{0,\theta}\Bigg]=0,
\end{aligned} \tag{4}$$

where the functions are computed at $r=R$. Since the right hand side of this equation is zero, the coeffcients of ε^i, $i=0,1,2,3,4$, on the left hand side of (4) are equal to zero. Using (4) we derive five boundary conditions for five unknown potentials $\phi_i(r,\theta)$, $i=0,1,2,3,4$, first two of them are:

$$\phi_{0,r}(R,\theta)=0, \tag{5}$$

$$\phi_{1,r}(R,\theta)=\frac{1}{R^2}f'(\theta)\phi_{0,\theta}(R,\theta)-f(\theta)\phi_{0,rr}(R,\theta). \tag{6}$$

It is clear that $\phi_0(r,\theta)$ is the velocity potential of the diffraction problem for the circular cylinder $r=R$ with the solution (see [1])

$$\phi_0(r,\theta)=\sum_{m=0}^{\infty}\epsilon_m i^m\left[J_m(kr)-\frac{J_m'(kR)}{H_m^{(1)\prime}(kR)}H_m^{(1)}(kr)\right]\cos[m(\theta-\alpha)],$$

which satisfies equation (5), where ϵ_m is the Neumann symbol which is given by $\epsilon_0=1$, $\epsilon_m=2$, $m\geq 1$. The series converges exponentially as $m\to\infty$.

The most general representations of $\phi_i(r,\theta)$, $i=1,2,3,4$, which satisfy the radiation condition at infinity are

$$\phi_i(r,\theta)=\sum_{m=0}^{\infty}\Big[C_{i,m}\cos[m(\theta-\alpha)]+D_{i,m}\sin[m(\theta-\alpha)]\Big]H_m^{(1)}(kr),$$

where the evanescent modes are not included (see [1]) and $C_{i,m}$ and $D_{i,m}$, $i=0,1,2,3,4$, are unknown coeffcients. The coefficients can be determined using the boundary conditions (5),(6) and the other 3 conditions and hence we can find the velocity potentials with the accuracy $\mathcal{O}(\varepsilon^5)$.

We also assume that $f(\theta)$ can be written as a Fourier series

$$f(\theta) = \frac{f_0^c}{2} + \sum_{m=1}^{\infty} [f_m^c \cos(m\theta) + f_m^s \sin(m\theta)],$$

where the coeffcients f_i^c and f_i^s, $i = 0, 1, 2, \ldots$ depend on a particular shape of the vertical cylinder in waves. If the function $f(\theta)$ is independent of ε then the right hand side of the conditions (5), (6) and the other 3 conditions depends only on θ. So we can write these conditions as $\phi_{i,r}(a, \theta) = G_i(\theta)$, $i = 0, 1, 2, 3, 4$, where $G_i(\theta)$ are represented by their Fourier series. After writing $G_i(\theta)$ as Fourier series, we can find the unknown coefficients $C_{i,m}$ and $D_{i,m}$, $i = 0, 1, 2, 3, 4$.

If the function $f(\theta, \varepsilon)$ depends on θ and ε, then we can use the asymptotic expansion of $f(\theta, \varepsilon)$ as $\varepsilon \to 0$:

$$f(\theta, \varepsilon) = f_0(\theta) + \varepsilon f_1(\theta) + \varepsilon^2 f_2(\theta) + \varepsilon^3 f_3(\theta) + \varepsilon^4 f_4(\theta) + \mathcal{O}(\varepsilon^5),$$

or higher order, and substituting this into (4) and then applying the same procedure as in the previous case we can find the unknown coefficients. As an example of this case, we have solved a problem for the cylinder with elliptic cross section of small eccentricity in the next section and calculated the hydrodynamic forces acting on this cylinder. The x and y components of the hydrodynamic force due to the fluid motion are given by

$$F_x = \Re\left\{ \frac{-i\rho g A \tanh(kh)}{k} \left[\int_0^{2\pi} \phi(a + \varepsilon f(\theta), \theta)[\varepsilon f'(\theta) \sin\theta + [a + \varepsilon f(\theta)] \cos\theta] \, \mathrm{d}\theta \right] e^{-iwt} \right\}, \quad (7)$$

$$F_y = \Re\left\{ \frac{-i\rho g A \tanh(kh)}{k} \left[\int_0^{2\pi} \phi(a + \varepsilon f(\theta), \theta)[-\varepsilon f'(\theta) \cos\theta + [a + \varepsilon f(\theta)] \sin\theta] \, \mathrm{d}\theta \right] e^{-iwt} \right\}. \quad (8)$$

Dividing F_x and F_y by $\rho g A \pi a^2 \tanh(kh)$, we arrive at the non-dimensionalized force components $\tilde{F}_x$ and $\tilde{F}_y$.

3 Example: Elliptic cylinder

The ellipse's equation in the polar coordinates with the origin at the focus reads

$$r = \frac{a(1 - e^2)}{1 - e\cos\theta}, \quad (9)$$

where $e = \sqrt{1 - \frac{b^2}{a^2}}$, $0 < e < 1$, is the eccentricity of the ellipse, a is semi-major axis, b is semi-minor axis. Assuming $e \ll 1$ and setting $e = \varepsilon$ we can write (9) in the form of Fourier series and then using Taylor expansion about $\varepsilon = 0$ we obtain

$$\begin{aligned} r = R + \varepsilon f(\theta) &= a\sqrt{1 - \varepsilon^2} + 2a\sqrt{1 - \varepsilon^2} \sum_{n=1}^{\infty} \left[\frac{\varepsilon}{1 + \sqrt{1 - \varepsilon^2}} \right]^n \cos(n\theta) \\ &= a + \varepsilon a \cos\theta - \varepsilon^2 a \sin^2\theta - \varepsilon^3 a \cos\theta \sin^2\theta + \varepsilon^4 a \cos^2\theta \sin^2\theta + \mathcal{O}(\varepsilon^5). \end{aligned}$$

Hence,

$$\begin{aligned} R &= a, \\ f(\theta) &= a\cos\theta - \varepsilon a \sin^2\theta - \varepsilon^2 a \cos\theta \sin^2\theta + \varepsilon^3 a \cos^2\theta \sin^2\theta + \mathcal{O}(\varepsilon^4) \end{aligned} \quad (10)$$

in (2). Rewriting conditions (5),(6) and the other 3 conditions for the function (10) we get:

$$\begin{aligned} \phi_{0,r}(a, \theta) &= 0, \\ \phi_{1,r}(a, \theta) &= -\frac{1}{a} \sin\theta \phi_{0,\theta}(a, \theta) - a\cos\theta \phi_{0,rr}(a, \theta), \\ \phi_{2,r}(a, \theta) &= -a\cos\theta \phi_{1,rr}(a, \theta) + a\sin^2\theta \phi_{0,rr}(a, \theta) - \frac{a^2 \cos^2\theta}{2} \phi_{0,rrr}(a, \theta) - \frac{1}{a} \sin\theta \phi_{1,\theta}(a, \theta). \end{aligned}$$

In the same manner, we can write the conditions for $\phi_{3,r}(a, \theta)$ and $\phi_{4,r}(a, \theta)$.

Substituting (10) into the equations (7), (8) and dividing them by $\rho g A \pi a^2 \tanh(kh)$, we get non-dimensionalized force components $\tilde{F}_x$, $\tilde{F}_y$ for elliptic cylinder.

4 Results and Conclusions

We have applied the asymptotic analysis described above to scattering problems of one-dimensional waves by a vertical cylinder with non-circular cross section. For an elliptic cylinder, we compared our results with the results by Williams [2] who used the expansion of the exact expressions for the forces which are given by the Mathieu functions for small values of the elliptic eccentricity parameter. The present asymptotic approach provides a good approximation for the forces exerted on the elliptic cylinder with eccentricity $\varepsilon = 0.5$ to the incident wave for values of $\alpha = 0°$ and $\alpha = 90°$ (see Figure 2, Figure 3). We found that, if the incident wave makes zero angle with the positive x-axis and $ka \to 0$, then

$$\tilde{F}_x = \left[2 - \frac{3}{2}\varepsilon^2 - \frac{1}{8}\varepsilon^4 + \mathcal{O}(\varepsilon^6)\right] \cos \omega t,$$

and if the incident wave makes the angle of $\frac{\pi}{2}$ with the positive x-axis and $ka \to 0$, then

$$\tilde{F}_y = \left[2 - \frac{1}{2}\varepsilon^2 - \frac{1}{8}\varepsilon^4 + \mathcal{O}(\varepsilon^6)\right] \cos \omega t,$$

which coincide with the asymptotic formulae from [2].

In conclusion, for different shapes of a vertical cylinder, $r = R + \varepsilon f(\theta)$, we can find the wave forces acting on the cylinder by using the formulae (7) and (8).

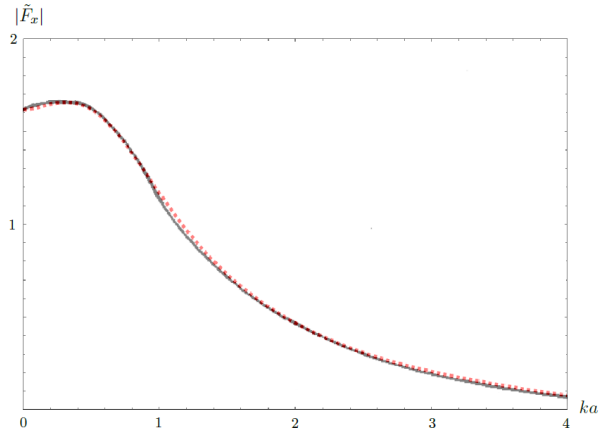

Figure 2: The x-component of the non-dimensionlized force on elliptic cylinder for $\varepsilon = 0.5$. (Solid curve is from [2], dotted curve is by the present method).

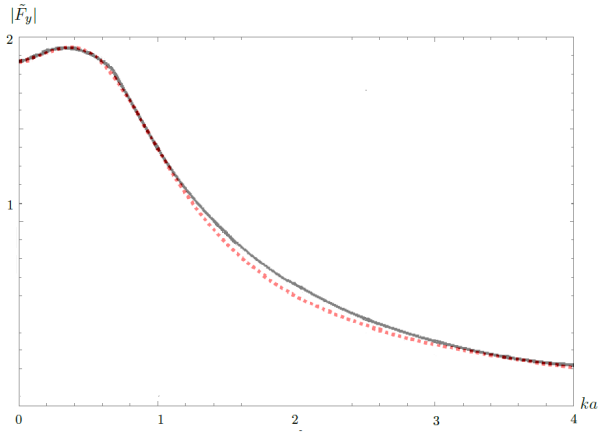

Figure 3: The y-component of the non-dimensionlized force on elliptic cylinder for $\varepsilon = 0.5$. (Solid curve is from [2], dotted curve is by the present method).

Acknowledgement: This research was performed while N. Buğurcan Dişibüyük was visiting the School of Mathematics, University of East Anglia as a visiting research scientist during the period from October 2014 to February 2015. Her visit was supported by YÖK (http://www.yok.gov.tr), The Council of Higher Education. This support is greatly acknowledged.

References

1. Mei C.C., Stiassnie M., K. Dick, Yue P. (2005) Theory And Applications of Ocean Surface Waves, Part1: Linear Aspects. World Scientific. Vol. 23, pp. 363-375.

2. Williams A. N. (1985) Wave Forces On An Elliptic Cylinder. Journal of Waterway, Port, Coastal and Ocean Engineering. Vol. 111, pp. 433-449.

3. Gradshteyn, I.S. & Ryzhik I.M. (1996) Tables of Integrals, Series, and Products. Academic Press.

Ship waves at finite depth in the presence of uniform vorticity

Simen Å. Ellingsen* and Yan Li
Department of Energy and Process Engineering,
Norwegian University of Science and Technology,
*Kolbjorn Hejes vei 2, N-7491 Trondheim, Norway**

Highlights

- Theory for ship waves in the presence of a shear flow of uniform vorticity is extended to the case of finite water depth.
- The presence of a shear flow, at arbitrary angle with the ship's direction of motion, introduces novel features such as asymmetric wakes, non-constant Kelvin wake angles and critical ship velocity above which transverse waves vanish.
- An explicit expression for the critical velocity with both shear and finite depth is derived, together with limits for the corresponding sector of wave propagation forbidden at supercritical velocities. A subtle interplay between shear flow and water depth is found.

I. INTRODUCTION

The theory of ship waves dates back to Lord Kelvin, who showed in 1887 that the angle formed by the waves in a ship's wake always forms the same angle, $\phi_K = 19°28'$[1]. The theory was developed further, in particular, by Havelock [2, 3], and is reviewed in the classical literature[4, 5]. Ship waves, and the Kelvin angle in particular, have lately received much attention in the literature [6–13]. Recently, the classical theory was extended by one of us to include the presence of a Couette-type shear flow of uniform vorticity below the surface [14], forming an arbitrary angle with the ship's direction of motion.

Several realistic situations involve the presence of shear flow beneath the water surface; examples include shallow rivers, sub-surface currents, and when the water near the surface is set in motion by wind (e.g. [15]). As a model flow we consider the simplest shear flow, namely a flow of uniform vorticity (Couette profile). While somewhat idealised compared to real flows (note that G.I. Taylor observed this kind of profile where a bubble curtain surfaces [16]), it allows reasonably straightforward analysis, and is an important stepping stone towards understanding the interaction of ship waves with more general shear profiles.

The presence of a shear flow below the surface was found in Ref. [14] to have a profound influence on the ship waves, determined mainly by the dimensional group $\mathrm{Fr}_S = VS/g$ where S is the shear (vorticity), V is the speed of the ship and g the acceleration of gravity. It may be interpreted as a "shear Froude number" based on the length g/S^2, and implies, crucially, that even moderate shear becomes important for fast–moving ships.

In the following we extend the theory to the case where the water has a finite depth h. While the re-derivation of the governing equations is only slightly complicated by the incorporation of the extra parameter, the introduction of a finite depth is by no means trivial, since the effects of water depth and shear flow interact with each other.

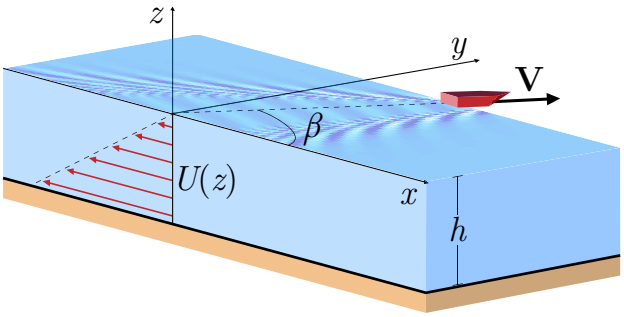

FIG. 1. The geometry considered.

A particularly interesting point reported in Ref. [14] is that the presence of the shear flow implies that in every direction of ship motion except exactly along the shear current, there exists a critical ship velocity V_{crit} beyond which no transverse waves are produced by the boat. The physical reason is that the shear limits the phase velocity of even very long waves, and that transverse waves, propagating in directions close to that of the ship's movement, cannot keep up with a ship moving faster than the maximum phase velocity. Exactly the same phenomenon is well known to appear in the case of ship waves at finite depth [3], where the phase velocity can never exceed $c_{\max} = \sqrt{gh}$.

II. THEORY

The geometry of the problem is shown in Fig. 1. A ship travels at velocity $\mathbf{V}$ relative to the surface of the water. We choose the coordinate system so that the surface velocity is zero, and the basic flow is $U(z) = Sz$ along the x axis. The water depth is h, the water density is ρ and we assume incompressible flow.

* simen.a.ellingsen@ntnu.no

We let β be the angle between the ship's motion and the shear flow as shown in Fig. 1. The ship perturbs the basic flow so that the velocity and pressure field become

$$\mathbf{v} = [U(z) + \hat{u}, \hat{v}, \hat{w}]; \quad p = -\rho g z + \hat{p}. \tag{1}$$

We work to linear order in these perturbations. Noting that ship waves must appear stationary as seen from the moving ship, the perturbed quantities can depend on time only through the combination $\boldsymbol{\xi} = \mathbf{r}_\perp - \mathbf{V}t$ where $\mathbf{r}_\perp = (x, y)$. We therefore subject all physical quantities to the plane Fourier transform

$$\hat{u}(\boldsymbol{\xi}, z) = \int \frac{\mathrm{d}^2 k}{(2\pi)^2} u(\mathbf{k}, z) \mathrm{e}^{i\mathbf{k}\cdot\boldsymbol{\xi}}, \tag{2}$$

etc. Here $\mathbf{k} = (k_x, k_y) = (k\cos\theta, k\sin\theta)$. The physical value is the real part.

Because of the presence of vorticity in an essentially three–dimensional problem, the velocity potential could not be used, and it was necessary to solve the full Euler equations, where the only assumptions made was incompressibility and that viscosity may be neglected. The Euler equations and continuity equation then read

$$ik_x u + ik_y v + w' = 0; \tag{3a}$$
$$i(k_x U - \mathbf{k}\cdot\mathbf{V})u + Sw = -ik_x p/\rho; \tag{3b}$$
$$i(k_x U - \mathbf{k}\cdot\mathbf{V})v = -ik_y p/\rho; \tag{3c}$$
$$i(k_x U - \mathbf{k}\cdot\mathbf{V})w = -p'/\rho, \tag{3d}$$

where a prime denotes derivation w.r.t. z. We can eliminate u, v and p from these equations to obtain an equation for w alone (Rayleigh equation): $w'' = k^2 w$. When subjected to the boundary condition $w(k, -h) = 0$ we obtain the solutions

$$u = iA\left[k_x \cosh k(z+h) + \frac{Sk_y^2 \sinh k(z+h)}{k(k_x U - \mathbf{k}\cdot\mathbf{V})}\right] \tag{4a}$$
$$v = iA\left[k_y \cosh k(z+h) - \frac{Sk_x k_y \sinh k(z+h)}{k(k_x U - \mathbf{k}\cdot\mathbf{V})}\right] \tag{4b}$$
$$w = kA \sinh k(z+h) \tag{4c}$$
$$p = -iA[(k_x U - \mathbf{k}\cdot\mathbf{V})\cosh k(z+h) - S\cos\theta \sinh k(z+h)]. \tag{4d}$$

where $A(\mathbf{k})$ is as yet undetermined.

The ship is modelled as a travelling pressure disturbance on the surface, chosen to have Gaussian form for ease of comparison with literature [7, 8]:

$$\hat{p}_{\mathrm{ext}} = p_0 \mathrm{e}^{-\pi^2\xi^2/b^2}; \quad p_{\mathrm{ext}} = (b^2 p_0/\pi)\mathrm{e}^{-k^2 b^2/(2\pi)^2} \tag{5}$$

where p_{ext} is the Fourier transform of $\hat{p}_{\mathrm{ext}}$ and $\xi = |\boldsymbol{\xi}|$. Here b is the "size" of the ship, and the ship's Froude number is $\mathrm{Fr}_b = V/\sqrt{gb}$. Moreover we define the surface elevation $\zeta(\boldsymbol{\xi})$ relative to an undisturbed surface to be

$$\zeta(\xi) = \int \frac{\mathrm{d}^2 k}{(2\pi)^2} B(\mathbf{k}) \mathrm{e}^{i\mathbf{k}\cdot\boldsymbol{\xi}}. \tag{6}$$

Inserting the above solutions and definitions into the dynamic and kinematic boundary conditions at the free surface now gives two equations with A and B as unknown, from which we eliminate A to produce

$$B(\mathbf{k}) = -\frac{1}{\rho}\frac{kp_{\mathrm{ext}}(k)}{gk - (\mathbf{k}\cdot\mathbf{V})^2 \coth kh - S\cos\theta(\mathbf{k}\cdot\mathbf{V})}. \tag{7}$$

This, in principle, is the full solution for the surface wave, where the generalisation from the infinite depth case reported in Ref. [14] is only the extra factor $\coth kh$ in the denominator. While seemingly innocuous, the added factor not only complicates the further analysis but its physical repercussions are also profound.

III. THE FAR-FIELD SOLUTION

The linear theory of ship waves, indeed of any waves generated by a localised source, encounter the same difficulty, that resulting expressions for the surface elevation contain a pole (or several) in the $\mathbf{k}$ plane. As discussed at length in the classical literature (e.g. [5, 17], the contribution from this pole contains the far-field, while further contributions to the integral vanish as $\xi \to \infty$. Physically this may be understood by noting that the zero of the denominator of (7) corresponds exactly to the condition

$$V\cos(\theta - \beta) = c(\mathbf{k}) \tag{8}$$

where [18]

$$c(\mathbf{k}) = \sqrt{(g/k)\tanh kh + (S/2k)^2\cos^2\theta\tanh^2 kh} - (S/2k)\cos\theta\tanh kh \tag{9}$$

is the phase velocity for a wave vector $\mathbf{k}$. Equation (8) results from insisting that waves seen in the far–field must satisfy the dispersion relation and have a phase velocity which produces waves which are stationary as seen from the source. In the following it will be convenient to work with the angle $\gamma = \theta - \beta$ instead of θ.

A complication is now that unlike the case of infinite depth, no explicit expression for the value of k at the pole may be found. The solution $K(\gamma)$ must instead be found numerically. The contribution from the pole is found by using the Sokhotsky-Plemelj theorem exactly as in Ref. [14], and the resulting expression in the far–field may be written

$$\zeta(\boldsymbol{\xi}) = -\frac{1}{4\rho\pi}\int_{-\pi/2}^{\pi/2} \mathrm{d}\gamma K(\gamma) p_{\mathrm{ext}}(K(\gamma)) \times \frac{\sin[K(\gamma)\xi\cos(\gamma + \beta - \phi)]}{\frac{\partial}{\partial k}G(k,\gamma)|_{k=K(\gamma)}}; \tag{10}$$

$$G(k,\gamma) = k - \frac{g}{V^2}\left[\frac{1}{\cos^2\gamma} - \frac{\mathrm{Fr}_S\cos(\gamma+\beta)}{\cos\gamma}\right]\tanh kh, \tag{11}$$

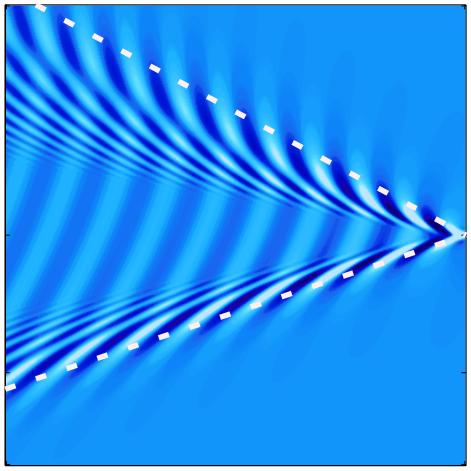

FIG. 2. Example of an asymmetric ship wake resulting from a sub–surface shear current normal to the ship's direction of motion. Here $\beta = \pi/2, \mathrm{Fr}_h = 0.8, \mathrm{Fr}_S = 0.5$ and $h = \infty$. The ship travels towards the right, and the dashed lines show the Kelvin angles (as defined in Ref. [14]) on either side of the wake.

where we have noted that only angles $|\gamma| < \pi/2$ can possibly satisfy Eq. (8), i.e., the wave propagation direction must have positive component along the direction of ship motion. $K(\gamma)$ now solves $G(k, \gamma) = 0$. An example of a boat wake with side–on shear is shown in figure 2, where the asymmetry both of the wake and of the Kelvin angles is clear to see.

IV. THE CRITICAL VELOCITY

When the velocity exceeds a critical value, it is necessary to further restrict the integration sector in Eq. (10), because waves propagating close to parallel with the ship motion (so–called transverse waves) are unable to keep up. To wit, equation (8) cannot be satisfied in a propagation direction θ for which $V\cos\gamma > c_{\max}(\theta)$ where $c_{\max}$ is the maximum phase velocity in said direction. From Eq. (9) one quickly verifies that the maximum velocity is found as $k \to 0$, hence the velocity V is supercritical when,

$$V\cos\gamma > \sqrt{gh + [\tfrac{1}{2}Sh\cos(\gamma+\beta)]^2} - \tfrac{1}{2}Sh\cos(\gamma+\beta).$$

We can re-write the condition for supercriticality as

$$\max_{\gamma}[\mathrm{Fr}_S\cos\gamma\cos(\gamma+\beta) + \mathrm{Fr}_h\cos^2\gamma] > 1 \qquad (12)$$

where $\mathrm{Fr}_h = V/\sqrt{gh}$ and the maximum is taken with respect to γ. Some straightforward but tedious algebra reveals that the maximum of the left hand side of (12) is found where $\tan\gamma = -\frac{1}{2}\mathrm{Fr}_S\sin\beta$. This is the propagation direction whose waves are first to vanish once the velocity exceeds the critical. Inserting this back into (12) we may write the condition for the velocity to be supercritical to be

$$\mathrm{Fr}_S(\cos\beta + \tfrac{1}{2}\mathrm{Fr}_S\sin^2\beta) + \mathrm{Fr}_h^2 > 1. \qquad (13)$$

At infinite depth ($\mathrm{Fr}_h \to 0$) the critical value of Fr_S was found in Ref. [14] to be $\mathrm{Fr}_{S,\mathrm{crit}} = 1/\cos^2(\beta/2)$. That what we have found is a generalisation of this is obvious when noting that Eq. (13) may be written instead as

$$\frac{\mathrm{Fr}_h^2}{1+\mathrm{Fr}_S\sin^2(\beta/2)} + \mathrm{Fr}_S\cos^2(\beta/2) > 1. \qquad (14)$$

Solved with respect to velocity, the critical value of V can be found as

$$V_{\mathrm{crit}} = 2\sqrt{gh}\frac{\sqrt{\mathrm{Fr}_{Sh}^2+4} - \mathrm{Fr}_{Sh}\cos\beta}{4+\mathrm{Fr}_{Sh}^2\sin^2\beta} \qquad (15)$$

where we defined the dimensionless group $\mathrm{Fr}_{Sh} = S\sqrt{h/g}$ (again a Froude number, with respect to length h and velocity Sh). Eq. (15) is readily found to have the appropriate limits as $h \to \infty$ and $S \to 0$.

We may finally derive, from Eq. (12), the angular sector in which waves are unable to keep up with the source and must be excluded from the integral of Eq. (10). A little algebra gives the two cutoff angles as

$$\gamma_{\mathrm{co}}^{\pm} = \arctan\Big[-\tfrac{1}{2}\mathrm{Fr}_S\sin\beta \pm \sqrt{(\tfrac{1}{2}\mathrm{Fr}_S\sin\beta)^2 + \mathrm{Fr}_h^2 + \mathrm{Fr}_S\cos\beta - 1}\Big].3g \qquad (16)$$

Angles $\gamma_{\mathrm{co}}^- < \gamma < \gamma_{\mathrm{co}}^+$ must be excluded from the integral, and only waves travelling at a sufficiently large angle with the ship's motion (diverging waves) may contribute to the wake.

V. DISCUSSION

The wake of waves behind a moving ship can change quite radically when a shear flow is present beneath the surface. The wake can be asymmetric and have a smaller or larger Kelvin angles than for uniformly flowing water, depending on the relative direction of motion of ship and shear flow. The presence of shear also limits the phase velocity of waves, introducing a critical velocity beyond which the transverse part of the wake disappears. This phenomenon is previously known from ship waves on water of finite depth. In the present endeavour we have laid out the theory for ship waves in the presence of both shear flow and finite depth, and found the critical ship velocity as an explicit function of shear, depth and the ship's direction of motion.

[1] Sir W. Thomson (Lord Kelvin), On ship waves, *Proc. Inst. Mech. Eng.* **38** 409–434 (1887).
[2] T.H. Havelock, The propagation of groups of waves in dispersive media, with applications to waves on water produced by a travelling disturbance, *Proc. R. Soc. London A* **81**, 398–430 (1908).
[3] T.H. Havelock, Wave resistance: Some cases of three–dimensional fluid motion, *Proc. R. Soc. London A* **95**, 354–365 (1919).
[4] Sir H. Lamb, *Hydrodynamics*, (Cambridge University Press, 1932).
[5] J. W. Wehausen and E. V. Laitone, Surface waves, in *Fluid Dynamics III* (ed. S. Flügge), Encyclopedia of Physics, vol. 9, 446–778, (Springer, 1960).
[6] M. Rabaud and F. Moisy, Ship waves: kelvin or Mach angle?, *Phys. Rev. Lett.* **110**, 214503 (2013).
[7] A. Darmon, M. Benzaquen, and E. Raphaël, Kelvin wake pattern at large Froude numbers, J. Fluid Mech. **738**, R3 (2014).
[8] M. Benzaquen, A. Darmon and E. Raphaël, Wake pattern and wave resistance for anisotropic moving disturbances, *Phys. Fluids* **26** 092106 (2014).
[9] G. Gomit, G. Rousseaux, L. Chatellier, D. Callaud, and L. David, Spectral analysis of ship waves in deep water from accurate measurements of the free surface elevation by optical methods, *Phys. Fluids* **26**, 122101 (2014).
[10] R. Pethiyagoda, S.W. McCue and T.J. Moroney, What is the apparent angle of a Kelvin ship wave pattern? *J. Fluid Mech.* **758** 468–485 (2014).
[11] F. Moisy and M. Rabaud, Scaling of far-field wake angle of nonaxisymmetric pressure disturbance, *Phys. Rev. E* **89** 063004 (2014).
[12] M. Rabaud and F. Moisy, Narrow ship wakes and wave drag for planing hulls, *Ocean Eng.* **90** 34–38 (2014)
[13] F. Moisy and M. Rabaud, Mach-like capillary-gravity waves, *Phys. Rev. E* **90** 023009 (2014).
[14] S.Å. Ellingsen, Ship waves in the presence of uniform vorcitity, *J. Fluid Mech.* **742** R2 (2014).
[15] D.H. Peregrine, Interaction of water waves and currents, *Adv. Appl. Mech.* **16** 9–117 (1976).
[16] G. Taylor, The action of a surface current used as a breakwater, *Proc. R. Soc. London A* **231** 466–478 (1955).
[17] J. Lighthill, *Waves in fluids*, (Cambridge University Press, 1978).
[18] S.Å. Ellingsen, Initial surface disturbance on a shear current: the Cauchy–Poisson problem with a twist, *Phys. Fluids* **26** 082104 (2014).

Total transmission through narrow gaps in channels

by D.V. Evans & R. Porter
University of Bristol, University Walk, Bristol, BS8 1TW, UK.
d.v.evans@bris.ac.uk

Highlights:

• A small gap approximation is used to show total transmission through multiple narrow gaps in barriers across a channel.

• Coupled integral equations are solved exactly on the basis of the small gap approximation.

1. Introduction

The phenomenon of 'extraordinary transmission' was first discovered in the field of optics. A recent review is given by Garcia de Abajo (2007).

Total transmission of a plane wave at a certain frequency is very familiar in the theory of linear water waves involving transmission over a long obstacle or past a pair of obstacles. See for example Newman (1965) and Porter & Evans (1995).

The solution to the problem of the transmission of plane waves through a gap in a barrier spanning a narrow channel is well-known. See for example Jones (1986) for an electromagnetic context. In this paper we show that 100% transmission can occur at a given frequency for an infinite sequence of spacings, when one or more extra identical barriers with small gaps are introduced. Specifically we consider the transmission of long waves down a channel of width $2d$ containing N equally-spaced thin rigid barriers spanning the channel each containing a central narrow gap of width $2a$. It is shown by comparison with a full numerical treatment that a small-gap approximation to the single barrier is remarkably accurate for a range of gap sizes. The technique is extended to obtain closed-form expressions for the reflection and transmission coefficients through the periodic array which are shown, as the spacing between the barriers increases, to reduce to the simple expressions based on a wide-spacing aproximation (WSA) given, for example, by Martin (2014). A key feature of the problem is the derivation of the condition under which we are in a pass or stop-band for the periodic structure. Also obtained is the condition for total reflection which disappears as the barrier spacing increases which is consistent with its non-appearance under the WSA.

2. The N-barrier problem

Since the channel walls and the barriers extend throughout the depth it is possible to factor out the depth dependence and we also assume a time harmonic dependence $\mathrm{e}^{-\mathrm{i}\omega t}$. Thus we seek a two-dimensional potential $\phi(x,y)$ satisfying

$$(\nabla^2 + k^2)\phi = 0 \tag{1}$$

in the fluid, where the wavenumber k is the real positive root of

$$\omega^2 = gk\tanh kh \tag{2}$$

where h is the depth of the channel. The barriers occupy $x = b_n = nb$, $n = 0, 1, 2, \ldots, N-1$, and the gaps occupy $L = \{|y| < a\}$. The no-flow condition on the walls demands

$$\phi_y(x, \pm d) = 0, \quad -\infty < x < \infty \tag{3}$$

whilst on the nth barrier ($n = 0, 1, 2, \ldots, N-1$)

$$\phi_x(b_n^{\pm}, y) = 0, \quad a < |y| < d. \tag{4}$$

For $x < 0$, general solutions of (1) satisfying (3) are

$$\phi(x,y) = \mathrm{e}^{\mathrm{i}kx} + R_N\mathrm{e}^{-\mathrm{i}kx} + \sum_{r=1}^{\infty} \frac{F_r^{(0)}\mathrm{e}^{\alpha_r x}\cos p_r y}{\alpha_r} \tag{5}$$

where $p_r = r\pi/d$, $\alpha_r = (p_r^2 - k^2)^{1/2}$, $\alpha_0 = -\mathrm{i}k$, $k < \pi/d$. For $x > (N-1)b$, we write

$$\phi(x,y) = T_N\mathrm{e}^{\mathrm{i}k(x-b_{N-1})} - \sum_{r=1}^{\infty} \frac{F_r^{(N-1)}e^{-\alpha_r(x-b_{N-1})}\cos p_r y}{\alpha_r}. \tag{6}$$

Finally, for $(n-1)b < x < nb$, $n = 1, 2, \ldots, N-1$, we write

$$\phi(x,y) = \sum_{r=0}^{\infty} \frac{(F_r^{(n)}\cosh\alpha_r(x-b_{n-1}) - \ldots}{\alpha_r\sinh\alpha_r b} \underline{\ldots F_r^{(n-1)}\cosh\alpha_r(b_n - x))\cos p_r y}. \tag{7}$$

In the above R_N and T_N are the reflection and transmission coefficients for N barriers and $F_r^{(n)}$ are undetermined coefficients. These definitions ensure that $\phi_x(b_n^+, y) = \phi_x(b_n^-, y)$, $|y| < d$, $n = 0, 1, 2, ..., N-1$ and we write

$$\phi_x(b_n, y) \equiv F^{(n)}(y) = \sum_{r=0}^{\infty} F_r^{(n)}\cos p_r y \tag{8}$$

whence (4) is used to give

$$F_r^{(n)} = \frac{1}{\epsilon_r}\int_L F^{(n)}(t)\cos p_r t\,dt \tag{9}$$

with $\epsilon_0 = 2d$, $\epsilon_r = d$, $r > 0$. In particular,

$$\mathrm{i}k(1-R_N) = F_0^{(0)}, \quad \mathrm{i}kT_N = F_0^{(N-1)}. \tag{10}$$

Continuity of pressure across the gap in the nth barrier demands $\phi(b_n^+, y) = \phi(b_n^-, y)$, $y \in L$ and gives, after using (5), (6), (7) and (9), $n = 1, 2, \ldots, N-2$,

$$\int_L \big(F^{(n+1)}(t)K_1(y,t) - 2F^{(n)}(t)K_2(y,t) + F^{(n-1)}(t)K_1(y,t)\big)\,dt = 0, \tag{11}$$

and

$$\int_L \big(F^{(1)}(t)K_1(y,t) - F^{(0)}(t)K_3(y,t)\big)\,dt = 2, \tag{12}$$

$$\int_L \big(F^{(N-1)}(t)K_3(y,t) - F^{(N-2)}(t)K_1(y,t)\big)\,dt = 0 \tag{13}$$

all for $y \in L$, in which

$$K_1(y,t) = \sum_{r=0}^{\infty} \frac{\cos p_r y \cos p_r t}{\epsilon_r \alpha_r \sinh \alpha_r b}, \tag{14}$$

$$K_2(y,t) = \sum_{r=0}^{\infty} \frac{\coth \alpha_r b\, \cos p_r y \cos p_r t}{\epsilon_r \alpha_r}, \tag{15}$$

and

$$K_3(y,t) = \sum_{r=0}^{\infty} \frac{(1+\coth \alpha_r b)\cos p_r y \cos p_r t}{\epsilon_r \alpha_r}. \tag{16}$$

3. The single barrier approximation

This generic problem forms the basis of the approach to the N-barrier problem. It is straightforward to show that $R_1 + T_1 = 1$ and that the horizontal velocity across L, $F^{(0)}(y)$ satisfies

$$\int_L F^{(0)}(t)K(y,t)\,dt = -R_1, \quad y \in L, \tag{17}$$

with

$$\int_L F^{(0)}(t)\,dt = 2\mathrm{i}kd\,T_1 \tag{18}$$

where

$$K(y,t) = \sum_{r=1}^{\infty} \frac{\cos p_r y \cos p_r t}{\alpha_r d}. \tag{19}$$

Note that the term $r = 0$ does not appear here. At this point we exploit the assumption that $a/d \ll 1$ so that the kernel $K(y,t)$ is dominated by a logarithmic term. Thus, we can write (e.g. Jones (1986) equn. (16.1))

$$K(y,t) = -\frac{1}{2\pi}\ln 2|\cos(\pi y/d) - \cos(\pi t/d)| + \sum_{r=1}^{\infty}\Big(\frac{1}{\alpha_r d} - \frac{1}{r\pi}\Big)\cos p_r y \cos p_r t \tag{20}$$

so that for $y, t \to 0$

$$K(y,t) \sim -\frac{1}{2\pi}\ln|y^2 - t^2| + \frac{1}{\pi}(S - \ln(\pi/d)) \tag{21}$$

where

$$S = \pi\sum_{r=1}^{\infty}\Big(\frac{1}{\alpha_r d} - \frac{1}{r\pi}\Big). \tag{22}$$

Substituting (21) into (17) and using the fact that $F^{(0)}(y)$ is even in y, gives

$$\int_L F^{(0)}(t)\ln|y-t|\,dt = A, \quad y \in L, \tag{23}$$

where $A = \pi R_1 + (S - \ln(\pi/d))\int_L F^{(0)}(t)\,dt$. The singular integral equation (23), where $F^{(0)}(y)(a^2 - y^2)^{1/2}$ is bounded, has an explicit solution, but all we require is the result

$$\int_L F^{(0)}(t)\,dt = A/\ln(a/2). \tag{24}$$

For a proof see Cooke (1970), and, for applications in water waves, Evans (1975), and Packham & Williams (1972) who also describe a three-dimensional version. It follows from (18), (23) and (24) that

$$\left.\begin{aligned} T_1 &= \cos\delta \mathrm{e}^{\mathrm{i}\delta} \\ R_1 &= -\mathrm{i}\sin\delta \mathrm{e}^{\mathrm{i}\delta} \end{aligned}\right\} \quad \tan\delta = 2\kappa(S(\kappa) - \ln\nu) > 0 \tag{25}$$

where

$$\kappa = kd/\pi < 1, \quad \nu = \pi a/2d. \tag{26}$$

The phase of T_1 will play a key role in the general theory and we make use of the result which follows from the above that if

$$\int_L F^{(n)}(t)K(y,t)\,dt = C, \quad y \in L, \tag{27}$$

then for $y, t \to 0$

$$\frac{1}{2d}\int_L F^{(n)}(y)dy = F_0^{(n)} = kC\cot\delta. \tag{28}$$

4. Solution for N barriers

Returning to the general case we have, from (14) to (16), as $y, t \to 0$,

$$K_1(y,t) \sim \frac{(-\mathrm{cosec}\, kb + E_1)}{2kd}, \tag{29}$$

$$K_2(y,t) - K(y,t) \sim \frac{(-\cot kb + E_2)}{2kd}, \tag{30}$$

and

$$K_3(y,t) - 2K(y,t) \sim \frac{(-\cot kb + E_2 + \mathrm{i})}{2kd}, \tag{31}$$

where

$$E_1 = \sum_{r=1}^{\infty}\frac{2kd}{\alpha_r d\sinh\alpha_r b}, \quad E_2 = \sum_{r=1}^{\infty}\frac{2kd\mathrm{e}^{-\alpha_r b}}{\alpha_r d\sinh\alpha_r b} \tag{32}$$

where the $E_i \to 0$ as $b/d \to \infty$, $i = 1, 2$. Substituting in (11)–(13), using (28) and defining $F_0^{(n)} = k\mu_n$ gives

$$\mu_{n+1} - 2\cos\alpha\mu_n + \mu_{n-1} = 0, \quad n = 1, 2, \ldots, N-2 \tag{33}$$

and

$$(p + \mathrm{i})\mu_0 + 2 = q\mu_1, \tag{34}$$

$$(p + \mathrm{i})\mu_{N-1} = q\mu_{N-2}. \tag{35}$$

In the above

$$p = 2\tan\delta - (\cot\kappa\lambda - E_2), \quad q = (-\mathrm{cosec}\,\kappa\lambda + E_1) \tag{36}$$

with $\kappa = kd/\pi$, $\lambda = \pi b/d$ and

$$\cos\alpha = \frac{(\cos\alpha_0 - E_2\sin kb)}{(1 - E_1\sin kb)} \tag{37}$$

where

$$\cos\alpha_0 = \frac{\cos(\delta + kb)}{\cos\delta} \equiv \frac{\cos(\delta + kb)}{|T_1|}. \tag{38}$$

Clearly $\alpha \to \alpha_0$ as $E_i \to 0$ which corresponds to $b/d \to 0$ or a wide-spacing approximation (WSA). For parameter values such that $|\cos\alpha| < 1$ it turns out we are in a pass-band which ensures wave transmission through the periodic array. For other values we are in a stop-band and transmission is not possible. See for example Linton & McIver (2001) equn. (6.52).
Finally,

$$R_N = 1 + \mathrm{i}\mu_0, \quad T_N = -\mathrm{i}\mu_{N-1}. \tag{39}$$

The solution of (33) satisfying (35) is, for $n = 0, 1, 2, \ldots, N-1$,

$$\mu_n = \mu_{N-1}\big((p + \mathrm{i})U_{N-n-2} - qU_{N-n-3}\big)/q \tag{40}$$

where $U_n(\alpha) = \sin(n+1)\alpha/\sin\alpha$, so that $U_{-2} = -1$, $U_{-1} = 0$, $U_0 = 1$. Thus from (39)

$$R_N = 1 + \mathrm{i}\mu_0 = \frac{q\mu_1 - (p - \mathrm{i})\mu_0}{q\mu_1 - (p + \mathrm{i})\mu_0} \tag{41}$$

after using (35). Now (40) can be used to show

$$R_N = \frac{(p^2+1)U_{N-2} - 2pqU_{N-3} + q^2U_{N-4}}{(p + \mathrm{i})^2U_{N-2} - 2q(p + \mathrm{i})U_{N-3} + q^2U_{N-4}}. \tag{42}$$

Similarly

$$T_N = \frac{2\mathrm{i}q}{(p + \mathrm{i})^2U_{N-2} - 2q(p + \mathrm{i})U_{N-3} + q^2U_{N-4}}. \tag{43}$$

The above expressions turn out to hold for $N = 2$ also where only (32) and (33) are required. The energy condition $|R_N|^2 + |T_N|^2 = 1$ can be shown to be satisfied exactly after some algebra.
It is clear from (43) that $T_N = 0$ if $q = 0$ for all $N > 1$ which is obvious on physical grounds. Less obvious is the fact that the condition is independent of the smallness of the gap. Now from (36) and (32), $q = 0$ implies

$$\sin\kappa\lambda = \left[\sum_{r=1}^{\infty} \frac{2\kappa}{(r^2 - \kappa^2)^{1/2}\sinh\lambda(r^2 - \kappa^2)^{1/2}}\right]^{-1}. \tag{44}$$

It is clear that provided the right-hand-side of (44) is less than unity, solutions of the form $\lambda(\kappa)$ exist, but that there will be a cut-off at, say, $\lambda = \lambda_c(\kappa)$ above which no solution is possible. This is consistent with the WSA valid for large λ which predicts no solution.
The vanishing of $|T_N|$ for any $N > 1$ is an unusual phenomenon, rare in water wave problems which was first shown by Evans & Morris (1972) in considering the scattering of waves by a pair of partially-immersed vertical barriers. For detailed and accurate computations see Porter & Evans (1995). However, it is the phenomenon of total transmission which is the main interest in this paper, particularly in the light of the assumption of small gaps. Thus the numerator in (42) is real so it can be expected that $R_N = 0$ for certain values of p, q, and α. As a special case we consider wide barrier spacing when the E_i in (32) tend to zero. After considerable algebra it can be shown that (42) and (43) become

$$R_N = \frac{U_{N-1}R_1}{U_{N-1} - T_1\mathrm{e}^{\mathrm{i}kb}U_{N-2}} \tag{45}$$

$$T_N = \frac{T_1}{U_{N-1} - T_1\mathrm{e}^{\mathrm{i}kb}U_{N-2}} \tag{46}$$

in agreement with Martin (2014) equn. (21). The condition $R_N = 0$ for total transmission is now simply $U_{N-1}(\alpha_0) = 0$ or $\alpha_0 = m\pi/N$, $m = 1, 2, \ldots, N-1$ so that from (38)

$$\cos\frac{m\pi}{N} = \frac{\cos(\delta + kb)}{\cos\delta}, \quad m = 1, 2, \ldots, N-1. \tag{47}$$

Thus for example, for $N = 2$ we have $\cos(\delta + kb) = 0$ or $\delta + kb = (2p-1)\pi/2$, p an integer.

5. Results

In Fig.1 the solid lines describe the variation of $|R_1|$ with kd for gap sizes $a/d = 0.1, 0.2, 0.3, 0.4$ using an accurate numerical method described in Porter & Evans (1995). The crosses are computed using the small-gap result given in (25). The agreement for $a/d = 0.1$ is excellent over the whole range of $kd < \pi$ and this value together with $kd = 1$ will be used in the further computations for multiple barriers.
The result (47) shows that a WSA approximation provides $N-1$ equations to determine when $R_N = 0$ and $|T_N| = 1$ for each region in which $\cos\alpha_0 < 1$ and we are in a pass-band, and we might expect that to be the case generally when the numerator of (42) vanishes. This is confirmed in Fig. 2 where $N = 4$ and $a/d = 0.1$ throughout. The solid lines show, in $(kd, b/d)-$space,

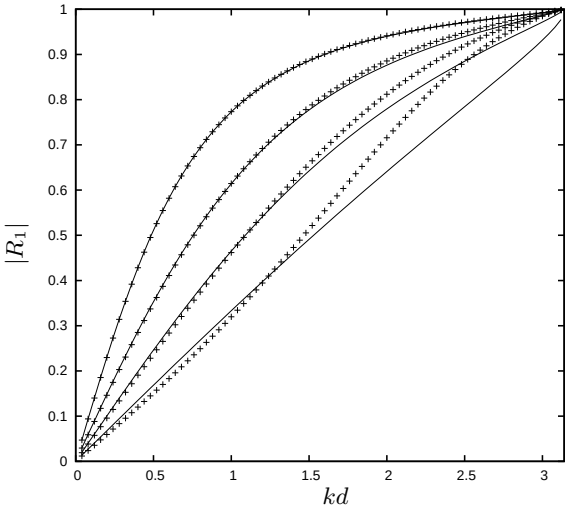

Figure 1: Comparison of small gap approximation against exact results for a single barrier.

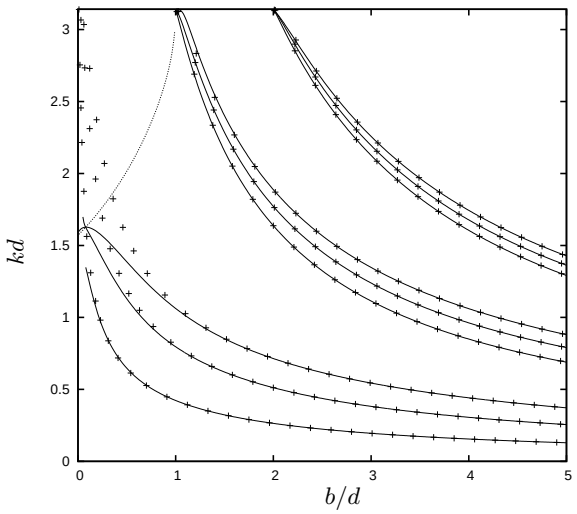

Figure 2: Solid curves/points show $R_4 = 0$ for $N = 4$ barriers with $a/d = 0.1$ using exact/WSA theory. The dotted line is $T_4 = 0$.

where $R_4 = 0$ and the crosses are based on the WSA. Thus for example for $kd = 1$ as b/d increases there are three different spacings at which $R_4 = 0$ followed by a gap before a further three cut in and so on. Alternatively, Fig. 2 shows that at a given spacing there are three distinct wavenumbers for which total transmission occurs with further groups of three at higher frequencies occurring for larger spacings. It is also clear that for most purposes the WSA is entirely adequate in predicting the results. The solution for $b/d \lesssim a/d$ is less clear as it conflicts with the small-gap approximation. Also shown in Fig. 2 is a dotted line on which $T_4 = 0$ derived from (44) and which has no counterpart in a WSA. It is possible to consider a semi-infinite array of barriers by ignoring condition (35) and assuming $\mu_n = A\mathrm{e}^{\pm \mathrm{i}n\alpha}$ as a solution of (33) whence (34) gives

$$R_\infty = \frac{q\mathrm{e}^{\pm \mathrm{i}\alpha} - (p - \mathrm{i})}{q\mathrm{e}^{\pm \mathrm{i}\alpha} - (p + \mathrm{i})} \tag{48}$$

the sign chosen so that $|R_\infty|$ does not exceed unity. The WSA counterpart of (48) requires replacing α by α_0. Fig. 3 shows a plot of $|R_4|$ and $|R_\infty|$ against b/d based on the exact small-gap theory with the WSA results overlaid. It shows clearly the triplets of zeros of R_4 separated by stop bands.

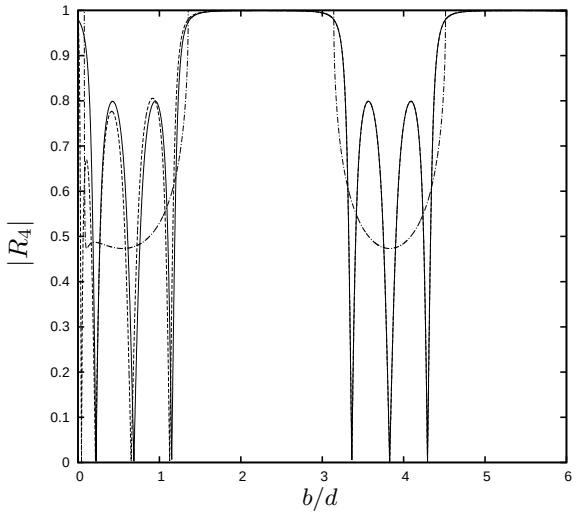

Figure 3: Solid/dashed lines are exact/WSA results for $N = 4$ barriers with $a/d = 0.1$ and $kd = 1$. The chained line is $|R_\infty|$.

References

1. Garcia de Abajo, F.J., 2007, *Rev. Mod. Phys.* **79** 1267.
2. Newman, J.N., 1965, Propagation of water waves past a long two-dimensional obstacle. *J. Fluid Mech.* **23** 23-29.
3. Porter, R. & Evans, D.V., 1995, Complementary approximations to wave scattering by vertical barriers. *J. Fluid Mech.* **294** 155-180.
4. Jones, D.S., 1986, Acoustic and Electromagnetic Waves. Clarendon Press Oxford.
5. Martin, P.A., 2014, N masses on an infinite string and related one-dimensional scattering problems. *Wave Motion* **51** 296-307.
6. Cooke, J.C., 1970, *Glasgow Math. J.* **17** 9-20.
7. Evans, D.V., 1975, A note on the total reflexion or transmission of surface waves in the presence of parallel obstacles. *J. Fluid Mech.* **67** 465-472.
8. Packham, B.A. & Williams, W.E., 1972, A note on the transmission of water waves through small apertures *J. Inst. Maths. Applics.* **10** 176-184.
9. Linton, C.M. & McIver, P., 2001, Handbook of Mathematical Techniques for Wave/Structure Interactions. CRC Press.
10. Evans, D.V. & Morris, C.A.N., 1972, Complementary approximations to the solution of a problem in water waves. *J. Inst. Maths. Applics.* **10** 1-9.

Numerical Simulation of Breaking Wave Impact on a Vertical Wall

Feng Gao, Jun Zang, Chris Blenkinsopp

Department of Architecture and Civil Engineering, University of Bath
Bath, United Kingdom
E-mail: f.gao@bath.ac.uk

Highlights:

- A compressible multiphase flow solver based on OpenFOAM has been successfully applied to simulate breaking wave impact on a vertical wall.
- Different types of wave impact on a vertical wall have been produced. The results of the pressure distribution near the impact area and the maximum impact pressure have been analysed.

1. Introduction

The loading caused by steep storm waves impacting coastal and offshore structures such as vertical sea walls, FPSOs and LNG carriers can cause significant damage. Accurate prediction of the breaking wave impact pressure is a key factor in the design of such structures. The fundamental role of the extreme impact pressures that are impulsively exerted on sea walls has been underlined by both experimental (e.g. Hattori *et al.* [1]; Bullock *et al.* [2]) and theoretical (e.g. Peregrine [3]) studies. In addition, numerous numerical works have been carried out to provide a reliable tool for the estimation of wave impact pressure. Lin and Liu [4] gave an overview and discussion of the different numerical techniques which have been used for interface tracking in breaking wave simulation, while Christensen *et al.* [5] undertook a comprehensive review of advances in numerical modelling and measurement techniques for the study of the surf zone.

In this study, a compressible multiphase flow solver based on the frame of open source CFD tool – OpenFOAM is used to simulate the breaking wave propagation, overturning and impact on a vertical wall. With a suitable predefined initial condition, different types of wave impact on a vertical wall have been produced. The results of the pressure distribution near the impact area and the maximum impact pressure will be analysed.

2. Numerical tools

OpenFOAM is a freely available set of applications developed to solve particular problems in continuum mechanics, which consists of a wide range of solvers and libraries. It has gained popularity in coastal and offshore engineering studies (Jacobsen *et al.* [6]; Chen *et al.* [7]; Morgan *et al.* [8]). *twoPhaseEulerFoam* is one of the component solvers included in the OpenFOAM package. In this solver, both air and water-air mixture are treated as compressible fluids, which are continuum and described by Eulerian conservation equations. The averaged inter-phase momentum transfer term accounts for the transfer of momentum between the two phases.

The averaged momentum and continuity equations for each phase φ can be written as:

$$\frac{\partial \alpha_\varphi \overline{U}_\varphi}{\partial t} + \nabla \cdot \left(\alpha_\varphi \overline{U}_\varphi \overline{U}_\varphi\right) + \nabla \cdot \left(\alpha_\varphi \overline{R}_\varphi^{eff}\right) = -\frac{\alpha_\varphi}{\rho_\varphi} \nabla \overline{p} + \alpha_\varphi g + \frac{\overline{M}_\varphi}{\rho_\varphi} \tag{1}$$

$$\frac{\partial \alpha_\varphi}{\partial t} + \nabla \cdot \left(\overline{U}_\varphi \alpha_\varphi\right) = \Gamma_\varphi \tag{2}$$

where the subscript φ denotes the phase, α is the phase fraction, $\overline{U}_\varphi$ is the averaged phase velocity, $\overline{R}_\varphi^{eff}$ is the combined Reynolds and viscous stress, $\overline{M}_\varphi$ is the averaged inter-phase momentum transfer term and Γ_φ stands for the mass gained by each phase per unit volume and time.

Combining equation (2) for the two phases when φ = a (for air) and φ = b (for water-air mixture) yields the volumetric continuity equation which can be formulated as an implicit equation for pressure.

The governing equations are solved by a pressure-based method PIMPLE, which is a hybrid PISO/SIMPLE algorithm used to couple the pressure and velocity fields. Whilst the free surface is handled by a volume of fluid (VOF) method with bounded compression techniques.

3. Numerical simulation

To avoid simulating waves from the wavemaker through to breaking, generation of breaking waves can be performed by starting from an initial deformed free surface. With a suitable initial free surface shape for the numerical simulation, different types of wave impact on the wall can be easily generated (Scolan *et al.* [9]). Here we use a hyperbolic tangent shape to define the initial free surface:

$$y = h + A\tanh\big(R(x - L/2)\big), \quad 0 < x < L \tag{3}$$

where L is the length of the wave tank, h is the mean water depth, A is the amplitude of the mode and R is the parameter controls the slope of the difference in height. The shape is defined in a coordinate system where the origin is located at the bottom left corner. By varying the parameters, a large range of wave shapes can be generated to simulate different types of wave impact on the vertical wall.

There are many different classifications being used for wave impact. According to Bullock *et al.* [2], there are four distinct types of wave impacts, where the impact type changes with decreasing distance between the breaking point and the wall:

(a): the aerated impact, where the wave has broken in front and hits the wall with an aerated water mass;
(b): the air pocket impact, where the wave crest hits the wall with enclosing a thin air bubble;
(c): the flip through impact, where the wave crest hits the wall and runs up without trapping air bubble;
(d): the slosh impact, where the run up of the wave is higher than the wave crest, so that the wave crest hits the water layer instead of the wall.

We focus on air pocket and flip through impact in this investigation for the maximum impact pressure on the vertical wall. By setting constant parameters L = 2m, A = 0.16m and R = 5, and varying the mean water depth h from 0.22m to 0.26m, several cases of wave impact on a vertical wall are numerically simulated. The height of the numerical domain is chosen as 0.6m, which is much higher than the height of the initial free surface, to leave enough space for the air flow and wave impact to be fully developed.

For a mean water depth of 0.22m, with wave overturning and breaking on the vertical wall, the wave crest hits the wall and encloses a large air-pocket. With increasing the mean water depth, the size of the entrapped air-pocket decreases, until it vanishes. After that, the wave impact type changes from air-pocket impact to flip through impact, where the wave crest hits the wall and runs up without trapping air bubble. These can be seen clearly in Fig. 1, for h = 0.22m and 0.24m, the wave impacts on the wall with entrapped air bubble (air-pocket impact), while for h = 0.25m and 0.26m, the wave impacts on the wall without trapping air bubble (flip through impact).

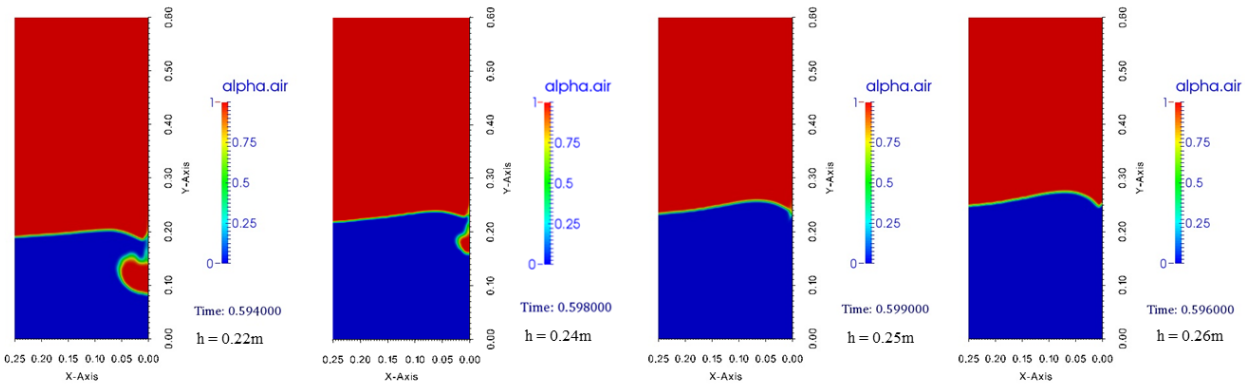

(a) air-pocket impact (b) flip through impact

Fig. 1. The free surface profiles at the time of peak impact for different initial water depths.

Fig. 2 shows the pressure distribution at the time of peak impact for different initial water depths relative to Fig. 1. The maximum pressure is located at the jet impact area. For an air-pocket impact, the pressure inside the air bubble is very high, and smaller air pockets tend to lead to higher pressures. For example, the air-pocket size for h = 0.24m is smaller than that for h = 0.22m, but the maximum pressure for h = 0.24m is 30kPa, which is much higher than 18kPa for h = 0.22m (Fig. 2 (a) and (b)). The flip through impact has a rather smaller impact area and generates a higher impact pressure (Fig. 2 (c) and (d)). For h = 0.25m, the maximum impact pressure reaches 51kPa, which is much higher than that of air-pocket impact.

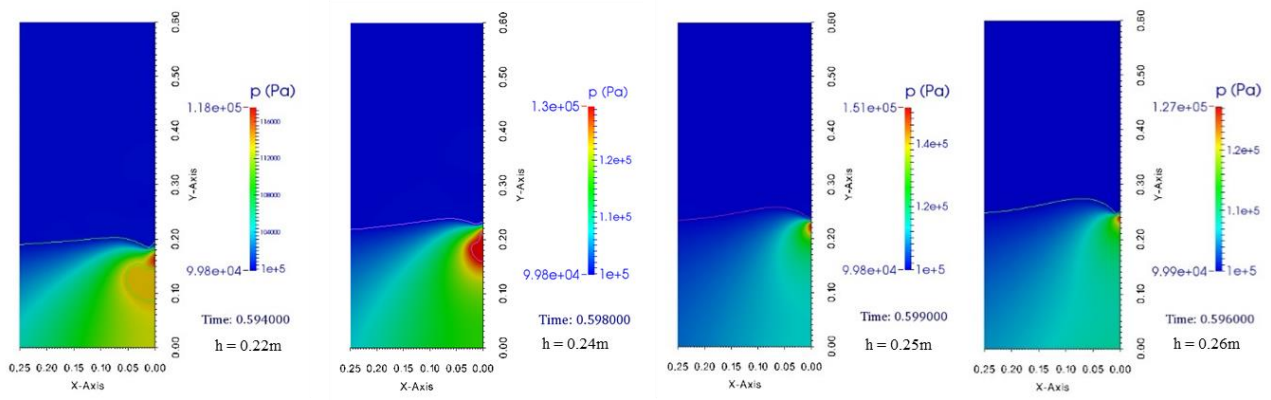

(a) air-pocket impact (b) flip through impact

Fig. 2. The pressure distributions at the time of peak impact for different initial water depths.

For the air-pocket impact, the entrapped air bubble is compressed horizontally against the wall by water pushing behind, and vertically by the trough run-up, which leads to oscillations of the air pocket (Bullock *et al.* [2]). The pressure on the wall will oscillate after the crest impact, associated with the compression and expansion of the air pocket. These phenomena can be seen clearly in Fig. 3 (a), the pressure on the wall oscillates after the peak impact where the measured points are located inside and below the air pocket. For the flip through impact, the pressure on the wall reaches to a sharp peak pressure when the wave crest hits the wall, and then damps very quickly with no pressure oscillation as shown in Fig. 3 (b). The duration of the high pressure impact is very small, less than 1ms.

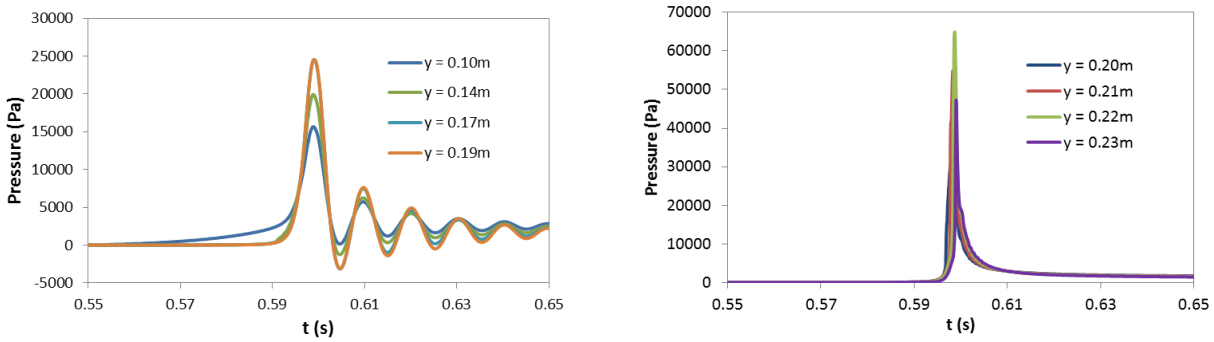

(a) air-pocket impact as h = 0.24 m (b) flip through impact as h = 0.25 m

Fig. 3. Time histories of impact pressure on the wall at different locations.

Fig. 4 shows the dimensionless pressure distributions along the wall for different initial water depths. It can be seen that the air-pocket impact causes a round peak pressure, which causes a larger impact area on the wall. The impact pressure for the small air pocket is larger than that for the big air pocket. The flip through impact exhibits a single sharp peak pressure, which indicates the larger impact pressure is not only related to smaller durations, but also to smaller impact areas. The largest pressure is created by flip through impact, for h = 0.25m, with the maximum dimensionless impact pressure reaching $p/\rho g h_o$=26. The mean water depth is also sensitive to the impact pressure. For ~1cm of difference in the mean water depth, the maximum impact pressure on the wall is reduced about 50%.

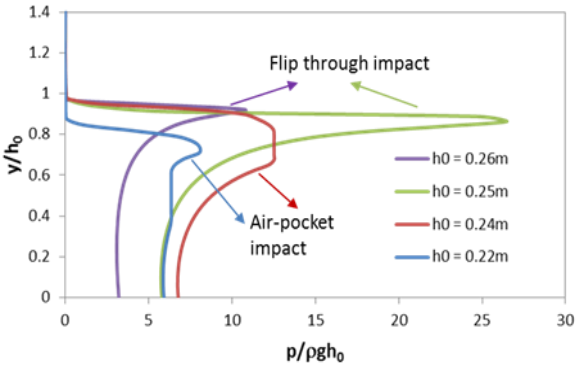

Fig. 4. Pressure along the wall at the moment of maximum impact pressure.

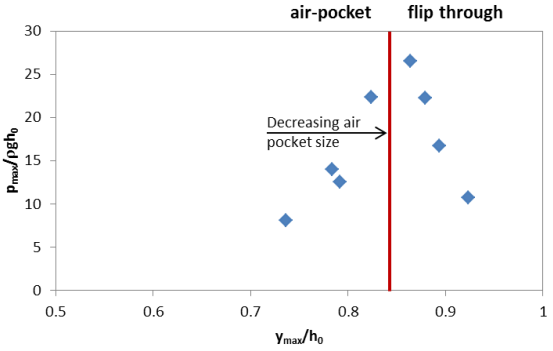

Fig. 5. Variation of dimensionless maximum impact pressures with impact locations

Fig. 5 shows the variation of dimensionless maximum impact pressures with impact locations. For the conditions of our predefined initial free surface, with increasing the mean water depth from mean water depth h = 0.22m to h = 0.26m, the wave impact point also occurs higher on the wall, whilst the trapped air pocket size decreases until it vanishes, corresponding maximum impact pressure reaches its peak value, and the impact type changes from air-pocket impact to flip through impact. After that, the maximum impact pressure will be reduced with increasing the mean depth, although impact location still grows higher

4. Conclusion

An open source compressible multiphase flow solver *twoPhaseEulerFoam* has been successfully used to simulate air-pocket and flip through wave impact on a vertical wall. The results show that the variability of the impact pressure is very large. The air pocket impact causes a round peak which happens at the location of the jet impact, whilst the flip through impacts exhibit a single sharp peak at the location where the wave crest and wave trough meet. The pressure oscillation inside the trapped air pocket has been recorded while the flip through impact does not generate pressure oscillation after the wave crest hits the wall.

Acknowledgements

This research was supported by the United Kingdom EPSRC Project: FROTH (Fundamentals and Reliability of Offshore Structure Hydrodynamics), under grant Ref: EP/J012777/1.

References

[1] Hattori M, Arami A & Yui T (1994) Wave impact pressure on vertical walls under breaking waves of various types. *Coastal Engineering.* Vol 22, pp 79-114.

[2] Bullock G, Obhrai C, Peregrine D, Bredmose H (2007). Violent breaking wave impacts. Part 1: Results from large-scale regular wave tests on vertical and sloping walls. *Coastal Engineering.* Vol 54, pp 602–617

[3] Peregrine DH (1993). Water-wave impact on walls. *Annual Review of Fluid Mechanics*. Vol 35, pp 23-43.

[4] Lin P and Liu PL-F (1999). Free surface tracking methods and their applications to wave hydrodynamics, Vol. 5 of Advances in Coastal and Ocean Engineering, World Scientific, pp 213-240.

[5] Christensen ED, Walstra DJ and Emarat N (2002). Vertical variation of the flow across the surf zone, *Coastal Engineering*, Vol 45, pp169-198.

[6] Jacobsen NG, Fuhrman DR and Fredsøe J (2012), A wave generation toolbox for the open-source CFD library: OpenFoam. *International Journal for Numerical Methods in Fluids*, Vol 70, Issue 9, pp 1073–1088.

[7] Chen LF, Zang J, Hillis AJ, Morgan GCJ and Plummer AR (2014), Numerical investigation of wave-structure interaction using OpenFOAM, *Ocean Engineering*, Vol 88, pp91-109.

[8] Morgan, G. and Zang, J. *et al.* (2010), Using the rasInterFoam CFD model for wave transformation and coastal modeling. The 32nd international Conference on Coastal Enginering (ICCE 2010).

[9] Scolan Y-M (2010), Some aspects of the flip-through phenomenon: A numerical study based on the desingularized technique, *Journal of Fluids and Structures*, Vol 26, Issue 6, pp 918-95.

Interaction distance for scattered and radiated waves in large wave energy parks

Malin Göteman, Jens Engström, Mikael Eriksson, and Jan Isberg

Department of Engineering Sciences, Uppsala University, Uppsala, Sweden
Email address of presenting author: malin.goteman@angstrom.uu.se

Highlights

- A multiple scattering method with an interaction distance is presented, which includes hydrodynamical interactions between devices that are within an arbitrarily specified distance from each other.
- The method allows for faster modelling and optimization of wave energy parks to a chosen degree of accuracy, as compared to well-established software. Irregular waves measured at the west coast of Sweden are used as input in a time-domain model where the motion and power of the devices are computed.
- The paper is an extension to the approximate method presented at the previous workshop [1].

1 Introduction

Wave energy technology is currently at the stage where several developers are taking the step to full-scale, commercial energy production. For most of the concepts, large-scale electricity production requires that single wave energy converters (WECs) are combined into larger arrays, or parks. In particular, this is true for the wave energy concept developed at Uppsala University, where the individual WECs are relatively small and consist of surface buoys connected to linear direct-driven generators at the sea bed, see figure 1. The devices in a wave energy park are not independent but will interact both hydrodynamically and electrically, and the interactions may cause large increase or decrease in the produced electricity, depending on the park geometry, wave direction, distance between devices, etc. With the present advancement of several wave energy concepts into the commercial and full-scale phase, the need for reliable simulation tools that can model full wave energy parks is immense, and the area is receiving increasing attention [2, 3, 4, 5].

This paper focuses on the hydrodynamical interactions between large arrays of floating buoys by scattered and radiated waves. In general, when the number of interacting structures in an array grows, the complexity of the model increases, and the numerical simulations are a challenge that call for new methods and theories. Here, a nearest-neighbour approach is taken to enable simulations of large WEC arrays. A model based on the multiple scattering theory [6, 7] is presented, which includes full hydrodynamical interaction between all bodies within an arbitrarily defined *interaction distance*, but excludes the interaction between devices that are further apart than this distance. The interaction distance is so defined that either the interaction by scattered waves is excluded for devices sufficiently far apart (point-absorber approximation [8, 9]), or that the interaction by radiated waves is excluded, or both. As such, the model resembles somewhat the hierarchical multiple scattering theory [10] or similar models of semi-infinite WEC arrays using asymptotic approaches [11, 12], or modules of multiple scales [13]. This method is a cruder, yet perhaps more flexible way to include only the most relevant hydrodynamical interaction. No dependency of different length scales is needed, and any park geometry can be studied; the distance between the WECs may vary, and the positions may be completely arbitrary. The method presented here is a work-in-progress to address multiple parameter optimization of large wave energy parks.

The hydrodynamical coefficients computed with this semi-analytical method are used as input in a time-domain method where the motion of the buoys are computed as a convolution with incident irregular waves, measured at the Lysekil test side on the west coast of Sweden. The power of each device can then be computed and serves as data for comparisons and optimization methods for wave energy parks. The results of the method are compared with results where the hydrodynamics is computed using the state-of-the art software WAMIT.

2 Theory

Coupled equations of motion Arrays of N point-absorber wave energy converters (WECs) are studied, each consisting of a cylinder buoy with radius R and draft d, connected by a stiff line to a direct-driven generator.

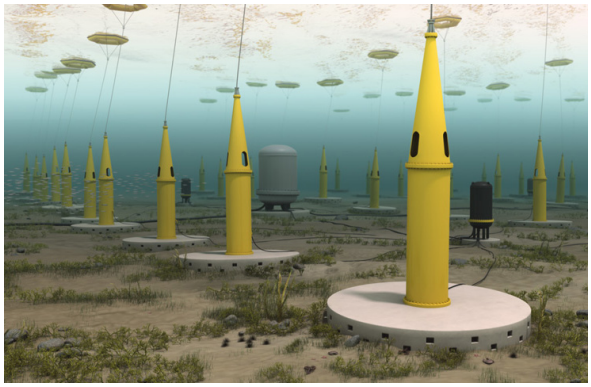

Figure 1: A wave energy park based on the concept of Uppsala University wave energy converters.

The total force determining the dynamics of the float is given as a sum of the exciting force $F_{\text{exc}}(t)$ from the incident waves, the radiation force $F_{\text{rad}}(t)$ from the oscillations of the floats, the hydrostatic restoring force $F_{\text{stat}}(t) = -\rho g \pi R^2 z(t)$ and the damping power take-off force of the generator $F_{\text{exc}}(t) = -\gamma \dot{z}(t) - k_s z(t)$, where k_s is the spring constant of a retracting spring. In this paper, the buoys are constrained to move in heave only. To compute the dynamical forces, we assume non-steep waves and that the fluid is non-viscous, irrotational and incompressible. Then, the fluid velocity potential satisfies the Laplace equation, the boundary constraints can be linearized, and the total fluid velocity potential will be the superposition of incoming, scattered and radiated waves, $\phi = \phi_0 + \phi_S + \phi_R$. In the frequency domain, the time-dependence is factored out and the dynamical forces are given as integrals of the fluid velocity potentials over the wetted surface of the buoys. The vertical coordinate in the frequency domain can be solved for in terms of a transfer function $H(\omega)$, see [1]. In irregular waves, the position is then obtained by a convolution between the inverse Fourier transform of the transfer function with the amplitude of the incident waves, $z(t) = (h * \eta_{\text{in}})(t)$. With the position in time determined, the absorbed power of the WEC can be calculated as $P(t) = \gamma \dot{z}(t)^2$. The irregular waves used to actuate the model are measured outside the Swedish west coast, where the wave climate in general is relatively moderate and the linear approximation can be used with good agreement with full-scale experiments [14].

Multiple scattering theory Divide the fluid domain with depth h into interior and exterior domains underneath and outside each buoy. A general solution to the Laplace equation and the boundary conditions can be found by separation of variables. In local cylindrical coordinates (r_j, θ_j, z) with origin in the center of the cylinder, the solution in the exterior domain takes the form

$$\phi^{j,\text{ext}} = \sum_{n=-\infty}^{\infty} \left[\sum_{m=0}^{\infty} \psi_m(z) \left(\alpha_{mn}^j \frac{K_n(k_m r_j)}{K_n(k_m R)} + \beta_{mn}^j \frac{I_n(k_m r_j)}{I_n(k_m R)} \right) \right] e^{in\theta_j}, \tag{1}$$

where $\psi_m(z)$ are normalized vertical eigenfunctions. The wave number $k_0 = -ik$ is a root to the dispersion relation $\omega^2 = gk \tanh(kh)$ and $K_n(k_0 r) \propto H_n^{(1)}(kr)$ and $I_n(k_0 r) \propto J_n(kr)$ correspond to propagating modes. The wave numbers k_m, $m > 0$ are roots to the dispersion relation $\omega^2 = -gk_m \tan(k_m h)$ and correspond to evanescent modes. A general potential in the interior domain underneath the cylinder can be written in the form

$$\phi^{j,\text{int}} = \sum_{n=-\infty}^{\infty} \left[\frac{V^j}{2(h-d)^2} \left((z+h)^2 - \frac{r^2}{2} \right) + \gamma_{0n}^j \left(\frac{r_j}{R} \right)^{|n|} + 2 \sum_{m=1}^{\infty} \gamma_{mn}^j \cos(\lambda_m (z+h)) \frac{I_n(\lambda_m r_j)}{I_n(\lambda_m R)} \right] e^{in\theta_j}, \tag{2}$$

where $\lambda_m = m\pi/(h-d)$. Consider an incoming wave ϕ_0 propagating along the x-axis. In the diffraction problem, all buoys are considered fixed ($V^j = 0$ for all $j \in N$). The diffracted wave in the exterior domain of a buoy $i \in N$ will be a superposition of the incident wave and the scattered waves from the remaining cylinders incident on a buoy, which can be added by applying addition theorems for Bessel functions, $\phi_D^{i,\text{ext}} = \phi_0^i + \phi_S^j\big|_i + \phi_S^i$. By requiring continuity between the exterior and interior domains and truncating the infinite sums, the unknown coefficients α_{mn}, β_{mn} and γ_{mn} can be solved for according to the multiple scattering theory [7].

In the radiation problem, the buoys are free to move but there is no incident wave ϕ_0. The exterior potential will in general be a superposition of the outgoing radiated and scattered waves, and the incoming radiated and scattered waves from the remaining buoys, $\phi_D^{i,\text{ext}} = \phi_R^i + \phi_S^i + \phi_S^j\big|_i + \phi_R^j\big|_i$. Again, continuity requirements across the domain borders will imply a system of linear equations where the unknown coefficients can be solved for.

Interaction distance The multiple scattering approach includes a diffraction matrix with all the interaction terms. We introduce an interaction distance $D_{\text{int},S}$ for the diffraction problem, and only include the interaction terms corresponding to devices that are within this distance from each other. The resulting diffraction matrix will be sparse and the computational costs are lowered. Further, a separate interaction distance $D_{\text{int},R}$ for the radiation problem is introduced, which specifies which devices should interact by radiated waves, i.e. which non-diagonal terms in the radiation force are to be computed. This further speeds up the simulations.

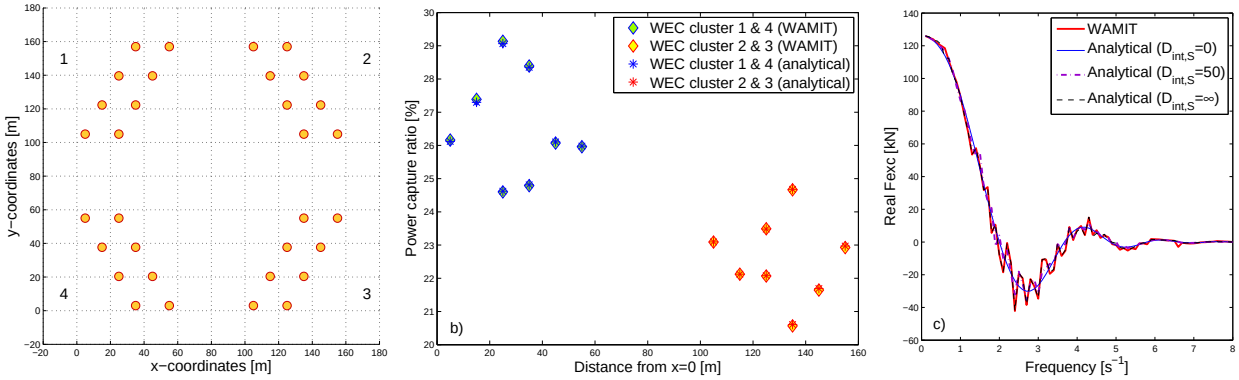

Figure 2: Array with 32 WECs in four clusters, numbered clockwise as in the left figure. b) Power capture ratio for all 32 devices, computed by both the analytical method with infinite interaction distance and with WAMIT. c) The real part of the excitation force in the array: without, with partial and with full multiple scattering.

3 Results

Accuracy and computational cost The hydrodynamical model has been implemented in a Matlab code and connected to a time-domain model with time-series of measured waves as input. The inversion of the diffraction matrix is computed using the object-oriented factorization algorithm of [15].

In figure 2, the power capture ratio $PCR = \bar{P}/(2JR)$, where J is the energy transport of the incident wave travelling along the x-direction, has been computed for each of the devices in an array with 32 WECs, using the analytical method with full multiple scattering (infinite interaction distance). As can be seen from the figure, due to symmetry, the WECs in the two clusters 1 and 4 (and 2 and 3) have identical PCR, and the agreement with WAMIT is good, but with only 28% of the computational cost of WAMIT. All simulations are performed on a standard desktop PC with Intel(R) Xeon(R) 3.07 GHz processor and 6 MB RAM.

In figure 2c), the real part of the excitation force in the same park with 32 WECs is computed without multiple scattering ($D_{\text{int},S} = 0$), with partial multiple scattering ($D_{\text{int},S} = 50$) and with full multiple scattering ($D_{\text{int},S} = \infty$). The partial multiple scattering includes diffraction between devices within 50 m distance from each other; the resulting excitation force will be a combination of single-body and full multiple scattering.

No hydrodynamical interaction for distant structures In figure 3, the power per device for an array with 9 WECs in a square configuration (shown in the figure) has been computed for different values of the interaction distance. The horizontal and vertical distance D between adjacent WECs in the array is increased from 4 m to 80 m. For interaction distances $D_{\text{int},S,R} = 0$ (blue crosses), no hydrodynamical interaction is computed, which implies that the average power per device is constant, independent of the separation distance between devices. For $D_{\text{int},S,R} = 50$ (purple plus signs), only hydrodynamical interaction between devices within 50 m from each other is accounted for. When full hydrodynamical interaction is included (black dots), the agreement with WAMIT is very good. From the figure it is clear that the approximation with $D_{\text{int},S,R} = 50$ agrees with the full multiple scattering simulation when the separating distance between adjacent devices is $D < D_{\text{int},S,R}/2\sqrt{2} = 17.7$, since all devices are within 50 m distance from each other. When D exceeds $D_{\text{int},S,R}/2\sqrt{2}$, the corner WECs lose hydrodynamical contact, and for D exceeding $D_{\text{int},S,R}/\sqrt{5}$, $D_{\text{int},S,R}/2$ and $D_{\text{int},S,R}/\sqrt{2}$, more of the hydrodynamical interactions within the park are lost. At $D > D_{\text{int},S,R}$, no hydrodynamical interactions are computed. These distances are indicated by vertical lines in figure 3. The computational time (lower plot) decreases with reduced number of hydrodynamical interaction terms to be computed.

No multiple scattering for distant structures It is also possible in the model to choose a different interaction distance for the radiation $D_{\text{int},R}$ and diffraction $D_{\text{int},S}$ problems. In figure 4, the average power per device has been computed as function of number of devices in square array with WECs at 20 m distance from each other. The agreement between the analytical method with full multiple scattering and WAMIT is very good, the deviation between the methods is never larger than 0.2%. Interaction distance $D_{\text{int},R} = D_{\text{int},S} = 50$ gives an approximation whose error increases with the number of WECs: 3% for an array with 25 WECs and 7% for 49 WECs. A better approximation, which gives the same time savings, is to include interaction by radiation for all WECs ($D_{\text{int},R} = \infty$), but neglect multiple scattering ($D_{\text{int},S} = 0$). Also here, the error increases with the number of devices, but is still less than 3% for an array with 49 WECs.

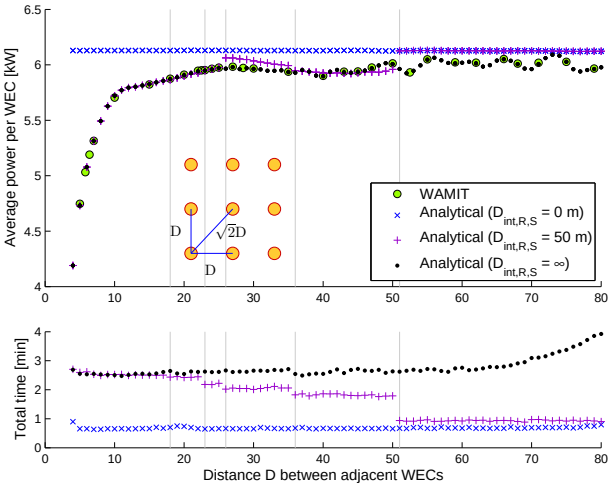

Figure 3: Power per device computed with the analytical model with different interaction distances in the array with 9 WECs, compared to the value computed using WAMIT. The lower plot shows the total computational time for each of the simulations.

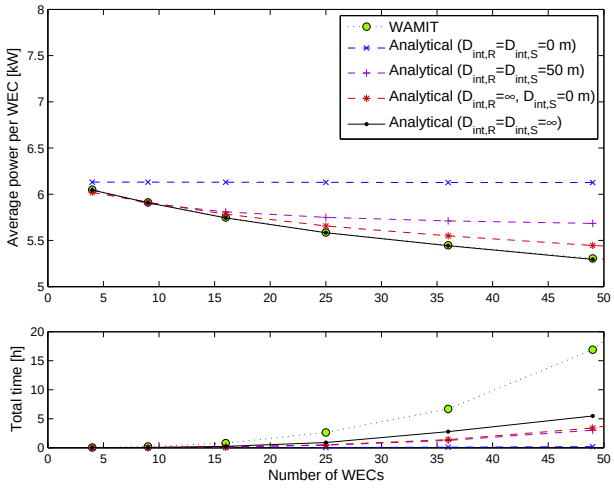

Figure 4: Average power per device computed with WAMIT, with the analytical method, and with the approximate analytical method with different interaction distances, as well as the corresponding computational time for each simulation.

4 Discussion

An advantage of having introduced the interaction distance in the model can be seen in figures 3: when WECs are far away from each other, the error of neglecting their hydrodynamical interactions is less than when they are close. Indeed, the point-absorber approximation has been found to give accurate results when the separating distance between devices is $D > 5R$ [16]. Hence, in a large park, a suitable interaction distance can be defined, such that both an acceptable accuracy and computational speed is achieved. Depending on the accuracy needed, this interaction distance can be increased or decreased as wanted. As figure 4 shows, for large parks it may be advantageous to choose different interaction distances for the radiation and diffraction problems.

Up to now, most optimization studies of wave energy parks have either compared different array configurations by trial-and-error, changed one-parameter at a time or studied only regular waves. Multiple parameter optimization of large-scale wave energy parks requires a hydrodynamical model which is both reasonably accurate and fast. This model is a work-in-progress to address optimization modelling of wave energy parks in a more systematic way and with realistic, irregular waves as input.

References

[1] M. Göteman, J. Engström, M. Eriksson, J. Isberg, and M. Leijon. In *29th IWWWFB*, Osaka, Japan, 2014.
[2] J. Cruz, R. Sykes, P. Siddorn, and R. Eatock Taylor. In *Proc. of the 8th EWTEC*, Uppsala, Sweden, 2009.
[3] B.F.M. Child and P. Laporte Weywada. In *Proc. of the 10th EWTEC*, Aalborg, Denmark, 2013.
[4] M. Vicente, M. Alves, and A. Sarmento. In *Proc. of the 10th EWTEC*, Aalborg, Denmark, 2013.
[5] J. Engström, M. Eriksson, M. Göteman, J. Isberg, and M. Leijon. *J. Appl. Physics*, 114:204502, 2013.
[6] M. Ohkusu. In *Intl. Symp. on Dynamics of Marine Vehicles and Structures in Waves*, volume 12, pages 107–112, London, UK, 1974.
[7] H. Kagemoto and D.K.P. Yue. *J. Fluid Mech.*, 166:189–209, 1986.
[8] D. Evans. pages 213–249. Power from Sea Waves. Academic Press, 1980.
[9] J. Falnes. *Appl. Ocean Res.*, 2:75, 1980.
[10] M. Kashiwagi. In *The 14th IWWWFB*, Port Huron, USA, April 1999.
[11] M. A. Peter and M. H. Meylan. *J. Fluid Mech.*, 575:473–494, 2007.
[12] B.G. Carter and P. McIver. *J. Eng. Math.*, 81:9–45, 2013.
[13] X. Garnaud and C.C. Mei. *J.Fluid Mech.*, 635, 2009.
[14] M. Eriksson, R. Waters, O. Svensson, J .Isberg, and M. Leijon. *J. Appl. Physics*, 102(084910), 2007.
[15] T.A. Davis. *ACM Transactions on Mathematical Software*, 39(4):28:1–28:18, 2013.
[16] S.A. Mavrakos and P. McIver. *Applied Ocean Research*, 19(5–6):283 – 291, 1997.

Validation of a nonlinear spectral model for water waves over a variable bathymetry

M. Gouin[1,2], G. Ducrozet[1], and P. Ferrant[1]

[1]Ecole Centrale Nantes, LHEEA Lab., UMR CNRS 6598, Nantes, France
[2]Institut de Recherche Technologique Jules Verne, Bouguenais, France
*maite.gouin@ec-nantes.fr

Highlights

- Presentation of an HOS scheme for modelling non-linear water waves over a variable bathymetry.
- Validation of the method for a small variation of the bottom with Bragg reflection.
- Application of the HOS model to wave propagation over a bathymetry with high variation of the bottom: submerged bar.

Introduction

The accurate modelling of surface gravity waves over non-negligible bottom topography is of major interest in the field of marine renewable energy. These marine renewable structures are intended to be located in limited water depth, where the effect of variable bathymetry is very significant on local wave conditions. Indeed, when entering shallow water, waves are strongly affected by the bottom through shoaling, refraction, diffraction, reflection and the resulting variations in local wave speed.

In [8] two different schemes for modelling a bathymetry with a High-Order Spectral (HOS) method have already been presented. This highly non-linear potential model has been initially developed [16, 5] for a flat bottom and extensively validated for different configurations in the LHEEA Lab [7, 6] from regular waves up to irregular multidirectional wavefields. This model, named HOS-ocean is available as an open-source version[1]. In the present paper, we focus on the efficient scheme allowing the use of FFTs presented in [8].

A few HOS applications consider a variable bathymetry. Liu and Yue [10] provided one simulation case with a bottom variation using the HOS method, but considering only a small variation of the bottom. This case reproduces Class I Bragg reflection and will be presented here as a validation of our model. The second case presented in this paper is more extreme with large bottom variations. Nevertheless, our method shows good results which are compared both to experimental results [11, 4] and numerical results obtained with other methods [1, 9].

[1]https://github.com/LHEEA/HOS-ocean/wiki

Methods and Algorithms

Hypothesis and formulation of the problem

In this section, the main hypothesis and equations are presented briefly. More details are available in [8].

$z = \eta(x,t)$ represents the free surface elevation, h the total water depth, h_0 the mean depth and $\beta(x)$ the bottom variation, such as $-h(x) = -h_0 + \beta(x)$. Thus we have : $-h_0+\beta(x) \leq z < \eta(x)$. A potential flow formalism is used (incompressible and inviscid fluid, irrotational flow) and we assume periodic boundary conditions in the horizontal plane so that the domain is considered infinite. We obtain the following set of equations:

- Laplace equation in the fluid domain:

$$\Delta\phi = 0 \tag{1}$$

- Free-surface boundary conditions (FSBC) written in terms of surface quantities η and $\tilde{\phi}$ ($\tilde{\phi}(x,t) = \phi(x, z=\eta, t)$):

$$\frac{\partial\eta}{\partial t} = \left(1 + \left|\frac{\partial\eta}{\partial x}\right|^2\right)\frac{\partial\phi}{\partial z} - \frac{\partial\tilde{\phi}}{\partial x}\cdot\frac{\partial\eta}{\partial x} \quad \text{on} \quad z=\eta(x,t) \tag{2}$$

$$\frac{\partial\tilde{\phi}}{\partial t} = -g\eta - \frac{1}{2}\left|\frac{\partial\tilde{\phi}}{\partial x}\right|^2 + \frac{1}{2}\left(1+\left|\frac{\partial\eta}{\partial x}\right|^2\right)\left(\frac{\partial\phi}{\partial z}\right)^2 \quad \text{on} \quad z=\eta(x,t) \tag{3}$$

- Bottom boundary condition (BBC):

$$\frac{\partial\phi}{\partial x}\frac{\partial\beta}{\partial x} - \frac{\partial\phi}{\partial z} = 0 \quad \text{on} \quad z = -h_0 + \beta(x) \tag{4}$$

To account for a bottom variation, an additional potential is introduced. The total potential ϕ_{tot} solution of the problem is expressed as:

$$\phi_{tot} = \phi_{h_0} + \phi_\beta \tag{5}$$

ϕ_{h_0} satisfies a Neumann condition on $z = -h_0$, therefore ϕ_{h_0} is solution of the problem at constant depth h_0. ϕ_β allows the definition of the correct bottom boundary condition (Eq.4) and satisfies a Dirichlet condition on $z = 0$.

In 2D, the potentials are expanded on basis functions taking into account the previous boundary conditions:

$$\phi_{h_0}(x,z,t) = \sum_j A_j(t)\frac{\cosh(k_j(z+h_0))}{\cosh(k_j h_0)}e^{ik_j x} \tag{6}$$

$$\phi_\beta(x,z,t) = \sum_j B_j(t) \frac{\sinh(k_j z)}{\cosh(k_j h_0)} e^{ik_j x} \quad (7)$$

with $k_j = \frac{j\ 2\pi}{L_x}$ and $(A_j(t), B_j(t))$ the modal amplitudes of ϕ_{h_0} and ϕ_β respectively.

High-Order-Spectral Method

The HOS model is a pseudo-spectral model initially developed in [16, 5]. The potential is expressed as a truncated power series of components $\phi^{(m)}$ for $m = 0$ to M (M is the order of the HOS method). Then, the potential evaluated at the free surface is expanded in a Taylor series with respect to the mean water level $z = 0$. Combining these two expansions gives a triangular set of Dirichlet problems for the components that can be solved by means of a spectral method (allowing the use of FFT's for efficient computations). One more equation is needed to find the modal amplitudes $A_{j_1}^{(m)}(t)$ and $B_{j_1}^{(m)}(t)$ at each order m.

These are given by the iterative method described hereafter (Fig.2). Once they are computed, the vertical velocity W at the free surface can be obtained from another triangular system. The solution ϕ_{tot} is then advanced in time as described in Fig.1, with W computed as represented in Fig.2.

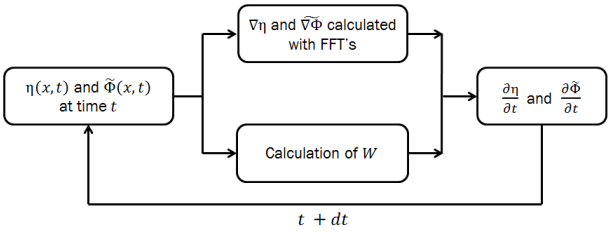

Figure 1: Temporal solution of the FSBC.

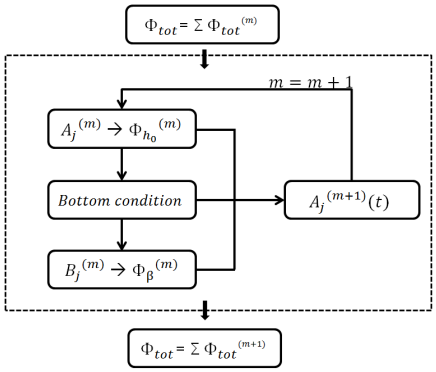

Figure 2: Use of the BBC in the temporal solution.

The bottom condition (Eq.4) reads:

$$\sum_{m=1}^{M} \frac{\partial \phi_{tot}^{(m)}}{\partial x}\frac{\partial \beta}{\partial x} - \sum_{m=1}^{M} \frac{\partial \phi_{tot}^{(m)}}{\partial z} = 0 \text{ on } z = -h_0 + \beta(x) \quad (8)$$

By assuming that $\beta << 1$ we can write a Taylor expansion with respect to the mean depth $z = -h_0$ at the order M. We also assume[2] that $O(\beta) \equiv O\left(\frac{\partial \beta}{\partial x}\right) \equiv O(\eta)$ and we keep only terms of order $\eta^{(m)}$. Thus we find the equations presented in [10]:

$$m = 1 : \frac{\partial \phi_{tot}^{(1)}}{\partial z}(x, -h_0, t) = 0$$

$$m = 2..M :$$

$$\frac{\partial \phi_{tot}^{(m)}}{\partial z}(x, -h_0, t) = \sum_{l=1}^{m-1} \frac{\partial}{\partial x}\left[\frac{\beta^l}{l!}\frac{\partial^{l-1}}{\partial z^{l-1}}\left(\frac{\partial \phi_{tot}}{\partial x}\right)^{(m-l)}\right]_{z=-h_0} \quad (9)$$

Perturbation expansions are truncated at order M. This new development Eq.(9) allows the computation of the modal amplitudes $B_{j_1}^{(m)}(t)$ at each order in function of the $A_{j_1}^{(m)}(t)$, and is independent of the position x, so FFT's can still be used, preserving the numerical efficiency of original HOS scheme as seen in [8].

Validations

In [8], a validation case has already been presented to assess the domain of applicability of our method. It allows to check the convergence of the scheme on the reconstruction of the vertical velocity with a wide variety of wave conditions and non-negligible (but constant) bottom variations. Here we present a test case to demonstrate the accuracy and efficiency of the proposed HOS model with a variable bathymetry. As an example of a small bottom variation, and in order to satisfy the conditions of the Taylor expansion ($\beta << 1$), the proposed test case considers Bragg reflection from a sinusoidal bottom patch.

[2]If Taylor expansions in η and β converge, the equality on the orders of magnitude is meaningless.

Bragg reflection

If the class I Bragg condition is satisfied, the reflected wave should be amplified as a result of resonant quadratic interaction between the incident wave and the bottom variation. For small incident waves and small bottom slopes, reflection near Bragg resonances is well predicted by multiple-scale linearized perturbation theory [12]. Here we analyse non-linear effects. The conditions of the experimental set-up [3] are used to compare with their experiments.

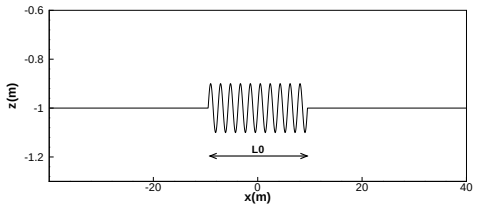

Figure 3: bottom topography with a patch of 10 sinusoidal ripples of amplitude $d = 0.1$ and slope $k_b d = 0.31$.

The bottom patch is defined as the variation around the mean water depth $h = h_0 + \beta(x)$ by :

$$\beta(x) = d\sin(k_b x) \quad \text{for } -L_0 \le x \le L_0 \quad (10)$$

as depicted in Fig.3, with k_b the bottom wavenumber. The free surface is located at $z = 0$. The ripple slope

is $k_b d = 0.31$, the ripple amplitude is $d = 0.1m$ and the length of the patch is $\frac{L_0}{\lambda_b} = 10$ (i.e. a patch of 10 sinusoidal ripples of wavelength $\lambda_b = \frac{2\pi}{k_b}$). The incident wave is at the linear resonance condition of $k = \frac{k_b}{2}$ with a wave steepness of $ka = 0.05$. In order to ensure periodicity relaxation zones are used to impose the Rienecker and Fenton solution at the beginning and at the end of the domain.

We perform simulations with $\frac{N}{\lambda} = 16$ nodes per wavelength and an order $M = 2$ to obtain the steady-state. This order of nonlinearity on the free-surface and on the bottom variation is sufficient to obtain converged results, because the Class I Bragg reflection is second order, as explained in [10]. The local reflection coefficient is then extracted using the method of Suh et al. [15].

The results appear in Fig.4 along with the experimental measurements of [3] and the solution given by the linear perturbation theory of [12]. It appears clearly that our numerical results are very closed to both the linear theory and the experiments. We will now focus on the next test case with a higher bottom variation, to check the ability of the proposed method is able to treat realistic bathymetry profiles with non-negligible variations.

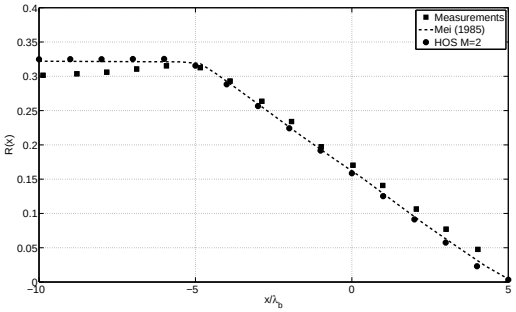

Figure 4: Bragg reflection from a sinusoidal bottom ripple patch over $-5\lambda_b \leq x \leq 5\lambda_b$. $ka = 0.05$ and $k_b d = 0.31$.

Application: harmonic generation over a submerged bar

Here we consider the transformation of non-linear regular waves as they travel up and over a submerged bar. As they propagate over the bar, they steepen and they decompose into higher-frequency free waves, as shown in the experiments [4, 11]. These higher harmonics produce an irregular pattern behind the bar. This validation case is particularly difficult because it requires the accurate propagation of waves in both deep and shallow water. Thus it is often used as a discriminating test case for non-linear models of surface waves propagation over a variable bottom [9, 1]. The bottom variation is defined by

$$\beta(x) = \begin{cases} 0.05\,(x-6) & \text{for } 6 \leq x \leq 12, \\ 0.3 & \text{for } 12 \leq x \leq 14, \\ 0.3 - 0.1\,(x-14) & \text{for } 14 \leq x \leq 17, \\ 0 & \text{elsewhere,} \end{cases}$$

and can be seen in Fig.5. It has been scaled with a factor of two in comparison with Dingemans experiments [4].

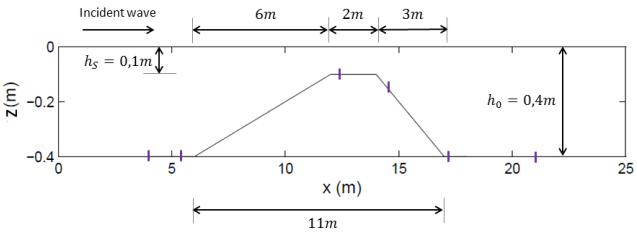

Figure 5: Submerged bar (Dingemans experiments).

Regular waves are generated at the left side of the domain thanks to a solution of Rienecker and Fenton [13] of steepness $ka = 0.0168$ and relative water depth $kh = 0.6725$. The period is fixed to 2.02s with an amplitude of 0.01m.

The convergence and steady-state are reached with 40 nodes per wavelength and an HOS order $M = 17$. Indeed, such a high-order is needed to represent all the non-linearities induced by the bottom variation.

Time series of surface elevations.

A snapshot of the surface elevation (scaled by a factor of 3) is represented in Fig.6 and the time histories of the surface elevations at various locations are shown in Fig.7. The experimental data comes from the experiment of [11].

The comparison between our numerical results and the experimental data is very good, and similar to the results obtained with other numerical methods [9, 1]. Thus, both free-surface non-linearities and bottom non-linearities are correctly solved and we are confident in the accuracy of the model even for large bottom variations.

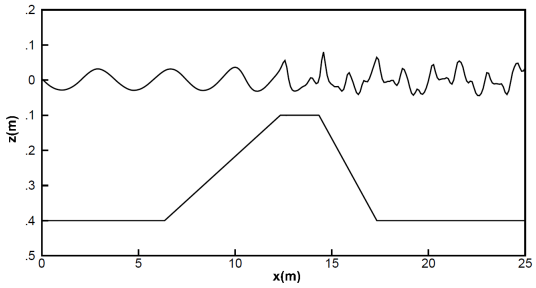

Figure 6: Snapshot of the surface elevation at steady-state.

Harmonic analysis.

For a deeper comparison, an harmonic analysis of the surface elevation is run as presented in [1]. Our results are visible in Fig.8.

As expected, we can clearly observe the generation of high-harmonics over the bar. Moreover, the comparison of all harmonics with the measurements is good even up to the fifth-harmonic. It is also very similar to the numerical results presented in [1], particularly on the slight discrepancies observed on the first harmonic. We can notice that even if $\frac{\beta}{h_0} = 75\%$ over the submerged bar (which represents a very large relative bottom variation), the steepness is weak ($ka = 0.017$), and the bottom variation does not take place on all the domain, so the model is able to solve this problem accurately.

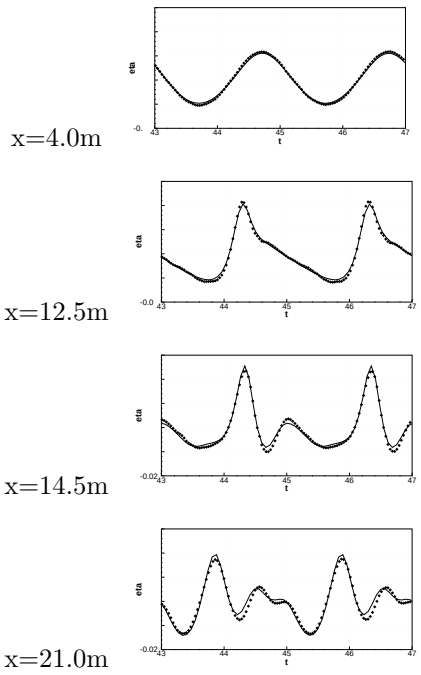

Figure 7: Time series of measured (points) and computed (lines) surface elevations.

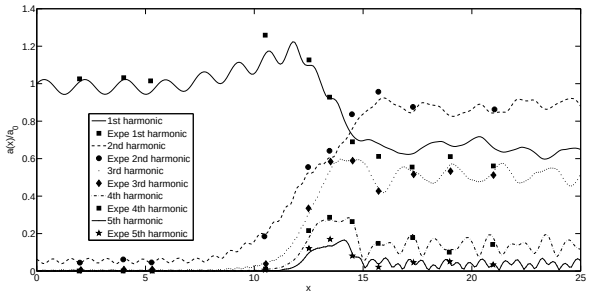

Figure 8: Harmonic analysis. $\frac{N}{\lambda} = 40$ and $M = 17$.

.

Conclusion

We have implemented a numerical method for the simulation of non-linear free surface waves over variable depth. It is based on a Taylor expansion of the bottom boundary condition with respect to the mean water depth.

A validation case with a constant bottom variation has already been presented in [8] to assess the domain of applicability of our method. By a series of two test cases, we have shown the accuracy of the method for non-constant bottom variations. The first test case reproduces Bragg reflection over small bottom variations and shows results conformed to [10, 1, 9]. The last case simulates highly and realistic varying bottom geometries. It shows very good agreement with both numerical and experimental data, and thus proves the ability of the method to accurately compute high variations of the bathymetry.

The required HOS order is very high for the harmonic generation over a submerged bar, and the bottom and the free-surface do not seem to require expansions with the same order of non-linearity. Thus we will try to improve the method by decoupling the orders of non-linearities on the free-surface and on the bottom to enhance the efficiency of our model. This has been presented with the DNO method [9, 2], a formalism which exhibits a formalism similar to the HOS method [14].

References

[1] H.B. Bingham and H. Zhang. On the accuracy of finite-difference solutions for nonlinear water waves. *J. Fluid Mech.*, 58:211–228, 2007.

[2] Walter Craig, Philippe Guyenne, David P. Nicholls, and Catherine Sulem. Hamiltonian long–wave expansions for water waves over a rough bottom. volume 461, pages 839–873. The Royal Society, 2005.

[3] A. G. Davies and A. D. Heathershaw. Surface-wave propagation over sinusoidally varying topography. *Journal of Fluid Mechanics*, 144:419–443, 7 1984.

[4] M.W. Dingemans. Comparison of computations with Boussinesq-like models and laboratory measurements. *Delft Hydraulics memo H1684.12.*, 1994.

[5] D.G. Dommermuth and D.K.P. Yue. A high-order spectral method for the study of non-linear gravity waves. *J. Fluid Mech.*, 184:267–288, 1986.

[6] G. Ducrozet, F. Bonnefoy, D. Le Touzé, and P. Ferrant. 3-D HOS simulations of extreme waves in open seas. *Nat. Hazards Earth Syst. Sci*, 7:109–122, 2007.

[7] G. Ducrozet, F. Bonnefoy, D. Le Touze, and P. Ferrant. A modified high-order spectral method for wavemaker modeling in a numerical wave tank. *Eur. J Mech. B, Fluid.*, 34:19–34, 2012.

[8] M. Gouin, G. Ducrozet, and P. Ferrant. Development of a highly nonlinear model for wave propagation over a variable bathymetry. In *26th international workshop on water waves and floating bodies, Proceedings*, 2014.

[9] P. Guyenne and D.P. Nicholls. A high-order spectral method for nonlinear water waves over moving bottom topography. *J. Sci. Comput.*, 30:81–101, 2007.

[10] Y. Liu and D.K.P. Yue. On generalized Bragg scattering of surface waves by bottom ripples. *J. Fluid Mech.*, 356:297–326, 1998.

[11] H.R. Luth, G. Klopman, and N. Kitou. Kinematics of waves breaking partially on an offshore bar. *Delft Hydraulics memo H1573*, 1994.

[12] Chiang C. Mei. Resonant reflection of surface water waves by periodic sandbars. *J. Fluid Mech.*, 152:315–335, 1985.

[13] M.M. Rienecker and J.D. Fenton. A Fourier approximation method for steady water waves. *J. Fluid Mech.*, 104:119–137, 1981.

[14] H.A. Schaffer. Comparison of Dirichlet-Neumann operator expansions for nonlinear surface gravity waves. *Coast. Engng.*, 55(4):288–294, 2008.

[15] Kyung Doug Suh, Woo Sun Park, and Beom Seok Park. Separation of incident and reflected waves in wavecurrent flumes. *Coastal Engineering*, 43(34):149 – 159, 2001.

[16] B.J. West, K.A. Brueckner, R. S. Janda, D. M. Milder, and R. L. Milton. A new numerical method for the surface hydrodynamics. *J. Geophys. Res.*, 92:11803–11824, 1987.

Strongly nonlinear evaluation of internal ship wakes

John Grue
Mechanics Division, Department of Mathematics, University of Oslo, Norway
johng@math.uio.no

• ship internal wave wakes at supercritical speed;
• strongly nonlinear interfacial model accounting for realistic ship geometries of draught comparable to the average depth of the pycnocline;
• similarities and differences between two- and three-layer fluids;
• numerical wake-induced amplitudes, currents, strain rate, with comparison to field experiments.

Background. There is a recent interest in internal wave wakes, generated by a ship moving in a stratified sea, at supercritical speed (Daniel Bourgault, 2014, personal communication). Watson et al. (1992) gives a summary of this research up to that date. Recent analyses and calculations given in the IWWWFB-community are obtained applying pressure distributions (Parau et al., 2007). Watson et al. (1992) analysed aspects of the ship generated internal waves using data from a set of experiments, with three different ships, in Loch Linnie, Scotland in 1989. They presented results for the wave wake amplitudes, wake-induced currents and quantity such as the strain rate at the sea surface. While existing models, at that time, basically assumed ships of very small draught, Watson et al. requested prediction tools that could allow for a finite draught of the ship. Such calculations are performed in the present account, with realistic ship models of draught comparable to the average depth of the pycnocline (see figure 3a,b).

Nonlinear interfacial model. Let $\mathbf{x} = (x_1, x_2)$ denote horizontal coordinates and y be vertical. $y = 0$ coincides with the interface at rest. A two-layer fluid has constant densities ρ_0 and $\rho_1 = \rho_0 + \Delta\rho$, where index 0 refers to the upper layer and index 1 to the lower. Layer depths at rest are h_0 and h_1, respectively. Assuming incompressible and irrotational motion in each of the layers, the fluid motion is governed by Laplacian potentials ϕ_0 and ϕ_1. The position of the ship geometry moving in the upper fluid, with speed U along the x_1-direction, is determined by $y = h_0 + \delta(\mathbf{x}, t)$ where $\delta(\mathbf{x}, t)$ determines the hull shape. The boundary condition at the ship geometry is given by $\delta_t + W_F = 0$ where $W_F = \mathbf{U} \cdot \nabla\delta$. The boundary of the upper fluid is denoted by F and is represented by a rigid lid at positions not occupied by the ship.

The interface, denoted by I, is determined by $y = \eta(\mathbf{x}, t)$. Values of the potentials along I are introduced by $\phi_{0I}(\mathbf{x}, t) = \phi_0(\mathbf{x}, y = \eta, t)$ and $\phi_{1I}(\mathbf{x}, t) = \phi_1(\mathbf{x}, y = \eta, t)$ on I, where indexes $0I$ and $1I$ indicate evaluation on the upper and lower side of the interface, respectively. Difference and sum potentials along I are introduced, where

$$\Psi(\mathbf{x}, t) = \phi_{1I}(\mathbf{x}, t) - \mu\phi_{0I}(\mathbf{x}, t) \quad \text{and} \quad \Phi(\mathbf{x}, t) = \phi_{0I}(\mathbf{x}, t) + \phi_{1I}(\mathbf{x}, t) \quad \text{at} \quad I, \tag{1}$$

and $\mu = \rho_0/\rho_1$. The interfacial motion and potential Ψ along I are integrated forward in time using the kinematic and dynamic boundary conditions at the interface:

$$\eta_t = V_I = W_I, \quad \Psi_t + g(1 - \mu)\eta = \mathcal{N}\mathcal{L}_2 \quad \text{at} \quad I, \tag{2}$$

where $\mathcal{NL}_2$ accounts for the full nonlinearity, $W_I = (\partial\phi_0/\partial n)\sqrt{1+|\nabla\eta|^2}$ and $V_I = (\partial\phi_1/\partial n)$ $\sqrt{1+|\nabla\eta|^2}$. Solution of the Laplace equation in each layer is obtained by use of Green's theorem. W_I, V_I and ϕ_{0F}, where the latter denotes the potential along the upper boundary F of fluid 0, including the ship surface, are expanded by $W_I = W_I^{(1)} + W_I^{(2)} + ...$, $V_I = V_I^{(1)} + V_I^{(2)} + ...$, $\phi_{0F} = \phi_{0F}^{(1)} + \phi_{0F}^{(2)} + ...$ In Grue (2015) it is shown that the quadratic approximation, i.e. truncating after the leading two terms of the expansions, fully accounts for the interfacial nonlinearity, for excursions η corresponding to the thinner layer depth. This approximation is used here.

Two- and three-layer fluids. The dispersion relation for a two-layer fluid reads $(ck_1)^2 = g(1-\mu)k_1/[\mu\coth(k_1h_0) + \coth(k_1h_1)]$, where k_1 denotes wavenumber and $c(k_1)$ wave speed (figure 1b). The dispersion relation for a three-layer fluid, where a pycnocline of thickness γ separates an upper mixed layer from a lower mixed layer, reads $K_\gamma^2 - k_1[\coth(k_1H_0) + \coth(k_1H_1)]K_\gamma\cot(K_\gamma\gamma) - k_1^2\coth(k_1H_0)\coth(k_1H_1) = 0$, where $K_\gamma^2 = N_0^2/c^2 - k_1^2$ and $N_0^2 = -(g/\rho)(\partial\rho/\partial y)$ denotes the buoyancy frequency, assumed to be constant in the three-layer model, see figure 1a, where also symbols are defined. The limit $k_1 \to 0$ obtains the linear long wave speed c_0. The wave phase speed $c(k_1)/c_0$ and group velocity $c_g(k_1)/c_0$ for the two- and three-layer fluids show small differences for kh_0 up to 0.7 (figure 1c).

Wave patterns and amplitudes. Ship geometries have a hull shape of $\delta = -b_0[1 - (x_1/(l_0/2))^6 - (x_2/(w_0/2))^6]$, where (l_0, w_0, b_0) denotes (length,width,draught). Calculations with $l_0/h_0 = 14.7, w_0/h_0 = 4$ and $b_0/h_0 = 1.2$ obtain the wave pattern for supercritical flow at speed $Fr = U/c_0 = 8$ (figure 2a). The pattern corresponds excellent to the patterns obtained by a linear kinematics analysis, for two- and three-layer fluids (Keller and Munk, 1970). Nonlinear calculations of the wave trough amplitudes show a small leading trough. Wave troughs number 2, 3, 4 and 5 have a common amplitude of $\sim 0.1h_0$, for a lateral distance of $x_2 \sim 100h_0$. The wave troughs follow power laws, i.e. $\eta_{min} = \beta x_2^{-\alpha}$ (figure 2b).

Other wake properties. A model similar to one of the ships in Watson et al. (1992) has a length of $38h_0$, width of $6.5h_0$ and draught of h_0. A mid depth of the pycnocline, in the field experiment, can be estimated to $h_0 = 3.06$ m. Calculations show the nonlinear interfacial depression and elevation below and right behind the ship (figure 3a,b), and the ship wake (figure 3c). Watson et al. showed measurements, obtained at an off-track distance of $55h_0$, of the cross-track current, u_2, and the strain rate, $\partial u_2/\partial x_2$, both at the sea surface, obtaining u_2/c_0 up to about $\sim \pm 0.1$, and $(\partial u_2/\partial x_2)/(c_0/h_0)$ up to about $\sim \pm 0.05$. The present calculations are very similar (figure 3d-f). In the simulations, wave tanks of lengths/widths of 300/300, 700/260, 500/400, have $\Delta x_1/h_0 \sim 0.4 - 0.8$ and $\Delta x_2/h_0 \sim 0.3 - 0.4$.

References.

J. Grue (2015), Nonlinear interfacial wave formation in three dimensions. J. Fluid Mech. (to appear).

J. B. Keller and W. H. Munk (1970), Internal wave wakes of a body moving in a stratified fluid. Phys. Fluids, 13(6):1425-1431.

E. I. Parau, J.-M. Vanden-Broeck and M. J. Cooker (2007), Nonlinear three-dimensional interfacial flows with a free surface. J. Fluid Mech., 591:481-494.

G. Watson, R. D. Chapman and J. R. Apel (1992), Measurements of the internal wave wake of a ship in a highly stratified sea loch. J. Geophys. Res. 97(C6):9689-9703.

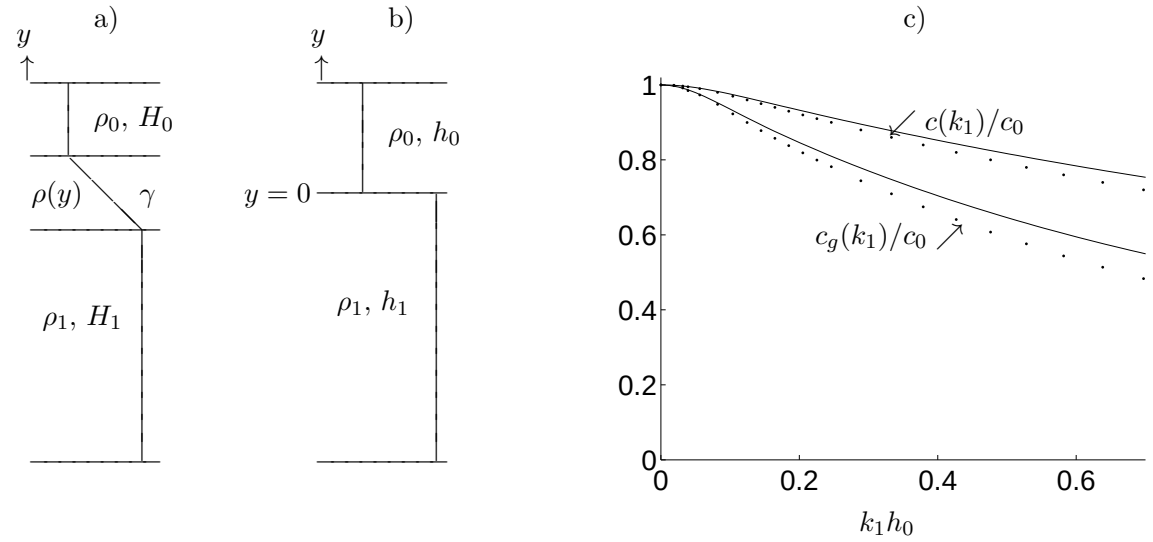

Figure 1: a) Sketch of theoretical three-layer fluid. b) Two-layer fluid. c) Wave phase speed $c(k_1)$ and group velocity $c_g(k_1)$, both normalized by the linear long wave speed of the respective density profiles. Two-layer configuration with $h_1/h_0 = 18$ (solid line) and three-layer configuration with $H_1/H_0 = 27.5$, $\gamma/H_0 = 1$ (dotted line).

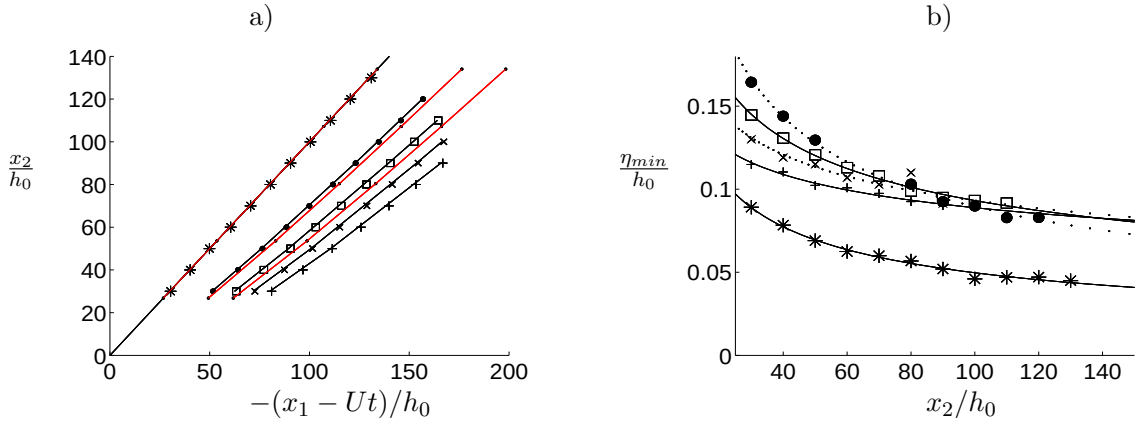

Figure 2: a) Nonlinear two-layer calculation of wake trough pattern (symbols); linear two-layer kinematics model with Keller-Munk equations (black solid line); linear three-layer kinematics model with Keller-Munk equations (red solid line). b) Trough amplitudes: trough 1 ($*$), trough 2 ($\bullet$), trough 3 (square), trough 4 ($\times$), trough 5 ($+$). $Fr = 8$. Ship model with length $29.4h_0$, width $4h_0$, draught $1.2h_0$.

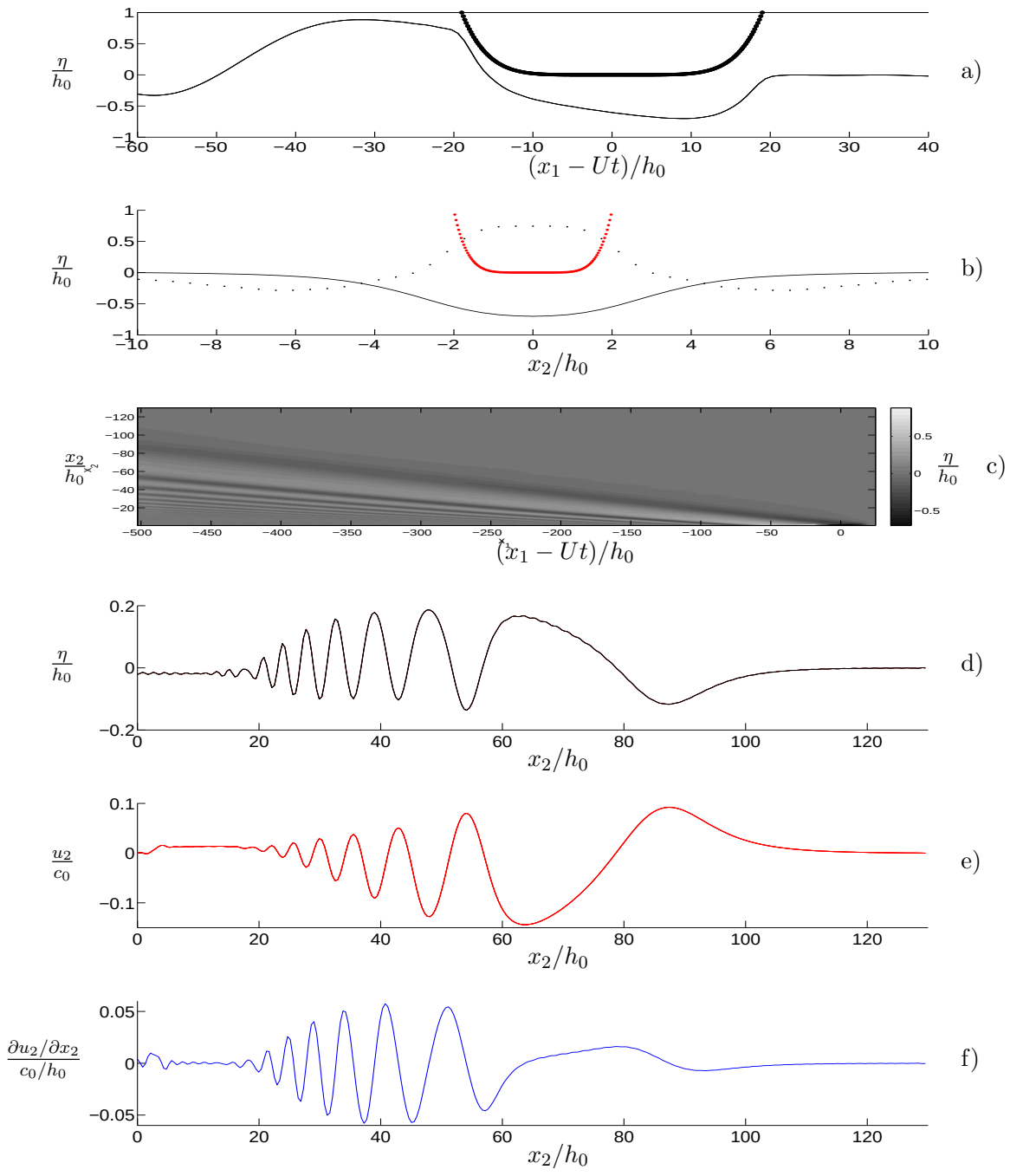

Figure 3: Interfacial wake properties for ship at $Fr = 6$. a) elevation η and hull geometry along centerplane of ship; b) η at two lateral cuts, at $(x_1 - Ut)/h_0 = 10$ (solid line) and $(x_1 - Ut)/h_0 = -30$ (dots) with ship geometry at mid beam (red solid line); c) $\eta(x_1 - Ut, x_2)$; d) cross-wake elevation η for $(x_1 - Ut)/h_0 = -504$; e) cross-wake velocity u_2 for $(x_1 - Ut)/h_0 = -504$; f) strain-rate $\partial u_2/\partial x_2$ for $(x_1 - Ut)/h_0 = -504$. Ship model with length $38h_0$, width $6.5h_0$, draught $1h_0$.

Second-order hydroelastic behavior of a flexible circular plate in monochromatic waves

S.Y. Han[(1)], S. Malenica[(2)], B.J. Kim[(1)], Y.J. Kim[(1)], S.H. Kwon[(1)]

[(1)] Pusan National University - Busan, Korea
[(2)] BUREAU VERITAS - Paris, France

E-mail :shkwon@pusan.ac.kr

Introduction

The hydroelastic behavior of a flexible circular plate with a concentric hole floating on the free surface is considered. The plate has zero thickness and homogeneous characteristics (constant density, constant flexural rigidity). It is also assumed that the fluid is the prefect fluid and the flow has irrotational characteristic. Furthermore, the thin plate theory is adopted to express the plate deflection. The right-handed coordinate system is introduced with $z = 0$ the undisturbed free surface. The bottom is assumed to be horizontal at $z = -h$. The incident wave propagates along positive x-axis. The basic configuration is shown in Figure 1.

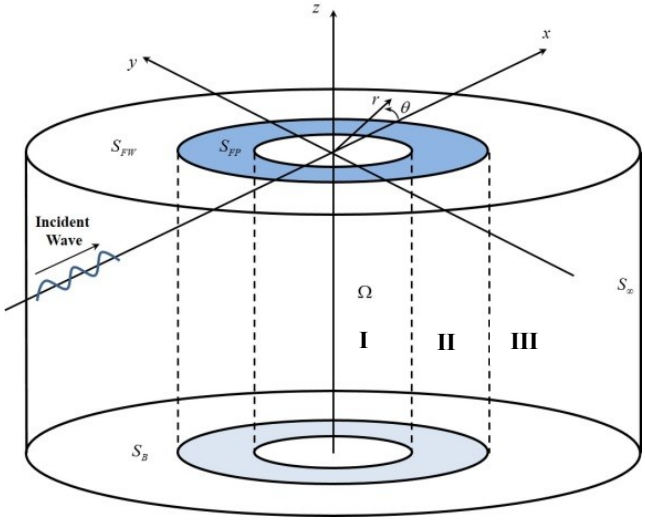

Figure 1. *Basic configuration*

Boundary condition for plate of zero thickness on the free surface

In order to express the boundary condition on the plate-wave interaction region, the kinematic condition and dynamic condition have to be considered. To do this, the governing equation of thin plate deflection is used. The governing equation is given by

$$M\frac{\partial^2 W}{\partial t^2} + D\Delta_0^2 W = P \tag{1}$$

where $W(x, y, t)$ is the deflection, M is the mass of unit area, D is flexural rigidity, P is the external pressure and Δ_0 denotes horizontal Laplace operator expressed as $\Delta_0 = \frac{1}{r}\frac{\partial}{\partial r}\left(r\frac{\partial}{\partial r}\right) + \frac{1}{r^2}\frac{\partial^2}{\partial \theta^2}$ to fit with the circular plate. The dynamic condition on the interaction region is that the pressure is equal to hydrodynamic pressure comes from the Bernoulli's equation.

$$M\frac{\partial^2 W}{\partial t^2} + D\Delta_0^2 W = -\rho\frac{\partial \Phi}{\partial t} - \frac{1}{2}\rho\nabla\Phi\cdot\nabla\Phi - \rho g W \qquad on\ z = W(x, y, t) \tag{2}$$

The kinematic condition in this domain states that the normal velocity of the plate is equal to that of water particle.

$$\frac{\partial W}{\partial t} = \frac{\partial \Phi}{\partial z} - \nabla\Phi \cdot \nabla W \qquad \text{on } z = W(x, y, \mathrm{t}) \tag{3}$$

These conditions have two difficulties which are nonlinear and are applied at the unknown position $z = W$. In order to transfer the boundary condition from the unknown position to its mean position $z = 0$, the classical way suggested by Stokes is introduced. For the small displacement assumption, we can expand the exact plate deflection to the mean position using the Taylor series expansions.
We can write the dynamic condition:

$$(1 + M\frac{\partial^2}{\partial t^2} + \frac{D}{\rho g}\Delta_0^2)W + \frac{1}{g}\frac{\partial \Phi}{\partial t} = -\frac{1}{2g}\nabla\Phi \cdot \nabla\Phi - \frac{1}{g}W\frac{\partial^2 \Phi}{\partial z \partial t} \qquad on\ z = 0 \tag{4}$$

The kinematic condition can be expressed as following:

$$\frac{\partial W}{\partial t} = \frac{\partial \Phi}{\partial z} - \nabla\Phi \cdot \nabla W + W\frac{\partial^2 \Phi}{\partial z^2} + o\left(\Phi^3\right) \tag{5}$$

This expression is written up to the second order with respect to Φ and the notation $o(\varepsilon)$ is used to represent the order higher than ε while $O(\varepsilon)$ denotes the order of ε.
Next step is to seek a solution, Φ and W, into a perturbation series with respect to wave steepness $\varepsilon = A/\lambda$ where A is the wave amplitude and λ is its length.

$$\Phi = \varepsilon\phi^{(1)} + \varepsilon^2\phi^{(2)} + o\left(\varepsilon^3\right) \ , \ W = \varepsilon W + \varepsilon^2 W^{(2)} + o\left(\varepsilon^3\right) \tag{6}$$

For monochromatic incident waves, the time dependency can be separated by using the time periodic assumption at frequency ω . The first- and second order velocity potential have the forms.

$$\phi^{(1)}(x,t) = \Re\left\{\varphi^{(1)}(x)e^{-i\omega t}\right\} \ , \ \phi^{(2)}(x,t) = \overline{\varphi}^{(2)}(x) + \Re\left\{\varphi^{(2)}(x)e^{-2i\omega t}\right\} \tag{7}$$

The similar notations are used for the plate deformation W.

$$W^{(1)}(x,y,t) = \Re\left\{w^{(1)}(x,y)e^{-i\omega t}\right\} \ , \ W^{(2)}(x,y,t) = \overline{w}^{(2)}(x,y) + \Re\left\{w^{(2)}(x,y)e^{-2i\omega t}\right\} \tag{8}$$

Because we focused on the high frequency phenomena, the over-bar expression for the steady parts of the second order is neglected in this study.
After inserting these expression into kinematic condition and dynamic condition, we obtain the combined plate-wave interaction boundary condition and plate deflection in frequency domain at corresponding orders.

$$\begin{aligned}
O(\varepsilon): \quad & -\nu\varphi^{(1)} + \mathcal{G}^{(1)}\frac{\partial \varphi^{(1)}}{\partial z} = 0, \\
& w^{(1)} = \frac{i}{\omega}\frac{\partial \varphi^{(1)}}{\partial z}; \\
O(\varepsilon^2): \quad & -4\nu\varphi^{(2)} + \mathcal{G}^{(2)}\frac{\partial \varphi^{(2)}}{\partial z} = \frac{i\omega}{g}[\frac{1}{2\nu}\mathcal{G}^{(1)}(\nabla_0\varphi^{(1)} \cdot \nabla_0\frac{\partial \varphi^{(1)}}{\partial z} - \frac{\partial \varphi^{(1)}}{\partial z}\frac{\partial^2 \varphi^{(1)}}{\partial z^2}) + \frac{1}{2}\nabla\varphi^{(1)} \cdot \nabla\varphi^{(1)} + \frac{\partial \varphi^{(1)}}{\partial z}\frac{\partial \varphi^{(1)}}{\partial z}], \\
& w^{(2)} = \frac{i}{2\omega}\left\{\frac{\partial \varphi^{(2)}}{\partial z} - \frac{1}{2}\nabla_0\varphi^{(1)} \cdot \nabla_0 w^{(1)} + \frac{1}{2}w^{(1)}\frac{\partial^2 \varphi^{(1)}}{\partial z^2}\right\};
\end{aligned} \tag{9}$$

where the mathematical operators $\mathcal{G}^{(1)}$ and $\mathcal{G}^{(2)}$ are defined as follows:

$$\begin{aligned}
\mathcal{G}^{(1)} &= (1 - \nu M/\rho + D/(\rho g)\Delta_0^2) \\
\mathcal{G}^{(2)} &= (1 - 4\nu M/\rho + D/(\rho g)\,\Delta_0^2)
\end{aligned} \tag{10}$$

Solution methodology

In order to solve the problem, the method of matched eigenfunction expansions is used. The eigenfunction expansion for the plate problem was introduced by Kim & Ertekin [2] and Malenica & Korobkin [4]. We divide the fluid domain

into three regions: an outer region defined by $R \le r \le \infty$, $0 \le \theta \le 2\pi$, $-h \le z \le 0$, a middle region (plate-wave interaction) defined by $a \le r \le R$, $0 \le \theta \le 2\pi$, $-h \le z \le 0$ and an inner region defined by $0 \le r \le a$, $0 \le \theta \le 2\pi$, $-h \le z \le 0$. To match the solutions, the continuity of the pressure and normal velocity are introduced at the common boundaries.

Potential decomposition in the inner and the outer regions

The total potential in the inner and outer regions (regions I and III in Figure 1) is divided into the incident and perturbation part. The incident potential, up to second order, is well known and can be written as follows:

$$\varphi_I^{(1)} = -\frac{igA}{\omega}\frac{\cosh k_0(z+h)}{\cosh k_0 h}\sum_{m=0}^{\infty}\varepsilon_m i^m J_m(k_0 r)\cos m\theta \tag{11}$$

$$\varphi_I^{(2)} = -\frac{3i\omega A^2}{8}\frac{\cosh 2k_0(z+h)}{\sinh^4 k_0 h}\sum_{m=0}^{\infty}\varepsilon_m i^m J_m(2k_0 r)\cos m\theta \tag{11}$$

where ε_m is equal to 1 for $m = 0$ and 2 for $m > 0$.

The perturbation potential, at each order *(j)* is now decomposed into two parts $\varphi_{PH}^{(j)}$ and $\varphi_{PQ}^{(j)}$ which satisfy the homogeneous and non-homogeneous free surface boundary conditions respectively:

$$\varphi^{(j)} = \varphi_I^{(j)} + \varphi_P^{(j)} = \varphi_I^{(j)} + \varphi_{PH}^{(j)} + \varphi_{PQ}^{(j)} \tag{13}$$

Since the potential $\varphi_{PH}^{\text{I or III},(j)}$ satisfies the homogeneous free surface boundary condition ($-\alpha\varphi_{PH}^{(j)} + \partial\varphi_{PH}^{(j)}/\partial z = 0$) can be found in the form:

$$\varphi_{PH}^{III,(j)}(r,\theta,z) = \sum_{m=0}^{\infty}\varepsilon_m\sum_{n=0}^{\infty}A_{mn}^{(j)} f_n^{(j)}(z) H_m^{(1)}(k_n r)\cos m\theta \tag{14}$$

$$\varphi_{PH}^{I,(j)}(r,\theta,z) = \sum_{m=0}^{\infty}\varepsilon_m\sum_{n=0}^{\infty}D_{mn}^{(j)} f_n^{(j)}(z) J_m(k_n r)\cos m\theta \tag{15}$$

where the vertical eigenfunction is $f_n^{(j)}(z) = \cosh k_n(z+h)/\cosh k_n h$ and the eigenvalues k_n are computed by using the dispersion relation, $\alpha = k\tanh kh$ (for the first order: $\alpha = \nu$, second order: $\alpha = 4\nu$). The dispersion relation gives one real root k_0 and infinite number of imaginary roots k_n.

The perturbation potential $\varphi_{PQ}^{\text{I or III},(j)}$ is chosen to satisfy the homogeneous boundary condition at the vertical boundaries of the domains ($\partial\varphi_{PQ}^{(j)}/\partial r = 0$ at $r = a$ or R) and the non-homogeneous free surface boundary condition ($-\alpha\varphi_{PQ}^{(j)} + \partial\varphi_{PQ}^{(j)}/\partial z = Q_P^{(j)}$). The corresponding solution at the vertical boundaries can be expressed in the following form:

$$\varphi_{PQ}^{III,(j)}(R,\theta,z) = \sum_{m=0}^{\infty}\varepsilon_m\sum_{n=0}^{\infty}L_{mn}^{(j)} f_n^{(j)}(\mathrm{z})\cos m\theta\,,\quad \varphi_{PQ}^{I,(j)}(a,\theta,z) = \sum_{m=0}^{\infty}\varepsilon_m\sum_{n=0}^{\infty}N_{mn}^{(j)} f_n^{(j)}(\mathrm{z})\cos m\theta \tag{16}$$

where the coefficients L_{mn}, N_{mn} can be deduced by using the Green's theorem as shown in [3].

$$L_{mn} = -\frac{2C_n\int_R^{\infty} H_m^{(1)}(k_n\rho)Q_{Pm}(\rho)\rho d\rho}{k_n R H_m^{(1)'}(k_n R)}\quad,\quad N_{mn} = \frac{2C_n\int_0^{a} J_m(k_n\rho)Q_{Pm}\rho d\rho}{k_n a J_m'(k_n a)} \tag{17}$$

Potential decomposition in the plate region

The potential in the plate region (region II in Figure 1) is also decomposed into two part $\varphi_{PH}^{II,(j)}$ and $\varphi_{PQ}^{II,(j)}$ where the potential $\varphi_{PH}^{II,(j)}$ satisfies the homogeneous plate-wave interaction boundary condition ($-\alpha\varphi_{PH}^{(j)} + \mathcal{G}^{(j)}\partial\varphi_{PH}^{(j)}/\partial z = 0$) can be written in the following form:

$$\varphi_{PH}^{II,(j)} = \sum_{m=0}^{\infty}\varepsilon_m\sum_{n=-2}^{\infty}F_n^{(j)}(B_{mn}^{(j)}J_m(\mu_n r) + C_{mn}^{(j)}Y_m(\mu_n r))\cos m\theta \tag{18}$$

where the vertical eigenfunction is $F_n^{(j)}(z) = \cosh\mu_n(z+h)/\cosh\mu_n h$ and the eigenvalues μ_n are the solution of the dispersion relation, $\alpha = (1 - \alpha\mathrm{M}/\rho + \mathrm{D}/(\rho\mathrm{g})\mu^4)\mu\tanh\mu h$). This equation gives one real root (μ_0),

infinite number of imaginary roots (μ_n), and two complex roots (μ_{-1} , μ_{-2}). These two complex roots are related to each other as $\mu_{-2} = \mu_{-1}^*$ with asterisk denoting the complex conjugate. The complex roots are introduced by Evans & Davies [1].

Finally, the remaining part of the perturbation potential $\varphi_{PQ}^{II,(j)}$, which satisfies the homogeneous boundary condition ($\partial\varphi_{PQ}^{(j)} / \partial r = 0$ at $r=a,\ R$) and the non-homogeneous boundary condition at the plate interface ($-\alpha\varphi_{PQ}^{(j)} + \mathcal{G}^{(j)}\partial\varphi_{PQ}^{(j)} / \partial z = Q_P^{II}$) can be expressed in the form:

$$\varphi_{PQ}^{II,(j)}(a,\theta,z) = \sum_{m=0}^{\infty}\varepsilon_m \sum_{n=-2}^{\infty} M_{mn}^{a,(j)} F_n^{(j)}(z)\cos m\theta\,,$$
$$\varphi_{PQ}^{II,(j)}(R,\theta,z) = \sum_{m=0}^{\infty}\varepsilon_m \sum_{n=-2}^{\infty} M_{mn}^{R,(j)} F_n^{(j)}(z)\cos m\theta \tag{19}$$

where coefficients M_{mn}^{a} , M_{mn}^{R} can be deduced by using the Green's theorem with the following Green's function:

$$G^{w} = \sum_{m=0}^{\infty}\varepsilon_m \sum_{n=-2}^{\infty} C_m \begin{pmatrix} H_m^{(1)}(\mu_n r) J_m(\mu_n \rho) \\ J_m(\mu_n r) H_m^{(1)}(\mu_n \rho) \end{pmatrix} F_n(z) F_n(\zeta)\cos m(\theta-\vartheta) \quad , \quad \begin{pmatrix} r>\rho \\ r<\rho \end{pmatrix} \tag{20}$$

Matching and the final linear system of equations for the unknown coefficients

In order to get the unknown coefficients $A_{mn}^{(j)}$, $B_{mn}^{(j)}$, $C_{mn}^{(j)}$ and $D_{mn}^{(j)}$, we need to truncate the infinite series in the expressions for the potentials and after that apply the matching conditions at the vertical boundaries of the different domains:

$$\left\{\varphi^{II,(j)} = \varphi^{III,(j)}\right\}_{r=R} \quad , \quad \left\{\frac{\partial\varphi^{II,(j)}}{\partial r} = \frac{\partial\varphi^{III,(j)}}{\partial r}\right\}_{r=R} \tag{21}$$

$$\left\{\varphi^{II,(j)} = \varphi^{I,(j)}\right\}_{r=a} \quad , \quad \left\{\frac{\partial\varphi^{II,(j)}}{\partial r} = \frac{\partial\varphi^{I,(j)}}{\partial r}\right\}_{r=a} \tag{22}$$

Finally, in order to properly close the problem we need to apply the plate end boundary conditions. In the case of free ends these conditions should ensure that the bending moment and shear force are zero at the plate ends:

$$\Delta_0 w^{(j)} - (1-\nu)\left[\frac{1}{r}\frac{\partial w^{(j)}}{\partial r} + \frac{1}{r^2}\frac{\partial^2 w^{(j)}}{\partial\theta^2}\right] = 0 \quad , \quad \frac{\partial\Delta_0 w^{(j)}}{\partial r} + \frac{1-\nu}{r}\frac{\partial}{\partial r}\left[\frac{1}{r}\frac{\partial^2 w^{(j)}}{\partial\theta^2}\right] = 0 \tag{23}$$

The numerical results for the first- and second order deflection of the plate will be presented at the Workshop.

Acknowledgment

This work was supported by the National Research Foundation of Korea (NRF) grant funded by the Korea government (MSIP) through GCRC-SOP (No. 2011-0030013).

References

[1] EVANS D.V. & DAVIES T.V., 1968. : "Wave-ice interaction", Technical report. 1313. Davidson Lab., Stevens Inst., of Techno., Hoboken, N.J.

[2] KIM J.W. & ERTEKIN R.C., 1998. : "An eigenfunction expansion method for predicting hydroelastic behavior of a shallow draft VLFS", 2nd. Int. Conf. on Hydroelasticity, Fukuoka, Japan.

[3] MALENICA S. & MOLIN B. 1995. : "Third harmonic wave diffraction by a vertical cylinder", Journal of Fluid Mechanics, vol. 302, pp.203-229.

[4] MALENICA S. & KOROBKIN A.A., 2003. : "Water wave diffraction by vertical circular cylinder in partially frozen sea", Proc. 18th IWWWFB Conf., April, Nantes, France.

Towards Efficient Generalized Wagner Solvers for Slamming in Oblique Seas

Jens B. Helmers[1] and Hui Sun[2]

[1]jens.bloch.helmers@dnvgl.com, DNV GL, Høvik 1363, Norway
[2]hui.sun@dnvgl.com, DNV GL, Høvik 1363, Norway

- For beam-sea calculations a simplification of the Generalized Wagner formulation is presented.
- The asymptotic corner flow model for beam sea is different from the head sea model.

1 Background and motivation

Ships operating in steep sea states may encounter critical loads due to wave slamming. In order to account for slamming loads in design, it is important to consider the frequency of occurrence for various load levels. As a consequence it is paramount to establish fast solvers for assessing a large number of impacts scenarios. The Generalized Wagner model first presented by Zhao et al. (1996) has previously been validated as a practical method in this context. Various formulations of the Generalized Wagner model has been discussed by Korobkin (2004). Based on full scale observations the largest slamming loads often occur in bow quartering seas. Most theoretical studies in this field have been focused on vertical impact of symmetric bodies. To some degree also for vertical impact of non-symmetric objects. Recently Lauzon (2014) presented a desingularized boundary element method for dealing with non-vertical impact velocity.

Towards impact simulation in oblique seas we will develop an efficient two-dimensional Generalized Wagner model applicable for beam sea calculations. The method is based on the meshless method presented by Helmers & Skeie (2013). In order to study important differences compared to the classical vertical drop tests, pure sway velocity in calm water is considered. By superposition of harmonic solutions this method can be combined with the theory of vertical impact models in order to handle general impact velocities. In the present study we only consider the spatial problem.

The target of this development is to establish a method suitable to be included in time domain seakeeping programs. Without loss of accuracy the theory is designed for exploiting preprocessor capabilities for efficient time domain calculations. As a consequence the spatial flow field needs to be accurately described by a very small number of parameters.

2 The spatial boundary value problem

Horizontal motion of a two-dimensional surface piercing body in calm water is considered. A Cartesian coordinate system (y, z) is introduced. The origin is located at the keel and the y-axis is parallel with the undisturbed free surface. The z-axis is pointing upwards. The body contour is defined by $\eta_b(y)$.

$$z = \eta_b(y), \qquad \eta_b(0) = 0, \qquad \eta_b(-y) = \eta_b(y), \qquad 0 < \frac{\partial \eta_b}{\partial y}|_{y>0} < \infty, \qquad |y| \leq y_{\max} \tag{1}$$

The fluid flow is assumed ideal and described by the velocity potential ϕ. The horizontal body velocity $\boldsymbol{V}_b$ is assumed large in the sense that gravity will not affect the flow. Adopted from Zhao et al. (1996)

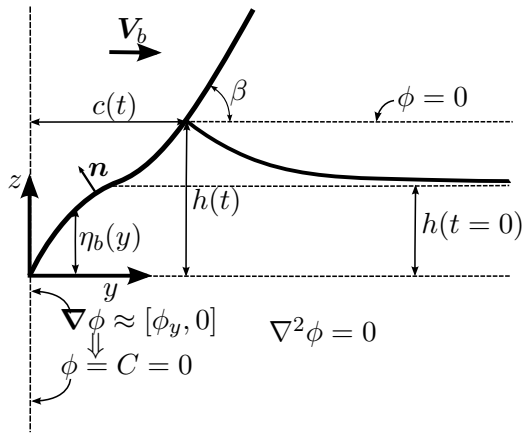

(a) The body velocity $\boldsymbol{V}_b$ is horizontal and the y-axis is parallel to the undisturbed free surface. At time t the intersection point between the body and the free surface is located at $y = c(t)$ and $z = h(t)$. On $y = 0$ we assume that the vertical fluid velocity is negligible compared to the horizontal component. The local deadrise angle at the intersection point is denoted β.

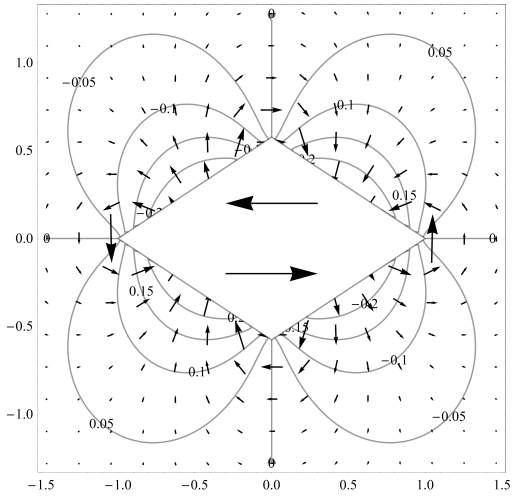

(b) The analytical flow field corresponding to the boundary value problem (2)-(4) induced by unit sway velocity of a wedge with $\beta = 30°$. The field vectors represent particle velocities and the curves are equipotential lines. The lower half is the physical space.

Figure 1: The boundary value formulation. The analytical solution for a wedge $\beta = 30°$.

the free surface flow is approximated by assuming a constant potential $\phi = 0$ on the horizontal line through the wave-body intersecting point as illustrated in figure 1a.

As a consequence of the impulsive nature of the flow and the pure horizontal body motion we will assume that the vertical fluid velocity at $y = 0$ is negligible compared to the horizontal component. The accuracy of this assumption is expected to be within the accuracy of neglecting horizontal fluid velocities on the free surface. It follows that ϕ is constant along the z-axis. By considering the assumption $\phi \to 0$ infinitely far away from the body we assume that $\phi = 0$ on $y = 0$. The spatial boundary value problem can be summarized as

$$\nabla^2\phi = 0, \qquad \text{in the fluid domain} \tag{2}$$

$$\boldsymbol{\nabla}\phi \cdot \boldsymbol{n} = \boldsymbol{V}_b \cdot \boldsymbol{n}, \qquad \text{on } z = \eta_b(y) \wedge y \leq c \tag{3}$$

$$\phi = 0, \quad \text{on } z = h \wedge y \geq c, \qquad \phi = 0, \quad \text{on } y = 0 \wedge z \leq 0, \qquad |\boldsymbol{\nabla}\phi| \to 0, \quad y^2 + z^2 \to \infty \tag{4}$$

where $\boldsymbol{n}$ is the unit surface normal pointing out of the fluid domain. The intersection point between the body surface and the true free surface is denoted $(y, z) = (c, h)$.

The meshless formulation (Helmers & Skeie 2013) is based on detailed knowledge of the flow characteristics. As a consequence we first need to consider the asymptotic properties of the boundary value problem (2)-(4).

Because of boundary conditions (4) it follows that the flow field far away from the body is represented by a quadrupole located at $(y, z) = (0, h)$ with unknown strength C_0.

$$\phi(y, z + h) = V_b \frac{C_0 yz}{(y^2 + z^2)^2}, \qquad y^2 + z^2 \to \infty \tag{5}$$

The decay rate of ϕ far away from the body is significant higher than for the vertical impact problem which is described by a vertical dipole. In the far field of the sway problem we note that the vertical fluid velocity is $\phi_z = C_0/y^3$ on the free surface.

The asymptotic flow close to the corners of the body is not evident for the sway problem. For the vertical impact problem success has been demonstrated by (e.g. Zhao et al. (1996)) using the classical corner flow formulation $\phi \sim r^{\sigma_1}$ where r is the asymptotic small distance between the corner and the

field point. For the free surface intersection point the geometrical parameter σ_1 is related to the local deadrise angle β as $\sigma_1 = \frac{\pi/2}{\pi-\beta}$.

However, for sway motion of a floating circle with center on the free surface it is straight forward to derive a closed form expression for the global spatial potential. It is well known that the asymptotic expansion of that solution close to the free surface contact point is $\phi \sim r\ln(r)$. The cylinder is wall sided ($\sigma_1 = 1$) at this location. Hence the model applied by Zhao et al. (1996) is not capable of describing this actual corner flow.

In order to establish a relevant corner flow model valid for sway motion for all bodies we first study the analytical solution of boundary value problem (2)-(4) in case of a wedge with deadrise β. We apply the following conformal mapping relating the body surface to a unit circle

$$A\left(\frac{Z}{c}-1\right) = \int_1^W \left(1+\frac{1}{w^2}\right)\left(\frac{w^2+1}{w^2-1}\right)^{-2\nu} dw \tag{6}$$

$$A = \frac{2\sin(\pi\nu)}{\sqrt{\pi}}\Gamma(1-\nu)\Gamma(\frac{1}{2}+\nu) \in [0,2], \qquad \nu = \frac{1}{2\sigma_1}-\frac{1}{2} \in [0,\frac{1}{2}], \qquad \sigma_1 = \frac{\pi/2}{\pi-\beta} \in [\frac{1}{2},1] \tag{7}$$

where the physical location $Z = y + i(h+z)$ is mapped to the position W. It can then be shown that

$$\phi(Z) = \mathfrak{Im}\{\sum_{n=1}^{\infty}\frac{b_n}{W^{2n}}\}, \qquad b_n = \frac{4hV_b\cos\beta}{\pi A}\cdot I_n^{\nu}, \qquad h = c\tan\beta, \qquad i = \sqrt{-1} \tag{8}$$

$$I_n^{\nu} = \frac{1}{n}\int_{3\pi/2}^{2\pi}\cos\theta(\tan^2\theta)^{\nu}\sin 2n\theta\, d\theta = (-1)^n\frac{\Gamma\left(\frac{3}{2}-\nu\right)\Gamma(n+\nu)}{\Gamma\left(\frac{3}{2}+n\right)}S_n \tag{9}$$

$$S_n = {}_3F_2\left((\frac{1}{2}-n, 1-n, \frac{3}{2}-\nu), (\frac{3}{2}, 1-n-\nu), 1\right) \tag{10}$$

This flow field is plotted in figure 1b for $\beta = 30°$. $\Gamma(x)$ is the Euler Gamma function. For some deadrise angles, $\beta \in \{0°, 45°, 90°\}$, the summation in $\phi(Z)$ can be expressed by closed-form expressions. For other deadrise angles the evaluation of the generalized hypergeometric functions ${}_3F_2$ needs to be carried out using asymptotic relations for high values of n.

The important thing to note in our context is that for all β we can establish closed-form expressions for the asymptotic flow close to the corners derived from equation (8). At the free surface intersection the flow is characterized by a polylogarithm function of order $2+2\nu$ which close to the corner takes the form of $F_\beta(r,\alpha)$:

$$\frac{\phi(Z)}{hV_b} = c_1\left(\frac{r}{h}\right)^{\sigma_1}\sin(\sigma_1\alpha) + F_\beta(r,\alpha), \qquad Z = c + ih + r\exp(i\alpha), \qquad r \to 0 \tag{11}$$

$$F_\beta(r,\alpha) = \tan(\beta)\left(-\frac{r}{h}\sin\alpha + c_2\left(\frac{r}{h}\right)^{\sigma_1}\sin(\sigma_1\alpha)\right) \tag{12}$$

$$c_2 = 2\,\zeta(1+2\nu)\frac{\sin(\pi\nu)}{\pi}\frac{\Gamma(1+\nu)}{\Gamma(1-\nu)}\left(\frac{2\cos(\pi\nu)}{\sqrt{\pi}}\Gamma(1-\nu)\Gamma(\frac{3}{2}+\nu)\right)^{\sigma_1} \tag{13}$$

where $\zeta(x)$ is the Riemann zeta function. A premature conclusion would be to include the c_2 term into c_1 and to neglect the only "body normal velocity" term $\tan(\beta)\frac{r}{h}\sin\alpha$ as a higher order effect ($\sigma_1 < 1$). The practical consequences of the latter strategy is shown in figure 2. It should be noted from our closed form expression for $F_\beta(r,\alpha)$ that for wall sided bodies $c_2 = 1$ and $F_\beta(r,\alpha) = \infty\cdot 0$. However by series expansion of $F_\beta(r,\alpha)$ it follows that

$$\lim_{\beta\to 90°} F_\beta(r,\alpha) = \frac{2}{\pi}\frac{r}{h}\left((1-\ln 2)\sin\alpha - \alpha\cos\alpha - \ln(\frac{r}{h})\sin\alpha\right) \tag{14}$$

which reflect the $r\ln r$ asymptotic nature related to wall sided bodies. An important observation from corner flow (11) is that there are no scaling factors related to $F_\beta(r,\alpha)$. The first term inside

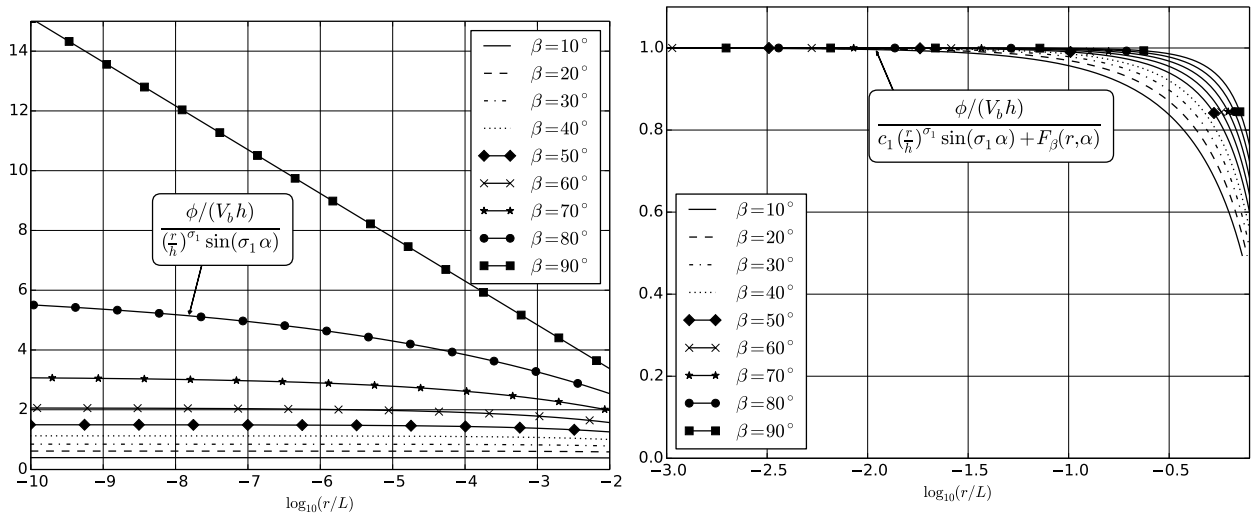

(a) The classical corner flow model is only applicable for small β in case of sway. For $\beta = 80°$ the model is not adequate even as close to the corner as $r = 10^{-10}L$.

(b) For all β the proposed corner flow model approximate the flow excellent for the upper 1% of the wetted surface. For large β the model describes the flow reasonable good for the upper 20% of the wetted surface.

Figure 2: The applicability range for the classical and proposed corner flow models along the body is presented ($\alpha = \beta - \pi$). At the distance r from the free surface corner relative to the wetted lenght L between the corner and the keel, the corner flow model is applicable if the ratio between the true potential ϕ and the corner flow model is constant (flat curve). ϕ is calculated by the analytical model given by equation (8). In combination with discrete boundary element methods the corner flow model should at least be applicable for $\log_{10}(r/L) \approx -3$ in order to avoid huge discretization cost.

$F_\beta(r, \alpha)$ match exactly the local body boundary condition and should not be scaled even for non-wedge bodies. For all other flow terms, at any expansion order, $\partial\phi/\partial n = 0$ on the body. For curved bodies geometrical corrections of c_2 can be exactly replaced by a corresponding adjustment of c_1 in equation (11). As a consequence we will keep the corner flow formulation (11) for general geometries.

At the keel the corner flow is more similar to the classical corner flow because the *horizontal* body velocity is less strenuous on the local $\phi = 0$ condition than at the free surface. A local expansion of flow field (8) at the keel reveals

$$\frac{\phi(Z)}{hV_b} = c_3\left(\frac{r}{h}\right)^{\sigma_2}\sin\left(\sigma_2\left(\alpha+\frac{\pi}{2}\right)\right) + \frac{r}{h}\cos\alpha, \quad \sigma_2 = \frac{\pi}{\pi+2\beta}, \quad Z = r\exp(i\alpha), \quad r \to 0 \qquad (15)$$

3 Conclusion and Further Work

A simplified spatial model for sway motion has been presented. The analytical results are now being implemented in the meshless Generalized Wagner formulation. A temporal model will follow.

References

Helmers, J. B. & Skeie, G. (2013), A meshless boundary element method for simulating slamming in context of generalized wagner, *in* 'Proc. ASME 2013 32nd Int'l Conf. OMAE 2013'.

Korobkin, A. (2004), 'Analytical models of water impact', *Euro. Jnl. of Appl. Math.* **15**, 821–838.

Lauzon, J. (2014), General wagner model with desingularized potential, Technical Report CRS report NT 3219 ATA 1649A, Bureau Veritas.

Zhao, R., Faltinsen, O. M. & Aarsnes, J. V. (1996), Water entry of arbitrary two dimensional sections with and without flow separation, *in* '21st Symp. on Naval Hydrodyn.', NTNU Trondheim, Norway.

The interaction of a waves with a Submerged Very Large Elastic Plate

A.J. Hermans
Delft Institute of Applied Mathematics, TU Delft, Mekelweg 4, 2628 CD Delft, The Netherlands,
E-mail: a.j.hermans@ewi.tudelft.nl

1 Introduction

Last year at the IWWWFB in Osaka Porter et al [1] discussed the phenomenon of cloaking. Among others results for a stiff plate underneath the free surface was considered. I asked myself the question whether for a flexible plate underneath the free surface the same phenomenon could be observed. In this presentation we extend the 'mode' method as derived for flexible plates at the free surface. It is well known, see for instance Hermans [2], that at certain frequencies the transmission coefficient may have an absolute value equal to unity $|T| = 1$. We will check by means of numerical calculations whether at such a point the phase shift equals zero, hence $T = 1$. In [2] a small phase shift is present at the frequency where $|T| = 1$.
In this abstract we extend the existing 'mode' method to the submerged flexible plate situation. We first consider a flexible plate and then a fixed rigid plate.

2 Flexible plate

We consider the two-dimensional interaction of an incident wave with a Very Large Flexible Platform (VLFP) with zero thickness located at finite depth $y = y_0$. We want to make use of the Green's theorem as we have done in the case where the platform is at the free surface.

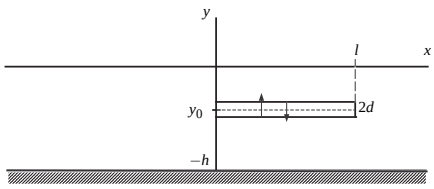

Figure 1: configuration

To do so we start with a plate of finite thickness, $2d$, as depicted in figure (1) and later take the limit $d \to 0$. The advantage is that we can make use of two different forms of the Green's function for points above or underneath the platform. The fluid is ideal, so we introduce the velocity potential $\mathbf{V}(\mathbf{x},t) = \nabla\Phi(\mathbf{x},t)$, where $\mathbf{V}(\mathbf{x},t)$ is the fluid velocity vector. Hence $\Phi(\mathbf{x},t)$is a solution of the Laplace equation $\Delta\Phi = 0$ in the fluid, together with the linearized kinematic condition, $\Phi_y = \tilde{v}_t$, and dynamic condition, $p/\rho = -\Phi_t - g\tilde{v}$, at the mean water surface $y = 0$, where $\tilde{v}(x,t)$ denotes the free surface elevation, and ρ is the density of the water.

The linearized free surface condition outside the platform, $y = 0$ and $x \in \mathcal{F}$, becomes:

$$\frac{\partial^2\Phi}{\partial t^2} + g\frac{\partial\Phi}{\partial y} = 0. \tag{1}$$

We assume that the velocity potential is a time-harmonic wave function, $\Phi(\mathbf{x},t) = \phi(\mathbf{x})\ \mathrm{e}^{-\mathrm{i}\omega t}$. The potential of the undisturbed incident wave is given by:

$$\phi^{\mathrm{inc}}(\mathbf{x}) = \frac{g\zeta_\infty}{\mathrm{i}\omega}\frac{\cosh(k_0(y+h))}{\cosh(k_0h)}\exp(\mathrm{i}k_0x) \tag{2}$$

where ζ_∞ is the wave height in the original coordinate system, ω the frequency, while the wave number k_0 is the positive real solution of the dispersion relation, $k_0\tanh(k_0h) = K$, for finite water depth.
A crucial step is the choice of the Green's function. It is possible to derive the Green's function $\mathcal{G}(x,y;\xi,\eta)$ by means of a Fourier transform with respect to the x-coordinate. It has the form:

$$\mathcal{G}^-(x,y;\xi,\eta) = \int_{\mathcal{L}'}\frac{1}{\gamma}\frac{K\sinh\gamma y + \gamma\cosh\gamma y}{K\cosh\gamma h - \gamma\sinh\gamma h}\cosh\gamma(\eta+h)\ \mathrm{e}^{\mathrm{i}\gamma(x-\xi)}\,\mathrm{d}\gamma \quad \text{for } y > \eta \tag{3}$$

and

$$\mathcal{G}^+(x,y;\xi,\eta) = \int_{\mathcal{L}'}\frac{1}{\gamma}\frac{K\sinh\gamma\eta + \gamma\cosh\gamma\eta}{K\cosh\gamma h - \gamma\sinh\gamma h}\cosh\gamma(y+h)\ \mathrm{e}^{\mathrm{i}\gamma(x-\xi)}\,\mathrm{d}\gamma \quad \text{for } y < \eta \tag{4}$$

The Green's function obeys the free surface boundary condition. The expression for the total potential $\phi^{\pm}$ becomes for $y > y_0 + d$ and for $y < y_0 - d$ resp.

$$\begin{aligned} 2\pi\phi^{\pm}(x,y) = 2\pi\phi^{\text{inc}}(x,y) - \int_0^l \left(\phi^{+}(\xi,\eta)\frac{\partial \mathcal{G}^{\mp}(x,y;\xi,\eta)}{\partial\eta} - \frac{\partial\phi^{+}(\xi,\eta)}{\partial\eta}\mathcal{G}^{\mp}(x,y;\xi,\eta)\right)\Big|_{\eta=y_0+d} \\ - \left(\phi^{-}(\xi,\eta)\frac{\partial \mathcal{G}^{\mp}(x,y;\xi,\eta)}{\partial\eta} - \frac{\partial\phi^{-}(\xi,\eta)}{\partial\eta}\mathcal{G}^{\mp}(x,y;\xi,\eta)\right)\Big|_{\eta=y_0-d} \mathrm{d}\xi. \end{aligned} \tag{5}$$

where we ignored the contributions of the endpoints.
To describe the vertical deflection $\tilde{v}(x,t)$ of the platform, we apply the isotropic thin-plate theory and use the kinematic and dynamic condition to arrive at the following equation for ϕ at $y = y_0$ in the platform area $x \in \mathcal{P}$:

$$\left\{ \mathcal{D}\frac{\partial^4}{\partial x^4} - \mu \right\} \frac{\partial\phi}{\partial y} = K(\phi^{-} - \phi^{+}), \tag{6}$$

where we used following parameters: $K = \frac{\omega^2}{g}$, $\mu = \frac{m\omega^2}{\rho g}$, $\mathcal{D} = \frac{D}{\rho g}$. Here m denotes the mass per length and D the flexural rigidity.
To apply the mode expansion we have to expand the potentials $\phi^{\pm}$ and the vertical velocity ϕ_y,and finally let d tend to zero, so we may pursue with this formulation.
However if we take $d = 0$ and differentiate (5) with respect to y we obtain the same result more directly. At first a hyper-singular equation does not look tractable. But it turns out that the equation of motion of the plate makes it possible to expand the vertical velocity at $y = y_0$ only.

$$2\pi\frac{\partial\phi}{\partial y} = 2\pi\frac{\partial\phi^{\text{inc}}(x,y)}{\partial y} + \frac{1}{K}\int_0^l \left| \left\{ \left(\mathcal{D}\frac{\partial^4}{\partial\xi^4} - \mu \right) \frac{\partial\phi}{\partial\eta} \right\} \frac{\partial^2 \mathcal{G}(x,y;\xi,\eta)}{\partial\eta\partial y} \right|_{\eta=y_0} \mathrm{d}\xi. \tag{7}$$

where

$$\frac{\partial^2 \mathcal{G}(x,y;\xi,\eta)}{\partial\eta\partial y} = \int_{\mathcal{L}'} \gamma \, \frac{K\cosh\gamma y + \gamma\sinh\gamma y}{K\cosh\gamma h - \gamma\sinh\gamma h} \sinh\gamma(\eta + h)\, \mathrm{e}^{\mathrm{i}\gamma(x-\xi)}\, \mathrm{d}\gamma \tag{8}$$

We now introduce the expansions for the vertical velocity at the surface of the plate

$$\frac{\mathrm{d}\phi}{\mathrm{d}y} = \sum_{n=0}^{N+1} a_n\, \mathrm{e}^{\mathrm{i}\kappa_n x} + b_n\, \mathrm{e}^{\mathrm{i}\kappa_n(l-x)} \tag{9}$$

We now can integrate with respect to ξ in (7) and let y tend to y_0. We consider $l = +\infty$ first and add some artificial damping to make the integrals with respect to ξ converge and work out the integral for $y > y_0$ and take $y = y_0$ afterwards.

$$\begin{aligned} &\int_0^{\infty} \left\{ \left(\mathcal{D}\frac{\partial^4}{\partial\xi^4} - \mu \right) \frac{\partial\phi}{\partial\eta} \right\} \frac{\partial^2 \mathcal{G}(x,y;\xi,\eta)}{\partial\eta\partial y}\, \mathrm{d}\xi = \frac{a}{\mathrm{i}}(\mathcal{D}\kappa^4 - \mu)\int_{\mathcal{L}'} \gamma \frac{(K\cosh\gamma y + \gamma\sinh\gamma y)\sinh\gamma(y_0+h)}{(K\cosh\gamma h - \gamma\sinh\gamma h)(\gamma - \kappa)}\, \mathrm{e}^{\mathrm{i}\gamma x}\, \mathrm{d}\gamma = \\ &2\pi a(\mathcal{D}\kappa^4 - \mu)\left(\kappa\frac{K\cosh\kappa y + \kappa\sinh\kappa y}{K\cosh\kappa h - \kappa\sinh\kappa h}\sinh\kappa(y_0+h)\, \mathrm{e}^{\mathrm{i}\kappa x} + \sum_{j=0}^{N-1} \frac{k_j(K\cosh k_j y + k_j\sinh k_j y)}{\frac{\mathrm{d}}{\mathrm{d}\gamma}(K\cosh\gamma h - \gamma\sinh\gamma h)|_{\gamma=k_j}} \frac{\sinh k_j(y_0+h)}{k_j - \kappa}\, \mathrm{e}^{\mathrm{i}k_j x} \right). \end{aligned} \tag{10}$$

If we take the coefficient of $\exp(\mathrm{i}\kappa x)$ in (7) equal to zero we arrive at the following dispersion relation for κ

$$\kappa(\mathcal{D}\kappa^4 - \mu)\sinh\kappa(y_0+h) = -K\frac{\kappa\sinh\kappa h - K\cosh\kappa h}{\kappa\sinh\kappa y_0 + K\cosh\kappa y_0} \tag{11}$$

If we take $y_0 = 0$ we recover the dispersion relation for the plate at the free surface.

$$\kappa(\mathcal{D}\kappa^4 - \mu + 1)\tanh\kappa h = K \tag{12}$$

The terms with $\exp(\mathrm{i}k_j x)$ will give us a set of equations for the unknown coefficients $A_n = \frac{-a_n}{\mathrm{i}\omega}$ and $B_n = \frac{-b_n}{\mathrm{i}\omega}$ determining the deflection of the finite platform.

$$w(x) = \sum_{n=0}^{N+1} A_n\, \mathrm{e}^{\mathrm{i}\kappa_n x} + B_n\, \mathrm{e}^{\mathrm{i}\kappa_n(l-x)} \tag{13}$$

We have $2N$ equations of the $2N+4$ unknowns A_n and B_n:

$$\begin{aligned}
&\sum_{n=0}^{N+1}(\mathcal{D}\kappa_n^4-\mu)\left[\frac{A_n}{\kappa_n-k_i}-\frac{B_n e^{i\kappa_n l}}{\kappa_n+k_i}\right]=-\delta_{0i}\frac{\sinh k_0 h}{\sinh k_0(y_0+h)}\frac{(K^2h-K-k_0^2h)}{Kk_0}\\
&\sum_{n=0}^{N+1}(\mathcal{D}\kappa_n^4-\mu)\left[\frac{A_n e^{i\kappa_n l}}{\kappa_n+k_i}-\frac{B_n}{\kappa_n-k_i}\right]=0.
\end{aligned}\tag{14}$$

for $i=0,\cdots,N-1$. The conditions at the endpoints of the platform $\frac{d^2w}{dx^2}=\frac{d^3w}{dx^3}=0$ result in four equations.

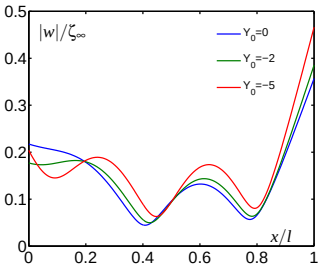

Figure 2: Deflection for different values of submergence

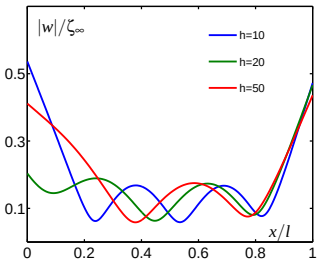

Figure 3: Deflection for different values of water depth

In figure (2) some results are shown for the deflection $|w|/\zeta_\infty$ of the plate with water depth $h=20$ m., $l=300$ m., $\mathcal{D}=10^7$ m. and $\lambda_0=2\pi/K=60$ m. for various values of submergence y_0. In figure (3) we have chosen a fixed value of submergence $y_0=-5$ m. and different values of water depth.

If we take $d=0$ in the expression for ϕ^+ in (5) we obtain the reflection and transmission coefficients.

$$R=\frac{Kk_0\sinh(k_0(y_0+h))}{(K(1-Kh)+k_0^2h)\sinh(k_0h}\sum_{n=0}^{N+1}(\mathcal{D}\kappa_n^4-\mu)\left[\frac{A_n}{k_0+\kappa_n}\left(e^{i(k_0+\kappa_n)l}-1\right)+\frac{B_n}{k_0-\kappa_n}\left(e^{ik_0l}-e^{i\kappa_n l}\right)\right]\tag{15}$$

and

$$T=\frac{Kk_0\sinh(k_0(y_0+h))}{(K(1-Kh)+k_0^2h)\sinh(k_0h)}\sum_{n=0}^{N+1}(\mathcal{D}\kappa_n^4-\mu)\left[\frac{A_n}{k_0-\kappa_n}\left(e^{-i(k_0-\kappa_n)l}-1\right)+\frac{B_n}{k_0+\kappa_n}\left(e^{-ik_0l}-e^{i\kappa_n l}\right)\right]+1\tag{16}$$

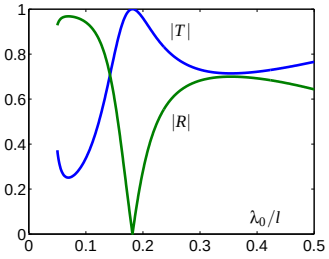

Figure 4: $\mathcal{D}=10^7$ m.

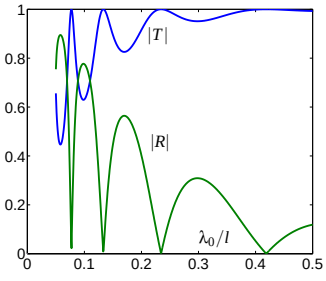

Figure 5: $\mathcal{D}=10^5$ m.

In figure (4) and (5) the reflection and Transmission coefficients are shown for two values of the flexural rigidity, $\mathcal{D}=10^7$ m. and $=10^5$ m. , at water depth $h=20$ m. and submergence of the plate $y_0=-5$ m. We study the points where $|T|=1$, it is more clear where $|R|=0$, in detail to see whether cloaking occurs in these points. We first notice that the relation $|R|^2+|T|^2=1$ very accurately.

The computations show that in none of these points $T=1$ exactly. In some points we find $\Re T$ close to -1 and in the other points where $\Re T$ is close to $+1$ the value of $\Im T\neq 0$.

3 Fixed rigid plate

If we consider a fixed rigid plate at $y=y_0$, thickness $d=0$. We notice that in the case of $\mathcal{D}\to\infty$ we find from the dispersion relation for the flexible plate (11) that either $\sinh\sigma(y_0+h)=0$ or $\kappa\sinh\kappa y_0+K\cosh\kappa y_0=0$, so we expect that we can use these realtions. To find proper relations for the modes we study the following hyper-singular equation obtained by means of we differentiation of (5) with respect to y, and take $y=y_0$.

$$2\pi\frac{\partial\phi^{\text{inc}}(x,y)}{\partial y}=\int_0^l\left(\phi^+(\xi,\eta)-\phi^-(\xi,\eta)\right)\frac{\partial^2\mathcal{G}(x,y;\xi,\eta)}{\partial\eta\partial y}\,d\xi.\tag{17}$$

This is a hyper-singular integral equation for the potential jump along the plate. We can solve this equation by means of the mode expansion method by introduction of:

$$\phi^+ - \phi^- = \sum_{n=0}^{N-1} \left(a_n \, \mathrm{e}^{\mathrm{i}\kappa_n x} + c_n \, \mathrm{e}^{\mathrm{i}\kappa_n (l-x)} \right) + \sum_{n=0}^{N-1} \left(b_n \, \mathrm{e}^{\mathrm{i}\sigma_n x} + d_n \, \mathrm{e}^{\mathrm{i}\sigma_n (l-x)} \right). \tag{18}$$

Using (10) it is easy to show that κ_n and σ_n are solutions of:

$$\kappa \sinh \kappa y_0 + K \cosh \kappa y_0 = 0, \qquad \sinh \sigma (y_0 + h) = 0. \tag{19}$$

So the solution consists of a combination of the eigen-modes of the flow above and below the plate resp. as expected. In [3] we studied the case of a rigid plate at the free surface, in that case only the the second condition of (19) played a role.
For the $2N$ coefficients in (18) we obtain, for $i = 0, \cdots, 2N-1$ the following set of equations

$$\begin{aligned} \sum_{n=0}^{N-1} \left[\frac{a_n}{\kappa_n - k_i} - \frac{c_n \mathrm{e}^{\mathrm{i}\kappa_n l}}{\kappa_n + k_i} \right] + \sum_{n=0}^{N-1} \left[\frac{b_n}{\sigma_n - k_i} - \frac{d_n \mathrm{e}^{\mathrm{i}\sigma_n l}}{\sigma_n + k_i} \right] &= -\delta_{0i} \frac{\sinh k_0 h}{\sinh k_0 (y_0 + h)} \frac{(K^2 h + K - k_0^2 h)}{K k_0} \\ \sum_{n=0}^{N-1} \left[\frac{a_n \mathrm{e}^{\mathrm{i}\kappa_n l}}{\kappa_n + k_i} - \frac{c_n}{\kappa_n - k_i} \right] + \sum_{n=0}^{N-1} \left[\frac{b_n \mathrm{e}^{\mathrm{i}\sigma_n l}}{\sigma_n + k_i} - \frac{d_n}{\sigma_n - k_i} \right] &= 0. \end{aligned} \tag{20}$$

The transmission and reflection coefficients are obtained accordingly.

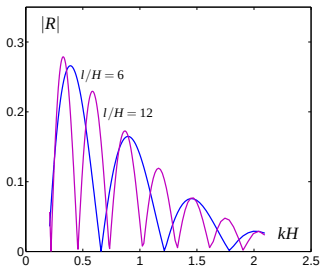

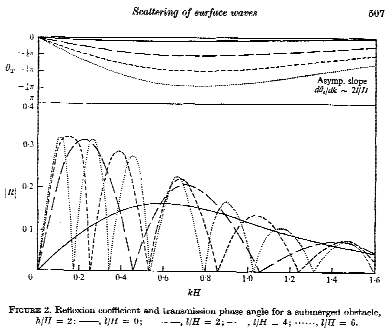

FIGURE 2. Reflexion coefficient and transmission phase angle for a submerged obstacle, $h/H = 2$: ——, $l/H = 0$; – – –, $l/H = 2$; – · –, $l/H = 4$; · · · · · ·, $l/H = 6$.

In a paper published in 1969 Mei and Black [5] studied the interaction of waves with fixed docks and object on the bottom. The figure shown is copied from that paper. In the figure next to it the plate is positioned at the same level as the top surface of the submerged object. The parameter H is the distance to the bottom.

4 Conclusions

We have extended the 'mode'method to the case of a flexible and fixed plate underneath the free surface. In contrast to the free surface plate one uses the hyper-singular integral equation for the vertical velocity instead of the equation for the potential function. The reflection coefficient computed by means of this method does not show frequencies where cloaking occurs. In [6] it is descibed how to extend the method to the configurations described in [5].

References

[1] D.V. Evans, M. McIver and R. Porter, Transparency of structures in water waves, *Proc. of the 29th International Workshop on Water Waves and Floating Bodies*, 2014, 37-41.

[2] A.J. Hermans, Free-surface wave interaction with a thick flexible dock or very large floating platform, *Journal of Engineering Mathematics* **58**, 2007, 77-90.

[3] A.J. Hermans, Interaction of free-surface waves with a floating dock, *Journal of Engineering Mathematics* **45**, 2003, 39-53.

[4] J.V. Wehausen and E.V. Laitone, Surface waves. *Encyclopedia of Physics* 9, Springer-Verlag, Berlin, (1960) 446-814, also http://www.coe.berkeley.edu/SurfaceWaves.

[5] C.C. Mei and J.L. Black, Scattering of surface waves by rectangular obstacles in waters of finite depth, *Journal of fluid mechanics*, **38**, 1969, 499-511.

[6] A.J. Hermans, Free-surface wave interaction with a thick flexible dock or very large floating platform, *Journal of Engineering Mathematics*, **58**, 2007, 7790.

Performance of "Salter's Cam" in 3-DOF Motion and in a Viscous Fluid

Yichen Jiang and Ronald W. Yeung*
Department of Mechanical Engineering
University of California at Berkeley, Berkeley, CA 94720-1740, USA
E-mail: yichen.e.jiang@gmail.com and rwyeung@berkeley.edu

Highlights:

- *Nonlinear time-domain solutions are obtained to predict the energy extraction by roll motion of the Salter cam in irregular waves, with the pivot point being compliant.*
- *Results illustrate that a flexible mooring system can extract more energy than that from a fixed-shaft Salter cam.*

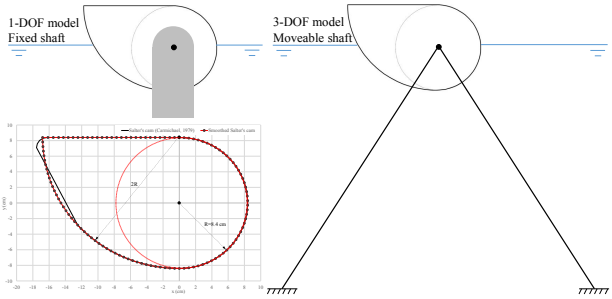

Figure 1: Smoothed Salter cam and mounting options.

1 Introduction

Mynett *et al.*(1979) investigated the performance of Salter cam with a partly constrained cam shaft and found that the shaft experiences a very large restraining force when it is fixed. This force can be reduced only by partially constraining the shaft and adding more degrees of freedom to the system. The flexible system appeared to lead to a decrease in the energy-extraction efficiency. Later, Greenhow (1981) calculated the energy-extraction efficiency of Salter's cam on a compliant shaft and found that increasing heave compliance beyond a certain value could lead to an increase of efficiency.

Parametric roll in beam seas had recently been identified in model experiments (Ikeda *et al.*, 2005). The large roll motion occurs in phase with heave, rather than pitch when the heave natural frequency is twice of the roll natural frequency. This brings up the question to be addressed in this paper: whether or not an appropriately adjusted heave resonance of the shaft support can be beneficial to the rolling performance of the Salter cam, thus allowing it to retain its distinctive high extraction efficiency?

To answer the question, two types of support system for mounting the Salter cam are examined and compared (see Fig. 1). The one degree-of-freedom (DOF) model has a fixed shaft, with no sway and heave motions. A 3-DOF system has a compliant shaft which is moored by taut (or pre-tensioned) but elastic cables. For convenience, as shown in Fig. 1, the frontal straight line of the original Salter shape is replaced by an arc so as to reduce flow-separation losses from roll motion. In this paper, the nonlinear time-domain solutions are sought to predict the roll motion and energy extraction from this mode in both regular and irregular waves with the presence of a power-take-off system (PTO) and a taut-line mooring system. Numerical results reveal that there are practical potential of applying the Salter cam with mooring cables in deep water, where fixed mounting would be unpractical.

2 Theoretical & Computational Model

The Free-Surface Random Vortex Method (FSRVM), reviewed in Yeung (2002), is a Lagrangian-Eulerian formulation for solving Navier-Stokes flows allowing for free-surface motion. The solution is obtained by decomposing the flow field into an irrotational component and a vortical component. The irrotational component of the flow is solved using a complex-variable Cauchy integral method, based on the instantaneous geometry of the computational domain and the vorticity field at that instant. The vorticity field is solved using a random vortex method for the diffusion effects and an "Order-N" multipole-accelerator interaction algorithm for convection effects (Yeung and Vaidhyanathan, 1994).

Various stages of development and validations have taken place to improve FSRVM to tackle the fully nonlinear problem and the current capabilities can model forced or free-body motion (see Yeung and Cermelli, 1998; Jiang and Yeung, 2012). It was recently extended to accommodate a mooring system and irregular incident waves in the time domain to study the per-

*Correspondence author

formance of wave-energy devices. More detailed information on the formulation of FSRVM can be found in the original work of Liao (2000). Here, we will expand that work to include the modeling of the mooring system and irregular incident waves.

2.1 Modeling of Irregular Waves

In the present study, the irregular waves are assumed to be a superposition of multiple components of linear waves: Eqn. (1)

$$\zeta = \sum_{j}^{N} A_j \sin(\omega_j t - k_j x + \theta_j), \tag{1}$$

where the component wave amplitude $A_j = \sqrt{2S(\omega_j) \triangle \omega}$ is calculated from by using, say, the Joint North Sea Wave Project (JONSWAP) spectrum. θ_j denotes a random phase and N represents the total number of linear waves.

The irregular incident waves can be generated by applying segments of external pressure on the free surface with the following pressure distribution (Stoker, 1992):

$$p(x,t) = \sum_{j}^{N} \begin{cases} \frac{\rho g A_j}{2} \sin(\omega_j t + \theta_j) \cos(\frac{x - x_c}{2L_j}\pi), & \text{for } |x - x_c| \leqslant L_j \\ 0, & \text{otherwise} \end{cases} \tag{2}$$

where x_c denotes the center of the pressure segment. L_j is one quarter of the corresponding wavelength.

To test this method, we simulate the irregular waves with a significant wave height $H_s = 2.00$cm and a peak period $T_p = 0.76$s, for a laboratory value of $R = 8.40$ cm, the reference value of the cam. Figure 2 shows the comparison between the JONSWAP spectral density and the spectral density computed from the irregular waves generated by FSRVM, using the pressure-distribution method. The two wave spectra are in good agreement.

2.2 Modeling of the Mooring System

A mooring system with four taut lines was devised to restrain the translational motion with a pair of lines emanating from each end of the finite width device, as shown Fig. 3. We assume the cable line to be a pretensioned massless rope, which behaves like a spring, when its length changes. In the figure, points A and B are the anchor locations which are respectively set at $(-10R, -10R)$ and $(10R, -10R)$. O' denotes the initial position of the body origin and $\overline{O}$ the instantaneous body origin, which is denoted by $(x_b(t), y_b(t))$. With the linear spring assumption, the mooring forces can be expressed by:

$$F_x^{\text{moor}} = -K_s[\beta_1(x_b - x_1) + \beta_2(x_b - x_2)] \tag{3}$$

$$F_y^{\text{moor}} = -K_s[\beta_1(y_b - y_1) + \beta_2(y_b - y_2)] \tag{4}$$

where K_s is the elastic stiffness of the cable; the factors $\beta_i = 1 - \frac{\sqrt{(x_0 - x_i)^2 + (y_0 - y_i)^2}}{\sqrt{(x_b - x_i)^2 + (y_b - y_i)^2}}$, for i=1,2.

2.3 Effectiveness of FSRVM Modeling

Carmichael (1979) carried out an experimental study to evaluate the performance of the Salter cam in regular waves. The performance characteristics of the device were determined in a two-dimensional wave channel. To evaluate the accuracy of FSRVM in simulating the response of rolling cams, these experimental results are chosen to be compared with our numerical simulations with fluid viscosity present in the model.

The time-average power of the extractor between t_1 and t_2 is

$$\overline{\dot{W}} = \frac{1}{t_2 - t_1} \int_{t_1}^{t_2} B_g \dot{\alpha}(t)^2 dt, \tag{5}$$

where B_g represents the PTO damping. In this section, the PTO power is averaged over the last five periods of the response for a 15 period simulation. The power of the two-dimensional regular waves is known to be:

$$P_w = \frac{1}{2} \rho g A^2 V_g, \tag{6}$$

where V_g is the group velocity of the incident wave of amplitude A. The extraction efficiency, representing the ratio of usable energy to the incident-wave energy, can be defined as: $\eta = \overline{\dot{W}}/P_w$.

In the experiments, the translational motions (sway and heave) were constrained, and the generator damping was adjusted until the maximum efficiency was achieved so that the performance was at optimum damping. In our simulations, we also tuned the numerical PTO damping and allowed the cam to roll only. A comparison between the extraction efficiency from the experiments and FSRVM simulations is presented in Fig. 4. It is found that the efficiency predicted by the numerical model closely matches that obtained from the experiments. The prediction tool is effective.

3 Results

The center of rotation of the smoothed Salter cam (see Fig. 1) is set on the calm water surface at $t = 0$, rather than below the water surface. The mooring cables are pretensioned in the 3-DOF model with the body weight being 75% of the buoyancy at $t = 0$. The center of gravity ($\bar{x}_G$, $\bar{y}_G$) is at $(-0.33R, 0)$. With the moment of inertia $I_{33}/(\rho R^4) = 1.40$, the roll resonance frequency is 8.32 rad/s or non-dimensionally, $\tilde{\omega}_{\text{roll}} \equiv \omega_{\text{roll}} \sqrt{R/g} = 0.77$. The elastic stiffness of the mooring cables is tuned to make the heave resonance frequency $\tilde{\omega}_{\text{heave}} = 1.54$, in order to satisfy the criteria of parametric roll.

The performance of the smoothed Salter cam in regular waves and irregular waves, with a fixed shaft or a moveable shaft, the latter held by the mooring system, will be examined.

3.1 Response in Regular Waves

In this sub-section, the 1-DOF and 3-DOF responses of the smoothed Salter cam in regular waves are simulated and compared for a range of different wave frequencies. All simulations are conducted with the incident waves of a wave height of 1.68 cm corresponding to $H/R = 0.20$.

Figure 5 shows the roll response amplitude operator (RAO) relative to the wave slope α_0/kA. From the figure, it can be seen that the 1-DOF model performs better than the 3-DOF model in the low-frequency regime ($\tilde{\omega} < 0.64$). However, in the rest of the region, the RAO is increased by the presence of sway and heave motions, especially at higher frequencies.

In addition, it is found that the sway and heave motions are excited with large motion in the higher frequency region, as shown in Fig. 6. From the energy point of view, we consider that part of the high-frequency wave energy is absorbed by the sway and heave motions and converted into kinetic energy of these modes, which in turn can be transferred into roll motion because of the motion coupling effects. Hence, the roll RAO of the 3-DOF model is larger than the 1-DOF case at higher frequencies. This fact indicates that the Salter cam with a moveable shaft in irregular waves have the potential to perform better than the fixed-shaft Salter cam.

3.2 Power Extraction in Irregular Waves

To quantify the motion coupling effects in irregular waves, the performance of the 1-DOF and 3-DOF smoothed Salter cams will be examined here.The significant wave height of the irregular waves is chosen to be $H_s = 2.00$ cm ($H_s/R = 0.24$) and its peak period is $T_p = 0.76$ s ($H_s/\lambda_p = 2.2\%$). The corresponding wave spectral density has been shown in Fig. 2. It is known that the PTO unit can absorb the maximum amount of energy, if the PTO damping matches the total hydrodynamic damping of the energy device. A free roll decay test of the smoothed Salter cam was conducted to obtain the hydrodynamic damping. The non-dimensional hydrodynamic damping is found to be $\lambda_{66}/(\omega_{\text{roll}}\rho R^4) = 0.81$, where ω_{roll} denotes the resonance frequency. Then, the non-dimensional PTO damping $B_g/(\omega_{\text{roll}}\rho R^4)$ is set to match this value at all time.

With the "optimal" PTO damping, we simulate the free response of the rolling cam with a fixed shaft or a moveable shaft for 200 peak periods. The statistics for the time-domain responses from the two models are given in Table 1. We find that the root-mean-square (RMS) value of the roll motion of the 3-DOF model is slightly larger than that of the 1-DOF model. Fig. 7 shows the roll spectral density computed from the roll responses of these two models. It can be seen that the spectral density curve of the 3-DOF model is higher and broader than that of the 1-DOF model. These results reveal that kinetic energy is transferred from the linear modes to the rotational mode, and the roll response of the Salter cam could be increased by mounting to a moveable shaft.

Table 1: Roll statistics in irregular waves (unit: deg).

Model	Mean	RMS	Max.	Min.
1-DOF	-0.1803	3.3522	8.8533	-10.1998
3-DOF	-0.2407	3.3949	8.2556	-9.6421

To investigate the power-extraction efficiency of the smoothed Salter cam in irregular waves, the PTO power is averaged over the last 150 periods of the response by using Eqn. (5). The power of the two-dimensional incident irregular waves is calculated by: $P_w = \frac{1}{2}\rho g \sum_{j=1}^{N} A_j^2 V_{g,j}$, where $V_{g,j}$ is the group velocity of the component of regular wave of amplitude A_j. Then, the extraction efficiency can be calculated by $\eta = \overline{\dot{W}}/P_w$. Based on the above equations, the extraction efficiency of the 1-DOF model is 62.88%, and the efficiency of the 3-DOF model is 67.58%. These results suggest that installing the Salter cam in deep water with mooring cables of the proper spring constant would not necessarily reduce the energy-extraction efficiency. More importantly, if the basic properties of the floater and the mooring system are designed properly, the performance of the wave-energy device can be enhanced.

Thus, we conclude that the criteria of parametric roll can be applied to a Salter cam with a moveable shaft so that it can retain the high energy extraction efficiency as the fixed-shaft cam. In the talk, we will also show how viscosity may not affect the results.

References

[1] Mynett, A.E., Serman, D.D., and Mei, C.C. (1979). *Applied Ocean Research*, Vol. 1, pp. 13-20.

[2] Greenhow, M. J. (1981). *Applied Ocean Research*, Vol. 3, 145-147.

[3] Ikeda, Y., Munif, A., Katayama, T., and Fujiwara, T. (2005). *Proc. of 8th International Ship Stability Workshop*, Istanbul, Turkey.

[4] Carmichael, A. D. (1979). Technical Report No. MITSG 78-22, Massachusetts Institute of Technology.

[5] Yeung, R. W. and Vaidhyanathan, M. *Proc. Intl Conference on Hydrodynamics*, pp. 118-128, October, 1994, Wuxi, China.

[6] Yeung, R. W. and Cermelli, C. A. (1998). *Adv in Fluid Mech*, Vol. 16, 1-36.

[7] Yeung, R. W. (2002). *Proc. Intl Society of Offshore and Polar Engineers (ISOPE)*, Vol. 3, pp. 1-11.

[8] Jiang, Y. and Yeung, R. W. (2012). *Proc. Intl Conference on Ocean, Offshore and Arctic Engineering*, Paper number: OMAE2012-84150, Rio de Janeiro, Brazil.

[9] Liao, S. (2000). Ph.D. dissertation, University of California, Berkeley.

[10] Stoker, J. J. (1992). *Water waves: The mathematical theory with applications*, Wiley, New York.

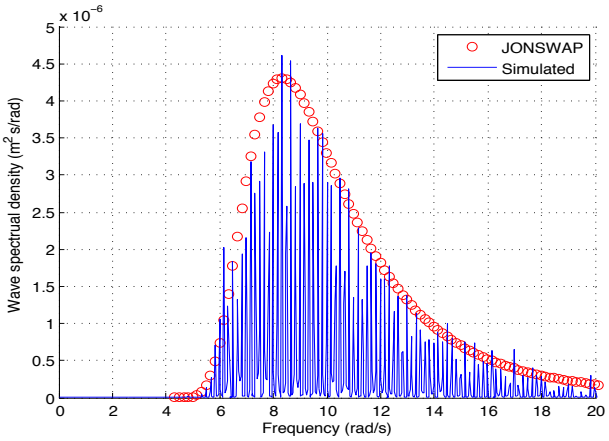

Figure 2: Spectral density of the simulated irregular waves.

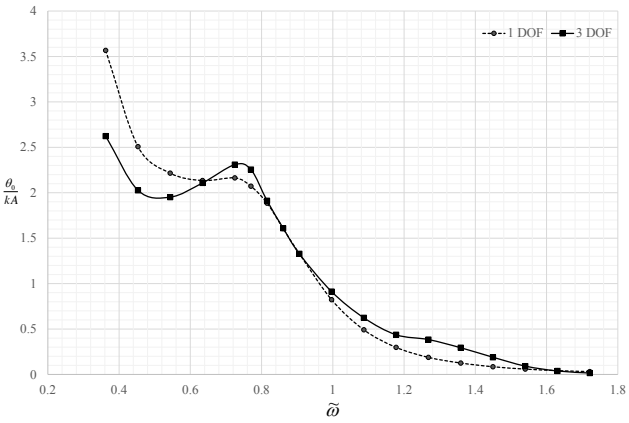

Figure 5: Comparison of the roll RAO between 1-DOF model and 3-DOF model.

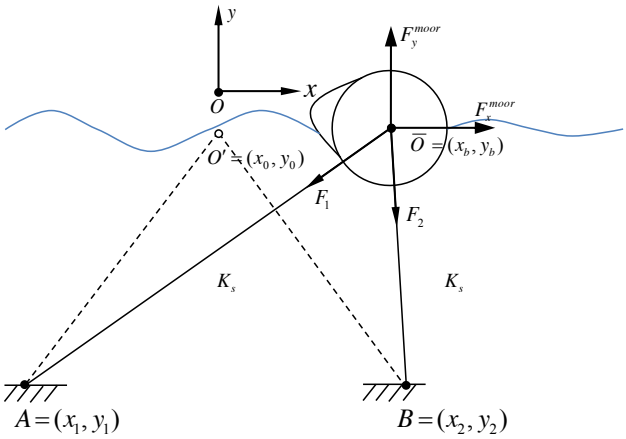

Figure 3: Mooring system of the 3DOF problem, utilizing four pre-tensioned elastic cables.

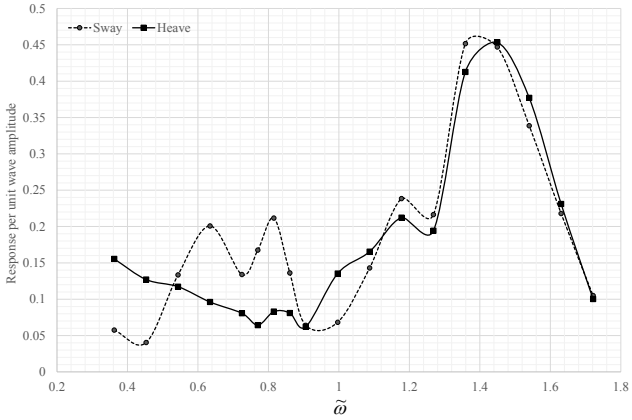

Figure 6: Sway and heave response per unit incident-wave amplitude obtained from the 3-DOF model.

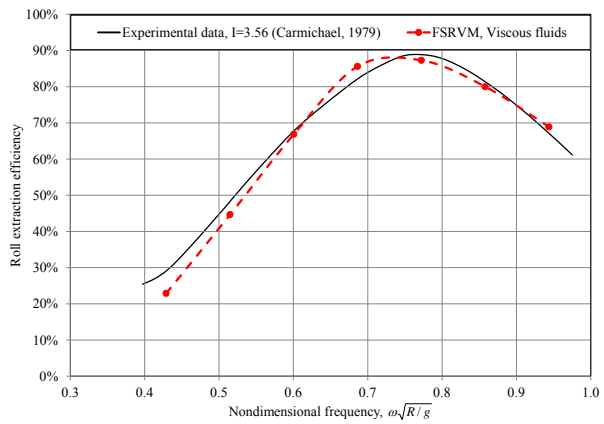

Figure 4: Comparison of the cam's efficiency between experiments and the FSRVM predictions, moment of inertia of the Salter Cam taken as: $\hat{I} = I/(\rho R^4) = 3.56$.

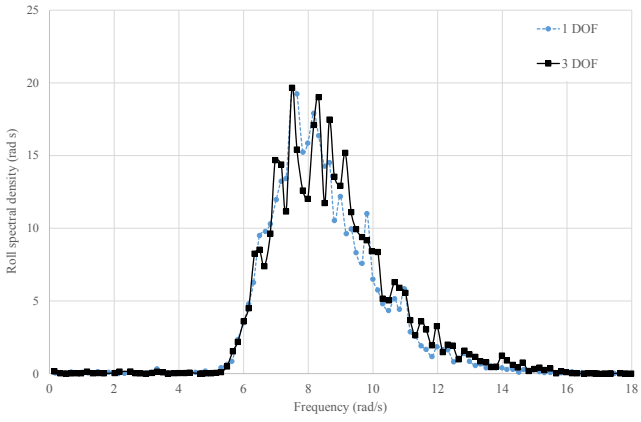

Figure 7: Comparison of the roll spectral density between 1-DOF model and 3-DOF model.

Singularization of Sloshing Impacts

M. R. Karimi[1,2,3*], L. Brosset[1], J.-M. Ghidaglia[3], M. L. Kaminski[2]
[1] Gaztransport & Technigaz, Saint-Rémy-lès-Chevreuse, France
[2] Delft University of Technology, Delft, The Netherlands
[3] École normale supérieure de Cachan, Cachan, France
Email: m.r.karimi@tudelft.nl

Highlights

- In the context of long duration sloshing model tests, it was investigated whether sloshing impacts selected from long model tests can be exactly generated with only a short test which was proven to be the case. In other words in order to regenerate a selected impact with any comfity, 15-60 s of relevant tank motions would be sufficient and there is no need to run the complete test until the impact time,
- Regenerating the most relevant impacts with such short test durations enables to quickly perform many repetitions and possibly gain more relevant statistics from samples of pressure peaks,
- Singularization enables a categorization of the impacts with their distinctive physical and statistical properties.

1 Introduction

As outlined by Gervaise et al. (2009) and Kuo et al. (2009), any sloshing assessment of LNG carrier membrane tanks is based on long duration sloshing model tests, usually at scale 1:40, performed with accurate 6 degree of freedom motion platforms. Clusters of pressure transducers are put on the most impacted areas of the tank walls, recording at a high sampling frequency. Samples of pressure peaks are gathered from tests corresponding to all the conditions that the ship will encounter during her life. Every model test is repeated several times in order to enrich the corresponding statistical sample of pressure peaks. Despite many repetitions of every model test the tails of the samples are often poor and statistical distributions (mostly Weibull) are fitted to data in order to extrapolate and predict the extreme loads. In every gathered sample of pressure peaks found from several repetitions of the same model test, peaks corresponding to different impact types (slosh, flip through, and gas pocket) are mixed together. Also every model test at scale $1:40$ corresponding to a 5 hour sea state would take about 50 minutes to complete and having many repetitions would take a long time.

An alternative would be to be able to focus on single impacts and necessarily the most relevant ones with a less time consuming method. One way to achieve this would be to first track down impacts of long sloshing model tests from the knowledge of *impact coincidence* as explained by Karimi and Brosset (2014). It would be then favorable not to spend a long time (in the order of a complete model test) to regenerate every selected single impact. The objective of the study is to show that only short tank motions right before the desired impact time are necessary to recreate the same exact impact conditions with the right statistical properties as obtained in long model tests. It will be demonstrated that there is only a short *effective memory* (m_e) in terms of tank motions, before the selected impact time that should be respected. A study based on 2D sloshing model tests is presented in order to verify the feasibility of this impact singularization.

2 Test Setup

s The internal geometry of the utilized tank (made of PMMA) corresponded to a transverse slice of a LNG carrier membrane tank at scale $1:40$. The tank was placed on an accurate six degree-of-freedom motion platform (hexapod) and filled at 20% of the tank height with water. The Ullage gas was air at atmospheric pressure and ambient temperature. 60 PCB pressure sensors were arranged in a 15×4 regular array with a

10 mm distance between the center of the sensors both horizontally and vertically. The array was placed on the vertical side of the tank, covering the area impacted by the breaking waves during the tests. The sampling frequency of the acquisition system was set at 40 kHz. Only sloshing events (impacts) for which one pressure signal exceeded a threshold were recorded. A Phantom V7.2 high speed video camera was fixed to the tank looking at the sensor array and recording at 4000 fps in order to capture the wave impacts. It was triggered by pressure sensors when exceeding another threshold and was synchronized with the data acquisition. A semi high speed video camera set at 96 fps was fixed to the platform in the plane of symmetry of the tank at the free surface level, far enough from the transverse tank wall in order to capture continuously the entire free surface.

3 Approach

Irregular motions were imposed on the tank by the hexapod. The motions were downscaled to scale 1:40 according to Froude similarity from BEM calculations of ship motions for a 5 hour sea state with a zero crossing period of $T_z = 8\,s$ and a significant wave height of $H_s = 6\,m$. Only the three degrees of freedom in the plane of the tank (sway, heave and roll) were used. The duration of one test was $2966\,s$ long including ramps at both ends.

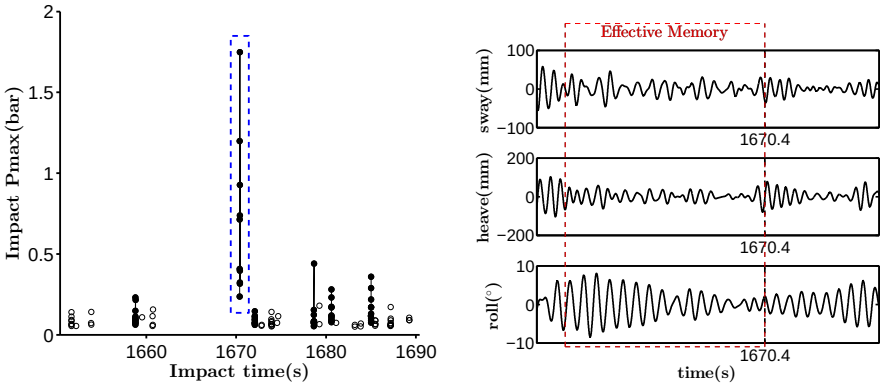

(a) (b)

Fig. 1: (a) The maximum pressure for the chosen impact as captured in 10 repetitions of long model tests (b) It is assumed that only a short duration of tank motions immediately before the impact governs the fluid flow at the impact time as if there is a short effective memory involved

10 repetitions of the same tank motions were performed. Based on the knowledge of impact coincidence as introduced by Karimi and Brosset (2014), an impact was selected occurring at exactly $t = 1670.4\,s$ in all the repetitions as shown in *Fig.* 1(a). Maximum impact pressures recorded at sensor level for the 10 impacts covered a rather large range which specially included high pressures.

The wave shapes corresponding to 9 out of 10 of these repetitions were recorded as depicted in *Fig.* 2. There were slight variations of the wave shape. The unique form of the crest made it distinctive. This impact made a target for the verification.

3DOF motions right before the expected time of the chosen impact were applied on the tank with a range of durations from 1 second to 120 seconds to be able to find the right *effective memory*. Fig. 3 shows the shortened heave signals (for sway and roll similar procedure was used) to respect effective memories of 15, 30, and 90 seconds. The motions continued for 1 second after the expected impact time. The extracted signals were completed by $5\,s$ and $1\,s$ long cubic-splines respectively at the beginning and the end for smooth transition to zero motion (continuous accelerations). In order to facilitate the comparison between the tests, a common initial time convention $t = 0$ was taken at the nominal impact time.

4 Results

For very short motions, global flow did not have time to match the global flow obtained from long duration tests. For durations of 15 seconds and more this matching was more obvious as depicted by *Fig.* 4 and continued until

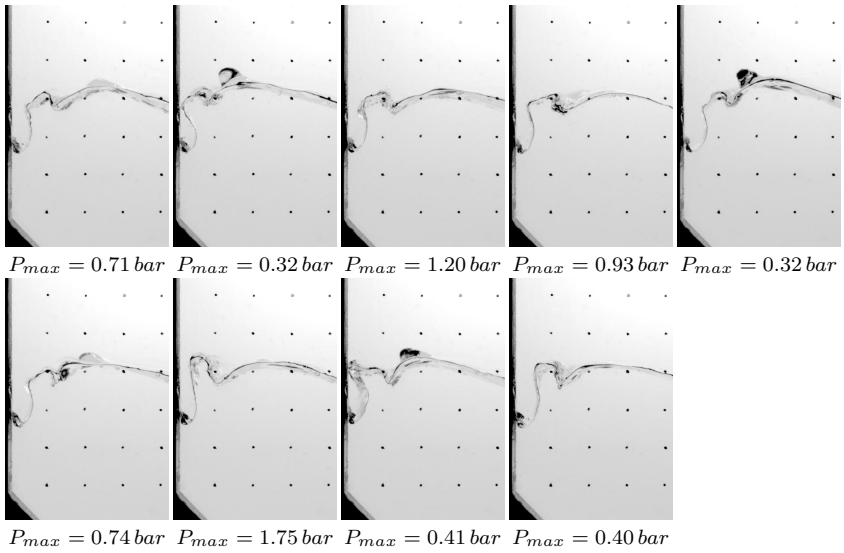

Fig. 2: The high-speed video recordings of the chosen impact captured in 9 out of 10 repetitions of long duration model tests and the maximum induced pressures at sensor level

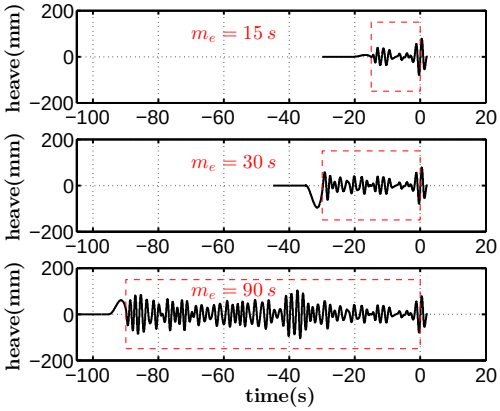

Fig. 3: The heave signals cut assuming 15, 30, and 90 seconds of effective memory. The same procedure was used to cut sway and roll signals.

the moment of the impact[1].

(a) (b) (c)

Fig. 4: The global flow in the 2D tank, 2.4 seconds before the impact time with assumed effective memories of (a) 15 seconds (b) 30 seconds (c) 90 seconds

At time $t = 0$ impacts were recorded as shown in *Fig.* 5 which geometrically looked very similar to the ones obtained from long duration tests. The differences between impacts obtained with different durations exist as was the case for impacts obtained from long tests and differences observed at the nominal impact time were comparable with the initial variations observed during the ten repetitions of the complete tests.

Taking benefit of the short excitation duration for recreating a given impact condition, 3000 repetitions of the same impact were created in GTT's laboratory. An excitation with the assumed $m_e = 30\,s$ was used for each test and a break time of one minute was applied in between every two repetitions. More repetitions could have

[1]Click on the *link* to watch the corresponding video or use the address: *http://youtu.be/1ibUgIqTsBs*. From the video, it is clear how the global flows progressively match together especially for the top one which has just started.

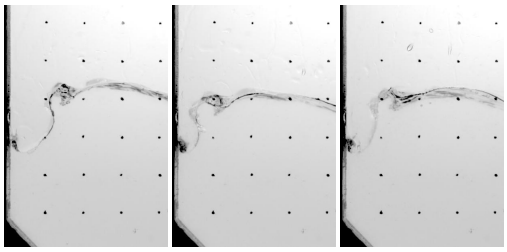

$P_{max} = 0.44\,bar$ (a) $P_{max} = 1.72\,bar$ (b) $P_{max} = 0.41\,bar$ (c)

Fig. 5: The impact geometry and maximum impact pressures obtained with assumed effective memories of (a) 15 seconds (b) 30 seconds (c) 90 seconds

been obtained considering a smaller excitation duration and no break between the tested conditions. Maximum pressure obtained from the 3000 repetitions was 3.14 bar to be compared with a maximum of 2.06 bar measured in all the impacts of the ten initial repetitions of the complete irregular test. Different sets of many repetitions for excitations of different durations are intended to be performed soon in GTT in order to complete the study and check whether the samples of pressure peaks are statistically equivalent or not.

5 Conclusions

For short 2D tank motions at scale 1 : 40 the global flow is able to match the global flow obtained from complete long excitations as long as the duration is larger than 15 s. In that case the variations obtained on the wave shape before the nominal impact for short durations are visually as small as the variations observed for repetitions of the long duration test. The study still needs to be continued and in order not to bias any statistics, it should be shown that the variability associated to the flow and finally to the pressure measurements remains similar to the variability that can be obtained from long duration tests.

Singularization of sloshing impacts could lead to new ways to quickly build more relevant pressure statistics for sloshing assessment as

- Instead of mixing measured pressure data from different impact types (a wide range of slosh, gas pocket, and flip-through) during statistical post processing, focus can be made on the same types of impacts and the statistical analysis would be more relevant,
- Instead of performing a limited number of long sloshing tests, thousands of repetitions for dedicated tests on single impacts could be done in a much shorter time with focus on the most relevant impacts which could save time and generate sounder statistical samples.

References

[1] GERVAISE, E., SÈZE, P.-E. D. & MAILLARD, S. (2009). Reliability-based methodology for sloshing assessment of membrane LNG vessels. *International Journal of Offshore and Polar Engineering*, 19(4).

[2] KARIMI, M. R., BROSSET, L. (2014). Global and Local Effects of Gas-Liquid Density Ratio on Shape and Kinematics of Sloshing Waves and Scaling Considerations. IWWWFB 2014, Osaka, Japan.

[3] KUO, J. F., CAMPBELL, R. B., DING, Z., HOIE, S. M., RINEHART, A. J., SANDSTRÖM, R. E., YUNG, T. W., GREER, M. N. & DANACZKO, M. A. (2009). LNG Tank Sloshing Assessment Methodology-the New Generation. *International Journal of Offshore and Polar Engineering*, 19(4).

The 30th International Workshop on Water Waves and Floating Bodies, Bristol UK, April 12-15, 2015

Wave Drift Force on Floating Bodies of Cloaking Configuration and Associated Wave Patterns

Masashi Kashiwagi, Takahito Iida and Mariko Miki

Department of Naval Architecture & Ocean Engineering, Osaka University
2-1 Yamada-oka, Suita, Osaka 565-0871, Japan E-mail: *kashi@naoe.eng.osaka-u.ac.jp*

Abstract

With a semi-analytical accurate computation method and model experiment, a study is made on the phenomenon of cloaking a floating cylinder by surrounding it with a finite number of smaller circular cylinders uniformly spaced on a circle concentric with the inner cylinder. It is shown that when the optimization of the geometrical parameters of surrounding cylinders is realized to minimize the total scattered-wave energy, the wave drift force reduces to nearly zero not only on the entire bodies but also on the inner cylinder and outer surrounding cylinders individually.

1. Introduction

Cloaking phenomenon is attracting attention recently in wave-body interaction problems on the free surface. 'Cloaking' refers to the condition that there is no wave scattering in the form of radial outgoing waves. Originally this phenomenon was studied by Pendry *et al.* (2006) in electromagnetic fields. Newman (2013) has also analyzed the phenomenon of cloaking a circular cylinder of finite draft by surrounding it with an array of smaller cylinders. He has shown numerically that the scattered-wave energy can be reduced to substantially zero by optimizing the geometrical parameters of the cylinders concerned and that the mean drift force on the entire bodies becomes also very small.

The present paper is concerned with the same problem, but care is paid on the accuracy of the solution by adopting Kagemoto & Yue's theory (1986) combined with a higher-order boundary element method (HOBEM). By expressing the solution with the cylindrical coordinate system and Graf's addition theorem for Bessel functions, it is made possible to compute the wave drift force not only on the entire bodies but also on each of the bodies in the array, only in terms of the complex amplitude coefficients of scattered and incident waves. Optimization of the geometrical parameters of the cylinders is performed using the real-coded genetic algorithm (RGA) such that the total scattered-wave energy is minimized.

In order to confirm correctness of computed results, a model experiment is also conducted for an optimized configuration at the normalized wavenumber $Kd_0 = 1$ (where d_0 is the draft of the central circular cylinder), measuring the wave drift forces and also the spatial distribution of the wave elevation. It is confirmed that when the cloaking phenomenon occurs, the wave drift force becomes very small not only on the entire bodies but also on the inner cylinder and outer surrounding cylinders individually.

2. Theory for Computation

2.1 Velocity potential

We consider a number of vertical circular cylinders of finite draft (total number equal to M), specifically a central cylinder (radius r_0 and draft d_0) is surrounded by smaller $N\,(=M-1)$ cylinders of same size with radius r and draft d which are uniformly spaced on a circle of radius R_0, concentric with the inner cylinder.

To analyze multiple wave interactions among these floating bodies, the linearized potential-flow problem is considered with coordinate systems shown in Fig. 1; where in addition to the global coordinate system O-$r\theta z$ (where $x = r\cos\theta$ and $y = r\sin\theta$) fixed at the central circular cylinder, the local coordinate system O_k-$r_k\theta_k z$ is considered, with its origin placed at the center of the k-th body. The z-axis is positive vertically downward, and the plane of $z = 0$ is placed on the undisturbed free surface.

Let us consider the diffraction problem with the velocity potential expressed in the form

$$\Phi(P;t) = \mathrm{Re}\left[\frac{g\zeta_a}{i\omega}\left\{\varphi_I(P)+\varphi_S(P)\right\}e^{i\omega t}\right]. \qquad (1)$$

Here $P = (r,\theta,z)$ denotes a field point in the fluid; g is the gravitational acceleration; ζ_a and ω are the amplitude and circular frequency of an incident wave, respectively; Re means the real part to be taken.

The velocity potential of incident wave $\varphi_I(P)$, propagating in the direction with incident angle β relative to the positive x-axis, can be expressed in the cylindrical coordinate

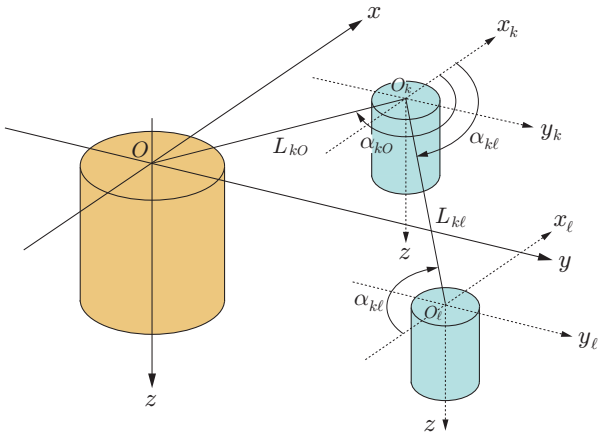

Fig. 1 Coordinate system and notations.

system as follows:

$$\varphi_I(P) = \sum_{m=-\infty}^{\infty} \alpha_m \, Z_0(z) \, J_m(k_0 r) \, e^{-im\theta} \tag{2}$$

where
$$\alpha_m = e^{im(\beta-\pi/2)}, \; Z_0(z) = \frac{\cosh k_0(z-h)}{\cosh k_0 h} \tag{3}$$

$$k_0 \tanh k_0 h = \frac{\omega^2}{g} \equiv K \tag{4}$$

with the fluid depth assumed constant and denoted as h.

The velocity potential $\varphi_S(P)$ in (1) is the scattering potential due to body disturbance. Since there are M bodies in the present analysis, it can be written as follows:

$$\varphi_S(P) = \sum_{\ell=1}^{M} \varphi_S^{\ell}(P) \simeq \sum_{\ell=1}^{M} \sum_{n=-\infty}^{\infty} A_n^{\ell} Z_0(z) H_m^{(2)}(k_0 r_\ell) \, e^{-in\theta_\ell}$$

$$= \sum_{m=-\infty}^{\infty} \mathcal{A}_m \, Z_0(z) \, H_m^{(2)}(k_0 r) \, e^{-im\theta} \tag{5}$$

where
$$\mathcal{A}_m = \sum_{\ell=1}^{M} \sum_{n=-\infty}^{\infty} A_n^{\ell} \, J_{n-m}(k_0 L_{\ell 0}) \, e^{-i(n-m)\alpha_{\ell 0}} \tag{6}$$

Evanescent wave components are ignored in (5) for brevity, and the complex amplitude of the scattered progressive wave around the ℓ-th body is denoted as A_n^{ℓ}, which is computed accurately with higher-order boundary element method (HOBEM) for computing the diffraction characteristics of elementary bodies and the wave-interaction theory of Kagemoto & Yue (1986). Here $J_m(k_0 r)$ and $H_m^{(2)}(k_0 r)$ denote the first kind of Bessel function of order m and the second kind of Hankel function of order m, respectively. The complex amplitude $\mathcal{A}_m$ in the global coordinate system, given by (6), is obtained through the coordinate transformation (see Fig. 1 for notations) and associated Graf's addition theorem for Bessel functions.

To summarize the above, the total velocity potential valid at a distance outside of all bodies can be given as the sum of (2) and (5) in the form

$$\phi(P) \equiv \varphi_I(P) + \varphi_S(P)$$

$$= \sum_{m=-\infty}^{\infty} \Big[\alpha_m J_m(k_0 r) + \mathcal{A}_m H_m^{(2)}(k_0 r) \Big] Z_0(z) \, e^{-im\theta} \tag{7}$$

For computing the wave drift force on each body, say on the ℓ-th body, we need an expression of the velocity potential valid around the ℓ-th body, in which the incident wave consists of not only the wave expressed by (2) coming from the outside but also disturbance waves due to other bodies. Thus it can be written with the ℓ-th local coordinate system in the form

$$\phi^{\ell}(P) \equiv \varphi_I^{\ell}(P) + \varphi_S^{\ell}(P)$$

$$= \sum_{m=-\infty}^{\infty} \Big[\alpha_m^{\ell} J_m(k_0 r_\ell) + A_m^{\ell} H_m^{(2)}(k_0 r_\ell) \Big] Z_0(z) \, e^{-im\theta_\ell} \tag{8}$$

where
$$\alpha_m^{\ell} = \alpha_m \, e^{-ik_0(x_{o\ell}\cos\beta + y_{o\ell}\sin\beta)} + \sum_{\substack{k=1 \\ k\neq\ell}}^{M} \sum_{n=-\infty}^{\infty} A_n^k \, H_{n-m}^{(2)}(k_0 L_{k\ell}) \, e^{-i(n-m)\alpha_{k\ell}} \tag{9}$$

and the second line in (9) is given with the coordinate transformation and associated Graf's addition theorem for Bessel functions.

2.2 Wave drift force and scattered-wave energy

According to the far-field method, the wave drift force can be computed from quadratic products of the total velocity potential valid at a distance from the body concerned. When the velocity potential is expressed with the cylindrical coordinate system, like (7) or (8), the integrals with respect to θ and z appearing in the formula by the far-field method can be analytically performed at a certain appropriate distance of r (where evanescent waves can be practically neglected), with the Wronskian relations for Bessel functions applied. After this kind of analytical integrations using (7), the calculation formula for the wave drift force on the entire bodies is given in the following complex form:

$$\frac{\overline{F}_x - i\overline{F}_y}{\frac{1}{2}\rho g \zeta_a^2 d_0} = \frac{i}{C_0 K d_0} \sum_{m=-\infty}^{\infty} \Big[2\mathcal{A}_m \mathcal{A}_{m+1}^* + \alpha_m \mathcal{A}_{m+1}^* + \alpha_{m+1}^* \mathcal{A}_m \Big], \tag{10}$$

where
$$C_0 = \frac{k_0}{K + (k_0^2 - K^2)h}. \tag{11}$$

In the same way using (8), the wave drift force on the ℓ-th body can be computed from

$$\frac{\overline{F}_x^{\ell} - i\overline{F}_y^{\ell}}{\frac{1}{2}\rho g \zeta_a^2 d_0} = \frac{i}{C_0 K d_0} \sum_{m=-\infty}^{\infty} \Big[2A_m^{\ell} A_{m+1}^{\ell *} + \alpha_m^{\ell} A_{m+1}^{\ell *} + \alpha_{m+1}^{\ell *} A_m^{\ell} \Big]. \tag{12}$$

Here the asterisk in superscript stands for the complex conjugate. It should be noted that hydrodynamic interactions among all bodies are exactly taken into account by including evanescent-wave effects in computing the complex amplitude of scattered waves, because Kagemoto & Yue's wave-interaction theory combined with HOBEM is adopted in the present theory.

Minimizing the scattered-wave energy may be used as an objective function in optimization of the parameters of outer surrounding circular cylinders. The scattered-wave energy can be computed with the same procedure as that used for computing the wave drift force. In the diffraction problem, the result can be expressed as

$$\frac{E_S}{\rho g \zeta_a^2 \frac{\omega}{k_0}} = \frac{1}{K C_0} \sum_{m=-\infty}^{\infty} \big| \mathcal{A}_m \big|^2. \tag{13}$$

3. Numerical Results

First, the real-coded genetic algorithm (RGA) was applied so as to minimize the total scattered-wave energy of all bodies, to be computed by (13), at the normalized wavenumber $K = 1$. (All parameters with length scale are nondimensionalized with the draft of central circular cylinder d_0.) Computed parameters of outer circular cylinders (r, d, R_0) are shown in Table 1; where E_S/E_{S0} denotes the energy ratio, with E_{S0} being the energy of scattered wave by the central cylinder alone.

Figure 2 shows the contour map of scattered-wave amplitude at $K = 1$ for the case of surrounding 8 bodies ($N = 8$, $M = N + 1 = 9$). It can be seen that no scattered waves exist outside of the entire bodies and almost all scattered waves are trapped between the central and surrounding bodies even for the case of $N = 8$.

Table 1 Optimized parameters of outer cylinders to minimize the total scattered-wave energy.

N	r	d	R_0	E_S/E_{S0}
4	0.2931	0.3509	2.2156	0.2948
8	0.2929	0.4834	2.2000	0.0254
16	0.1960	0.4871	2.1483	0.0199
32	0.1311	0.4506	2.1051	0.0127

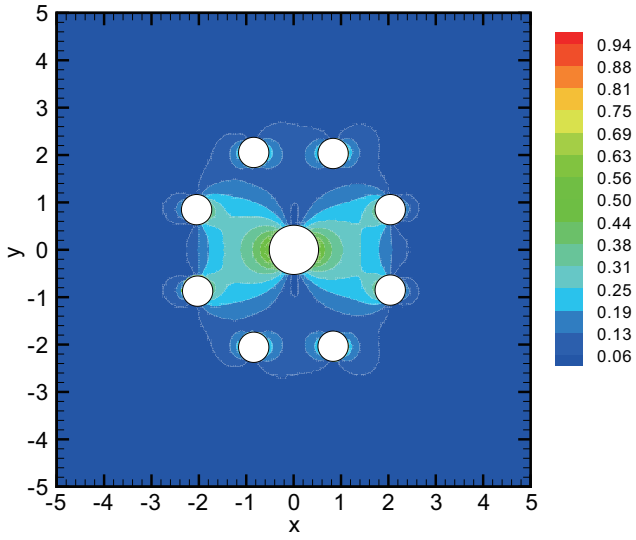

Fig. 2 Contour map of scattered-wave amplitude at $K = 1.0$ for the case of $N = 8$ shown in Table 1.

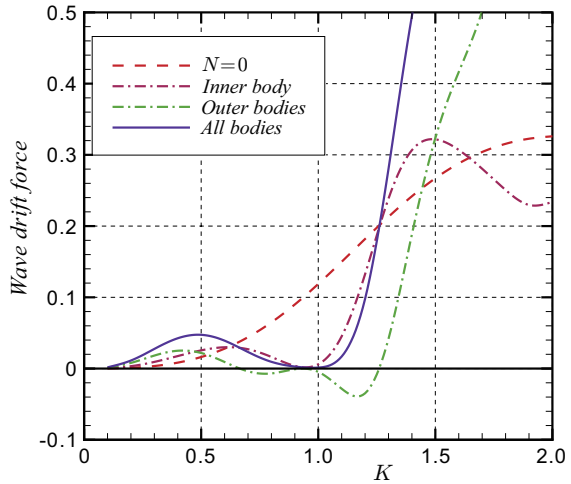

Fig. 3 Wave drift forces on the entire structure of $N = 8$ configuration and separate components acting on the inner cylinder and outer surrounding cylinders. The broken line is the force on the inner cylinder alone ($N = 0$).

The wave drift force is associated with the scattered wave, as observed by (10) and (11). However, it is not obvious whether the wave drift force becomes zero, when the scattered-wave energy of (13) is zero. Computed results for the wave drift force are shown in Fig. 3 for the case of $N = 8$. We can see at $K = 1$ that not only the force on the entire bodies (indicated by solid line) but also the individual components acting on the inner and outer bodies are also almost zero. This is because the scattered-wave pattern, shown in Fig. 2, looks symmetric with respect to the y-axis penetrating the center of inner cylinder and orthogonal to the direction of incident-wave propagation.

4. Experimental Confirmation

A model experiment has been conducted, corresponding to the numerical computations for the case of surrounding 8 circular cylinders. A photo of the model set in the wave basin is shown in Fig. 4, where the radius (r_0) and draft (d_0) of the central circular cylinder were selected as r_0 =0.134 m and d_0 =0.240 m. By referring to computed results at $K = 1$, the parameters of outer circular cylinders are selected as shown in Table 2.

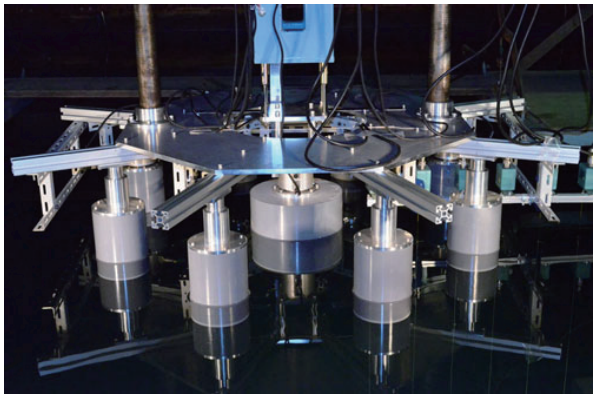

Fig. 4 Experimental model set in a wave basin.

Table 2 Parameters of outer circular cylinders used in the model experiment.

Radius	r	0.070 m	$(r/d_0 = 0.292)$
Draft	d	0.120 m	$(d/d_0 = 0.500)$
Distance	R_0	0.515 m	$(R_0/d_0 = 2.146)$

It should be noted that the length ratios shown in Table 2 are slightly different from corresponding normalized values in Table 1 for $N = 8$, on account of practical limitation in selecting materials for circular cylinders.

Although the wave elevation was measured at a number of different points, the results are shown only for the wave drift force acting on the central cylinder and also on each of outer surrounding cylinders (4 bodies due to symmetry).

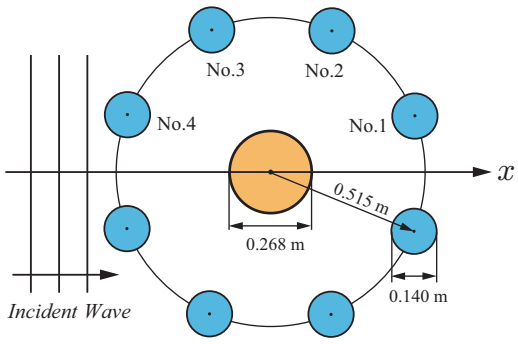

Fig. 5 Arrangement and numbering of outer cylinders.

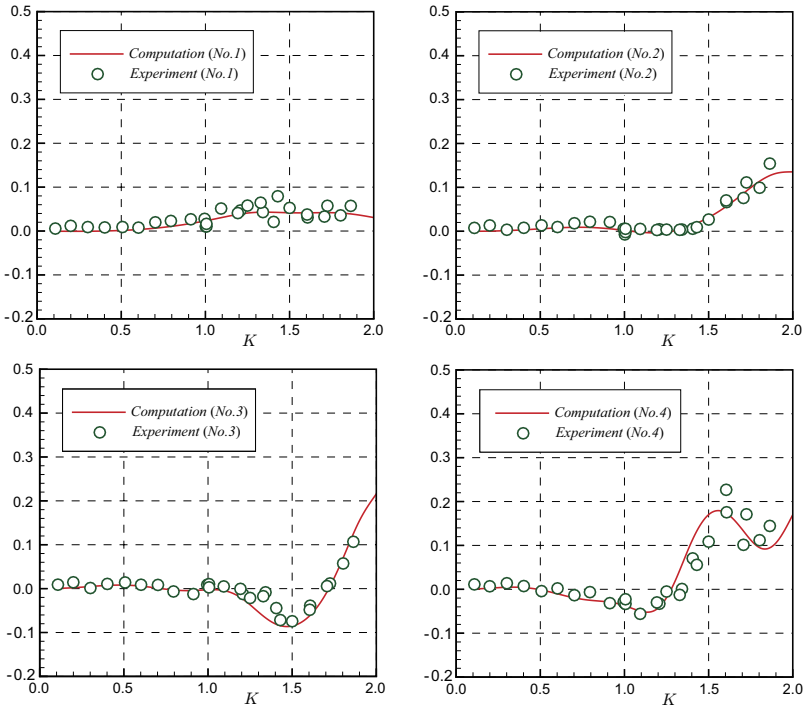

Fig. 6 Wave drift forces on each of outer cylinders (No. 1 through No. 4).

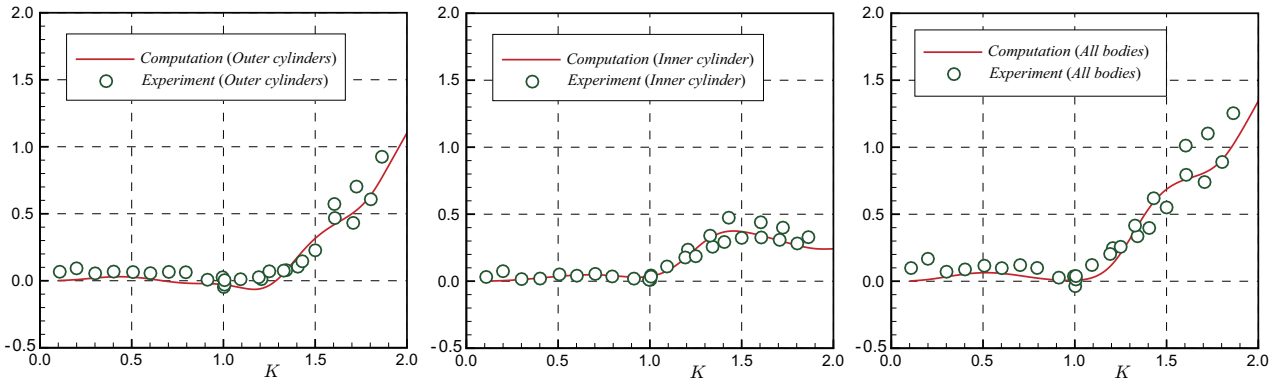

Fig. 7 Wave drift forces on outer cylinders, inner cylinder, and all cylinders.

The outer cylinders are numbered with No. 1 through No. 4 from the downwave side, as depicted in Fig. 5.

We can see in Fig. 6 relatively good agreement between computed and measured results, and at the cloaking frequency of $K = 1$ the value of No. 4 cylinder becomes negative, whereas the corresponding value of No. 1 cylinder is positive with almost the same magnitude. In fact, summing up all values acting on the outer surrounding bodies, we can obtain the result shown in Fig. 7, from which we can see that the wave drift forces on both the inner cylinder and outer surrounding cylinders are almost zero at $K = 1$.

5. Conclusions

Using a semi-analytical method with higher accuracy, the occurrence of cloaking in the surface-wave problem was confirmed for an array of smaller cylinders which surround the inner cylinder of finite draft. It was demonstrated that when the cloaking is realized, the wave drift force becomes practically zero both on the inner and outer cylinders individually. The wave pattern around the bodies was also computed and a relationship between the wave pattern and zero drift force at the cloaking frequency was noted.

Furthermore, a model experiment was conducted to confirm correctness of computed results, measuring hydrodynamic forces and the spatial distribution of the wave elevation around the bodies. Measured results for the wave elevation and their comparison with computed results will be presented at the Workshop.

References

[1] Pendry, JB, Schurig, D and Smith, DR (2006). "Controlling electromagnetic fields", *Science*, Vol 312, pp 1780–1782.

[2] Kagemoto, H and Yue, DKP (1986). "Interactions among Multiple Three-Dimensional Bodies in Water Waves: An Exact Algebraic Method", *Journal of Fluid Mechanics*, Vol 166, pp 189–209.

[3] Newman, JN (2013). "Cloaking a circular cylinder in deep water", *Proc of 28th IWWWFB* (L'Isle sur la Sorgue, France), pp 157–160.

A linearized exit model for prediction of forces on a body within the 2D+T framework

T.I. Khabakhpasheva[1], A.A. Korobkin[1] and Kevin J. Maki[2]

[1] School of Mathematics, University of East Anglia, Norwich, UK,
e-mail: t.khabakhpasheva@uea.ac.uk, a.korobkin@uea.ac.uk
[2] Department of Naval Architecture and Marine Engineering University of Michigan Ann Arbor, MI, 48109 USA, e-mail: kjmaki@umich.edu

The present study is motivated by hydrodynamics of high-speed vessels and aircraft ditching on the water surface, where the wetted part of the hull is streamlined and the hull is elongated in the direction of the motion. Hydrodynamic loads over the wetted part of the elongated hull can be estimated by using the 2D+T approximation [1]. In this approximation, the three-dimensional nonlinear stationary problem is reduced to a two-dimensional transient problem of water entry and exit. This two-dimensional problem can be linearized if both the draft of the body and the deadrise angles of the body cross sections are small. For the stationary three-dimensional problem of a smooth body moving at a constant speed along the water surface, it is convenient to introduce a vertical plane perpendicular to the direction of the body motion and consider the unsteady two-dimensional flow in this plane caused by the body passing through the plane. The intersection of the body surface with this control plane provides a two-dimensional contour which changes its shape in time and interacts with the water surface. For a three-dimensional body with smooth surface the penetration stage ends when the two-dimensional contour stops expanding. During the next stage, which is referred below as the exit stage, the contour contracts and exits from the water. The entry stage was investigated in [2] by the modified Logvinovich model [3]. It was found that the theoretical results are very close to the CFD results obtained by numerical simulations of the Navier- Stokes equations (see [4-6] for details of the simulations). However, the theoretical results from [2] for the exit stage were not as good as for entry stage. During the exit stage, the von Karman model was used in [2]. Recently a linearized exit model was developed in [7]. The exit model is formulated in terms of the linearized pressure with the condition that the speed of the contact points is proportional to the local speed of the flow. This model does not account for the shape of the body but still corresponds quite well to the CFD results from [4]. The model was developed further in [8] to account for a varying in time acceleration of the body. The bodies in [7] and [8] were rigid and only vertical motions were allowed. The two-dimensional problem of a body whose shape varies in time was studied in [2] for an expanding and contracting circular cylinder. The numerical and theoretical forces were very close to each other during the expansion (entry) stage but rather different during the contraction (exit) stage.

In the present paper, we apply the exit model from [7] to the bodies of varying shapes together with corrections accounting for the shape of the body (see [2]) and nonlinear effects. The entry stage is considered below within the original Wagner theory of water impact. It is known (see [2]) that the MLM provides better prediction of the hydrodynamic loads during the entry but here we are concentrated on the negative loads during the exit stage. In the next sections, we provide the solution of the linearized exit model for a body of varying shape, introduce the correction terms and compare the theoretical forces with the CFD results from [2]. Then we apply the model to the problem of an ellipsoid which moves horizontally at a fixed penetration depth and compare the distributions of the sectional forces and pressures with the CFD results. Finally we summarize our findings and draw conclusions.

Exit model for a body shape of which varies in time

The linearized exit model [7] for a body with a shape that is described by the equation $y = y_b(x,t)$, is formulated in terms of the acceleration potential $\varphi_t(x,y,t)$:

$$\nabla^2\varphi_t = 0 \quad (y<0), \qquad \varphi_t = 0 \quad (y=0,\ |x|>c(t)),$$
$$\partial\varphi_t/\partial y = y_{b,tt}(x,t) \quad (y=0,\ |x|<c(t)), \qquad \varphi_t \to 0 \quad (x^2+y^2\to\infty), \tag{1}$$

where $y=0$ corresponds to the level at which the problem is linearized, the function $y_b(x,t)$ is given and the function $c(t)$ is calculated by using the condition that the velocity of the contact points $c'(t)$ is proportional to the local velocity of the flow at these points

$$dc/dt = \gamma\varphi_x[c(t),0,t], \qquad c(0)=c_0, \tag{2}$$

where c_0 is the solution of the equation $y_b(c_0,0)=0$. The coefficient γ is equal to two in the present analysis as in all previous calculations (see [7,8]). The pressure is given by the linearized Bernoulli equation $p(x,y,t) = -\rho\varphi_t(x,y,t)$, where ρ is the water density, and the hydrodynamic force $F_L(t)$ is given by (the subscript L stand for the linearized exit model)

$$F_L(t) = \int\limits_{-c(t)}^{c(t)} p(x,0,t)\,dx. \tag{3}$$

The solution of the boundary problem (1) with the acceleration potential being continuous at the contact points $x=\pm c(t)$, $y=0$ is given by

$$\varphi_{xt}(x,0,t) = \frac{1}{\pi\sqrt{c^2-x^2}}\ \text{p.v.}\int\limits_{-c(t)}^{c(t)} y_{b,tt}(\xi,t)\frac{\sqrt{c^2-\xi^2}}{\xi-x}\,d\xi, \qquad \varphi_x(x,0,t) = \int\limits_0^t \varphi_{xt}(x,0,\tau)\,d\tau. \tag{4}$$

Equations (3) and (4) yield the formula for the hydrodynamic force in term of the functions $c(t)$ and $y_{b,tt}(x,t)$

$$F_L(t) = -2\rho c^2(t)\int\limits_0^{\pi/2} y_{b,tt}(c\sin\theta,t)\cos^2\theta\ d\theta. \tag{5}$$

Equations (2) and (4) provide the equation for the function $c(t)$

$$\frac{dc}{dt} = \frac{\gamma}{\pi}\int\limits_0^t\left(\int\limits_{-c(\tau)}^{c(\tau)}\frac{y_{b,tt}(\xi,\tau)\sqrt{c^2(\tau)-\xi^2}}{\xi-c(t)}\,d\xi\right)\frac{d\tau}{\sqrt{c^2(\tau)-c^2(t)}}. \tag{6}$$

To transform equation (6) to a form suitable for numerical integration, we introduce a function

$$H(t) = \frac{2}{\pi}\int\limits_0^{c(t)}\frac{y_{b,tt}(\xi,t)}{\sqrt{c^2(t)-\xi^2}}\,d\xi,$$

which plays a role of an averaged acceleration of the body. Then we introduce new unknown functions $\sigma(t)$ by $c^2(t) = c_0^2(1-\sigma(t))$ and $f(\sigma)$ by

$$H(t) = f(\sigma)\frac{dc^2(t)}{dt} = -c_0^2 f(\sigma)\frac{d\sigma}{dt} \tag{7}$$

(see [7] for details). Then equation (6) can be written as

$$H\Big(\sigma,t(\sigma)\Big) = 2\gamma c_0^3(1-\sigma)f(\sigma)\int\limits_0^{\sigma}\frac{f(\sigma)}{\sqrt{\sigma-\alpha}}R\Big(\sigma,\alpha,t(\alpha)\Big)\,d\alpha, \tag{8}$$

$$H\Big(\sigma,t(\sigma)\Big) = \frac{2}{\pi}\int\limits_0^{\pi/2} y_{b,tt}\Big(c_0\sqrt{1-\sigma}\sin\theta,t(\sigma)\Big)\,d\theta, \qquad R\Big(\sigma,\alpha,t(\alpha)\Big) = 1-2(\sigma-\alpha)\,\frac{L\Big(\sigma,\alpha,t(\alpha)\Big)}{H\Big(\alpha,t(\alpha)\Big)},$$

$$L\Big(\sigma,\alpha,t(\alpha)\Big) = \int\limits_0^{\pi/2}\frac{y_{b,tt}\Big(c_0\sqrt{1-\alpha}\sin\theta,t(\alpha)\Big) - y_{b,tt}\Big(c_0\sqrt{1-\sigma}\sin\theta,t(\sigma)\Big)}{(1-\alpha)\sin^2\theta-(1-\sigma)}\,d\theta.$$

For parabolic shapes with time-dependent curvature we have

$$y_b(x,t) = B(t)x^2+h(t), \qquad H(\sigma,t) = \frac{1}{2}B''(t)c_0^2(1-\sigma)+h''(t), \qquad L(\sigma,\alpha,t) = \frac{\pi}{2}c_0^2B''(t). \tag{9}$$

Equations (7) and (8) serve to determine the functions $f(\sigma)$ and $t(\sigma)$, where $0 \le \sigma < 1$. Equations (7) and (8) are solved numerically by the generalized version of the algorithm from [8]. Note that the hydrodynamic force (5) and the size of the wetted area predicted by (8) depend on the acceleration of the body but not on its shape within the linearized exit model. In order to account for the shape of the body and, at least partly, for the nonlinear terms in the Bernoulli equation, we use the ideas from the modified Logvinovich model [3], where the pressure distribution along the wetted part of the entering water contour is given by

$$p(x, y_b(x,t), t) = -\rho\Big(\phi_t - \phi_x y_{b,t} y_{b,x}/(1+y_{b,x}^2) + (\phi_x^2 - y_{b,t}^2)/(2(1+y_{b,x}^2))\Big).$$

In this formula, we neglect ϕ_x, $y_{b,x}$ and approximate

$$\phi_t(x,t) \approx \varphi_t(x,0,t) + +vp_{ty}(x,0,t)(y_b(x,t) - y_b(c,t)) = \varphi_t(x,0,t) + y_{b,tt}(x,t)(y_b(x,t) - y_b(c,t)).$$

The term $y_b(c,t)$, the splash-up height, indicates that the problem (1) is obtained by the linearization on the splash-up level as in the generalized Wagner model. In the parabolic approximation (9), the corrected pressure is given by

$$p(x, y_b(x,t), t) = -\rho\phi_t + \rho(x^2 B'' + h'')(c^2 - x^2)B(t) + \rho(B'x^2 + h')^2/2, \tag{10}$$

where $\varphi_t(x,0,t)$ is given by Wagner theory at the entry stage and by the linearized exit model at the exit stage. Correspondingly the force is decomposed as

$$F(t) = F_L(t) + F_b(t), \tag{11}$$

where $F_L(t)$ is given by the linearized models of entry and exit and the corrections term $F_b(t)$ is obtained by integration of the second and third terms in (11) over the wetted interval, $-c(t) < x < c(t)$, both during the entry and exit stages.

Numerical results

The introduced model is applied to the water entry and exit of an expanding and contracting circular cylinder. This problem was studied numerically and by using the MLM during the expansion stage and von Karman model during the contraction stage in [2]. The forces calculated numerically and by the MLM during the expansion stage are very closed to each other, but the numerical and theoretical predictions of the forces during the contraction stage are rather different. Here we are concentrated on the contraction stage describing the expansion stage by the simplified model (10), (11), where the cylinder was approximated by the parabolic contour (9). The conditions of calculations are the same as in [2]. The non-dimensional forces for different ratios $k = R_{max}/R_0$, where R_{max} is the maximum radius of the cylinder and R_0 is its initial radius, are presented in Fig. 1 as functions of the non-dimensional time t^*, where $F^* = Ft_0^2/(4\rho R_0^3(k-1)^2)$, $t^* = t/t_0$ and t_0 is the duration of the impact stage. Here line 1 corresponds to $F_L^*(t^*)$ without any corrections of the linearized model, line 2 shows the total force $F^*(t^*)$ by (10) and (11), line 3 is for the total force $F^*(t^*)$ but the linearization is performed at the equilibrium water level $y = 0$, and line 4 is for the CFD resulting force from [2]. Star stands for non-dimensional variables. It is seen that the present model provides the force closest to the CFD results. Calculations were also performed for the actual shape of the cylinder without the parabolic approximation to demonstrate the accuracy of the approximation (9).

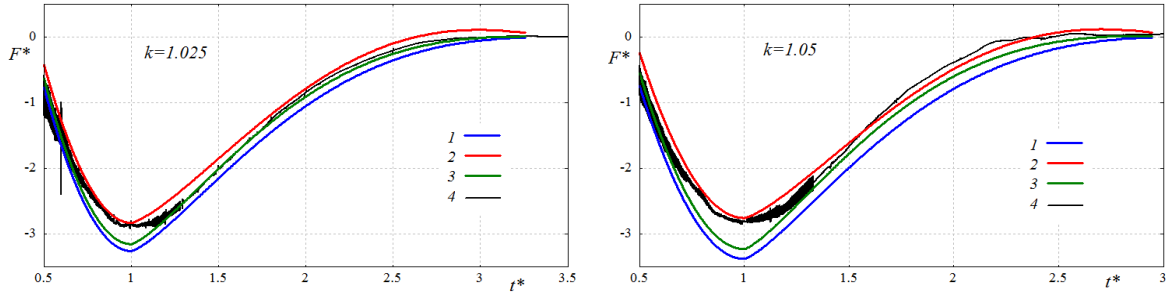

Fig. 1 Non-dimensional forces acting on the expanding/contracting circular cylinder as functions of the non-dimensional time for different values of the parameters k.

Finally we apply the developed model to a three-dimensional steady problem of a rigid ellipsoid

$$(x - Ut)^2/a^2 + y^2/b^2 + (z - h)^2/c^2 = 1$$

with semi-axes a, b and c, which is slightly submerged at $c - h$ and moves along the water surface in the x-direction with constant speed V within the 2D+T approximation. The hydrodynamic loads are determined for each section of the body by using the Wagner theory if the section penetrates water, and by the linearized exit model if the section exits from the water. The control plane is introduced at $x = a$. The forces are calculated for sections of the body

$$z = z_b(y, t) = h - c\sqrt{\tau(2 - \tau) - y^2/b^2}, \qquad \tau = Ut/a,$$

which are approximated by parabolic shapes (9). The distributions of the pressure at $y = 0$ and the sectional forces are shown in Fig. 2 together with CFD results obtained within the Navier-Stokes three-dimensional model without gravity and surface tension. Calculations were performed for $a = 10$m, $b = c = 1$m and $V = 50$m/s. The present linearized model with corrections (10) and (11) over-predicts the loads for the sections in entry but well corresponds to the CFD predictions for the sections in exit. The loads for the sections in entry can be potentially improved by using the MLM and a local three-dimensional model close to the jet overturning region.

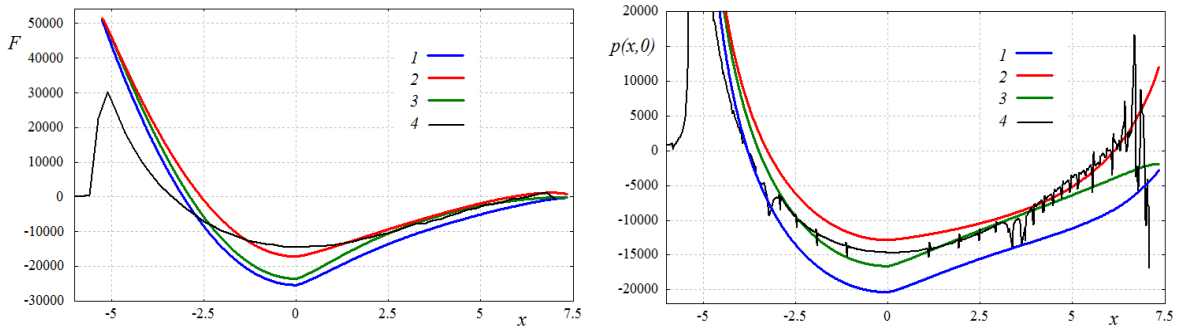

Fig. 2 The hydrodynamic sectional force (on the left) and the pressure at $y = 0$ (on the right) as functions of the longitudinal coordinate x. The correspondences of the lines are the same as in Fig. 1 (see the text).

Acknowledgment: This work has been supported by the NICOP research grant "Fundamental Analysis of the Water Exit Problem" N62909-13-1-N274, through Dr. Woei-Min Lin. Any opinions, findings, and conclusions or recommendations expressed in this material are those of the authors and do not necessarily reflect the views of the Office of Naval Research.

References

1. Fontaine, E., Cointe, R. (1997). A slender body approach to nonlinear bow waves. Philosophical Transactions of the Royal Society of London. Series A: Mathematical, Physical and Engineering Sciences, 355(1724), 565-574.
2. Tassin, A., Piro, D. J., Korobkin, A. A., Maki, K. J., Cooker, M. J. (2013). Two-dimensional water entry and exit of a body whose shape varies in time. Journal of Fluids and Structures, 40, 317-336.
3. Korobkin, A. (2004). Analytical models of water impact. Eur. Journal of Applied Mathematics, 15(06), 821-838.
4. Piro, D. J., Maki, K. J. (2011). Hydroelastic wedge entry and exit. In Eleventh International Conference on Fast Sea Transport. 26-29 September, Honolulu, Hawaii, USA.
5. Piro, D. J., Maki, K. J. (2012). Water exit of a wedge-shaped body. Proc. 27th IWWWFB, Copenhagen, Denmark.
6. Piro, D. J., Maki, K. J. (2013). Hydroelastic analysis of bodies that enter and exit water. Journal of Fluids and Structures, 37, 134-150.
7. Korobkin, A. A. (2013). A linearized model of water exit. Journal of Fluid Mechanics, 737, 368-386.
8. Korobkin A.A., Khabakhpasheva T.I., Maki K.J. (2014). Water-exit problem with prescribed motion of a symmetric body. Proc. 29th IWWWFB, , Osaka, Japan, p. 117-120.

Experimental description of long time evolution of Akhmediev breathers

O. Kimmoun[1,2], A. Chabchoub[3], H. Branger[2], H.C. Hsu[4], Y.Y. Chen[4], C. Kharif[2], M.S. Li[4].

1 Introduction

Deep water waves in the ocean and wave propagation in optical fibers can be described by the nonlinear Schrödinger (NLS) equation. One class of solutions of this equation is called breather and corresponds to the evolution of solitary waves on finite amplitude background. Due to nonlinear interaction between the solitary waves and the background, the solitons are pulsating. A fundamental analytical solution of these breathers is the Peregrine soliton, which was first presented by Peregrine [1]. The Peregrine soliton is a localized solution in both time and space, and is a limiting case of Akhmediev breathers [2]. For ideal conditions, Peregrine or Akhmediev breathers exhibit only one growth and return cycle. More realistic studies have shown that this behavior is not generally observed and a more complex evolution is observed [3]. In order to verify this complex behavior for water wave, experiments have been conducted in the "mid-size observation Flume" at the Tainan Hydraulics Laboratory (THL) of National ChengKung University, Taiwan. This flume permits to observe the long time evolution of Akhmediev breather.

2 Theoretical preliminaries

The NLS equation describes the evolution in space and time of weakly nonlinear wave trains of amplitude $A(x,t)$ in various media [4]. In finite water depth h it can be derived by applying the method of multiple scales [5, 6] and is given by:

$$-i\left(\frac{\partial A(x,t)}{\partial t}+c_g\frac{\partial A(x,t)}{\partial x}\right)+\alpha\frac{\partial^2 A(x,t)}{\partial x^2}+\beta|A(x,t)|^2A(x,t)=0$$

with

$$\begin{cases}\alpha = & -\frac{1}{2}\frac{\partial^2\omega}{\partial k^2}\\ \beta = & \dfrac{\omega\,k^2}{16\sinh^4(kh)}\left(\cosh(4kh)+8-2\tanh^2(kh)\right)\\ & -\dfrac{\omega}{2\sinh^2(2kh)}\dfrac{(2\omega\cosh^2(kh)+kc_g)^2}{gh-c_g^2}\end{cases}$$

with $\omega^2=gk\tanh(kh)$ and $c_g=\frac{\partial\omega}{\partial k}$. Using rescaling variables:

$$X=x-c_g\,t\quad T=-\alpha\,t\quad\text{and}\quad q(X,T)=\sqrt{\frac{\pm\beta}{2\alpha}}A(X,T)$$

When $kh>1.363$, then $\alpha\beta>0$, and a sign + takes place in the square root. Then the NLS equation becomes:

$$i\,q_T\;+\;q_{XX}\;+\;2\,|q|^2\,q=0$$

In this case, a regular wave train is unstable and the Benjamin-Feir instability grows exponentially. The free surface elevation is given by:

$$\eta(x,t)=\Re\left(A(x,t)\;.\;\mathrm{e}^{i\,(kx-\omega t)}\right)$$

An exact first-order solution of this NLS equation is given by Akhmediev [7]

$$q(X,T)=-\left(1+\frac{2(1-2a)\cosh(2bT)+ib\sinh(2bT)}{\sqrt{2a}\cos(\omega_{mod}X)-\cosh(2bT)}\right)\mathrm{e}^{2iT}$$

[1]email: olivier.kimmoun@centrale-marseille.fr
[2]Aix-Marseille University, CNRS, Centrale Marseille, IRPHE, Marseille, France
[3]Swinburne University of Technology, John St, Hawthorn, Australia
[4]Tainan Hydraulics Laboratory, National Cheng Kung University, Taiwan

with $b = \sqrt{8a(1-2a)}$ and $\omega_{mod} = 2\sqrt{1-2a}$ and with a a parameter related to the period of the wave envelope. An example of $q(X,T)$ for $a = 0.45$ is displayed in Fig.1(Left) and an example of the free surface in front of the wave-maker $\eta(x,t)$ for $x = -70m$ is displayed in Fig.1(Right).

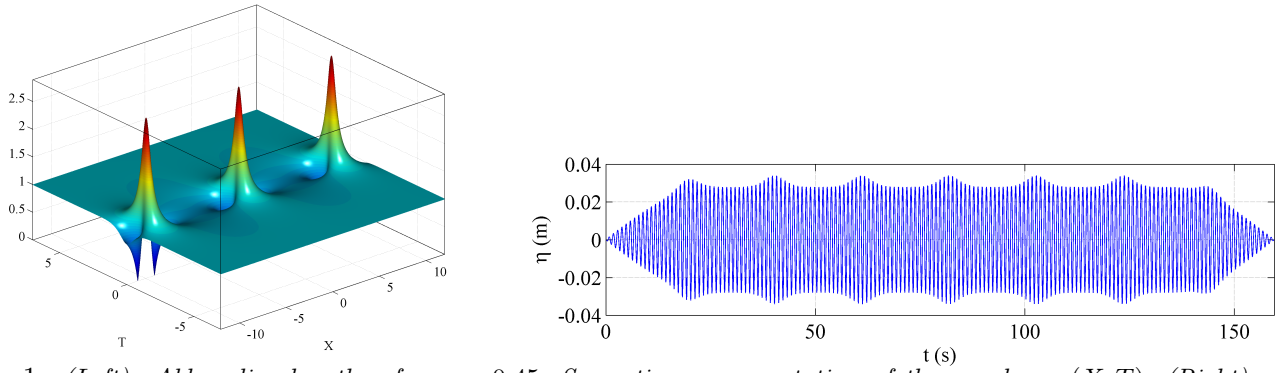

Figure 1: *(Left): Akhmediev breather for $a = 0.45$, Space-time representation of the envelope $q(X,T)$, (Right): wave elevation $\eta(x,t)$ for $x = -70m$ in front of the wave-maker for $T = 1s$, $a_0k = 0.12$ and $a = 0.45$*

3 Experimental setup

Experiments have been conducted at the Tainan Hydraulics Laboratory (THL) of National ChengKung University, Taiwan, in the so-called "mid-size observation flume". This facility is 200m long and 2m wide. The water depth was set to 1.35m. At one end, the tank is equipped with a piston wave-maker and at the other end with an absorbing beach made with rocks. In order to measure wave elevation, 60 capacitance-type wave gauges were used with a sample rate of 100Hz. The first one was located at 2.1m from the wave-maker and the last one at 176.1m. The spatial distribution of the wave gauges is presented in Fig.2.

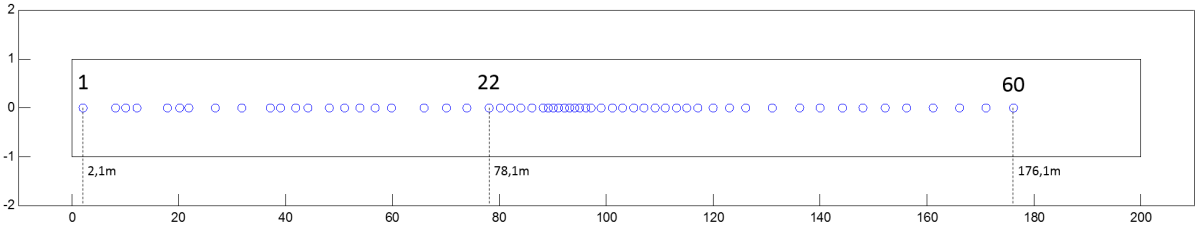

Figure 2: Distribution of the 60 wave gauges along the wavetank

3.1 A weakly nonlinear case

Among all the cases performed during this experiment, a typical case with a small steepness is chosen. In Fig.3(Left), the time evolution of the free surface and the envelope at different wave gauges is displayed. This case corresponds to $T = 1s$, $ak = 0.07$ and $a = 0.45$. In this representation, the x-axis is shifted according to the group velocity in order to have the maxima at the same location. For cases where the steepness is relatively small, the amplitude of the envelope increases and decreases after a maximum is reached, in this case at a distance from the wave-maker equal to 70m. It is noteworthy that the maximum of the envelope is always located at the same place whatever the distance from the wave-maker. In order to estimate the repeatability of the tests, the space evolution of the maximum of the amplitude of the envelope along the tank for three similar wave conditions is displayed in Fig.3(Right). The good agreement between the three curves shows that repeatability is achieved. In the next section, the repeatability for a more nonlinear case (see Fig.5(Left)) is also displayed and shows the same agreement. In Fig.4(Left), the space-time evolution of the envelope is displayed. This figure shows that the evolution of the envelope is regular all along the wave tank. As it can be noticed in Fig.3(Right), for distance to the wave-maker larger than 120m, a second maximum appears just before the main one. This feature is explained in the next section for more nonlinear cases. Another important issue

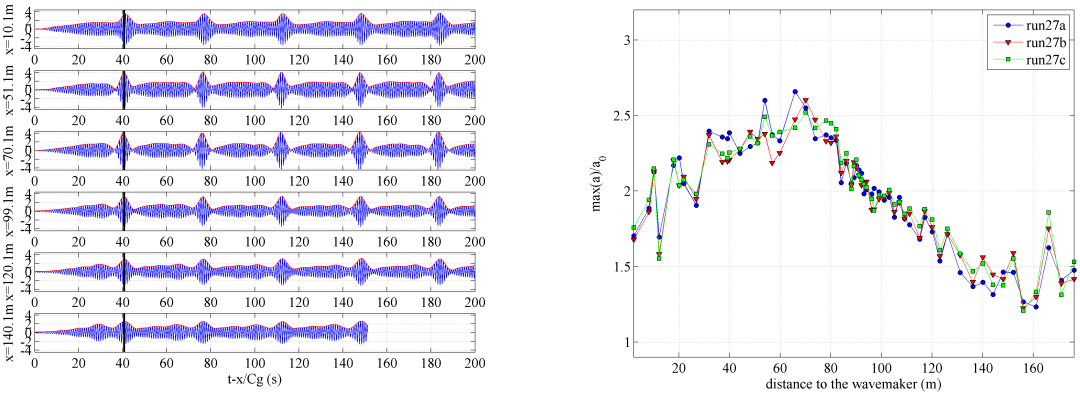

Figure 3: $T = 1s$, $a_0k = 0.07$ *and* $a = 0.45$. *(Left): Time evolution of the free surface and the envelope for different wave gauges. (Right): Space evolution of the maximum of the normalized amplitude of the envelope*

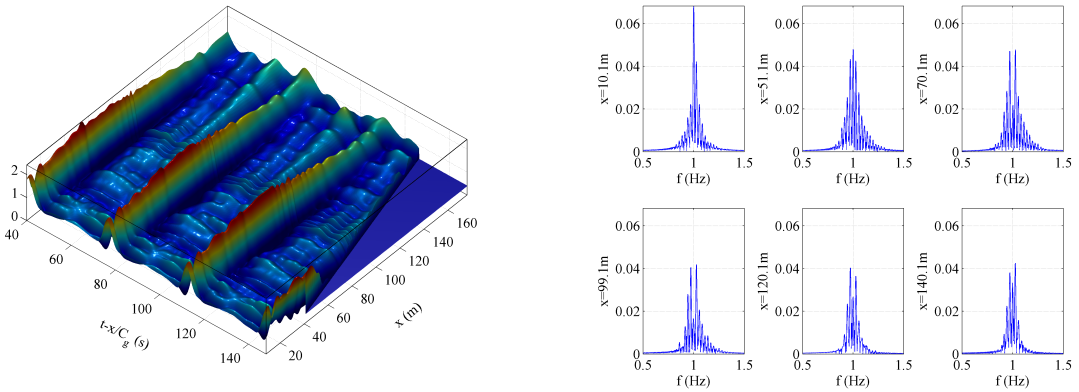

Figure 4: $T = 1s$, $a_0k = 0.07$ *and* $a = 0.45$. *(Left): Time-space evolution of the normalized amplitude of the envelope. (Right): Spectra of the wave elevations for different wave gauges. Values are expressed in* (cm/Hz)

concerns the spectral content of the wave train. In Fig.4(Right), spectra for different wave gauges along the wave tank are displayed. For the wave gauge near the wave-maker, the central peak is dominant with sidebands present on either side of the peak. As the wave train evolves, the central peak decreases up to a minimum and increases again. At the same time, the spectral content of the sidebands increases.

3.2 Highly nonlinear case

While the behavior of the different quantities is relatively simple in the weakly nonlinear case, it becomes more complex when the steepness increases. The considered case corresponds to the same wave period and Akhmediev parameter but for a steepness $ak = 0.12$. In Fig.5(Left) the space evolution of the maximum of the envelope is displayed for three similar tests. Firstly, even for higher values of the steepness, the repeatability is still very good. Secondly, when the steepness increases, we can observed three stages in the evolution: an increasing phase up to a maximum reached at 70m, a decreasing phase up to a minimum reached at 110m and a new increasing phase. In Fig.5(Right) the time evolution of the wave elevation for different wave gauges is presented. As in the previous example, over almost one hundred meters, before the minimum is reached, the maximum is located at the same time. But during the second increasing stage, we can observe that instead of one maximum, two maxima appear at either side of the previous one. This splitting can be observed more easily on the three dimensional representation displayed in Fig.6(Left). This phenomenon has been observed before experimentally for fiber optics by Hammani et al. (2011)[8] and Erkintalo et al. (2011)[9] and corresponds to high-order modulational instability. In these previous experiments, the two subpulses are of the same magnitude. In the present case, the first one with respect to the time is higher than the second one.

As we have presented for the weakly nonlinear case, the spectra for different wave gauges are presented in Fig.6(Right). As in the weakly nonlinear case, the peak at the carrier frequency decreases down to a minimum and increases again. At the same time the frequency contents of the sidebands increase.

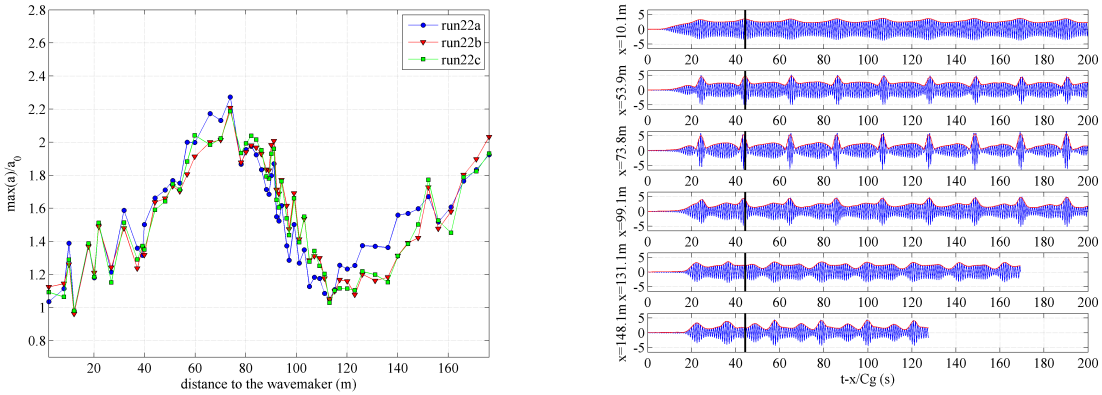

Figure 5: $T = 1s$, $a_0k = 0.12$ *and* $a = 0.45$. *(Left): Space evolution of the maximum of the normalized amplitude of the envelope. (Right): Time evolution of the free surface and the envelope for different wave gauges*

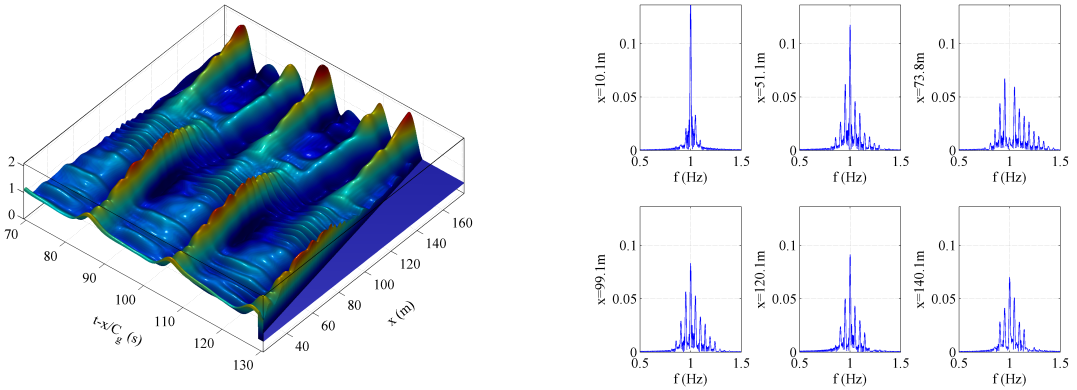

Figure 6: $T = 1s$, $a_0k = 0.12$ *and* $a = 0.45$. *(Left): Time-space evolution of the normalized amplitude of the envelope. (Right): Spectra of the wave elevations for different wave gauges. Values are expressed in* (cm/Hz).

References

[1] D. H. Peregrine (1983). Water waves, nonlinear Schrödinger equations and their solutions. The Journal of the Australian Mathematical Society. Series B. Applied Mathematics, 25, pp 16-43.

[2] N. Akhmediev and V. I. Korneev, (1986) Modulation instability and periodic solutions of the nonlinear Schödinger equation, Theor. Math. Phys. (USSR) , 69, 1089-1093.

[3] Akhmediev N. N. and Ankiewicz A., (1997), Solitons, Nonlinear Pulses and beams, Chapman and Hall, London.

[4] V. E. Zakharov, (1968), Stability of periodic waves of finite amplitude on a surface of deep fluid, J. Appl. Mech. Tech. Phys. 2, 190–194.

[5] H. Hasimoto, and H. Ono, (1972), Nonlinear modulation of gravity waves, J. Phys. Soc. Japan 33, 805–811.

[6] C. C. Mei, (1983), ,The Applied Dynamics Of Ocean Surface Waves, Advanced Series on Ocean Engineering 1.

[7] N. N. Akhmediev, V. M. Eleonskii and N. E. Kulagin, (1987), Exact first-order solutions of the nonlinear Schrödinger equation. Theoretical and mathematical physics, 72(2), 809–818.

[8] K. Hammani, B. Kibler, C. Finot, P. Morin, J. Fatome, J. Dudley and G. Millot, (2011), Peregrine soliton generation and breakup in standard telecommunications. Optics Letters, Optical Society of America, 36 (2), pp.112-114.

[9] M. Erkintalo, K. Hammani, B. Kibler, C. Finot, N. Akhmediev, J.M. Dudley and G. Genty, (2011), Higher-order modulation instability in nonlinear fiber optics, Physical Review Letters 107, 253901.

Non-linear problem on unsteady free surface flow forced by submerged cylinder

Vasily K. Kostikov[1,2], Nikolay I. Makarenko[1,2],
[1]Lavrentyev Institute of Hydrodynamics, [2] Novosibirsk State University, Novosibirsk, Russia
E-mail: vasilii_kostikov@mail.ru

A fully nonlinear problem on unsteady water waves generated by submerged circular cylinder is considered semi-analytically. Main purpose is to evaluate impact of non-linearity acting at early stage of non-stationary wave motion when the cylinder accelerates impulsively near the free surface. Effect of non-linearity was originally studied by Tuck [1] who used the Wehausen scheme [2] by constructing power expansion on radius of the cylinder for the solution which describes stationary wave train past horizontally moving body. We apply here analytical method developed by Ovsyannikov [3] for a class of initial boundary value problems on unsteady free surface flows. By this way, the mathematical formulation reduces to an integral-differential system of equations for the functions defining the free surface shape and the normal and tangential components of fluid velocity. This method was extended by Makarenko [4] to the problem on unsteady water waves forced by circular cylinder, as well as the problem on elliptic cylinder moving under free surface [5] or under ice cover [6] was considered. Small-time solution expansions were obtained systematically starting from the papers by Tyvand & Miloh [7, 8] devoted to the case of unsteady motion of a circular cylinder. We revisit here this problem in order to accent the role of non-linearity in the mechanism of formation of finite amplitude surface waves.

Statement of the problem

The plane irrotational flow of a heavy inviscid deep fluid is considered in the coordinate system Oxy with a vertical y–axis. The circular cylinder of nondimensional radius r centered at $(x_{cyl}(t), y_{cyl}(t))$ moves totally submerged in the deep fluid with free surface $y = \eta(x,t)$, having the equillibrium level $y = 0$. Dimensionless variables use the initial depth of submergence h as the length scale, characteristic speed of cylinder u_0 as the velocity scale, ρu_0^2 as the pressure scale and h/u_0 as the time scale. The Euler equations for the fluid velocity $\mathbf{u} = (U, V)$ and pressure p are

$$\begin{cases} U_t + UU_x + VU_y + p_x = 0, \\ V_t + UV_x + VV_y + p_y = -\lambda, \\ U_x + V_y = 0, \quad U_y - V_x = 0. \end{cases} \tag{1}$$

Here $\lambda = gh/u_0^2$ is the square of the inverse Froude number. The fully non-linear kinematic and dynamic free-surface boundary conditions

$$\eta_t + U\eta_x = V, \quad p = 0, \quad (y = \eta(x,t)), \tag{2}$$

together with the exact rigid body surface condition

$$(\mathbf{u} - \mathbf{u}_{cyl}) \cdot \mathbf{n} = 0, \qquad (x - x_{cyl}(t))^2 + (y - y_{cyl}(t))^2 = r^2 \tag{3}$$

are employed. Here $\mathbf{n}$ is the unit normal to the cross-section of the cylinder. We suppose that the fluid is at rest at infinity ($U, V \to 0, \quad \eta \to 0, \quad |\mathbf{x}| \to \infty$) and initial velocity field satisfies compatibility conditions, i.e. it is potential and irrotational.

We reduce equations (1)–(3) to an equivalent system of boundary integral-differential equations which are one-dimensional with respect to spatial variables. Let $u = U + \eta_x V$ and $v = V - \eta_x U$ be tangential and normal fluid velocitites at the free surface $y = \eta(x,t)$. Excluding the pressure p from momentum equations (1) we obtain under conditions (2) an evolution system for η, u, v

$$\eta_t = v, \qquad u_t + \frac{1}{2}\frac{\partial}{\partial x}\left(\frac{u^2 - 2\eta_x uv - v^2}{1 + \eta_x^2}\right) + \lambda\eta_x = 0. \tag{4}$$

Differential equations (4) are complemented by the integral equation which follows from the representation of complex velocity $F = U - iV$ using the boundary integrals on the free surface only

$$2\pi i F(z,t) = \int\limits_\Gamma \frac{F(\zeta,t)d\zeta}{\zeta - z} + \frac{r^2}{(z - z_{cyl})^2}\overline{\int\limits_\Gamma \frac{F(\zeta,t)d\zeta}{\zeta - z_*}} + \frac{\gamma}{z - z_{cyl}} + \frac{2\pi i r^2 z'_{cyl}}{(z - z_{cyl})^2}. \tag{5}$$

Here $z_* = z_{cyl} + r^2/\overline{z}$ is the inversion image of $z = x + iy$ with respect to the circle centered at the point $z_{cyl}(t) = x_{cyl}(t) + iy_{cyl}(t)$. The constant γ is the velocity circulation around the cylinder. Combining real and imaginary parts of the formula (5) with $z = x + i\eta(x,t)$ taken on the free surface gives the real-valued form of boundary integral equation as follows:

$$\pi v(x) + v.p. \int_{-\infty}^{\infty} (A_f(x,s) + r^2 A_r(x,s)) v(s) ds = v.p. \int_{-\infty}^{+\infty} (B_f(x,s) + r^2 B_r(x,s)) u(s) ds + v_{curl}(x) + v_{dip}(x), \quad (6)$$

where the kernels of integral operators are given by

$$A_f + iB_f = \frac{i[1 + i\eta'(x)]}{x - s + i[\eta(x) - \eta(s)]}, \quad A_r + iB_r = \frac{i[1 - i\eta'(x)]}{[x - i\eta(x)][r^2 - (x - i\eta(x))(s - i\eta(s))]}.$$

The functions v_{curl} and v_{dip} are the normal velocities induced at the free surface by vortex and dipole:

$$v_{curl}(x) = \gamma \mathrm{Re}\Big[\log(x + i\eta(x) - z_{cyl}(t))\Big]_x, \quad v_{dip}(x) = \mathrm{Re}\left[\frac{2iz'_{cyl}(t)}{x + i\eta(x) - z_{cyl}(t)}\right]_x.$$

The time variable t was omitted in (6) because it appears in this integral equation only as a parameter. It should be noted that the kernels A_f and B_f correspond to the problem on free waves in deep water without cylinder. The terms A_r and B_r describe the interaction between the cylinder and free surface.

Small-time asymptotic solution

We consider the unsteady flow which starts from the rest and is caused by the motion of the circular cylinder along the trajectory $z_{cyl}(t) = -i + e^{i\theta} t^2$. The angle θ of the motion direction relative to the horizon remains constant. We look for a solution in the form of power series

$$\eta(x,t) = t^2\eta_2(x) + t^3\eta_4(x) + \ldots, \quad u(x,t) = t^3 u_3(x) + t^4 u_4(x) + \ldots, \quad v(x,t) = tv_1(x) + t^2 v_2(x) + \ldots$$

It is easy to see that the coefficients η_n for $n \geq 1$ and u_n for $n \geq 3$ may be evaluated via v_n by recursive formulas following from equations (4)

$$\eta_{n+1} = \frac{1}{n+1} v_n, \quad u_3 = \frac{1}{6}(v_1^2 - \lambda v_1)_x, \quad u_4 = \frac{1}{4}(v_1 v_2)_x - \frac{1}{12}\lambda v_{2x}, \quad u_5 = \frac{1}{10}(2v_1 v_3 + v_2^2)_x - \frac{1}{20}\lambda v_{3x}. \quad (7)$$

Using the expansion of free surface elevation η one can determine the power series for integral operators

$$A_f = t^2 A_f^{(2)} + t^3 A_f^{(3)} + \ldots, \quad B_f = B_f^{(0)} + t^2 B_f^{(2)} + \ldots, \quad A_r = A_r^{(0)} + t^2 A_r^{(2)} + t^3 A_r^{(3)} + \ldots, \quad B_r = B_r^{(0)} + t^2 B_r^{(2)} + \ldots$$

The operators $B_f^{(0)}$ and $A_r^{(0)}$ are important for the solution construction. First of them is the Hilbert transform $H = B^{(0)}$

$$Hu(x) = v.p. \int_{-\infty}^{+\infty} \frac{u(s)ds}{x - s}, \qquad A_r^{(0)} v(x) = \frac{1}{\pi} \int_{-\infty}^{+\infty} \frac{(1 - r^2 p(x))q'(x) + (r^2 q(x) - s)p'(x)}{(1 - r^2 p(x))^2 + (r^2 q(x) - s)^2} v(s) ds$$

and the operator $A_r^{(0)}$ is nonlinear with respect to the Poisson kernels

$$p(x) = \frac{1}{1 + x^2}, \quad q(x) = \frac{x}{1 + x^2}.$$

The integral equation (6) for the normal velocity v leads to a set of equations for coefficients v_n ($n \geq 1$)

$$\pi v_n(x) + r^2 \int_{-\infty}^{+\infty} A_r^{(0)}(x,s) v_n(s) ds = \varphi_n(x) \qquad (n = 1, 2, ...), \quad (8)$$

where the functions φ_n can be evaluated via the coefficients v_1, v_2, …, v_{n-1} by the formulas

$$\varphi_1 = v_{dip}^{(1)}, \quad \varphi_2 = 0, \quad \varphi_3 = v_{dip}^{(3)} + Hu_3 + r^2\Big(B_r^{(0)} u_3 - A_r^{(2)} v_1\Big) - A_f^{(2)} v_1.$$

Here $v_{dip}^{(n)}$ are the coefficients of small-time expansion for normal velocity v_{dip} generated by dipole.

Thus nonlinearity realizes in two different ways if the solution expansion is constructed. Firstly, nonlinear terms arise from the integral operators depending linearly on the coefficients u_n which are nonlinear with respect to v_1, v_2, …, v_{n-1} due to the recursive formulas (7). In addition, nonlinearity is also presented by the kernels of integral operators depending on the coefficients η_n. The Table 1 illustrates the leading order terms of integral equation (8) collected by the powers of the time variable t and the cylinder radius r.

Table 1. Coefficients in the expansion of the functions φ_n from equations (8).

	t^2	t^4	…
r^2	$v_{dip}^{(1)}$	$v_{dip}^{(3)}$, Hu_3	…
r^4	$A_r^{(0)}v_1$	$A_r^{(0)}v_3$, $B_r^{(0)}u_3$, $A_f^{(2)}v_1$	…
…	…	…	…

Analytic solution of the equation (8) can be constructed explicitly by using the Neumann series of integral operator $A_r^{(0)}$. It is important here that the leading-order coefficient v_1 results as linear combination of the Poisson kernels $p(x)$, $q(x)$ and their derivatives $p'(x)$, $q'(x)$. Subsequently, calculation of higher order coefficients v_n involves nonlinear combinations of derivatives $p^{(k)}(x)$ and $q^{(k)}(x)$ with $k = 1, \ldots, n$. This version of multi-pole expansion procedure can be simplified essentially by using special identities such as follows:

$$p'(x)q'(x) = -\frac{1}{12}p'''(x), \quad p'^2(x) = \frac{1}{4}p(x) + \frac{1}{4}q'(x) + \frac{1}{12}q'''(x), \quad q'^2(x) = \frac{1}{4}p(x) + \frac{1}{4}q'(x) - \frac{1}{12}q'''(x), \quad \ldots$$

The main difficulty appears by evaluation of integral terms like $A_f^{(2)}v_1$ that can be rewritten as follows:

$$A_f^{(2)}v_1(x) = \text{v.p.}\frac{1}{\pi}\int\limits_{-\infty}^{+\infty}\frac{\eta_2(x)-\eta_2(s)}{(x-s)^2}v_1(s)ds - \eta_2'(x)\,\text{v.p.}\frac{1}{\pi}\int\limits_{-\infty}^{+\infty}\frac{v_1(s)ds}{x-s}. \tag{9}$$

As will readily be observed the first integral in the equation (9) is a commutator of the Hilbert transform H with some differential operator. To be exact:

$$\frac{1}{\pi}\int\limits_{-\infty}^{+\infty}\frac{\eta_2(x)-\eta_2(s)}{(x-s)^2}v_1(s)ds = \eta_2 Hv_{1x} - H(\eta_2 v_1)_x.$$

Finally combining all the terms of integral equation (8) we obtain under recursive formulas (7) the power expansion for the leading-order solution coefficients as follows:

$$\eta_2(x) = 2\left(r^2 - r^4\right)\Big(q'(x)\sin\theta - p'(x)\cos\theta\Big) + O(r^6), \tag{10}$$

$$\eta_4(x) = r^2\Big(p''(x)\cos 2\theta - q''(x)\sin 2\theta\Big) + \frac{\lambda(r^2-r^4)}{6}\Big(p''(x)\sin\theta + q''(x)\cos\theta\Big) + \\ + \frac{r^4}{9}\Big(p''''(x)\cos 2\theta - q''''(x)\sin 2\theta\Big) + \frac{r^4}{3}\Big(p''(x) - q'(x)\Big) + O(r^6).$$

Calculations and visualization of the flow

Non-linear theory contribute to the analytical solution (10) by the terms of the order $O(r^4)$, so the correction to linear theory becomes essential at the time scales when the cylinder approaches the free surface closely. The Fig. 2 shows that constructed solution gives the correction not only in the elevation of the free surface but also in its formation rate. In addition, asymptotic solution (10) allows one to calculate velocity field in the whole fluid domain. Subsequent flow can be constructed effectively by the representation of complex velocity (5), this solution has the form

$$F(z,t) = -2r^2\left(e^{i\theta}\frac{t}{(z-i)^2} + 2e^{2i\theta}\frac{t^3}{(z-i)^3}\right) + +2r^2\left(e^{i\theta}\frac{t}{(z+i)^2} + 2e^{2i\theta}\frac{t^3}{(z+i)^3}\right) + \\ + 2r^4\left(e^{i\theta}\frac{t}{(z-i)^2} + 2e^{2i\theta}\frac{t^3}{(z-i)^5}\right) + \frac{r^4}{2}\left(e^{-i\theta}\frac{t}{(z+i)^2} + ie^{-2i\theta}\frac{t^3}{(z+i)^2} + 2\frac{t^3}{(z+i)^3}\right) + O(r^6). \tag{11}$$

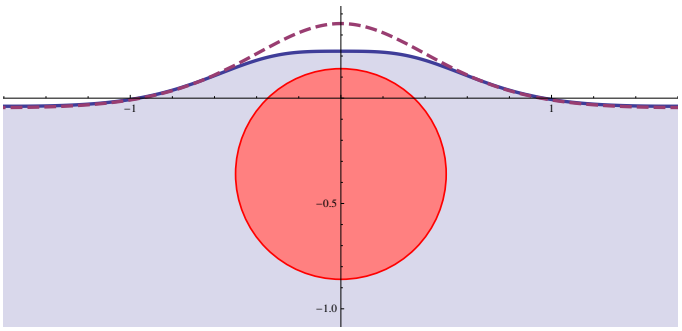

Fig 1: The shape of free surface at $t = 0.7$ ($r = 0.5$, $\lambda = 5$) predicted by the non-linear approximation (10) (solid line) and by the linear approximation [4] (dashed line).

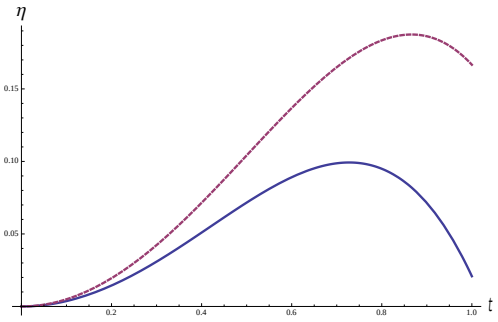

Fig 2: Free surface elevation at $x = 0$ ($r = 0.5$, $\lambda = 5$) predicted by the non-linear approximation (10) (solid line) and by the linear approximation [4] (dashed line).

Fig 3: Velocity field around the cylinder of radius $r = 0.5$ at the time $t = 0.7$ ($\lambda = 10$) moving in an infinite fluid (a) and downwards under the free surface (b).

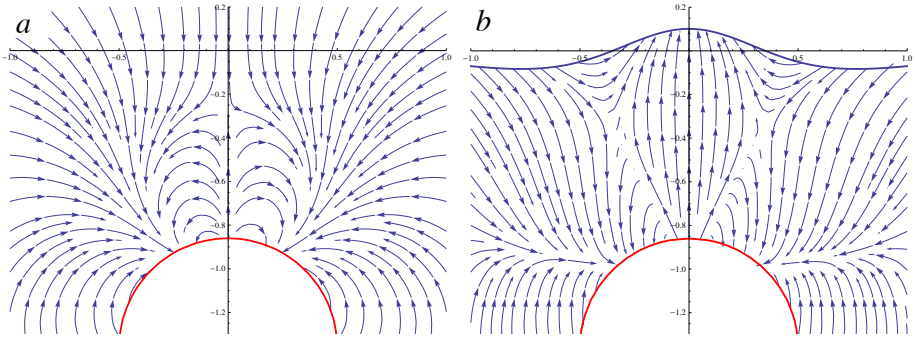

From relation (11) we see that in the leading order as $r \to 0$ the flow is determined by the two poles located at the points $z = \pm i$ symetrically with respect to undisturbed free surface $y = 0$. The effect of self-induced dipole that takes into account non-linear effects appears only when cylinder moves close to the free surface.

In this paper the nonlinear problem of free surface flow in the presence of a submerged circular cylinder has been studied analytically. The leading-order solution with the accuracy $O(r^4)$ was constucted in explicit form. The effect of non-linearity was clarified for the case of circular cylinder moving with constant acceleration from the rest.

Acknowledgement

This work was supported by the Russian Foundation for Basic Research (grant no. 15-01-03942).

References

[1] Tuck E.O. (1965) The effect of non-linearity at the free surface on flow past a submerged cylinder. J. Fluid. Mech. Vol. 22, part 2, pp. 401-414.

[2] Wehausen J.V., Laitone E.V. (1960) Surface Waves. Handbuch der Physik. Vol. 9. Springer Verlag. Berlin. pp. 446-778.

[3] Ovsyannikov L.V., Makarenko N.I., Nalimov V.I. et al. (1985) Nonlinear problems on theory of surface and internal waves. Novosibirsk, «Nauka».

[4] Makarenko N.I. (2003) Nonlinear interaction of submerged cylinder with free surface. JOMAE Transactions of the ASME. Vol.125. No 1, pp. 72-75.

[5] Makarenko N.I., Kostikov V.K. (2013) Unsteady motion of an elliptical cylinder under a free surface. Journal of Applied Mechanics and Technical Physics. Vol. 53, No. 3, pp. 367-376.

[6] Kostikov V.K., Makarenko N.I., Korobkin A.A. (2012) Unsteady motion of elliptic cylinder under ice cover. Proc. of 27th Int. Workshop on Water Waves and Floating Bodies. pp. 89–92.

[7] Tyvand P.A., Miloh T. (1995). Free surface flow due to impulsive motion of a small submerged circular cylinder. J. Fluid Mech. Vol. 286, pp. 67-101.

[8] Tyvand P.A., Miloh T. (1995). free-surface flow generated by a small submerged circular cylinder starting from the rest. J. Fluid Mech. Vol. 286, pp. 103-116.

When no axisymmetric modes are trapped by a freely floating moonpool

Nikolay KUZNETSOV

Laboratory for Mathematical Modelling of Wave Phenomena,
Institute for Problems in Mechanical Engineering, Russian Academy of Sciences,
V.O., Bol'shoy pr. 61, St. Petersburg 199178, Russian Federation.
E-mail: nikolay.g.kuznetsov@gmail.com

We study the coupled time-harmonic motion of an axisymmetric moonpool (toroidal, surface-piercing body) floating freely in infinitely deep water bounded above by a free surface. The surface tension is neglected and the water motion is assumed to be irrotational. The motion of both water and body is of small amplitude near equilibrium which allows us to apply the linearized model proposed by John [2]. We use it in the form of a coupled spectral problem; its two- and three-dimensional versions were developed in [4] and [7], respectively.

In the framework of this model, two theorems proved in [7] guarantee the absence of trapped modes in the presence of a single body freely floating in water of constant finite depth; it is either totally submerged or surface piercing, but the free surface is assumed to be connected in the latter case. On the other hand, single bodies and structures consisting of multiple bodies [either motionless or heaving] were constructed in [8] and [9] so that they trap axisymmetric wave modes in water of infinite depth. A characteristic feature of these bodies and structures, all of which have axisymmetric immersed parts and float freely, is that they divide the free surface into at least two connected components.

In the present note, our aim is to find frequency intervals within which no axisymmetric modes exist that are trapped by a freely floating moonpool provided its geometry satisfies the assumptions used in [5] to guarantee the absence of modes trapped by the same moonpool being fixed. The frequency intervals obtained here only partly coincide with those in [5] because an extra condition is due to the equation of body's motion.

1 Statement of the problem

We take the Cartesian coordinates $(\boldsymbol{x},y)$ $[\boldsymbol{x}=(x_1,x_2)]$ so that the y-axis is directed upwards and the $\boldsymbol{x}$-plane coincides with the mean free surface. It divides $\widehat{B}$ — an axisymmetric toroidal domain occupied by a surface-piercing body in its equilibrium position — into two non-empty parts and $B=\widehat{B}\cap\mathbb{R}^3_-$ denotes the submerged part $[\mathbb{R}^3_-=\{(\boldsymbol{x},y):\boldsymbol{x}\in\mathbb{R}^2,y<0\}]$. Furthermore, $W=\mathbb{R}^3_-\setminus\overline{B}$ is the water domain, $S=\partial\widehat{B}\cap\mathbb{R}^3_-$ is the wetted surface of the moonpool and $\boldsymbol{n}$ denotes the unit normal pointing to the exterior of W. Finally, the free surface $F=\partial W\setminus\overline{S}$ is the union $F_0\cup F_\infty$; its circular part $F_0=\{0\leqslant|\boldsymbol{x}|<b,y=0\}$ is separated from infinity by the annulus $D=\widehat{B}\cap\partial\mathbb{R}^3_-$ of finite width and F_∞ is the infinite part of the free surface outside of D.

In the general linearised setting (see [2]), the time-dependent motion is described by the following first-order variables: the real-valued velocity potential $\Phi(\boldsymbol{x},y;t)$ and the vector $\boldsymbol{q}(t)\in\mathbb{R}^6$, characterising the motion of the body's centre of mass about its rest position $\bigl(\boldsymbol{x}^{(0)},y^{(0)}\bigr)$. The horizontal and vertical displacements are q_1, q_2 and q_4, respectively, whereas q_3 and q_5, q_6 are the angles of rotation about the axes that go through the centre of mass and are parallel to the y and x_1, x_2 axes, respectively.

We do not formulate the problem for Φ and $\boldsymbol{q}$ (see [7] for its condensed form), but assume that the motion is time-harmonic with the radian frequency $\omega>0$, in which case $\bigl(\Phi(\boldsymbol{x},y,t),\boldsymbol{q}(t)\bigr)=\operatorname{Re}\bigl\{\mathrm{e}^{-\mathrm{i}\omega t}\bigl(\varphi(\boldsymbol{x},y),\boldsymbol{\chi}\bigr)\bigr\}$. Then the bounded complex-valued function φ and $\boldsymbol{\chi}\in\mathbb{C}^6$ must satisfy the following problem:

$$\nabla^2\varphi=0\ \text{ in } W;\ \ \partial_y\varphi-\nu\varphi=0\ \text{ on } F;\ \ \partial_{\boldsymbol{n}}\varphi=-\mathrm{i}\omega\,\boldsymbol{n}^{\mathsf{T}}\boldsymbol{D}_0\boldsymbol{\chi}\ \text{ on } S; \tag{1}$$

$$\omega^2\boldsymbol{E}\boldsymbol{\chi}=-\mathrm{i}\omega\int_S\varphi\,\boldsymbol{D}_0^{\mathsf{T}}\boldsymbol{n}\,\mathrm{d}s+g\,\boldsymbol{K}\boldsymbol{\chi};\quad \int_{W\cap\{|\boldsymbol{x}|=a\}}\bigl|\partial_{|\boldsymbol{x}|}\varphi-\mathrm{i}\nu\varphi\bigr|^2\,\mathrm{d}s=o(1)\ \text{ as }\ a\to\infty. \tag{2}$$

Here ω is the spectral parameter [$\nu=\omega^2/g$ for the sake of brevity], which is sought together with the eigenvector $(\varphi,\boldsymbol{\chi})$; also the following notation is used: $\nabla=(\partial_{x_1},\partial_{x_2},\partial_y)$ is the spatial gradient, g is the acceleration due to gravity acting in the direction opposite to the y-axis, $^{\mathsf{T}}$ is the symbol of matrix transposition; $\boldsymbol{D}_0=\boldsymbol{D}\bigl(\boldsymbol{x}-\boldsymbol{x}^{(0)},y-y^{(0)}\bigr)$ is an auxiliary 3×6 matrix, where $\boldsymbol{D}(\boldsymbol{x},y)=\begin{bmatrix}1&0&x_2&0&0&-y\\0&1&-x_1&0&y&0\\0&0&0&1&-x_2&x_1\end{bmatrix}$. In the equation of body's motion [the first condition (2)], the 6×6 matrices $\boldsymbol{E}$ and $\boldsymbol{K}$ are defined as follows:

$\boldsymbol{E} = \rho_0^{-1} \int_{\widehat{B}} \rho(\boldsymbol{x},y)\, \boldsymbol{D}_0^{\mathsf{T}}(\boldsymbol{x},y)\, \boldsymbol{D}_0(\boldsymbol{x},y)\, \mathrm{d}\boldsymbol{x}\, \mathrm{d}y$, where $\rho(\boldsymbol{x},y) \geqslant 0$ is the distribution of density within the body and $\rho_0 > 0$ is the constant density of water;

$$\boldsymbol{K} = \begin{pmatrix} \mathbb{O}_3 & \mathbb{O}_3 \\ \mathbb{O}_3 & \boldsymbol{K}' \end{pmatrix}, \quad \text{where} \quad \boldsymbol{K}' = \begin{pmatrix} I^D & I_2^D & -I_1^D \\ I_2^D & I_{22}^D + I_y^B & -I_{12}^D \\ -I_1^D & -I_{12}^D & I_{11}^D + I_y^B \end{pmatrix}, \quad I^D = \int_D \mathrm{d}\boldsymbol{x}, \quad I_y^B = \int_B \bigl(y - y^{(0)}\bigr)\, \mathrm{d}\boldsymbol{x}\, \mathrm{d}y,$$

$$I_i^D = \int_D \bigl(x_i - x_i^{(0)}\bigr)\, \mathrm{d}\boldsymbol{x}, \quad I_{ij}^D = \int_D \bigl(x_i - x_i^{(0)}\bigr)\bigl(x_j - x_j^{(0)}\bigr)\, \mathrm{d}\boldsymbol{x}, \ \ i,j = 1,2, \quad \text{and } \mathbb{O}_3 \text{ is the } 3\times 3 \text{ null matrix.}$$

The elements of the mass-inertia matrix $\boldsymbol{E}$ are various moments of the whole body $\widehat{B}$ and this matrix is symmetric and positive definite; the symmetric matrix $\boldsymbol{K}$ is related to buoyancy (see [2, 7]).

Along with relations (1) and (2), the following subsidiary conditions must hold [they concern the equilibrium position of the floating body and its stability]: • $\rho_0^{-1} \int_{\widehat{B}} \rho(\boldsymbol{x},y)\, \mathrm{d}\boldsymbol{x}\, \mathrm{d}y = \int_B \mathrm{d}\boldsymbol{x}\, \mathrm{d}y$ [Archimedes' law]; • $\int_B \bigl(x_i - x_i^{(0)}\bigr)\, \mathrm{d}\boldsymbol{x}\, \mathrm{d}y = 0$, $i = 1,2$ [the center of buoyancy lies on the same vertical line as the centre of mass]; • $\boldsymbol{K}'$ is a positive definite matrix which implies that the body's equilibrium position is stable, [2, § 2.4].

2 Definition of a trapped mode

First we list some properties of φ under the assumption that $\widehat{B}$ is an axisymmetric freely floating moonpool with $x_1^{(0)} = x_2^{(0)} = 0$. The boundedness of φ implies that $\nabla\varphi$ decays as $y \to -\infty$, whereas the radiation condition [the second condition (2)] guarantees that φ describes outgoing waves at infinity (see [3]). In the same way as in [7], one proves the following assertion about the energy of $(\varphi, \boldsymbol{\chi})$ satisfying problem (1) and (2):

The first component φ belongs to the space $H^1(W)$ and $\int_F |\varphi|^2\, \mathrm{d}\boldsymbol{x} < \infty$, that is, the kinetic and potential energy of the water motion is finite. The following equality expresses the equipartition of energy of the coupled motion

$$\int_W |\nabla\varphi|^2\, \mathrm{d}\boldsymbol{x}\, \mathrm{d}y + \omega^2 \overline{\boldsymbol{\chi}}^{\mathsf{T}} \boldsymbol{E} \boldsymbol{\chi} = \nu \int_F |\varphi|^2\, \mathrm{d}\boldsymbol{x} + g\, \overline{\boldsymbol{\chi}}^{\mathsf{T}} \boldsymbol{K} \boldsymbol{\chi}. \tag{3}$$

Definition. Let the conditions concerning the equilibrium position of the moonpool $\widehat{B}$ hold, then a non-trivial pair $(\varphi, \boldsymbol{\chi})$ belonging to $H^1(W) \times \mathbb{C}^6$ is called a *trapped mode* provided relations (1) and the first relation (2) are satisfied for some value of ω; the latter is called a *trapping frequency*.

Since $\varphi \in H^1(W)$ relations (1) must be understood as the integral identity

$$\int_W \nabla\varphi \nabla\psi\, \mathrm{d}\boldsymbol{x}\, \mathrm{d}y = \nu \int_F \varphi\, \psi\, \mathrm{d}\boldsymbol{x} - \mathrm{i}\omega \int_S \psi\, \boldsymbol{n}^{\mathsf{T}} \boldsymbol{D}_0 \boldsymbol{\chi}\, \mathrm{d}s, \tag{4}$$

which involves only the first-order derivatives of φ; here ψ is an arbitrary smooth function having a compact support in $\overline{W}$.

Below we restrict our considerations to axisymmetrc trapped modes, that is, $\boldsymbol{\chi} = (0,0,0,H,0,0)$, whereas $\varphi = \varphi(|\boldsymbol{x}|, y)$. We recall that several examples of geometries of bodies [and also of multi-body structures] that trap modes with $H = 0$ [$\widehat{B}$ is motionless] and $H \neq 0$ [$\widehat{B}$ is heaving] were constructed in [8] and [9], respectively.

3 Conditions guaranteeing the absence of axisymmetric trapped modes

We recall that a body satisfies John's condition [3] if no point of its wetted surface lies on vertical lines going through the free surface (see Fig. 1 in [5], illustrating the case of an axisymmetric moonpool). This condition is essential for proving the following assertion about the absence of axisymmetric trapped modes.

Let an axisymmetric freely floating moonpool satisfy John's condition. If $(\varphi, \boldsymbol{\chi}) \in H^1(W) \times \mathbb{C}^6$ is an axisymmetric solution of problem that consists of the first relation (2) *and identity* (4)*, then this solution vanishes identically provided the following two conditions are fulfilled:*

(i) *the inequalities $j_{0,m} \leqslant \nu b \leqslant j_{1,m}$ hold for some $m = 1,2,\ldots$, where $j_{0,m}$ ($j_{1,m}$) is the m-th zero of the Bessel function J_0 (J_1, respectively)*;

(ii) $\omega^2 > \lambda_*$, *where $\lambda_* > 0$ is the largest λ such that* $\det(\lambda \boldsymbol{E} - g\boldsymbol{K}) = 0$.

What follows outlines main points of the proof. As in the case of a fixed moonpool (see [5]), we assume

that there exists a non-trivial φ and define the following function which was originally introduced by John [3] under the assumption that $F_0 = \emptyset$:

$$w(|\boldsymbol{x}|) = \int_{-\infty}^{0} \varphi(|\boldsymbol{x}|, y)\, \mathrm{e}^{\nu y}\, \mathrm{d}y. \tag{5}$$

Then the Laplace equation and the free surface boundary condition [the first and second relations (1)] imply that

$$w_{x_1x_1} + w_{x_2x_2} + \nu^2 w = 0 \quad \text{in } F = F_0 \cup F_\infty. \tag{6}$$

Since φ decays at infinity, this gives that $w \equiv 0$ in F_∞ (see [3], p. 78), a consequence of which is the inequality

$$\nu \int_{F_\infty} |\varphi|^2\, \mathrm{d}\boldsymbol{x} \leqslant \frac{1}{2} \int_{W_\infty} |\partial_y \varphi|^2\, \mathrm{d}\boldsymbol{x}\, \mathrm{d}y \leqslant \frac{1}{2} \int_{W_\infty} |\nabla\varphi|^2\, \mathrm{d}\boldsymbol{x}\, \mathrm{d}y. \tag{7}$$

Furthermore, (6) yields that $w(|\boldsymbol{x}|) = CJ_0(\nu|\boldsymbol{x}|)$ in F_0 because φ is non-singular on $|\boldsymbol{x}| = 0$; here C is, generally speaking, a non-zero constant. Thus, we get that the following equalities are valid for $|\boldsymbol{x}| < b$:

$$CJ_0(\nu|\boldsymbol{x}|) = \int_{-\infty}^{0} \varphi(|\boldsymbol{x}|, y)\, \mathrm{e}^{\nu y}\, \mathrm{d}y, \qquad \nu C J_1(\nu|\boldsymbol{x}|) = -\int_{-\infty}^{0} \varphi_{|\boldsymbol{x}|}(|\boldsymbol{x}|, y)\, \mathrm{e}^{\nu y}\, \mathrm{d}y,$$

$$\varphi(|\boldsymbol{x}|, 0) = \nu C J_0(\omega^2|\boldsymbol{x}|) - \int_{-\infty}^{0} \varphi_y(|\boldsymbol{x}|, y)\, \mathrm{e}^{\nu y}\, \mathrm{d}y.$$

Here the second and third equalities follow from the first one by virtue of differentiation and integration by parts, respectively. After some manipulations with inequalities obtained by squaring these relations and applying the Schwarz inequality to the integrals (see [5], pp. 570–572), one arrives at the inequality

$$\nu \int_{F_0} |\varphi|^2\, \mathrm{d}\boldsymbol{x} \leqslant \int_{W_0} |\nabla\varphi|^2\, \mathrm{d}\boldsymbol{x}\, \mathrm{d}y \tag{8}$$

under the assumption that νb satisfies condition (i). From this inequality and (7) we get that

$$\nu \int_{F} |\varphi|^2\, \mathrm{d}\boldsymbol{x} < \int_{W} |\nabla\varphi|^2\, \mathrm{d}\boldsymbol{x}\, \mathrm{d}y. \tag{9}$$

Then the equipartition of energy [equality (3)] gives

$$\omega^2 \overline{\boldsymbol{\chi}}^{\mathsf{T}} \boldsymbol{E} \boldsymbol{\chi} - g \overline{\boldsymbol{\chi}}^{\mathsf{T}} \boldsymbol{K} \boldsymbol{\chi} < 0, \tag{10}$$

which is incompatible with (ii) unless $\boldsymbol{\chi}$ vanishes, but this is impossible because then (9) contradicts (3) for a non-trivial φ. Hence the problem under consideration has only a trivial axisymmetric solution.

4 Discussion

• If the free surface F is connected and $N \geqslant 1$ bodies float freely each satisfying John's condition, then condition (i) is unnecessary for obtaining inequality (9). However, condition (ii) must hold for each body and λ_* in this case is equal to the largest λ_j, where the latter is the largest λ such that $\det(\lambda \boldsymbol{E}_j - g\boldsymbol{K}_j) = 0$, $j = 1, \ldots, N$.

• If a moonpool is fixed, then the uniqueness follows directly from inequality (9) because it contradicts (3) since the latter does not contain the two terms depending on $\boldsymbol{\chi}$.

• In the case when W is bounded below by a horizontal bottom $\{y = -d\}$ with $d > \max\{-y : (x, y) \in S\}$, the uniqueness theorem similar to that obtained in § 3 for deep water is also true, but the non-dimensional parameter νb in condition (i) must be changed to $k_0 b$, where k_0 is the unique positive root of $k_0 \tanh k_0 d = \nu$. In the proof, one has to use $w(|\boldsymbol{x}|) = \int_{-d}^{0} \varphi(|\boldsymbol{x}|, y) \cosh k_0 y\, \mathrm{d}y$ instead of (5) when deriving inequalities (7) and (8) for the axisymmetric mode φ.

• The above theorem can be improved by allowing the submerged part B of a moonpool to be bulbous on the side directed to infinity. Namely, let B lies outside the cylinder $\{|\boldsymbol{x}| = b\}$ and within the cone whose generator going through the waterline $\overline{S} \cap \overline{F}_\infty$ forms an angle less than 38° with the negative y-axis. Then the inequality

$$\nu \int_{F_\infty} |\varphi|^2\, \mathrm{d}\boldsymbol{x} \leqslant \int_{W_\infty} |\nabla\varphi|^2\, \mathrm{d}\boldsymbol{x}\, \mathrm{d}y$$

holds as is shown in [10]; here W_∞ is the part of $\mathbb{R}^3_-$ lying outside the cone described above. Combing the last inequality [instead of (7)] and (8) [a consequence of condition (i)], one obtains the theorem for a bulbous axisymmetric moonpool. Below we explain why condition (i) which plays a key role in our considerations

is incompatible with a moonpool's geometry bulbous on the side directed to W_0.

• A result similar to the above theorem is true for an azimuthal mode of the form $\varphi_n(|x|,y)\cos n\theta$, where θ is the polar angle in the x-plane and $n = 1,2,\ldots$, in which case condition (i) must be changed to the following one. *The inequalities $j_{n,m} \leqslant \nu b \leqslant j'_{n,m}$ hold for some $m = 1,2,\ldots$; here $j_{n,m}$ ($j'_{n,m}$) is the m-th zero of the Bessel function J_n (J'_n, respectively)*. According to formulae 9.5.12 and 9.5.13 in [1] [they give the asymptotics of these zeroes as $m \to \infty$], the intervals in νb, for which there are no trapped modes with any azimuthal number, are asymptotically of length $\pi/2$.

• For values of b, belonging to a certain interval adjacent to $j_{1,m}/\nu$ and located on the left of it, there exist freely floating moonpools both heaving and motionless [the latter can be also treated as fixed] trapping axisymmetric modes and enclosing the circular free surface of radius b. When $m = 1$ such values of b lie between $|\mathring{x}| \in (0, j_{1,1}/\nu)$ and $j_{1,1}/\nu$ as follows from Proposition 5 (c) in [8]; here $|\mathring{x}|$ stands for the unique positive zero of the trace $\psi(\nu|x|,0)$ of the stream function that has its singularity at $(j_{1,1},0)$. If the singularity is at $(j_{1,m},0)$, then the behaviour of the left end of the interval occupied by values νb corresponding to trapping moonpools is as follows: it tends to $j_{0,m}$ as m goes to infinity. Hence, the intervals in which trapped modes exist are also asymptotically of length $\pi/2$.

• Results similar to those in § 3 are valid for the properly formulated two-dimensional problem. Let a pair of infinitely long surface-piercing cylinders have a vertical cross-section symmetric about the y-axis (see Fig. 4.7 in [6]). In this case, it is natural to consider symmetric and antisymmetric modes of waves as is shown in [6], § 4.2.2, for fixed cylinders. Indeed, conditions guaranteeing the absence of trapped modes of each type are given there. It occurs that the same results are valid when the cylinders have symmetric density distributions and float freely. In particular, for the parameter νb [here $2b$ is the spacing between the cylinders] there are segments, where antisymmetric and symmetric modes are absent and these segments are interlacing. However, the additional restriction which is unnecessary for fixed cylinders must be imposed when cylinders are freely floating; it says that frequencies must be sufficiently large [cf. condition (ii)]. It is also worth mentioning that if $\nu b = \pi m/2$ and $m > 0$ is sufficiently large, then there are no trapped modes at all in deep water.

5 Conjecture

Given the proof of a theorem guaranteeing the uniqueness of a solution to the linearised problem about time-harmonic water waves in the presence of a fixed obstacle, then this proof admits amendments transforming it into the proof of an analogous theorem for the same obstacle floating freely with additional restrictions on the non-trapping frequencies [they must be sufficiently large; see condition (ii) above] and, in some cases, on body's geometry and on the type of non-trapping modes.

References:

[1] M. Abramowitz & I. A. Stegun, 1965 *Handbook of Mathematical Functions*.

[2] F. John, 1949 *CPAM* **2**, 13–57.

[3] F. John, 1950 *CPAM* **3**, 45–101.

[4] N. Kuznetsov, 2011 *St. Petersburg Math. J.* **22**, 985–995.

[5] N. Kuznetsov & P. McIver, 1997 *QJMAM* **50**, 565–580.

[6] N. Kuznetsov, V. Maz'ya & B. Vainberg, 2002 *Linear Water Waves: A Mathematical Approach*.

[7] N. Kuznetsov & O. Motygin, 2011 *JFM* **679**, 616–627.

[8] N. Kuznetsov & O. Motygin 2012 *JFM* **703**, 142–162.

[9] N. Kuznetsov & O. Motygin 2013 *Proc. 28th IWWWFB*, 121–124.

[10] N. Kuznetsov, M.J. Simon 1999 *JFM* **386**, 5–14.

Study on a Semi-Analytic Approach for Analysis of Parametric Roll in Regular and Irregular Head Seas

By Jae-Hoon Lee[1], Yonghwan Kim[1*], and Kang-Hyun Song[2]
[1]Dept. of Naval Architecture and Ocean Engineering, Seoul National University, Seoul, Korea
[2]Korean Register of Shipping, Korea
E-mail: **yhwankim@snu.ac.kr*

Highlights:

- A semi-analytic approach for the simulation of parametric roll motions is proposed from the investigation on the characteristics of metacentric height (GM) variation and the relationship between GM and the restoring lever (GZ) in waves.
- To validate the accuracy and efficiency of the present method, the computational results are compared with those obtained by the direct simulation based on an impulse response function (IRF) method.
- The stochastic properties of parametric roll in irregular waves are discussed, considering the uncertainties due to the computational parameters such as time-window and the phases of wave components.

1. Introduction

Parametric roll motion in head sea is a rapidly increasing large-amplitude motion induced by the variations of restoring forces over several wave periods. Due to the nonlinear change in transverse stability, there is a difficulty in quantifying the amplitude of parametric roll. Also, this phenomenon in irregular waves is a non-ergodic and non-Gaussian process, which leads to the large number of realizations to obtain the stable probabilistic qualities. Therefore, an efficient and accurate scheme which can consider the nonlinearities in parametric roll is required for the practical application.

In a time-domain numerical computation, the nonlinear restoring lever in waves can be considered in a more accurate manner for the quantitative calculation. Shin et al. (2004) applied the Rankine panel method to develop the susceptibility criteria for parametric roll motions of large container ships while Spanos and Papanikolaou (2007) used IRF method to analyze the phenomenon of fishing vessels in regular waves. However, large computational costs are incurred for many realizations and for many sea states in wave scatter diagram. On the other hand, Bulian (2004) and Umeda et al. (2004) derived the simplified analytical approaches for prediction of amplitude of parametric roll by applying their own modellings for the nonlinearities in the variations in GZ. Since then, led by the International Maritime Organization (IMO), various models such as Belenky's, Umeda's, and Song's methods (IMO, 2010, 2011, 2012) have been developed to establish dynamic stability criteria and operational guidance, but the accuracies of these conventional methods are still concern.

In this study, a semi-analytical approach to simulate the parametric roll motion of a large container ship in head sea conditions is proposed. The accuracy and efficiency of the present approach are validated by the comparison with the results obtained by the IRF method in respect of the occurrence and amplitude of parametric roll in regular and irregular waves. Also, the probabilistic qualities of the parametric rolling in irregular waves as obtained from the both a semi-analytical and numerical approach are compared considering the sensitivities and uncertainties of to the computation parameters.

2. Semi-analytic approach

Based on the assumption that the coupling effects from roll motion to vertical motions are neglected, the 1.5 degree of freedom (DOF) equation of roll motion in head seas can be written as follows:

$$\left(M_{44}+A_{44}\right)\ddot{\xi}_4+b_{roll}\dot{\xi}_4+\Delta GZ\left(\xi_3,\xi_4,\xi_5,\eta\right)=0 \tag{1}$$

where M_{44}, A_{44}, and Δ are the rolling moment of inertia, the roll- added moment of inertia, and the displacement, respectively. In Eq. (1), the damping force acting on roll motion is modelled by an equivalent linear damping to for an easy implementation. Also, the restoring lever, GZ in the equation depends on the actual wetted surface considering vertical and roll motions of ship relative to the wave elevation. Because large computation costs are incurred for the direct integration of the external pressure up to wave surfaces in time domain, the simplified and efficient modelling for the time-varying restring force is required.

2.1. Approximation of GM

Containerships which have the large bow and overhang transom show a large variation in the water plane area according to the change in the draft at the fore and after body. The resulting variations of GM in waves can be approximated by the mean value and harmonic components, such that:

$$GM\left(A,\omega,t\right)=GM_{still}+GM_0\left(A,\omega\right)+\sum_{i=1}^{\infty}GM_i\left(A,\omega\right)\cos\left(i\omega t\right)\approx GM_{still}+GM_0\left(A,\omega\right)+GM_1\left(A,\omega\right)\cos\left(\omega t\right) \quad (2)$$

where GM_{still} indicates the GM in still water, and GM_0 and GM_i are the difference between the mean and GM_{still}, and the i-th harmonic component, respectively. The time history of GM is calculated at the actual water plane area considering vertical motions obtained by the IRF method. According to Eq. (2), the transfer functions of GM_0 and GM_1 are computed by applying the Fourier transform to the time histories of GM in regular waves as shown in Fig. 1. The higher order harmonic components are assumed to be negligible since these values are relatively small and are not directly related with the mechanism of occurrence of parametric roll.

In this study, GM_0 which represents the static stability performance is regarded as being a second order quantity with respect to the wave amplitude based on the assumption that the second order effects on the mean value are dominant. On the other hand, GM_1 which is the amplitude of variation is a linear component as proven by Dunwoody (1989). It can be seen that these hypotheses are valid by the fact that the normalized transfer functions computed for different wave amplitudes show good correspondences between each other. Therefore, the variations of GM in random seas can be approximated under the "assumption of superposition", such that:

$$GM_0\left(H_s,T_p\right)=\sum_{i=1}^{N}A_i^2RAO_{GM_0/A^2}\left(\omega_i\right)=2\int_0^{\infty}RAO_{GM_0/A^2}S_\eta\left(\omega\right)d\omega=2\int_0^{\infty}S_{GM_0/A^2}\left(\omega\right)d\omega \quad (3)$$

$$GM_1\left(H_s,T_p,t\right)=\sum_{i=1}^{N}A_iRAO_{GM_1/A}\left(\omega_i\right)\cos\left(\omega_i t+\varepsilon_i\right) \quad (4)$$

where $RAO_{GM0/A2}$ and $RAO_{GM1/A}$ are the transfer functions of GM_0 and GM_1, respectively. S_η and $S_{GM0/A2}$ indicate the spectrum of the wave and normalized GM_0, respectively.

2.2. Approximation of GZ

The variation in GZ is proportional to the variation in GM at small heel angles while the variation shows nonlinearities from the body geometry due to the small change in the wetted surface at large heel angles. Therefore, the GZ in waves is expressed by the GM_{still}, GM in waves, and the "GZ factor function", $f(\xi_4)$ as follows:

$$GZ\left(\xi_4,t\right)=GZ_{still}\left(\xi_4\right)+\frac{GM\left(t\right)-GM_{still}}{GM_{still}}f\left(\xi_4\right). \quad (5)$$

The accuracy of quantitative prediction is closely relevant to how to model the higher order term in the GZ factor function to consider the nonlinearities at large heel angles. Eq. (6) denotes the present modeling which is a modified form of the Song's method (IMO, 2012), such that:

$$f\left(\xi_4\right)=GM_{still}\left(\sin\left(\xi_4\right)-\frac{\sin^{\alpha}\left(\xi_4\right)}{\sin^{\alpha-1}\left(\xi_{4,\max}\right)}\right) \quad (6)$$

where $\xi_{4,\max}$ indicates the x-intercept of the GZ curve in still water. In the current method, α is adopted to represent the order of the higher-order term.

The proposed GZ factor function is compared with that from the "direct calculation" which is based on the instantaneous hydrostatically computed maximum and minimum GZ curves in waves as shown in Fig. 2. For an appropriate value of α, the present function shows good agreement with that of the direct calculation in overall heel angles. It should be noted that the validated values are different according to the type of ships (for the 6500 TEU containership, α=2.0-3.0, for the MARIN model 8004-2, α=5.0-7.0), which means that α depends on the geometry of ship, especially at fore and after body.

3. Parametric roll in regular waves

The equation of roll motion in a regular wave can be solved by using the time integration such as the 4th-order Runge-Kutta method. In the integration, the disturbance of roll motion induced by gusts or currents is modelled by an impulsive roll angle (3-10 degrees) at a certain instant. After parametric roll arises, the roll motion does not diverge, and is bounded with the quasi-steady state amplitude owing to the damping force and the decreases of GZ in waves at large heel angles.

Fig. 3 shows the comparison of the quasi-steady state amplitudes obtained by the present method and the IRF method which is based on the hydrodynamic coefficients of the strip theory and the weakly nonlinear approach. The discrepancies with regard to the amplitudes and occurrences of parametric roll come from the difference between the calculation methods for the hydrodynamic forces and the errors in the approximation of variations in GZ at large heel angels. For the validated value of α, however, the similar solutions are produced by the semi-analytical and the numerical method.

4. Parametric roll in irregular waves

The solutions of equation of roll motion in random seas exhibit the stochastic nature such as non-Gaussianities and non-ergodicities because of the nonlinear restoring term which can be regarded as a random process. In the solutions, there exist strong uncertainties and sensitivities with respect to the length of time window, the method of discretization for the wave spectrum. Therefore, the stochastic analysis instead of the deterministic calculation is required to investigate the statistical properties of parametric roll in irregular waves.

The test condition is the "Run 307004" case (Tp=14.4 sec, Hs=5.25 m) from the benchmark study conducted by the ITTC specialist committee on stability in waves (Reed, 2011). The randomly discretized 80 wave components for a wave spectrum are given, and the 20 sets of wave phases are distributed to represent the wave train of the experiment in the study. For these wave conditions, it was proved that parametric roll occurs easily. In the both applications of the semi-analytical and numerical approach, the same impulsive angle is imposed, and the damping coefficient is set based on the roll decay test of the study. Also, α of the present method is in the range of 2.0-3.0 according to the validation for the model ship, the MARIN model 8004-2.

For all 20 realizations in which the 2500-sec simulations are conducted, the variances of parametric roll motions and their 95% confidence bands are computed as shown in Fig. 4. The IRF method shows the more scattered variances along with larger bands. This phenomenon indicates that the results of numerical approach are more sensitive to the phases of wave components than those of the semi-analytic approach because the higher-order components in nonlinear restoring forces and Froude-Krylov forces are taken into account based on weakly nonlinear approach. On the other hand, the simplified variations of GM in the present method lead to the more consistent results for different set of wave phases. If the value of α, which denotes how large the variations of restoring forces in waves increases, the variations and the uncertainties becomes large owing to the stronger nonlinearities in the equation of roll motion.

Fig. 5 shows the cumulative density functions (CDFs) of parametric roll motions for different time windows. Even for the 86400-sec simulation, the numerical method exhibits still diverged CDFs (the absence of the "practical ergodicities") while the semi-analytical method show the converged functions which has the similar form with the Rayleigh distribution. For larger value of α, the differences from the Rayleigh distribution increase with the stronger non-Gaussianities, as expected. Despite the more accurate considerations for the nonlinear restoring forces in the numerical computation, in conclusion, the present method can be a more rational way because the converged statistical properties can obtained much more efficiently.

References

Bulian, G., 2004. Approximate analytical response curve for a parametrically excited highly nonlinear 1-DOF system with an application to ship roll motion prediction. Nonlinear analysis: real world applications. 5 (4), 725-748.

IMO SLF/52/INF.2, 2010. Information collected by correspondence group.

IMO SLF/53/INF.10, 2011. Information collected by correspondence group.

IMO SLF/54/INF.12, 2012. Information collected by correspondence group.

Reed, AM., 2011. 26th ITTC parametric roll benchmark study. In: Proceedings of the 12th International Ship Stability Workshop, Washington DC, USA.

Shin, Y.S., Belenky, V.L., Paulling, J.R., Weems, K.M., Lin, W.M., 2004. Criteria for parametric roll of large containerships in longitudinal seas. In: SNAME Annual Meeting, Washington DC, USA.

Spanos, D., Papanikolaou, A., 2007. Numerical simulation of parametric roll in head seas. Int. Shipbuild. Prog. 54 (4), 249-267.

Umeda, N., Hashimoto, H., Vassalos, D., Urano, S., Okou, K., 2004. Nonlinear dynamics on parametric roll resonance with realistic numerical modelling. Int. Shipbuild. Prog. 51 (2), 205-220.

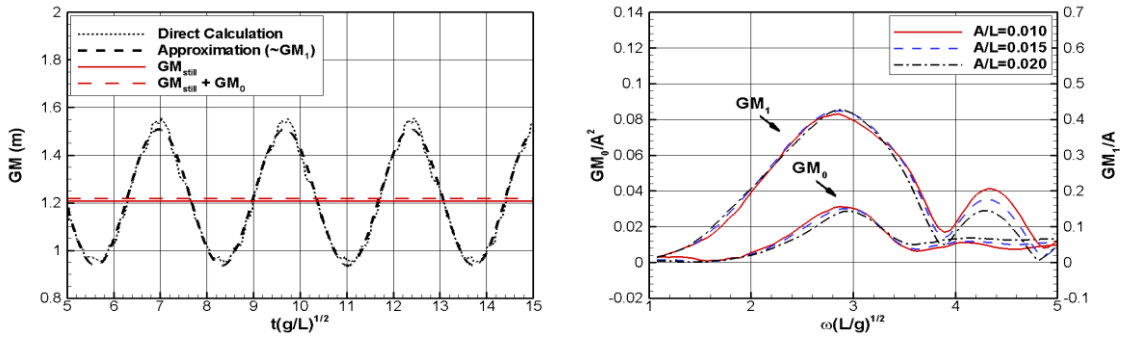

Fig. 1 Time history of GM in a regular wave and its approximation, $\omega(L/g)^{1/2}$=2.11 (left), Transfer functions of GM (right): 6500 TEU containership, V (forward speed)=5 knots

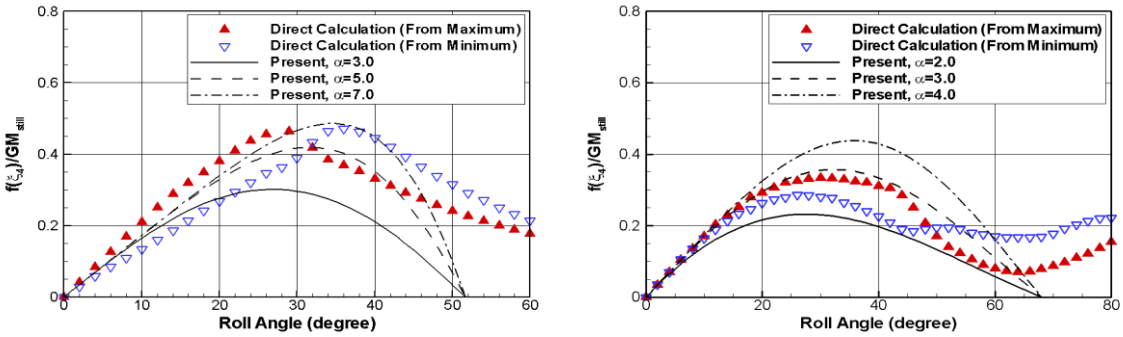

(a) 6500 TEU containership, $\omega(L/g)^{1/2}$=2.11 (b) MARIN model 8004-2, $\omega(L/g)^{1/2}$=2.27

Fig, 2 GZ factor functions: *A/L*=0.010, *V*=5 knots

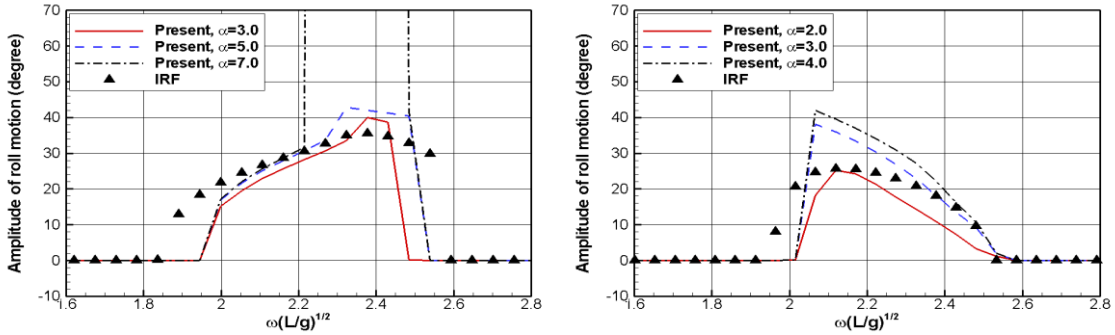

(a) 6500 TEU containership (b) MARIN model 8004-2

Fig, 3 Quasi-steady state amplitude of parametric roll motion: *A/L*=0.010, *V*=5 knots

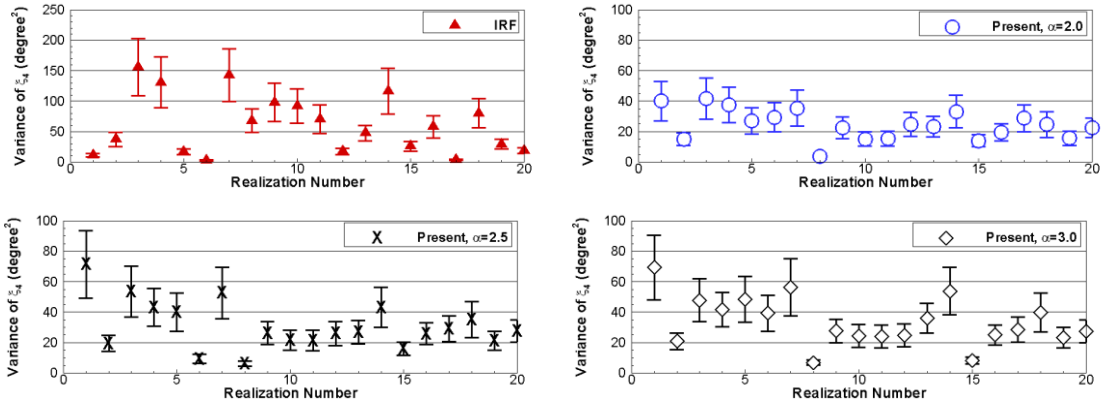

Fig. 4 Variances of parametric roll with 95% confidence bands: Run 307004 (Reed, 2011), 2500 sec

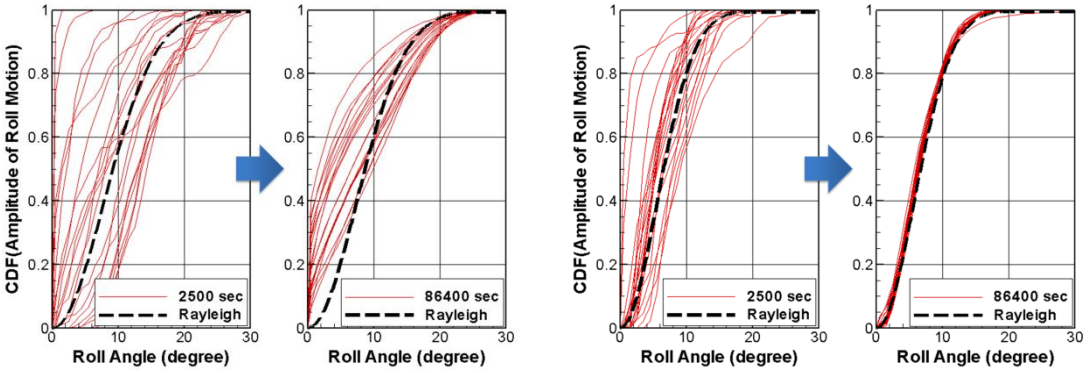

Fig. 5 Cumulative density functions: Run 307004 (Reed, 2011), IRF method (left), Present, α=2.5 (right)

Forces on vertical cylinders due to steep asymmetric and breaking waves based on the Froude Krylov approximation x2

S. J. Lind and P. K. Stansby

steven.lind@manchester.ac.uk
p.k.stansby@manchester.ac.uk
School of Mechanical, Aerospace and Civil Engineering, University of Manchester, Manchester, UK, M13 9PL

Highlights

- Novel implementation of state-of-the-art incompressible SPH with Froude-Krylov forcing to determine 3D loads on cylinders in breaking wave conditions, and with good experimental agreement.
- Determination of the asymmetric wave profile likely to exert maximum loading during wave breaking.

1 Introduction

Studies of wave forces on cylinders is a fundamental problem in fluid mechanics and is of particular interest in offshore and coastal engineering given the many structures with semi-submerged cylindrical supports. Interest has been renewed in recent years with the increased deployment of offshore wind turbines in ever challenging offshore environments and high sea-states. The prediction of forces exerted on these wind turbine columns is key to designing and deploying structures with maximal functionality and survivability. Breaking waves are likely, and, despite being the subject of sustained research for seven decades, there is still debate over the loads and forces exerted due to wave breaking. In this paper, we present the novel numerical approach of using state-of-the-art incompressible SPH with Froude-Krylov forcing to determine 3D loads on cylinders due to 2D plane incident waves - both breaking and non-breaking. The effectiveness of this approach is demonstrated through thorough comparisons with recent experimental work on breaking and non-breaking regular [5] and focused waves [2, 7]. The applicability of this approach is remarkable, and it benefits from relatively low computational cost and ease of implementation. Following validation, the method is also used to gain insight into the maximum forces exerted due to wave breaking, and considers at what point in the breaking process maximum loading occurs.

2 Model and Numerical Method

2.1 The Problem Set-Up and Governing Equations

A two dimensional numerical wave basin of length L and maximum water depth, D, is constructed with a piston wave paddle positioned at the left hand side of the domain, centred at x=0. A cylinder of diameter d_c is centred at a distance x_c from the origin. To enable breaking in the regular wave studies, as in the experiments of [5], a 2.5% gradient ramp is inserted such that the local water depth at the cylinder is then D_{loc}. The governing equations of a low viscosity Newtonian fluid are to be solved: namely, the conservation of momentum,

$$\frac{d\mathbf{u}}{dt} = -\frac{1}{\varrho}\nabla p + \nu\nabla^2\mathbf{u} + \mathbf{f},$$

and the conservation of mass,

$$\nabla\cdot\mathbf{u} = 0$$

The symbols $\mathbf{u}$, p, ϱ, ν, and $\mathbf{f}$ denote the fluid velocity, pressure, density, constant kinematic viscosity, and constant gravity body force, respectively.

2.2 Incompressible Smoothed Particle Hydrodynamics

The Lagrangian particle method, incompressible SPH (ISPH) is used to solve the governing equations [4]. In SPH a variable A at a point $\mathbf{r}$ is approximated by a convolution product of the variable A with a smoothing kernel function $\omega_h(|\mathbf{r}-\mathbf{r}'|)$, with a smoothing length h, and is written as

$$A(\mathbf{r}) \approx \int_{\Omega} A(\mathbf{r}')\omega_h(|\mathbf{r}-\mathbf{r}'|)\, d\mathbf{r}',$$

where Ω is the supporting domain. When discretised over surrounding Lagrangian fluid particles the interpolation can be written as

$$A(\mathbf{r_i}) \approx \sum_j V_j A(\mathbf{r_j}) \omega_h(r_{ij}),$$

where V_j is the particle volume, $\mathbf{r}_{ij}$ is a distance vector between particle i and j. Incompressibility is imposed through a projection method, which provides a pressure Poisson equation from which the pressure is obtained [4].

2.3 Wave Generation and Froude-Krylov Forcing

A piston-type wavemaker is used to generate all waves, with its motion prescribed using linear wave theory. In the case of focused waves, a JONSWAP spectrum provides the amplitude distribution. In both the experimental studies of interest, the Keulegan-Carpenter numbers are moderate to small and the Reynolds numbers are large, meaning that inertial forces dominate the wave-cylinder interaction. Horizontal forces on the cylinder are calculated using the Froude-Krylov approximation, with an added mass multiplier based on uniform potential flow:

$$F_x = -2 \int_C p n_x \, dS.$$

3 Results

3.1 Regular Wave Loading

The first wave type to be considered and compared with experiment is that of a plane regular wave incident on a cylinder placed on a slope. The slope has a gradient of 2.5% and the cylinder (diameter 0.2m) is positioned at x_c=10m. A water depth at the cylinder of D_{loc}=0.4m is considered here. The test case considers a regular wave of period T=1.6 s interacting with the cylinder for a range of (local) wave heights. Figure 1 presents the horizontal forces on the cylinder due to experiments of [5] (circles), ISPH (joined black squares), and semi-analytical results (thick black line) from non-linear stream function theory for periodic water waves used in combination with the Morison equation (calculated using the SAWW software [1]). For all wave heights, the ISPH results lie centrally within the experimental measurements recorded by [5], and begin to deviate significantly from SAWW predictions for wave heights above 0.15m. Indeed, for heights above approximately 0.15m, the waves begin to break.

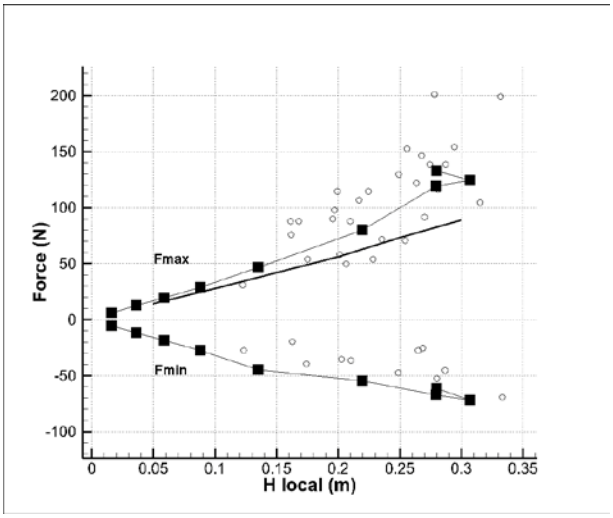

Figure 1: Comparison with experimental results [5] (circles) for loading on cylinder due to regular waves on a slope. Black squares are ISPH, and the thick black line denotes predictions from SAWW.

3.2 Focused Wave Loading

The second type of wave-cylinder interaction considered is that due to focused wave groups as in the experimental study detailed in [7, 2]. There is no slope in this case, as breaking waves may be formed by the focusing of the wave group into an unstable wave form at the front of the cylinder. The numerical wave tank is taken to be of length L=12m and still water depth D=0.505m (as in the experiment). The cylinder (diameter 0.25m) is centred at x_c=7.52m.

The focused wave case considered is that which results in a plunging breaker with jet impact direct on the cylinder (H=0.22m, f=0.82Hz). Figure 2a shows the breaking wave (with pressure contours) at time t≈11.8s. Quite remarkably, subsequent force measurements up to and including the plunging jet impact at t≈11.8s are well predicted by the FK modelling (Fig. 2b). At later times agreement worsens, but this is to be expected as full cylinder interaction would be required for accurate modelling after such an impact. It seems that in this case a consideration of the undisturbed flow field alone is sufficient to get reasonable agreement in the *total loading* on the cylinder - including at jet impact.

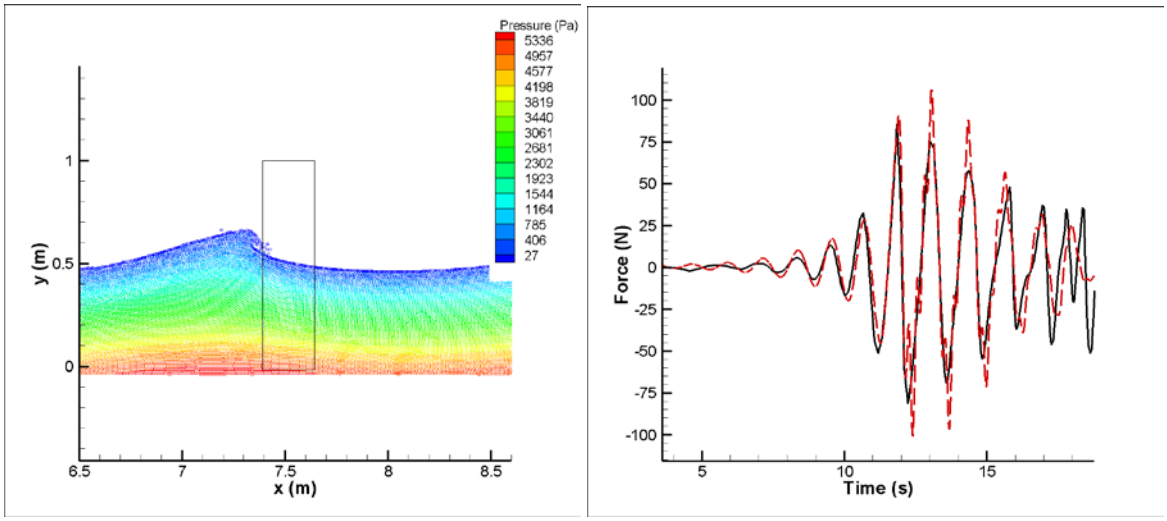

(a) (b)

Figure 2: (a) Wave profile and pressure contours at select times near the focal point at the cylinder. (b) Comparison between experimental and numerical results for the total horizontal force on the cylinder for a focused wave case. The dashed lines denote experimental measurements, the black line is ISPH.

For this case, the cylinder position is moved incrementally about the original experimental position x_c=7.52m, in order to vary the form of the breaking wave at impact. For each cylinder location, the local wave height at the cylinder is determined and input into the SAWW program to determine the loading at that wave height for the equivalent fully non-linear but symmetric (non-breaking) wave profile. Figure 3a plots the maximum horizontal force determined from ISPH and SAWW against various cylinder positions. There is clearly an amplification region ($6.5 \lesssim x \lesssim 7.5$m) as highlighted approximately by the arrow, that produces an increased load for ISPH resulting purely from asymmetry in the impacting wave crest. From Figure 3a the globally maximum force occurs at a cylinder location x_c=7.22m, which corresponds to an impact as displayed in Figure 3b, where the wave is at the point of overturning and the wave front vertical. This supports the numerical study of [3], and the experimental findings of [6], where maximum forces were observed with impact at the point of overturning when newly-formed jets remain horizontal.

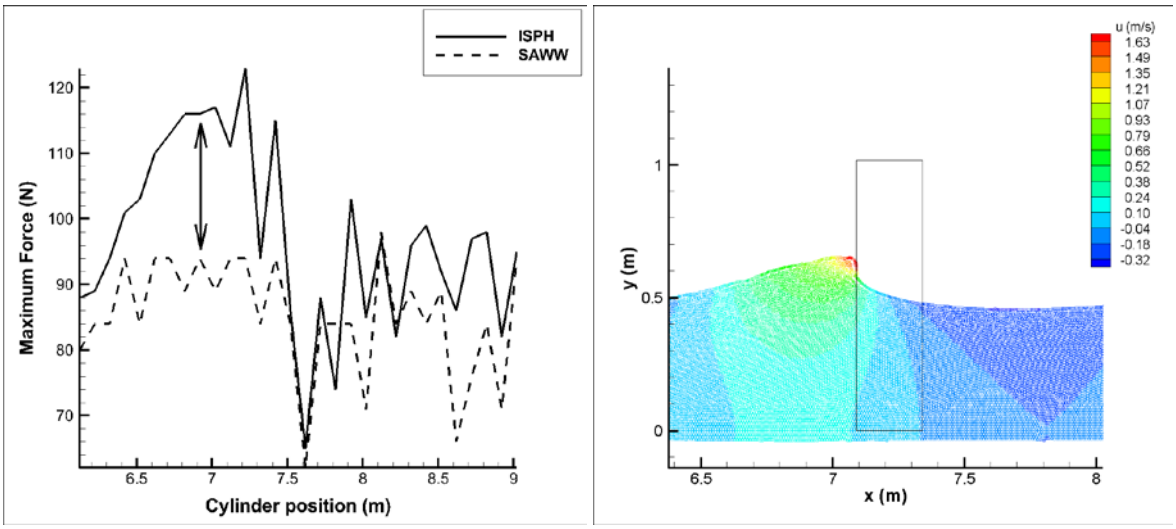

(a) (b)

Figure 3: (a) Maximum predicted loads on the cylinder at various cylinder locations. (b) The wave profile that exerts the largest load on the cylinder during the breaking process as determined through ISPH predictions. Contours denote the horizontal velocity values.

4 Conclusions

This paper presents a novel and efficient numerical approach to the calculation of three dimensional loads on cylinders due to breaking and non-breaking waves. Fully non-linear wave profiles and dynamics are determined accurately using a state-of-the-art incompressible SPH method. Forces on the cylinder are then determined from the undisturbed flow field using the Froude-Krylov force with theoretical added mass for a uniform flow. Two wave types are studied (regular and focused) and thorough comparisons are made with experimental data [5, 7]. The Froude-Krylov approximation with theoretical added mass is remarkably accurate, and is able to predict loads on cylinders due to waves in various stages of breaking. The numerical simulations remain two dimensional and of moderate resolution, meaning that computations are comparatively fast.

Acknowledgement

Support through the EPSRC Supergen Marine Grand Challenge Project X-MED EP/J010235/1 is acknowledged.

References

[1] G. Y. Buss and P. K. Stansby. SAWW - a computer program to calculate the properties of steady water waves. Technical report, Simon Engineering Laboratories, University of Manchester, 1982.
[2] L.F. Chen, J. Zang, A.J. Hillis, G.C.J. Morgan, and A.R. Plummer. Numerical investigation of wave-structure interaction using openfoam. *Ocean Engineering*, 88:91–109, 2014.
[3] A. Hildebrandt and T. Schlurmann. Breaking wave kinematics, local pressures, and forces on a tripod support structure. *Proceedings of the 33rd International Conference on Coastal Engineering; ICCE, Santander, Spain*, 2012.
[4] Lind, S.J., Xu, R., Stansby, P.K. & Rogers, B.D. Incompressible smoothed particle hydrodynamics for free-surface flows: A generalised diffusion-based algorithm for stability and validations for impulsive flows and propagating waves. *J. Comput. Phys.* 231 (4), 1499, 2012.
[5] M. Luck and M. Benoit. Wave loading on monopile foundation for offshore wind turbines in shallow-water areas. *in Coastal Engineering 2004. World Scientific Publishing Co. Pte. Ltd.: Lisbon, Portugal.*, page 4595, 2004.
[6] J. Wienke and H. Oumeraci. Breaking wave impact force on a vertical and inclined slender pile - theoretical and large-scale model investigations. *Coastal Engineering*, 52:435–462, 2005.
[7] J. Zang, P. H. Taylor, G. Morgan, R. Stringer, J. Orszaghova, J. Grice, and M. Tello. Steep wave and breaking wave impact on offshore wind turbine foundations - ringing revisited. *25th International Workshop on Water Waves and Floating Bodies, Harbin*, 2010.

Hydroelastic response of a floating thin plate due to a surface-piercing load*

D. Q. Lu[1, 2, †]

[1] *Shanghai Institute of Applied Mathematics and Mechanics, Shanghai University, Yanchang Road, Shanghai 200072, China*
[2] *Shanghai Key Laboratory of Mechanics in Energy Engineering, Yanchang Road, Shanghai 200072, China*

1. INTRODUCTION

A thin elastic plate floating on an inviscid fluid is an ideal model for the very large floating structure in offshore engineering [1] and the homogeneous ice sheet in the polar region [2]. A fundamental problem for this model is the flexural response due to a moving concentrated load [3–7], in which the Euler–Bernoulli plate was commonly employed. Recently, the effect of compression of the plate on the hydroelastic dynamics were considered [8]. A general model the effect of lateral stress is presented here for the elastic plate floating on an infinitely deep fluid. A special case of this model is capillary–gravity waves on an inertial surface. The wave response and the wave resistance are analytically investigated for steadily moving, suddenly starting and suddenly stopping concentrated loads on the surface of the floating plate. For the purpose of analytical study, two-dimensional problems are considered.

2. GENERAL MATHEMATICAL FORMULATION

We consider an inviscid, incompressible and homogeneous fluid of infinite depth, being covered by a thin elastic plate of infinite extent. As a starting point for the analytical study, a two-dimensional problem is addressed here. The Cartesian coordinates oxz are chosen in such a way that the z axis points vertically upwards. The fluid occupies the domain $(-\infty < x < \infty, \ -\infty < z \leqslant 0)$ with $z = 0$ being the undisturbed plate–fluid interface. Under the assumption that the motion is irrotational, the velocity potential $\phi(x, z, t)$ for the fluid satisfies the Laplace equation $\nabla^2\phi = 0$. For an infinitely deep fluid, we have $\partial\phi/\partial z = 0$ as $z \to -\infty$.

Let $\zeta(x, t)$ represent the vertical plate deflection subjected to a downward external load $-P_{\text{ext}}(x, t)$. It is assumed that the wave amplitudes generated are small in comparison with the wavelengths. Thus the linearized boundary conditions will be applied on the plate–fluid interface ($z = 0$). The kinematic boundary condition on $z = 0$ reads $\partial\zeta/\partial t = \partial\phi/\partial z$, which implies that there is no cavitation between the plate and the fluid and the fluid particles once on the interface will always remain there. The dynamic boundary condition on $z = 0$ reads

$$D\nabla^4\zeta + Q\nabla^2\zeta + M\frac{\partial^2\zeta}{\partial t^2} = -\rho\left(\frac{\partial\phi}{\partial t} + g\zeta\right) - P_{\text{ext}}, \tag{1}$$

where the flexural rigidity of the plate D is determined by Young's modulus E, Poisson's ratio ν and the plate thickness d as $D = Ed^3/12(1-\nu^2)$; Q is related to the lateral stress of the plate (with compression at $Q > 0$ and stretch at $Q < 0$) [8]; $M = \rho_{\text{e}}d$; ρ_{e} and ρ denote the densities of the plate and the fluid, respectively; and g is the acceleration due to gravity.

Obviously, Eq. (1) indicates the balance among the elastic, inertial, hydrodynamic forces and the downward external load. Equation (1) is a general linear model for a floating elastic plate. In particular, as $D = 0$ and $Q = -T$, Eq. (1) is for the capillary–gravity waves on an inertial ($M \neq 0$) or a free ($M = 0$) surface, where T with $T > 0$ is the coefficient of the surface tension.

To have a formal solution, we introduce the Fourier transforms as $\{\widetilde{\phi}(\alpha, z, t), \widetilde{\zeta}(\alpha, t), \widetilde{P}_{\text{ext}}(\alpha, t)\} = \int_{-\infty}^{\infty}\{\phi(x, z, t), \zeta(x, t), P_{\text{ext}}(x, t)\}\exp(-\text{i}\alpha x)\text{d}x$. Upon some mathematical derivation, we obtain, for $z = 0$,

$$\frac{\partial^2\widetilde{\zeta}}{\partial t^2} + \omega^2\widehat{\zeta} = -\frac{\hat{P}_{\text{ext}}k}{\rho(1+\sigma k)}, \tag{2}$$

where

$$\omega^2 = \frac{gk(\Gamma k^4 - \Lambda k^2 + 1)}{1 + \sigma k}, \tag{3}$$

$$\Gamma = D/\rho g, \quad \Lambda = Q/\rho g, \quad \sigma = M/\rho, \tag{4}$$

and $k = |\alpha|$ is the wave number.

Equation (3) is the dispersion relation between the frequency $\omega(k)$ and the wave number k for the flexural–gravity wave motion on the elastic plate floating on the inviscid fluid of infinite depth. Three parameters, Γ, Λ and σ, are associated with the effects of flexural rigidity, lateral stress and the inertia of the thin plate. For the capillary–gravity waves on

*This research was sponsored by the National Basic Research Program of China under Grant No. 2014CB046203, the Natural Science Foundation of Shanghai under Grant No. 14ZR1416200, and the National Natural Science Foundation of China under Grant No. 11472166.
†dqlu@shu.edu.cn

an inertial ($\sigma \neq 0$) or a free ($\sigma = 0$) surface, the corresponding dispersion relation follows from Eq. (3) by setting $\Gamma = 0$ and $\Lambda = -\tau$, where $\tau = T/\rho g > 0$.

3. STEADILY TRANSLATING LOADS

Let $\boldsymbol{e}_x$ be the unit vector along the positive x-axis. We consider a concentrated load steadily moving with a constant velocity $-U\boldsymbol{e}_x$ and a constant magnitude of strength P_0, namely $P_{\rm ext} = P_0\delta(x-x_0)$, where $\delta(\cdot)$ is the Dirac delta function and $x_0 = -Ut$ is the source point namely the location of the concentrated load. In this case the right-hand side of Eq. (2) reads $-P_0 k\exp(\mathrm{i}\alpha Ut)/[\rho(1+\sigma k)]$. Neglecting the transient effect, we have the particular solution of Eq. (2) with $P_{\rm ext} = P_0\delta(x-x_0)$, denoted by $\widetilde{\zeta}^{\rm S}(\alpha,t)$, for the ultimately steady-state plate deflection as follows

$$\widetilde{\zeta}(\alpha,t) = \widetilde{\zeta}^{\rm S}(\alpha,t) = -\frac{P_0}{\rho\Delta}\exp(\mathrm{i}\alpha Ut), \tag{5}$$

where

$$\Delta(k) = k(1+\sigma k)(c^2 - U^2), \tag{6}$$

and $c(k) = \omega/k$ is the phase speed.

By the inverse Fourier transform for Eq. (5), the steady plate deflection, denoted by $\zeta^{\rm S}$, due to a steadily translating load is given by

$$\zeta^{\rm S}(X,U) = -\frac{P_0}{2\pi\rho}\int_{-\infty}^{\infty}\frac{\exp(\mathrm{i}\alpha X)}{\Delta}\mathrm{d}\alpha, \tag{7}$$

where $X = x - x_0 = x + Ut$. Taking X as a new coordinate, one can see from Eq. (7) that the wave is time-independent, which can be seen as a system of steady waves in a reference frame steadily moving with the load. It is noted that the denominator of the integrand in Eq. (7) is an even function with respect to α since $k = |\alpha|$. To have an explicit expression for the plate deflection, the Jordan lemma will be used. The contribution to the integral comes from the pole of the integrand, namely the roots of the equation

$$c^2 - U^2 = 0. \tag{8}$$

One can find that there is a minimal phase speed $c_{\rm min}$ for the flexural–gravity waves in the floating plate with a given d. $c_{\rm min}$ is usually referred to as the critical speed of the moving load. The critical wave number $k_{\rm cr}$ at which the minimal phase speed occurs satisfies

$$\frac{\mathrm{d}c}{\mathrm{d}k} = \frac{1}{k}(c_{\rm g} - c) = 0, \tag{9}$$

where $c_{\rm g}(k) = \mathrm{d}\omega/\mathrm{d}k$ is the group speed of the wave generated. Equation (9) implies $c_{\rm g} = c = c_{\rm min}$ at $k = k_{\rm cr}$. For $k < k_{\rm cr}$, $c_{\rm g} < c$ while for $k > k_{\rm cr}$, $c_{\rm g} > c$.

The nature of the real roots of Eq. (8) depends crucially on the relation between U and $c_{\rm min}$. As $U < c_{\rm min}$, Eq. (8) has no real roots. As $U = c_{\rm min}$, Eq. (8) has one real root $k_{\rm cr}$. As $U > c_{\rm min}$, Eq. (8) has two real roots, denoted by k_1 and k_2 with $k_1 < k_{\rm cr} < k_2$.

As $U < c_{\rm min}$, the plate deflection profile can be numerically calculated by the fast Fourier transform [4]. According to Schulkes and Sneyd [4], there is no wave propagation. As $U < c_{\rm min}$ the deflection profile is similar to a static one. As $U > c_{\rm min}$, it is noted that the poles of the integrand $\pm k_1$ and $\pm k_2$ lie on the real α axis, which is due to the use of potential theory for an inviscid fluid. For the viscous fluid, the poles are automatically off from the axis since the viscosity coefficient appears in the imaginary part, as shown by Lu and Chwang [9]. To perform the α integration for the wave motion in an inviscid fluid, an artificial viscosity is necessary to move the poles off the axis. According to Lighthill's method [10], the artificial viscosity, denoted by ϵ with $\epsilon > 0$, can be introduced as $\alpha = \alpha_0 - \mathrm{i}\epsilon/(c_{\rm g} - U)$, where $\alpha_0 = \pm k_1, \pm k_2$ is the original pole. For $\alpha_0 = k_1 < k_{\rm cr}$, we have $c_{\rm g} < c = U$. For $\alpha_0 = k_2 > k_{\rm cr}$, we have $c_{\rm g} > c = U$. Therefore, with the aid of the artificial viscosity, $\pm k_1$ and $\pm k_2$ are moved into the upper and lower half α-plane, respectively.

According to the Jordan lemma, infinite semicircles in the upper and lower half α-planes are chosen for $X > 0$ and $X < 0$, respectively. Thus the wave profile for $U > c_{\rm min}$ is given by

$$\zeta^{\rm S}(X,U) = \begin{cases} \zeta_1^{\rm S}, & (X > 0), \\ \zeta_2^{\rm S}, & (X < 0), \end{cases} \tag{10}$$

where $\zeta_j^{\rm S} = 2(-1)^{j+1}P_0\sin(k_j X)\mathrm{H}(U - c_{\rm min})/\rho\Delta_j'$, $\Delta_j' = \mathrm{d}\Delta(k_j)/\mathrm{d}k$, and $\mathrm{H}(\cdot)$ is the Heaviside step function. k_1 is the wave number of the long gravity-dominated wave trailing the moving object ($x_0 < x$), while k_2 is the wave number of the short elasticity-dominated (capillarity-dominated) wave leading the moving object ($x < x_0$). This theoretical perdition is in agreement with the experimental observatories conducted by Squire et al. [5]

According to the formula of wave resistance given by Kim and Webster [11], the wave resistance $\boldsymbol{R} = R^{\rm S}\boldsymbol{e}_x$ for a moving load can be given by

$$R^{\rm S}(U) = \int_{-\infty}^{\infty} P_{\rm ext}\frac{\partial\zeta}{\partial x}\mathrm{d}x = \frac{1}{2\pi}\int_{-\infty}^{\infty}\mathrm{i}\alpha\widetilde{P}_{\rm ext}^{*}\widetilde{\zeta}\mathrm{d}\alpha, \tag{11}$$

where $\widetilde{P}_{\rm ext}^{*}(\alpha,t)$ is the conjugate function of $\widetilde{P}_{\rm ext}(\alpha,t)$. It follows from Eq. (5) that the steady-state wave resistance reads

$$R^{\rm S}(U) = -\frac{P_0^2}{2\pi\rho}\int_{-\infty}^{\infty}\frac{\mathrm{i}\alpha}{\Delta}\mathrm{d}\alpha. \tag{12}$$

By the residue theorem developed by Lighthill [10] for the dispersive waves, the far-field wave resistance for $V > c_{\rm min}$ can be analytically given by

$$R^{\rm S}(U) = \frac{2P_0^2}{\rho}\sum_{j=1}^{2}\frac{k_j}{\Delta_j'}\mathrm{H}(U - c_{\rm min}). \tag{13}$$

4. SUDDENLY STARTING LOADS

We assume that the concentrated load suddenly starts from rest at $t = 0$ and then moves with a constant velocity $-U\boldsymbol{e}_x$, then we have $P_{\rm ext} = P_0\delta(x - x_0)\mathrm{H}(t)$. The initial conditions for Eq. (2) read

$$\widetilde{\zeta}|_{t=0} = 0, \quad \frac{\partial\widetilde{\zeta}}{\partial t}|_{t=0} = 0. \tag{14}$$

The solution for Eq. (2) with $P_{\rm ext} = P_0\delta(x - x_0)\mathrm{H}(t)$ and (14) can readily be given by

$$\widetilde{\zeta}(\alpha, t) = \widetilde{\zeta}^{\rm S}(\alpha, t) + \widetilde{\zeta}^{\rm T}(\alpha, t), \tag{15}$$

where

$$\widetilde{\zeta}^{\rm T}(\alpha, t) = \frac{P_0}{\rho\Delta}\Big[\cos(\omega t) + \frac{\mathrm{i}\alpha U}{\omega}\sin(\omega t)\Big], \tag{16}$$

and $\widetilde{\zeta}^{\rm S}(\alpha, t)$ is given by Eq. (5). One can see that $\widetilde{\zeta}^{\rm S}(\alpha, t)$ and $\widetilde{\zeta}^{\rm T}(\alpha, t)$ are the steady-state and transient responses due to a suddenly starting load, respectively.

The analysis on $\hat{\zeta}^{\rm S}(\alpha, t)$ follows Section 3. Equation (16) can be rewritten as

$$\widetilde{\zeta}^{\rm T}(\alpha, t) = A\exp(\mathrm{i}\alpha U t)\sum_{\pm}\frac{\exp(\mp\mathrm{i}\Omega_{\pm}t)}{\Omega_{\pm}}, \tag{17}$$

where $A(k) = P_0/2\rho(1 + \sigma k)c$ and $\Omega_{\pm}(\alpha) = \omega \pm \alpha U$. The transient plate deflection, denoted by $\zeta^{\rm T}$, due to a suddenly starting load is given by

$$\zeta^{\rm T} = \frac{1}{2\pi}\sum_{\pm}\int_{-\infty}^{\infty} A\exp(\mathrm{i}\alpha X)\frac{\exp(\mp\mathrm{i}\Omega_{\pm}t)}{\Omega_{\pm}}\mathrm{d}\alpha. \tag{18}$$

Equation (18) with large t will be performed by means of the method of stationary phase. Ω_- with $\alpha > 0$ and Ω_+ with $\alpha < 0$ have the same stationary points, which make the main contribution to the integral for $\zeta^{\rm T}$. Equation (18) can be rewritten as

$$\zeta^{\rm T} = \sum_{n=1}^{2}\int_0^{\infty}\frac{A}{\Omega}\exp\left[(-1)^{n+1}\mathrm{i}(kX + \Omega t)\right]\mathrm{d}k, \tag{19}$$

where $\Omega(k) = \omega - kU$. The stationary point of $\Omega(k)$ is determined by

$$\frac{\mathrm{d}\Omega}{\mathrm{d}k} = c_{\rm g} - U = 0. \tag{20}$$

There exists a minimal group velocity $c_{\rm gmin}$. The nature of the real roots of Eq. (20) depends crucially on the relation between U and $c_{\rm gmin}$. Equation (20) has no roots for $U < c_{\rm gmin}$, one real root (denoted by $\kappa_{\rm gm}$) for $U = c_{\rm gmin}$, and two real roots (denoted by κ_1 and κ_2) for $U > c_{\rm g}$. Obviously, $\kappa_1 < \kappa_{\rm gm} < \kappa_2$.

5. SUDDENLY STOPPING LOADS

We consider a concentrated load steadily moving with a constant velocity $-U\boldsymbol{e}_x$ and a constant magnitude of strength P_0 for $t < 0$. The load suddenly stops at $t = 0$ and keeps at rest for $t > 0$. The governing equation is Eq. (2) with $\hat{P}_{\rm ext} = 0$. The initial values at $t = 0$ for the plate defection and the velocity are taken as those for the steady-state solution. The initial conditions are given by

$$\Big\{\widetilde{\zeta}|_{t=0}, \frac{\partial\widetilde{\zeta}}{\partial t}|_{t=0}\Big\} = -\frac{P_0}{\rho\Delta}\Big\{1, \mathrm{i}\alpha U\Big\}. \tag{21}$$

The corresponding solution reads $\widetilde{\zeta} = -\widetilde{\zeta}^{\rm T}(\alpha, t)$, where $\widetilde{\zeta}^{\rm T}(\alpha, t)$ is given in Eq. (16). It should be noted that $\widetilde{\zeta} = -\widetilde{\zeta}^{\rm T}(\alpha, t)$ is similar to the transient part due to a suddenly starting load.

6. DISCUSSION

6.1. Flexural–gravity waves

In this Subsection, we consider the flexural–gravity waves on an elastic surface with $\Gamma > 0$ and $\Lambda \neq 0$. The general case with $\sigma \neq 0$ is discussed at first. Then the special case with $\sigma = 0$ is of interest since the inertial effect of the thin plate can be neglected in comparison with the effects of the elastic force and lateral stress of the plate and with the fluid inertia. This assumption is justified since the wavelength of the plate deflection is usually much large than the plate thickness [3].

From the dispersion relation of the flexural–gravity waves on an elastic surface, some remarkable characteristics can be found due to the presence of lateral stress ($\Lambda \neq 0$). As $Q = Q_{\rm max} = 2\sqrt{D\rho g}$ (namely $\Lambda = 2\sqrt{\Gamma}$), we have $c_{\rm min} = 0$ at $k = k_{\rm p0} = (\rho g/D)^{1/4}$. Therefore $Q < Q_{\rm max}$ is a necessary condition for the wave propagation. Close examination on $c_{\rm g}$ shows that there exists a critical value of Q (denoted by $Q_{\rm g0}$) at which $c_{\rm gmin} = 0$, and $c_{\rm g} > 0$ holds if and only if $Q < Q_{\rm g0}$. As $Q_{\rm g0} < Q < Q_{\rm c0}$, we have $c_{\rm g} < 0$ and $c > 0$. As $\sigma \neq 0$, the values of $Q_{\rm g0}$ and the wave number $k_{\rm g0}$ at which $c_{\rm g} = 0$ holds satisfy quintic equations which can be solved numerically. As $\sigma = 0$, we have the analytical expressions $Q_{\rm g0} = 2\sqrt{5D\rho g}/3$ (namely $\Lambda = 2\sqrt{5\Gamma}/3$) and $k_{\rm g0} = (\rho g/25D)^{1/4}$.

As $\sigma \neq 0$, the solutions for $k_{\rm cr}$ and $\kappa_{\rm gm}$, which satisfy respectively $\mathrm{d}c/\mathrm{d}k = 0$ and $\mathrm{d}c_{\rm g}/\mathrm{d}k = 0$, can be obtained numerically. As $\sigma = 0$, exactly analytical solutions for $k_{\rm cr}$ and $\kappa_{\rm gm}$ can be given as

$$k_{\rm cr} = \left(\frac{\sqrt{F} + \sqrt{12 + F}}{6\sqrt{\Gamma}}\right)^{1/2}, \tag{22}$$

$$\kappa_{\rm gm} = \left(\frac{\sqrt{E_1} - \sqrt{D_1} + 11\sqrt{F}}{30\sqrt{\Gamma}}\right)^{1/2}, \tag{23}$$

where $F = \Lambda^2/\Gamma$, $E_1 = 363F - D_1 - 90(10+F) + 8(900-209F)\sqrt{F/D_1}$, $D_1 = 15C_1 + 121F - 30(10+F) + 15(80-24F+F^2)/C_1$, $C_1 = (8\sqrt{B_1} + 1600 - 272F - 36F^2 + F^3)^{1/3}$, and $B_1 = (4-F)^2(2000 + 600F - 19F^2)$. Accordingly, the analytical expressions for the minimal phase and group speeds are given by $c_{\min} = c(k_{\rm cr})$ and $c_{\rm gmin} = c_{\rm g}(\kappa_{\rm gm})$, respectively.

As $\sigma \neq 0$, we have, for the steady-state flexural–gravity wave elevation and wave resistance,

$$\Delta_j' = g(4\Gamma k_j^3 - 2L_2 k_j - L), \tag{24}$$

where $L_2 = \Lambda + \sigma L$ and $L = U^2/g$. The exact solutions for the wave numbers k_1 and k_2 of the steady-state response can be given by

$$k_j = \frac{\sqrt{K_2}}{2} + \frac{(-1)^j}{2}\sqrt{-K_2 + \frac{2L}{\sqrt{K_2}\Gamma} + \frac{2L_2}{\Gamma}}, \tag{25}$$

where $K_2 = [l_2/2^{1/3} + 2^{1/3}(12\Gamma + L_2^2)/l_2 + 2L_2]/3\Gamma$, $l_2 = [L_6 + \sqrt{L_6^2 - 4(12\Gamma + L_2^2)^3}]^{1/3}$, $L_6 = 27L^2\Gamma + 72L_2\Gamma - 2L_2^3$. As $\sigma = 0$, the solutions for Δ_j' and k_j can readily be obtained from Eqs. (24) and (25) by setting $\sigma = 0$.

As $\sigma \neq 0$ or $\sigma = 0$, the solutions for the wave numbers κ_1 and κ_2 of the transient flexural–gravity waves can be calculated numerically.

6.2. Capillary–gravity waves

Another special case with $\Gamma = 0$ and $\Lambda = -\tau < 0$ corresponds to the capillary–gravity waves on an inertial ($\sigma \neq 0$) or a free ($\sigma = 0$) surface. There is a maximal phase and group speeds for the capillary–gravity waves on an inertial surface, namely

$$\lim_{k\to+\infty} c = \lim_{k\to+\infty} c_{\rm g} = \sqrt{g\tau/\sigma}. \tag{26}$$

The analytical solutions for $k_{\rm cr}$ and $\kappa_{\rm gm}$ are given as

$$k_{\rm cr} = \frac{1}{\sqrt{\tau}}[\sqrt{C} + \sqrt{C+1}], \tag{27}$$

$$\kappa_{\rm gm} = \frac{\sqrt{D_2}}{2} + \frac{1}{2}\sqrt{2D_2 - 3C_2 + \frac{E_2}{4\sqrt{D_2}}} - \frac{\sigma}{B_2}, \tag{28}$$

where $E_2 = 32\sigma(1/B_2\tau - 2\sigma^2/B_2 + 3)/B_2^2$, $D_2 = 4(\sigma^2/B_2 - 1)/B_2 + C_2$, $C_2 = 4(C+1)^{2/3}/B_2$, $B_2 = \tau(4C+3)$, and $C = \sigma^2/\tau$.

For the the steady-state capillary–gravity wave elevation and wave resistance, we have

$$\Delta_j' = g[2(\tau - \sigma L)k_j - L], \tag{29}$$

where $k_j = [L + (-1)^j\sqrt{L^2 - 4\tau + 4\sigma L}]/2(\tau - \sigma L)$.

As $\sigma \neq 0$, the solutions for the wave numbers κ_1 and κ_2 of the transient capillary–gravity waves can be calculated numerically. For $\sigma = 0$, the exact solution for κ_j is

$$\kappa_j = \frac{\sqrt{C_3}}{2} + \frac{L}{9\tau} + \frac{(-1)^j}{2}\sqrt{\frac{D_3}{4\sqrt{C_3}} + \frac{4L^2}{27\tau^2} - \frac{4}{3\tau} - C_3},$$

where $D_3 = 4(L^2 - 9\tau)/27\tau^2$, $C_3 = 4(3^{4/3}B_3^2 + L^2B_3 - 9B_3\tau - 3^{5/3}L^2\tau + 3^{8/3}\tau^2)/81B_3\tau^2$, and $B_3 = \{9L^2\tau^2 + L\tau[3\tau(L^4 + 18L^2\tau - 27\tau^2)]^{1/2} - 9\tau^3\}^{1/3}$.

7. CONCLUSIONS

Analytical solutions are explicitly derived for the wave response and the wave resistance due to steadily moving, suddenly starting and suddenly stopping concentrated loads on the surface of the floating plate, taking the effects of lateral stress into consideration. It is found that there is a critical value for the compression effect, at which the phase speed of flexural–gravity waves is zero.

[1] Kashiwagi, M. 2000 Research on hydroelastic responses of vlfs: Recent progress and future work. *Int. J. of Offshore Polar Eng.* **10**(2), 81–90.

[2] Porter, R. & Evans, D. V. 2006 Scattering of flexural waves by multiple narrow cracks in ice sheets floating on water. *Wave Motion* **43**(5), 425–443.

[3] Davys, J. W., Hosking, R. J. & Sneyd, A. D. 1985 Waves due to a steadily moving source on a floating ice plate. *J. Fluid Mech.* **158**, 269–287.

[4] Schulkes, R. M. S. M. & Sneyd, A. D. 1988 Time-dependent response of floating ice to a steadily moving load. *J. Fluid Mech.* **186**, 25–46.

[5] Squire, V. A., Robinson, W. H., Langhorne, P. J. & Haskell, T. G. 1988 Vehicles and aircraft on floating ice. *Nature* **333**(6169), 159–161.

[6] Squire, V. A., Hosking, R. J., Kerr, A. D. & Langhorne, P. S. 1996 *Moving Loads on Ice Plates*. Dordrecht: Kluwer Academic Publishers.

[7] Lu, D. Q. & Zhang, H. 2013 Flexural–gravity wave resistances due to a surface-moving line source on a fluid covered by a thin elastic plate. *Theor. Appl. Mech. Lett.* **3**(2), 022002.

[8] Sturova, I. V. 2013 Unsteady three-dimensional sources in deep water with an elastic cover and their applications. *J. Fluid Mech.* **730**, 392–418.

[9] Lu, D. Q. & Chwang, A. T. 2005 Interfacial waves due to a singularity in a system of two semi-infinite fluids. *Phys. Fluids* **17**(10), 102107.

[10] Lighthill, J. 1978 *Waves in Fluids*. Cambridge: Cambridge University Press.

[11] Kim, J. W. & Webster, W. C. 1998 The drag on an airplane taking off from a floating runway. *J Mar.Sci. Tech.* **3**, 76–81.

Abstract for the 30th Intl Workshop on Water Waves and Floating Bodies, Bristol (UK), April 12 - April 15, 2015

On Stokes' Coefficients and the Wave Resistance of a Towed Body

by Dmitri V. Maklakov[1] and Alexander G. Petrov[2]
[1]Kazan (Volga region) Federal University, Kazan, Russia
[2]Moscow Institute of Physics and Technology (State University),
Institute for Problems in Mechanics of RAS, Moscow, Russia
dmaklak@kpfu.ru, petrovipmech@gmail.com

Highlights:

In this work we have deduced an infinite system of quadratic equations with respect to the Stokes coefficients which define the periodic progressive waves in water of finite depth. The system has a compact form and has been derived by means of a new variational equation for steady periodic flows above a level bottom. By solving the system we have constructed an analytical ten-termed expansion in the amplitude for the wave resistance of a two-dimensional body that creates the waves. The coefficients of the expansion depend only on the mean depth of the waves. The obtained expansion has been compared with Kelvin's one-termed formula and with an accurate numerical solution.

1 Introduction

In the scientific literature there is a considerable number of works devoted to finding the Stokes coefficient which define the periodic progressive waves in water of finite depth. The first computer algorithm has been developed by Schwartz (1974). As in the initial work by Stokes (1880), Schwartz has used the boundary condition of constant pressure at the free surface and obtained a cubic system of equations with respect to the Stokes coefficients. Longuet-Higgins (1978) has demonstrated that after some transformations the cubic system can be reduced to a quadratic one. In this work we have derives a simple variational equation for steady periodic flows above a level bottom which is especially convenient for studying steady periodic gravity waves in water of finite depth. The equation leads to a very compact system of quadratic equations with respect to the Stokes coefficients. We have developed an effective algorithm of computing the coefficients in the form of a series in powers of the wave amplitude. The exact formula for the wave resistance R_w derived in Maklakov & Petrov (2014) allows us to deduce new analytical formulae for R_w.

2 Variational equations for steady periodic flows and gravity waves

Consider a steady flow of an ideal fluid bounded by a λ-periodic line l_z from above and by a horizontal bottom $y = 0$ from below. Under the λ-periodicity we understand the property $z = x + iy \in l_z \Rightarrow z + \lambda \in l_z$. The complex potential of the flow $w = \phi + i\psi$ satisfies the following boundary conditions

$$\begin{array}{lll} \mathrm{Im}\, w = \psi = Q & \text{for} & z \in l_z, \\ \mathrm{Im}\, w = \psi = 0 & \text{for} & y = 0, \end{array} \tag{1}$$

where Q is the volume flux. In the flow domain the complex conjugate velocity dw/dz is a λ-periodic function, but the complex potential $w(z)$ increases by an increment C (by a circulation) on every period:

$$w(z + \lambda) - w(z) = C.$$

For a fixed upper boundary l_z the flow is defined uniquely by specifying either the volume flux Q, in this case the increment of the potential C should be found in solving, or by specifying C to determine Q.

In the flow domain consider one period, shown in Fig. 1(a). Let s be the arc abscissa of the line l_z, reckoned from a certain point L.

Proposition. *Consider a steady λ-periodic flow bounded from above by the line l_z with the velocity distribution $v(s)$ on l_z. Assume that the flow flux is Q and the circulation is C. Let the boundary l_z be varied by shifting each of its points on the distance $\delta n(s)$ in the direction of the normal in so manner that the new line l_z^* be also λ-periodic. Let for the new λ-periodic flow, bounded from above by the line l_z^*, the flux and circulation be $Q + \delta Q$ and $C + \delta C$, respectively (fig. 1a). Then the following variational equation holds*

$$\int_{LS} v^2(s)\delta n(s) ds = C\delta Q - Q\delta C, \tag{2}$$

where the curve LS is any period of the line l_z.

The prove of the proposition is based on the Cauchy theorem for analytic functions.

Consider a system of periodic gravity waves in the wave-fixed reference frame in which the flow is steady. Then the parameter of periodicity λ is the wavelength. Let the density of the fluid be ρ. As in Longuet-Higgins (1975) we non-dimensionalize all wave parameters by choosing $\lambda/(2\pi)$, $\sqrt{g\lambda/(2\pi)}$ and ρ as the scales for length, velocity and density, respectively. In what follows all physical quantities will be dimensionless with accordance to the chosen scales. Now the dimensionless wavelength is 2π, in the boundary conditions (1) and in the variational equation (2) the parameters Q and C are scaled by $\sqrt{g\lambda^3/(2\pi)^3}$.

For the periodic wave problem we should add to the boundary conditions (1) the Bernoulli equation on the unknown free surface l_z: $\frac{v^2}{2}+y=R$, where R is the dimensionless Bernoulli constant (total head).

It is easy to demonstrate that for any λ–periodic line and any differentiable function $P(y)$ the following variational equation holds

$$\delta\int_{LS}P(y)dx=\int_{LS}P'(y)\delta n(s)ds, \tag{3}$$

where LS is one period of the line.

Consider now one wave period located between neighboring wave crests (Fig. 1 a). On the free surface the boundary condition $v^2=2R-2y$ is satisfied. Let us vary the free-surface by a function $\delta n(s)$. Then by virtue of (3)

$$\begin{aligned}\int_{LS}v^2(s)\delta n(s)ds&=\int_{LS}(2R-2y)\delta n(s)ds\\&=\delta\int_{LS}(2Ry-y^2)dx=2\pi\delta M[\eta],\end{aligned} \tag{4}$$

where the functional

$$M[\eta]=2R\,d-D^2$$

depends only on the shape of the free surface with the equation $y=\eta(x)$, d and D are the mean and root-mean-square depths, respectively:

$$d=\frac{1}{2\pi}\int_x^{x+2\pi}\eta(x)dx,\quad D^2=\frac{1}{2\pi}\int_x^{x+2\pi}\eta^2(x)dx.$$

It follows from (2) that

$$2\pi\,\delta M[\eta]=C\delta Q-Q\delta C=C^2\delta\left(\frac{Q}{C}\right). \tag{5}$$

For the wave period the domain of the complex potential $w=\varphi+i\psi$ is a rectangle, shown in Fig. 1 b. We map conformally this rectangle onto an annulus (see Fig. 1 c) with an outer radius of unity and inner radius of

$$r_0=\exp\left(-\frac{2\pi Q}{C}\right). \tag{6}$$

A usual assumption (see e.g. Longuet-Higgins, 1975; Cokelet, 1977) in the theory of nonlinear periodic waves is that in the bottom-fixed reference frame the waves propagate with the velocity c_a, equal to the average fluid velocity at any horizontal level completely within the fluid in the wave-fixed reference frame (in steady flow). That is $c_a=\frac{C}{2\pi}$. Now the equation (5) can be rewritten as

$$\delta M[\eta]=-c_a^2\frac{\delta r_0}{r_0}, \tag{7}$$

which is just the variational equation for steady periodic waves.

3 System of quadratic equations for the Stokes coefficients

We shall seek the conformal mapping of the annulus (Fig. 1 c) in the parametric ζ-plain onto the flow domain of the one wave period in the form

$$z(\zeta)=2\pi+i\log\zeta+iy_0+i\sum_{n=1}^{\infty}y_n\left(\zeta^n-\frac{r_0^{2n}}{\zeta^n}\right). \tag{8}$$

The representation (8), being a variant of the Stokes method (see Stokes, 1880), is often used in the nonlinear wave theory (see e.g. Schwartz, 1974). By virtue of symmetry the Stokes coefficients y_n ($n=0,1,2\dots$) are real. Because on the bottom $\operatorname{Im} z=0$, we find from (8) that $y_0=-\log r_0$. The parametric equations of the free surface are

$$\begin{aligned}x_s(\gamma)&=2\pi-\gamma-\sum_{n=1}^{\infty}\alpha_n\sin n\gamma,\\y_s(\gamma)&=-\log r_0+\sum_{n=1}^{\infty}\beta_n\cos n\gamma,\end{aligned} \tag{9}$$

where $\alpha_n=1+r_0^{2n}$, $\beta_n=1-r_0^{2n}$, γ is a polar angle in the ζ-plane. After some algebra it is possible to demonstrate that

$$M=(R+\log r_0)\,\Lambda-\frac{1}{2}\,(\Lambda_1+\Lambda_2)-\log^2 r_0-2R\,\log r_0,$$

where

$$\begin{aligned}\Lambda=\sum_{n=1}^{\infty}n\beta_{2n}y_n^2,\quad \Lambda_1=\sum_{n=1}^{\infty}\beta_n^2y_n^2,\\ \Lambda_2=\sum_{k=2}^{\infty}y_k\sum_{n=1}^{k-1}\gamma_{k-n,n}\,y_n\,y_{k-n},\end{aligned} \tag{10}$$

$$\gamma_{m,n}=m\beta_n\beta_{2m+n}+n\beta_m\beta_{m+2n}.$$

Now in the variational equation (7) the left-hand side is a function of the Stokes coefficients y_n ($n=1,2,3,\dots$) and the parameter r_0. Differentiating M with respect to y_n at fixed r_0, we come to the following infinite system of quadratic equations:

$$\begin{aligned}(n\beta_{2n}K-\beta_n^2)\,y_n&=\frac{1}{2}\sum_{n=1}^{n-1}\gamma_{n-m,m}\,y_{n-m}\,y_m\\&+\sum_{m=1}^{\infty}\gamma_{m,n}\,y_{m+n}y_m,\quad n=1,2,3,\dots,\end{aligned} \tag{11}$$

where

$$K=2(R+\log r_0). \tag{12}$$

After finding y_n at a fixed r_0 we are able to calculate

$$c_a^2=-r_0\frac{\partial M}{\partial r_0}=K-\Lambda+\frac{r}{2}\left(\frac{\partial\Lambda_1}{\partial r_0}+\frac{\partial\Lambda_2}{\partial r_0}-K\frac{\partial\Lambda}{\partial r_0}\right). \tag{13}$$

We shall seek the coefficients y_n and the parameter K in the form of expansions in powers of the wave amplitude $a = (h_c - h_t)/2$, where h_c and h_t are the heights of the wave crests and troughs, respectively. The coefficients of these expansions are functions of the parameter $\varepsilon = \exp(-2d)$. Let the highest power of a in these expansions be N, where N is an odd number. Then

$$K = \sum_{k=0}^{(N-1)/2} \varkappa_{2n} a^{2n} + \mathrm{O}(a^{N+1}), \tag{14}$$

$$y_i = \sum_{n=0}^{[(N-i)/2]} a_{i,2n} a^{i+2n} + \mathrm{o}(a^N), \quad i = 1, 2, \ldots, N, \tag{15}$$

and because the parameters a and ε are given we should add to the system (11) two more equations

$$a = \sum_{n=1}^{(N+1)/2} \beta_{2n-1} y_{2n-1}, \quad r_0^2 = \varepsilon \exp\left(\sum_{n=1}^{N} n \beta_{2n} y_n^2 \right).$$

The first equation follows from the second equation in (9), the latter one follows from the identity

$$d = \Lambda/2 - \log r_0. \tag{16}$$

We have developed an effective algorithm of finding the coefficients $\varkappa_{2n}$, $a_{i,2n}$. The algorithm can be easily programmed (for example, by the MATHEMATICA package) and allows one to use exact arithmetics and symbolic computations. After determination the coefficients by making use of (13) one can calculate

$$c_a^2 = \sum_{n=0}^{(N-1)/2} c_{2n} a^{2n} + \mathrm{O}(a^{N+1}), \tag{17}$$

where c_{2n} are functions of the parameter ε.

4 Analytical formulae for the wave resistance

Consider a two-dimensional body that moves horizontally from right to left at constant speed c in a channel of finite depth h. Assume that in the body frame of reference the flow is steady. Then the wave train generated by the body also moves from right to left with the same velocity c. In the body frame of reference we have far upstream a uniform stream with velocity c and far downstream the train of steady periodic waves (Fig. 2).

Due to the generation of waves the body experiences a resistance, which we denote by R_w. Maklakov & Petrov (2014) have deduced an exact analytical formula for R_w:

$$R = 3V + \frac{1}{2}(\Delta d)^2 + (c^2 - d)\Delta d, \tag{18}$$

where V is the mean potential energy of the wave:

$$V = \frac{1}{4\pi} \int_x^{x+2\pi} [\eta(x) - d]^2 dx = \frac{1}{4} \left(-\frac{\Lambda^2}{2} + \Lambda_1 + \Lambda_2 \right), \tag{19}$$

and $\Delta d = h - d$ is the defect of levels (the difference between the undisturbed level far upstream and the mean level far downstream).

Let us assume that the mean depth d and amplitude a of the waves are known. By means of equations (10), (15), (19) it is easy to derive an expansion for the mean potential energy V. Now to determine R_w by equation (18) one needs to find the defect of levels Δd and the speed of the body c. Because the flux Q and the Bernoulli constant R far upstream and far downstream of the body are equal we can write

$$c(d + \Delta d) = Q, \quad c^2 + 2\Delta d = 2(R - d).$$

From equations (6), (12), (16) we deduce that $Q = c_a(d - \Lambda/2)$, $2(R - d) = K - \Lambda$. This allows us to derive a cubic equation with respect to Δd:

$$(K - \Lambda - 2\Delta d)(\Delta d + d)^2 = c_a^2 \left(d - \Lambda/2\right)^2.$$

In this equation the parameters Λ, c_a^2 and K are expressed by ε and a by formulae (10), (14), (15) and (17). The solution is represented as an expansion in even powers of a up to the terms of order a^{N-1}. After finding Δd we determine $c^2 = K - \Lambda - 2\Delta d$. Inserting the found Δd and c^2 in (18), we get the wave resistance in the form

$$R_w = R_2 a^2 + R_4 a^4 + R_6 a^6 + \cdots + R_{N-1} a^{N-1} + \mathrm{O}(a^{N+1}), \tag{20}$$

where the coefficients R_{2k} depends on $\varepsilon = \exp(-2d)$. The first coefficient $R_2 = \frac{1}{4}\left(1 - \frac{2d}{\sinh 2d}\right)$ coincides with that at a^2 obtained by Kelvin (1887).

The computations of the wave resistance by the Stokes method have been carried out at $N = 21$, i. e with the asymptotic accuracy up to the terms of a^{20}, and all ten coefficients R_{2k} have been found analytically. But an analytical representation of the coefficient R_6 is already very cumbersome. For the coefficient R_4 we have

$$R_4 = R_{40} + R_{41} d + R_{42} d^2,$$

$$R_{40} = \frac{11\cosh 2d + \cosh 4d + 2\cosh 6d - 5}{128 \sinh^5 d \, (d\cosh d - \sinh d)},$$

$$R_{41} = \frac{10\cosh 2d - 118\cosh 4d - 14\cosh 6d - 3\cosh 8d - 19}{1024 \sinh^6 d \cosh d \, (d\cosh d - \sinh d)},$$

$$R_{42} = \frac{-7\cosh 2d + 10\cosh 4d + \cosh 6d + 5}{128 \sinh^7 d \, (d\cosh d - \sinh d)}.$$

Comparison of the wave resistance obtained by analytical formulae and by the accurate numerical method of the paper by Maklakov (2002) is presented on the graphs of Fig. 3.

The work was supported by the Russian Science Foundation, project No 14-19-01633.

References

COKELET, E. D. 1977 Steep gravity waves in water of arbitrary uniform depth. *Proc. R. Soc. Lond.* A **286**, 183–230.

KELVIN, LORD 1887 On ship waves. *Proceedings of the Institution of Mechanical Engineers* **38**, 409–434.

LONGUET-HIGGINS, M. S. 1975 Integral properties of periodic gravity waves of finite amplitude. *Proc. R. Soc. Lond.* A **342**, 157–174.

LONGUET-HIGGINS, M. S. 1978 Some new relations between Stokes's coefficients in the theory of gravity waves. *J. Inst. Maths Applics* **22**, 261–273.

MAKLAKOV, D. V. 2002 Almost highest gravity waves on water of finite depth. *Euro. J. Appl. Maths* **13**, 67–93.

MAKLAKOV, D. V. & PETROV, A.G. 2014 Determination of the wave resistance of a towed body by the parameters of generated waves. In *Abstract for the 29th Intl Workshop on Water Waves and Floating Bodies, Osaka (Japan), March 30 - April 02, 2014*. (http://www.iwwwfb.org/Workshops/29.htm).

SCHWARTZ, LEONARD W. 1974 Computer extension and analytic continuation of Stokes expansion for gravity waves. *J. Fluid Mech.* **62**, 553–578.

STOKES, G. G. 1880 Supplement to a paper on the theory of oscillatory waves. In *Mathematical and Physical Papers, Volume I*, pp. 314–326. Cambridge University Press.

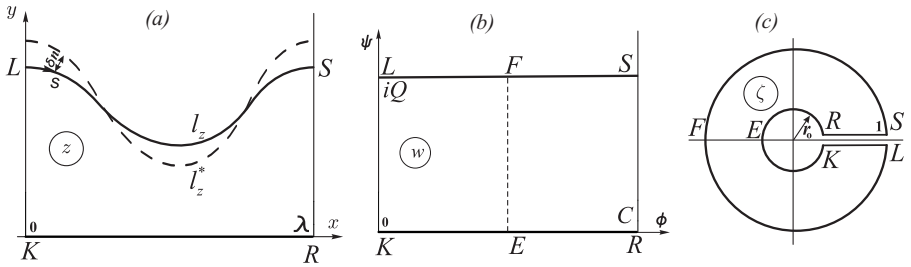

Figure 1: (a) One period. (b) Domain of the complex potential $w = \varphi + i\psi$. (c) Parametric ζ-plane.

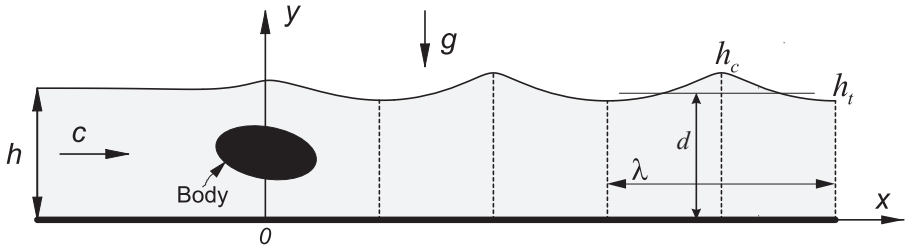

Figure 2: Scheme of the steady flow

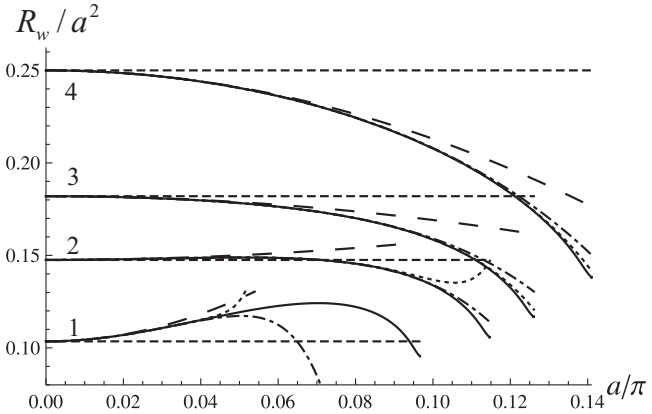

Figure 3: Comparison of accurate numerical results with analytical formulae at the depths $\frac{d}{2\pi} = 0.15$ (1), 0.2 (2), 0.25 (3) ∞ (4): solid lines, the waves have been computed by the method of the paper by Maklakov (2002); dashed lines, $n = 1$ (Kelvin's one-termed formula), dashed lines with long dashes, $n = 2$; dot-and-dash lines, $n = 5$; dotted lines, $n = 10$, where n is the number of terms in (20).

Abstract for the 30th Intl Workshop on Water Waves and Floating Bodies, Bristol (UK), 12-15th April 2015

A note on convergence of expansion formulae for wave-structure interaction problems

S. Mandal[1], T. Sahoo[1] and A. Chakrabarti[2]

[1]Department of Ocean Engineering and Naval Architecture, Indian Institute of Technology, Kharagpur -721302, India
[2]Department of Mathematics, Indian Institute of Science, Bangaluru -560012, India
E-mail: *souravmath88@naval.iitkgp.ernet.in*

Highlights

- Convergence of the expansion formulae for problems of gravity wave-interaction with floating flexible structure are demonstrated using Green's function approach in both the cases of finite and infinite water depth.
- In the present approach, the Green's function for the differential operator associated with the wave-structure interaction problems is integrated over the complex plane to derive the spectral representation. This approach is independent of whether the spectrum for the differential operator is discrete or continuous.

1. Introduction

In recent decades, emphasis is given to the dynamic analysis of large class of problems in the field of hydroelasticity and hydroacoustics involve higher order conditions on a wavy boundary. Apart from the development of expansion formulae and associated mode-coupling relations as in Manam et al. [1], emphasis is given to study the convergence of the various infinite series and integrals (see Evans & Porter [2]). Lawrie [3], [4] proved the point-wise convergence of a class of problems associated with Helmholtz equation satisfying higher order boundary conditions arising in hydroacoustics in two and three dimensions. Later, Mondal et al. [5] demonstrated the convergence of the expansion formulae in case of infinite depth for a class of wave-structure interaction problems associated with Laplace equation satisfying higher order boundary conditions in the broad field of hydroelasticity. In the present study, convergence of the expansion formulae for wave-structure interaction problems arising in hydroelasticity are demonstrated in both the cases of finite and infinite water depth. In the present approach, the Green's functions for the differential operator associated with the wave-structure interaction problems along the water depth is integrated over the complex plane to derive the spectral representation. This approach is independent of water depth.

2. Mathematical formulation

Under the assumption of the linearized theory of water waves, the wave-structure interaction problem is formulated in a two-dimensional channel in both the cases of water of finite and infinite depth. The physical problem is studied in the Cartesian co-ordinate system with x axis being in the horizontal direction and y-axis being positive in the vertically downward direction. Assuming that a flexible plate acting under the action of uniform compression being infinitely extended along the positive direction of x-axis, is floating on the mean free surface. Thus, the fluid domain occupies the region $0 < x < \infty$ and $0 < y < h$ in case of finite water depth ($0 < x < \infty$ and $0 < y < \infty$ in case of infinite water depth). The fluid is assumed to be incompressible, inviscid with the fluid motion being irrotational and simple harmonic in time with angular frequency ω. Thus, there exists a velocity potential $\Phi(x, y, t)$ of the form $\Phi(x, y, t) = Re\{\phi(x, y)e^{-\mathrm{i}\omega t}\}$ with Re being the real part. Hence, in the fluid region, the spatial velocity potential $\phi(x, y)$ satisfies the Laplace equation

$$\nabla^2\phi = 0, \tag{1}$$

along with the linearized plate covered boundary condition on the mean free surface

$$(D\partial_{yyyyy} - Q\partial_{yyy} + \partial_y + K)\phi = 0, \quad \text{on } y = 0, \tag{2}$$

with D, Q, K being known positive constants as in Manam et al.[1], and the bottom boundary condition

$$\left.\begin{aligned} \phi_y = 0 \qquad & \text{on} \quad y = h \text{ in case of finite water depth,} \\ \phi, |\phi_y| \to 0 \quad & \text{on } y \to \infty \text{ in case of infinite water depth.} \end{aligned}\right\} \tag{3}$$

The spatial velocity potentials ϕ satisfying Eq.(1) along with the boundary conditions in Eqs.(2) - (3) are expressed as (see Manam et al. [1])

$$\phi(x, y) = \sum_{n=0,I}^{IV} A_n(x)\psi_n(y) + \sum_{n=1}^{\infty} A_n(x)\psi_n(y), \quad \text{in case of finite water depth} \tag{4}$$

$$\phi(x,y) = \sum_{n=0,I}^{IV} A_n(x)\psi_n(y) + \frac{2}{\pi}\int_0^\infty \frac{A(k,x)M(k,y)}{T^2+K^2}dk, \quad \text{in case of infinite water depth} \tag{5}$$

where $A_n(x)$ and $A(k,x)$ are of the forms $A_n(x) = A_n \mathrm{e}^{\mathrm{i}k_n x}$ and $A(k,x) = A(k)\mathrm{e}^{-kx}$ and are given by

$$A_n(x) = \frac{1}{D_n}\left[\int_0^h \phi(x,y)\psi_n(y)dy - \frac{Q}{K}\phi_y(x,0)\psi_{ny}(0) + \frac{D}{K}\{\phi_y(x,0)\psi_{nyyy}(0) + \psi_{ny}(0)\phi_{yyy}(x,0)\}\right], \tag{6}$$

$$A(k,x) = \frac{1}{D_n}\left[\int_0^\infty \phi(x,y)M(k,y)dy - \frac{Q}{K}\phi_y(x,0)M_y(k,0) + \frac{D}{K}\{\phi_y(x,0)M_{yyy}(k,0) + M_y(k,0)\phi_{yyy}(x,0)\}\right], \tag{7}$$

with $h = \infty$ in case of infinite water depth and $D_n = \mathcal{G}'(k)\psi_y(0)/\{2k_nK\}$, $M(k,y) = T\cos ky - K\sin ky$ with $T = (Dk^5 - Qk^3 + k)$. In Eqs. (4) - (5), the eigenfunctions $\psi_n(y)$s are given by

$$\psi_n(y) = \begin{cases} \dfrac{\cosh k_n(h-y)}{\cosh k_n h}, & 0 < y < h, \quad n = 0, I, II, III, IV, 1, ..., \quad \text{(for finite water depth)}, \\ e^{k_n y}, & 0 < y < \infty, \quad n = 0, I, II, III, IV, \quad \text{(for infinite water depth)}, \end{cases} \tag{8}$$

with k_ns satisfying the dispersion relation

$$\mathcal{G}(k) = 0, \tag{9}$$

where $\mathcal{G}(k) = K - (Dk^4 - Qk^2 + 1)k\tanh kh$ for finite water depth and $\mathcal{G}(k) = K - (Dk^4 - Qk^2 + 1)k$ for infinite water depth. We assume that the dispersion relation in Eq. (9) has one real positive roots $k = k_0$, two complex conjugate pairs of the form $k_I, k_{II}(= \bar{k_I})$ and $k_{III}, k_{IV}(= \bar{k_{III}})$ and infinitely many imaginary roots of the form $\pm \mathrm{i}k_n$ for $n = 1, 2, ...$, whilst no imaginary root exists for infinite water depth. Further, the eigenfunctions $\psi_n(y)$s in Eq. (8) satisfy the orthogonal mode-coupling relation (as in Manam et al. [1])

$$\langle \psi_m(y), \psi_n(y)\rangle = \int_0^h \psi_m(y)\psi_n(y)dy - \left\{\frac{Q}{K}\psi_{my}\psi_{ny} + \frac{D}{K}(\psi_{my}\psi_{nyyy} + \psi_{myyy}\psi_{ny})\right\}\Big|_{y=0} = D_n\delta_{mn}, \tag{10}$$

with δ_{mn} being the Kroneckar delta, D_n being the same as in Eqs. (6)-(7) and $h = \infty$ in case of infinite water depth.

2.1. Characteristics of the eigenfunctions in case of finite water depth

In order to understand various characteristics of the eigenfunctions $\psi_n(y)$, consider the boundary value problem

$$\psi_{yy} - k^2\psi = 0, \quad \text{for} \quad 0 < y < h, \tag{11}$$

subject to the boundary conditions as in Eqs. (2) - (3) in terms of ψ. It can be easily observed that $\psi_n(y)$ as in Eq. (8) satisfies the boundary value problem defined in Eqs. (2), (3) and (11). Next, the Green's function $G(y, y_0; k)$ associated with the boundary value problem in $\psi(y)$, where y is the field point and y_0 is the source point, is derived followed by various characteristics of the eigenfunctions which are expressed in terms of certain lemmas.

Lemma 1 *The Green's function $G(y, y_0; k)$, satisfying*

$$G_{yy} - k^2G = \delta(y - y_0), \quad \textit{for} \quad 0 < y, y_0 < h, \tag{12}$$

subject to the conditions in Eqs. (2) - (3) with the continuity and jump conditions in water of finite depth,

$$G\big|_{y=y_{0+}} - G\big|_{y=y_{0-}} = 0 \quad \textit{and} \quad G_y\big|_{y=y_{0+}} - G_y\big|_{y=y_{0-}} = 1 \quad \textit{at} \quad y = y_0 \tag{13}$$

is given by

$$G = \begin{cases} \{\cosh ky(Dk^5 - Qk^3 + k) + K\sinh ky\}\cosh k(h - y_0)/\{k\mathcal{G}(k)\}, & 0 < y < y_0, \\ \{\cosh ky_0(Dk^5 - Qk^3 + k) + K\sinh ky_0\}\cosh k(h - y)/\{k\mathcal{G}(k)\}, & y_0 < y < h. \end{cases} \tag{14}$$

Lemma 2 *The eigenfunctions $\psi_n(y)$ in water of finite depth have the following spectral representation*

$$\delta(y - y_0) = \sum_{n=0,I,II,1}^{\infty} Y_n\psi_n(y)\psi_n(y_0), \quad 0 < y, y_0 < h, \tag{15}$$

where $\delta(y)$ is the Dirac delta function and Y_n is given by $Y_n = -(\sinh 2k_nh)/(2D_n)$.

Proof: Proceeding in a similar manner as in Friedman [6], it can be proved that

$$\lim_{R\to\infty}\frac{1}{\pi \mathrm{i}}\oint G(y,y_0;k)kdk=-\delta(y-y_0), \tag{16}$$

where $G(y,y_0,k)$ is the Green's function as in Eq. (14), R being the radius of a closed semi-circular contour of large radius in the upper half of the complex $k-$plane. Thus, to prove the Lemma, it is necessary to evaluate the contour integral as $R\to\infty$. It may be noted that $k=0$ is neither a pole nor a branch point of $G(y,y_0;k)$. Further, it is found that the poles of the integrand $G(y,y_0;k)$ in Eq. (16) are the simple zeros of the relation as in Eq. (9), with one of these zeros k_0 being on the real axis, $k_n, n=I,II,III,IV$, are four complex roots lie on in four quadrants and the other infinity number of zeros $\pm k_n$, $k_n>0, n=1,2,3,...$, being on the imaginary axis. For the sake of boundedness of the Green's function, k_{III} and k_{IV} have been neglected. The path of integration of the closed contour is deformed onto a semicircular arc (Γ) of large radius $R(\to\infty)$ on upper half plane, the line segments $[-R,k_0-\epsilon]$, a semi circle (γ_ϵ) from $-\epsilon$ to ϵ and the line segment $[k_0+\epsilon,R]$ which contains all the poles in the upper half plane. Now

$$\frac{1}{\pi \mathrm{i}}\oint G(y,y_0;k)kdk=\frac{1}{\pi \mathrm{i}}\oint kdk\Big\{G_1(y,y_0;k)H(y_0-y)+G_2(y,y_0;k)H(y-y_0)\Big\}, \tag{17}$$

where G_1 (for $y<y_0$) and G_2 (for $y>y_0$) are the Green's functions given in Eq. (14) with $H(y)$ being the Heaviside step function. Now using Jordan's lemma and applying Cauchy residue theorem one can find

$$\frac{1}{\pi \mathrm{i}}\oint G_1(y,y_0;k)H(y_0-y)kdk=-\sum_{n=0,I,II,1}^{\infty}Y_n\psi_n(y)\psi_n(y_0)H(y_0-y), \tag{18}$$

with $Y_n=-(\sinh 2k_nh)/(2D_n)$. Proceeding in a similar manner, it can be proved that

$$\frac{1}{\pi \mathrm{i}}\oint G_2(y,y_0;k)H(y-y_0)kdk=-\sum_{n=0,I,II,1}^{\infty}Y_n\psi_n(y)\psi_n(y_0)H(y-y_0),\quad \text{for}\quad y_0<y. \tag{19}$$

Thus, Eqs. (17) - (19) yields

$$\frac{1}{\pi \mathrm{i}}\oint G(y,y_0;k)kdk=-\sum_{n=0,I,II,1}^{\infty}Y_n\psi_n(y)\psi_n(y_0)\Big\{H(y_0-y)+H(y-y_0)\Big\}. \tag{20}$$

Eliminating the integral in Eqs. (16) and (20), the spectral representation given in Eq. (15) is obtained. □
It may be noted that Lawrie [3]) derived similar spectral representations for the eigenfunctions associated with acoustic wave structure interaction problems following a different approach.

2.2. Characteristics of the eigenfunctions in case of infinite water depth

In this subsection, the spectral representation of the eigenfunctions and the associated results of convergence for the velocity potential is discussed in the case of infinite water depth using a similar approach as discussed in case of finite water depth in the previous Section.

Lemma 3 *The Green's function $G(y,y_0;k)$ satisfying*

$$G_{yy}+k^2G=\delta(y-y_0),\quad \textit{for}\quad 0<y,y_0<\infty, \tag{21}$$

subject to the boundary conditions in Eqs. (2) - (3) and the continuity and jump conditions as in Eq. (13) in case of infinite water depth, is given by

$$G=\begin{cases} M(k,y)/\{k\mathcal{G}(\mathrm{i}k)\}e^{-\mathrm{i}ky_0}, & 0<y<y_0,\\ M(k,y_0)/\{k\mathcal{G}(\mathrm{i}k)\}e^{-\mathrm{i}ky}, & y_0<y<\infty,\end{cases} \tag{22}$$

where $M(k,y)$ is same as in Eq. (5).

Lemma 4 *The eigenfunctions $\psi_n(y)$ and $M(k,y)$ defined in Eqs. (8) and (5) have the following spectral representation*

$$\delta(y-y_0)=\sum_{n=0,I}^{II}Z_n\psi_n(y)\psi_n(y_0)+\frac{2}{\pi}\int_0^\infty\frac{M(k,y)M(k,y_0)}{T^2+K^2}dk, \tag{23}$$

with $Z_n=-1/(2D_n)$ and D_n being the same as in Eqs. (6)-(7).

Proof: As discussed in case of finite water depth in Eq. (16), in case of infinite water depth

$$\frac{1}{\pi \mathrm{i}} \oint G(y, y_0; k) k dk = -\delta(y - y_0), \tag{24}$$

where $G(y, y_0, k)$ is the Green's function as in Eq. (22) and the integration to be performed in the complex $k-$ plane as in Eq. (16). In this case, since G has a branch point singularity at $k = 0$, a branch cut is introduced in the complex plane along the positive real axis and the closed contour is chosen as a large circle not crossing the branch cut as in Friedman [6]. Using the fact that the poles of the integrand $G(y, y_0; k)$ are the simple zeros of the relation as in Eq. (9), with one of these zeros k_0 being on the real axis and $k_n, n = I, II$, the two complex roots contributing to the boundedness of the Green's function. Thus, using complex function theory and proceeding in a similar manner as in Lemma 2, it can be easily derived that

$$\begin{aligned} \frac{1}{\pi \mathrm{i}} \oint G(y, y_0; k) k dk = \quad & -Z_n \psi_n(y) \psi_n(y_0) - \frac{1}{\pi \mathrm{i}} \int_0^\infty \Big[\{G_1(k) - G_1(-k)\} H(y_0 - y) \\ & + \{G_2(k) - G_2(-k)\} H(y - y_0) \Big] k dk, \end{aligned} \tag{25}$$

where G_1 (for $y < y_0$) and G_2 (for $y > y_0$) are the Green's functions given in Eq. (22) with $H(y)$ being the Heaviside function as in Lemma 2. Now substituting G_1 and G_2 one can find that

$$\frac{1}{\pi \mathrm{i}} \oint G(y, y_0; k) k dk = -\sum_{n=0,I}^{II} Z_n \psi_n(y) \psi_n(y_0) - \frac{2}{\pi} \int_0^\infty \frac{M(k, y) M(k, y_0) dk}{T^2 + K^2}. \tag{26}$$

Now, eliminating the integral in Eqs. (24) and (26), the spectral representation given in Eq. (23) is obtained. □
It may be noted that the relation in Eq. (23) was derived in Mondal et al. [5] using a different approach.

Theorem 1 *Given the coefficients $A_n(x)$ and $A(k, x)$ in Eqs. (6) and (7) where the velocity potential $\phi(x, y)$ satisfies the Laplace equation as in Eq. (1) along with the boundary conditions in Eqs. (2) - (3), the sums*

$$S(x, y) = \begin{cases} \displaystyle\sum_{n=0,I}^{II} A_n(x) \psi_n(y) + \sum_{n=1}^{\infty} A_n(x) \psi_n(y), & \textit{in case of finite water depth,} \\ \displaystyle\sum_{n=0,I}^{II} A_n(x) \psi_n(y) + \frac{2}{\pi} \int_0^\infty \frac{A(k, x) M(k, y)}{T^2 + K^2} dk, & \textit{in case of infinite water depth} \end{cases} \tag{27}$$

converge to $\phi(x, y)$ in water of finite and infinite depth, as appropriate.

Proof: Using the spectral representation of the eigenfunctions as in Eqs. (15) and (23), the expression for the unknowns $A_n(x)$ and $A(k, x)$ and the orthogonal mode-coupling relation defined in Eq. (10), it can be easily shown that $S(x, y)$ converges to $\phi(x, y)$ in finite and infinite water depth. □

Acknowledgement

SM gratefully acknowledges the financial support received from CSIR, New Delhi to pursue this research work.

References

[1] MANAM, S. R., BHATTACHARJEE, J. & SAHOO, T. (2006) Expansion formulae in wave structure interaction problems. Proc. R. Soc. A, 462, 263–287.

[2] EVANS, D. V. & PORTER, R. (2003) Wave scattering by narrow cracks in ice sheets floating on water of finite depth. J. Fluid Mech, 484, 143–165.

[3] LAWRIE, J. B. (2007) On eigenfunction expansions associated with wave propagation along ducts with wavebearing boundaries. IMA J. Appl. Math., 72, 376–394.

[4] LAWRIE, J. B. (2009) Orthogonality relations for fluid-structural waves in a three-dimensional, rectangular duct with flexible walls. Proc. R. Soc. A, 465, 2347–2367.

[5] MONDAL, R., MOHANTY, S. K. & SAHOO, T. (2011) Expansion formulae for wave structure interaction problems in three dimensions. IMA J. Appl. Math, 78,181–205.

[6] FRIEDMAN, B. (1956) Principles and techniques of applied mathematics. New York: Wiley.

Scattering by rings of vertical cylinders

by P. A. Martin

Department of Applied Mathematics and Statistics, Colorado School of Mines, Golden, CO 80401, USA

pamartin@mines.edu

Highlights:

• Foldy-type methods are developed to study the title problem with equally spaced cylinders around a ring.

• Explicit solutions are obtained by exploiting the circulant structure implied by the special geometry.

1. Introduction

It is 25 years since the publication of "Linton & Evans" [1] on "The interaction of waves with arrays of vertical circular cylinders"; it is their most cited joint work. The paper describes an exact method in which separation of variables and addition theorems are combined, leading to an infinite system of linear algebraic equations. The method itself is much older, and goes back to a paper by Záviška from 1913. It has been used in many contexts, and extended in many directions; for discussion and many references, see [2, Chapter 4]. Apart from using the basic method for water-wave problems, Linton & Evans [1] also showed that the computation of the pressure near, or on, any one cylinder could be simplified considerably.

In this paper, we are interested in the scattering of an incident plane wave by N identical vertical circular cylinders arranged in a particular way: in a horizontal plane (plan view), there are N circles (radius a) with their centres located on, and equally spaced around, a larger circle (radius b). We call this geometrical configuration a *ring* or a *cage*.

Of course, the Linton–Evans method can be, and has been, applied to scattering by a ring of cylinders. See, for example, [3, 4, 5]. However, we are especially interested when N is large, so that we have many small circles around the ring with small gaps between them.

Intuitively, we expect that, in the limit (when there are no gaps), we should approach the solution for scattering by a single large cylinder (with cross-section of radius b). Can this be shown, and, if so, how fast is the limit achieved?

The problem we have described is reminiscent of a problem in electrostatics, a *Faraday cage*. Thus, a metal enclosure protects its inhabitants from external electrical discharges, as first demonstrated by Michael Faraday in 1836. If the metal has small holes or gaps, protection is no longer perfect.

In a recent paper [6], we gave an analysis of such problems, for both electrostatics (Laplace's equation) and acoustics (Helmholtz equation); the latter is of most relevance here. The cylinders comprising the wires in the cage were assumed to be small, both geometrically ($a \ll b$) and acoustically ($ka \ll 1$, where $2\pi/k$ is the incident wavelength). For the scattering itself, we used a much simplified version of Linton–Evans, one in which the scattering by each circular cylinder is represented by a single term (proportional to $H_0(kr)$, see below) instead of the usual infinite separation-of-variables series. This leads to *Foldy's method* [7], [2, §8.3], which takes account of all the multiple scattering effects. The result is an $N \times N$ linear algebraic system. This reduction works for N scatterers at more-or-less arbitrary locations. However, for a ring of equally-spaced identical scatterers, the matrix occurring has a special structure: it is a *circulant* matrix. This means that it can be inverted explicitly, using a discrete Fourier transform, and then the behaviour of the solution as N grows can be analysed. It turns out that the expected limit is achieved but the limit is approached slowly, as $N^{-1} \log N$.

So far, we have not mentioned the boundary condition on each cylinder. The exact Linton–Evans approach can accommodate any choice, such as a Dirichlet condition (pressure or potential specified, "sound-soft" in acoustics) or a Neumann condition (normal velocity specified, "sound-hard" in acoustics). In the context of water waves, the usual case is the Neumann condition, as imposed in [1].

For the simplified Foldy-type analysis described above, the underlying assumption is that each cylinder scatters *isotropically*: note the presence of $H_0(kr)$ with no dependence on the polar angle. This is entirely appropriate for Dirichlet problems because we know that small ($ka \ll 1$) sound-soft circles really do scatter like a monopole. On the other hand, sound-hard circles do not scatter isotropically: both monopole and dipole contributions are equally important and must be retained. The dipole gives a directional dependence to the waves scattered by one circle, and this must be incorporated into the calculation of the multiply scattered waves when there are N circles.

2. Basic formulation

A plane wave is incident upon N vertical cylinders in water of depth H. As usual, we factor out the depth dependence and write the velocity potential for the scat-

tered waves as

$$\mathrm{Re}\{u(x,y)\,\cosh k(H-z)\,\mathrm{e}^{-\mathrm{i}\omega t}\}$$

where $z=0$ is the free surface, $z=H$ is the flat bottom and k is the positive real solution of $\omega^2 = gk\tanh kH$. Denote the cross-section of the jth cylinder in the xy-plane by $\mathcal{C}_j$; it is centred at $\boldsymbol{r}_j$. Then u satisfies $(\nabla^2 + k^2)u = 0$ outside all the $\mathcal{C}_j$, together with a radiation condition and a boundary condition on each $\mathcal{C}_j$.

3. Basic Foldy approach

Foldy's method starts by assuming isotropic scattering. This means that, near $\mathcal{C}_j$, the scattered field at $\boldsymbol{r}$ is approximated by

$$A_j G(\boldsymbol{r}-\boldsymbol{r}_j),$$

where A_j is an unknown amplitude, $G(\boldsymbol{r}) = H_0(k|\boldsymbol{r}|)$ is the free-space Green's function and $H_n(w) \equiv H_n^{(1)}(w)$ is a Hankel function. The total field is represented as

$$u(\boldsymbol{r}) = u_{\mathrm{inc}}(\boldsymbol{r}) + \sum_{j=1}^{N} A_j G(\boldsymbol{r}-\boldsymbol{r}_j), \tag{1}$$

where we will take $u_{\mathrm{inc}}(\boldsymbol{r}) = u_{\mathrm{inc}}(x,y) = \mathrm{e}^{\mathrm{i}kx}$.

The field incident on $\mathcal{C}_n$ in the presence of all the other scatterers is

$$\begin{aligned} u_n(\boldsymbol{r}) &\equiv u(\boldsymbol{r}) - A_n G(\boldsymbol{r}-\boldsymbol{r}_n) \\ &= u_{\mathrm{inc}}(\boldsymbol{r}) + \sum_{\substack{j=1\\ j\neq n}}^{N} A_j G(\boldsymbol{r}-\boldsymbol{r}_j). \end{aligned} \tag{2}$$

This "incident" field is scattered by $\mathcal{C}_n$. We characterize this process by

$$A_n = g u_n(\boldsymbol{r}_n). \tag{3}$$

This makes the strength of the scattered wave from $\mathcal{C}_n$, A_n, proportional to the field acting on it, $u_n(\boldsymbol{r}_n)$. The parameter g (Foldy's "scattering coefficient") can be chosen as $g = -[J_0(ka)]/[H_0(ka)]$, where J_n is a Bessel function and each $\mathcal{C}_j$ has radius a; if the scatterers were different, we would have written g_n in (3).

Finally, evaluating (2) at $\boldsymbol{r}_n$ gives, after using (3),

$$\frac{1}{g}A_n = u_{\mathrm{inc}}(\boldsymbol{r}_n) + \sum_{\substack{j=1\\ j\neq n}}^{N} A_j\, G(\boldsymbol{r}_n-\boldsymbol{r}_j), \tag{4}$$

for $n = 1, 2, \ldots, N$. This is a linear $N\times N$ system for A_j. Then the total field is given by (1).

4. Application to a ring of soft cylinders

Here, we summarise the results from [6]. There are N small sound-soft circles arranged so that their centres (at $\boldsymbol{r}_j$) are equally spaced around a larger circle of radius b, centred at the origin. Let $h = 2\pi/N$ be the angular spacing between adjacent scatterers. Then, using plane polar coordinates, r and θ, $\boldsymbol{r}_j$ is at $r=b$, $\theta = \theta_j = jh$. The distance between the jth and nth scatterers is

$$|\boldsymbol{r}_n - \boldsymbol{r}_j| = 2b\,|\sin([n-j]\pi/N)|\,. \tag{5}$$

Then the $N\times N$ Foldy system (4) simplifies to

$$\sum_{j=1}^{N} K_{n-j} A_j = f_n, \quad n = 1,2,\ldots,N, \tag{6}$$

where $f_n = -u_{\mathrm{inc}}(\boldsymbol{r}_n)$, $K_0 = -g^{-1}$,

$$K_j = H_0(2kb\,|\sin(j\pi/N)|), \quad j \neq 0 \bmod N \tag{7}$$

and K_j is N-periodic: $K_{j+mN} = K_j$, $m = \pm1, \pm2, \ldots$.

Richmond [8] and Wilson [9] gave numerical solutions of (6). Much later, Vescovo [10] noticed that the system matrix in (6) is a circulant matrix, which means that (6) can be solved explicitly using the discrete Fourier transform. Thus, let $\varpi = \mathrm{e}^{2\pi\mathrm{i}/N}$. Multiply (6) by ϖ^{mn}, sum over n and use the N-periodicity of K_n. This gives

$$\tilde{A}_m = \tilde{f}_m / \tilde{K}_m, \tag{8}$$

where

$$\tilde{A}_m = \sum_{j=1}^{N} A_j \varpi^{mj}, \quad A_n = \frac{1}{N}\sum_{j=1}^{N} \tilde{A}_j \varpi^{-nj}, \tag{9}$$

$$\tilde{f}_m = \sum_{j=1}^{N} f_j \varpi^{mj}, \quad \tilde{K}_m = \sum_{j=1}^{N} K_j \varpi^{mj}. \tag{10}$$

Finally, invert the discrete Fourier transform of $\{A_j\}$, $\{\tilde{A}_m\}$, using the second of (9).

Having determined A_n, we can calculate the field everywhere, using (1). In addition, we can investigate analytically what happens as N grows.

Thus, for $u_{\mathrm{inc}} = \mathrm{e}^{\mathrm{i}kx}$, we obtain

$$\tilde{f}_m = -\sum_{j=1}^{N} \mathrm{e}^{\mathrm{i}kb\cos jh}\,\mathrm{e}^{\mathrm{i}mjh}.$$

Write this formula (suggestively) as

$$\frac{\tilde{f}_m}{N} = h\sum_{j=1}^{N} f(jh) \quad \text{with} \quad f(\theta) = -\frac{1}{2\pi}\mathrm{e}^{\mathrm{i}kb\cos\theta}\mathrm{e}^{\mathrm{i}m\theta}.$$

We recognise the sum. It is what we would have obtained if we had used the repeated trapezium rule to compute $\int_0^{2\pi} f(\theta)\,\mathrm{d}\theta$, noting that f is 2π-periodic. As f is also very smooth, we know that the convergence is exponentially fast. Hence, evaluating the integral gives

$$N^{-1}\tilde{f}_m \sim -\mathrm{i}^m J_m(kb) \quad \text{as } N\to\infty. \tag{11}$$

This rapid convergence is encouraging, but the behaviour of $\tilde{K}_m$ is quite different. From (7) and (10),

$$\tilde{K}_m = -\frac{1}{g} + \sum_{j=1}^{N-1} v(jh), \tag{12}$$

where

$$v(\theta) = \mathrm{e}^{\mathrm{i}m\theta} H_0(2kb\,|\sin(\theta/2)|)$$

is 2π-periodic but has log singularities at $\theta = 0$ and $\theta = 2\pi$. The sum in (12) looks like the trapezoidal rule in which the endpoint contributions have been "ignored"; the properties of such sums have been analysed by Sidi [11]. Using his results, we find that

$$\frac{1}{N}\tilde{K}_m \sim -\frac{1}{Ng} + \frac{1}{2\pi}\int_0^{2\pi} v(\theta)\,\mathrm{d}\theta + \frac{2\mathrm{i}}{\pi N}\log N$$

as $N \to \infty$. The integral can be evaluated. Eventually, after combining with (8) and (11), we find that

$$\tilde{A}_n = -\mathrm{i}^n/H_n(kb) + O(N^{-1}\log N) \quad \text{as } N \to \infty. \tag{13}$$

The leading approximation can be used to confirm our expectations. For example, the far-field pattern of the ring approaches that for scattering by a sound-soft circle of radius b [2, eqn (4.10)], but this limit is approached very slowly. Similarly, the total field at the origin is $O(N^{-1}\log N)$ as $N \to \infty$.

4. Extended Foldy approach

Rigid (sound-hard) scatterers always induce a dipole field. Foldy's method can be generalized to cover these situations [2, §8.3.3]. Thus, suppose that, near the jth scatterer, the scattered field is given by

$$A_j G(\boldsymbol{r} - \boldsymbol{r}_j) + \boldsymbol{q}_j \cdot \boldsymbol{g}(\boldsymbol{r} - \boldsymbol{r}_j), \tag{14}$$

where A_j is an amplitude, $\boldsymbol{q}_j$ is a vector,

$$\boldsymbol{g}(\boldsymbol{r}) = -\frac{1}{k}\,\mathrm{grad}\,G(\boldsymbol{r}) = -\frac{\hat{\boldsymbol{r}}}{k}\frac{\mathrm{d}}{\mathrm{d}r}G(\boldsymbol{r}) = \hat{\boldsymbol{r}}\,H_1(kr),$$

with $\hat{\boldsymbol{r}} = \boldsymbol{r}/r$ and $r = |\boldsymbol{r}|$. Each component of $\boldsymbol{g}$ is an outgoing solution of the Helmholtz equation.

The first term in (14) is a source at $\boldsymbol{r}_j$; the strength of the source (given by A_j) is unknown. The second term is a dipole at $\boldsymbol{r}_j$; the direction and strength of the dipole (given by $\boldsymbol{q}_j$) are unknown. The basic Foldy method assumes that $\boldsymbol{q}_j \equiv \boldsymbol{0}$. We remark that the approximation (14) was used successfully in [12, Appendix A] for scattering by an infinite grating of sound-hard circular cylinders.

For more detail, define polar coordinates R_j and Θ_j at $\boldsymbol{r}_j$, $\boldsymbol{r} = \boldsymbol{r}_j + R_j(\hat{\mathbf{i}}\cos\Theta_j + \hat{\mathbf{j}}\sin\Theta_j)$, where $\hat{\mathbf{i}}$ and $\hat{\mathbf{j}}$ are unit vectors in the x and y directions, respectively. Then (14) becomes

$$A_j H_0(kR_j) + \{(\boldsymbol{q}_j \cdot \hat{\mathbf{i}})\cos\Theta_j + (\boldsymbol{q}_j \cdot \hat{\mathbf{j}})\sin\Theta_j\}H_1(kR_j).$$

Next, we represent the total field as

$$u(\boldsymbol{r}) = u_{\mathrm{inc}}(\boldsymbol{r}) + \sum_{j=1}^{N}\{A_j G(\boldsymbol{r}-\boldsymbol{r}_j) + \boldsymbol{q}_j \cdot \boldsymbol{g}(\boldsymbol{r}-\boldsymbol{r}_j)\}. \tag{15}$$

The field incident on $\mathcal{C}_n$ in the presence of all the other scatterers is

$$\begin{aligned} u_n(\boldsymbol{r}) &\equiv u(\boldsymbol{r}) - A_n G(\boldsymbol{r}-\boldsymbol{r}_n) - \boldsymbol{q}_n \cdot \boldsymbol{g}(\boldsymbol{r}-\boldsymbol{r}_n) \qquad (16)\\ &= u_{\mathrm{inc}}(\boldsymbol{r}) + \sum_{\substack{j=1\\ j\neq n}}^{N}\{A_j G(\boldsymbol{r}-\boldsymbol{r}_j) + \boldsymbol{q}_j \cdot \boldsymbol{g}(\boldsymbol{r}-\boldsymbol{r}_j)\}. \end{aligned}$$

This "incident" field is scattered by $\mathcal{C}_n$. We characterize this process by

$$A_n = g u_n(\boldsymbol{r}_n) \quad \text{and} \quad \boldsymbol{q}_n = \mathbf{Q}\,\boldsymbol{v}_n(\boldsymbol{r}_n),$$

where

$$\boldsymbol{v}_n(\boldsymbol{r}) = k^{-1}\mathrm{grad}\,u_n. \tag{17}$$

The quantity g is a scalar whereas $\mathbf{Q}$ is a 2×2 matrix. Thus, A_n is proportional to the value of the exciting field at $\boldsymbol{r}_n$, whereas $\boldsymbol{v}_n$ is related to the gradient of the exciting field at $\boldsymbol{r}_n$.

Low-frequency asymptotics for scattering by one sound-hard circle lead to good choices for g and $\mathbf{Q}$. Thus

$$g = -\frac{J_0'(ka)}{H_0'(ka)} \sim \frac{\pi}{4\mathrm{i}}(ka)^2, \quad \mathbf{Q} = -2g\mathbf{I},$$

where $\mathbf{I}$ is the 2×2 identity matrix.

Evaluating (16) at $\boldsymbol{r}_n$ gives

$$\frac{1}{g}A_n = u_{\mathrm{inc}}(\boldsymbol{r}_n) + \sum_{\substack{j=1\\ j\neq n}}^{N}\{A_j G(\boldsymbol{R}_{nj}) + \boldsymbol{q}_j \cdot \boldsymbol{g}(\boldsymbol{R}_{nj})\}, \tag{18}$$

where $\boldsymbol{R}_{nj} = \boldsymbol{r}_n - \boldsymbol{r}_j$. Also, from (16) and (17),

$$\begin{aligned} \boldsymbol{v}_n(\boldsymbol{r}) &= \boldsymbol{v}_{\mathrm{inc}}(\boldsymbol{r}) \qquad (19)\\ &+ \sum_{\substack{j=1\\ j\neq n}}^{N}\{-A_j\,\boldsymbol{g}(\boldsymbol{r}-\boldsymbol{r}_j) + k^{-1}\mathrm{grad}\,[\boldsymbol{q}_j \cdot \boldsymbol{g}(\boldsymbol{r}-\boldsymbol{r}_j)]\}, \end{aligned}$$

where $\boldsymbol{v}_{\mathrm{inc}}(\boldsymbol{r}) = k^{-1}\mathrm{grad}\,u_{\mathrm{inc}}$. Direct calculation gives

$$(kR_{nj})^{-1}H_1(kR_{nj})\,\boldsymbol{q}_j - \widehat{\boldsymbol{R}}_{nj}(\boldsymbol{q}_j \cdot \widehat{\boldsymbol{R}}_{nj})H_2(kR_{nj})$$

for $k^{-1}\mathrm{grad}\,[\boldsymbol{q}_j \cdot \boldsymbol{g}(\boldsymbol{r}-\boldsymbol{r}_j)]$ at $\boldsymbol{r} = \boldsymbol{r}_n$, where $R_{nj} = |\boldsymbol{R}_{nj}|$ and $\widehat{\boldsymbol{R}}_{nj} = \boldsymbol{R}_{nj}/R_{nj}$. Hence, evaluating (19) at $\boldsymbol{r}_n$, we obtain

$$\begin{aligned} \mathbf{Q}^{-1}\boldsymbol{q}_n = \boldsymbol{v}_{\mathrm{inc}}(\boldsymbol{r}_n) + \sum_{\substack{j=1\\ j\neq n}}^{N}\Bigg\{ &\frac{H_1(kR_{nj})}{kR_{nj}}\,\boldsymbol{q}_j\\ &- \widehat{\boldsymbol{R}}_{nj}(\boldsymbol{q}_j \cdot \widehat{\boldsymbol{R}}_{nj})H_2(kR_{nj}) - A_j\boldsymbol{g}(\boldsymbol{R}_{nj})\Bigg\}. \end{aligned} \tag{20}$$

Equations (18) and (20) hold for $n = 1, 2, \ldots, N$. They give a system of linear algebraic equations for A_n and the two components of $\boldsymbol{q}_n$. For N scatterers, there are $3N$ equations for the $3N$ scalar unknowns.

5. Application to a ring of hard cylinders

We define the geometry as in §3. It is convenient to write $\boldsymbol{q}_j$ in terms of its radial and tangential components with respect to the ring. Let $\hat{\boldsymbol{\theta}}_j = \hat{\mathbf{j}}\cos\theta_j - \hat{\mathbf{i}}\sin\theta_j$ be a unit tangent vector, so that $\hat{\boldsymbol{r}}_j \cdot \hat{\boldsymbol{\theta}}_j = 0$. Write

$$\boldsymbol{q}_j = B_j\hat{\boldsymbol{r}}_j + C_j\hat{\boldsymbol{\theta}}_j,$$

so that the $3N$ unknowns are A_j, B_j and C_j, $j = 1, 2, \ldots, N$. We have

$$\begin{aligned} b^{-1}\boldsymbol{q}_j \cdot \boldsymbol{R}_{nj} &= (B_j\hat{\boldsymbol{r}}_j + C_j\hat{\boldsymbol{\theta}}_j)\cdot(\hat{\boldsymbol{r}}_n - \hat{\boldsymbol{r}}_j) \\ &= -(2b^2)^{-1}R_{nj}^2 B_j + C_j\sin\theta_{nj}, \end{aligned}$$

where we have used (5) and we have defined

$$\theta_{nj} = \theta_n - \theta_j = (n-j)h.$$

Hence

$$\boldsymbol{q}_j \cdot \widehat{\boldsymbol{R}}_{nj} = -(2b)^{-1}R_{nj}B_j + bR_{nj}^{-1}C_j\sin\theta_{nj}.$$

This will be used in (18) and (20). We will also form the inner product of (20) with $\hat{\boldsymbol{r}}_n$ and with $-\hat{\boldsymbol{\theta}}_n$. Thus, we require

$$\begin{aligned} &\hat{\boldsymbol{r}}_n \cdot \boldsymbol{q}_j = B_j\cos\theta_{nj} + C_j\sin\theta_{nj}, \\ &\hat{\boldsymbol{\theta}}_n \cdot \boldsymbol{q}_j = -B_j\sin\theta_{nj} + C_j\cos\theta_{nj}, \\ &\hat{\boldsymbol{r}}_n \cdot \widehat{\boldsymbol{R}}_{nj} = (2b)^{-1}R_{nj}, \\ &\hat{\boldsymbol{\theta}}_n \cdot \widehat{\boldsymbol{R}}_{nj} = bR_{nj}^{-1}\sin\theta_{nj}. \end{aligned}$$

Assembling all the pieces, we obtain the system

$$\sum_{j=1}^{N}\mathbf{K}_{n-j}\mathbf{x}_j = \mathbf{f}_n, \quad n = 1, 2, \ldots, N, \tag{21}$$

where $\mathbf{x}_j = (A_j, B_j, C_j)^T$,

$$\mathbf{f}_j = (-u_{\mathrm{inc}}(\boldsymbol{r}_n),\, -\hat{\boldsymbol{r}}_n \cdot \boldsymbol{v}_{\mathrm{inc}}(\boldsymbol{r}_n),\, \hat{\boldsymbol{\theta}}_n \cdot \boldsymbol{v}_{\mathrm{inc}}(\boldsymbol{r}_n))^T$$

and $\mathbf{K}_j$ is a symmetric 3×3 matrix. In detail,

$$\mathbf{K}_0 = \mathbf{K}_N = \begin{pmatrix} -g^{-1} & 0 & 0 \\ 0 & (2g)^{-1} & 0 \\ 0 & 0 & -(2g)^{-1} \end{pmatrix}$$

and, for $j \neq 0 \bmod N$,

$$\mathbf{K}_j = \begin{pmatrix} K_{11} & K_{12} & K_{13} \\ K_{12} & K_{22} & K_{23} \\ K_{13} & K_{23} & K_{33} \end{pmatrix},$$

with entries as follows:

$$\begin{aligned} &K_{11} = H_0, \quad K_{12} = -(2b)^{-1}R_jH_1, \\ &K_{13} = bR_j^{-1}H_1\sin\theta_j, \\ &K_{22} = \frac{H_1}{kR_j}\cos\theta_j + H_2\frac{R_j^2}{4b^2}, \\ &K_{23} = \frac{H_1}{kR_j}\sin\theta_j - \frac{1}{2}H_2\sin\theta_j, \\ &K_{33} = -\frac{H_1}{kR_j}\cos\theta_j + H_2\frac{b^2}{R_j^2}\sin^2\theta_j. \end{aligned}$$

All the Hankel functions have argument kR_j with $R_j = 2b|\sin(j\pi/N)|$. Evidently, $\mathbf{K}_j$ is N-periodic: $\mathbf{K}_{j+mN} = \mathbf{K}_j$, $m = \pm1, \pm2, \ldots$.

The system (21) gives $3N$ equations for $3N$ unknowns. Application of the discrete Fourier transform breaks the system into N 3×3 systems, one for each $\mathbf{x}_j$.

6. Discussion

This is a work in progress. The current intention is to develop the approach outlined in §5 so as to analyse the effects of letting N grow. One question is: how well does a ring of small vertical cylinders shield the interior of the ring? We hope to present results in this direction at the Workshop.

References

[1] C. M. Linton and D. V. Evans, The interaction of waves with arrays of vertical circular cylinders. *J. Fluid Mech.* **215** (1990) 549–569.

[2] P. A. Martin, *Multiple Scattering*, Cambridge University Press, 2006.

[3] A. Z. Elsherbeni and A. A. Kishk, Modeling of cylindrical objects by circular dielectric and conducting cylinders. *IEEE Trans. Antennas & Propag.* **40** (1992) 96–99.

[4] D. V. Evans and R. Porter, Near-trapping of waves by circular arrays of vertical cylinders. *Appl. Ocean Res.* **19** (1997) 83–99.

[5] L. Pajewski, G. Schettini and F. Frezza, Cylindrical-wave approach for the electromagnetic scattering problem by buried two-dimensional objects. *J. Appl. Geophys.* **67** (2009) 318–326.

[6] P. A. Martin, On acoustic and electric Faraday cages. *Proc. Roy. Soc.* A **470** (2014) 20140344.

[7] L. L. Foldy, The multiple scattering of waves. I. General theory of isotropic scattering by randomly distributed scatterers. *Phys. Rev.* **67** (1945) 107–119.

[8] J. H. Richmond, Scattering by an arbitrary array of parallel wires. *IEEE Trans. Microwave Theory & Techniques* **13** (1965) 408–412.

[9] L. O. Wilson, The shielding of a plane wave by a cylindrical array of infinitely long thin wires. *IEEE Trans. Antennas & Propag.* **22** (1974) 689–696.

[10] R. Vescovo, Electromagnetic scattering from cylindrical arrays of infinitely long thin wires. *Electronic Lett.* **31** (1995) 1646–1647.

[11] A. Sidi, Euler–Maclaurin expansions for integrals with endpoint singularities: a new perspective. *Numerische Math.* **98** (2004) 371–387.

[12] P. A. Martin and R. A. Dalrymple, Scattering of long waves by cylindrical obstacles and gratings using matched asymptotic expansions. *J. Fluid Mech.* **188** (1988) 465–490.

The Sign of the Added Mass Coefficients for 2-D Structures

by M. McIver and P. McIver
Department of Mathematical Sciences, Loughborough University, Loughborough, LE11 3TU, UK
m.mciver@lboro.ac.uk

Highlights:

- The diagonal coefficients in the added mass matrix, for a single two-dimensional structure which satisfies the John condition in water of infinite depth, are proven to be non-negative.
- The heave added mass coefficient for a symmetric pair of structures, which individually satisfy the John condition but move as a single structure, is shown to be non-negative in the range $(2n-1)\pi \leq Ks \leq 2n\pi$. The corresponding sway coefficient is shown to be non-negative when $2n\pi \leq Ks \leq (2n+1)\pi$. Here n is an integer, K is the infinite-depth wave number and s is the length of the free surface between the structures.

1 Introduction

A structure is forced to make small oscillations in water of infinite depth in a single mode of motion. The coefficient of proportionality in the part of the complex-valued hydrodynamic force on the structure that is proportional to minus its acceleration, is a diagonal term in the added mass matrix. Numerical calculations show that this coefficient is positive at all frequencies for many structures. However, if the structure is shallowly-submerged, it may be negative in some frequency ranges [1, 2]. Negative added mass also occurs when one or more elements of the structure enclose a portion of the free surface, for example a pair of surface-piercing cylinders in two dimensions [3, 4, 5].

Falnes [6] showed that the diagonal coefficients in the added mass matrix are proportional to the difference in the time averaged kinetic and potential energies of the relevant fluid motion. A similar argument to that employed in [7] is used here to show that the potential energy is less than or equal to the kinetic energy for a single two-dimensional structure which satisfies the John condition and oscillates in a single mode of motion. So the diagonal coefficients in the added mass matrix are non-negative for such a structure at all frequencies. The work is extended to find frequency ranges in which the added mass coefficients for a symmetric pair of such structures are non-negative, using the method in [8]. The ranges for non-negative symmetric and antisymmetric added mass coefficients are shown to be complementary. Numerical calculations for two semi-circular cylinders show that the frequencies at which negative added mass occurs are consistent with these results.

2 Formulation

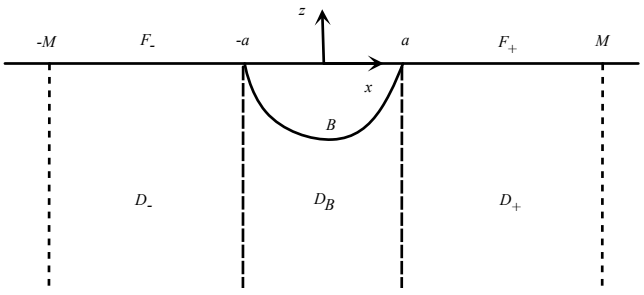

Figure 1: A single structure which satisfies the John condition

A two-dimensional, surface-piercing structure makes small amplitude oscillations at angular frequency ω, in water of infinite depth. In its equilibrium position, the structure is assumed to intersect the mean free surface at two points only $(\pm a, 0)$, as illustrated in Figure 1, and to be such that a vertical line drawn down through the fluid from each point on the mean free surface does not intersect the structure. John [9] showed that the linear, unforced frequency domain potential for such a body is zero and so the structure is said to satisfy the John condition.

If the component of the velocity of the structure in the pth mode of motion is given by $Re[v_p \mathrm{e}^{-\mathrm{i}\omega t}]$ then the corresponding velocity potential is $Re[v_p \phi_p(x,z)\mathrm{e}^{-\mathrm{i}\omega t}]$, where ϕ_p is harmonic and satisfies

$$\frac{\partial \phi_p}{\partial n} = n_p \quad \text{on the structure,} \tag{1}$$

where n_p is the pth component of the unit inward normal. The linearised free surface condition is

$$K\phi_p - \frac{\partial \phi_p}{\partial z} = 0 \quad \text{on } z = 0,\ x < -a, \quad x > a, \quad K = \omega^2/g. \tag{2}$$

There is no motion at large depths and only outward propagating waves as $x \to \pm\infty$.

3 The sign of the added mass coefficient for a single structure

An application of the divergence theorem to $\phi_p \nabla \overline{\phi}_p + \overline{\phi}_p \nabla \phi_p$ in the fluid yields the relationship between the non-dimensional diagonal coefficient in the added mass matrix μ_{pp} and the difference between the time-averaged kinetic and potential energies derived in [6], namely

$$\mu_{pp} = Re\left[\frac{1}{A_0}\int_B \phi_p\, n_p \,\mathrm{d}S\right] = \frac{1}{A_0}\lim_{M\to\infty}\left[\int_{D_-\cup D_+\cup D_B} |\nabla\phi_p|^2 \,\mathrm{d}V - K\int_{F_-\cup F_+} |\phi_p|^2 \,\mathrm{d}x\right], \tag{3}$$

where A_0 is the cross-sectional area of the structure. Green's theorem is applied to ϕ_p and $\mathrm{e}^{iK(x-s)+Kz}$ in the region $x \geq s > a$. Both functions represent outgoing waves at infinity and so the only contribution comes from the line $x = s$ and yields

$$\int_{-\infty}^{0}\left[\frac{\partial \phi_p}{\partial x}\mathrm{e}^{Kz} - \mathrm{i}K\phi_p \mathrm{e}^{Kz}\right]_{x=s} \mathrm{d}z = 0. \tag{4}$$

The second term in (4) is integrated by parts and then the equation is rearranged to give

$$\phi_p(s,0) = \int_{-\infty}^{0}\left[\frac{\partial \phi_p}{\partial z} - \mathrm{i}\frac{\partial \phi_p}{\partial x}\right]_{x=s} \mathrm{e}^{Kz}\,\mathrm{d}z. \tag{5}$$

Now

$$\left|\frac{\partial \phi_p}{\partial z} - \mathrm{i}\frac{\partial \phi_p}{\partial x}\right|^2 = 2\left(\left|\frac{\partial \phi_p}{\partial z}\right|^2 + \left|\frac{\partial \phi_p}{\partial x}\right|^2\right) - \left|\frac{\partial \phi_p}{\partial z} + \mathrm{i}\frac{\partial \phi_p}{\partial x}\right|^2 \leq 2\,|\nabla\phi_p|^2\,, \tag{6}$$

so an application of the Cauchy-Schwarz inequality to (5) and then integration over F_+ yields

$$K\int_{F_+} |\phi_p(x,0)|^2 \,\mathrm{d}x \leq \int_{D_+} |\nabla\phi_p|^2 \,\mathrm{d}V. \tag{7}$$

A similar analysis in $x < -a$ produces the same inequality but with F_+ and D_+ replaced by F_- and D_-. Both inequalities are substituted into (3) to give

$$\mu_{pp} = Re\left[\frac{1}{A_0}\int_B \phi_p\, n_p \,\mathrm{d}S\right] \geq \frac{1}{A_0}\int_{D_B} |\nabla\phi_p|^2 \,\mathrm{d}V \geq 0. \tag{8}$$

Thus the diagonal terms in the added mass matrix are non-negative for a single structure which satisfies the John condition.

4 The sign of the added mass coefficient for two structures

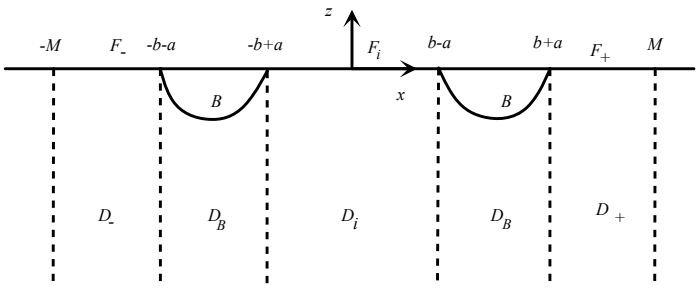

Figure 2: Two structures which individually satisfy the John condition

The analysis used in §3 is performed for two structures which individually satisfy the John condition but move as a single structure and yields

$$\mu_{pp} = Re\left[\frac{1}{A_0}\int_B \phi_p\, n_p\, \mathrm{d}S\right] \geq \frac{1}{A_0}\left[\int_{D_i} |\nabla\phi_p|^2\, \mathrm{d}V - K\int_{F_i} |\phi_p|^2\, \mathrm{d}x\right], \tag{9}$$

where F_i represents the free surface between the structures and D_i the fluid region below. It remains to determine where the right-hand side of (9) is non-negative. On F_i the function w_p is defined as in [8] by

$$w_p(x) = \int_{-\infty}^{0} \phi_p(x,z)\mathrm{e}^{Kz}\, \mathrm{d}z. \tag{10}$$

The operator $\mathrm{d}^2/\mathrm{d}x^2$ is applied to (10) and yields $\mathrm{d}^2 w_p/\mathrm{d}x^2 + K^2 w_p = 0$. If the system of structures is symmetric, the heave potential ϕ_3 is symmetric in x, and so

$$w_3(x) = B_3 \cos Kx = \int_{-\infty}^{0} \phi_3(x,z)\mathrm{e}^{Kz}\, \mathrm{d}z, \quad x \in F_i, \tag{11}$$

where B_3 is a complex constant. Integration by parts in (11) followed by applications of the Cauchy and Schwarz inequalities yields an inequality which is integrated over F_i to give

$$K\int_{F_i} |\phi_3(x,0)|^2\, \mathrm{d}x \leq K^2|B_3|^2\,[2K(b-a) + \sin 2K(b-a)] + \int_{D_i}\left|\frac{\partial\phi_3}{\partial z}\right|^2 \mathrm{d}V. \tag{12}$$

Differentiation of (11) with respect to x and an application of the Cauchy-Schwarz inequality followed by integration over F_i yields

$$K^2|B_3|^2\,[2K(b-a) - \sin 2K(b-a)] \leq \int_{D_i}\left|\frac{\partial\phi_3}{\partial x}\right|^2 \mathrm{d}V. \tag{13}$$

A combination of (12) and (13) gives

$$K\int_{F_i} |\phi_3(x,0)|^2\, \mathrm{d}x \leq 2K^2|B_3|^2 \sin 2K(b-a) + \int_{D_i} |\nabla\phi_3|^2\, \mathrm{d}V \leq \int_{D_i} |\nabla\phi_3|^2\, \mathrm{d}V \tag{14}$$

if $\sin 2K(b-a) \leq 0$, that is if $(2n-1)\pi \leq 2K(b-a) \leq 2n\pi$, where n is a positive integer. Substitution of (14) into (9) shows that the heave added mass is non-negative in this range. The sway potential ϕ_1 is antisymmetric in x and so $w_1(x) = B_1 \sin Kx$ and a similar analysis gives

$$K\int_{F_i} |\phi_1(x,0)|^2\, \mathrm{d}x \leq -2K^2|B_1|^2 \sin 2K(b-a) + \int_{D_i} |\nabla\phi_1|^2\, \mathrm{d}V \leq \int_{D_i} |\nabla\phi_1|^2\, \mathrm{d}V \tag{15}$$

if $\sin 2K(b-a) \geq 0$, that is if $2n\pi \leq 2K(b-a) \leq (2n+1)\pi$, where n is a non-negative integer. Substitution of (15) into (9) shows that the sway added mass is non-negative in this range.

Numerical calculations of the heave and sway added mass coefficients, μ_{33} and μ_{11}, are presented in Figure 3 for a pair of surface-piercing, semi-circular cylinders for which $b = 2a$. The shaded area represents the frequency ranges in which μ_{11} must be non-negative and the complementary frequency ranges are where μ_{33} must be non-negative. It should be noted that μ_{11} and μ_{33} are not negative everywhere outside these intervals and work is currently in progress to use the wide-spacing approximation to find ranges of frequencies at which negative values of μ_{11} and μ_{33} occur.

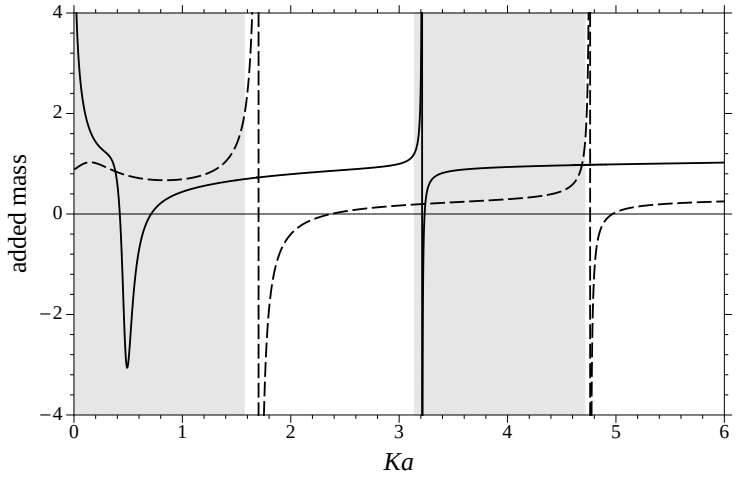

Figure 3: The heave —— and sway − − − added mass for 2 semi-circular cylinders, $b = 2a$

References

[1] J. N. Newman, B. Sortland, and T. Vinje. Added mass and damping of rectangular bodies close to the free surface. *J. Ship Res.*, 28(4):219–225, 1984.

[2] P. McIver and D. V. Evans. The occurrence of negative added mass in free-surface problems involving submerged oscillating bodies. *J. Engng Maths*, 18:7–22, 1984.

[3] S. Wang and R. Wahab. Heaving oscillations of twin cylinders in a free surface. *J. Ship Res.*, 15:33–48, 1971.

[4] R. W. Yeung and R. K. M. Seah. On Helmholtz and higher-order resonance of twin floating bodies. *J. Engng Maths*, 58:251–265, 2007.

[5] R. Porter and D.V. Evans. Estimation of wall effects on floating cylinders. *J. Engng Maths*, 70:191–204, 2011.

[6] J. Falnes and P. McIver. Surface wave interactions with systems of oscillating bodies and pressure distributions. *Appl. Ocean Res.*, 7:225–234, 1985.

[7] D.V. Evans, M. McIver, and R. Porter. Transparency of structures in water waves. *International Workshop on Water Waves and Floating Bodies, Osaka*, 2014.

[8] C. M. Linton and N. G. Kuznetsov. Non-uniqueness in two-dimensional water-wave problems: numerical evidence and geometrical restrictions. *Proc. Roy. Soc. Lond. A*, 453:2437–2460, 1997.

[9] F. John. On the motion of floating bodies, II. Simple harmonic motions. *Communications Pure Applied Mathematics*, 3:45–101, 1950.

Numerical and experimental modelling of cylindrical tuned liquid dampers

B. Molin, F. Remy, J. Bonnici, J.-B. Lacaze

Aix Marseille Université, CNRS, Centrale Marseille, IRPHE UMR 7342,
13451 Marseille cedex 20, France

I. Introduction

So-called Tuned Liquid Dampers (TLDs) are gaining interest as devices to mitigate the resonant response of slender buildings under wind or earthquake excitation. Some TLDs are of sloshing type, consisting in tanks partly filled with water, with the natural frequency of their first sloshing mode adjusted to the resonant frequency of the structure. Energy dissipation is enhanced by perforated screens. The two-dimensional case of rectangular TLDs has been extensively investigated numerically and experimentally — e.g. see Warnitchai & Pinkaew (1998), Tait (2008), Faltinsen *et al.* (2011), Crowley & Porter (2012) or Molin & Remy (2013).

Figure 1: Considered geometries: circular screen (left) or along a diameter (right).

In the case of axisymmetric buildings such as airport or wind towers TLDs should preferably be axisymmetric as well. Ghaemmaghami *et al.* (2012) have proposed an annular TLD with two horizontal solid baffles at the outer wall. Here we consider cylindrical tanks with vertical perforated screens, either radial or circular, or a combination of both. There are two basic cases: one circular screen or one screen along a diameter, perpendicular to the direction of forced motion (Fig. 1). We have investigated both cases through numerical and experimental modelling.

II. Numerical models

The theoretical frame closely follows Molin & Remy (2013): potential flow theory is assumed with the free surface equations linearized. With the velocity potential written as

$$\Phi(R,\theta,z,t) = A\,\omega\,\Re\left\{\varphi(R,\theta,z)\,\mathrm{e}^{-\mathrm{i}\,\omega t}\right\} \tag{1}$$

where (R,θ,z) are cylindrical coordinates from the bottom of the tank, A is the surge motion amplitude and ω the frequency, the boundary value problem writes

$$\Delta\varphi = 0 \qquad 0 \le R \le b \qquad 0 \le z \le h \tag{2}$$

$$g\,\varphi_z - \omega^2\,\varphi = 0 \qquad z = h \tag{3}$$

$$\varphi_z = 0 \qquad z = 0 \tag{4}$$

$$\varphi_R = \cos\theta \qquad R = b \tag{5}$$

(b the radius of the tank and h the filling height of water).

At the porous screen a quadratic discharge law is assumed (Molin, 2011):

$$P_- - P_+ = \rho\,\frac{1-\tau}{2\,\mu\,\tau^2}\,V_r\,|V_r|, \tag{6}$$

with $P_- - P_+$ the pressure drop, τ the porosity or open-area ratio, μ a discharge coefficient, and V_r the relative velocity of the flow with respect to the screen.

II.1 Circular screen

The velocity potential is written as

$$\varphi_1 = \cos\theta \left\{ \varphi_{NS} + B_0 \frac{J_1(k_0 R)}{k_0\, J_1'(k_0 a)} \frac{\cosh k_0 z}{\cosh k_0 h} + \sum_{n=1}^{\infty} B_n \frac{I_1(k_n R)}{k_n\, I_1'(k_n a)} \cos k_n z \right\} \tag{7}$$

in the inner sub-domain ($0 \le R \le a$), and

$$\begin{aligned} \varphi_2 &= \cos\theta \left\{ \varphi_{NS} + B_0 \frac{Y_1'(k_0 b)\, J_1(k_0 R) - J_1'(k_0 b)\, Y_1(k_0 R)}{k_0\, (Y_1'(k_0 b)\, J_1'(k_0 a) - J_1'(k_0 b)\, Y_1'(k_0 a))} \frac{\cosh k_0 z}{\cosh k_0 h} \right. \\ &+ \left. \sum_{n=1}^{\infty} B_n \frac{I_1'(k_n b)\, K_1(k_n R) - K_1'(k_n b)\, I_1(k_n R)}{k_n\, (I_1'(k_n b)\, K_1'(k_n a) - K_1'(k_n b)\, I_1'(k_n a))} \cos k_n z \right\} \end{aligned} \tag{8}$$

in the annular sub-domain ($a \le R \le b$). In these equations k_0, k_n are the roots of the dispersion equation $\omega^2 = g\, k_0 \tanh k_0 h = -g\, k_n \tan k_n h$ and φ_{NS} stands for the solution in the absence of screen:

$$\varphi_{NS} = A_0 \frac{J_1(k_0 R)}{k_0\, J_1'(k_0 b)} \frac{\cosh k_0 z}{\cosh k_0 h} + \sum_{n=1}^{\infty} A_n \frac{I_1(k_n R)}{k_n\, I_1'(k_n b)} \cos k_n z \tag{9}$$

with $A_0 = 2\, \sinh 2k_0 h / (2\, k_0 h + \sinh 2k_0 h)$, $A_n = 4\, \sin k_n h / (2\, k_n h + \sin 2\, k_n h)$.

Only the discharge equation (6) remains to be verified. The relative flow velocity at the screen is

$$V_r(z,\theta,t) = A\,\omega\, \cos\theta\, \Re\left\{ \left[(\alpha_0 + B_0) \frac{\cosh k_0 z}{\cosh k_0 h} + \sum_n (\alpha_n + B_n) \cos k_n z \right] \mathrm{e}^{-\mathrm{i}\,\omega t} \right\} \tag{10}$$

with $\alpha_0 = A_0\, (J_1'(k_0 a)/J_1'(k_0 b) - 1)$, $\alpha_n = A_n\, (I_1'(k_n a)/I_1'(k_n b) - 1)$, while the pressure drop is

$$P_1 - P_2 = A\,\rho\,\omega^2\, \cos\theta\, \Re\left\{ \mathrm{i} \left[\beta_0\, B_0 \frac{\cosh k_0 z}{\cosh k_0 h} + \sum_n \beta_n\, B_n \cos k_n z \right] \mathrm{e}^{-\mathrm{i}\,\omega t} \right\} \tag{11}$$

and the β_i coefficients have complicated expressions not reproduced here.

The following derivations closely follow Molin & Remy (2013) with Lorentz linearization being applied both to the time and angular coordinate dependencies:

$$\Re\left\{ f\, \mathrm{e}^{-\mathrm{i}\,\omega t} \right\} \left| \Re\left\{ f\, \mathrm{e}^{-\mathrm{i}\,\omega t} \right\} \right| \simeq \frac{8}{3\,\pi} \|f\|\, \Re\left\{ f\, \mathrm{e}^{-\mathrm{i}\,\omega t} \right\} \qquad\qquad \cos\theta\, |\cos\theta| \simeq \frac{8}{3\,\pi} \cos\theta$$

II.1 Screen along a diameter

In the case of a solid wall, Bauer (1963) has proposed a solution written as the solid motion plus a combination of natural modes, that is eigen-functions satisfying an homogeneous Neumann condition at the vertical walls. In the case of a porous wall it turns out to be more handy to use eigen-functions satisfying the linearized free surface condition, alike in the circular case.

That is, in the sub-domains ① and ② of Fig. 1 the velocity potential φ_i is written as

$$\begin{aligned} \varphi_{1,2} &= \sum_{m=0}^{\infty} \cos 2m\theta \left\{ \pm A_{m0} \frac{J_{2m}(k_0 R)}{k_0\, J_{2m}'(k_0 b)} \frac{\cosh k_0 z}{\cosh k_0 h} \pm \sum_{n=1}^{\infty} A_{mn} \frac{I_{2m}(k_n R)}{k_n\, I_{2m}'(k_n b)} \cos k_n z \right\} \\ &+ \sum_{m=0}^{\infty} \cos(2m+1)\theta \left\{ B_{m0} \frac{J_{2m+1}(k_0 R)}{k_0\, J_{2m+1}'(k_0 b)} \frac{\cosh k_0 z}{\cosh k_0 h} + \sum_{n=1}^{\infty} B_{mn} \frac{I_{2m+1}(k_n R)}{k_n\, I_{2m+1}'(k_n b)} \cos k_n z \right\} \end{aligned} \tag{12}$$

In this equation $\pm$ means $+$ in sub-domain ① and $-$ in sub-domain ②. When the screen is solid the B_{mn} coefficients are zero identically. When there is no screen the A_{mn} and B_{mn} coefficients are zero except for the B_{0n} which are identical with the A_n in (9).

There remains to verify the no flow condition at the outer wall and the discharge equation at the porous screen. From the development

$$\cos(2m+1)\theta = \pm\alpha_{m0} \pm \sum_{n=1}^{\infty} \alpha_{mn} \cos 2n\theta \qquad 0 \le \theta \le \pi \tag{13}$$

where, again, $\pm$ means $+$ in subdomain ① and $-$ in subdomain ②, and

$$\alpha_{m0} = \frac{2}{\pi}\,\frac{(-1)^m}{2m+1} \qquad \alpha_{mn} = \frac{4}{\pi}\,\frac{(-1)^{m+n}\,(2m+1)}{(2m+1)^2 - 4\,n^2} \tag{14}$$

the no-flow condition at the outer wall results in

$$A_{mn} + \sum_{p=0}^{\infty} \alpha_{pm}\, B_{pn} = \alpha_{0m}\, B_{0nNS} \qquad m, n = 0, \infty \tag{15}$$

where B_{0nNS} is the No Screen case solution (9). Equivalently, in vector form:

$$\overrightarrow{A} = \mathbf{AB} \cdot \overrightarrow{B} + \overrightarrow{R_A} \tag{16}$$

where $\overrightarrow{A} = (A_{01}, A_{02}, \ldots, A_{0N}, A_{11}, \ldots, A_{MN})$, $\overrightarrow{B} = (B_{01}, B_{02}, \ldots, B_{0N}, B_{11}, \ldots, B_{MN})$ and M, N are the truncation orders of the m and n series. There remains to verify the discharge equation at the screen which takes the form

$$\sum_{m=0}^{\infty} (-1)^m \left\{ A_{m0}\, \frac{J_{2m}(k_0 R)}{k_0\, J'_{2m}(k_0 b)}\, \frac{\cosh k_0 z}{\cosh k_0 h} + \sum_{n=1}^{\infty} A_{mn}\, \frac{I_{2m}(k_n R)}{k_n\, I'_{2m}(k_n b)}\, \cos k_n z \right\}$$

$$= \mathrm{i}\; F(R,z) \left[\sum_{m=0}^{\infty} (2m+1)\,(-1)^m \left\{ B_{m0}\, \frac{J_{2m+1}(k_0 R)}{k_0\, J'_{2m+1}(k_0 b)}\, \frac{\cosh k_0 z}{\cosh k_0 h} + \sum_{n=1}^{\infty} B_{mn}\, \frac{I_{2m+1}(k_n R)}{k_n\, I'_{2m+1}(k_n b)}\, \cos k_n z \right\} - R \right] \tag{17}$$

with

$$F(R,z) = \frac{2}{3\pi}\,\frac{1-\tau}{\mu\tau^2}\,\frac{A}{R^2}\; \times \left\| \sum_{m=0}^{\infty} (2m+1)\,(-1)^m \left\{ B_{m0}\, \frac{J_{2m+1}(k_0 R)}{k_0\, J'_{2m+1}(k_0 b)}\, \frac{\cosh k_0 z}{\cosh k_0 h} + \sum_{n=1}^{\infty} B_{mn}\, \frac{I_{2m+1}(k_n R)}{k_n\, I'_{2m+1}(k_n b)}\, \cos k_n z \right\} - R \right\|$$

Alike in the two-dimensional case an iterative procedure is devised where $F(R,z)$ is given from the previous two steps. Both sides of equation (17) are first multiplied by $\cosh k_0 z / \cosh k_0 h$ (then $\cos k_n z$) and integrated in z from 0 to h. Then they are multiplied by $J_{2p}(k_0 R)/(k_0\, J'_{2p}(k_0 b))$ (then $I_{2p}(k_n R)/\,(k_n\, I'_{2p}(k_n b))$) and integrated in R from 0 to b. In this way one gets the vectorial equation

$$\mathbf{M_A} \cdot \overrightarrow{A}^{(j)} = \mathrm{i}\; \mathbf{M}_B^{(j)} \cdot \overrightarrow{B}^{(j)} + \mathrm{i}\; \overrightarrow{R}_C^{(j)} \tag{18}$$

Combination with (16) yields a linear system in $\overrightarrow{B}$. In the implementation numerical convergence problems were encountered associated with the evanescent components. In the numerical results shown further down in this paper, related to relatively shallow depth cases, the evanescent modes are just neglected.

III. Experiments

Experiments were carried out with the Hexapode bench of Centrale Marseille. The internal diameter of the tank was 0.97 m, the circular screen diameter 0.5 m. In the circular case the screen porosity was 23 %, in the diameter case it was 18 %. The screens had the same thickness, 2 mm, and circular openings with a diameter of 4 mm. Tests were done at 15 cm, 25 cm and 35 cm filling heights. Here we show results at a depth of 25 cm.

The range of frequencies was from 2 through 12 rad/s. When there is no screen, the first natural frequencies (below 12 rad/s) of the sloshing modes are 5.25 rad/s and 10.34 rad/s. With a solid circular screen they are 8.29 rad/s for the inner sub-domain and 4.02 rad/s and 11.67 rad/s for the annular sub-domain. With a solid diameter, they are 7.53 rad/s, 8.64 rad/s, 10.33 rad/s, 11.64 rad/s, 11.90 rad/s.

In the computations the discharge coefficient μ was taken equal to 0.5.

In the circular case, Fig. 2 shows the experimental and numerical added mass (left) and damping (right) coefficients, for different amplitudes of motion.

In the perforated diameter case, Fig. 3 shows the numerical and experimental added mass coefficients, while Fig. 4 shows the damping coefficients.

Good agreement is generally observed between the experimental and numerical hydrodynamic coefficients.

More results, with other screen arrangements, will be shown at the workshop.

References

Bauer H.F., 1963. Liquid sloshing in a cylindrical quarter tank. *AIAA Journal*, **1**, 2601–2606.

Crowley S., Porter R., 2012. An analysis of screen arrangements for a tuned liquid damper. *Journal of Fluids and Structures*, **34**, 291–309.

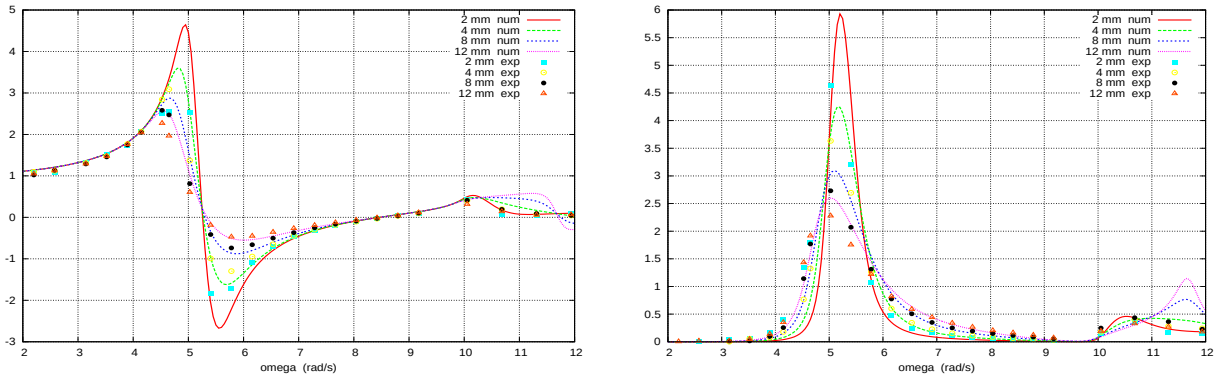

Figure 2: Circular screen. Added mass (left) and damping (right) coefficients.

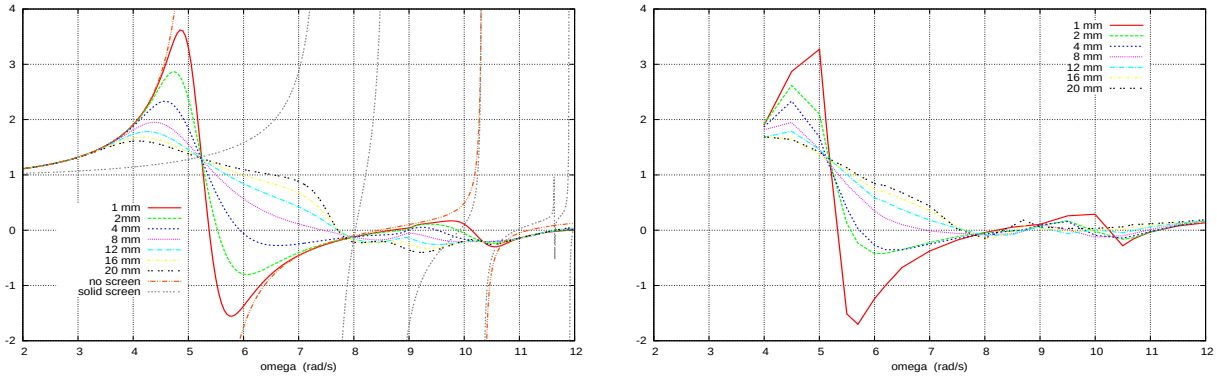

Figure 3: Screen along a diameter. Numerical (left) and experimental (right) added mass coefficients.

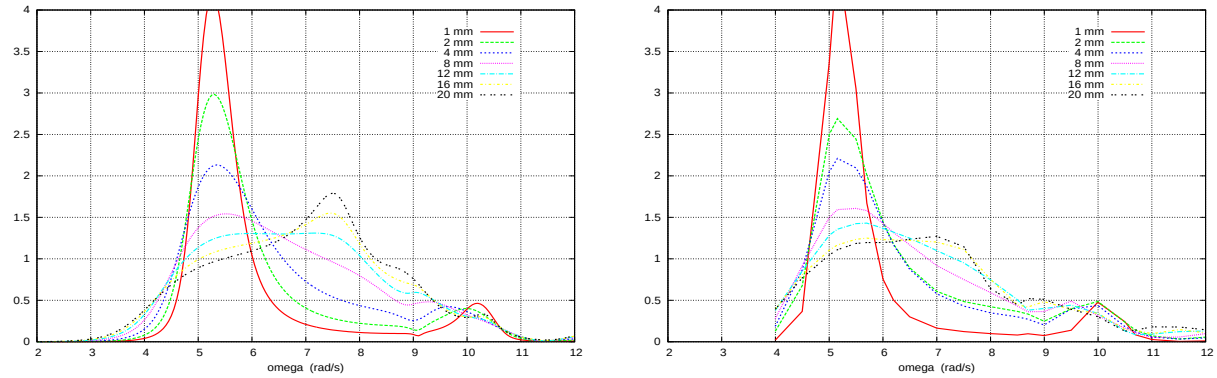

Figure 4: Screen along a diameter. Numerical (left) and experimental (right) damping coefficients.

Faltinsen O., Firoozkoohi R., Timokha A.N., 2011. Steady-state liquid sloshing in a rectangular tank with a slat-type screen in the middle: Quasilinear modal analysis and experiments. *Physics of Fluids*, **23**, 042101.

Ghaemmaghami A.R., Kianoush M.R., Mardukhi J. 2012. Numerical study on annular tuned liquid dampers for controlling the response of wind towers subjected to seismic loads. In *Proc. 15th World Conference on Earthquake Engineering*, Lisbon.

Molin B., 2011. Hydrodynamic modeling of perforated structures. *Applied Ocean Research*, **33**, 1–11.

Tait M.J., 2008. Modelling and preliminary design of a structure-TLD system. *Engineering Structures*, **30**, 2644–2655.

Warnitchai P., Pinkaew T., 1998. Modelling of liquid sloshing in rectangular tanks with flow-dampening devices. *Engineering Structures*, **20**, 593–600.

Amplification of waves by submerged plates

J. N. Newman
jnn@mit.edu

(Submitted to the 30th IWWWFB – Bristol, UK – 12-15 April 2015)

1 Introduction

The possibility of using submerged structures to focus waves is of special interest for wave-energy converters. Mehlum and Stamnes used a 'wave lens' in a large outdoor experimental facility (cf. [1] and references therein). Subsequent analyses have been made by Murashige & Kinoshita [2], Teigen [3], Griffiths & Porter [4], and others. Most of this work is motivated by the concept of optical refraction, at least as a first approximation, which implies that the structure is large relative to the wavelength λ. The lens described in [1] is a transverse array of small elements extending over a width of 33λ, with amplification factors of 3-4 at the focal point. Slender-body approximations are used in [2] to achieve amplification factors of 5 with a width of 16λ. Submerged plates with simple planforms and smaller dimensions are used in [3], with amplification factors of 2. Bathymetry with an elliptical plateau is considered in [4], with horizontal dimensions on the order of 10λ and amplification factors of 4-4.5. (The amplification factor is defined here as the maximum value of the free-surface elevation, for an incident wave of unit amplitude.) For the configurations in [3] and [4] the point of maximum elevation is in the shallow region above the plate or plateau.

For practical applications it is desirable to reduce the size of the structure. In the present work submerged horizontal plates are considered with dimensions comparable to the wavelength. Instead of assuming a simple geometrical shape, the planform is represented by a Fourier series with optimized coefficients to maximize the amplification factor. The computational approach combines the multivariate optimization code PRAXIS with the radiation/diffraction code WAMIT, as in [5]. Planforms are found with amplification factors between 5 and 15 at one wavenumber. Other planforms are found which maximize the average amplitude over a range of wavenumbers. As in [3] and [4] the point of maximum amplitude is in the shallow region above the plate. This may be an important restriction for wave-energy converters, since the power may be substantially less than for a plane progressive wave with the same amplitude.

2 Formulation

Plane waves of unit amplitude and wavenumber K propagate in the $+x$-direction toward a submerged horizontal plate of zero thickness. The fluid depth is infinite and linear potential theory is assumed. The plate is stationary, and occupies the space $0 \le r \le R(\theta)$ in the plane $z = -d$, where d is the depth below the undisturbed free surface and (r, θ) are polar coordinates with $x = r\cos\theta, y = r\sin\theta$. The coordinates and wavenumber are nondimensional. Symmetry is assumed about $y = 0$, and the outer radius R is represented by the Fourier series

$$R(\theta) = \sum_{n=0}^{N} c_n \cos n\theta. \tag{1}$$

The free surface is defined as $z = \mathrm{Re}\left[\zeta(x, y)\mathrm{e}^{\mathrm{i}\omega t}\right]$, where ω is the wave frequency and $K = \omega^2/g$. The amplification factor A is defined as the maximum value of $|\zeta(x, y)|$ over the domain of the free surface. The coefficients c_n are determined by optimization, with the objective to maximize A. The 'half-length' $a = R(0)$ is fixed to constrain the size of the plate, with the value $a = 2$. Except where noted the wavenumber $K = 1$ is used for the optimizations.

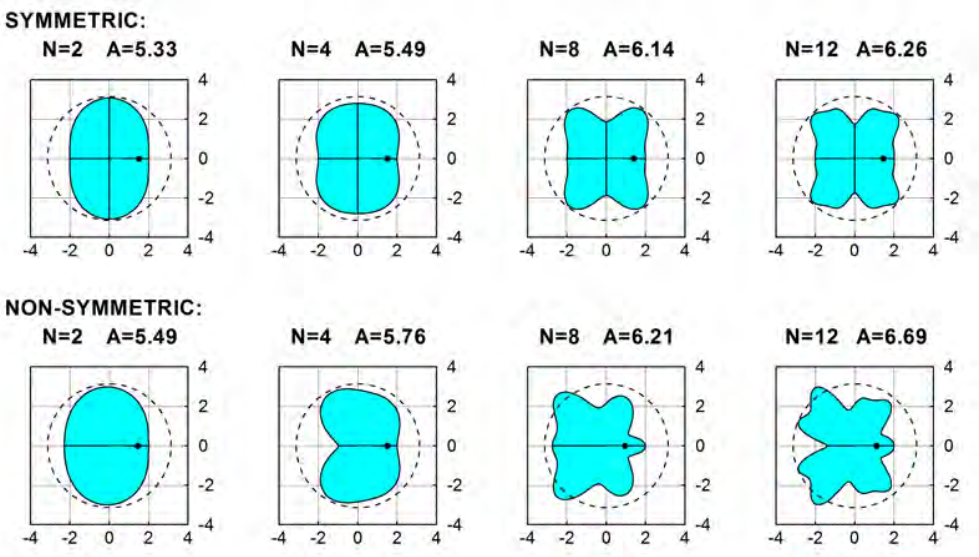

Figure 1: Planforms of the plates defined by the Fourier series (1) with $N = 2, 4, 8, 12$ and $d = 0.25$. The diameter of the dashed circles is equal to the wavelength 2π of the incident waves, which propagate from left to right. The maximum amplitude A occurs at the points shown by filled black circles.

3 Results

Figure 1 shows the planforms of optimized plates for the depth $d = 0.25$, with the upper limit N of the Fourier series equal to 2,4,8,12. Only the Fourier coefficients of even order are used in the upper row, to represent plates which are symmetrical about $x = 0$. In the lower row all $N+1$ coefficients are included to allow for non-symmetry. The parameter A increases with increasing N, but at a relatively slow rate. Allowing for non-symmetry introduces interesting details in the planform, but does not increase the maximum amplitude substantially.

The diameter of the dashed circles in Figure 1 is equal to the wavelength of the incident waves in deep water. Accounting for the finite depth above the plates reduces the wavelength by about one half. Thus the planforms in Figure 1 have maximum dimensions which are approximately equal to one deep-water wavelength, or two wavelengths for waves of the same frequency in depth d.

Figure 2 shows the planforms of symmetrical plates with $N = 8$, for different values of the depth d. The Fourier coefficients for these plates are listed in Table 1. The planform with $d = 0.25$ differs from the corresponding plate in Figure 1, due to the different initial conditions used for each optimization. This is an example of local convergence of the optimizations, which are not unique, and other planforms may exist with larger values of A. (Another planform was found for $d = 0.15$ with $A = 19.02$, but with twice the width of the plate shown here.)

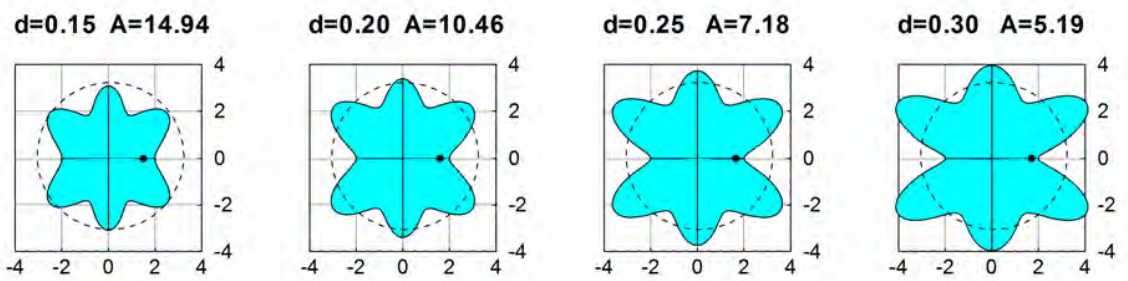

Figure 2: Planforms of symmetrical plates defined by the Fourier series (1) with $N = 8$ and depths d as shown.

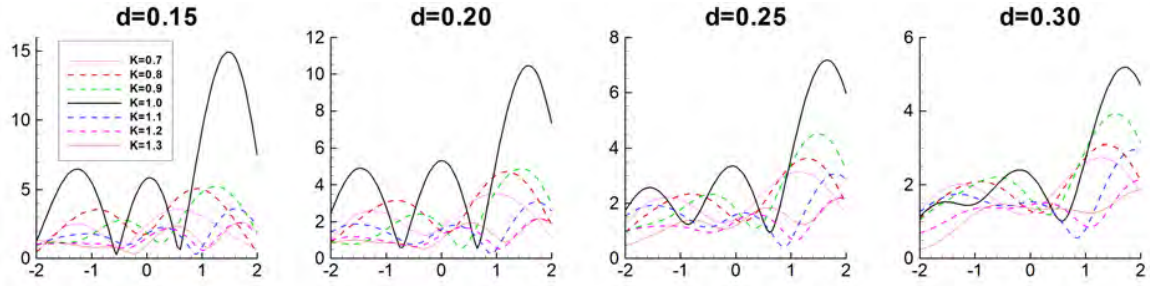

Figure 3: Free-surface elevation $|\zeta|$ as a function of the position x along the centerline of the plates shown in Figure 2, for different values of the wavenumber K. Note that the vertical scales are different.

The free-surface elevations $|\zeta(x,0)|$ above the plates in Figure 2 are plotted in Figure 3, for different values of the wavenumber K. The solid curves correspond to the wavenumber $K = 1$ used for the optimizations. For other values of K the amplification factors are reduced substantially.

Figure 4 shows planforms which are optimized for a range of wavenumbers. Here the average of the amplitudes at seven uniformly-spaced wavenumbers $K = 0.7(0.1)1.3$ is used, instead of the amplitude at $K = 1$, and $\bar{A}$ is defined as the maximum value of this average at all the field points x. The Fourier coefficients are listed in Table 2. The corresponding elevations of the free surface are shown in Figure 5. In these cases the maximum amplitudes occur at longer wavelengths ($K < 1$). These planforms are smaller and the free-surface elevations are more uniform with respect to the wavenumber K, but the maximum amplitudes are much less than for the plates in Figure 2.

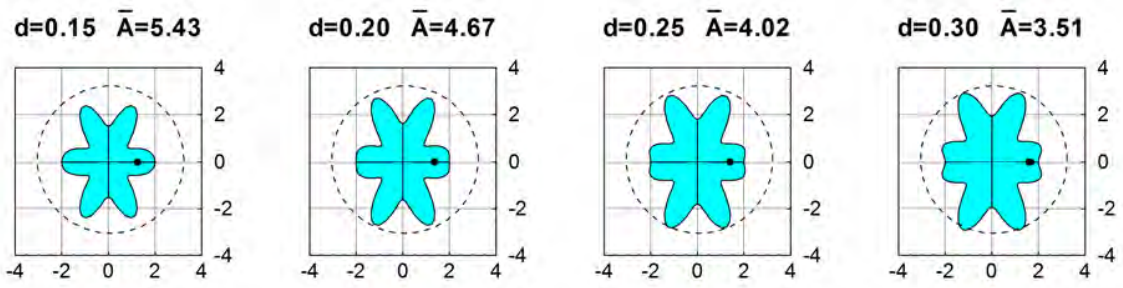

Figure 4: Planforms of the symmetric plates optimized for the range of wavenumbers $0.7 \le K \le 1.3$. The diameter of the dashed circles is equal to the wavelength at $K = 1$.

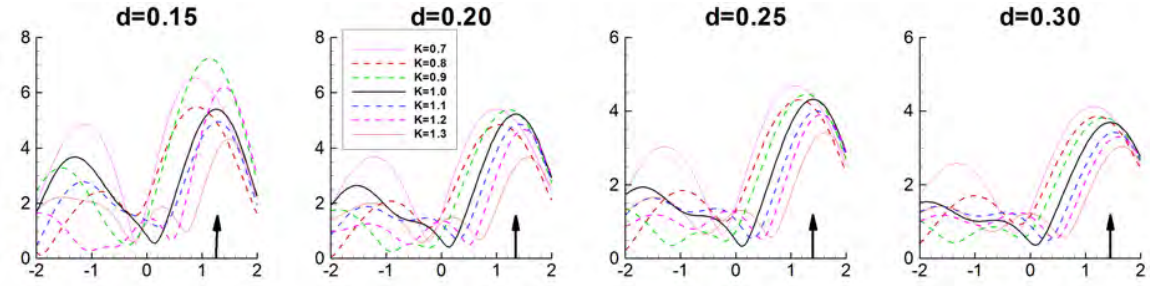

Figure 5: Free-surface elevation $|\zeta|$ as a function of the position x along the centerline of the plates shown in Figure 4, for different values of the wavenumber K. The vertical arrows show the points x where the averaged amplitude has its maximum value $\bar{A}$.

4 Conclusions

Submerged horizontal plates are found with planforms which maximize the local amplitude of the free-surface elevation. These plates are relatively compact, with horizontal dimensions comparable to the wavelength. Amplification factors between 5 and 15 are achieved at the wavenumber $K = 1$ used for the optimizations, but these factors are reduced substantially at other wavenumbers. An alternative set of plates are optimized for the range of wavenumbers $0.7 \leq K \leq 1.3$, with their average amplitude factors $\bar{A}$ between 3.5 and 5.4. Some reduction of the amplitude is expected for oblique waves, but this may be less important in a typical spectrum compared to the effect of different frequencies and corresponding wavenumbers.

For applications to wave-energy converters it should be noted that the point of maximum amplification is above the plate, where the elevation of the free surface is affected by three-dimensional effects and by reflection at the edge of the plate. Thus the relation between the amplitude of free-surface elevation and the power is more complicated than for a plane progressive wave and the available power may be much less than would be implied by a simple analysis based on the maximum amplitude. An interesting possible extension of the present work would be to combine a simple point absorber with a submerged plate and optimize both to maximize the power output.

Viscous and nonlinear effects are obvious issues. Separation may be mitigated by using finite thickness with a rounded edge. Nonlinear effects are important if the amplitude is comparable to the depth of the plate. Notwithstanding these practical issues, it is surprising that such large amplification factors can be achieved simply by optimizing the planform, when the dimensions are comparable to the wavelength.

References

[1] Stamnes, J.J., Løvhaugen, O., Spjelkavik, B., Mei, C.C., Lo, E. & Yue, D.K.P. 'Nonlinear focusing of surface waves by a lens - theory and experiment,' J. Fluid Mech. **135**, 71-94 (1983).

[2] Murashige, S. & Kinoshita, T. 'An ideal ocean wave focusing lens and its shape,' Applied Ocean Research **14**, 275-290 (1992).

[3] Teigen, P. 'On wave amplification over submerged lenses,' 23rd IWWWFB, Jeju, Korea (2008).

[4] Griffiths, L.S. & Porter, R. 'Focusing of surface waves by variable bathymetry,' Applied Ocean Research **34**, 150-163 (2012).

[5] Newman, J.N. 'Cloaking a circular cylinder in deep water,' 28th IWWWFB, l'Isle sur la Sorgue, France (2013).

d	A	c_0	c_2	c_4	c_6	c_8
0.15	14.94	2.5609	-0.0570	-0.2119	-0.4854	0.1934
0.20	10.46	2.9254	-0.1069	-0.3614	-0.5967	0.1397
0.25	7.18	3.2355	-0.0508	-0.3449	-0.8274	-0.0123
0.30	5.19	3.4775	-0.0179	-0.3254	-0.9663	-0.1679

Table 1: Fourier coefficients of the plates shown in Figure 2.

d	$\bar{A}$	c_0	c_2	c_4	c_6	c_8
0.15	5.43	1.7807	-0.2641	0.2219	0.5128	-0.2514
0.20	4.67	1.9693	-0.3242	0.2058	0.5221	-0.3730
0.25	4.02	2.0953	-0.3441	0.1998	0.4515	-0.4025
0.30	3.51	2.2020	-0.3514	0.1833	0.3869	-0.4207

Table 2: Fourier coefficients of the plates shown in Figure 4.

Bursting of a high pressure bubble through a free surface

B.Y. Ni *[a,b]
a. College of Shipbuilding Engineering, Harbin Engineering University, Harbin 150001, P. R. China;(nibaoyu@hrbeu.edu.cn)
b. Department of Mechanical Engineering, University College London, London WC1E 7JE, UK;

Highlights:

- The bursting of a fully submerged bubble with high internal pressure has been simulated.
- A methodology has been developed to deal with the sharp corner formed when the bubble surface merges with the free surface after it breaks up.
- Physics of the oscillation of the free surface in the form of a long and thin jet with a much higher second peak after bubble bursting has been discussed.

1. Introduction

Bubble bursting at the free surface can be found in biological, chemical and geophysical fields, as well as in nuclear engineering. It is suggested that it plays an important role in the natural production of liquid nuclei at the sea surface (Wu, 2002, Zhang et al., 2012), in the damages caused by the underwater explosion bubbles (LeMéhauté & Wang, 1995), as well as the cell damage observed in bioreactors as a result of bursting bubbles (Boulton-Stone & Blake, 1993, Boulton-Stone,1995).

In mathematical modelling and numerical simulations, bubble bursting at the free surface always presents a huge challenge due to the complex deformation and rapid motion of the air/liquid interfaces. Especially for a fully submerged bubble with large initial internal pressure relative to the ambient pressure, it will rise to the free surface and burst open very violently. Once it is open, this is often accompanied by a jet shooting up from the bottom of the bubble. When the jet reaches its peak height, it will fall down due to the gravity. The free surface will then oscillate and a second peak or more may appear before its deformation diminishes gradually through wave propagation away to the far field (Kedrinskii, 1978, LeMéhauté & Wang, 1995, Georgescu et al., 2002). Longuet-Higgins (1983) adopted a Dirichlet hyperboloid to model the bursting of an axisymmetric bubble. Since the deformation of the bubble surface could be expressed in an analytical form in this problem, he was able to show when the angle between the asymptotes of the hyperboloid reduces and approaches to $2\arctan\sqrt{2}$, both the velocity and acceleration at the tip of the hyperboloid become infinity. Based on this critical condition, LeMéhauté & Wang (1995) assumed that the bubble would simply break up at the apex at this very moment. In this kind of problem, as soon as the bubble bursts, there arises a major challenge in the numerical scheme. This is because two different directional normals exist at the intersection point of the bubble surface and free surface. This may cause a singularity which would greatly affect the stability of the numerical procedure if it is not properly resolved. LeMéhauté & Wang (1995) assumed that the unknown normal velocity remained single valued at the sharp corner, the same as other collocation points on the free surface and it was obtained by solving boundary integral equation directly. The tangential velocity was taken as the weighted average of those on the two elements attached to the corner. The normal direction at the corner was chosen as that perpendicular to the tangential velocity direction. However, mathematically to assume the normal at the sharp tip of the jet is single valued is not wholly justifiable. When the tip is an important part of the solution, this may cause numerical inaccuracy and instability. Thus a suitable scheme has been developed in this work to deal with the sharp tip after bubble bursting. This allows such a highly complex problem to be modelled successfully. In the present work the whole process of bubble motion and the free surface motion will be simulated, including the bubble rising/bursting, jet development, free surface rising/falling, wave oscillation and propagation.

2. Mathematical Model and Numerical Method

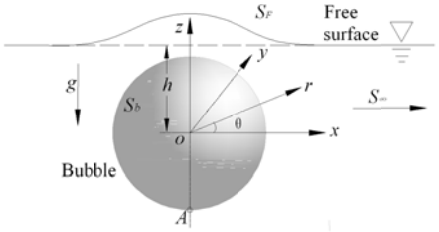

Fig. 1 Sketch of the problem with Cartesian and cylindrical coordinate systems

Fig.1 gives a sketch of the problem, which shows an initial spherical bubble close to a free surface. The distance between the initial bubble centre and the undisturbed free surface is h. When the internal pressure is spatially constant, the mathematical problem is axisymmetric about z. The fluid is assumed inviscid and incompressible, and the flow is irrotational. Thus, a velocity potential Φ can be introduced, which satisfies Laplace's equation

$$\nabla^2\Phi = 0, \tag{1}$$

in the fluid domain.

On the bubble surface and free surface, the fully nonlinear kinematic and dynamic boundary conditions can be written as below in the Lagrangian framework:

$$\frac{Dr}{Dt} = \frac{\partial\Phi}{\partial r}, \qquad \frac{Dz}{Dt} = \frac{\partial\Phi}{\partial z}, \tag{2}$$

$$\frac{D\Phi}{Dt} = \frac{1}{2}|\nabla\Phi|^2 - gz + \frac{P_\infty - P_l}{\rho}, \tag{3}$$

where D/Dt is the substantial derivative following a fluid particle, ρ is the density of the liquid, g is the acceleration due to gravity, P_∞ is the ambient pressure. Because the origin of the coordinate system is set at the

initial bubble centre, one has $P_\infty = P_{atm} + \rho g h$, where P_{atm} is the atmospheric pressure. P_l is the local fluid pressure on the surface, one has $P_l = P_g - \sigma\kappa$ when considering the surface tension, where σ is the surface tension coefficient, κ is the local surface curvature, and $P_g = P_b$ on the bubble surface, or $P_g = P_{atm}$ on the free surface.

It is assumed that the gas inside the bubble satisfies an isentropic law. Thus the pressure P_b inside the bubble is related to the volume V through the following equation (Lamb, 1975):

$$P_b = P_0 (V_0 / V)^\tau , \tag{4}$$

where P_0 and V_0 are respectively the initial gas pressure and volume when the bubble is generated, τ is the ratio of specific heat of gas. This state equation is applicable up to the moment of bubble breaking up, after which the bubble pressure is just taken as the atmospheric pressure $P_b = P_{atm}$.

Just before the rupture of the bubble, when the water layer between the bubble surface and the free surface becomes very thin, the element sizes used must be comparable to the thickness of the liquid layer. However, the element size cannot be reduced continuously indefinitely, which is one of the main reasons for the difficulty in analysing the micro details of extremely thin water layer. One way forward is to assume the water layer will break up when this is sufficiently thin (Ni et al., 2013). Here it is assumed that when the smallest distance between the nodes on the bubble surface and on the free surface is less than a critical value $\Delta\bar{s}_{c1}$, the bubble will open up at this point at the next time step. Also the bubble surface near this point with its distance to the free surface is smaller than another critical distance $\Delta\bar{s}_{c2} \geq \Delta\bar{s}_{c1}$ will open up. In this way $\Delta\bar{s}_{c1}$ will decide the moment of bubble bursting and $\Delta\bar{s}_{c2}$ will decide the size of the bubble surface being opened up.

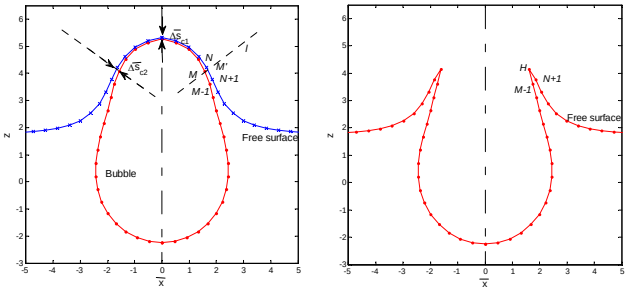

(a) Before bubble breaking (b) After bubble breaking

Fig. 2 Sketch of numerical procedure for a bubble bursting through the free surface

For the axisymmetric case considered here, it is observed during the simulation that the node on the bubble with the shortest distance to the free surface is its top point, as shown in Fig.2. The distance between the nodes on the bubble surface and on the free surface with $\bar{x} = 0$ is firstly defined as $\Delta\bar{s}_1$. When $\Delta\bar{s}_1 \leq \Delta\bar{s}_{c1}$, the water layer is regarded to be sufficiently thin and the bubble will burst in the next time step. To decide the size of the opening, we define a line l through point M on the bubble surface along its normal direction. The line intersects with the free surface at M', which is located in the element with nodes N and N+1. Variables such as velocity potential on M' are obtained by interpolation from nodes N and N+1. When the distance between points M and M' $\Delta\bar{s}_2 < \Delta\bar{s}_{c2}$ the water layer will be just cut there in the next time step, as shown in Fig.2(b). After the bubble is opened up, the point of intersection between the bubble surface and free surface is marked as H, whose location and velocity potential are taken as the average of those at points M and M'.

In the subsequent calculation, care must be taken at the intersection point H, because the normal derivatives Φ_{n1} and Φ_{n2} from the both sides of the sharp corner of H are different. When calculating the corresponding coefficient in the matrix at the intersection, the integral can be split into two parts: one from the integration over the left side surface and the other from the right side surface. However, there exists one more unknown in this case, and one extra condition needs to be found before solving the matrix equation.

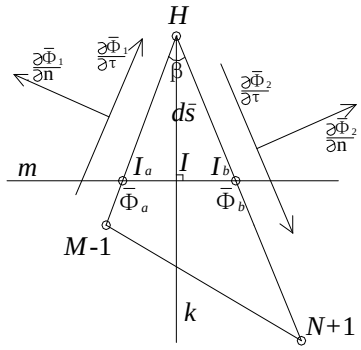

Fig. 3 Numerical treatment on the sharp corner

This is provided from a numerical scheme shown in Fig.3. Assume the angle between the two segments at the sharp corner is β. Bisect the angle β by using a line k. Draw a line m perpendicular to k with the intersection point I, whose distance to point H is $d\bar{s}$ which is quite small, and line m will intersect the two segments at I_a and I_b respectively. Assume the potentials at these points are Φ_a and Φ_b respectively. One can get the derivative $\Phi_{(I_b I_a)} = (\Phi_b - \Phi_a)/s_{ba}$, where s_{ba} is the distance between the points I_a and I_b. The weighted average of projections along the line m of normal derivatives Φ_{n1} and Φ_{n2}, as well as tangential derivatives $\bar{\Phi}_{\tau 1}$ and $\bar{\Phi}_{\tau 2}$ should be equal to $\bar{\Phi}_{(I_b I_a)}$. This gives a link between Φ_{n1} and Φ_{n2}, which can be used an extra condition for the matrix equation. Then the total velocity (Φ_r, Φ_z) at H can be obtained by the weighted average of those on the two sides of the corner, which is used to update the potential and the free surface shape. The calculation is then allowed to continue.

3. Results and discussions

A case is chosen here to show the jet formations after bubble bursting, rapid free surface deformation and wave propagation. Results for the velocity field and pressure contour are provided. Nondimensionalisation is applied based on the initial bubble radius R_0, the ambient pressure P_∞ and the density of the fluid ρ. Thus $Fr = \sqrt{P_\infty / \rho g R_0}$ as the Froude number, $\varsigma = P_0 / P_\infty$ as the strength parameter, $We = R_0 P_\infty / \sigma$ as the Weber number and $\lambda = h / R_0$ as the distance parameter are introduced. The dimensionless parameters in this case are taken as: $\varsigma = 20$, $Fr = 2.5$, $We = 2.2 \times 10^6$, $\lambda = 1.7$ and $\tau = 1.25$ (Cole, 1965).

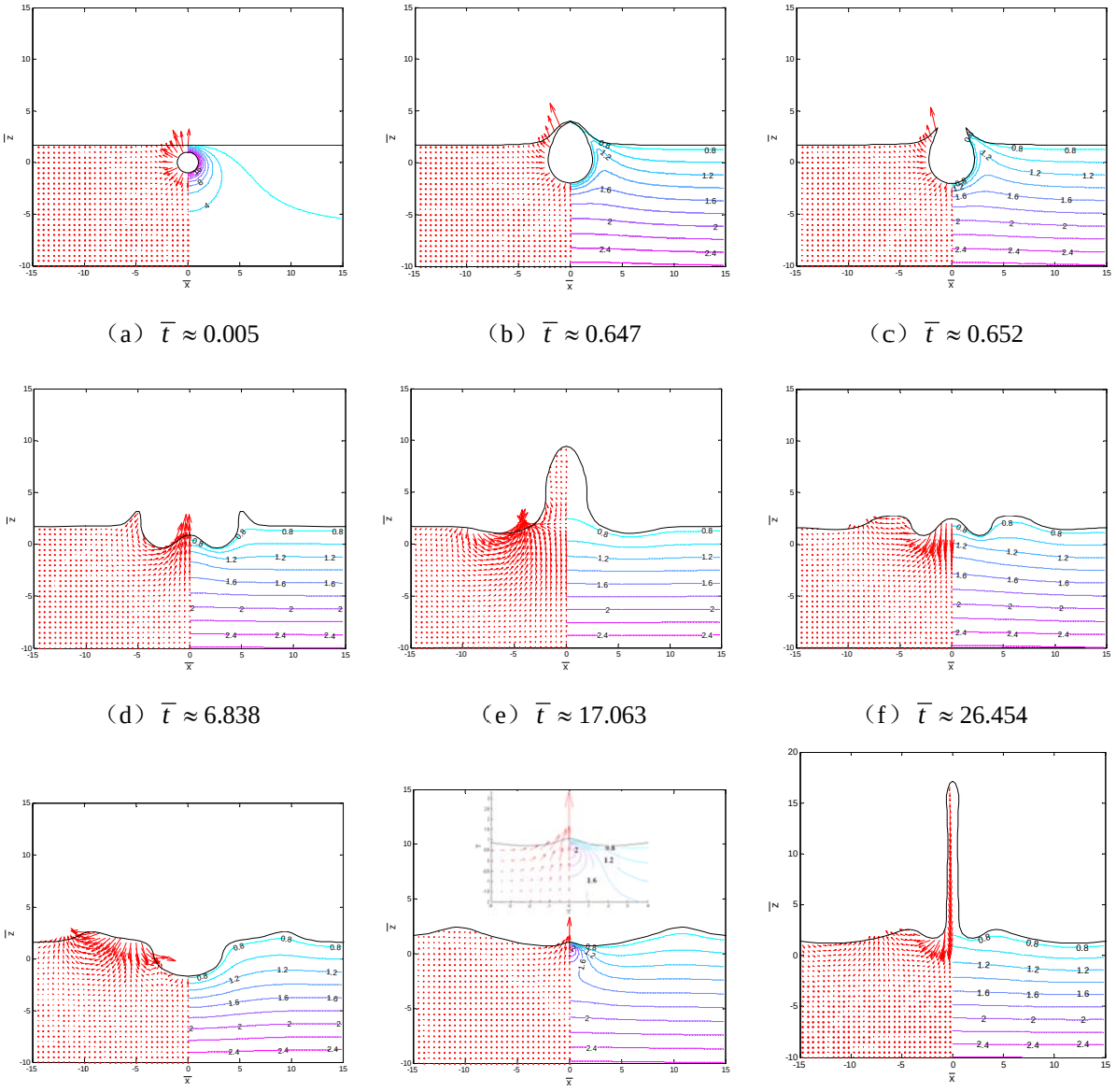

（a） $\overline{t} \approx 0.005$　（b） $\overline{t} \approx 0.647$　（c） $\overline{t} \approx 0.652$

（d） $\overline{t} \approx 6.838$　（e） $\overline{t} \approx 17.063$　（f） $\overline{t} \approx 26.454$

（g） $\overline{t} \approx 31.629$　（h） $\overline{t} \approx 34.677$　（i） $\overline{t} \approx 48.993$

Fig.4 Velocity vectors and pressure contours for $\varsigma = 20$, $Fr = 2.5$, $We = 2.2 \times 10^6$ and $\lambda = 1.7$. Arrow lengths are scaled with respect to the maximum instantaneous velocity in each frame.

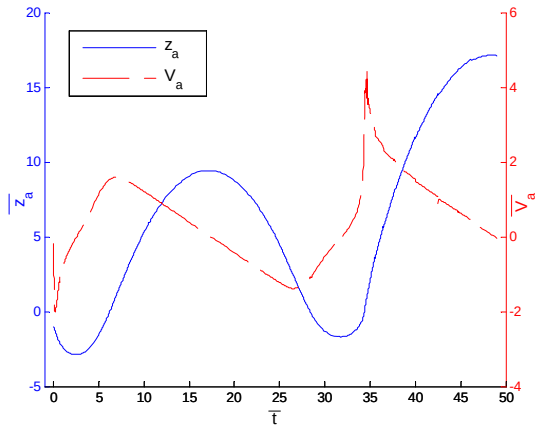

Fig.5 The time-history of the vertical coordinate and velocity of point *A*

Fig. 4 provides the pressure contours and velocity vectors near the bubble and free surface as well as the evolution of the bubble and free surface and Fig.5 gives the variation of the vertical coordinate and the velocity of point *A*, which is the lowest point initially on the bubble surface as shown in Fig.1. Initially the gradient of the pressure at the top of the bubble is higher than that at the bottom of the bubble because of the difference in the hydrostatic pressure. Thus the induced radial velocity at the top of the bubble is larger due to a larger initial acceleration, as shown in Fig.4(a). As the bubble expands, its top moves towards the free surface, while its bottom or point *A* moves downwards as shown in Fig.5. The pressure inside the bubble then reduces gradually. Fig.4(b) presents the surfaces right before bubble bursting and it is found that at this time step $P_b / P_{atm} \approx 1.01$. The water layer is removed in the next time step, and the bubble is opened up as shown in Fig.4(c). After this moment $\overline{t} \approx 0.652$, the pressure at point *A* becomes P_{atm}. This creates a larger local pressure gradient shown in Fig.4(c), which leads to a larger acceleration, as shown in Fig.5. Due to momentum point *A* still goes downwards. It continues until it reaches the first bottom at $\overline{t} \approx 2.584$. Due to the large hydrostatic pressure at lower position, point *A* then moves up with rapidly rising velocity. The velocity reaches a peak and then it slows down and becomes zero at $\overline{t} \approx 17.063$ when point *A* reaches its first peak, as shown in Fig.5. A large hump of the free surface around point *A* is formed, as shown in Fig.4(e), and much of the kinetic energy of fluid is converted into the potential energy. It can also be seen in Fig.4(e) that the hydrodynamic pressure inside the hump is almost P_{atm}. This means that gradient of the pressure is near zero. From the momentum equation, one can infer that the vertical acceleration of the fluid particle is $-g$. This coincides well with what has been observed in Fig.5, in which there is a section with a constant acceleration $-g$ during $6.84 \le \overline{t} \le 26.66$. The elevated free surface is pulled down by the gravity as the time progresses. Point *A* reaches the bottom second time at $\overline{t} \approx 31.629$ as shown in Fig.5. Fig.4(g) gives the surface shape at this moment. The location of point *A* is not as low as that of the previous trough. The deformation of the free surface becomes evident over a larger area, which indicates disturbance or generated wave is propagating outwards. Almost right after point *A* reaches the second trough, the surrounding water starts rushing towards the centre, leading to a higher pressure gradient at point *A*, as shown in the local magnification in Fig.4(h). The acceleration at point *A* becomes extremely large, shown by the nearly vertical velocity curve in Fig.5. It leads to a much larger velocity peak of 4.34 at $\overline{t} \approx 34.677$ before it slows down. Consequently, point *A* reaches a much higher peak. However, this is followed only by those points near point *A* or those slightly away from the centre. As a result a long and thin jet is formed at $\overline{t} \approx 48.993$, as shown in Fig.4(i). Then the jet column will be pulled down by the gravity and point *A* will continue to oscillate but with gradually reduced peaks as the disturbance propagates outwards in the form of the surface wave.

Acknowledgements

This work is supported by Lloyd's Register Foundation through the joint centre involving University College London, Shanghai Jiaotong University and Harbin Engineering University, the National Natural Science Foundation of China (Nos. 11302056 and 11302057), and the International Postdoctoral Exchange Fellowship Program (No. 20140068), to which the authors are most grateful. Lloyd's Register Foundation helps to protect life and property by supporting engineering-related education, public engagement and the application of research.

References:

[1] Boulton-Stone J. M., Blake J. R., Gas bubbles bursting at a free surface, Journal of Fluid Mechanics, 1993, 254: 437–466P

[2] Boulton-Stone J. M., The effect of surfactant on bursting gas bubbles, Journal of Fluid Mechanics,1995, 302: 231–257P

[3] Cole R.H., Underwater explosion, New York: Dover, 1965.

[4] Georgescu S. C., Achard J. L., Canot E., Jet drops ejection in bursting gas bubble processes, European Journal of Mechanics B/Fluids, 2002, 21:265-280P

[5] Kedrinskii V. K., Surface effects from an underwater explosion (Review), translated from Zhurnal Prikladnoi Mekhanikii Tekhnicheskoi Fiziki. 1978, 4: 66-87

[6] Lamb H., Hydrodynamics, sixth edition, Cambridge University Press, 1975

[7] LeMéhauté B., Wang S., Water waves generated by underwater explosion, Advanced series on ocean engineering: v.10, 1995, World Scientific Publishing.

[8] Longuet-Higgins M. S. Bubbles, breaking waves and hyperbolic jets at a free surface, Journal of Fluid Mechanics, 1983, 127: 103–121P

[9] Ni B. Y., Zhang A. M., Wu G. X., Numerical and experimental study of bubble impact on a solid wall, ASME-Journal of Fluid Engineering, 2015, 137(3),031206

[10] Wu J., Jet drops produced by bubbles bursting at the surface of seawater. J. Phys. Oceanogr. 2002, 32, 3286–3290.

[11] Zhang J. Q., Chen J. J., Zhou N. J., Characteristic of jet droplet produced by bubble bursting on the free liquid surface, Chemical Engineering Science, 2012, 68:151-156

A fully submerged flap-type wave energy converter

by I.F. Noad† and R. Porter*
University of Bristol, University Walk, Bristol, BS8 1TW, UK.
†imogen.noad@bris.ac.uk
*richard.porter@bris.ac.uk

Highlights:

• A novel solution method for the diffraction and radiation of waves by a fully submerged flap is presented.

• Insight is given into the effects on performance seen as a result of fully submerging the device.

1. Introduction

The abundance of energy available in ocean waves has long been of interest as a potentially significant source of renewable energy, numerous devices having been conceived over the years with the intent of converting it into a usable form. However, difficulties arise in engineering devices which are both efficient and able to survive the harsh marine environment. One of the devices which has recently emerged as a promising candidate for large scale commercial success in the UK is the Oyster device, a buoyant flap-type device under development by Aquamarine Power LTD[1]. Although engineering development challenges remain this has been successfully demonstrated in terms of numerical modelling, laboratory testing and in full-scale deployment. Thus, interest has turned to mathematically modelling devices of this type with a significant contribution having been made by Renzi & Dias (2013).

With the issue of survivability firmly in mind, the purpose of the present paper is to investigate the impact on the performance characteristics of such devices when they are fully submerged and thus sheltered from the most extreme conditions which are seen in the surface region. To that end a novel semi-analytic solution method is developed.

2. Formulation

Cartesian coordinates have been chosen with the origin at the mean free surface level and z pointing vertically upwards. The fluid has density ρ and is of constant, finite depth h. The hydrodynamic model assumes the flap to be infinitely thin and buoyant so that when at rest it occupies the vertical plane $\{x = 0, -a < y < a, -h < z < -h + b\}$, where $b < h$. It is hinged along a horizontal axis $(x, z) = (0, -h + c)$, which is denoted in figure 1 by P. Above its pivot the flap is free to move and below it is held fixed and vertical. The fluid is incompressible and inviscid, the flow

[1]http://www.aquamarinepower.com/

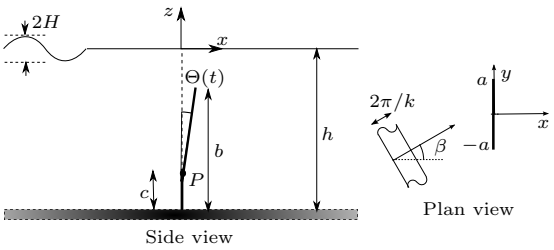

Figure 1: Side and plan views of the flap converter used in the hydrodynamic model.

is irrotational and the flap oscillations are assumed to be of small amplitude. A standard linearised theory of water waves is used.

Small amplitude plane waves of radian frequency ω are incident from $x < 0$, making an anti-clockwise angle $\beta \in (-\pi/2, \pi/2)$ with the positive x-direction.

After removing the harmonic time-dependence, the velocity potential is decomposed as

$$\phi(x, y, z) = A\phi^S(x, y, z) + \Omega\phi^R(x, y, z) \qquad (1)$$

where Ω is the complex angular velocity, $A = igH/2\omega\psi_0(0)$ ensures an incident wave height H and ψ_0 is a normalised depth eigenfunction which will be defined later. Here ϕ^S and ϕ^R are associated with the scattered and radiated wave fields respectively. They satisfy

$$\nabla^2\phi^{S,R} = 0 \qquad (2)$$

in the fluid,

$$\phi^{S,R}_z - \frac{\omega^2}{g}\phi^{S,R} = 0 \qquad (3)$$

on $z = 0$, and

$$\phi^S_z = 0 \qquad \text{and} \qquad \phi^R_z = 0 \qquad (4)$$

on $z = -h$. Further, we have

$$\phi^S_x(0^\pm, z) = 0 \qquad \text{and} \qquad \phi^R_x(0^\pm, z) = u(z) \qquad (5)$$

for $-a < y < a$ and $-h < z < -h + b$, where

$$u(z) = \begin{cases} 0, & z \in [-h, -h + c] \cup [-h + b, 0] \\ z + h - c, & z \in [-h + c, -h + b]. \end{cases} \qquad (6)$$

The incident wave is given by

$$\phi^I(x,y,z) = e^{ik(x\cos\beta - y\sin\beta)}\psi_0(z) \tag{7}$$

where k satisfies $\omega^2 = gk\tanh kh$ and $\psi_0(z)$ is a normalised depth eigenfunction defined by

$$\psi_0(z) = N_0^{-1/2}\cosh k(z+h), \tag{8}$$

with $N_0 = \frac{1}{2}(1+\sinh(2kh)/(2kh))$. The potentials ϕ^R and $\phi^D \equiv \phi^S - \phi^I$ describe outgoing waves at large distances from the flap.

In the frequency domain, the equation of motion of the flap is

$$-i\omega I\Omega = -\frac{iC}{\omega}\Omega + F_w + F_e \tag{9}$$

where I denotes the moment of inertia and C the restoring moment, quantities determined by the physical properties of the flap. F_w is the time-independent wave torque and is written as

$$F_w = AF_S + \Omega F_R \tag{10}$$

where

$$F_{S,R} = -i\omega\rho\int_{-a}^{a}\int_{-h}^{0} P^{S,R}(y,z)u(z)\,dz\,dy \tag{11}$$

and

$$P^{S,R}(y,z) = \phi^{S,R}\left(0^+,y,z\right) - \phi^{S,R}\left(0^-,y,z\right) \tag{12}$$

is the pressure difference across $x=0$. Further decomposition of the radiation force F_R yields

$$F_w = AF_S + (i\omega\mathcal{A} - \mathcal{B})\Omega \tag{13}$$

where the real quantities $\mathcal{A}(\omega)$ and $\mathcal{B}(\omega)$ are the added mass and radiation damping coefficients. Finally, we decide the mechanism for power take-off should take the form of a linear damping force and write

$$F_e = -\lambda\Omega \tag{14}$$

where λ is assumed to be a real constant so that the power and velocity are in phase. It may then be shown (see Evans & Porter (2012) for example) that the capture factor can be written as

$$\hat{l} = \hat{l}_{max}\frac{2\mathcal{B}}{\mathcal{B}+|Z|}\left(1 - \frac{(\lambda-|Z|)^2}{|\lambda+Z|^2}\right) \tag{15}$$

where

$$\hat{l}_{max} = \frac{1}{2a}\frac{|AF_S|^2}{8\mathcal{B}W_{inc}} \tag{16}$$

is the maximum capture factor, achieved through optimal tuning ($\lambda = |Z|$) at resonance ($|Z| = \mathcal{B}$), W_{inc} is the power per unit width of incident wave and

$$Z = \mathcal{B} - i\omega\left(\mathcal{A} + I - \frac{1}{\omega^2}C\right). \tag{17}$$

Further, the optimal capture factor is given by

$$\hat{l}_{opt} = \frac{2\mathcal{B}}{\mathcal{B}+|Z|}\hat{l}_{max} \tag{18}$$

and is achieved through optimal tuning.

Thus, in order to study the performance of the device we must first determine the hydrodynamic coefficients $\mathcal{A}$ and $\mathcal{B}$ along with the exciting force F_S. These depend on the solution of the hydrodynamic problems for ϕ^S and ϕ^R and that is where our attention turns now.

3. Solution of the hydrodynamic problems

3.1 The scattering problem

The scattering problem deals with the diffraction of the incident wave when the flap is held fixed vertically. We consider the potential $\phi^D \equiv \phi^S - \phi^I$ associated with the diffracted waves. By antisymmetry we have $\phi^D(x,y,z) = -\phi^D(-x,y,z)$ and so we only need the solution in $x>0$. We define the Fourier transform of $\phi^D(x,y,z)$ by

$$\overline{\phi}^D(x,l,z) = \int_{-\infty}^{\infty}\phi^D(x,y,z)e^{-ily}\,dy. \tag{19}$$

Then, taking Fourier transforms with respect to y of the governing Laplace equation (2) gives

$$\left(\nabla_{xz}^2 - l^2\right)\overline{\phi}^D = 0. \tag{20}$$

The most general solution of (20) which also satisfies (3) and (4) with the correct outgoing wave behaviour is

$$\overline{\phi}^D(x,z) = \sum_{r=0}^{\infty} B_r(l)e^{-\lambda_r x}\psi_r(z) \tag{21}$$

where $B_r(l)$ are unknown coefficients,

$$\psi_r(z) = N_r^{-1/2}\cos k_r(z+h), \tag{22}$$

$N_r = \frac{1}{2}(1+\sin(2k_rh)/(2k_rh))$ and k_r are the positive roots of $\omega^2 = -gk_r\tan k_rh$ for $r=1,2,....$ This is consistent with the definition of $\psi_0(z)$ if we let $k_0 = -ik$ and the functions $\psi_r(z)$ for $r=0,1,2,...$ form a complete set of normalised depth eigenfunctions. Further,

$$\lambda_r(l,k_r) = \begin{cases} \left(k_r^2+l^2\right)^{1/2}, & \text{for } r=1,2,... \\ \left(l^2-k^2\right)^{1/2}, & \text{for } r=0 \text{ and } |l|\geq k \\ -i\left(k^2-l^2\right)^{1/2}, & \text{for } r=0 \text{ and } |l|<k \end{cases}$$

where the choice of branch for λ_0 ensures the radiation condition is satisfied.

We formulate the problem in terms of the unknown pressure difference across the flap, defined in (12). Taking Fourier transforms and using the orthogonality of

the depth eigenfunctions we gain the following equations for the unknown coefficients

$$B_r(l) = \frac{1}{2h}\int_{-h}^{-h+b} \overline{P}^S(l,z')\psi_r(z')dz' \equiv \frac{1}{2h}\int_{-h}^{-h+b}\int_{-a}^{a} P^S(y',z')\psi_r(z')e^{-ily'}dy'\,dz' \tag{23}$$

for $r = 0, 1, 2, ...$

Invoking the inverse Fourier transform of (21) results in an integral representation for $\phi^D(x, y, z)$

$$\phi^D(x,y,z) = \frac{1}{2\pi}\int_{-\infty}^{\infty}\sum_{r=0}^{\infty} B_r(l)\, e^{-\lambda_r x}\psi_r\,(z)\, e^{ily}\, dl \tag{24}$$

where $B_r(l)$ for $r = 0, 1, 2, ...$ are expressed in terms of $P^S(y', z')$ in (23). Applying the condition on the flap,

$$\frac{\partial\phi^D}{\partial x}(0^{\pm}, y, z) = -\frac{\partial\phi^I}{\partial x}(0^{\pm}, y, z) \tag{25}$$

for $-a < y < a$ and $-h < z < -h+b$, then results in an integral equation for $P^S(y, z)$. This may not be solved analytically, instead we employ a Galerkin expansion method. We incorporate the known square-root endpoint behaviour through the approximation

$$P^S(y,z) \simeq \sum_{n=0}^{2N+1}\sum_{p=0}^{P}\alpha_{np}w_n(y)\tau_p(z) \tag{26}$$

where

$$w_n(y) = \frac{e^{in\pi/2}}{a(n+1)}\sqrt{a^2-y^2}U_n\left(\frac{y}{a}\right) \tag{27}$$

and

$$\tau_p(z) = \frac{2e^{ip\pi}}{\pi b(2p+1)}\sqrt{b^2-(z+h)^2}U_{2p}\left(\frac{z+h}{b}\right) \tag{28}$$

and $U_n(\cos\theta) = \sin((n+1)\theta)/\sin\theta$ are Chebyshev polynomials of the second kind. Substituting for $P^S(y', z')$ in the integral equation, multiplying through by $-(1/\pi)w_m^*(y)\tau_q(z)$ and integrating over $-a < y < a$, $-h < z < -h+b$ results in the following system of linear equations

$$\sum_{n=0}^{2N+1}\sum_{p=0}^{P}\alpha_{np}M_{npmq} = D_m(\beta)G_{q0} \tag{29}$$

for $m = 0, ..., 2N+1$ and $q = 0, ..., P$, where

$$M_{npmq} = \sum_{r=0}^{\infty} G_{pr}G_{qr}K_{nm}^{(r)} \tag{30}$$

with

$$K_{nm}^{(r)} = \frac{1}{4}\int_{-\infty}^{\infty}\frac{\lambda_r(l,k_r)}{l^2}J_{n+1}(al)J_{m+1}(al)\,dl \tag{31}$$

and

$$G_{pr} = \begin{cases} N_r^{-1/2}J_{2p+1}(k_r b)/k_r h & \text{for } r \geq 1 \\ (-1)^p N_0^{-1/2}I_{2p+1}(kb)/kh & \text{for } r = 0 \end{cases} \tag{32}$$

and

$$D_m(\beta) = \begin{cases} -i\cot\beta J_{m+1}(ka\sin\beta) & \text{if } \beta \neq 0 \\ -\frac{1}{2}ika\delta_{m0} & \text{if } \beta = 0. \end{cases} \tag{33}$$

The integrals which determine $K_{nm}^{(r)}$ vanish when $n+m$ is odd, a rendundancy which allows us to reduce our consideration to elements for which $n + m$ is even. In order to ensure rapid convergence we use an integral result involving products of Bessel functions (Gradshteyn & Ryzhik (1981) §6.538(2)) to gain an integrand which decays like $O\left((ka)^2/l^4\right)$. Ultimately (29) then reduces to a coupled pair of systems which may be solved for the unknown expansion coefficients α_{np}.

The exciting torque on the flap may be expressed in terms of the Galerkin expansion coefficients as

$$F_S = \frac{1}{2}i\omega\rho ah^2\pi\sum_{p=0}^{P}\alpha_{0p}\hat{g}_p \tag{34}$$

where

$$\hat{g}_p = -\int_{-h}^{0}\tau_p(z)u(z)dz, \tag{35}$$

an integral which may be expressed in closed form.

3.2 The radiation problem

Applying the same solution method to the radiation problem, this time making the approximation

$$P^R(y,z) \simeq ah\sum_{n=0}^{2N+1}\sum_{p=0}^{P}\beta_{np}w_n(y)\tau_p(z) \tag{36}$$

for the unknown pressure difference across the flap, results in the following system of linear equations

$$\sum_{n=0}^{2N+1}\sum_{p=0}^{P}\beta_{np}M_{npmq} = E_m\hat{g}_q \tag{37}$$

for $m = 0, ..., 2N+1$ and $q = 0, ..., P$. Here M_{npmq} is defined identically to before,

$$E_m = \frac{1}{2}\delta_{m0} \tag{38}$$

and $\hat{g}_q$ is given in (35).

More rapid convergence of the integrals defining $K_{nm}^{(r)}$ may be achieved as before. Ultimately, having solved for the unknown expansion coefficients β_{np}, we find that the radiation torque is given by

$$F_R = -\frac{1}{2}i\omega\rho a^2h^3\pi\sum_{p=0}^{P}\beta_{0p}\hat{g}_p. \tag{39}$$

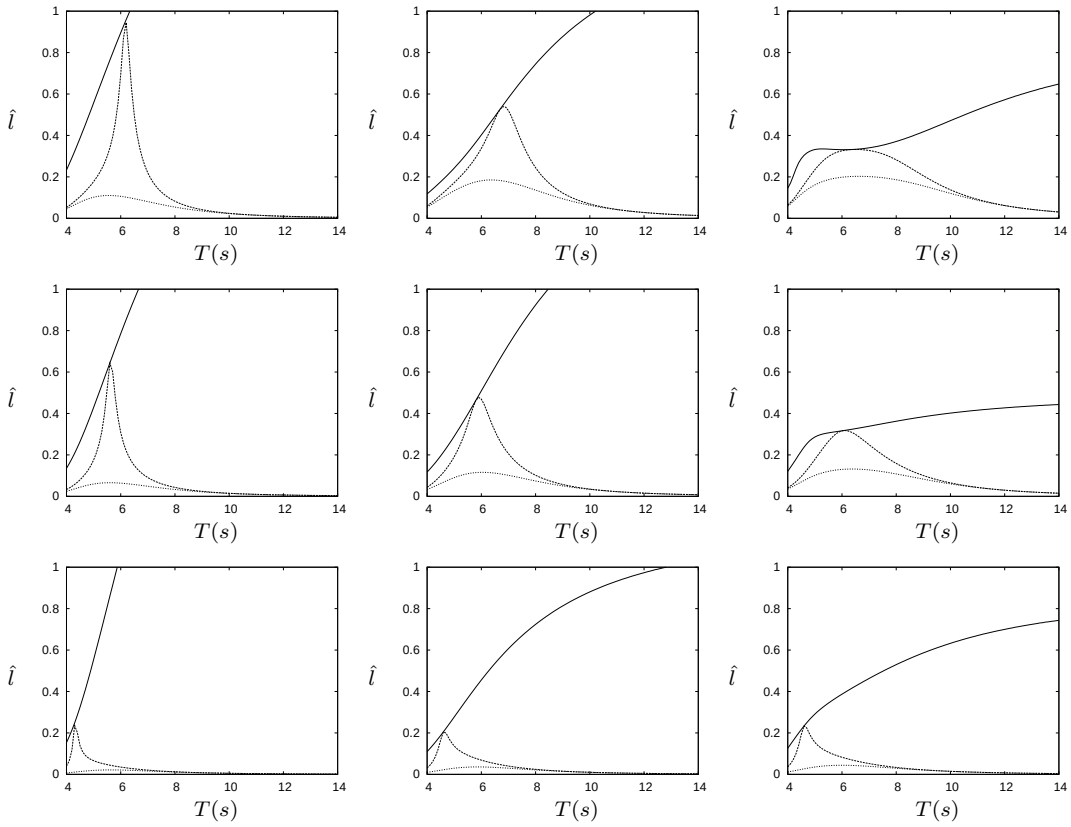

Figure 2: Capture factors plotted as a function of wave period $T(s)$ for flaps of various lengths and heights in water of fixed depth $h = 12m$. The hinge height is fixed at $c = 0.2h$ and the power take-off at $\lambda = 8$. The rows show results for $b/h = 0.9, 0.8$ and 0.6 respectively, moving down the page, whilst the columns show results for $a/h = 0.5, 1.0$ and 2.0, from left to right. The dotted, dashed and solid curves show $\hat{l}$, $\hat{l}_{opt}$ and $\hat{l}_{max}$ respectively.

4. Results

Figure 2 shows the actual, optimum and maximum capture factors for a range of flap lengths and proportions of the depth taken up by the device. The results appear to be best when $b/h = 0.9$ and the top of the flap is nearest to the surface. The theoretical maximum, which forms an upper bound, is at its highest when $a/h = 0.5$ and the flap is short. However, this also corresponds to a narrower resonant peak than that seen for longer devices. Whilst an improvement in the actual capture factors over those plotted may be achieved through optimal tuning, this unfortunate combination of characteristics leads to a narrow peak and actual capture factors being limited to a mean value of about 0.3. By comparison, when optimally configured, the results for a surface piercing device are close to 0.7 for a broad range of periods (Noad & Porter, 2015). It is not obvious that such a deterioration in performance should be seen as a result of complete submersion. Indeed, high capture factors are maintained for some devices and this is the case for the fully submerged device of Crowley, Porter & Evans (2014) for example.

References

1. Renzi, E. and Dias, F., 2013, Hydrodynamics of the oscillating wave surge converter in the open ocean. *Eur. J. Mech. B/Fluids* **41** 1-10.

2. Evans, D.V. and Porter, R., 2012, Wave energy extraction by coupled resonant absorbers. *Phil. Trans. Royal Soc. A* **370** 315-344.

3. Gradshteyn, I.S. and Ryzhik, I.M., 1981, Tables of integrals, series and products. *Academic Press, New York 10003.*

4. Noad, I.F. and Porter, R., 2015, Optimisation of arrays of flap-type oscillating wave surge converters. *Submitted to Applied Ocean Research.*

5. Crowley, S.H., Porter, R. and Evans, D.V., 2014, A submerged cylinder wave energy converter with internal sloshing power take-off. *Eur. J. Mech. B/Fluids* **47** 108-123.

30th International Workshop on Water Waves and Floating Bodies
12-15th April 2015, Bristol (UK)

A new linearization method for vectorial Morison equation

C. Ouled Housseine, C. Monroy and F. Bigot

Research Department, Bureau Veritas
67-71, Boulevard du Chateau
Neuilly-sur-Seine, France

Introduction

For offshore and naval applications, the wave forces acting on slender parts of the bodies can be described by the Morison equation, which expresses the overall force in terms of a nonlinear drag force and a linear inertia force that define an additional damping and added mass.

In frequency domain, the drag term of the Morison force needs to be linearized. In case of irregular waves, Borgman [1] linearized the wave drag force in the Morison Equation using the random Gaussian process assumption for the wave velocity. This linearized form was developed for a fixed vertical cylinder under the action of a unidirectional wave.

However, for seakeeping and mooring analysis, the vectorial Morison equation is used to evaluate the wave force on slender bodies in multi-directional flows. Therefore, this linearized form needs to be modified since it does not obey vector operation rules.

The purpose of this paper is to present a new linearization method for the multi-directional flow. A comparison between the new and the classical linearization will be presented against the time domain simulation in the case of cylinder.

Morison equation and limitations of the existing linearization

In unidirectional wave flow, the Morison load on a fixed circular cylinder (per unit length), without current, is given by:

$$f_{Morison} = (1 + C_m)\rho S\dot{u} + \frac{1}{2}C_d\rho D\,|u|\,u \tag{1}$$

Where D stands for the cylinder diameter and S its section, C_d the drag coefficient, C_m the inertia coefficient and u the wave field velocity projected on the perpendicular plane to the principal axis element. If the cylinder is in motion x, the velocity is replaced by the relative-velocity projected on the same plane:

$$f_{Morison} = (1 + C_m)\rho S\dot{u} - C_m\rho S\ddot{x} + \frac{1}{2}C_d\rho D\,|u - \dot{x}|\,(u - \dot{x}) \tag{2}$$

The drag f_d and the inertia f_i loads can be written as:

$$f_i = (1 + C_m)\rho S\dot{u} - C_m\rho S\ddot{x} \tag{3}$$

$$f_d = \frac{1}{2}C_d\rho D\,|u - \dot{x}|\,(u - \dot{x}) \tag{4}$$

In the vectorial case, the Morison equation involves only the two velocity components along the plane normal to the axis of the element. Therefore, for the cylinder local coordinate system (O, x, y, z) such as (Oz) the element axis, the Morison equation can be written as:

$$f_{Morison} = (1 + C_m)\rho S\begin{bmatrix} \dot{u_x} \\ \dot{u_y} \end{bmatrix} - C_m\rho S\begin{bmatrix} \ddot{x} \\ \ddot{y} \end{bmatrix} + \frac{1}{2}C_d\rho D\sqrt{(u_x - \dot{x})^2 + (u_y - \dot{y})^2}\begin{bmatrix} u_x - \dot{x} \\ u_y - \dot{y} \end{bmatrix} \tag{5}$$

In irregular waves and without current, u is a zero mean Gaussian random process. With the same assumptions as above, Borgman showed that the autocorrelation function $R_{f_df_d}$ of the drag force, can be written simply in terms of the wave velocity autocorrelation function R_{uu} ([2] and [1]):

$$R_{f_df_d}(\tau) = (\frac{1}{2}C_d\rho D)^2 R_{uu}(0)^2 G(r) \tag{6}$$

Where:

$$r = \frac{R_{uu}(\tau)}{R_{uu}(0)} \tag{7}$$

$$G(r) = \frac{1}{\pi}\left((4r^2 + 2)arsin((r) + 6r\sqrt{1 - r^2}\right) \tag{8}$$

With the first order linearization of the function $G(r)$ (because $0 \leqslant r \leqslant 1$), it is possible to write:

$$R_{f_d f_d}(\tau) \approx (\frac{1}{2} C_d \rho D)^2 R_{uu}(0)^2 \frac{8}{\pi} r \tag{9}$$

The Energy spectral density is then calculated, using the Fourier transform of the above equation:

$$S_{f_d f_d}(f) \approx (\frac{1}{2} C_d \rho D)^2 \frac{8}{\pi} \sigma_u^2 S_{uu}(f) \tag{10}$$

Finally, the linearized force is given by:

$$f_d \approx \frac{1}{2} \rho C_d D \sqrt{\frac{8}{\pi}} \sigma_u u \tag{11}$$

Where σ_u is the standard deviation of the wave velocity. In the case where the cylinder is in motion, we suppose that the relative-velocity is also a zero mean random Gaussian process so we can write:

$$f_d \approx \frac{1}{2} C_d \rho D \sqrt{\frac{8}{\pi}} \sigma_{u-\dot{x}} (u - \dot{x}) \tag{12}$$

In the vectorial case, this method faces two problems:

1. A common linearization constant cannot be calculated for the two components of the Morison drag force.
2. The characteristics of water particle velocity (orbital velocity for example) cannot be modeled efficiently without considering the correlation between between the 2 directional velocities.

One way to solve the first problem is to linearize each component of the drag force separately by considering a unidirectional flow following each wave velocity direction:

$$\overrightarrow{f_d} = \begin{bmatrix} f_x \\ f_y \end{bmatrix} = \frac{1}{2} C_d \rho D \sqrt{\frac{8}{\pi}} \begin{bmatrix} \sigma_{u_x} & 0 \\ 0 & \sigma_{u_y} \end{bmatrix} \begin{bmatrix} u_x \\ u_y \end{bmatrix} \tag{13}$$

However, this method will underestimate the drag force since in its original form (Eq.5), the velocity norm depends on the two other velocity components and will be always higher than the norm of one component. Thus, a more complete model needs to be developed for an accurate linearization form.

Analytical model

We consider a fixed cylinder in 3D random wave flow. The cylinder is not supposed to be necessarily vertical since we will work on its local coordinate system $(\overrightarrow{e_1}, \overrightarrow{e_2}, \overrightarrow{n})$ with $\overrightarrow{n}$ the cylinder's vector axis. We will be limited in our study to a two-dimensional case since the Morison equation depend on the projected wave velocity as mentioned previously. Thus, the drag force and the wave velocity can be written in the local coordinate system $(\overrightarrow{e_1}, \overrightarrow{e_2}, \overrightarrow{n})$ as:

$$\overrightarrow{u} = \begin{bmatrix} u_1 \\ u_2 \end{bmatrix} \quad , \quad \overrightarrow{f_d} = \begin{bmatrix} f_1 \\ f_2 \end{bmatrix} \tag{14}$$

Extending the Borgman's linearization to a two-dimensional case seems to be difficult for the reason that the autocorrelation function of each force component is complicated to determine analytically (need to calculate multiple integrals of 4 variables: $u_1(t)$, $u_2(t)$, $u_1(t+\tau)$ and $u_2(t+\tau)$). For simplification, a classic random Gaussian vector model will be used for $\overrightarrow{u}$ so its probability density function can be defined as:

$$p(u_1, u_2) = \frac{1}{2\pi\sigma_1\sigma_2\sqrt{1-{\rho_{12}}^2}} exp\left(- \frac{\frac{{u_1}^2}{{\sigma_1}^2} + \frac{{u_1}^2}{{\sigma_1}^2} - \frac{2u_1u_2\rho_{12}}{\sigma_1\sigma_2}}{2(1-\rho_{12}^2)} \right) \tag{15}$$

Where σ_1 and σ_2 are respectively the standard deviations of the two zero mean random Gaussian variables u_1 and u_2 and $\rho_{12} = \frac{cov(u_1,u_2)}{\sigma_1\sigma_2}$ the correlation coefficient. The idea of this linearization is based on the energy dissipation of the Morison drag force which will be calculated for the exact and the linearized formulations. The linearization coefficient must provide the same energy dissipation for each model.

Mathematically, we define the energy dissipation as the expected value $< . >$ of the drag force mechanical power $\overrightarrow{f_d}.\overrightarrow{u}$. For the linear model, we can write:

$$\overrightarrow{f_L} = \frac{1}{2} C_d \rho D K \overrightarrow{u} = K_D K \overrightarrow{u} \tag{16}$$

So the dissipated energy E_L is calculated by:

$$E_L = < \overrightarrow{f_L}.\overrightarrow{u} > = K_D K < u_1^2 + u_2^2 > = K_D K \left(\sigma_1^2 + \sigma_2^2\right) \tag{17}$$

For the exact model, we can write:

$$E = < \overrightarrow{f_d}.\overrightarrow{u} > = K_D < \left(u_1^2 + u_2^2\right) \| \overrightarrow{u} \| > = K_D < \left(u_1^2 + u_2^2\right)^{\frac{3}{2}} > \tag{18}$$

Using the expected value mathematical definition:

$$E = \frac{K_D}{2\pi\sigma_1\sigma_2\sqrt{1-{\rho_{12}}^2}} \iint_{\mathbb{R}^2} \left(u_1^2 + u_2^2\right)^{\frac{3}{2}} exp\left(-\frac{\frac{{u_1}^2}{{\sigma_1}^2} + \frac{{u_1}^2}{{\sigma_1}^2} - \frac{2u_1u_2\rho_{12}}{\sigma_1\sigma_2}}{2(1-\rho_{12}^2)} \right) \mathrm{d}u_1 \mathrm{d}u_2 \tag{19}$$

With the polar transformation: $u_1 = rcos(\theta)\sigma_1$ and $u_2 = rsin(\theta)\sigma_2$, the previous double integral can be simplified in a single elliptic integral:

$$E = \frac{3K_D}{2\sqrt{2\pi}} \int_0^{2\pi} \frac{\left(\left(\sigma_1 cos(\theta)\right)^2 + \left(\sigma_2 sin(\theta)\right)^2 \right)^{\frac{3}{2}}}{\sqrt{1-\rho_{12}sin(2\theta)}} \mathrm{d}\theta \tag{20}$$

By considering $E = E_L$, we obtain:

$$K = \frac{3}{2\sqrt{2\pi}} \int_0^{2\pi} \frac{\left(\left(acos(\theta)\right)^2 + \left((1-a)sin(\theta)\right)^2 \right)^{\frac{3}{2}}}{\sqrt{1-\rho_{12}sin(2\theta)}} \mathrm{d}\theta \ \sqrt{\sigma_1^2 + \sigma_2^2} \tag{21}$$

Where:

$$a = \frac{\sigma_1^2}{\sigma_1^2 + \sigma_2^2} \tag{22}$$

Finally, the linearized force is given by:

$$\overrightarrow{f_L} = \frac{3K_D}{2\sqrt{2\pi}} \int_0^{2\pi} \frac{\left(\left(acos(\theta)\right)^2 + \left((1-a)sin(\theta)\right)^2 \right)^{\frac{3}{2}}}{\sqrt{1-\rho_{12}sin(2\theta)}} \mathrm{d}\theta \ \sqrt{\sigma_1^2 + \sigma_2^2} \ \overrightarrow{u} \tag{23}$$

As the result shows, the linearization coefficient is expressed as a function of two non-dimensional parameters. Using this two-parameter model, we fulfill requirements imposed by the two problems mentioned in the previous section:

- The parameter a represents the two-dimensional aspect of the flow (problem 1).
- The parameter ρ_{12} expresses the correlation relation between the two velocity components u_1 and u_2 and therefore the wave field characteristics: linear, orbital, ... (problem 2).

For verification, in the case of a unidirectional wave field following $\overrightarrow{e_1}$ direction ($a = 1$ and $\rho_{12} = 0$), we have:

$$K = \frac{3}{2\sqrt{2\pi}} \int_0^{2\pi} |cos(\theta)|^3 \mathrm{d}\theta \ \sigma_1 = \sqrt{\frac{8}{\pi}} \sigma_1 \tag{24}$$

We obtain the Borgman linearization constant in the unidirectional case.

For a 3D wave field, with a structure containing several Morison elements, each element is discretized on Gauss integration points. The relative velocity of each integration point is projected in the local coordinate system of the element. Next, K and $\overrightarrow{f_L}$ are calculated in the local coordinate system then expressed in the global system coordinate and summed.

Simulation results and discussion

In order to test this linearization, the Morison drag force is calculated in irregular waves for a fixed cylinder in time and frequency domains. Cylinder dimensions are ($R = 1m$ x $H = 3m$) and $C_d = 0.7$. As a wave model, a JONSWAP spectrum is used with the parameters $H_s = 1.0m$, $T_p = 12.0s$ and $\gamma = 1.0$. The water

depth is infinite. The wave time signal has been generated for 3 hours using a linear reconstruction of the wave spectrum with a random phase for each frequency component. The power spectral density (PSD) of each signal has been calculated in order to obtain the drag force RAOs.

To show the difference between the two linearizations (scalar and vectorial) in different configurations, the force is calculated for the vertical and the horizontal position of the cylinder (linear and orbital wave fields) for two headings $\beta = 0°$ (head) and $\beta = 45°$ (diagonal). The axis of cylinder is (Oz) in the vertical case and (Ox) in the horizontal case. The wave heading is defined by the angle between the propagation direction and the positive direction of the axis (Ox).

The figures bellow give the RAOs of the drag force components. As the results show, the frequency domain solution seems to underestimate the drag force, due to the linearization effect. In addition, for $\beta = 0°$, the projected wave field is unidirectional so the two linearizations give the same results (figure 1 for the horizontal and vertical case and are in agreement with the time domain solution (green plot).

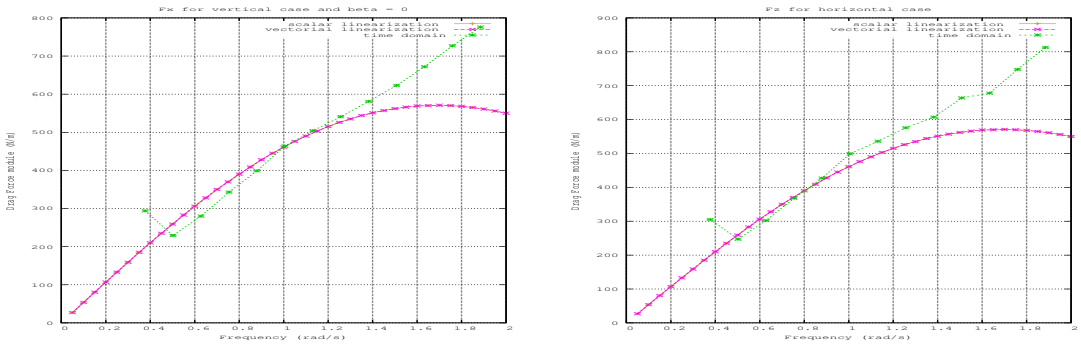

(a) F_x Vertical case (b) F_z Horizontal case

Figure 1: $\beta = 0°$

However, for the diagonal heading $\beta = 45°$ (figure 2), since the drag force will depend on more than one velocity direction ((Ox) and (Oy) in the vertical case and (Oz) and (Oy) in the horizontal case), the vectorial linearization (pink plot) is more accurate and the scalar linearization (brown plot) underestimates the drag force especially for the horizontal case which corresponds to the circular wave filed.

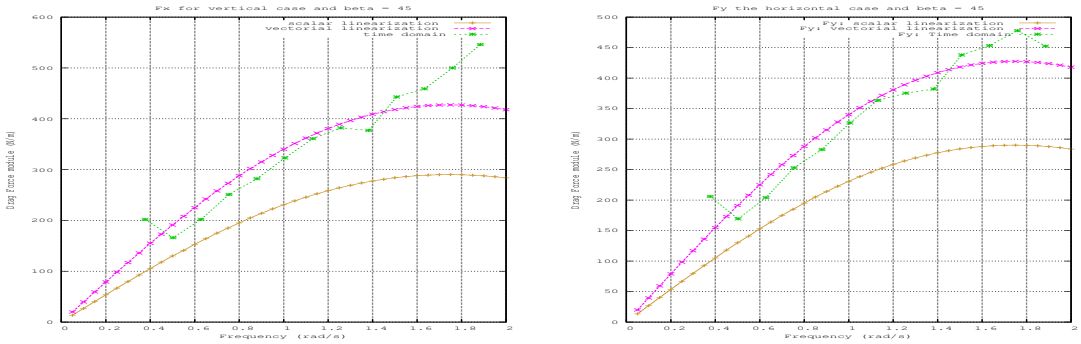

(a) F_x Vertical case (b) F_y Horizontal case

Figure 2: $\beta = 45°$

References

[1] Leon E. Borgman. Random hydrodynamic forces on objects. *Ann. Math. Statist.*, pages 37–51, 1967.

[2] R. L. Wiegel. Waves and their effects on pile-supported structures. pages 1–10, 1969.

30th International Workshop on Water Waves and Floating Bodies
April 12-15, 2015, Bristol, UK

Hydrodynamic Interaction of Two Bodies in Waves

Heather Peng, Md. Ashim. Ali and Wei Qiu*
Advanced Marine Hydrodynamics Laboratory
Faculty of Engineering and Applied Science, Memorial University
St. John's, NL, Canada
*Email: qiuw@mun.ca

Introduction

When multiple vessels or floating bodies are in a close proximity, the large resonant elevations of free surface occur in the gap. Most of the linear seakeeping programs currently used by the industry, for example, those solving the body interaction problem in the frequency domain, over-predict free surface elevations between vessels and hence the low-frequency loadings on the hull. This can cause problems in the design of the fenders, hawsers and loading arms and lead to unsafe operations.

Many researchers have made contributions to overcome this problem. Huijsmans et al. (2001) developed a lid technique to suppress the unrealistic values of low-frequency forces and wave elevations. In their work, the free surface in the gap is replaced by a flexible plate. A generalized mode technique was used by Newman (2003) to model the free surface. Chen (2005) proposed a linear dissipation term to modify the free-surface equation.

These methods however require to input the artificial damping factors. Efforts have made to determine the damping factors. For example, Pauw et al. (2007) compared the experimental data and numerical results for two side-by-side LNG carriers in head seas. The numerical results were based on a panel method code using a flexible damping lid in the gap region. Various gap widths were used in an attempt to obtain rationale for predicting suitable damping factors. No unique value for the damping factor was found to cover all the measured cases. Molin et al. (2009) used a set of massless plates in the gap between two fixed barges and a quadratic damping force was applied to the plates. The numerical results were compared to the model tests of two rectangular barges in irregular waves. A drag coefficient of 0.5 for determining the quadratic damping force led to good agreement with experimental data.

Since these potential-flow based methods are inadequate to give reasonable predictions without providing the experimental data beforehand, it is desirable to determine the damping contribution due to viscous flow based on CFD methods.

This paper presents the preliminary numerical and experimental studies of wave elevations between two bodies in close proximity with an objective to quantify the contribution of viscosity. Model tests were carried out to two identical box-like bodies with round corner in waves. Motions of the bodies and wave elevations in the gap between the two bodies were measured. CFD methods solving RANS equations, based on OpenFoam and Star-CCM+, were applied to simulate the hydrodynamic interaction of the two bodies in head seas. A panel-free method based seakeeping program, MAPS0, was also used for the prediction of motions and wave elevations. The computed motions and wave elevations by CFD and MAPS0 were compared with experimental data and the solutions by the potential-flow code, WAMIT.

Numerical Methods

A frequency-domain program, MAPS0, a sub-suite of Motion Analysis Program Suite (MAPS), was used to compute the motions and wave elevations in the gap between the two bodies. MAPS is based on the panel-free method (Qiu et al., 2006) and includes programs for both frequency-domain and time-domain analysis based on the potential-flow theory. The CFD computations are based on OpenFoam and Star-CCM+.

Experimental Tests

Model tests were carried out at the towing tank of the Ocean Engineering Research Center (OERC) at Memorial University to measure the motions of two bodies and the wave elevations for a variety of wave headings and frequencies. The tank is 60 m long, 4.5 m wide and 3 m deep.

Two identical 1:60 box-like simplified FPSO models, as shown in Fig. 1, were used, which have round bilges. Each model was restrained in the tank by two soft mooring lines which allow for body motions in six degrees of freedom but prevent excessive drift motions. The body motions were measured by a Qualisys system and wave elevations at three locations in the gap were measured by wave probes. Note that model tests were also carried out for a single body.

Figure 1: Two bodies in head seas

The particulars of the model-scale ships are listed in Table 1. In this phase, model tests were conducted in regular waves. The frequencies of waves are from 3.92 rad/s to 7.16 rad/s, which is corresponding to 0.51 rad/s to 0.92 rad/s in full scale. The wave steepness was 1/30.

Table 1: Model Particulars

	Model 1	Model 2
Length(m)	1.997	1.998
Breadth(m)	0.397	0.397
Depth(m)	0.301	0.300
Draught(m)	0.103	0.104
$\Delta(kg)$	76.6	76.6
KG(m)	0.131	0.124
$R_{xx}(m)$	0.135	0.125
$R_{yy}(m)$	0.535	0.502
$GM_T(m)$	0.054	0.053

Table 2: Gaps and Locations of Wave Probes

	Unit	Model Scale
Wave Heading	*degree*	180
Gap Width 1	m	0.40
Gap Width 2	m	0.45
Gap Width 3	m	0.55
Wave Probe 1	m	(0,0,0)
Wave Probe 2	m	(0.5,0,0)
Wave Probe 3	m	(-0.5,0,0)

Numerical Results

To quantify the viscous effect on the free surface elevation in the gap between two bodies, computations were performed for head seas using Star-CCM+, OpenFoam, MAPS0 and the low-order frequency-domain program WAMIT. The numerical results were then compared with the experimental data. Three gaps, 0.4m, 0.45m and 0.55m in model scale, were investigated. The full-scale results are presented below.

Figures 2 to 4 present the comparison of predicted wave elevations with experimental data at wave probe 1 for the three gaps, respectively. The predictions by MAPS0 and WAMIT, which are both based on the potential-flow theory, agree very well and are in good agreement with the experimental results at low frequency band. It

is also observed that there are less oscillations in the predicted elevations by MAPS0 than those by WAMIT. At the resonant frequencies, both MAPS0 and WAMIT over-predicted the wave elevations.

The predicted heave and pitch motions by MAPS0 and WAMIT for body 1 are presented in Figs. 5 to 8 for the two gaps (0.40m and 0.45m). They are in good agreement with the experimental data. The predicted heaves by MAPS0 are slight better than those by WAMIT.

Figure 9 presents the effect of gap width on the predicted wave elevations. It can be seen that the resonant wave elevation decreases with the gap width increases.

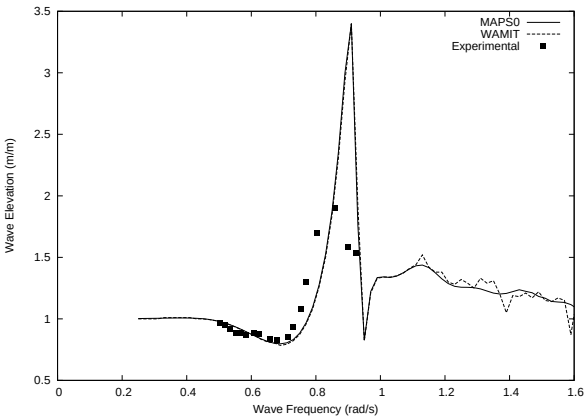

Figure 2: Wave elevation at location 1, gap=0.40m

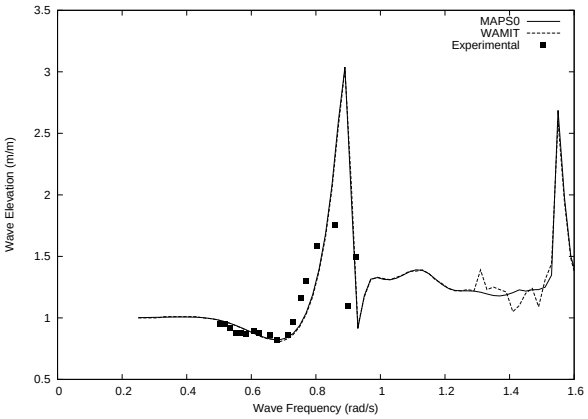

Figure 3: Wave elevation at location 1, gap=0.45m

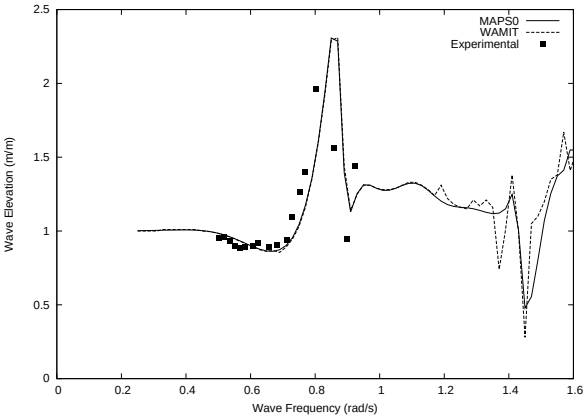

Figure 4: Wave elevation at location 1, gap=0.55m

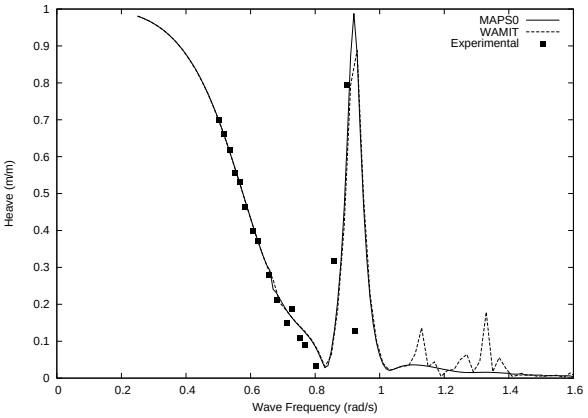

Figure 5: Heave of body 1, gap=0.40m

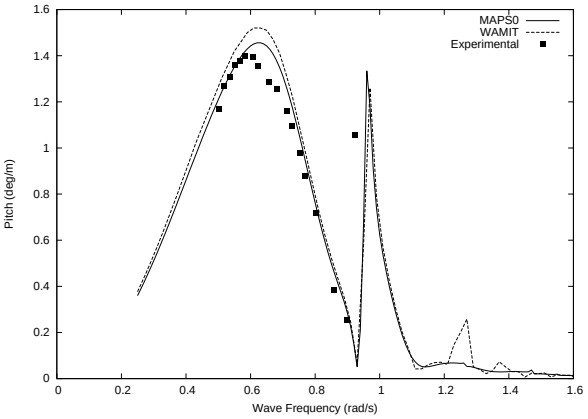

Figure 6: Pitch of body 1, gap=0.40m

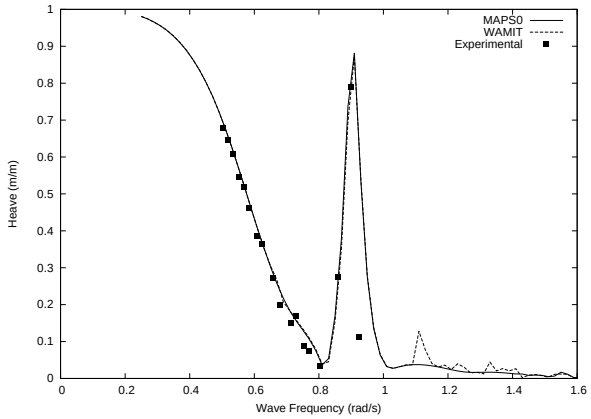

Figure 7: Heave of body 1, gap=0.45m

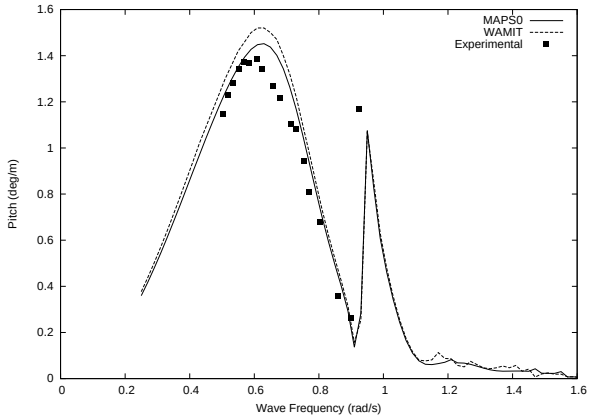

Figure 8: Pitch of body 1, gap=0.45m

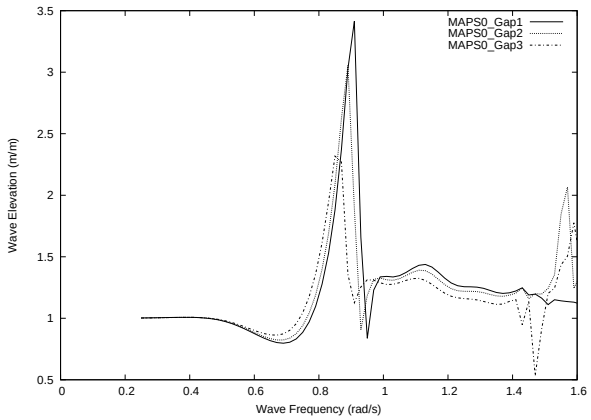

Figure 9: Wave elevations at location 1 for three gaps

Concluding Remarks

Experimental and numerical studies were carried out to investigate the hydrodynamic interaction of two side-by-side bodies in waves. Potential-flow programs based on the the panel-free method and the panel method and the CFD methods were used to compute motions of bodies and wave elevations in the gap between two bodies. The computational results were compared with experimental data. It is anticipated that the CFD results will be presented and the viscous effect will be discussed at the Workshop.

Acknowledgement

This work was supported by the Natural Sciences and Engineering Research Council (NSERC) of Canada.

References

Chen, X.B., 2005, "Hydrodynamic Analysis for Offsore LNG Terminals," Proc. International Workshop on Applied Offshore Hydrodynamics.

Huijsmans, R.H.M., Pinkster, J.A. and de Wilde, J.J., 2001, "Diffraction and Radiation of Waves Around Side by Side Moored Vessels," Proc. ISOPE2001.

Molin, B., Remy, F., Camhi, A. and Ledoux, A., 2009, "Experimental and Numerical Study of the Gap Resonances in-between Two Rectangular Barges," Proc. IMAM2009, Istanbul, Turkey.

Newman, J.N., 2003, "Application of Generalized Models for the Simulation of Free Surface Patches in Multi Body Hydrodynamics," WAMIT Consortium Report.

Pauw, W.H., Huijsmans, R.H.M. and Voogt, A., 2007, "Advances in the Hydrodynamics of Side-By-Side Moored Vessels," Proc. OMAE2007.

Qiu, W., Peng, H. and Chuang, J.M., 2006, "Computation of Wave-Body Interactions Using the Panel-Free Method and Exact Geometry," J. Offshore Mechanics and Arctic Engineering, Vol. 128, pp. 31-38.

The 30th International Workshop on Water Waves and Floating Bodies, April 2015, Bristol and Bath, UK

Long-period waves and current variations in a port due to a passing vessel

Jo Pinkster, PMH bv and Arne van der Hout , Deltares

Highlights

Comparisons are made between the results of measurements of ship-induced long waves and current variations in a port and results of computations. The computations are based on a combination of potential flow calculations using the double-body assumption to determine the initial forcing due to the sailing ship and linear 3-d diffraction computations are used to determine the response of the port structure and a moored vessel to the forcing. In the process FFT methods are used to transform time-domain forcing to frequency-domain input for diffraction computations .RAOs generated by the 3d-diffraction are transformed to transient time-domain results which are directly comparable with measured data. Comparisons of wave elevations and currents are given for three port configurations.

Introduction

In this contribution results of model tests and computations on ship-induced long waves and current velocities will be presented. The model test program was part of the Joint Industry Project (JIP) ROPES, acronym for Research On Passing Effects of Ships. The objective of the ROPES JIP was to increase insight in the factors influencing forces on ships moored in ports caused by passing vessels. A review of this project may be found in Ref. (1). The objective of a part of the scale model tests carried out by Deltares was to investigate and to better understand the hydrodynamic forces on a moored ship due to a passing ship, especially related to the influence of (complex) harbour geometries. In complex harbour geometries, a large passing vessel will generate long waves consisting of so-called 'draw-down' which travel with the passing vessel and transient long period oscillatory waves in the form of standing waves or seiches. Such effects may also be of influence on the forces on moored vessels.The objective of the model tests carried out by Deltares was to produce a high-quality dataset, which included the effects of currents and the influence of harbour geometries on mooring forces , transient long waves and current effects.

The following sections describe briefly the model test set-up and the measurement set-up with respect to wave elevations and currents induced by a passing vessel. The results of the measurements are compared with the results of computations based on potential flow including free surface effects. The forces on the moored vessel are not treated.

Set-up of the model tests

The model tests were carried out in the Atlantic Basin at Deltares. An overview of these tests excluding comparisons with computed results is given in Ref. (2). The basin has a total length of 74.7 m which included , among others ,a dissipative beach at both ends. The effective length of the test section is 43.9 m with a width of 8.7 m. For the model tests , the basin was fitted with a towing carriage to which the a model of a Post-Panamax container vessel was connected. The vessel was captive in the surge, sway, roll and yaw directions while it was able to squat and trim freely. The model scale amounted to 1: 100.Several lay-outs of a straight channel with a width of 270 m with different basins to one side of the channel were modeled. The water depth in the channel and the basins amounted to 18 m full scale.

The vessels

The main dimensions of the passing Post-Panamax and the moored Panamax vessels are given below:

	Units	Post-Panamax	Panamax
Lpp	m	331.5	255.0
Beam	m	42.9	32.26
Draft	m	14.5	12.0
Displacement	m^3	127037	58660

Measurement equipment

A total of five capacitance type Wave Height Measurement (WHM) gauges were used to measure surface elevation at different positions in the basin. The measurement positions of the WHM gauges for each layout are indicated in the figures of the layouts. The WHM01 gauge was placed at the reference position x, y = (0 m, 12 m) for all tests.

The other WHM gauges were placed at strategic positions throughout the basin. In general, one gauge was placed in ahead , one aft, and one next to the mid ship position of the moored ship. In the test with a side basin, also two WHM gauges were placed in the corners of the basin to detect standing waves, since this is where the largest standing wave amplitudes are expected. In the tests of Layout 1 (straight channel), one wave gauge (WHM05) was placed outside the measurement channel on the other side of the channel wall. This was done to check the amount of wave penetration underneath or between the concrete building blocks of the channel wall (unwanted leakage).
The horizontal velocity components of the water was measured using five Electro Magnetic Velocity probes (EMS). A sample rate of 30 Hz was used. During the measurements, the signal was filtered by the data-acquisition software using a moving average filter with a window of 0.1 s (model scale). The measurement positions of the EMS probes for each layout are specified in the accompanying figures. EMS probes measure the flow velocity at a certain vertical position in the water column. In almost all cases the probes measured the flow velocity at a depth of 7 m under the water surface, which is approximately at half draught of the passing vessel. Only in Layout 1, EMS04 was positioned to measure at a water depth of z=-12 m, to check the variation of flow velocity over the draught of the passing vessel.

Test program
In this contribution some results of wave elevations and current velocities is shown for three port layouts. For all three cases the passing speed of the Post-Panamax vessel corresponded with 10.4 kn and the centerline of the vessel was 107 m from the bank nearest the side-basin. In the model tests the passing vessel started from X= +3000 m and slowly accelerated up to the required speed in order to minimize additional transient waves due to the start-up. Measurements were carried out with the vessel at a constant speed. At the end of the run the vessel was decelerated and stopped at about X= -1000m. The vessel was at 10.4 kn for the part of the channel shown in the layouts. In the computations a similar procedure was followed regarding the speed of the vessel.

Computations
The computational procedure was similar to that described in Ref. (3). The computations are based on potential flow which are solved using zero-order panel methods. The procedure is carried out in four phases : firstly the time-dependent flow due to the passing vessel is solved assuming double-body flow i.e. no free-surface effects. At each time-step the strengths of the sources on the passing vesssel are solved based on the near-field assumption i.e. both vessels and the fairway are modeled and included in the solution process. Secondly , the thus derived time-dependent source strengths on the passing vessel are used to compute the time-dependent velocity and pressure disturbances at the fairway boundaries and the moored vessel i.e. 'undisturbed' velocity components and pressure due only to the sources on the passing vessel. These time-dependent disturbances are transformed to frequency-domain vectors (FFT) which form the input to the third phase which consists of solving a zero-speed frequency-domain 3-d diffraction problem involving the fairway and the moored vessel but which excludes the passing vessel. Based on the frequency-domain solutions, RAOs of fluid velocity components , wave elevations and forces on the moored vessel are computed. Finally, the RAOs are transformed to transient time-domain results using Inverse FFT methods. These records are directly comparable with the measured time-records of velocity components and wave elevation.
In a previous IWWWFB workshop Ref. (4) some preliminary comparisons of results of measurements and computations of wave elevations were shown for a simple rectangular barge entering a restriction in a straight canal. In the contribution we are presenting new data for more realistic hull forms and port geometries and a more detailed flow analyses.

Results
In fig. 1 through fig. 6 the layout and comparisons of computed and measured results for three selected cases are shown. All data are for full scale. Computed results are given in red.
The results for Layout 1 show a lack of oscillatory waves and current variations compared to the results for Layout 2 which clearly shows strong seiching in the side basin. Layout 7 shows slightly more seiche effects than Layout 1 but clearly significantly less than Layout 2. Small, short secondary waves are discernable in the measured wave records only.

References
1. van den Boom, H.J.J, Pluijm, M. and Pauw, W. :" Ropes; Joint Industry Project on Effect of Passing Ships on Moored Vessels" , PIANC , San Francisco, USA, 1-5 June 2014.
2. Hout, A.J. van der, M.P.C de Jong and S.P. Reijmerink, “Passing-ship effects in complex geometries and currents”, PIANC, San Francisco, USA, 1-5 June 2014.
3. Pinkster, J.A. ,“The Influence of a Free Surface on Passing Ship Effects,” Int. Shipbuilding Progress, 51, No. 4, 2004.
4. Pinkster, J.A. and Naaijen, P. " Predicting the effect of passing ships" , IWWWFB , 2003

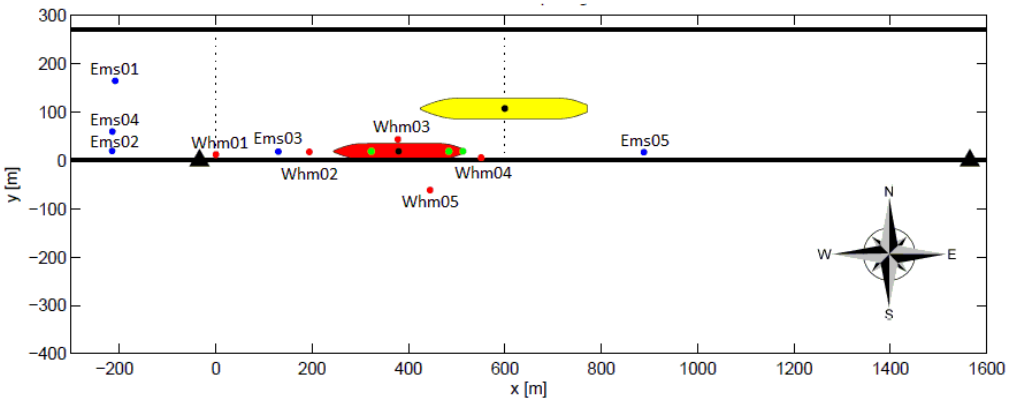

Figure 1 Laout 1 ; Straight channel. Width 270 m, waterdepth 18.0 m

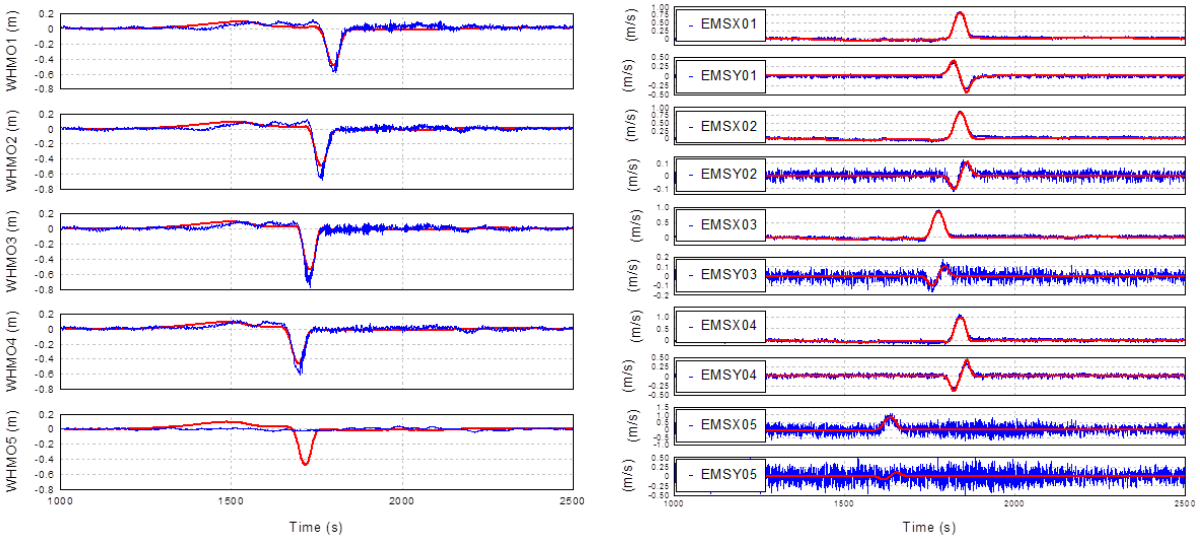

Figure 2 Results for Layout 1. Wave elevations left, X- and Y- Current velocity components right.

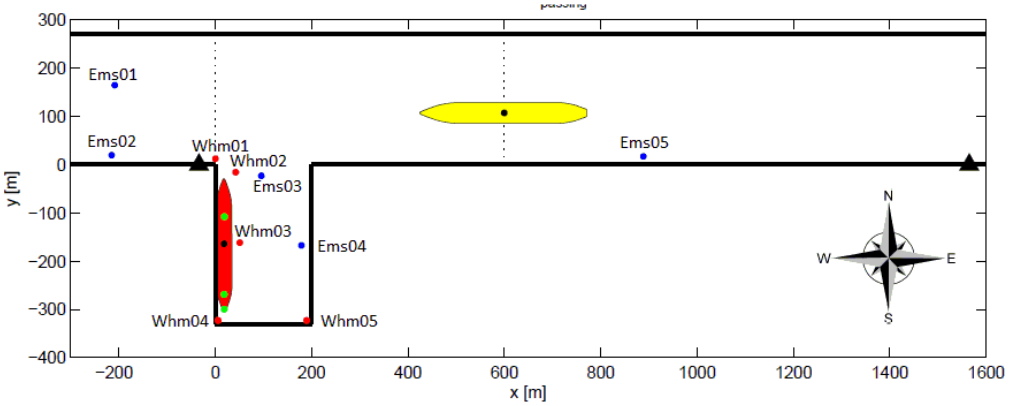

Figure 3 Layout 2 ; Narrow basin at right-angle to channel axis. Water depth in basin 18 m.

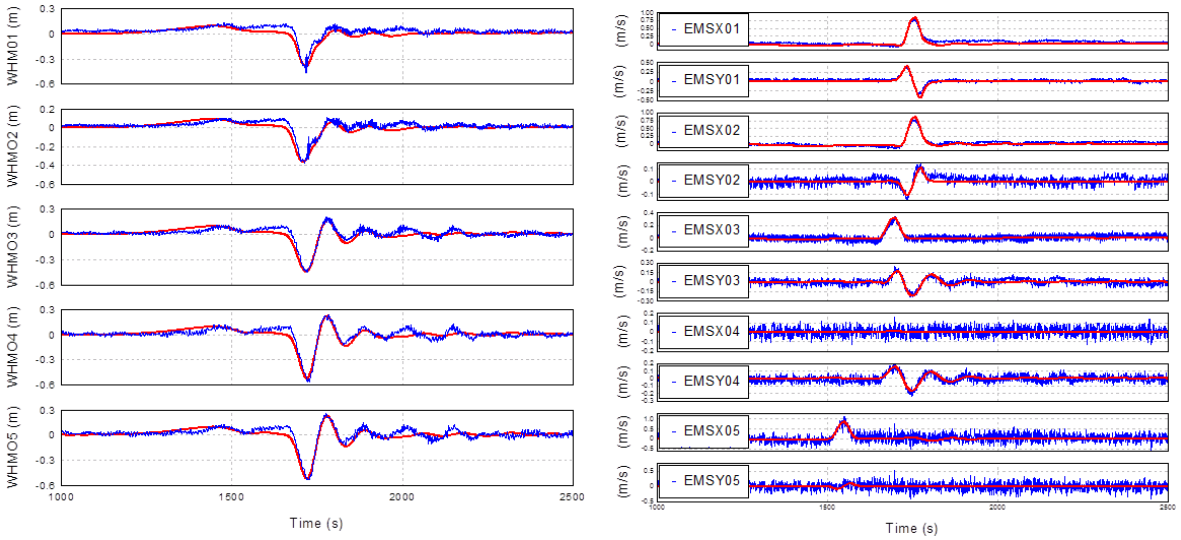

Figure 4 Results for Layout 2. Wave elevations left, X- and Y- Current velocity components right.

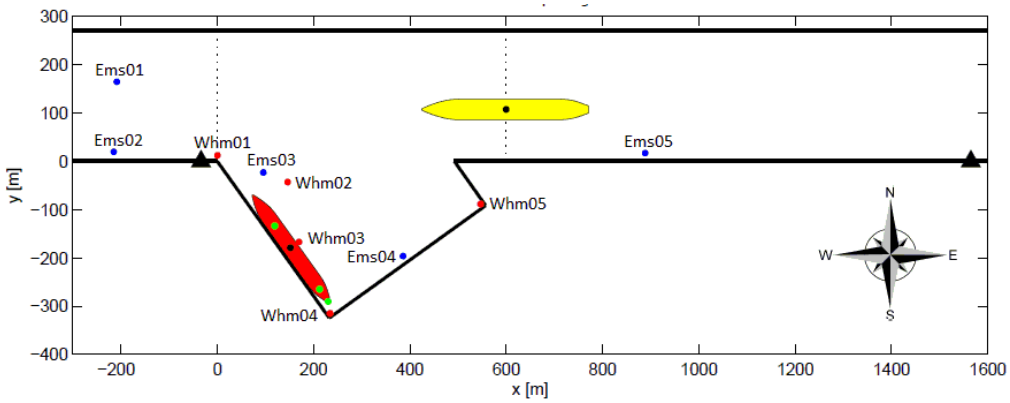

Figure 5 Layout 7 ; Basin at an angle to the channel axis. Water depth in basin 18 m.

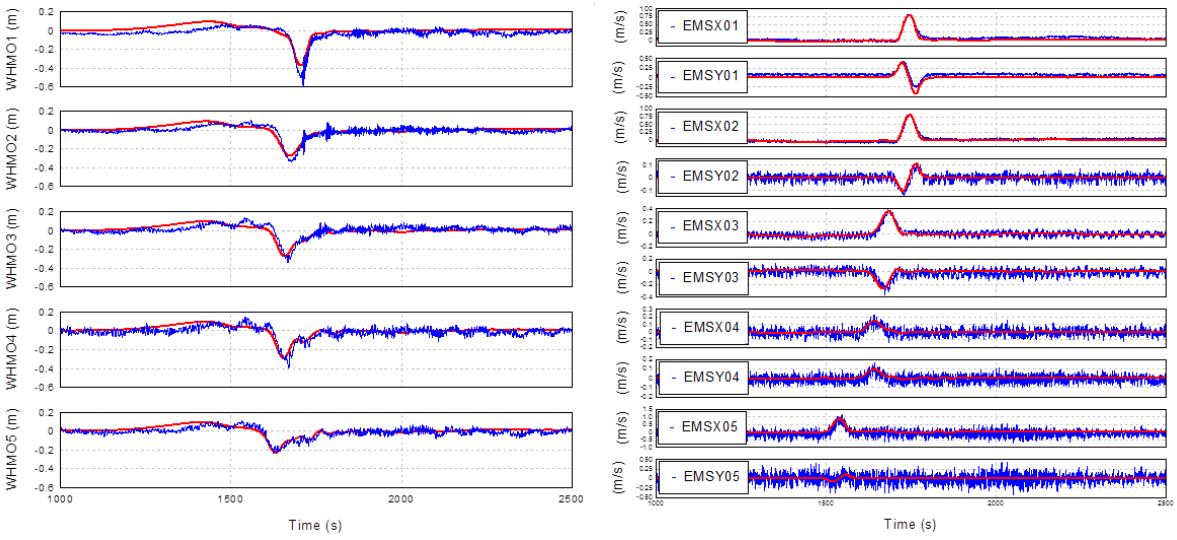

Figure 6 Result for Layout 7. Wave elevations left, X- and Y- Current velocity components right.

Extended Mild-Slope Equations for Compressible Fluids

E. Renzi[1*], C. Cecioni[2], G. Bellotti[2], P. Sammarco[3], F. Dias[1]

[1] Earth Institute, UCD School of Mathematical Sciences
University College Dublin, Belfield Dublin 4, Ireland.
[2] Department of Engineering, University of Roma Tre,
Via Vito Volterra 62, 00146 Rome, Italy
[3] Department of Civil and Computer Science Engineering,
University of Rome Tor Vergata, Via del Politecnico 1, 00133 Rome, Italy
email: emiliano.renzi@ucd.ie

1 Introduction

In this paper we derive new forms of the mild-slope equation (MSE) for water waves in a weakly compressible fluid on a slowly varying bathymetry, with surface and bottom disturbances. The MSE is a powerful tool to model the refraction-diffraction dynamics of water waves propagating on a variable bathymetry [1]. Traditionally, mild-slope models are derived by assuming that the wave steepness is small, the fluid is inviscid and incompressible and the motion is irrotational. Furthermore, no disturbances are normally considered both on the free surface and at the bottom of the fluid domain [2]. In this paper we shall find new expressions of the MSE by relaxing the incompressibility hypothesis and considering both surface and bottom disturbances. We shall name the set of new formulae as the extended acoustic-gravity mild-slope equations (EAG-MSE). Such a system of equations can be implemented in numerical models for the early detection of coastal flooding based on the hydro-acoustic precursors of surface gravity waves (see [3]–[5]).

*New address: Department of Mathematical Sciences, Loughborough University, Loughborough, Leics, LE11 3TU, UK.

2 Mathematical model

Let us consider the motion of a slightly compressible fluid on a variable bathymetry with surface and bottom disturbances. The wave field is described by the wave equation

$$\nabla^2\Phi + \Phi_{zz} = \frac{1}{c^2}\Phi_{tt} \tag{1}$$

in the fluid domain, together with the kinematic-dynamic boundary condition on the free surface (see [5])

$$\Phi_{tt} + g\Phi_z = -\frac{P(x,y,t)}{\rho_0}, \quad z = 0, \tag{2}$$

and the no-flux condition at the bottom

$$\Phi_z + \nabla h \cdot \nabla\Phi = -h_t, \quad z = -h(x,y,t), \tag{3}$$

as in [1]. Here, $\Phi(x,y,z,t)$ is the velocity potential, ∇ is the horizontal gradient, $P(x,y,t)$ is a prescribed surface pressure disturbance, $h(x,y,t)$ denotes the seafloor, g is the acceleration due to gravity, ρ_0 is the density of the undisturbed fluid, c is the (assumed constant) speed of sound in water. A reference system $O(x,y,z)$ is set such that (x,y) lie on the horizontal plane and z is the vertical coordinate originating from the undisturbed water plane, positive upwards; t is time. Physically, P represents the action of an atmospheric pressure front, which is responsible for the generation of storm surges, while $h(x,y,t)$ is a seafloor deformation which generates tsunamis [1]. Initially we shall retain both

disturbances and derive a generalised form of the EAG-MSE. Then we shall find particularised expressions of our novel equation for each disturbance. Following [4], let us expand the velocity potential in a Galerkin series

$$\Phi(x,y,z,t) = \sum_{n=0}^{\infty} \psi_n(x,y,t)\, f_n(z, h(x,y,t)), \tag{4}$$

where the $\psi_n(x,y,t)$ are unknown functions and the $f_n(z,h)$ are the solutions of the homogeneous boundary-value problem with the local and instantaneous water depth $h(x,y,t)$ (see [1]):

$$f_n(z, h(x,y,t)) = \frac{\cosh \beta_n(z+h)}{\cosh \beta_n h}. \tag{5}$$

In the latter, the $\beta_n = \beta_n(h(x,y,t))$ solve

$$\beta_0 \quad : \quad \omega^2 = g\beta_0 \tanh \beta_0 h \tag{6}$$

$$\beta_n = i\bar{\beta}_n \quad : \quad \omega^2 = -g\bar{\beta}_n \tan \bar{\beta}_n h, \tag{7}$$

where the mathematical problem is formulated for a generic single frequency ω of the forcing spectrum [4]. The solution for the complete spectrum is easily obtained by simple Fourier superimposition of the single spectral components ([4], [1]). Physically, $n = 0$ represents the propagating gravity mode, while $n > 0$ represents propagating and evanescent hydro-acoustic modes [3]. Let us now introduce the inner product

$$\langle f(x,y,z,t), g(x,y,z,t)\rangle = \int_{-h}^{0} f(x,y,z,t)\, g(x,y,z,t)\, dz, \tag{8}$$

so that $\langle f_n, f_m\rangle$=0 if $n \neq m$. We shall also expand the surface and bottom disturbances accordingly, i.e.

$$P(x,y,t) = \sum_{n=0}^{\infty} P_n(x,y,t)\, f_n(x,y,z,t), \tag{9}$$

$$h(x,y,t) = \sum_{n=0}^{\infty} h_n(x,y,t)\, f_n(x,y,z,t) \tag{10}$$

respectively, where

$$P_n(x,y,t) = \frac{\langle P, f_n\rangle}{\langle f_n, f_n\rangle} \tag{11}$$

and

$$h_n(x,y,t) = \frac{\langle h, f_n\rangle}{\langle f_n, f_n\rangle}. \tag{12}$$

Following [2] (Section 7.2.3.3), first calculate

$$\left\langle f_m,\, \nabla^2\Phi + \Phi_{zz} - \frac{1}{c^2}\,\Phi_{tt} \right\rangle = 0, \tag{13}$$

from Eq.(1), with $m = 0, 1, \ldots$ Then substitute the expansion (4) into (13) to get

$$\begin{aligned} &\sum_{n=0}^{\infty} \left[\nabla^2\psi_n \langle f_m, f_n\rangle + 2\nabla\psi_n \cdot \langle f_m, \nabla f_n\rangle \right. \\ &+\psi_n \left\langle f_m, \nabla^2 f_n\right\rangle + \psi_n \langle f_m, f_{n_{zz}}\rangle \\ &-\frac{1}{c^2}\left(\psi_{n_{tt}} \langle f_m, f_n\rangle + 2\psi_{n_t} \langle f_m, f_{n_t}\rangle \right. \\ &\left.\left. +\ \psi_n \langle f_m, f_{n_{tt}}\rangle\right)\right] = 0, \end{aligned} \tag{14}$$

for the governing equation. Similarly, substituting (4) into (2) and (3), one gets

$$\begin{aligned} &\sum_{n=0}^{\infty} \psi_n f_m f_{n_z} = -\frac{1}{g}\sum_{n=0}^{\infty} (\psi_{n_{tt}} f_m f_n \\ &+2\psi_{n_t} f_m f_{n_t} + \psi_n f_m f_{n_{tt}}) \\ &-\frac{1}{\rho_0 g}\sum_{n=0}^{\infty} \left(P_{n_t} f_m f_n + P_n f_m f_{n_t}\right),\ z = 0 \end{aligned} \tag{15}$$

and

$$\begin{aligned} &\sum_{n=0}^{\infty} \psi_n f_m f_{n_z} = -\sum_{n=0}^{\infty} (\psi_n f_m \nabla f_n \cdot \nabla h \\ &+ \nabla\psi_n \cdot \nabla h\, f_m f_n + h_{n_t} f_m f_n + \\ &+ h_n f_m f_{n_t}),\ z = -h \end{aligned} \tag{16}$$

for the boundary conditions, respectively. Further application of the Green integral formula

$$\langle f_m, f_{n_{zz}}\rangle = -\langle f_{m_z}, f_{n_z}\rangle + [f_m f_{n_z}]_{z=-h}^{z=0} \tag{17}$$

and usage of (15)–(16), together with the properties

$$f_{n_t} = f_{n_h}\, h_t, \quad f_{n_{tt}} = f_{n_{hh}}\,(h_t)^2 + f_{n_h} h_{tt}$$

and

$$(f_{n_h})_{z=0} = (f_{n_{hh}})_{z=0} = 0,$$

transforms (14) into the sought system of expressions:

$$\sum_{n=0}^{+\infty} \left[a_{mn}\nabla^2\psi_n + \mathbf{b}_{nm} \cdot \nabla\psi_n \right.$$

$$+\left(c_{mn}-\frac{\omega^2}{g}\right)\psi_n-\frac{1}{g}\,\psi_{ntt}\Big]$$
$$=\frac{1}{c^2}\sum_{n=0}^{\infty}\left(a_{mn}\,\psi_{n_{tt}}+d_{mn}\,\psi_{n_t}\right.$$
$$\left.+\,e_{mn}\,\psi_n\right)+\frac{1}{\rho_0 g}\sum_{n=0}^{+\infty}P_{n_t}$$
$$-\sum_{n=0}^{+\infty}\left[g_{mn}\,h_{n_t}+l_{mn}\,h_n\right],\ m\in\mathbb{N},\quad(18)$$

after lengthy algebraic simplifications. In Eq. (18),

$$\begin{aligned}
a_{mn} &= \langle f_m, f_n\rangle\,,\\
\mathbf{b}_{mn} &= 2\,\langle f_m, \nabla f_n\rangle + (f_m\,f_n)_{z=-h}\,\nabla h,\\
c_{mn} &= -\,\langle f_{m_z}, f_{n_z}\rangle + \left\langle f_m, \nabla^2 f_n\right\rangle\\
&\quad + (f_m\,\nabla f_n)_{z=-h}\cdot\nabla h + \frac{\omega^2}{g},\\
d_{mn} &= 2\,\langle f_m, f_{n_h}\rangle\,h_t,\\
e_{mn} &= \langle f_m, f_{n_{hh}}\rangle\,h_t^2 + \langle f_m, f_{n_h}\rangle\,h_{tt},\\
g_{mn} &= (f_m\,f_n)_{z=-h}\\
l_{mn} &= (f_m\,f_{n_h})_{z=-h}\,h_t,
\end{aligned}$$

All the above terms depend on x, y, t via the f_n and h (see Eq.5). Expression (18) is the novel EAG-MSE for waves in a weakly compressible fluid generated by surface pressure disturbances and seafloor deformations. It represents both gravity ($n = 0$) and hydro-acoustic ($n > 0$) waves of given frequency ω [4, 5]. Note that in the limit $c \to \infty$, assuming $P = h_t = 0$ and steady-state harmonic oscillations of frequency ω, (18) fully corresponds to Massel's MSE (see equation 16 in [2]).

3 The adiabatic approximation

The adiabatic hypothesis is a frequent approximation undertaken in the modelling of acoustic-gravity waves. Within such an approximation, one neglects the cross-coupling terms in the governing equations, not allowing the normal modes to interact among themselves. This framework allows for much quicker computations, usually without significant loss of accuracy [6]. Assuming that each mode propagates without interacting with the others, the EAG-MSE (18) simplifies into

$$a_{nn}\nabla^2\psi_n + \mathbf{b}_{nn}\cdot\nabla\psi_n + \left(c_{nn}-\omega^2/g\right)\,\psi_n$$
$$-\frac{1}{g}\psi_{n_{tt}} = \frac{1}{c^2}\left(a_{nn}\psi_{n_{tt}} + d_{nn}\psi_{n_t} + e_{nn}\psi_n\right)$$
$$+\frac{1}{\rho_0 g}P_{n_t} - g_{nn}h_{n_t} - l_{nn}h_n,\quad n=0,1,\ldots\quad(19)$$

which we name the adiabatic acoustic-gravity mild-slope equation (AAG-MSE).

3.1 AAG-MSE for tsunamis (Sammarco *et al.*'s MSEWC)

Let us consider the case $P = 0$, $h = h(x, y, t)$. For a geophysical flow over a large area with a slowly varying bottom, such as a tsunami, the dependence of f_n on h can be safely neglected, so that $f_n = f_n(z)$ (see [4]) and

$$d_{nn} = e_{nn} = l_{nn} = 0. \qquad (20)$$

Furthermore, for a slowly varying depth, the higher-order terms

$$\nabla^2 f_n = O\left(\nabla^2 h\right),\quad \nabla f_n\cdot\nabla h = O\left(|\nabla h|^2\right),$$

can be neglected too, so that

$$c_{nn} = \beta_n^2 a_{nn}. \qquad (21)$$

Finally note that

$$a_{nn}\nabla^2\psi_n = \nabla\cdot(a_{nn}\nabla\psi_n) - \nabla a_{nn}\cdot\nabla\phi_n, \quad (22)$$

where

$$\nabla a_{nn} = a_{nn_h}\nabla h = \frac{\partial}{\partial h}\int_{-h}^{0} f_n^2\,dz\,\nabla h = \mathbf{b}_{nn} \qquad (23)$$

as an application of the Leibniz integral rule. Substituting (20)–(23) into (19), the latter yields finally

$$\psi_{n_{tt}}\left(\frac{C_n}{c^2}+\frac{1}{g}\right) - \nabla\cdot(C_n\nabla\psi_n)$$
$$+\left(\frac{\omega^2}{g}-\beta_n^2 C_n\right)\psi_n = D_n\,h_t. \qquad (24)$$

In Eq. (24),

$$C_n = a_{nn} = \frac{2\beta_n h + \sinh(2\beta_n h)}{4\beta_n\cosh^2(\beta_n h)}, \qquad (25)$$

$$D_n = \frac{\langle g_{nn}, f_n\rangle}{\langle f_n, f_n\rangle} = \frac{4\tanh(\beta_n h)}{2\beta_n h + \sinh(2\beta_n h)}. \qquad (26)$$

Expression (24) is the MSE for weakly compressible fluids (MSEWC) found by Sammarco *et al.* [4]. The latter allows to model the hydro-acoustic waves travelling fast ahead of an incoming tsunami generated by a seafloor movement. Such hydro-acoustic waves leave a distinctive signature on the bottom pressure that can be used for the early detection of tsunamis [3, 4].

3.2 AAG-MSE for storm surges

We shall now consider the case of a fixed bathymetry $h = h(x, y)$ and a surface pressure distribution $P(x, t)$. In such a case, $d_{nn} = e_{nn} = l_{nn} = 0$. Therefore, using again (23), expression (19) simplifies to

$$\psi_{n_{tt}} \left(\frac{C_n}{c^2} + \frac{1}{g} \right) - \nabla \cdot (C_n \nabla \psi_n) + \left(\frac{\omega^2}{g} - \beta_n^2 C_n \right) \psi_n = -\frac{B_n}{\rho_0 g} P_t, \qquad (27)$$

where

$$B_n = \frac{2 \sinh(2\beta_n h)}{2\beta_n h + \sinh(2\beta_n h)}. \qquad (28)$$

Expression (27) allows to model the hydro-acoustic precursors of storm waves over a variable 3D bathymetry.

4 Numerical computations

Numerical computations of the MSEWC have already been performed in [4], where equation (24) has been solved for constant and mild-slope domain configurations. Numerical analysis of the AAG-MSE for storm waves (27) is currently being performed for a travelling pressure perturbation. Preliminary results will be presented at the workshop.

The numerical model solves the partial differential equation by means of the Finite Element Method. The three dimensional domain is discretised into tetrahedral elements, whose minimum element size is set to be at least 1/10 of the simulated wave length, in order to correctly reproduce the wave field. Neumann type boundary conditions are applied at the boundaries of the domain. Since the mathematical problem is hyperbolic, it is solved by means of a time-marching numerical scheme. For the efficiency of the time-stepping algorithm, it is important to assemble the time independent matrices only once. We use the generalised-α method, which is a one-step implicit method for solving the transient problem. Frequency bands of defined width are selected to discretise the forcing spectrum and to solve a set of equations, as (27), each one calculated using the carrier frequency of the selected band. Then a broad frequency spectrum can be simulated by superimposing the results. The numerical solution is obtained using the software COMSOL Multiphysics.

The work of E.R. is funded by the AXA Research Fund. F.D. is supported by the ERC-2011-AdG 290562-MULTIWAVE.

References

[1] Mei, C.C., Stiassnie, M. & Yue, D. K.-P. 2005 *Theory and applications of ocean surface waves*. World Scientific, USA.

[2] Massel, S.R. 2013 *Ocean Surface Waves*. World Scientific, USA.

[3] Stiassnie, M. 2010 Tsunamis and acoustic-gravity waves from underwater earthquakes. *J. Eng. Math.* 67, 23–32.

[4] Sammarco, P., Cecioni, C., Bellotti, G. & Abdolali, A. 2013 Depth-integrated equation for large-scale modelling of low-frequency hydroacoustic waves. *J. Fluid Mech.* 722 (R6), 1–10.

[5] Renzi, E. & Dias, F. 2014 Hydro-acoustic precursors of gravity waves generated by surface pressure disturbances localised in space and time. *J. Fluid Mech.* 754, 250–262.

[6] Jensen, F.B., Kuperman, W.A., Porter, M.B., Schmidt, E. 2011 *Computational Ocean Acoustics*. Springer, USA.

Localisation in water wave and thin plate problems

Sebastian Rupprecht[1] **Malte A. Peter**[1] **Luke G. Bennetts**[2] **Hyuck Chung**[3]

[1]**Institute of Mathematics, University of Augsburg, Germany**

[2]**School of Mathematics, University of Adelaide, Australia**

[3]**School of Computer and Mathematical Sciences, Auckland University of Technology, NZ**

E-mail addresses: sebastian.rupprecht@math.uni-augsburg.de, peter@math.uni-augsburg.de, luke.bennetts@adelaide.edu.au, hchung@aut.ac.nz

Highlights

- Simulations obtained for water waves over rough seabed and waves in rough in vacuo plate.
- Attenuation rates of effective and individual wave fields extracted, compared and found to differ.

1 Introduction

Ocean surface waves attenuate with distance travelled into the sea-ice covered ocean (Meylan et al., 2014). This is reminiscent of the wave localisation phenomenon, which occurs in many branches of wave science. For an incident wave train propagating into a rough (randomly disordered) medium, wave localisation refers to exponential attenuation (on average) of the wave train in the rough medium. (Alternative theories have also been proposed to explain wave attenuation in the ice-covered ocean, e.g. the viscous ice model of Keller, 1998.)

Wave propagation in the ice-covered ocean is conventionally modelled using linear potential-flow theory for the water and thin-plate theory for the ice cover. Bennetts & Peter (2012) conducted a preliminary investigation of wave localisation in the ice-covered ocean due to ice roughness. They modelled the roughness as variations in stiffness and mass of the ice, which are known up to a characteristic length and a root-mean-square amplitude. They extended the multiple-scale method of Mei & Hancock (2003) and Mei et al. (2005) for free-surface waves over a rough seabed to derive a semi-analytic expression for the attenuation rate.

The multiple-scale method is based on the effective wave field, i.e. the mean wave field with respect to realisations of the random medium. Bennetts et al. (2015) showed individual wave fields attenuate far slower than the effective wave field for the rough seabed problem, using large ensembles of numerical solutions for randomly generated realisations of the bed profile.

Here, we extend the study of Bennetts et al. (2015) to problems involving thin plates, with the aim of establishing if effective media theory is valid to study wave propagation in the ice-covered ocean. We begin by summarising the methods and results of Bennetts et al. (2015) for a rough seabed in intermediate depth. Then, we apply the method to a rough thin plate in vacuo. In both cases, we compare the mean attenuation rates of individual wave fields to the attenuation rates of corresponding effective wave fields.

2 Free-surface/rough-bed problem

Let spatial locations in a long transect of the ocean be defined by the Cartesian coordinate system (x, z). Horizontal locations are defined by the coordinate x. Vertical locations are defined by the coordinate z. The vertical coordinate points upwards and has its origin set to coincide with the equilibrium position of the ocean surface.

Consider a monochromatic wave propagating in the positive x-direction. The wave amplitude is assumed to be sufficiently small with respect to the wavelength, λ, that linear theory is applicable. In open water, the wavenumber, $k = 2\pi/\lambda$, is related to the angular frequency, ω, via the dispersion relation $k\tanh(kh) = K$, where $K = \omega^2/g$, h denotes the fluid depth and $g \approx 9.81\,\mathrm{m\,s^{-2}}$ denotes acceleration due to gravity.

Consider a seabed that fluctuates about $z = -\bar{h}$, where $\bar{h}$ is an intermediate depth, i.e. $k\bar{h} = \mathrm{O}(1)$. The fluctuations have a known characteristic length, l, and root-mean-square amplitude, ε, which is also referred to as the roughness amplitude. We assume $\varepsilon \ll 1$ for consistency with the multiple-scale method although this is not required for a numerical scheme. The function $z = -h(x)$, where $h(x) = \bar{h} - \varepsilon p(x)$ and $p = \mathrm{O}(1)$, is used to denote the location of the bed.

Under the usual assumptions of linear, time-

harmonic wave theory, the velocity field of water particles in the ocean is defined as the gradient of $\mathrm{Re}\{(g/\mathrm{i}\omega)\phi(x,z)\mathrm{e}^{-\mathrm{i}\omega t}\}$. The (complex-valued) velocity potential, ϕ, satisfies Laplace's equation in the undisturbed fluid domain, i.e.

$$\partial_x^2\phi + \partial_z^2\phi = 0 \quad (-h < z < 0). \tag{1a}$$

An impermeability condition is applied on the seabed, i.e.

$$\partial_z\phi + h'(\partial_x\phi) = 0 \quad \text{on} \quad z = -h(x). \tag{1b}$$

The velocity potential is coupled to the wave elevation, denoted $z = \mathrm{Re}\{\eta(x)\mathrm{e}^{-\mathrm{i}\omega t}\}$, via free-surface conditions applied at the equilibrium ocean surface. The free-surface conditions are

$$\phi = \eta \quad \text{and} \quad \partial_z\phi = K\eta \quad \text{on} \quad z = 0, \tag{1c}$$

which are combined into the single condition $\partial_z\phi = K\phi$ $(z = 0)$ for the velocity potential.

Consider the problem in which the roughness extends over a long, finite interval $x \in (0, L)$. The bed is otherwise flat and extends to infinity in both positive and negative horizontal directions. A unit-amplitude incident wave is prescribed at $x \to -\infty$. The incident wave is defined by the velocity potential $\phi = \mathrm{e}^{\mathrm{i}kx}w(z)$, where $w(z) = \cosh\{k(z+h)\}/\cosh(kh)$. We seek the resulting wave elevation in the interval containing the rough bed.

Let the rough bed profile, $h(x)$ $(0 < x < L)$, be approximated by a piece-wise constant function on M sub-intervals — the so-called step approximation — and let $(-\infty, 0)$ and (L, ∞) be the 0th and $(M+1)$th sub-intervals, respectively. We denote the value of the function in the mth sub-interval as h_m, and set it to be equal to the value of the continuous bed profile at the mid-point.

In the mth sub-interval, we have

$$\phi(x,z) = \left(a_m\mathrm{e}^{\mathrm{i}k_m x} + b_m\mathrm{e}^{-\mathrm{i}k_m x}\right)w_m(z), \tag{2}$$

where k_m is the wavenumber for depth h_m and w_m is the corresponding vertical mode. The quantities a_m and b_m are the wave amplitudes. Incident wave forcing from $x \to -\infty$ only is set via $a_0 = 1$ and $b_{M+1} = 0$.

Wave fields in adjacent sub-intervals are related to one another at the interface between the sub-intervals via continuity conditions, which are enforced in a weak sense. An iterative algorithm is used to calculate the amplitudes a_m $(m = 1, \ldots, M+1)$ and b_m $(m = 0, \ldots, M)$. Bennetts and Squire (2009) give full details of the algorithm. The wave elevation, η, is subsequently recovered via the first component of equation (1c).

Wave elevations are calculated for a large ensemble of randomly generated realisations of the bed profile. The bed profiles share the same amplitude, ε, and characteristic length, l. The relationship between the ensemble of bed profiles is expressed via the autocorrelation condition

$$\langle p(x)p(x-\xi)\rangle = q(|\xi|), \tag{3}$$

where $\langle\cdot\rangle$ denotes the ensemble average of the included quantity with respect to realisations. We prescribe the Gaussian autocorrelation function $q(\xi) = \mathrm{e}^{-\xi^2/l^2}$, noting Mei & Hancock (2003) showed an exponential autocorrelation function gives almost identical results. The characteristic length, l, is hence referred to as the correlation length from here on.

Two measures of the exponential attenuation rate are obtained from the ensemble of wave elevations. First, an attenuation rate, $Q_{\mathrm{eff}}^{(\mathrm{rs})}$, is extracted from the effective wave elevation, $\langle\eta\rangle$. The attenuation rate, in this case, is defined via

$$|\langle\eta\rangle| \propto \mathrm{e}^{-Q_{\mathrm{eff}}^{(\mathrm{rs})}x} \quad (0 < x < L). \tag{4}$$

It is calculated using a least-squares minimisation routine. Second, an attenuation rate, $Q_{\mathrm{ind}}^{(\mathrm{rs})}$, is calculated as the ensemble average of attenuation rates of individual wave elevations. The attenuation rate is defined as $Q_{\mathrm{ind}}^{(\mathrm{rs})} = \langle Q_i\rangle$, where Q_i is the attenuation rate extracted from the individual wave elevation $\eta = \eta_i$, i.e.

$$|\eta_i| \propto \mathrm{e}^{-Q_i x} \quad (0 < x < L). \tag{5}$$

We generate individual realisations of p using a harmonic random process of the form

$$p(x) = \sqrt{\frac{2}{N}}\sum_{n=1}^{N}\cos\left(f_n x + g_n\right) \quad (N \gg 1). \tag{6}$$

The frequencies f_n and phases g_n $(n = 1, \ldots, N)$ are independently chosen and identically distributed random variables. The standard deviation of the bed profile, with respect to realisations, at all spatial locations x is normalised to unity. We prescribe probability density functions for frequencies f_n and phases g_n $(n = 1, \ldots, N)$ to satisfy the Gaussian autocorrelation condition (3). The phases are selected from a uniform distribution over the interval $[0, 2\pi)$. The frequencies are selected from a Gaussian distribution with zero mean and standard deviation equal to $\sqrt{2}/l$.

Fig. 1 shows example individual wave elevations and corresponding effective wave elevations,

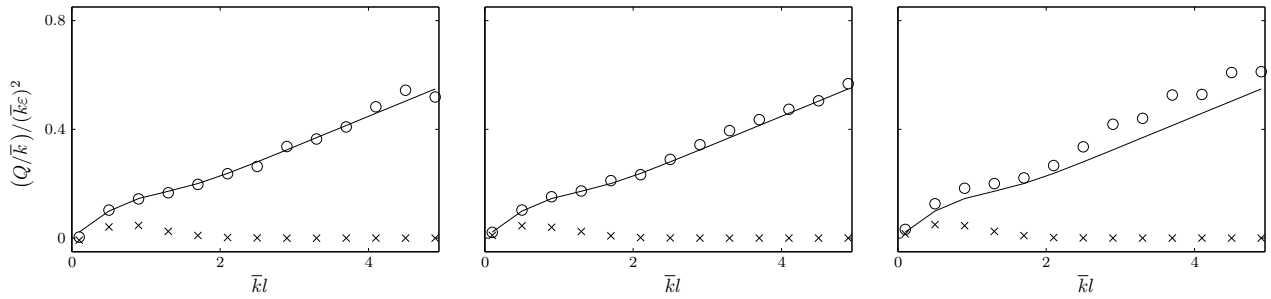

Fig. 2: Attenuation of individual (×) and effective (○) wave elevations, for $\bar{k}\varepsilon = 10^{-2}$ (left), 10^{-1} (middle) and 2×10^{-1} (right). Multiple-scale approximation is shown for comparison (—).

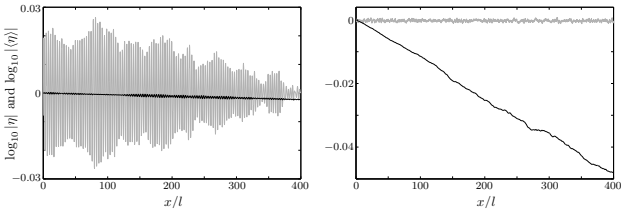

Fig. 1: Example individual wave elevations (grey) and corresponding effective wave elevations (black), for $\bar{k}\varepsilon = 10^{-2}$ and $\bar{k}l = 0.9$ (left) and 5 (right).

for a non-dimensional roughness amplitude $\bar{k}\varepsilon = 10^{-2}$, and correlation lengths $\bar{k}l = 0.9$ and 5. The wavenumber $\bar{k}$ corresponds to the mean depth $\bar{h}$, and the intermediate water depth $\bar{k}\bar{h} = 1$ is set.

The smaller correlation length is chosen to produce visible (although weak) attenuation of the individual wave elevation. The corresponding effective wave elevation attenuates slightly more rapidly than the individual wave elevation.

The largest correlation length is chosen to produce maximal attenuation of the effective wave elevation. The corresponding individual elevation does not attenuate (on the scale shown). Attenuation of the effective elevation is, therefore, not related to the individual elevations.

Fig. 2 shows attenuation rates predicted by the numerical simulations, scaled by $(\bar{k}\varepsilon)^2$, as functions of non-dimensional correlation length, for non-dimensional roughness amplitudes $\bar{k}\varepsilon = 10^{-2}$, 10^{-1} and 2×10^{-1}. The multiple-scale approximation (Bennetts et al., 2015) is also shown for comparison.

Attenuation rates of the individual wave elevations have qualitative and quantitative properties markedly different from those of the effective wave elevations. The qualitative behaviour of the attenuation rate of individual wave elevations is intuitive. The attenuation rate is approximately zero (on the linear scale shown) for the smallest non-dimensional correlation length considered, $\bar{k}l = 0.1$. In this regime the random bed fluctuations are too rapid to be seen by the waves (homogenisation limit). The attenuation rate is also approximately zero for correlation lengths greater than two. The roughness in this regime is too mild to modulate the waves. The attenuation rate is only non-zero for correlation lengths between these two regimes, where the roughness is long enough to be seen by the waves and short enough to modulate the waves.

Attenuation of the effective wave elevation is therefore not indicative of attenuation of individual wave elevations for the regime studied. Although the rough seabed forces a random component of the individual wave elevations, the individual wave elevations do not attenuate. We deduce that the dominant source of attenuation of the effective wave elevation is wave cancellation, i.e. decoherence.

3 In vacuo plate problem

Next, we consider an infinitely long rough thin plate in vacuo. The problem is one-dimensional in the horizontal coordinate x. The spatial part $u(x)$ of the plate deflection $\mathrm{Re}\{u(x)\mathrm{e}^{-\mathrm{i}\omega t}\}$ satisfies the thin plate equation

$$\beta\partial_x^4 u - \gamma\omega^2 u = 0 \quad (-\infty < x < \infty), \qquad (7)$$

where β is the constant plate stiffness and $\gamma(x)$ is its varying mass.

With the same step approximation as in the rough-bed problem, the deflection in the mth subinterval can be expressed as

$$u(x) = a_m^{(0)}\mathrm{e}^{\mathrm{i}\kappa_m x} + a_m^{(1)}\mathrm{e}^{-\kappa_m x} + b_m^{(0)}\mathrm{e}^{-\mathrm{i}\kappa_m x} + b_m^{(1)}\mathrm{e}^{\kappa_m x}, \qquad (8)$$

where the wavenumber κ_m is $\kappa(x) = (\omega^2\gamma(x)/\beta)^{\frac{1}{4}}$, evaluated at the midpoint of the mth sub-interval. The wave amplitudes $a_m^{(0)}$ and $b_m^{(0)}$ correspond to right- and left-travelling waves, respectively, whereas $a_m^{(1)}$ and $b_m^{(1)}$ correspond to the evanescent waves, which decay to the right and left, respectively.

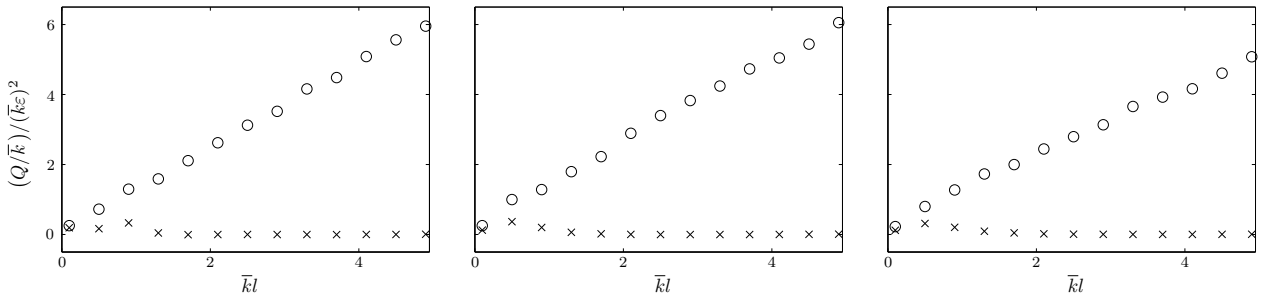

Fig. 4: As in Fig. 2 but for in vacuo plate problem.

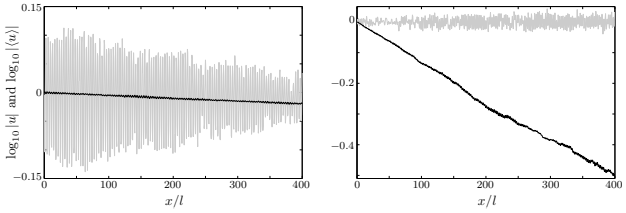

Fig. 3: As in Fig. 1 but for in vacuo plate problem.

The wavenumber is written as $\kappa(x) = \bar{\kappa} - \varepsilon p(x)$, where $\bar{\kappa}$ is its mean. The fluctuation p is as defined in Section 2.

As for the rough-bed problem, the extent of the plate roughness is restricted to the long finite interval $x \in (0, L)$. Outside of this interval, the wavenumber is constant. A unit amplitude wave is incident from $x \to -\infty$.

Wave fields in adjacent sub-intervals are coupled via continuity conditions of displacement, displacement velocity, bending moment and shear stress. An extended version of the iterative algorithm is used to calculate the step approximation for a given realisation of the varying wavenumber, i.e. to calculate the amplitudes $a_m^{(0)}$, $a_m^{(1)}$ $(m = 1, \ldots, M+1)$ and $b_m^{(0)}$, $b_m^{(1)}$ $(m = 0, \ldots, M)$.

Again, solutions are calculated for large ensembles of different realisations of the varying wavenumber, which share a common correlation length and roughness amplitude. Then, attenuation rates $Q_{\text{eff}}^{(\text{rs})}$ and $Q_{\text{ind}}^{(\text{rs})}$, defined in analogy to the rough bed problem, are extracted.

Figures 3 and 4 show the results for the in vacuo plate, in analogy to figures 1 and 2 for the rough bed, respectively. As can be seen, the behaviour is very similar and the analogous conclusions are drawn.

4 Summary and discussion

Numerical results were used to show that, for small-amplitude roughness, individual wave elevations attenuate at a far slower rate than the effective wave elevation for ocean waves travelling over a rough seabed in intermediate depth and also for waves in a thin plate in vacuo. In particular, in most cases attenuation rates of individual wave elevations are too small for wave localisation to be realised.

It was found that the effective wave elevation attenuates due to wave cancellation in the averaging process. The attenuated wave energy is transferred to the random components of the individual wave fields. Use of the effective wave elevation, therefore, results in misleading predictions of attenuation, and, hence, localisation.

Acknowledgements

This work was supported by the Group of Eight, Australia, and German Academic Exchange Service (DAAD) Joint Research Co-operation Scheme. LB acknowledges funding support from the Australian Research Council (DE130101571) and the Australian Antarctic Science Grant Program (Project 4123).

References

L. G. Bennetts and M. A. Peter, Approximations of wave propagation in one-dimensional multiple scattering problems with random characteristics, In: Proc. 27th IWWWFB (ed. H. B. Bingham et al.), Copenhagen (Denmark), pp. 9–12 (2012).

L. G. Bennetts, M. A. Peter, and H. Chung, Absence of localisation in ocean wave interactions with a rough seabed in intermediate water depth *Q. J. Mech. Appl. Math.* (2015), in press.

L. G. Bennetts and V. A. Squire, Wave scattering by multiple rows of circular ice floes, *J. Fluid Mech.* **639** (2009) 213–238.

J. B. Keller, Gravity waves on ice covered water, *J. Geophys. Res. 103* (1998), 7663–7669.

C. C. Mei and M. J. Hancock, Weakly nonlinear surface waves over a random bed, *J. Fluid Mech.* **475** (2003) 247–268.

C. C. Mei, M. Stiassnie, and D. K.-P. Yue, *Theory and applications of ocean surface waves. Part I: linear aspects* (World Scientific, 2005).

M. H. Meylan, L. G. Bennetts, and A. L. Kohout, In-situ measurements and analysis of ocean waves in the Antarctic marginal ice zone *Geophys. Res. Let.* **14** (2014), 5046–5051.

Inertia forces on conductor arrays in a jacket model in regular waves

H. Santo[1] (harrif.santo@eng.ox.ac.uk), P. H. Taylor[1], A. H. Day[2]

[1] Department of Engineering Science, University of Oxford,
Parks Road, Oxford OX1 3PJ, UK

[2] Department of Naval Architecture and Marine Engineering, University of Strathclyde,
Henry Dyer Building, 100 Montrose Street, Glasgow G4 0LZ, UK

- A wave phase-based force decomposition allows inertia and drag forces to be separated, we focus here on the inertia force on conductor arrays (closely spaced vertical cylinders).
- The measured inertia force coefficient of the 1st harmonic force component is very close to 2 for waves both with and without current. For waves without current, the coefficient of the 2nd harmonic force is within 10% of 5/4, the corresponding term in the FNV model. For waves with current, the coefficient of the 2nd harmonic force increases noticeably as the current increases.
- The effect of conductor spacing is investigated numerically. For the jacket end-on, even when the closest conductors touch, the change in effective C_M ~ –5%. In contrast for broadside where the spacing is effectively closer, the change is ~ +45%.

1. Introduction

The hydrodynamic loading on space-frame offshore structures has been re-visited recently by Taylor et al. (2013) and Santo et al. (2014) because of the growing interest in the oil industry in the re-assessment of ageing offshore infrastructure. For space-frame structures, the Morison equation has been used universally for design; this describes the total hydrodynamic force as a sum of drag and inertia forces (Morison et al. 1950). Typically the most extreme fluid-loading regime is dominated by drag; hence the study of Taylor et al. (2013) was focused on the behaviour of the drag term. For regular waves with in-line current, the drag term has been shown to be overestimated by the Morison equation because of the occurrence of additional blockage which further reduces the mean flow on the structure. This additional flow reduction is in addition to the standard industry practice of including a simple current blockage factor as documented in API (American Petroleum Institute 2000).

Here we report observations on what we assume are the linear and nonlinear potential flow (inertia) forces in recent experiments on a jacket model. We compare the force coefficients for the first three frequency harmonics of the measured force (those components out of phase with the wave crests) with the FNV-force equation from Faltinsen et al. (1995), see also Malenica & Molin (1995), for the total horizontal load on vertical cylinders. This allows us to investigate the contribution of the linear and non-linear components of the total inertia force. Previous experimental studies have been carried out by Chaplin et al. (1997) and others to look at the force on a single or a few vertical cylinders. Here, we also look at the force on arrays of cylinders representing conductors, examining the interaction effects on the linear inertia term on arrays of cylinders for different wave directions.

2. Experimental set up & data analysis

A series of experiments were conducted in the towing tank in the Kelvin Hydrodynamics Laboratory of Strathclyde University, Glasgow, as an extension of previous work to verify the improved fluid loading recipe on a scaled jacket model, as well as to formulate an appropriate current blockage recipe for irregular waves. A 1:80 jacket model was constructed from stainless steel (figure 1 shows the model); this resembles a typical second generation North Sea jacket 4-leg structure. The jacket was hung below the carriage, such that the still-water submerged height of the jacket was 1.45 m. The carriage was moved at constant speed along the tank to simulate uniform current, and the model was exposed to regular waves of various wave heights with a fixed wave period of 1.4 sec on a water depth of 2.1 m. The jacket was mounted in such a way that the total horizontal reaction due to the hydrodynamic load was measured directly by a force transducer. A wave gauge was mounted on the carriage between the jacket model and the side of the tank to provide phase information of the undisturbed incoming waves. A combination of 5 different heights of regular wave and 3 towing speeds (current) were tested.

The jacket model is tapered when viewed end-on and rectangular broadside (see figure 1 for the plan view). Also shown are the conductor support frames and the arrangement of the conductor arrays (vertical closely spaced uniform cylinders). The conductor support frames, made of square hollow members instead of cylindrical members, were supported on the horizontal bracings at end-on instead of extending from the jacket legs (as commonly found in actual offshore jackets) to ease the fabrication process. The conductors in the jacket model were designed to be removed

easily from the carriage so a combination of cases with and without conductors for the same wave loading direction is possible. For hydrodynamic loading in the broadside direction, there are rows of four conductor tubes side-by-side orthogonal to the flow direction. In contrast, for end-on direction, there are rows of only two conductor tubes. Interaction effects are expected in the inertia forces of broadside and end-on, both with conductors. In total, three configurations of the jacket model were tested: broadside with conductors, end-on with conductors, and end-on without conductors. No cases of broadside without conductors were tested.

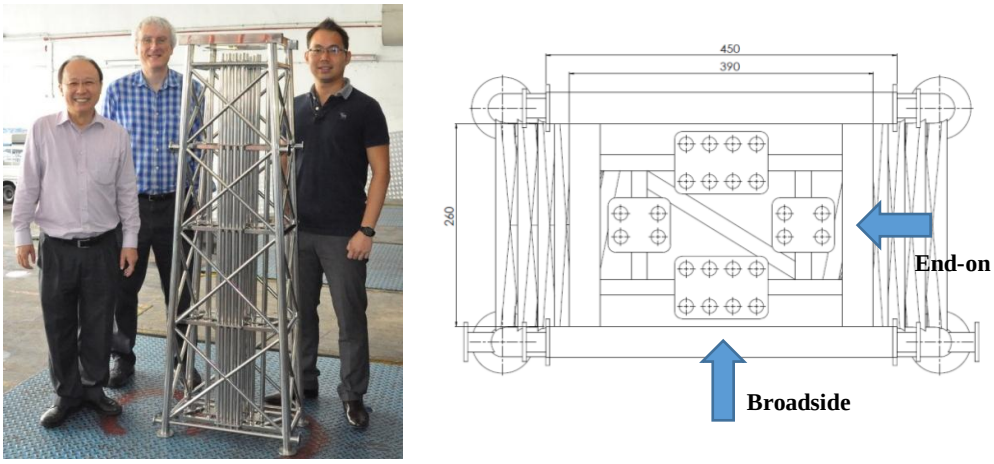

Figure 1: (Left) 3D view of the jacket model and (Right) plan view of the model showing the arrangement of conductor arrays.

The total measured forces were decomposed into a sum of drag and inertia forces following the decomposition method outlined in Santo et al. (2014). The phase information of the wave is required, and the key assumption made is force symmetry around the wave crest/horizontal velocity peak. The total force was extracted after the starting transients when the force is periodic in time, and phase-averaged (cycle-by-cycle) over a record of 10 – 20 wave cycles before the decomposition. That part of the total force in-phase with the wave velocity is assumed to be drag, the remainder that is out of phase is assumed to arise from potential flow load components, with the linear part (in both frequency and wave amplitude) being the Morison inertia term. Figure 2 (left) shows a plot of the decomposition for 0.24 m regular waves in the end-on direction with no current. The drag force will be compared with the new blockage theory (Taylor et al. 2013) elsewhere. Here, we focus on the inertia force and its harmonics (Fig. 2 top right).

3. Inertia force on conductor arrays in end-on

To investigate the experimentally measured inertia force, we chose to look at the measured inertia force on the conductor arrays only, by subtracting the inertia force on the model without conductors for waves end-on from the inertia force for the same model tested with conductors. Thus, the effects of legs, braces, and other cylindrical members that are non-orthogonal to the flow as well as square hollow members which have different C_M values should be removed. This will allow a cleaner investigation: all the conductor tubes run vertically the full height of the jacket, forming an array of uniform, closely spaced cylinders of diameter 1.6 cm.

We fit the measured inertia forces using the MATLAB curve fitting toolbox. The phase of the wave is obtained from the wave gauge signal, so the phases of both drag and inertia terms are known. We take a -90° phase shift for the harmonic term of the inertia force relative to the wave crest and obtain force coefficients of the 1st up to 3rd harmonic terms in frequency. We compare the force fits with those of the nonlinear potential flow FNV force on a single uniform vertical surface-piercing cylinder (Faltinsen et al. 1995): with $\eta = A\,cos\,\omega t$ as the linear part of the wave profile, the FNV force is $F_{Inertia}/\pi r^2 = -2\rho g A\,sin\omega t - 5/4\rho g A^2 k\,sin2\omega t - 2\rho g A^3 k^2\,sin3\omega t$, where r is the cylinder radius and the other symbols have their usual meanings. The FNV force model assumes the linear inertia coefficient $C_M = 2$ and contains force coefficients of 1.25 and 2 for the 2nd and 3rd harmonic terms, respectively.

For waves with no current, the mean value of force coefficients on the conductor array are 2.08 (1st harmonic), 1.35 (2nd harmonic) and 6.02 (3rd harmonic). The first two harmonics agree reasonably well with the predictions from the FNV model, the 3rd harmonic term differs considerably but the signal is small and noisy. We also believe that there may be some small phase leakage across from the drag term for the 3rd frequency harmonic. In calculating the force coefficients, the effect of finite water depth was taken into account (a 5% correction to deep water kinematics assumption). Figure 2 (right) shows the forces on the conductor arrays for 0.24 m regular waves with no current.

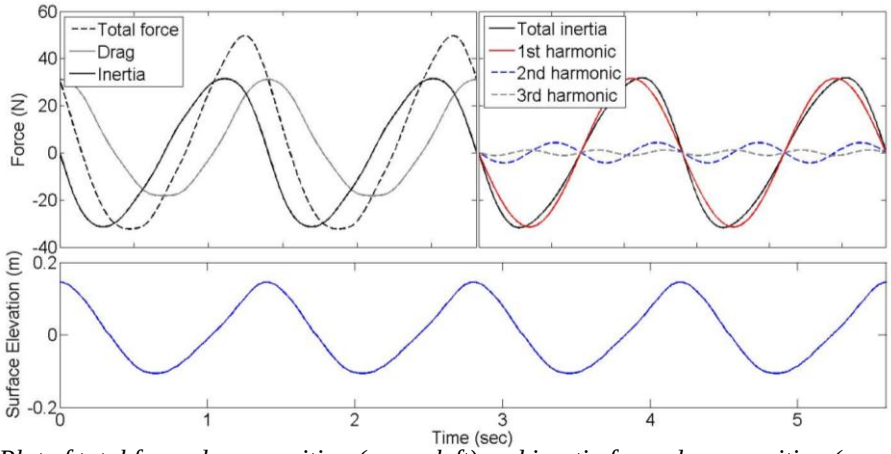

Figure 2: Plot of total force decomposition (upper left) and inertia force decomposition (upper right), both for 0.24 m regular waves with no current. The bottom figure shows the surface elevation.

The current is simulated by towing the jacket model along the tank, so the wave kinematics are unaffected by the current, but the encounter rate of the model with the waves changes. Hence, in a moving frame of reference (moving with jacket), the wave horizontal velocity can be written as: $U_{Wave} \sim \omega A \cos[(\omega + U_C k)t - kx]$. Therefore, the linear inertia term contains the encounter frequency due to current: $\partial U_{Wave}/\partial t \sim -\omega(\omega + U_C k)A \sin[(\omega + U_C k)t - kx]$ and as a result, the total linear contribution in the inertia force with $C_M = 2$ can be expressed as $\sim(2 \cdot \partial U_{Wave}/\partial t + U_C \, \partial U_{Wave}/\partial x)$. When integrated over the height of the model to mean sea level, this yields a factor of $-2\left(1 + \frac{U_C}{2C_\emptyset}\right)\times$, where $C_\emptyset = \omega/k$ is the phase speed of the wave. The additional term $(U_C/2C_\emptyset)$ arises from the current contribution to the 1st harmonic term. We assume that the rest of the FNV-model is unaltered. Clearly for the case with current, the 2nd order term in wave amplitude could be expected to be generalised to have current × wave terms contributing to the 1st harmonic component. The 3rd order term for waves with no current would be expected to produce 1st and 2nd harmonic contributions with the current present. Unfortunately we know of no extension of the FNV-model to account for the effect of current on the 2nd and higher harmonic terms.

Figure 3 shows the values of the force coefficients for all cases with and without current. For the 1st harmonic term (left), the measured C_M values are all close to the theoretical $C_M = 2$ (solid line). For the coefficient of the 2nd harmonic term (right), with the theoretical FNV value of 5/4 (solid line), the experimental mean of 1.35 (for no current – dashed black line) is quite close. As the current speed is increased the 2nd order coefficients also increase, from 1.35 to 1.92 (for 0.14 m/s current – red line) and 2.18 (for 0.28 m/s current – blue line). We suspect the increase is associated to the current but have no model to account for it.

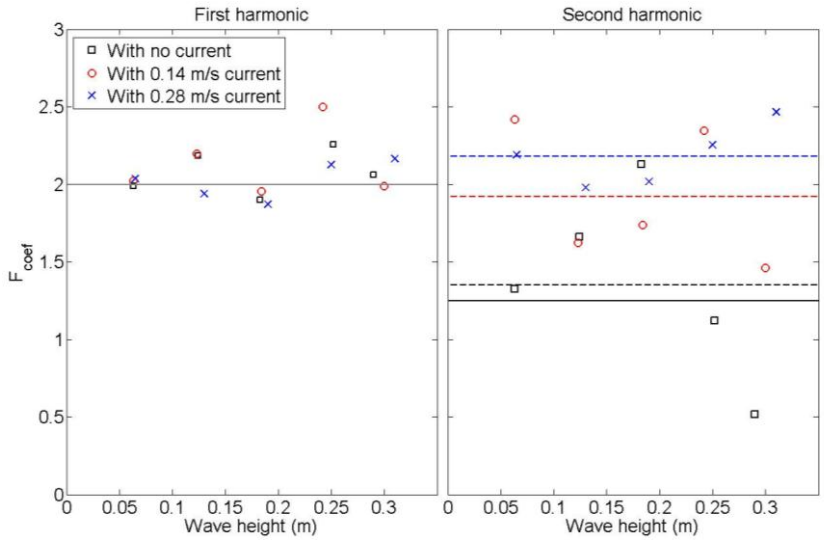

4. Interactions within conductor arrays

The effect of conductor arrays in regular waves is known to induce (wake) shielding, which can be captured with a reduced drag coefficient in the Morison equation, and either the full current blockage model from Taylor et al. (2013) or the API standard (figure C.3.2-4) can be used to account for such an effect. The effect on the inertia term however, is less clear.

Figure 3: Plot of force coefficient variations with wave height and current speed.

From the measured inertia forces, we obtain C_M of about 2.0 for the conductor array in the end-on orientation, suggesting that the experimental evidence is compatible with potential flow theory prediction. What about the same structure in the broadside orientation? Would the arrangement of the conductor tubes end-on vs. broadside matter in terms of C_M? We have no experimental data as yet, but a simple potential flow model (Walker & Eatock Taylor 2005), based on Linton & Evans (1990) analysis of multiple cylinders, was used to examine this.

For the arrangement of conductor arrays we have for the jacket model, the smallest spacing (centre to centre) to diameter ratio of conductor tubes (S/D) is 1.7 for both end-on and broadside directions. From the potential flow model, the net effective C_M for end-on is 0.96× the undisturbed C_M, for broadside is 1.07×. The increase/decrease in C_M is associated with the interaction effects of neighbouring cylinders. For broadside, there are four rows of four cylinders, while for end-on there are only rows of two cylinders. Whilst for the experimental configuration there are only small perturbations away from the undisturbed values, it is interesting to ask how much closer would the conductor tubes have to be to produce large changes in C_M?

Figure 4 shows the variation of force coefficients for end-on and broadside. The S/D ratio was adjusted by increasing/decreasing the diameter of the conductor tubes while keeping their centres fixed, with $S/D = 1$ being the limit when the closest conductors touch. The interaction effect for waves end-on is small; the force coefficient decreases as S/D reduces up to the point when the two conductors at the first two and last two rows in the end-on direction are about to touch. The interaction effect is larger in the broadside direction, where the increase in C_M is now up to 45% in the limit when the conductors in the rows of four cylinders are touching. Whilst closely-spaced conductor arrays are known to reduce the drag term in the Morison equation due to blockage, in contrast the linear inertia term could increase, depending on the arrangement of the conductor arrays. Any increase in the inertia term is obviously relevant to fatigue prediction.

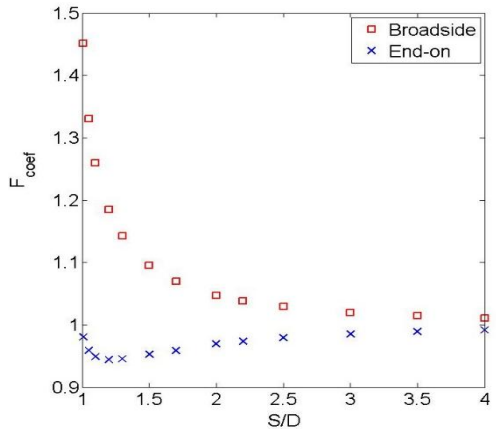

Figure 4: Plot of force coefficients versus S/D for end-on and broadside.

Acknowledgements:

The authors are grateful to Prof. Y.S. Choo of the National University of Singapore and Prof. R. Eatock Taylor of University of Oxford for their help with this work.

References

American Petroleum Institute, 2000. Recommended practice for planning, designing, and constructing fixed offshore platforms: working stress design. API RP2A-WSD 21st Edition with Errata and Supplements.

Chaplin, J. R., Rainey, R. C. T., & Yemm, R. W., 1997. Ringing of a vertical cylinder in waves. *J. Fluid Mech.* **350**, 119–147.

Faltinsen, O. M., Newman, J.N., & Vinje, T., 1995. Nonlinear wave loads on a slender vertical cylinder. *J. Fluid Mech*. **289**, 179–198.

Linton, C. M., & Evans, D. V., 1990. The interaction of waves with arrays of vertical circular cylinders. *J. Fluid Mech.* **215**, 549–569.

Malenica, S., & Molin, B., 1995. Third-harmonic wave diffraction by a vertical cylinder. *J. Fluid Mech.* **302**, 203–229.

Morison, J. R., Johnson, J. W., & Schaaf, S. A., 1950. The force exerted by surface waves on piles. *J. Petroleum Technology*, ***2***(5), 149–154.

Taylor, P. H., Santo, H., & Choo, Y. S., 2013. Current blockage: Reduced Morison forces on space frame structures with high hydrodynamic area, and in regular waves and current. *Ocean Eng.* **57**, 11–24.

Santo, H., Taylor, P. H., Williamson, C. H. K., & Choo, Y. S., 2014. Current blockage experiments: Force time histories on obstacle arrays in combined steady and oscillatory motion. *J. Fluid Mech*. **739**, 143–178.

Walker, D. A. G., & Eatock Taylor, R., 2005. Wave diffraction from linear arrays of cylinders. *Ocean Eng*, ***32***, 2053–2078.

30^{th} *International Workshop on Water Waves and Floating Bodies, Bristol-Bath, UK, April 2015.*

Some aspects of the eigenfrequency computation in a two-dimensional tank filled with two non miscible fluids.

Y.-M. Scolan
ENSTA-Bretagne, yves-marie.scolan@ensta-bretagne.fr
2 rue François Verny, 29806 Brest cedex 13, France

Highlights

- the eigenfreqencies of the sloshing modes of a two fluid layer system are computed,
- the convergence of a desingularized technique is commented,
- the variations of the eigenfrequencies with the density ratio are detailed.

1) Introduction

Determining the natural frequencies of the sloshing modes in a two-dimensional tank is a well-known problem in potential theory (see Ibrahim, 2005, or Faltinsen and Timokha, 2009, among recent textbooks on that topic). In practice the computational effort reduces to the determination of eigenvalues of a matrix. A first (and non sophisticated) approach consists in formulating a classical integral equation where singularities are distributed all over the fluid boundaries, including the tank walls and the free surface itself. On the former surface, a homogeneous Neumann condition is prescribed whereas on the latter surface a Fourier condition is prescribed. Then the matrix follows from the discretization of the surface integrals into panels. An improvement is to use harmonic solutions which implicitely account for the wall boundary condition. Faltinsen and Timokha (2010, 2012, 2014) deal with the case of the circular tank or prismatic tank in that way, since they need an analytic continuation above the linearized free surface. This is obviously required when the fully nonlinear free surface flow problem is solved. This is why the technique initially proposed by Tuck (1998) is appealing. A conformal mapping turns the domain bounded by the tank walls into a half space and a desingularized technique provides a simple expression of the velocity potential. The computational effort then focuses on the free surface description only. That combination has proved to be very effective and robust even for more complicated tank geometries than a simple rectangular tank (see Scolan, 2010). The same technique can be used to deal with a two fluid layer system in a closed tank with a more or less complicated boundaries (see Scolan *et al*, 2014).

This technique and other analytical approaches are detailed in the next developments in order to determine the frequencies of the sloshing modes of a two fluid layer system in a closed tank. First a numerical analysis is performed for a rectangular tank to assess the convergence criteria in terms of the number of singularities and the desingularizing distance. Then the technique proposed by McIver (1989) is applied to a two fluid layer system in a circular tank.

2) Eigenfrequency in a rectangular tank by MFS

Much work has been done for a single phase flow neglecting the gas above the free surface, considered as vacuum. However in most practical situations there is a gas above the liquid. From the analysis of Lord Rayleigh (1883) in potential theory, the dispersion relation of wave travelling at the interface of two non miscible fluids in an unbounded fluid domain, is well-known. This dispersion relation reads $\omega^2 = gkA_t$ where ω is the circular frequency, k the wavenumber, g the acceleration of gravity and $A_t = (1-r)/(1+r)$ is the Atwood number with r being the ratio of densities. If the two fluid layers are contained in a closed tank, the two fluid domains must be perfectly symmetric with respect to the interface so that the n^{th} eigenfrequency $\omega_n(r)$ varies as

$$\omega_n(r) = \sqrt{\frac{1-r}{1+r}}\omega_n(0) \tag{1}$$

When the geometry is rectangular (with length L and liquid depth h), then $\omega_n^2(0) = \frac{n\pi g}{L}\tanh\frac{n\pi h}{L}$, the proof for (1) is straigtforward. For an arbitrary domain with the interface as a plane of symmetry, it is easy to show that both the velocity potentials and their normal derivative along the interface are equal but opposite in sign; then the identity (1) follows.

In previous works it has been shown that Method of Fundamental Solutions (also known as Desingularized Methods) is effective in simulating nonlinear free surface motions (see Mrabet *et al*, 2014). The main reasons are this method does not require regridding or smoothing during the time marching scheme. Conformal mapping is an essential aspect of the present technique. As a matter of fact, by turning the physical computational domain into a simpler domain, as a half space for example, the impermeability condition on the tank walls is easily accounted for. To this end the following conformal mappings

$$w = -\cos\frac{\pi z}{L}, \qquad w = \cos\frac{\pi}{L}(z - ih_{roof}) \tag{2}$$

are used for a rectangular tank as described below

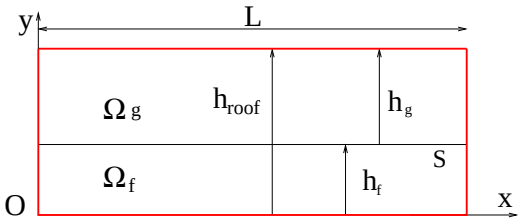

These two independent transformations "flatten" the two vertical walls of the rectangular tank. In practice, the velocity potentials attached to each phase are written as a finite summation of Rankine sources placed at some distance from the actual interface. The number of sources is denoted N and $\delta L/(N-1)$ is the desingularizing distance. When the density ratio is zero, it is shown that the relative error on the n^{th} eigenfrequency varies like

$$E_n = A_n e^{-\pi\delta L\frac{N-n}{N-1}} \tag{3}$$

The same result holds when the density ratio is non zero but the analysis of convergence follows from numerical analysis. The figures below illustrate that result for $r = 0.5$. It shows the decreasing error as a function of δ for the first and tenth modes. On these curves the theoretical error follows from (3).

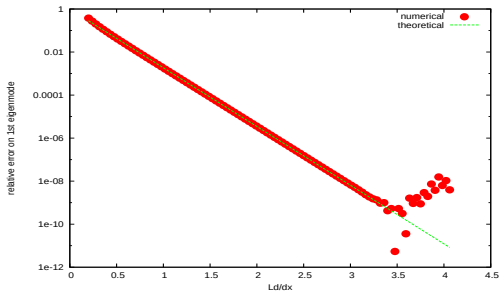

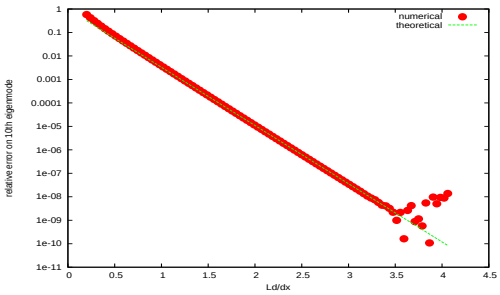

Christiansen (1976) and Pozrikidis (2000) arrived at the same conclusion: the farther the singularities, the better the convergence. However that (non intuitive) result is rather paradoxical. As a matter of fact, when using the same numerical technique but for solving the nonlinear free surface equations, it is shown that the desingularizing distance must be adapted to a small enough value in order to fulfill the criteria of mass and energy conservation (see Scolan, 2010).

2) Eigenfrequencies in a circular tank

We consider a circular tank with radius c filled with two fluids which are not miscible, say Ω_g and Ω_f the corresponding fluid domains as shown in figure below.

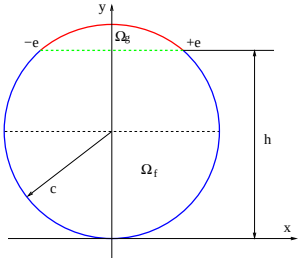

The indices f and g refer to the liquid and gas respectively. The density ratio of the two fluids is $r = \rho_g/\rho_f$. The filling height is h measured from the bottom (south pole). The dimension of the interface is defined by $e = \sqrt{c^2 - (h-c)^2}$. The analysis by McIver (1989) provides us with the conformal mapping $x + iy = ih - e\tanh(\zeta/2)$ with $\zeta = \alpha + i\beta$, which turns the physical domain (inner circle) into an infinite strip $\beta \in [-\pi, +\pi]$ and $\alpha \in]-\infty, +\infty[$. The surface of the circle is described by $\beta = C^{ste}$: $\beta = \beta_f$ (such that $\cos\beta_f = \frac{c-h}{c}$) is the image of the circular arc bounding Ω_f and $\beta = \beta_g$ (such that $\cos\beta_g = \frac{h-c}{c}$) is the image of the circular arc bounding Ω_g. It is worth noting that the two angles β_f and β_g are not independent, they are opposite in sign and verify the identity $\beta_f - \beta_g = \pi$.

Following McIver (1989), the general solutions which verify both Laplace equation and impermeability conditions on the wall, read

$$\phi_j(\alpha, \beta, \beta_j) = \int_0^\infty A_j(\tau)\cosh\tau(\beta - \beta_j) \left\{ \begin{array}{c} \sin\tau\alpha \\ \cos\tau\alpha \end{array} \right\} d\tau, \qquad j = f \text{ or } g \tag{4}$$

where cos and sin yield the symmetric and antisymmetric modes respectively. These solutions are such that the pressure and the normal velicity at the interface are continuous, yielding the following integral equation for the function B,

$$(1-r)B(\tau') = \lambda \int_0^\infty B(\tau)K(\tau,\tau')d\tau, \qquad \tau' \geq 0, \qquad \lambda = \frac{e\omega^2}{g} \tag{5}$$

$$B(\tau) = A_f(\tau)\sqrt{\tau f(\tau)\sinh\tau\beta_f\cosh\tau\beta_f}, \qquad f(\tau) = 1 - r\frac{\tanh\tau\beta_f}{\tanh\tau\beta_g} \tag{6}$$

$$K(\tau,\tau') = \left[\frac{\tau-\tau'}{\sinh(\tau-\tau')\pi} \mp \frac{\tau+\tau'}{\sinh(\tau+\tau')\pi}\right]\sqrt{\frac{f(\tau)f(\tau')}{\tau\tau'\tanh\tau\beta_f\tanh\tau'\beta_f}} \tag{7}$$

where $\pm$ depends on sin / cos in equation (4), namely the antisymmetric or symmetric modes. Numerically, the integral in (5) is discretised by using a Gauss quadrature formula. To this end, Legendre type sounds better than Laguerre type; after the appropriate change of variable has been done. The next figure shows the variation of the eigenfrequency $\lambda(r)/A_t$ with the filling ratio h/c for the first nine modes. The density ratio varies in the range $(0, 0.2, 0.5, 0.9)$.

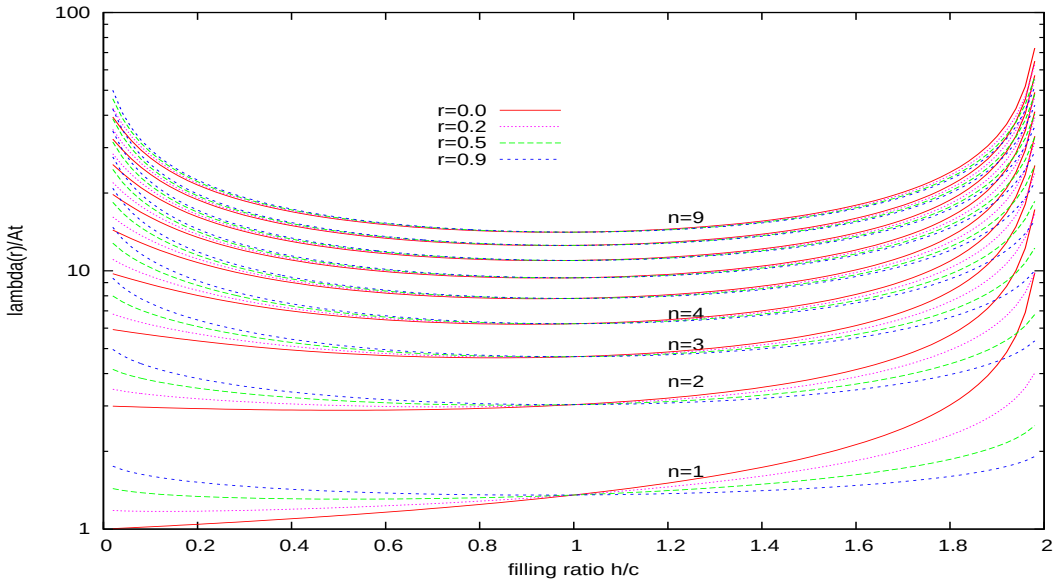

When the tank is half filled, equation (1) is perfectly valid. Otherwise, that equation is a rough approximation. It is worth noting that for low filling ratio the frequencies increase with increasing density ratio. This variation is reversed at high filling ratio.

4) Conclusions

The sloshing modes in a tank are rarely computed by accounting for the two fluid system *i.e.* non miscible fluids in a closed tank (see La Rocca *et al*, 2002, 2005). This problem is addressed here by using different approaches. For a rectangular tank, some numerical aspects and convergence criteria of the desingularized technique are detailed. For a circular tank, the quasi-analytical approach proposed by McIver is extended to a two layer system.

5) References

• Lord Rayleigh S. J. W., 1883, Investigation of the character of the equilibrium of an incompressible heavy fluid of variable density, Proceedings of the London mathematical society Vol.14, 170-177.

• Faltinsen O.M., Timokha A., 2009, Sloshing, Cambridge University Press, Cambridge.

• Faltinsen O.M., Timokha A.N., 2010, A multimodal method for liquid sloshing in a two-dimensional circular tank. J. Fluid Mech. vol. 665, pp. 457-479.

• Faltinsen O.M., Timokha A.N., 2012, On sloshing modes in a circular tank, J. Fluid Mech. 695, 467-477.

• Faltinsen O.M., Timokha A.N., 2014, Analytically approximate natural sloshing modes and frequencies in two-dimensional tanks European Journal of Mechanics B/Fluids,47, 176-187.

• Ibrahim R., 2005, Liquid Sloshing Dynamics, Cambridge University Press.

• McIver, P. 1989 Sloshing frequencies for cylindrical and spherical containers filled to an arbitrary depth. J. Fluid Mech. 201, 243-257.

• Tuck E.O., 1998, Solution of Nonlinear Free-Surface Problems by Boundary and Desingularised Integral Equation Techniques, Invited Lecture, Computational Techniques and Applications: CTAC'97 Eds J. Noye, M. Teubner, A. Gill, World Scientific, Singapore, 11-26.

• Scolan Y.-M., 2010 Some aspects of the flip-through phenomenon: A numerical study based on the desingularized technique Journal of Fluids and Structures, Volume 26, Issue 6, pp 918–953.

• Scolan Y.-M., M. R. Karimi, F. Dias, J.-M. Ghidaglia, J. Costes, 2014 Highly nonlinear wave in tank with small density ratio. 29^{th} International Workshop on Water Waves and Floating Bodies, Japan, April 2014.

• Christiansen, S., 1976, On Kupradze's functional equations for plane harmonic problems, Function Theoretic Methods in Differential Equations, eds. R.P. Gilbert and R.J. Weinacht (Pitman, London, 1976) 205–243.

• Pozrikidis, C., 2000, On the method of functional equations and the performance of desingularized boundary element methods. Engineering analysis with boundary elements, vol. 24, N^o 1, 3-16.

• La Rocca M., G. Sciortino, and M. A. Boniforti, 2002, Interfacial gravity waves in a two-fluid system, Fluid Dyn. Res. 30, 31.

• La Rocca M., G. Sciortino, C. Adduce, and M. A. Boniforti, 2005, Experimental and theoretical investigation on the sloshing of a two-liquid system with free surface, Phys. Fluids 17, 062101.

• Mrabet A.A., Costes J., Ghidaglia J.-M., Guilcher P.-M., Le Touzé D. and Scolan Y.-M., 2014, Highly nonlinear dynamics of the interface between two non miscible fluids in a closed tank. 15^{th} Int. Workshop on Trends in Numerical and Physical Modelling for Industrial Multiphase Flows, Cargèse, Corsica, France, October 2014.

HYDRODYNAMIC IMPACT ON AN ERODIBLE BODY

Y.A. Semenov, G.X. Wu

Department of Mechanical Engineering University College London, London, UK
E-mail: semenov@a-teleport.com, g.wu@ucl.ac.uk

1. INTRODUCTION

Liquid/structure or liquid/liquid impact is widely observed in nature. Examples include wave impact on marine structures and coastline, droplet impact or waterfalls on solid floor, a solid body passing through a liquid surface. While high speed liquid impacts can cause structural damage or failure and many other adverse effects, these processes are also used in applications such as 3-D printing technology, cool jet-cutting and cleaning of metals, coating and painting.

In many water impact studies, the bodies are treated as rigid and impermeable. However, in many other fluid/solid impact processes, the body surface may be non rigid or permeable. There may be surface erosion or other types of material removal that changes the body shape during impacts, such as liquid drop impacting a soil or granular materials [1], metal cutting through jets [2,3], surface penetration through shaped charges [4,5], and cavitation erosion by high-speed jets generated during collapse of vapour bubbles [6,7]. In maritime engineering, liquid may penetrate through a perforated or porous surface, and typical examples can be found in [8 – 11].

In this study we consider the two dimensional self similar velocity potential flow problem for impact between a liquid wedge and a permeable or/and erodible body [12]. Integral hodograph method [13] is used. It enables the original partial differential equation with the nonlinear boundary conditions on the unknown free surface to be converted into a system of intergro-differential equations along straight lines in the parameter plane. The method has been successfully used in variety of impact problems [12 - 14]. However, the application of the method to the present problem has some new difficulties. On the impermeable solid surface, the normal velocity is prescribed, while on the free surface the pressure is provide. On the permeable body surface or the moving wetted surface caused by erosion, neither of these functions is known in advance explicitly. Instead the boundary condition is written in terms of a relationship between the pressure and the normal component of the velocity trough the body surface. This leads to a new singularity on the mathematical formulation. Further in the case of an erodible body, the wetted surface of the solid deforms and body material moves away, and its shape into the body is determined by the local speed of erosion or melting. The formulation of the problem includes an additional equation through a law relating the speed of erosion with other flow parameters, which gives the means to determine the unknown shape of the interface.

Various case studies are considered. The first one is porous body, for which a linear relationship between the pressure and normal velocity through non deforming body boundary is employed. The second case is a perforated body, for which the quadratic relationship between the pressure and the normal velocity trough the non deforming body surface is used. These two cases are related to the problems in coastal and offshore engineering [8, 9, 15] where the porous/perforated bodies are used to reduce the hydrodynamic impact loading on a structure. The third case considered here is associate with jet-cutting or penetration of the shaped charge, in which the solid material is removed by the hydrodynamic pressure and shear stress. There are some previous studies related to this case, in particular, that done by Pool [5], which are based on a further development of the classical Birkhoff-problem of steady impinging jets.

2. FORMULATION OF THE PROBLEM

We consider the impact problem between a liquid wedge of half-angle α and a permeable and/or erodible body. A sketch of the problem and the definitions of the geometric parameters are shown in Fig. 1*a*. The flow is self similar and will be studied in the frame of reference with its origin attached to the stagnation point A which may move during the erosion of the body surface.

The liquid wedge has uniform velocity at infinity, which is indicated as V in figure 1*a* and it is relative to point A. The symbol v_{ni} in the figure is the normal velocity of surface OA, which is zero at point A, as the origin of the coordinate system is fixed there. Within

this surface, AD is the wetted surface of the body after erosion and forms an angle $\alpha_A < \pi/2$ with the y-axis at point A. The symbol v_{np} in the figure is the velocity due to the body surface permeability. Thus, the total normal component of the velocity of the liquid along OA can be expressed as $v_n = v_{ni} + v_{np}$, in which $v_{np} = 0$ on the free surface OD.

For a constant impact velocity of the liquid wedge, the time-dependent problem in the physical complex plane $Z = X + iY$ can be written in the stationary similarity plane $z = x + iy$ in terms of the self-similar variables $x = X/(Vt)$, $y = Y/(Vt)$ where t is the time. The complex velocity potential $W(Z,t)$ for the self-similar flow can be written as

$$W(Z,t) = V^2 t w(z) = V^2 t\left[\phi(x,y) + i\psi(x,y)\right]. \qquad (1)$$

The problem is to determine the function $w(z)$ which conformally maps the similarity plane z onto the complex-velocity potential region w. We choose the first quadrant of the $\zeta-$plane in figure 1*b* as the parameter region to derive expressions for the nondimensional complex velocity, dw/dz, and for the derivative of the complex potential, $dw/d\zeta$, both as functions of the variable ζ. Once these functions are found, the velocity field and the relation between the parameter region and the physical flow region can be determined as follows:

$$v_x - iv_y = \frac{dw}{dz}(\varsigma), \quad z(\varsigma) = z(0) + \int_0^{\varsigma} \frac{dw}{d\varsigma} \Big/ \frac{dw}{dz} d\varsigma. \quad (2)$$

The boundary-value problems for the complex velocity function, dw/dz, and for the derivative of the complex potential, $dw/d\zeta$, can be formulated in the parameter plane. Then, applying the integral formulae [13] determining an analytical function from its modulus and argument, and from its argument on the boundary of the first quadrant, respectively, we obtain the following expression for the complex velocity and for the derivative of the complex potential [16]

$$\frac{dw}{dz} = v_0 \exp\left[\begin{array}{l} \dfrac{1}{\pi}\displaystyle\int_0^1 \frac{d\beta}{d\xi}\ln\left(\frac{\xi-\zeta}{\xi+\zeta}\right)d\xi \\ -\dfrac{i}{\pi}\displaystyle\int_0^{\infty} \frac{d\ln v}{d\eta}\ln\left(\frac{i\eta-\zeta}{i\eta+\zeta}\right)d\eta - i\beta_0 \end{array}\right], \quad (3)$$

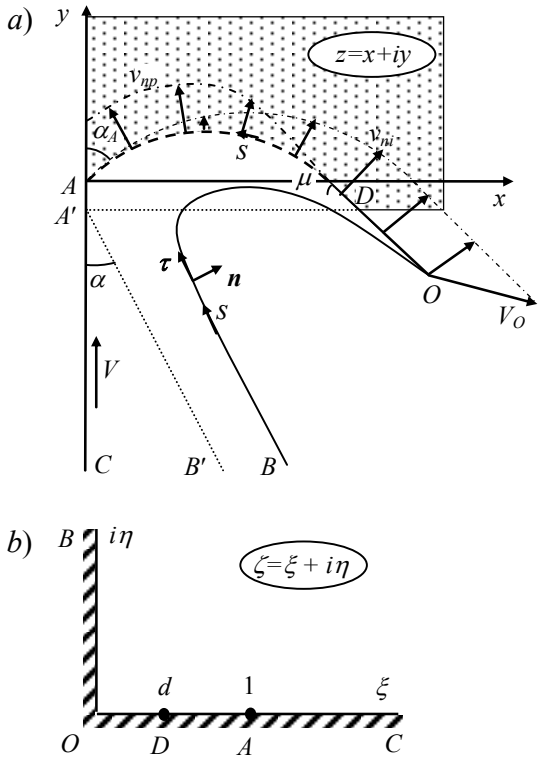

Figure 1. Sketch of the problem for impact between a liquid wedge (dotted line at the time of impact) and an erodible/permeable wall: (*a*) similarity plane and (*b*) parameter plane.

$$\frac{dw}{d\zeta} = K\frac{\zeta^{2\mu/\pi-1}}{(1-\zeta^2)^{\alpha_A/\pi}}\exp\left[\begin{array}{l} \dfrac{1}{\pi}\displaystyle\int_0^1 \frac{d\gamma}{d\xi}\ln(\xi^2-\zeta^2)d\xi \\ +\dfrac{1}{\pi}\displaystyle\int_0^{\infty} \frac{d\theta}{d\eta}\ln(\eta^2+\zeta^2)d\eta \end{array}\right]. \quad (4)$$

where K is a real scale factor, $v_0 = v(\eta)_{\eta=0}$ is the velocity magnitude at point O, $\theta(\eta) = \tan^{-1}(v_n/v_s)$ is the angle between the velocity vector and the free surface, and $\gamma(\xi) = \tan^{-1}(v_n/v_s)$ is the angle between the velocity vector and the interface.

The functions $v(\eta)$ and $\theta(\eta)$ are determined from dynamic and kinematic boundary conditions. In contrast to the impact between the liquid and impermeable/ no eroding solid wedges [14], the functions $\beta(\xi)$ and $\gamma(\xi)$ now become unknown on AD, as well as OD. According to the definitions, these functions can be found if the normal component of the velocity, $v_n = v_{ni} + v_{np}$ on the body surface is known.

The normal component of the velocity, v_{ni}, determines by the shape of the interface, i.e. $v_{ni} = \mathrm{Im}(\bar{z}e^{i\delta})$, where $\bar{z}$ is complex conjugate coordinate and δ is the slope to the interface. The normal component of the velocity due to the permeable interface, v_{np}, depends on the pressure on the body. For porous or/and permeable surfaces, the following equations were proposed in [9, 10]

$$v_{np} = \alpha_0 c_p, \qquad v_{np} = \chi_0 \sqrt{c_p}, \tag{5}$$

where c_p is the pressure coefficient, α_0 and χ_0 are the non-dimensional coefficients characterizing the porosity and perforation of the thin wall, respectively.

The method of successive approximations is used to solve the total system of integral equations through the iteration procedure.

3. NUMERICAL RESULTS

Results for the angles of the liquid and solid wedges $\alpha = \alpha_A = 45°$ are shown in figure 2. For the impermeable surface in case (*a*), the pressure decreases almost linearly from the wedge apex to the root of the tip jet, while in case (*b*) the pressure decreases more mildly and then faster near the root of the tip jet. This is caused by larger pressure reduction near the apex of the wedge due to the larger flowrate into the wedge side there.

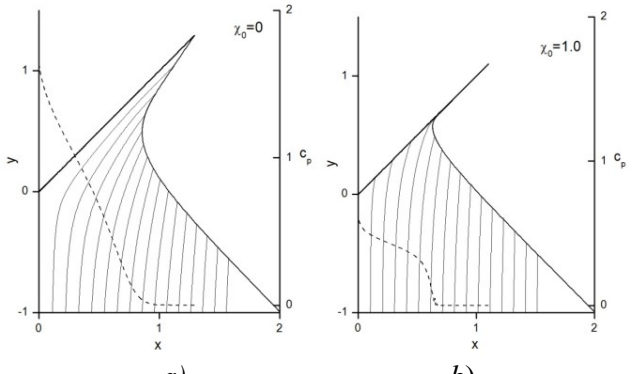

a) *b)*

Figure 2. Streamline patterns, free surfaces (solid lines), and the pressure distribution for the liquid and solid wedges $\alpha_A = 45°$ and $\alpha = 45°$, increment in the stream function $\Delta\psi = 0.1$, and (*a*) χ_0=0 and (*b*) χ_0=1.0.

For the part *AD* of the interface, the body surface erosion considered in the present study is assumed to be due to an extremely high normal or/and shear stresses during impact by liquid. This behaviour occurs when the stress has exceeded the yield stress of the material. The problem of flow/structure interaction of eroding bodies has some analogy to the classical Stefan problem for bodies undergoing melting, dissolution, or other similar processes of phase change. The choice of an appropriate model of erosion significantly depends on a particular problem and the cause of the erosion. For the present impact problem, the local normal velocity V^* of the eroding surface is assumed to be linearly related to the pressure *P* and the shear stress τ. In non-dimensional form the constitute equation of erosion takes the form

$$v^* = -K_p c_p - K_\tau v_s^2, \tag{6}$$

where v_s is dimensionless tangential component of the velocity, K_p and K_τ are the material-dependent constants. In physical reality, the erosion of the body surface is due to both the pressure and the shear stress, as shown in Eq. (6). However, if $K_\tau = 0$ and $K_p \neq 0$ in Eq. (6), it gives $v^* = 0$ at point *D*, since c_p at point *D* equals to zero. Thus, we introduce a minimal velocity $v^*_{\min}$. When the v^* obtained from Eq.(6) is smaller than $v^*_{\min}$, we set $v^* = v^*_{\min}$. The obtained results are shown in figure 3. More results will be provided in the workshop and can be found in Semenov and Wu [12] (submitted for publication).

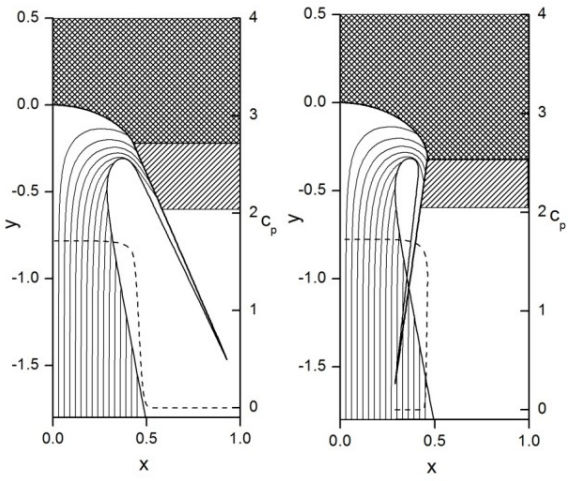

(*a*) (*b*)

Figure 3. Impact between a liquid wedge of half-angle $\alpha = 10°$ and an initially flat solid wall with $v^*_A = 0.6$, (*a*) $v^*_{\min} / v^*_A$ =0.9, (*b*) $v^*_{\min} / v^*_A$ =0.7. The lower dashed region corresponds to the restriction $v^*(s) \geq v^*_{\min}$ along the interface.

4. CONCLUSIONS

The present work gives an extended summary to the work of Semenov & Wu [12] submitted for publication. Its calculations confirmed the expected reduction of the hydrodynamic pressure on a porous or perforated wedge.

For an eroding wall, the interface between the liquid and the body is assumed to change according to the constitute law relating the rate of erosion and the normal pressure. The result shows that in this case the erosion shapes the cavity in such way to provide nearly constant pressure on most part of the cavity surface. The cavity shape is composed of an arc of a near circle, where the pressure is almost constant, and an almost straight line where the restriction $v^*_{\min} \le v^*(s)$ is applied.

This work is supported by Lloyd's Register Foundation (LRF) through the joint centre involving University College London, Shanghai Jiaotong University and Harbin Engineering University, to which the authors are most grateful. LRF supports the advancement of engineering-related education, and funds research and development that enhances safety of life at sea, on land and in the air.

4. REFERENCES

1. Delon, G., Terwagne, D., Dorbolo, S. Vandewalle, N. and Caps, H. (2011) Impact of liquid droplets on granular media. *Phys. Rev. E* **84**, 046320.
2. Daehwan, A., Changho, S. and Kim, D. (2012) Removal of metals and ceramics by combined effects of micro liquid jet and laser pulse. *J. of Appl. Phys*. **112**, 124916.
3. Kalyanasundaram, D. Shehata, G., Neumann, C., Shrotriya, P. and Molian, P. (2008) Design and vali-dation of a hybrid laser/water-jet machining system for brittle materials. *J. of Laser Applications*, **20**.
4. Walters, W. P. and Zukas, J. A. (1989) *Fundamentals of Shaped Charges.* John Wiley and Sons.
5. Poole, C. (2005) Penetration of a Shaped Charge. Ph.D. thesis. University of Oxford.
6. Isselin, J.-C., Alloncle, A.-P. and Autric, M. (1998) On laser induced single bubble near a solid boundary: contribution to the understanding of erosion pheno-mena. *J. Appl. Phys*. **84**, 5766.
7. Knepp, R.T., Daily, J.W., Hammitt, F.G. (1970) C*avitation*. New York: Mcgraw-Hill.
8. Molin, B. (1992) *Motion Damping by Slotted Struc-tures*. *In Hydrodynamics: Computations, Model Tests and Reality, Developments in Marine Technology*, 10. Elsevier.
9. Molin, B. and Korobkin, A.A. (2001) Water entry of perforated wedge. *In 16th IWWWFB Proc.* (Eds. K. Mori and H. Iwashita).
10. Iafrati, A. and Korobkin, A.A. (2005) Self-similar solutions for porous/perforated wedge entry problem. *In 20th IWWWFB Proc*., Oslo, 29 May – 1 June.
11. Iafrati, A., Miloh, T. and Korobkin, A.A. (2007) Oblique water entry of a block sliding along a sloping beach. *Proceedings of International Conference on Violent Flows*. Fukuoka, Japan.
12. Semenov, Y.A. and Wu, G.X. (2015) Liquid Impact on a Permeable/Erodible Body. Phys. Fluids, Submitted.
13. Semenov, Y.A. and Cummings, L.J. (2006) Free boundary Darcy flows with surface tension: analytic-cal and numerical study. *Euro. J. Appl. Math*., **17**, p. 607 – 631.
14. Semenov, Y. A. and Wu, G. X. (2013) Asymmetric impact between liquid and solid wedges. *Proc. R. Soc. A* **469**, 1.
15. Huang, Z. Li, Y. and Liu, Y. (2011) Hydraulic perfo-rmance and wave loadings of perforated/slotted coas-tal structures: A review. *Ocean Engn.* **38**, 1031–1053.
16. Semenov, Y.A. and Wu, G.X., Korobkin A.A. (2015) Impact of Liquids with Different Densities. *J. of Fluid Mech.* In press.
17. Curtis, J. P. and Kelly, R. J. (1994) Circular stream-line model of shaped-charge jet and slug formation with asymmetry. *J. Appl. Phys*., **75**(12):7700–7709.

Abstract for the 30th International Workshop on Water Waves and Floating Bodies, Bristol, UK, 12-15th Apr. 2015

Optimising power take-offs for maximizing wave energy conversions

Wanan Sheng, Raymond Alcorn and Anthony Lewis
Beaufort-Hydraulics and Maritime Research Centre, University College Cork, Ireland
(w.sheng@ucc.ie, r.alcorn@ucc.ie, t.lewis@ucc.ie)

1 Introduction

The paper presents a study on the different power take-off (PTO) dampers (linear and nonlinear) and their optimizations for maximising wave energy conversions on a point absorber wave energy converter.

To simplify the problem, a bottom-fixed point absorber and the single heave motion is considered for power conversion and analysis. For such a system, theoretical work has been widely carried out in optimising the damping levels in maximising wave power conversion if the power take-off is linear and under the assumption of the linear hydrodynamics of wave energy conversion. It has been shown that the relevant optimised damping can be easily obtained analytically in regular waves [1, 2]. However, when it comes to the nonlinear power take-off, the problem becomes more complicated, and much less research work has been conducted and optimised for nonlinear power take-offs.

It has been wondered, however, whether the nonlinear power take-offs are better than the linear ones, because some claims have been made that the nonlinear power take-offs can convert more power than those of linear power take-offs. Though there is limited evidence for the claims, it is not evident whether it is coincident or not. For instance, if these PTOs are not optimised, then the comparison among the different PTO damping coefficients may be meaningless and even unfair in some cases. In this research work, the power conversions from the linear and nonlinear PTOs will be conducted appropriately. More importantly, the comparisons will be made for the optimised damping coefficients for both linear and nonlinear PTO damping coefficients so that the maximum power conversions from different PTOs are comparable.

From the study, it is shown that the averaged power conversion from the optimised linear damper and nonlinear dampers can be very similar. The maximum power conversion using the nonlinear PTOs may be marginally higher than that of the optimised linear PTO, both in regular waves and in irregular waves. That is, the maximised power conversion using a nonlinear PTO may exceed theoretical maximum from the linear analysis, but it must be noted that the exceedance is only marginal.

One difference in optimizing the linear and nonlinear PTOs is that the optimised nonlinear damping coefficient is both wave period and height dependent, whilst the optimised linear damping coefficient is only wave period dependent.

2 Dynamic equations

Figure 1 shows a schematic drawing of the wave energy converter. Under the wave excitation, the buoy is supposed to move up and down (heave motion). When a PTO is applied to connect the buoy and the fixed reference (for example, the seabed), the heave motion of the buoy can drive the PTO to convert the mechanical power into useful energy. The generic dynamic equation can be expressed as

$$\begin{aligned}&[M + A_{33}(\infty)]\ddot{x}_3(t) + \int_0^t K_{33}(t-\tau)\dot{x}_3(\tau)d\tau + C_{33}x_3(t) \\ &= F_3(t) - F_{pto}(t)\end{aligned} \quad (1)$$

where M is the mass of the device; A_{33} the added mass at infinite frequency for heave motion; K_{33} the impulse function; C_{33} the restoring coefficient; F_3 the excitation; F_{pto} the power take-off (PTO) force due to the power conversion; x_3 the heave motion; v_3 the heave velocity ($v_3 = \dot{x}_3$). All parameters in eq. (1) except F_{pto} can be assessed using the boundary element method for potential flow theory (in this case, WAMIT), in which the hydrodynamics of the float has been taken as a linear dynamic system, thus a frequency domain can be conducted, and the relevant time-dependent parameters can be also easily obtained using a Fourier transform.

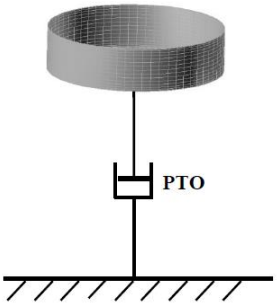

Figure 1 Seabed referenced point absorber

If nonlinear effects are considered, for instance, a nonlinear power take-off, they are only external forces, rather than the hydrodynamic forces. When we consider the wave energy conversion, the wave heights may be medium, hence the nonlinear hydrodynamic effects may not be evident. Hence in this research, linear hydrodynamics is assumed. Under the assumption of the linear hydrodynamics, the dynamic equation (1) is correct whilst the PTO force can be considered to be nonlinear or even piecewise type, like in latching control (see Sheng et al. [3]). Overall, this convention will be applied throughout this research.

For a linear PTO, a pure damper PTO can be simply expressed as a linear relation between the PTO force and the motion velocity as

$$F_{pto}(t) = b_0 v_3(t) \tag{2}$$

where b_0 is the constant damping coefficient of the PTO, and v_3 the velocity of the device in heave (i.e., $v_3 = \dot{x}_3$).

For the nonlinear PTOs, we will examine different types of PTO. The first type is inspired by the nonlinear air turbine, for example, the impulse turbine (see Falcao et al.[4]), in which the PTO force can be expressed as a nonlinear function of the velocity as,

$$F_{pto}(t) = b_1 |v_3(t)|^2 \, sign(v_3(t)) \tag{3}$$

where b_1 is the nonlinear damping coefficient, and the PTO force is proportional to the velocity squared, |*| means an absolute value.

The second type of nonlinear PTO is inspired by the relation of the newly invented bi-radical turbine (see Falcao et al. [5]), in which the PTO force can be expressed as

$$F_{pto}(t) = b_2 \sqrt{|v_3(t)|} sign(v_3(t)) \tag{4}$$

where b_2 is the nonlinear damping coefficient, and the PTO force is proportional to the velocity square root.

Once the dynamic equation (1) is solved, the power conversion is simply calculated as

$$P(t) = \left| F_{pto}(t) * v_3(t) \right| \tag{5}$$

the corresponding average power is given by

$$\overline{P} = \frac{1}{T} \int_0^T P(t) dt \tag{6}$$

where T is the time interval for calculating the average power.

3 Results and analysis

3.1 Power conversion in regular waves

Figure 2 shows the averaged power conversions using linear and nonlinear PTOs in the regular waves of a height H=2m and a period T_w=8s. In the calculations, time-domain simulations and averaged power conversion have been conducted using the procedure shown in the previous section. It can be seen that the linear PTO has an averaged power conversion close to (never larger than) the theoretical maximum in the frequency domain analysis, i.e., 40.77 kW. Using the optimized damping coefficient, the linear PTO could extract the maximal power close to the theoretical maximum. It can be seen that away from the optimised damping coefficient, the captured power is decreased when the damping coefficient is either increased or decreased ('solid line' in Figure 2). When the nonlinear PTOs are considered in the forms of Eqs. (3) and (4), the maximised power conversions can be slightly larger than that of the linear PTO.

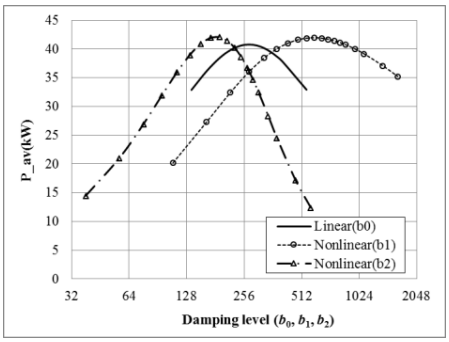

Figure 2 Damping level for regular waves (H=2m and T_w=8s)

The optimised damping coefficients are b_0=271.14 kN*s/m, b_1=596.5 kN*s^2/m^2 and b_2=189.8 kN*s$^{1/2}$/m$^{1/2}$ for the respective linear and nonlinear PTOs. It must be noted that the optimised nonlinear PTO coefficients given above are based on both the specific wave height H=2m and period, T_w=8s, whilst for the linear PTO, the optimised damping coefficient is only decided by the wave period.

Figure 3 to Figure 6 show the time series of the simulations in the specific regular wave. It can be seen that the motions for different optimised PTOs are very similar, only small differences can be discerned in the peaks and troughs (Figure 3). Relatively, the velocities of the heave motions for different PTOs are quite different in amplitude (Figure 4).

The PTO forces are very close again in the magnitudes, and no large difference can be seen (Figure 5), whilst as a combination of the PTO force and the velocity, the power conversions are quite different in peaks. It must be noticed that though the difference in peaks in the power conversion, their average power conversions are very similar, 40.77kW, 41.92kW and 42.01kW for b_0, b_1 and b_2 respectively. The nonlinear PTO could exceed the maximal power conversion given by the linear PTO by 2.82% and 3.04% respectively.

For a reference, the ratio of the maximal power over the average power is 2.284 for the nonlinear PTO (b_2), 1.806 for the nonlinear PTO (b_1), compared to the case with a linear PTO, which is a constant of 2 (Figure 6).

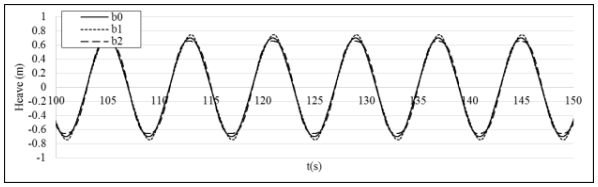

Figure 3 Motion (H=2m &T_w=8s)

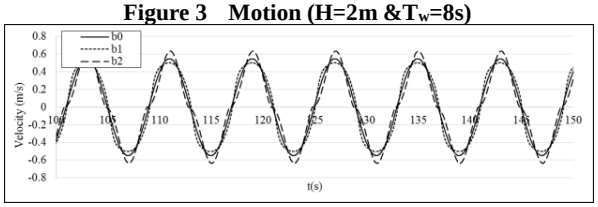

Figure 4 Velocity (*H*=2m & T_w=8s)

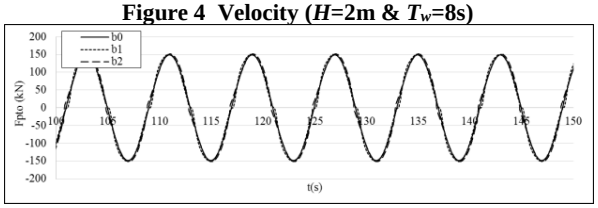

Figure 5 PTO force (*H*=2m & T_w=8s)

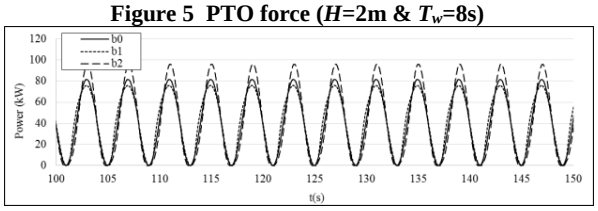

Figure 6 Power conversion (*H*=2m & T_w=8s)

3.2 Power conversion in irregular waves

Figure 7 shows the averaged power conversions using linear and nonlinear PTOs in the irregular wave of a significant height H_s=2m and a peak period T_p=8s (for a Bretschneider spectrum). From the calculations, it can be seen that the linear PTO has a maximal averaged power conversion for the optimised damping coefficient based on the wave energy period, T_e=6.86s, that is, b_0=210.77 kN*s/m in this case. The corresponding maximal power conversion for the linear PTO is 17.76 kW. Away from the optimised damping coefficient, the captured power decreases whenever the damping coefficient is either increased or decreased ('solid line' in Figure 7). When the nonlinear PTOs are used, the maximised power conversions can be slightly larger than that of the linear PTO.

Based on the simulations, the optimised damping coefficients for the irregular waves are b_0=210.77 kN*s/m, b_1=505.5 kN*s^2/m^2 and b_2=132.79 kN*s$^{1/2}$/m$^{1/2}$ for the respective linear and nonlinear PTOs. And all optimised linear and nonlinear PTO coefficients given above are based on the wave condition of a significant height H_s=2m and a peak period, T_p=8s.

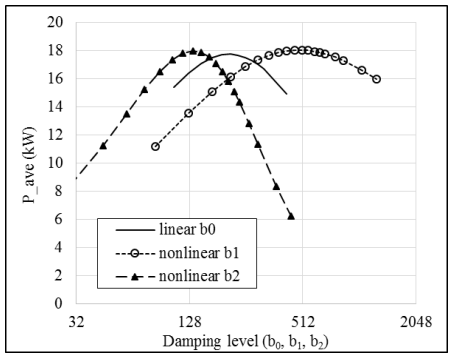

Figure 7 Damping level for irregular waves (H_s=2m & T_p=8s)

Figure 8 to Figure 11 show the time series of the simulations for the specific irregular waves. It can be seen that the motions in different optimised PTOs are very similar, though some differences can be seen in the peaks and troughs (Figure 8). Similarly, the velocities of the heave motions for different PTOs are different, again in peaks and troughs (Figure 9).

Figure 10 shows the differences of the PTO forces in the magnitudes (Figure 10).

Though the power conversions in time series are quite different in peaks, but the averaged power conversion are very similar, 17.76 kW, 18.05kW and 17.98 kW respectively. The nonlinear PTOs may increase power output by 1.63 % and 1.24% for b_1 and b_2 respectively. Again, a very small increase of the power conversion can be only possible using the optimized nonlinear PTOs. For this particular case, the ratio of the maximal power over the average power is 10.09 with the nonlinear PTO (b_2), 9.12 with the nonlinear PTO (b_1), compared to the linear PTO, which is 10.29 (Figure 11). These statistic values are based on the simulations for about 150 wave cycles.

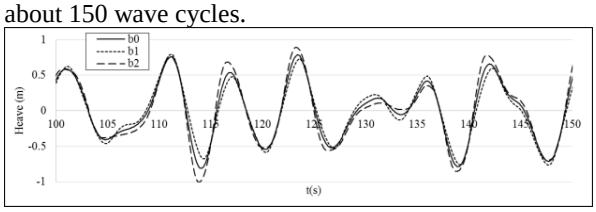

Figure 8 Motion (H_s=2m & T_p=8s)

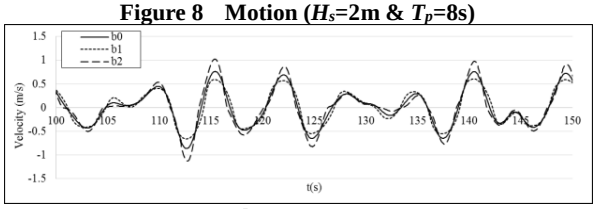

Figure 9 Velocity (H_s=2m & T_p=8s)

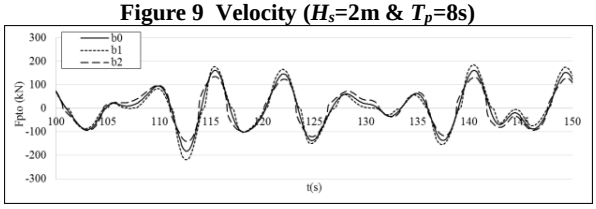

Figure 10 PTO force (H_s=2m & T_p=8s)

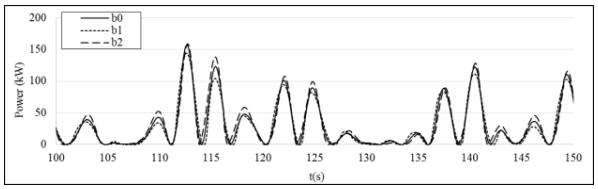

Figure 11 Power conversion (H_s=2m & T_p=8s)

3.3 Maximised power conversion in irregular waves

Figure 12 shows the maximised power conversions for different significant wave heights in irregular waves (peak period T_p=8s). It can be seen that if the damping coefficients are optimised, the linear and nonlinear PTOs can extract very similar maximised powers from waves. The maximised power conversions are generally proportional to the wave height squared with slightly different coefficients for each PTO. From Figure 13, it is interesting to note that for the linear PTO, for the specific wave period, T_p=8s, the optimised damping coefficient is a constant, regardless of the wave heights. But for the nonlinear PTOs, the optimised damping coefficients are both wave period and height dependent. To reach optimised power conversions for different wave heights, the optimised damping coefficient b_1 decreases with the increase of the wave height, whilst the optimised damping coefficient b_2 increases with the increase of the wave height.

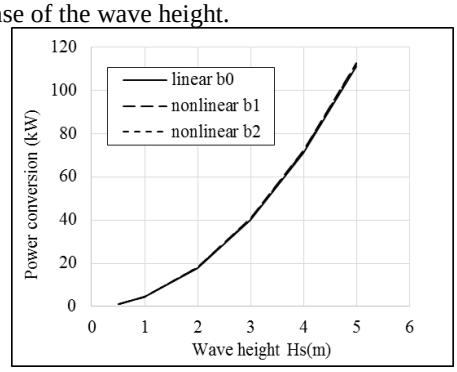

Figure 12 Optimised damping levels with the wave height in irregular waves (T_p=8s)

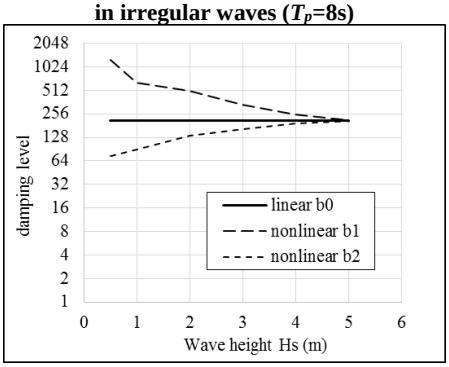

Figure 13 Power conversion with the optimised damping levels for irregular waves (T_p=8s)

4 Conclusions

In this investigation, some comparisons have been made for the linear and nonlinear PTOs in converting wave power into useful energy in which the nonlinear power take-offs are inspired by the practical PTOs. From the investigation, the following conclusions can be drawn:

- For maximising power conversion for the linear and nonlinear PTOs, the damping coefficients must be optimised. Under the optimised damping coefficients (b_0, b_1 and b_2), the averaged power conversions are very similar for the linear and nonlinear PTO dampers. The nonlinear PTOs may extract the maximised power more than that of the linear PTO, by 2-4% in regular waves, and 1-2% in irregular waves, respectively.
- For linear PTOs, the optimisation of the damping coefficient is only based on the wave period in regular waves and in irregular waves, regardless of the wave height. For the nonlinear PTOs, the optimised damping coefficients are based both on the wave period and wave height. For a specific wave period, the optimised damping coefficient decreases with the increase of the wave height for the nonlinear PTO (b_1), and the nonlinear PTO (b_2) has an opposite trend with regard to the nonlinear PTO (b_1).

Acknowledgements

This material is based upon works supported by the Science Foundation Ireland (SFI) under the Charles Parsons Award at Beaufort -Hydraulics and Maritime Research Centre (HMRC). Statistics and data were correct at the time of writing the article; however the authors wish to disclaim any responsibility for any inaccuracies that may arise.

References

1. Falnes, J., *Ocean Waves and Oscillating Systems: Linear Interaction Including Wave-Energy Extraction*. 2002: Cambridge University Press.
2. Sheng, W. and Lewis, A., *Assessment of wave energy extraction from seas: numerical validation.* Journal of Energy Resources Technology, 2012. **134**(Dec. 2012).
3. Sheng, W., Alcorn, R., and Lewis, A., *On improving wave energy conversion, part II: development of latching control technologies.* Renewable Energy, 2014. http://dx.doi.org/10.1016/j.renene.2014.09.049.
4. Falcao, A. and Gato, L.M.C., eds. *Air Turbines*. Comprehensive Renewable Energy, ed. A. Sayigh. Vol. 8. 2012, Elsevier: Oxford. 111-149.
5. Falcao, A., Gato, L.M.C., and Nunes, E.P.A.S., *A novel radial self-reectifying air turbine for use in wave energy converters.* Renewable Energy, 2013. **50**: p. 289-298.
6. Sheng, W., Alcorn, R., and Lewis, A., 2013, *Latching control for improving wave energy conversion*, submitted to Renewable Energy for publication.

Modelling Water Wave Overwash of a Sea Ice Floe

David Skene[1], Luke Bennetts[1,†], Michael Meylan[2], Alessandro Toffoli[3] and Jason Monty[4]

[1]School of Mathematical Sciences, University of Adelaide, 5005 Australia
[2]School of Mathematical and Physical Sciences, University of Newcastle, 2308 Australia
[3]Centre for Ocean Engineering Science and Technology, Swinburne University of Technology, 3122 Australia
[4]School of Mechanical Engineering, University of Melbourne, 3010 Australia
[†]luke.bennetts@adelaide.edu.au

Highlights

· Experimental validation of a mathematical model of wave-induced flexural motion of a thin floating plate.
· First model of wave overwash of an ice floe, which is validated by laboratory measurements.

Introduction

Mathematical models of ocean surface waves travelling through the sea ice covered ocean and impacting the ice cover have been developed for over 40 years now. The kernel of the models is a model of water waves interacting with a solitary ice floe. The ice floe is conventionally modelled as thin floating elastic plate. Water motions are conventionally modelled using potential flow theory.

Moreover, linear motions are assumed. However, as the floe has a small freeboard, incident waves of modest amplitudes are easily able to overwash the floe (run over its upper surface). The presence of overwash violates the assumption that motions are small perturbations from the equilibrium, which undergirds linear theory.

The impact of overwash on the motions of the floe and the surrounding wave field have not been investigated previously. More fundamentally, few attempts have been made to validate the linear thin-plate/potential-flow model.

In one notable exception, Montiel *et al.* (2013*a*,*b*) conducted a series of laboratory wave tank experiments to study the flexural motion of a floating thin plastic disk, as a model ice floe. They showed the linear model was able to predict the motions accurately. However, they attached a barrier to the edge of the model floe to prevent overwash in the experiments. Subsequently, their results provide no information on the impacts of overwash.

Results of a new series of wave tank experiments are reported here. In the experiments, no edge barrier was used and the incident waves were able to overwash the floe. The experimental measurements are used to show the linear model is able to predict the motions of the floe accurately, and, hence, that overwash does not significantly affect floe motions for the chosen parameter range.

This finding is used as the basis of a mathematical model of a wave overwashing an ice floe. The model is validated by measurements of the overwash depth recorded during the experiments. The model-data comparison shows generally very pleasing agreement and indicates the limit of validity of the model.

Experimental model

Experimental models of water waves interacting with an ice floe were implemented at the Mitchell Hydrodynamics Laboratory, University of Melbourne, Australia, and the Coastal Ocean and Sediment Transport (COAST) laboratories, Plymouth University, U.K. The models investigated one- and two-dimensional wave motions, respectively. The latter model is described here, and a selection of corresponding results is presented.

A thin plastic plate was installed in the COAST wave basin, as a model ice floe, on water of depth $H = 0.5\,\mathrm{m}$. The floe was loosely moored. Two different plastics, with distinct material properties, were used. First, a relatively dense and rigid polypropylene plastic, with a manufacturer specified density of $\rho_{\mathrm{pl}} = 905\,\mathrm{kg\,m^{-3}}$ and Young's modulus $E = 1600\,\mathrm{MPa}$. Second, a relatively light and compliant polyvinyl chloride (PVC) plastic with density $\rho_{\mathrm{pl}} = 500\,\mathrm{kg\,m^{-3}}$ and Young's modulus $E = 500\,\mathrm{MPa}$. Both plastics were provided with thicknesses $D = 5\,\mathrm{mm}$ and $10\,\mathrm{mm}$, and $20\,\mathrm{mm}$ and $40\,\mathrm{mm}$ (polypropylene) and $19\,\mathrm{mm}$ (PVC). The plates were cut into squares with side lengths $2L = 1\,\mathrm{m}$.

A series of tests were conducted in which the model floes were set in motion by regular incident waves. The motions were recorded stereoscopically by the Qualysis motion tracking system. Wave periods $T = 0.6\,\mathrm{s}$, $0.8\,\mathrm{s}$ and $1\,\mathrm{s}$ were used for the incident waves. The corresponding wavelengths are $0.56\,\mathrm{m}$, $1\,\mathrm{m}$ and $1.51\,\mathrm{m}$, respectively, i.e. approximately half

the floe length, equal to the floe length and 1.5 times the floe length. Four incident wave steepnesses were tested: $ka = 0.04$, 0.08, 0.1 and 0.15, where k and a denote the incident wave number and amplitude, respectively.

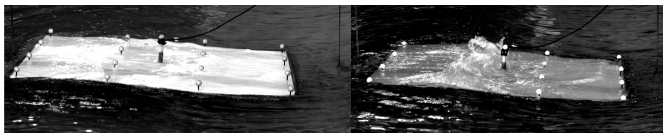

Figure 1: Photos of mild and severe overwash.

A small gauge was deployed in the middle of the upper surface of the floe to measure the depth of overwashed fluid. Overwash occurred in approximately 60% of the cases tested. The polypropylene floes, which have a relatively small freeboard, experienced the strongest overwash.

Figure 1 shows photos of overwash occurring in the tests. The left-hand panel shows mild overwash occurring for a 10 mm thick PVC floe and a 1 s period incident wave with steepness 0.15. A bore wave is visible in the shallow overwash. Bores are typical when overwash occurs. The right-hand panel shows severe overwash occurring for a 10 mm thick polypropylene floe and a 1 s period incident wave with steepness 0.15. In this case bore waves travelling up and down the plate have collided and, subsequently, caused breaking.

For each test conducted, the recorded flexural motions of the floe are converted into a spectral representation via a decomposition into the floe's natural modes of vibration. Thus, let $\eta_m(t)$ denote the vertical displacement of the mth marker. After the initial transients have passed, the signal is approximately periodic in time at the angular frequency of the incident wave, ω. Therefore, a complex amplitude A_m is calculated such that $\eta_m(t) \approx \mathrm{Re}\{A_m \mathrm{e}^{-\mathrm{i}\omega t}\}$, using least-squares minimization.

Horizontal locations on the surface of the floe are define by a Cartesian coordinate system (x, y). The origin of the coordinate system is the geometric center of the floe. The x coordinate points in the direction of the incident wave.

The floe's orthonormal natural modes of vibration are denoted $w_j(\mathbf{x})$, where $\mathbf{x} = (x, y)$. Following Kirchoff-Love thin-plate theory the modes satisfy the governing equation

$$\Delta^2 w_j = \lambda_j^4 w_j,$$

where λ_j are eigenvalues, plus free-edge conditions. They are calculated using the finite element method outlined by Meylan (2002).

The complex amplitudes A_m are projected onto a finite-dimensional space spanned by the dominant natural modes of vibration, i.e.

$$A_m \approx \sum_{j \in \Lambda} \xi_j^{\mathrm{ex}} w_j(\mathbf{x}_m)$$

where $\mathbf{x}_m$ denotes the location of the mth marker. The set $\Lambda = \{1, 2, 5, 6, 7, 9, 11\}$ contains indices of the modes used for computations. Only motions symmetric with respect to the direction of the incident wave are considered. The first two modes represent the rigid body motions of the floe: heave and pitch, respectively. The final five modes represent the primary flexural motions. The weights ξ_j^{ex} are obtained via a least squares minimization routine.

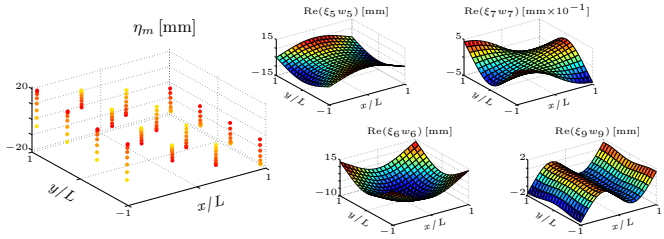

Figure 2: Motion of floe markers (left), and corresponding four dominant flexural modes (right).

Figure 2 shows an example decomposition of the floe motion into the natural modes. The example is for a 5 mm thick polypropylene floe, and a 0.8 s period incident wave with steepness 0.1. The left-hand panel shows the recorded vertical displacements of the markers over a short time interval. The right-hand panels show the corresponding four dominant weighted flexural modes.

Linear mathematical model

Following potential flow theory and assuming time-harmonic conditions, the water's velocity field is defined by the gradient of the scalar velocity potential $\mathrm{Re}\{\phi(x, y, z)\mathrm{e}^{-\mathrm{i}\omega t}\}$. Locations in the water are defined by the Cartesian coordinate system (x, y, z), where $\mathbf{x} = (x, y)$ defines horizontal locations and z is the vertical coordinate. The time-independent component of the velocity potential, ϕ, satisfies Laplace's equation throughout the water domain, i.e.

$$\Delta\phi = 0 \quad \text{for} \quad \mathbf{x} \in \mathbb{R}^2 \quad \text{and} \quad -H < z < 0, \quad \text{(1a)}$$

and a zero normal flow bed condition

$$\phi_z = 0 \quad \text{for} \quad \mathbf{x} \in \mathbb{R}^2 \quad \text{and} \quad z = -H. \quad \text{(1b)}$$

On the linearised water surface away from the floe, the potential satisfies the free-surface condition

$$\phi_z = \frac{\omega^2}{g}\phi \quad \text{for} \quad \mathbf{x} \notin \Omega \quad \text{and} \quad z = 0. \quad \text{(1c)}$$

On the linearised interface between the water surface and the underside of the floe, the potential is coupled

to the floe motion via kinematic and dynamic conditions, respectively

$$\phi_z = -\mathrm{i}\omega \sum_{j=1}^{\infty} \xi_j^{\mathrm{ma}} w_j \qquad \text{and} \tag{1d}$$

$$\frac{\mathrm{i}\omega}{g}\phi = \sum_{j=1}^{\infty} \left(1 + \beta\lambda_j^4\right) \xi_j^{\mathrm{ma}} w_j - \omega^2 \gamma \sum_{j=1}^{\infty} \xi_j^{\mathrm{ma}} w_j, \tag{1e}$$

Here, $\gamma = \rho_{\mathrm{pl}} D/\rho g$ is the scaled mass of the floe and $\beta = ED^3/\{12(1-\nu^2)\rho g\}$ is the scaled flexural rigidity, where $\nu = 0.4$ (polypropylene floes) and 0.3 (PVC) are typical values of Poisson's ratio.

The velocity potential is expanded as

$$\phi = \phi^{\mathrm{I}} + \phi^{\mathrm{D}} - \mathrm{i}\omega \sum_{j=1}^{\infty} \xi_j^{\mathrm{ma}} \phi_j^{\mathrm{R}} \tag{2}$$

where ϕ^{I} is the incident wave potential with amplitude a. The sum of the incident wave and diffraction potentials, $\phi^{\mathrm{I}} + \phi^{\mathrm{D}}$, is the solution of the problem in which the floe is held in place, i.e. equations (1a–d) with $\xi_j^{\mathrm{ma}} = 0$ $(j = 1, 2, \dots)$. The radiation potentials, ϕ_j^{R} $(j = 1, 2, \dots)$ are solutions of the problems in which the floe oscillates in one of its degrees of freedom with unit amplitude, i.e. equations (1a–d) with $\xi_i^{\mathrm{ma}} = \delta_{ij}$ $(i = 1, 2, \dots)$. The diffraction and radiation potentials are calculated by using a Green's function to convert the boundary value problems to integral equations, which are solved numerically via a constant panel method (Meylan, 2002).

A linear system for the modal weights, ξ_j^{ma}, is obtained by applying the dynamic coupling condition (1e) to the expanded velocity potential (2) and taking inner-products with respect to the subset of the modes defined by Λ. The system is expressed is

$$\left(\mathbf{K} + \mathbf{C} - \omega^2\mathbf{M} - \omega^2\mathbf{A}(\omega) - \mathrm{i}\omega\mathbf{B}(\omega)\right)\boldsymbol{\xi}^{\mathrm{ma}} = \mathbf{f}(\omega).$$

Here $\mathbf{K}$, $\mathbf{C}$ and $\mathbf{M}$ are the stiffness, hydrostatic-restoring and mass matrices:

$$\mathbf{K} = \lceil \beta\lambda_j^4 \rfloor, \qquad \mathbf{M} = \gamma\mathbf{I} \qquad \text{and} \qquad \mathbf{C} = \mathbf{I},$$

where $\lceil \dots \rfloor$ denotes a diagonal matrix and $\mathbf{I}$ is the identity matrix. The real matrices $\mathbf{A}$ and $\mathbf{B}$ are known as the added-mass and damping matrices, respectively, and are defined element-wise by

$$\omega^2\mathbf{A}_{ij} + \mathrm{i}\omega\mathbf{B}_{ij} = \frac{\omega^2}{g} \iint_{\Omega} \phi_j^{\mathrm{R}}(\mathbf{x}, 0) w_i(\mathbf{x}) \, \mathrm{d}\mathbf{x}.$$

The forcing vector, $\mathbf{f}$, is defined by

$$\mathbf{f}_j = \frac{\mathrm{i}\omega}{g} \iint_{\Omega} \left(\phi^{\mathrm{I}}(\mathbf{x}, 0) + \phi^{\mathrm{D}}(\mathbf{x}, 0)\right) w_j(\mathbf{x}) \, \mathrm{d}\mathbf{x}.$$

The system is solved for the modal weights, which are contained in the vector $\boldsymbol{\xi}^{\mathrm{ma}}$.

Results

Figure 3 shows linear-model predictions of the magnitudes of the dominant modes and values calculated from the experimental data. The magnitudes of the modal amplitudes are scaled with respect to the incident amplitude, a. Results shown are for the polypropylene floes, which experience stronger overwash. The corresponding results for the PVC floes are consistent.

The experimental data indicate the floe's motion is, essentially, linear, i.e. the modal weights scale with the incident amplitude. Small discrepancies are notable for certain cases, for example, the 1 s period, 0.08 steepness incident waves for a 10 mm thick polypropylene floe. However, no consistent dependence is evident in those cases, and experimental errors are a probable cause of the discrepancies.

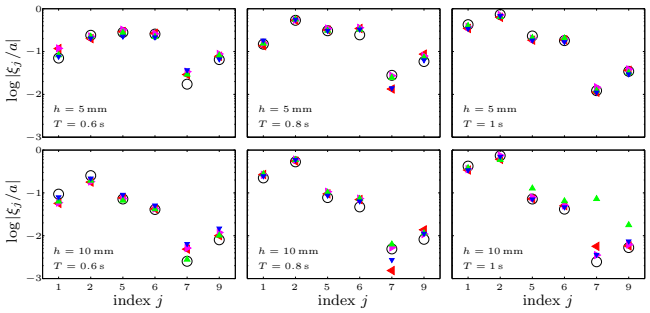

Figure 3: Comparisons of scaled modal weight magnitudes extracted from experimental data (triangles) and predicted by theoretical model for polypropylene floes (black circles). Incident steepnesses are: $ka = 0.04$ (blue, triangles down); 0.08 (green, up); 0.1 (magenta, right); and 0.15 (red, left).

The model is able to capture the magnitudes of the modal weights accurately. The model predictions are marginally more accurate for the thinner floes. Note that the logarithmic scale used to display the results emphasises errors for modal weights with small magnitudes. The model-data agreement found indicates that nonlinear phenomena inherent in wave-floe interactions, in particular, overwash, but also slamming and drift, have only a negligible effect on flexural motions.

Overwash model

The linear model is extended to a nonlinear model that incorporates overwash, by assuming:

(i) floe motions are governed by linear theory;

(ii) the height of the wave above the floe edges and its horizontal velocity forces overwash; and

(iii) overwash does not influence the surrounding wave field.

The model is two-dimensional (one horizontal dimension and one vertical dimension). Figure 6 shows an example snapshot of motions predicted by the model.

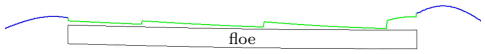

Figure 4: Overwash model: overwash fluid surface (green) and surrounding fluid surface (blue).

The overwashed fluid is modelled by the shallow-water equations, which, in conservative form, are

$$(h)_t + (hu)_x = 0 \qquad (3a)$$

and $$(hu)_t + (hu^2 + 1/2 * gh^2)_x = 0. \qquad (3b)$$

Here $h(x,t)$ is the depth of the overwashed fluid, $u(x,t)$ is the depth-averaged horizontal fluid velocity. Equations (3) account for the motion of the floe beneath the fluid. They are solved numerically using the finite volume method outlined in Kurganov & Tadmor (2000) and Kurganov *et al.* (2001) for spatial discretisation in conjunction with a total variation diminishing Runge-Kutta method for time stepping. The numerical scheme accurately resolves the bores produced by the shallow-water equations which is evident in figure 6.

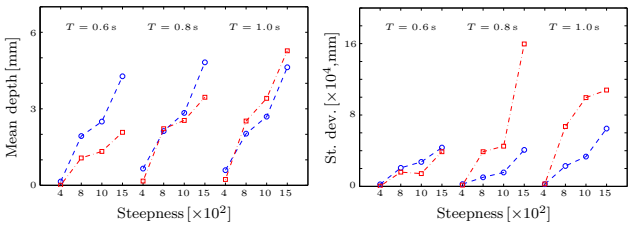

Figure 5: Comparisons of model overwash predictions (blue circles) with experimental data (red squares) for 5 mm thick polypropylene floes.

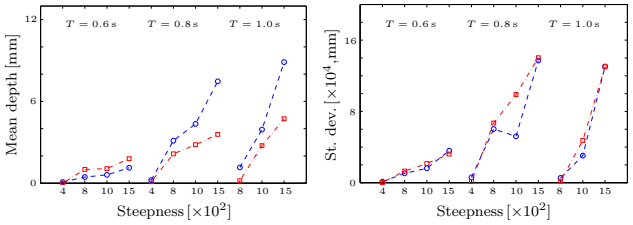

Figure 6: As in figure 5 but for a 10 mm thick floe.

Figures 5–6 show example comparisons of model predictions of the overwash depth mean and standard deviation at the centre of the floe and values calculated from the experimental data. Results are, again, for polypropylene floes.

In general:

- overwash becomes deeper as incident waves become steeper and the incident period increases;
- and overwash tends to be deepest for the thinner floes.

In terms of the model-data agreement:

- the model tends to slightly overestimate the mean depth and underestimate the standard deviation;
- the model is marginally more accurate for the polypropylene floes; and
- the model is least accurate for deep overwash (greater than approximately 5–6 mm), presumably because the model assumptions are no longer valid in the deep overwash regime.

Summary

1. A linear model accurately predicts the motions of a model floe induced by regular incident waves.
2. A relatively simple model, in which overwash is forced by the linear model, predicts mean overwash depth with pleasing accuracy.

Acknowledgements

The Universities of Plymouth, Melbourne and Newcastle funded the experiments. The Australian Antarctic Science Program funds DS and LB. The Australian Research Council funds LB and JM. The US Office of Naval Research funds MM.

References

Kurganov, A. & Tadmor, E. 2000 New high-resolution central schemes for nonlinear conservation laws and convectiondiffusion equations *J. Comp. Phys.* **160**, 241–282.

Kurganov, A., Noelle, S. & Petrova, G. 2001 Semidiscrete central-upwind schemes for hyperbolic conservation laws and Hamilton–Jacobi equations *SIAM J. Sci. Comput.* **23**, 707–740.

Meylan, M. H. 2002 Wave response of an ice floe of arbitrary geometry. *J. Geophys. Res.* **107**.

Montiel, F., Bonnefoy, F., Ferrant, P., Bennetts, L. G., Squire, V. A. & Marsault, P. 2013*a* Hydroelastic response of floating elastic disks to regular waves. Part 1: Wave tank experiments. *J. Fluid Mech.* **723**, 604–628.

Montiel, F., Bennetts, L. G., Squire, V. A., Bonnefoy, F. & Ferrant, P. 2013*b* Hydroelastic response of floating elastic disks to regular waves. Part 2: Modal analysis. *J. Fluid Mech.* **723**, 629–652.

Wave Radiation by a Cylinder Submerged in Water with an Ice Floe or a Polynya

by I.V. Sturova and L.A. Tkacheva

Lavrentyev Institute of Hydrodynamics of SB RAS, pr. Lavrentyeva 15, Novosibirsk, 630090, Russia
sturova@hydro.nsc.ru, tkacheva@hydro.nsc.ru

Highlights:

• Radiation problem for a cylinder submerged in the fluid with a finite elastic plate is solved in two ways: Wiener-Hopf technique and matched eigenfunction expansions.
• The influence of a finite patch of ice-free water in an ice sheet on the hydrodynamic characteristics of oscillating cylinder is investigated.

1. Introduction

The linear 2-D time-harmonic water-wave problem describing small oscillations of a horizontal cylinder is considered for two classes of a hydroelastic system. The fluid surface is either open, except in a finite region where it is covered by a thin-elastic plate, which represents an ice floe, or covered by two semi-infinite thin elastic plates with different properties, except in a finite patch of ice-free water (polynya). In both cases, the fluid domain is of infinite horizontal extent and finite depth.

Radiation of waves by a cylinder submerged in fluid having mixed boundary conditions on the upper surface were studied in [1,2] for a floating semi-infinite elastic plate and in [3,4] for two semi-infinite elastic plates connected by the vertical and flexural rotational springs as a model of a partially frozen crack in ice sheet. These problems were solved by the method of matched eigenfunction expansions for the velocity potentials. The interaction of a submerged body with a floating elastic platform of finite length was considered by Hermans [5] using the Green's function method.

In this paper, Hermans's problem is solved by two different methods: Wiener-Hopf technique and matched eigenfunction expansions. Wave generation by an oscillating submerged cylinder in the presence of a polynya is studied only by using the method of matched eigenfunction expansions. The hydrodynamic load and the amplitudes of vertical displacements of the free surface and elastic plates are calculated.

2. Mathematical formulation

The problem is analyzed in 2-D Cartesian coordinate system with the x-axis directed along the undisturbed mean water surface perpendicular to the cylinder axis, and the y-axis pointing vertically upwards. The fluid is assumed to be inviscid and incompressible, its motion is irrotational. The depth of fluid is equal to H. The plates are in contact with the water at all points for all time. The plate drafts are neglected. It is assumed that the edges of the plates are free.

The wave motions are generated by the small oscillations of submerged rigid body with wetted surface S at a frequency ω with amplitudes ζ_j $(j = 1, 2, 3)$ for the sway, heave and roll problems, respectively. Under the usual assumptions of linear theory, the time-dependent velocity potential can be written as

$$\Phi(x, y, t) = \Re\left[i\omega \sum_{j=1}^{3} \zeta_j \varphi_j(x, y) \exp(i\omega t)\right], \quad (1)$$

where $\varphi_j(x, y)$ are complex valued functions and t is time. The vertical displacements of the free surface and elastic plates $W(x, t)$ can be determined from the relation

$$\frac{\partial W}{\partial t} = \left.\frac{\partial \Phi}{\partial y}\right|_{y=0}.$$

By analogy with representation (1), the expression for $W(x, t)$ can be written in the form:

$$W(x, t) = \Re\left[\sum_{j=1}^{3} \zeta_j w_j(x) \exp(i\omega t)\right],$$

$$w_j(x) = \left.\frac{\partial \varphi_j}{\partial y}\right|_{y=0}. \quad (2)$$

The radiation potentials $\varphi_j(x, y)$ satisfy the Laplace equation in the fluid domain

$$\nabla^2 \varphi_j = 0 \quad (-\infty < x < \infty,\ -H < y < 0) \quad (3)$$

except in the region occupied by the cylinder.

The boundary condition on the closed smooth contour of the submerged body S has the form:

$$\frac{\partial \varphi_j}{\partial n} = n_j \quad (x, y \in S). \quad (4)$$

Here, $\mathbf{n} = (n_x, n_y)$ is the inward normal to the contour S. The notations

$$n_1 = n_x, \quad n_2 = n_y, \quad n_3 = (y - y_0)n_1 - (x - x_0)n_2 \quad (5)$$

are used where $x_0,\ y_0$ are the coordinates of the center of the roll oscillations.

The boundary condition at the bottom is

$$\frac{\partial\varphi_j}{\partial y} = 0 \quad (-\infty < x < \infty,\ y = -H). \tag{6}$$

In the far field a radiation condition should be imposed that requires the radiated waves to be outgoing.

Finite plate. The upper boundary of the fluid is covered partly with an elastic homogeneous plate $(0 < x < L,\ y = 0)$ with mass density ρ and thickness d. The free surface condition in the open water regions is given by

$$\frac{\partial\varphi_j}{\partial y} - \frac{\omega^2}{g}\varphi_j = 0, \quad (x < 0,\ x > L,\ y = 0), \tag{7}$$

where g is the acceleration due to gravity.

On the elastic covered surface, the radiation potentials $\varphi_j(x, y)$ satisfy the boundary condition in the form

$$\left(D\frac{\partial^4}{\partial x^4} - \omega^2 M + g\rho_0\right)\frac{\partial\varphi_j}{\partial y} - \rho_0\omega^2\varphi_j = 0 \tag{8}$$

$$(0 < x < L,\ y = 0),$$

where $D = Ed^3/[12(1-\nu^2)]$, $M = \rho d$, E is the Young's modulus for the elastic plate, ν is its Poisson's ration, ρ_0 is the fluid density. At the plate edges, free edge conditions require vanishing the bending moment and the shear force:

$$\frac{\partial^3\varphi_j}{\partial x^2\partial y} = \frac{\partial^4\varphi_j}{\partial x^3\partial y} = 0 \quad (x = 0^+, L^-,\ y = 0). \tag{9}$$

Polynya. Two semi-infinite elastic plates Λ_1 $(x < 0)$ and Λ_2 $(x > L)$ float on water surface. The left plate Λ_1 and the right plate Λ_2 have the characteristics $E_1,\ d_1,\ \rho_1,\ \nu_1$ and $E_2,\ d_2,\ \rho_2,\ \nu_2$, respectively. The boundary conditions for the fluid in contact with the plates Λ_1 and Λ_2 are similar (8) using the corresponding values of $E,\ d,\ \rho,\ \nu$. Free edge conditions (9) are fulfilled at $(x = 0^-, L^+,\ y = 0)$. The free surface condition (7) takes place at $(0 < x < L,\ y = 0)$.

3. Method of solution.

In solving the problem (3), (4), (6)-(9), for each of the body oscillation modes we introduce an unknown mass source distribution $\sigma_j(x, y)$ over the contour S. The radiation potentials at any point of fluid can be represented in the form

$$\varphi_j(x, y) = \int_S \sigma_j(\xi, \eta)G(x, y; \xi, \eta)ds. \tag{10}$$

The Green function $G(x, y; \xi, \eta)$ satisfies the following equation

$$\nabla^2 G = 2\pi\delta(x - \xi)\delta(y - \eta)$$

with the boundary conditions analogous to (6)-(9) and the radiation condition in the far field, and δ is the Dirac delta-function.

We describe briefly the determination of the Green function for the case of finite plate by the Wiener - Hopf technique. The characteristic length $l = g/\omega^2$ and dimensionless variables and parameters are used:

$$x' = \frac{x}{l}, \quad y' = \frac{y}{l}, \quad t' = \omega t, \quad H' = \frac{H}{l}, \quad L' = \frac{L}{l},$$

$$\beta = \frac{D}{\rho_0 g l^4}, \quad \gamma = \frac{M}{\rho_0 l}.$$

Below, the primes are omitted. Then boundary conditions on the upper surface of the fluid (7), (8) have the form

$$\Omega_1(\varphi_j) \equiv \frac{\partial\varphi_j}{\partial y} - \varphi_j = 0,\ (x < 0,\ x > L,\ y = 0), \tag{11}$$

$$\Omega_2(\varphi_j) \equiv \left(\beta\frac{\partial^4}{\partial x^4} + 1 - \gamma\right)\frac{\partial\varphi_j}{\partial y} - \varphi_j = 0, \tag{12}$$

$$(0 < x < L,\ y = 0).$$

Two different expressions for the same Green functions are used. For the first one we seek the Green function in the form

$$G(x, y; \xi, \eta) = G_0(x, y; \xi, \eta) + G_1(x, y; \xi, \eta),$$

where G_0 is the Green function for the fluid with the infinite free upper surface and the condition of non-flow on the bottom, G_1 is the added function to fulfil the conditions (8), (9) on the plate. This expression is convenient when the points (x, y) and (ξ, η) are at short distance, because the logarithmic singularity is expressed evidently. For the determination of the function of G_1 we obtain the same problem (3), (6), (9), (11), (12), only in the condition (12) the right side is non-zero function. This problem is solved by the Wiener - Hopf technique in [6]. For other case we express the Green function in the form of series. We use the Fourie transformation on x

$$\Psi_+(\alpha, y) = \int_L^\infty \mathrm{e}^{i\alpha(x-L)}G(x, y)dx, \tag{13a}$$

$$\Psi_-(\alpha, y) = \int_{-\infty}^0 \mathrm{e}^{i\alpha x}G(x, y)dx, \tag{13b}$$

$$\Psi_1(\alpha, y) = \int_0^L \mathrm{e}^{i\alpha x}G(x, y)dx, \tag{13c}$$

$$\Psi(\alpha, y) = \Psi_-(\alpha, y) + \Psi_1(\alpha, y) + e^{i\alpha L}\Psi_+(\alpha, y),$$

$$\partial^2\Psi/\partial y^2 - \alpha^2\Psi = 2\pi\mathrm{e}^{i\alpha\xi}\delta(y - \eta). \tag{13d}$$

The solution of Eq. (13d) with the condition (6) on the bottom has the form

$$\Psi(\alpha, y) = C(\alpha)Y(\alpha, y) +$$

$$\frac{2\pi}{\alpha}\mathrm{e}^{i\alpha\xi}\begin{cases}\sinh(\alpha(y + H))\cosh(\alpha(\eta + H)) & (y > \eta)\\ \cosh(\alpha(y + H))\sinh(\alpha(\eta + H)) & (y < \eta),\end{cases}$$

$$Y(\alpha, y) = \frac{\cosh(\alpha(y + H))}{\cosh(\alpha H)}.$$

We denote $D_{\pm}(\alpha)$, $D_1(\alpha)$ the integrals of the type (13a-c) where the function G is replaced by the expression $\Omega_1(G)$ and $F_{\pm}(\alpha)$, $F_1(\alpha)$ are analogous integrals where G is replaced by $\Omega_2(G)$. Further the functions $D(\alpha)$ and $F(\alpha)$ are introduced:

$$D(\alpha) = D_-(\alpha) + D_1(\alpha) + e^{i\alpha L} D_+(\alpha),$$

$$F(\alpha) = F_-(\alpha) + F_1(\alpha) + e^{i\alpha L} F_+(\alpha),$$

$$D(\alpha) = \frac{2\pi}{\alpha} \mathrm{e}^{i\alpha\xi} [\alpha \cosh(\alpha H) - \sinh(\alpha H)] \times \cosh(\alpha(\eta + H)) + C(\alpha) K_1(\alpha), \quad (14)$$

$$F(\alpha) = \frac{2\pi}{\alpha} \mathrm{e}^{i\alpha\xi} [(\beta\alpha^4 + 1 - \gamma)\alpha \cosh(\alpha H) - \sinh(\alpha H)] \times \cosh(\alpha(\eta + H)) + C(\alpha) K_2(\alpha). \quad (15)$$

From the conditions (11) and (12) we have $D_-(\alpha) = D_+(\alpha) = 0$, $D_1(\alpha) = D(\alpha)$, $F_1(\alpha) = 0$.

We express $C(\alpha)$ from (14) and substitute to (15). After transformations we obtain

$$F_-(\alpha) + e^{i\alpha L} F_+(\alpha) = \left[2\pi \mathrm{e}^{i\alpha\xi} (\gamma - \beta\alpha^4) Y(\alpha, \eta) + D_1(\alpha) K_2(\alpha)\right] / K_1(\alpha).$$

This equation is solved in a similar manner as in [6]. The solution of this equation and expressions for the Green function are detailed in [7]. An alternative method of determining the Green function is the method of matched eigenfunction expansions which was used in [1-4].

Using boundary condition (4) on the body surface S, we obtain the integral equation for the functions $\sigma_j(x, y)$

$$\pi\sigma_j(x, y) - \int_S \sigma_j(\xi, \eta) \frac{\partial G}{\partial n} ds = n_j.$$

Once the distribution of the singularities $\sigma_j(x, y)$ has been calculated, we can determine the radiation potentials (10). The vertical deflections of the free surface and elastic plates can be determined from (2):

$$w_j(x) = \int_S \sigma_j(\xi, \eta) \frac{\partial G}{\partial y}\bigg|_{y=0} ds.$$

The radiation load acting on the oscillating body is determined by the force $\mathbf{F} = (F_1, F_2)$ and the moment F_3 which, without account for the hydrostatic term, have the form

$$F_k = \sum_{j=1}^{3} \zeta_j \tau_{kj} \quad (k = 1, 2, 3),$$

$$\tau_{kj} = \rho\omega^2 \int_S \varphi_j n_k ds = \omega^2 \mu_{kj} - i\omega\lambda_{kj}$$

where μ_{kj} and λ_{kj} are the added mass and damping coefficients, respectively. There is the symmetry condition $\tau_{kj} = \tau_{jk}$. Reciprocity relations between the damping coefficients and wave characteristics in the far field agree with the case of infinitely extended free surface (see, *e.g.,* [8]) for a finite elastic plate and with the case of a crack between two semi-infinite elastic plates [3,4] for a polynya.

4. Numerical results

The calculations are performed for the elliptic contour $S : (x - c)^2/a^2 + (y + h)^2/b^2 = 1$, where a and b are the major and minor axes of the ellipse, respectively, and the coordinates of its center are equal to $x = c$, $y = -h$ $(h > 0)$. Rotational oscillations occur with respect to the point $x_0 = 0$, $y_0 = -h$ in (5). The following input data are used: $E = 5GPa$, $\rho = 922.5kg/m^3$, $\nu = 0.3$, $\rho_0 = 1025kg/m^3, d = 2m$, $b = 10m$, $a = h = 20m$, $H = 500m$.

Figures 1, 2 represent dimensionless values of the coefficients of hydrodynamic load as functions of dimensionless frequency $b/l = \omega^2 b/g$:

$$\mu^*_{kj} = \frac{\mu_{kj}}{\pi\rho_0 b^2}, \quad \lambda^*_{kj} = \frac{\lambda_{kj}}{\pi\rho_0\omega b^2},$$

$$\mu^*_{k3} = \frac{\mu_{k3}}{\pi\rho_0 b^3}, \quad \lambda^*_{k3} = \frac{\lambda_{k3}}{\pi\rho_0\omega b^3} \quad (k, j = 1, 2),$$

$$\mu^*_{33} = \frac{\mu_{33}}{\pi\rho_0 b^4}, \quad \lambda^*_{kj} = \frac{\lambda_{kj}}{\pi\rho_0\omega b^4}.$$

More detailed results for the hydrodynamic load on the cylinder and the amplitudes of the displacements of the ice sheets and the free surface will be presented at the Workshop.

References

[1] Sturova, I.V. 2013, Wave forces on oscillating horizontal cylinder submerged under non-homogeneous surface. *IWWWFB28.*

[2] Sturova, I.V. 2014, Wave generation by an oscillating submerged cylinder in the presence of a floating semi-infinite elastic plate, *Fluid Dynamics*, Vol. 49, No. 4, pp. 504-514.

[3] Sturova, I.V. 2014, Radiation of waves by a cylinder submerged in the fluid beneath an elastic ice sheet with a partially frozen crack. *IWWWFB29.*

[4] Sturova, I.V. 2014, Effect of a crack in an ice sheet on hydrodynamic characteristics of submerged oscillating cylinder, *J. Appl. Maths Mechs* (accepted).

[5] Hermans, A.J. 2014, The interaction of a submerged object with a Very Large Floating Platform. *IWWWFB29.*

[6] Tkacheva, L.A. 2005, Action of a periodic load on an elastic floating plate, *Fluid Dynamics*, Vol. 40, No. 2, pp. 282-296.

[7] Tkacheva, L.A. 2014, Oscillations of submerged cylinder in fluid in the presence of an ice cover, *J. Appl. Mech. Tech. Phys.* (submitted).

[8] Linton, C.M., McIver, P., 2001, *Handbook of Mathematical Techniques for Wave/Structure Interactions*, Chapman & Hall/CRC Press, London/ Boca Raton, FL.

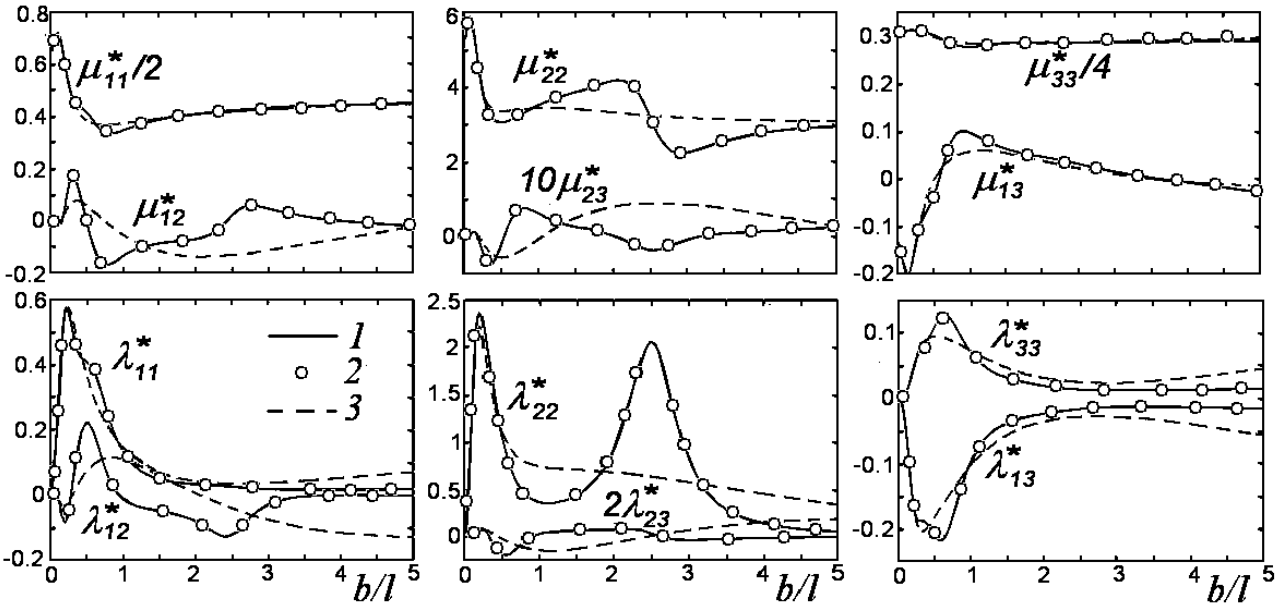

Figure 1: The hydrodynamic load of a cylinder beneath an ice floe at $c/b = 5$. Curves *1* and *2* correspond to solutions obtained at $L/b = 15$ by Wiener-Hopf technique and matched eigenfunction expansions, respectively. Curve *3* shows the results for a semi-infinite ice sheet [2].

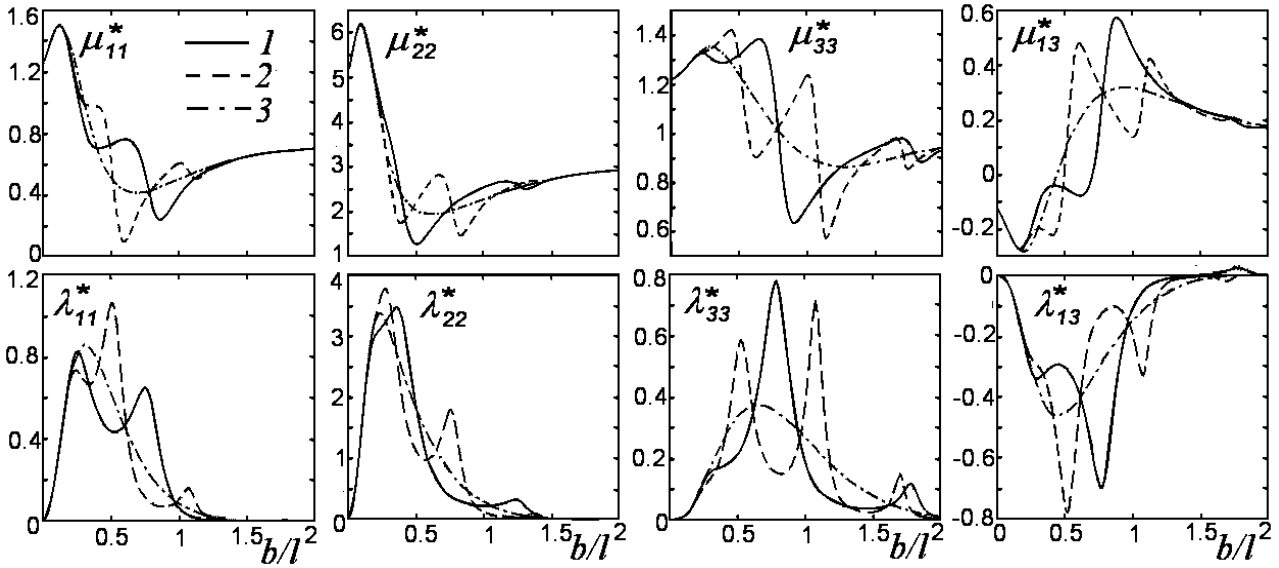

Figure 2: The hydrodynamic load of a cylinder beneath a polynya between two ice sheets with identical properties. Curves *1* and *2* correspond to $L/b = 6,\ c/b = 3$ and $L/b = 10,\ c/b = 5$, respectively. Curve *3* shows the results for infinitely extended free surface.

A Time-Domain Twice Expansion Method for Wave Interaction with a Body of Large Amplitude Motion

Bin Teng, Ruijia Jin
State Key Laboratory of Coastal and Offshore Engineering
Dalian University of Technology
Dalian, 116024, Liaoning, China
E-mail: bteng@dlut.edu.cn

1. Introduction

Deep water structures are usually positioned in sea by mooring lines, which perform strong nonlinearity. The structure system usually has a very low natural frequency, and can be inspired lager reciprocating drift motion by nonlinear wave force at low frequency.

To deal with the problem due to mooring nonlinearity, Sarkar and Eatock Taylor (1998, 2001) proposed a two-scale perturbation method to investigate the interactions of nonlinear mooring stiffness and wave hydrodynamics, and established a frequency domain perturbation method for this problem.

The nonlinear problem is more widely studied in the time domain, and coupling analysis must be carried out for wave interaction with floater and mooring system. As the total time domain coupling analysis is complex and tremendous, hydrodynamic load is often computed by a perturbation expansion method (as Yang et al (2012)), or by Cummins method based on the frequency domain perturbation expansion (as Kim et al (2013)).

Perturbation method is powerful when body motion is not very large. However, in deep water the floater may oscillate with an amplitude larger than wave lengths. At this condition, the traditional perturbation expansion is obviously not correct. The most obvious disadvantages of the present perturbation method are that the phase change of the wave load due to body motion and the change of the encountering frequency of incident waves are unable to be considered. To solve those problems, a time domain twice expansion method is proposed in this study. The displacement of floater motion is divided into two part: one is a large amplitude motion with low frequency, and the other is an oscillation about the low frequency motion at higher frequency. The large amplitude motion at low frequency is obtained by numerical filtering of body response with progress of the simulation. This position is called as the instantaneous mean position. The smaller amplitude motion about the mean position is computed by perturbation expansion method. Thus, it can be guaranteed that the perturbation expansion factor is always smaller.

The numerical filtering is implemented by a wavelet transform method in this study, and a HOBEM is applied to calculate the wave field at each time step. At each time step, the overall body and free surface meshes vary with the low frequency movement, but the relative location of the computational grids is invariant. Recursive interpolation is used to get the physical values for those nodes inside the free surface mesh, and Taylor series expansion is used for the boundary nodes after the body and the mesh have translated to a new position. At the new position, computation is similar with that for wave interaction with a body moving in a steady current.

2. Definition of coordinate systems and decomposition of body motion

To describe the motion of a floating body, three coordinate systems (**Fig. 1**) are defined. The first is an earth-fixed coordinate system $Oxyz$ at the initial equilibrium position of the body, the second is an instantaneous mean coordinate system $\overline{O}\overline{x}\overline{y}\overline{z}$ translating horizontal with the body at low frequency and the third is a body-fixed coordinate system $O'x'y'z'$. The origins of the coordinate systems $Oxyz$ and $\overline{O}\overline{x}\overline{y}\overline{z}$ are at the still water surface, and the z and the $\overline{z}$ axes measure vertically upward.

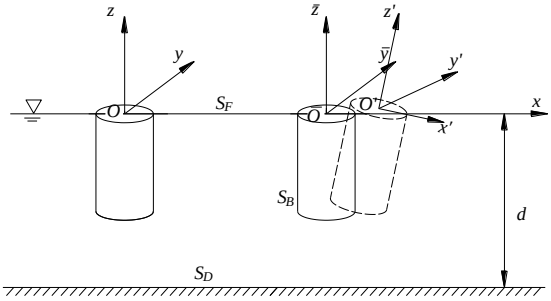

Fig. 1 Definition sketch of coordinate systems

When the body is undergoing a large drift motion, the second coordinate system will be far away from the first one. For any point on the body, the coordinate vector X in the earth-fixed coordinate system can be

represented by the coordinate vector $\boldsymbol{X}'$ in the body-fixed coordinate system and it motion components in the following relationship:

$$\boldsymbol{X} = \boldsymbol{X}'(t) + \Xi(t) \tag{1}$$

and

$$\Xi(t) = \bar{\boldsymbol{X}}(t) + (\boldsymbol{\xi} + \boldsymbol{\alpha} \times (\boldsymbol{X}'(t) - \boldsymbol{X}'_0(t)) \tag{2}$$

where $\overline{\mathbf{X}}(t)$ is the displacement of the instantaneous mean coordinate system $\overline{O}xyz$ with only the horizontal translation, $\boldsymbol{X}'_0$ is the body rotation center, $\boldsymbol{\xi}$ and $\boldsymbol{\alpha}$ are the body translation and rotation components relative to the instantaneous mean coordinate system. $\overline{\mathbf{X}}(t)$ will be obtained by a numerical filtering method with the simulation of body response, which will be introduced in the next section.

Following the Stokes expansion procedure, we expand the body motion relative to the instantaneous mean position $\overline{\mathbf{X}}(t)$ into perturbation series as follows:

$$\xi(t) = \varepsilon\xi^{(1)}(\bar{\mathbf{X}}, t) + \varepsilon^2\xi^{(2)}(\bar{\mathbf{X}}, t) + \cdots \tag{3}$$

$$\alpha(t) = \varepsilon\alpha^{(1)}(\bar{\mathbf{X}}, t) + \varepsilon^2\alpha^{(2)}(\bar{\mathbf{X}}, t) + \cdots \tag{4}$$

The superscripts (1) and (2) indicate separately the wave components at the first-order and the second-order of ε respectively.

In the same way, the velocity potential ϕ and wave elevation η can be expanded as

$$\phi(\bar{\mathbf{X}}, t) = \varepsilon\phi^{(1)}(\bar{\mathbf{X}}, t) + \varepsilon^2\phi^{(1)}(\bar{\mathbf{X}}, t) + \cdots \tag{5}$$

$$\eta(\bar{\mathbf{X}}, t) = \varepsilon\eta^{(1)}(\bar{\mathbf{X}}, t) + \varepsilon^2\eta^{(1)}(\bar{\mathbf{X}}, t) + \cdots \tag{6}$$

at the instantaneous mean positions by the parameter ε.

Then the Stokes perturbation expansions are substituted into the Laplace equation and the corresponding boundary conditions are expanded about the still water surface and the instantaneous mean body surface. The boundary value problems at the order of ε and ε^2 in the perturbation expansions can be established.

As the instantaneous mean coordinate system moves with very low frequency, the acceleration of the system is a higher order term of ε, and the system can be approximated as an inertial system. Thus, the governing equation, boundary conditions, wave force and motion equation are the same as in the earth-fixed coordinate system, and computation can be done in the same way as for a steady moving body in waves (Liu et al, 2012).

3. Computation of mean position and mesh translation

Deep water moored platforms may move to far distances from their initial positions. For accurate computation, an instantaneous mean position is needed to get and carries out perturbation expansion about the position. According to the time sequence of the motion response simulated, we use a wavelet transform to get the mean position of the motion response (Chritopher and Gilbert, 1998).

Assuming that the time sequence of the motion response is $\Xi(t)$ (0, t), and is progressing with the time, the continuous wavelet transform of a discrete sequence is defined as the convolution of Ξ with a scaled and translated version of $\Psi_0(\eta)$. By the convolution theorem, the wavelet transform is the inverse Fourier transform of the product

$$WT(s,t) = \sum_{n=0}^{N-1} \hat{\Xi}\hat{\psi}^*(s\omega_k) e^{i\omega_k n\Delta t} \tag{7}$$

In the actual application of wavelet transform, the selection of mother wavelet function has a crucial impact on the analysis results. For the same problem, the analysis results may differ very much if different mother wavelets are chosen. In the present analysis, the instantaneous mean displacement $\overline{\mathbf{X}}(t)$ is not needed to be unique, but only the total displacement $\boldsymbol{\Xi}(t)$ to be needed unique. The study in this paper is based on the Morlet wavelet as the mother wavelet. Since the wavelet transform is a band pass filter with a known response function, it is possible to reconstruct the original time series using either deconvolution or the inverse filter.

$$\Xi(t) = \frac{\delta j \Delta t^{1/2}}{C_\delta \psi_0(0)} \sum_{j=0}^{J} \frac{\mathrm{Re}\{WT(s_j, t)\}}{s_j^{1/2}} \tag{8}$$

where C_δ is the reconstruct coefficient. For the mean position of the displacement time series, there is no need to evaluate all the scales. The small scales just should be left out and the expected results $(\bar{X}_x(t), \bar{X}_y(t))$ will be obtained.

When the Morlet wavelet is selected as the mother wavelet, the value of reconstruct coefficients C_δ and $\psi_0(0)$ will be 0.776 and $\pi^{-1/4}$.

Let the body surface mesh and free surface mesh drift horizontally with the body mean displacement. When the meshes moving to new mean positions, the right-hand side of integration equation, i.e. the known quantities, would be evaluated based on the values at the last time step. The wave elevation also needs to conduct recursive calculation by the free surface conditions. Due to the meshes moving as a whole, the grid shape will not change, so that the velocity potentials and wave elevations at the new time step can be determined by interpolation for those points inside the free surface meshes or by using Taylor expansion for those points at the boundaries of the free surface mesh as

$$f_{t+\Delta t}^{(1)}(x,y) = f_t^{(1)}(x_0,y_0) + \frac{\partial f_t^{(1)}}{\partial x}\nabla x + \frac{\partial f_t^{(1)}}{\partial y}\nabla y$$

$$f_{t+\Delta t}^{(2)}(x,y) = f_t^{(2)}(x_0,y_0) + \frac{1}{2}\frac{\partial^2 f_t^{(1)}}{\partial x^2}\nabla x^2 + \frac{1}{2}\frac{\partial^2 f_t^{(1)}}{\partial y^2}\nabla y^2 + \frac{\partial^2 f_t^{(1)}}{\partial x \partial y}\nabla x \nabla y + \frac{\partial f_t^{(2)}}{\partial x}\nabla x + \frac{\partial f_t^{(2)}}{\partial y}\nabla y \tag{8}$$

where f indicates scattered potential ϕ_s or scattered wave evaluation η_s at the free surface.

4. Example analyses

To validate the present method, a forced moving truncated cylinder in monochromatic waves and a free moving truncated cylinders in bichromatic waves are considered.

4.1. Forced motion in waves

The first evaluation is about forced oscillation of a truncated cylinder in monochromatic waves. The cylinder has a radius of 1m and a draft of 0.5m in a water depth of 1.5m. The incident waves have an amplitude of A=0.1m with a frequency of ω=2.98rad/s (k=0.6m^{-1}), and propagating in the x-direction.

The cylinder is under a forced dual-frequency motion:

$$\Xi_x = A_1 \sin(\omega_1 t + \varphi_1) + A_2 \sin(\omega_2 t + \varphi_2) \qquad (9)$$

where A_1=0.4m, ω_1=2.98rad/s (k_1=1.0m^{-1}) and φ_1=45° are the amplitude, frequency and initial phase of the higher-frequency small-amplitude motion, and A_2=2.0m, ω_2=0.19rad/s (k_2=0.05m^{-1}) and φ_2=0° are the amplitude, frequency and initial phase of the lower-frequency large-amplitude motion.

The wave exciting force on the moving body is decomposed into the components due to the incident potential and the scattered potential, which are defined as F_w and F_s. Fig. 2 and 3 how the comparison of the first order and the second order forces by the present method with the original expanded method in the earth-fixed coordinate system. From Fig. 2, it can be seen that there exists obvious phase difference between the incident wave forces from the two methods. When body mean position is positive, the phase of the incident wave force obtained by the present method is later than that by the original one, as the incident waves reach the present body position later than the original position. In turn, when the mean position is negative, the phase of incident wave force obtained by the present method is earlier than that by the original method. This conclusion is consistent with the actual situation. While to the wave force generated by the scattered potential, the phases of wave forces obtained by the two methods are the same, but the envelop shapes are different. The present results fluctuate around the original ones, and the oscillating period is equal to the period of the low frequency forced motion. The difference is from the motion velocity of the instantaneous mean position which is neglected in the original method.

The total force is the summation of the two parts. It was observed the total forces from the two methods are quite different. The amplitude of the total force from the original method is steady and uniform, but the force amplitude from the present method oscillating with the time. When body moves to a position where incident wave force and scattered wave force have the same phase, the total force from the present method are much bigger than that from the original ones. Oppositely, the present results are smaller than the original ones.

The second-order total wave force contains more complex components. There are more differences between the present and the original methods.

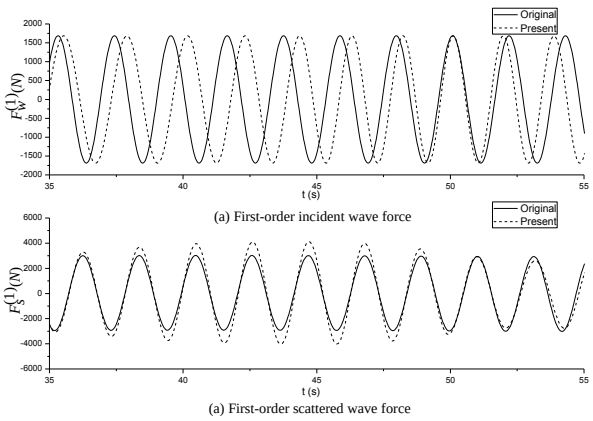

Fig. 2 Comparison of the first-order wave force

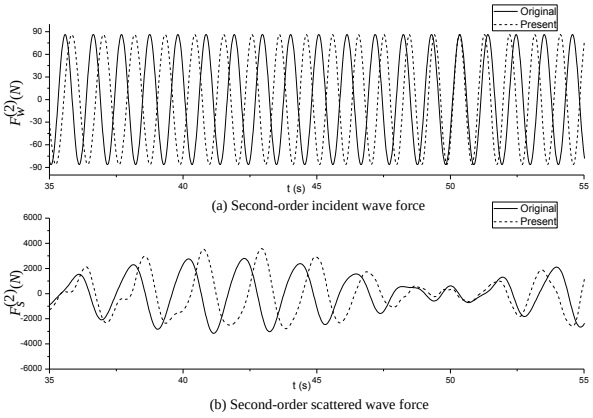

Fig. 3 Comparison of the second-order wave force

4.2. Free motion in waves

It is seen that the present method gets quite different results for a body undergoing a large amplitude motion from that by the original method. Through analysis and comparison, it is believed that the present method is more reasonable and more suitable for realistic conditions.

This example shows the analysis for a free moving truncated cylinder moored by linear elastic constrain under the action of bichromatic waves. The cylinder has a radius of 1.0m and a draft of 3.0m in a water depth of 10.0m. A linear spring is arranged in the surge direction to constrain the motion of the cylinder and the stiffness of the spring is 4×10^2N/m. The natural vibration frequency of the system is about 0.151rad/s. The parameters of the bichromatic waves are shown in

Tab. 1 as follow.

Tab. 1 Parameters of the bichromatic waves

Items	Wave Amplitude(m)		Wave Frequency(rad/s)		Wave Direction(°)	
	A_1	A_2	ω_1	ω_2	θ_1	θ_2
Value	0.20	0.18	2.20	2.40	0.00	0.00

From the above table, we can see that the difference frequency of the bichromatic waves is 0.2rad/s that is in the same order of the natural frequency of the system.

Fig. 4 shows the comparison of the wave forces from the present and the original methods. **Fig. 5** shows the comparison of the surge displacements from the present and the original methods. From Figs. 4 and 5, it can be seen that the first order wave forces and the body motion from the two methods are almost the same, as the total surge displacement is much less than the wave lengths. The second-order wave forces from the two method exist some differences, and difference between the second order displacements is very obvious. It can also be seen that the second order displacement is much larger than the first order displacement as the difference frequency of the bichromatic waves is close to the natural frequency of the moored cylinder.

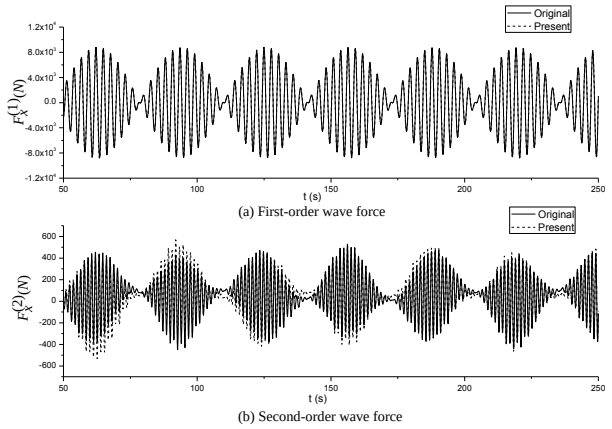

Fig. 4 Comparison of wave forces

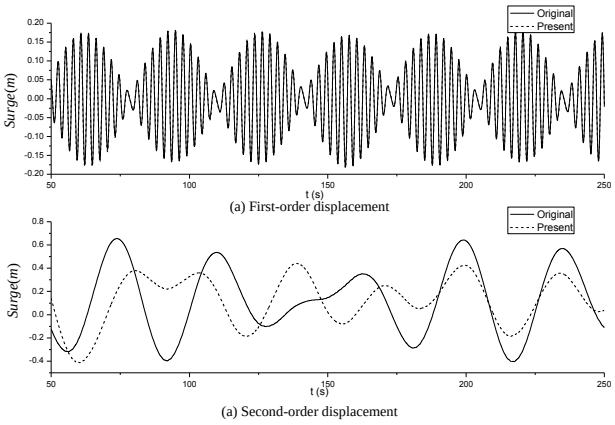

Fig. 5 Comparison of surge displacement

5. Conclusion

A twice expansion method in the time domain is developed in this study. The present method firstly gets the instantaneous mean position with the simulation by filtering the total motion response, and then carries out perturbation expansion about the mean position to assure the perturbation expansion factor is always smaller. The present method can deal with the problems of the phase change of incident wave action with the body motion and the change of encountering frequency of the incident waves with body moving velocity.

Two numerical examples are carried out, and comparisons are made between the present and the original methods. One is the forced motion of a truncated cylinder with dual-frequencies in a monochromatic waves, and the other is the free motion of a moored truncated cylinder in a bichromatic waves. Comparisons show that when the displacement of the body motion is large, both the first order and the second order force are different for the two methods, and when the displacements are smaller comparing to wave lengths the first order forces and displacements are almost the same, but the second order responses still have obvious difference.

Acknowledgements

This work was supported by the National Natural Science Foundation of China (Grant Nos. 51379032, 51490672), and the National Basic Research Program of China ("973" Program) (Grant No. 2011CB013703).

REFERENCES

[1] Kim BW, Hong GS, Kim JH, Hong SY, 2013, Comparison of linear spring and nonlinear FEM methods in dynamic coupled analysis of floating structure and mooring system, *Journal of Fluids and Structures*, 42, 205-227.

[2] Liu Z, Teng B, Ning DZ, Gou Y, 2010, Wave-current interactions with three-dimensional floating bodies, *Journal of Hydrodynamics*, 22(2), 229-240.

[3] Sarker A, Eatock Taylor R, 1998, Low-frequency responses of non-linearly moored vessels in random waves: development of a two-scale perturbation method, *Applied Ocean Research*, 20, 225-236.

[4] Sarker A, Eatock Taylor R, 2001, Low-frequency responses of non-linearly moored vessels in random waves: coupled surge, pitch and heave motions, *Journal of Fluids and Structures*, 15, 133-150.

[5] Chritopher T, Gilbert CP, 1998, A practical guide to wavelet analysis, *Bulletin of American Meteorological Society*, 79(1), 64-78.

[6] Yang MD, Teng B, Ning DZ, Shi ZM, 2012, Coupled dynamic analysis for wave interaction with a truss spar and its mooring linear/riser system in time domain, *Ocean Eng*, 39, 72-87.

Experimental observation of near-motion-trapped mode

H. Wolgamot[1], **P. H. Taylor**[2], **R. Eatock Taylor**[2], **C.J. Fitzgerald**[2], **T. van den Bremer**[2], **C. Whittaker**[3], **A. Raby**[3]

[1] Faculty of Engineering, Computing and Mathematics, University of Western Australia 35 Stirling Highway, CRAWLEY WA 6009, Australia. hugh.wolgamot@uwa.edu.au

[2] Department of Engineering Science, University of Oxford, OX1 3PJ, UK

[3] School of Marine Science and Engineering, Plymouth University, PL4 8AA, UK

Highlights

- Near-motion-trapping in heave is demonstrated experimentally;
- Tuned and detuned geometries tested;
- Range of radiation damping values is apparent from body motion;
- Small differences in damping apparent in analysis of radiated field.

1 Introduction

Trapped modes and near-trapped modes have been of considerable interest in water-wave problems for some time; sloshing trapped modes around fixed structures were found by Callan et al. [1991] and many subsequent authors, while sloshing near-trapped modes were found in arrays of vertical circular cylinders by Evans and Porter [1997]. Motion-trapped modes, in which a structure moves with a local oscillation of the free surface, but no oscillation in the far-field, were discovered by McIver and McIver [2006]. A previous contribution to this workshop, subsequently published as Wolgamot et al. [2014], identified a structure which approximated motion-trapping characteristics to high accuracy: 8 heaving truncated circular cylinders, evenly spaced around the circumference of a circle. The theoretical investigations above (and other similar works) have used potential flow theory.

Experimental investigations of sloshing trapped modes were undertaken by Cobelli et al. [2011], while various authors have investigated sloshing near-trapped modes experimentally. However, no attempt has been made to investigate motion-trapped (or near-trapped) modes experimentally to the authors' knowledge. Hence this paper describes a small experimental campaign to investigate the 8 cylinder structure referred to above.

2 Experimental methods

As the theory of motion-trapped modes assumes an ideal fluid it was desirable to minimise viscous effects in the experiments. To this end, the 8 cylinder structure investigated had hemispherical ends on each cylinder - the predicted trapping behaviour was not significantly altered compared to the truncated cylinders, though the trapping frequency changed as a result of the change in added mass. Each cylinder was fabricated from 160mm dia. PVC pipe, with a (clear) plastic hemisphere of the same diameter attached to the bottom. The cylinders were attached by radial spokes to a central hub, and could be attached at different positions along the spokes to change the radius of the ring, while adjusting the ballast in the cylinders adjusted the draft. Water was used as ballast - no internal sloshing was observed so there was no need to attempt to suppress such oscillations.

Tests were carried out in the Coastal Basin at Plymouth University's COAST Laboratory. This facility is a rectangular basin 15.5m x 10m, with an array of piston-type wavemakers (switched off throughout testing) and a beach on opposite short sides and 0.5m water depth during testing. The model was suspended from a beam across the tank (with the hemispherical ends completely immersed in all cases) and then released using a latch system. The motion of the model was tracked using a 6 DOF motion tracking system and the motion

of the free surface measured by wave gauges at seven points (both systems sampling at 128 Hz). The wave gauge locations are shown in Figure 1; Figure 2 is a photo of the experimental set-up.

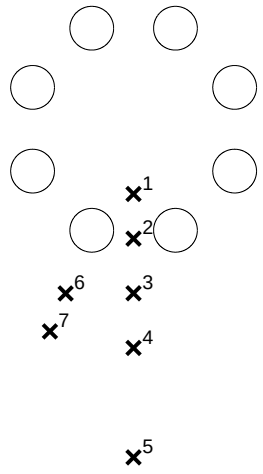

Figure 1: Layout of wave gauges WG1-WG7 (indicated by numbered crosses) relative to the cylinders for ring radius $5a$. Note that the wave gauges were not moved when the ring radius was changed.

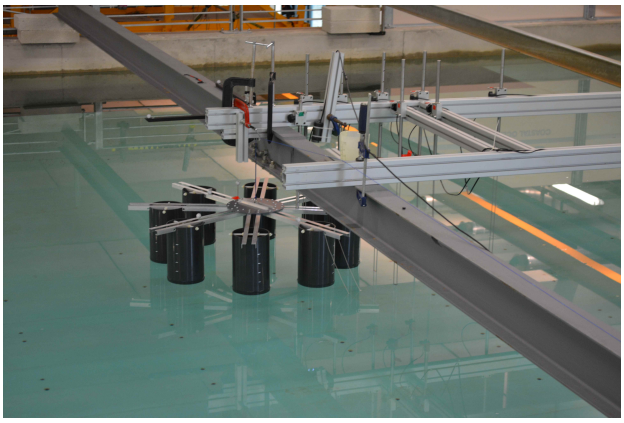

Figure 2: Experimental set-up showing model and wave gauges attached to the support beams.

The near-motion-trapped geometry had a ring radius of $5a$, where a is the cylinder radius, and an equilibrium draft of $2.5a$. In addition to this tuned case, a number of de-tuned cases, with different ring radii and drafts, were tested in the same way. The test geometry matrix is given in Table 1.

3 Results

One problem affecting both body motion and wave gauge data is reflection from the sidewalls of the tank. Based on the wave gauge readings it is estimated that the reflected waves from the sidewall reached the model about 5 seconds after release.

Draft \ Radius	$4a$	$5a$	$6a$
$2a$		$0.5a$	
$2.5a$	$0.5a$ $0.75a$ a	$0.5a$ $0.75a$ a	$0.5a$ $0.75a$ a
$3a$		$0.5a$ $0.75a$ a	
$3.5a$	$0.5a$ $0.75a$	$0.5a$ $0.75a$	

Table 1: Test matrix of different 8 cylinder configurations tested. Entries of the table correspond to initial release height. The near-motion-trapped mode occurs at draft $2.5a$ and ring radius $5a$.

3.1 Model heave

The model heave motion was found to behave linearly - no higher harmonics were evident when the frequency content was examined and the time series for different release heights, scaled by the initial value, matched extremely well (as seen in Figure 3). This behaviour suggests that nonlinear viscous damping of the model was negligible and that the viscous damping present can be considered linear. The different geometries were predicted to exhibit a range of radiation damping values - as indicated in Table 2.

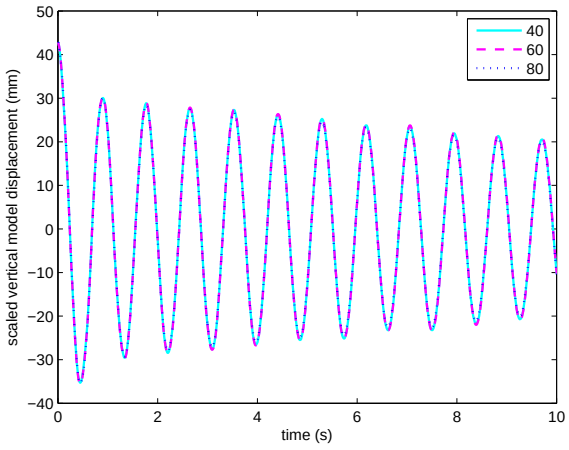

Figure 3: Heave oscillations of model at three different release heights, normalised by initial release height (to match nominal 40mm, actual release 43mm) to indicate linear scaling.

A number of methods were used to investigate the damping of the model. Dramatically different behaviour was observed for the most and least damped cases, as shown in Figure 4. However, it was difficult to differentiate between the decay

Draft \ Radius	$4a$	$5a$	$6a$
$2a$		2.7	
$2.5a$	1.9	0.0018*	0.9
$3a$		3.0	
$3.5a$	29	10	

Table 2: Predicted linear radiation damping of the various geometries tested (kg/s). *Note that this geometry is still slightly mistuned - at a frequency $\simeq 0.002$ Hz higher the predicted damping is more than 2 orders of magnitude lower, though this has little relevance experimentally.

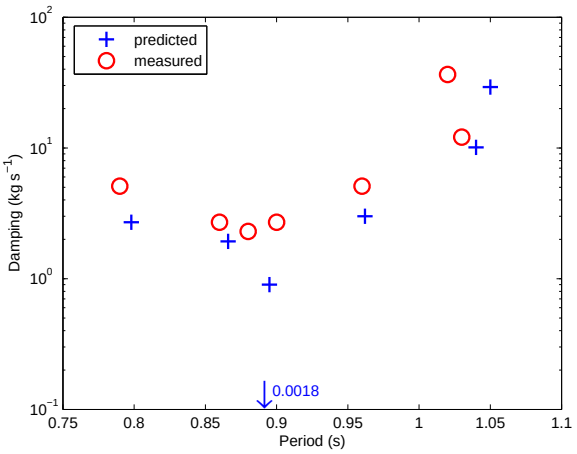

Figure 5: Predicted and measured model oscillation period and damping. The arrow indicates the predicted values for the tuned case (third from left).

rates of the models with small radiation damping, where the differences were masked by viscous damping. No simple theoretical way of accurately calculating the viscous damping to eliminate it from the problem could be found, but further analysis will be reported at the workshop. Figure 5 illustrates the behaviour of the different models by means of a plot of the predicted and measured natural periods and damping coefficients for each of the geometries given in Table 2. The damping is shown on a log scale. Note also in this figure the generally good agreement between predicted and measured oscillation period.

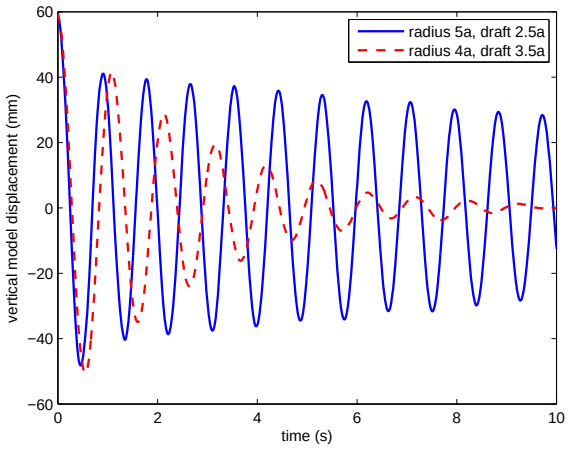

Figure 4: Measured time series of model oscillations in heave for the tuned geometry and geometry with the highest radiation damping.

3.2 Free surface elevation

The free surface elevation data was filtered in the frequency domain to remove the signal due to vibrations of the supporting beam (which supported both the model and wave gauges). As this beam vibration frequency occurred at approximately 5.5Hz, much higher than the wave frequencies, this was straightforward. In contrast to the model heave data, and as expected, higher harmonics were found to be present in the free surface elevation data. The radiated field data distinguished between the near-motion-trapped case and the other cases with moderately low damping. This is shown in Figure 6, where the time series and the Fourier transformed data (calculated using 2^{12} points, i.e. 32 seconds, commencing at 1.5 seconds after release) are shown for the near-motion-trapping geometry and the geometry with the 2nd lowest radiation damping (ring radius $6a$, draft $2.5a$).

Figure 6a shows the time series of the free surface elevations for the tuned case. It may be seen that in the tuned case, after the initial transient has passed, there is negligible radiation at linear frequencies outside the array (WG3) despite the fact that the internal free surface continues to oscillate. A comparison of the power spectral density at the heave frequency for wave gauges 1 and 3 (inside and outside the array) shows a ratio of almost 10^3 for the optimised geometry. There is noticeable radiation at double the linear frequency and the arrival of reflections at about 5 seconds may be seen. Figure 6b shows this pronounced 2nd harmonic and the absence of a linear signal outside the array. In Figures 6c and 6d, by contrast, there is a clear linear signal outside the array which dominates over the 2nd harmonic. It should be noted that the relative position of WG3 is closer to the model when the ring radius is increased, but as WG4 to 7 (omitted here for clarity) show similar behaviour this point is not significant.

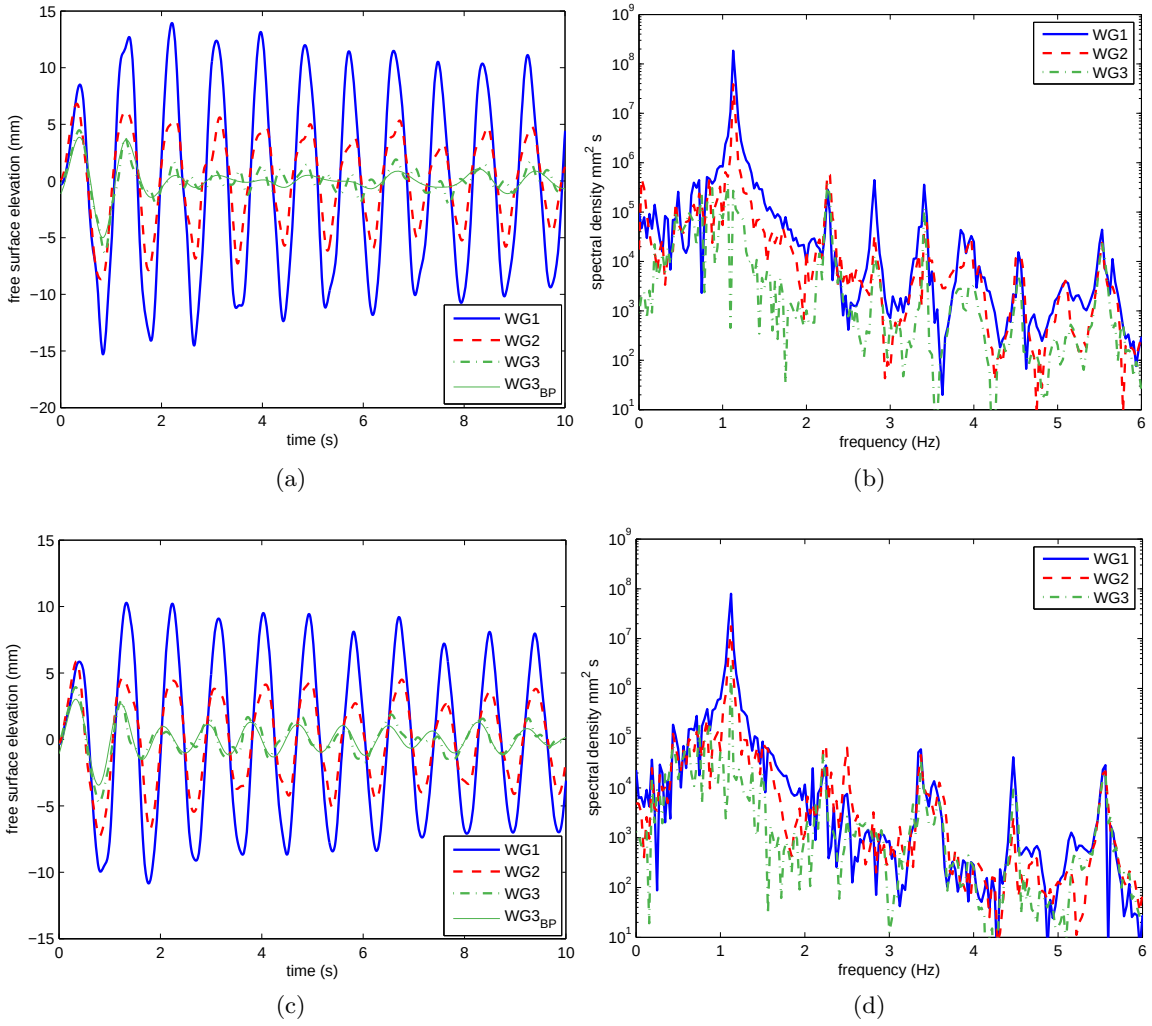

Figure 6: (a) time series of free surface elevations for the tuned case (ring radius $5a$, draft $2.5a$). $\mathrm{WG3}_{BP}$ is band pass filtered to eliminate frequencies outside the range $0.5f_1 < f < 1.5f_1$, where $f_1 =$ peak linear frequency; (b) power spectrum for case (a); (c) time series for ring radius $6a$, draft $2.5a$; (d) power spectrum for case (c).

4 Conclusions

Even though viscous damping is present in the experiments, the behaviour of the near-trapped mode is retained and is clearly visible: the heave motion persists for longer, and there is little wave radiation at the heave frequency after a starting transient. Further analysis, including fully nonlinear simulations of the experiment and videos taken during the testing will be presented at the Workshop.

Acknowledgement

The authors are grateful to the Lubbock Trustees in Oxford for a small grant to cover the costs of construction of the model. The first author acknowledges financial support from Shell Australia.

References

M. Callan, C.M. Linton, and D.V. Evans. Trapped modes in two-dimensional waveguides. *Journal of Fluid Mechanics*, 229:51–64, 1991.

P.J. Cobelli, V. Pagneux, A. Maurel, and P. Petitjeans. Experimental study on water-wave trapped modes. *Journal of Fluid Mechanics*, 666:445–476, 2011.

D.V. Evans and R. Porter. Near-trapping of waves by circular arrays of vertical cylinders. *Applied Ocean Research*, 19:83–99, 1997.

P. McIver and M. McIver. Trapped modes in the water-wave problem for a freely floating structure. *Journal of Fluid Mechanics*, 558(1):53–67, 2006.

H.A. Wolgamot, R. Eatock Taylor, and P.H. Taylor. Radiation, trapping and near-trapping in arrays of floating truncated cylinders. *Journal of Engineering Mathematics*, Published online 23 October 2014; DOI: 10.1007/s10665-014-9734-1, 2014.

A linearized free-surface RANS method for unsteady ship maneuvering problems

Marc O. Woolliscroft, Kevin J. Maki

Department of Naval Architecture and Marine Engineering
University of Michigan, Ann Arbor, MI, 48109 USA
[mowoolli, kjmaki]@umich.edu

Highlights

- The unsteady linearized free-surface condition is implemented within a numerical framework based on the Reynolds-Averaged Navier-Stokes equations. The target application for the novel solver is the simulation of ship maneuvering, and in particular, cases in which the fluid viscosity and turbulence are important and the rudders and propellers are moving.
- The method is more computationally efficient than viscous-flow methods that satisfy the fully-nonlinear free-surface conditions and is computationally equivalent to a numerical method that solves for a velocity potential via discretization of the flow domain (not the domain boundary).
- The new solver is validated by comparing with results from other numerical methods and physical experiments of the waves generated by a heaving catamaran, and the force on the hull of the naval destroyer 5415 moving with prescribed horizontal-plane motion.

Introduction

This paper discusses the pursuit of simulating the unsteady Reynolds-Average Navier-Stokes (URANS) equations for problems in which ship-wave interaction and fluid turbulence are both important. The primary engineering problem of interest is the prediction of the trajectory of a maneuvering ship, although many other related problems are well suited for analysis with the proposed method, such as ship seakeeping and powering predictions. The key idea of the method is that state-of-the-art URANS technology can be employed together with the linearized free-surface conditions to produce a computational tool that is both accurate and efficient such that the results can be useful within the time constraints of the ship design process.

Prediction of ship maneuvering is challenging due to the complex relationship between the ship motion and the unsteady manner in which the flow separates (forms a recirculation region) from the body. The physical process of viscous separation is influenced by the wave system generated by the ship, and has a substantial role on the flow seen by the propeller and rudder. Thus it is necessary to consider the effects of viscosity and turbulence for accurate prediction of ship maneuvering. Indeed, methods that neglect viscosity are severely challenged to predict the force, moment, and trajectory of the ship in a general maneuver. While URANS methods are capable of simulating maneuvering flows, the computational expense of solving the URANS equations with the fully nonlinear free-surface boundary conditions is very large, and their use is limited to academic or research applications [5], and not widely used for industrial benefit. Indeed, the objective of this work is to substantially reduce the computational burden, by simplifying the algorithm with respect to the free-surface solution, so that RANS-based maneuvering simulations can be brought into engineering practice more immediately.

Two problems are studied in this abstract to motivate our approach. The first is the prediction of the unsteady wave generated by a heaving catamaran. This problem has been studied experimentally and numerically by several authors [1, 2, 3]. Although turbulence is not necessarily important for the model tests, the resonance behavior of the wave system can be grossly overpredicted by methods that do not rationally account for the dissipation and transport of energy away from the body. Furthermore, using this problem, the novel URANS approach is compared to a method in which the linearized problem is solved in terms of a velocity potential. This grants the opportunity to directly compare computational expense of each approach. It is shown that the costs are very similar between the two methods. Although the URANS approach has more than three unknowns (in two spatial dimensions), the bulk of the expense is due to the solution of the pressure variable that is governed by a partial differential equation that is elliptic in nature, just like the governing equation of the velocity potential. This implies that for problems in which viscosity and turbulence play an important role, a breakthrough in accuracy is available for the small incease in expense due to the addition of the primitive RANS variables.

The second problem studied in this abstract is the prediction of the force on the naval destroyer hull form DTMB 5415 that is undergoing prescribed horizontal-plane motion. In this problem, the turbulent-boundary

layer on the body interacts with the unsteady-ship-generated wave system. Model-test results are available for a setup in which the hull is fitted with bilge keels, but otherwise unappended. Compared to fully nonlinear viscous flow methods, the linearized free-surface approach offers an extreme advantage in terms of the computational requirements. The novel method is more efficient for several reasons. First, the domain is inherently smaller since only the water portion is discretized. Second, the need for highly-resolved cells to capture or track an interface is eliminated. Instead, relatively large cells can be used, especially far from a body, while still accurately resolving the first-order wave field.

Numerical Approach

All problems are solved in a *earth-fixed* Cartesian coordinate system, with z oriented upwards. The linearized flow domain is below $z = 0$. The governing equations are solved using the finite-volume method on a discretization of the flow domain comprised of non-overlapping polyhedra of arbitrary number of sides. The kinematic condition for the free-surface elevation is solved using a finite-area method on the linearized free-surface boundary $z = 0$. The solvers used in this work are developed using the OpenFOAM open-source CFD library.

URANS The URANS equations are solved in the arbitrary-Lagrangian-Eulerian (ALE) form to allow for a moving grid. The fluid velocity in the earth-fixed coordinate is denoted $\vec{U}$, and the velocity of the mesh is $\vec{U}_{\text{mesh}}$. The relative velocity is defined as $\vec{U}_{\text{rel}} = \vec{U} - \vec{U}_{\text{mesh}}$. The free-surface elevation is represented by η. The fluid pressure is p, and the effective viscosity is the sum of the molecular and turbulent viscosities $\mu_{\text{eff}} = \mu + \mu_t$.

The conservation of momentum and mass equations are written for each computational cell that has volume V and is bounded by the surface S with outward normal $\vec{n}$.

$$\frac{d}{dt}\int_V \rho\vec{U}\, dV + \int_S \rho\vec{U}\vec{U}_{\text{rel}}\cdot\hat{n}\, dS = \int_V (-\nabla\, p + \rho\vec{g})\, dV + \int_S \mu_{\text{eff}}\left(\nabla\vec{U} + \nabla\vec{U}^T\right)\cdot\hat{n}\, dS \quad \text{and} \quad \int_S \vec{U}\cdot\hat{n}\, dS = 0 \tag{1}$$

Two fundamental steps are taken to numerically approximate the conservation equations on each cell. The flow unknowns are interpolated from the cell centers to the cell face centers, and then the surface integrals are approximated with a mid-point quadrature rule. Both the interpolation and quadrature are second-order accurate, with upwind-biased schemes used for the interpolation of the convection term and centered schemes otherwise.

Similarly, the ALE form of the kinematic free-surface boundary condition is used to evolve the free-surface elevation η via:

$$\frac{\partial}{\partial t}\int_{S_0} \eta\, dS - \int_l \eta\vec{U}_{\text{mesh}}\cdot\hat{n}\, dl = \int_{S_0} w\, dS \quad \text{on} \quad z = 0 \tag{2}$$

where S_0 is the portion of the boundary of a computational cell that is adjacent to the plane $z = 0$, and l is the contour of this area. The pressure boundary condition is applied according to the linear dynamic free-surface boundary condition:

$$p - \rho g\eta = 0 \quad \text{on} \quad z = 0 \tag{3}$$

Field potential The velocity-potential method used in the results section solves the discretized form of the Laplacian in the field. The Laplacian solver is second-order accurate in space. In the calm-water plane, the unsteady, zero-forward speed, combined free-surface boundary condition is satisfied. This equation is discretized with a second-order backward scheme for the time term, and a one-sided, second-order scheme for the vertical gradient of the potential.

$$\frac{\partial^2\phi}{\partial t^2} = -g\frac{\partial\phi}{\partial z} \quad \text{on } z = 0 \tag{4}$$

Results

Heaving catamaran with gap resonance The problem of a heaving catamaran is studied to demonstrate the ability to accurately predict the wave motion between the hulls and in the far field for a wide range of oscillation frequency. The experiments were performed at MARINTEK in 2010 [3]. The experiments were performed in a wave flume so that the radiated wave is practically two dimensional. The flow domain is two-dimensional and comprised of rectangular cells that are clustered around the body. The body boundary condition is satisfied on the mean position of the body for both the linearized RANS and potential-flow simulations.

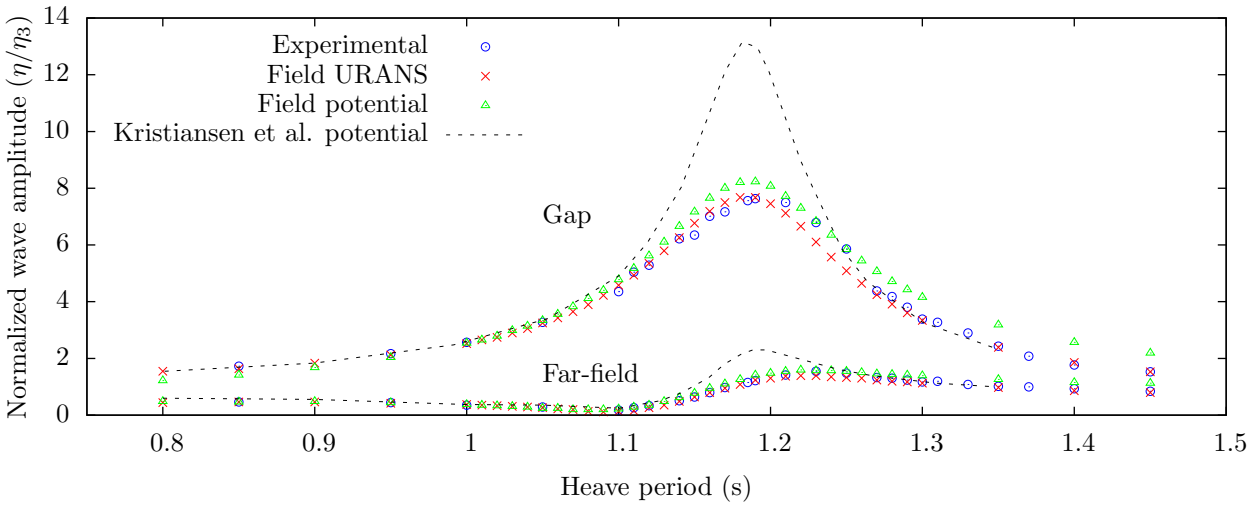

Figure 1: Wave amplitudes from heaving catamaran

A summary of the results appears in Figure 1. In this figure, two groups of data are shown, one for the wave amplitude in the gap, and another for the wave amplitude in the far-field. For each group of data, four sources of prediction are represented: the experimental measurements, the present linearized URANS, the present field potential, and potential results from [3], labeled Kristiansen et al. potential. The Kristiansen et al. potential results are said to be consistent with the linear analytical potential solution from [1].

As shown in Figure 1, the Kristiansen et al. potential results significantly overpredict the wave amplitude both in the gap and the far-field near the resonant frequency. On the other hand, the field potential only slightly over predicts the wave amplitude near resonance, with an increasing over-prediction as the oscillation period increases. The substantial improvement in the potential-flow prediction for the wave amplitude in the gap can be attributed by the fact that the second-order-accurate field discretization has a dissipative quality that is sufficient to prevent the artificial accumulation of energy in the gap between the hulls. The dissipation in the scheme depends on the grid resolution, but for the set of grids tested in our work, the results are very weakly dependent on the grid. Between the medium and fine grids, the relative error of the wave amplitude in the gap is only 0.3% for the period of 1.2 s.

The field URANS approach shows very strong agreement with the experimental measurements throughout the frequency range, and a small improvement over the field potential results. In addition, the computational time required for the field potential and linearized URANS formulations is nearly identical.

DTMB 5415 in pure yaw motion A pure yaw planar motion mechanism (PMM) test is simulated for the DTMB 5415 hull form. Experiments are included for testing done on a model of length $L = 3.048$ m [4]. The Froude number is 0.28, and length-based Reynolds number is 4.46 million. The hull is unappended with the exception of bilge keels. The hull is fixed at the dynamic sinkage and trim for both the simulation and the experiment. The sway motion has amplitude $\eta_0/L = 0.1073$ and period 7.48 s. The body-boundary condition is satisfied exactly as $\vec{U} = \vec{U}_{\text{body}}$.

Three numerical grids are used, denoted coarse, medium, and fine. The coarse grid contains about 200,000 cells, and the fine grid about 920,000 cells. Figure 2 (left) shows the discretization of the free-surface plane for the coarse grid. The posteriori calculation of the dimensionless near-wall spacing indicates the average y^+ value is 60 for the coarse grid and 40 for the fine grid. The Spalart-Allmaras turbulence model is used with a universal wall-function. The numerical simulations are performed on the parallel computer flux hosted by the University of Michigan.

Figure 2 (right) presents the time series of the yaw moment through one PMM period. The numerical results from each grid are compared to the experimental measurements. It is striking to note the manner in which the numerical results converge with refinement of the grid. This behavior is not frequently seen for fully nonlinear URANS results because it is rarely possible to use a sufficiently fine discretization such that the solution has converged. In the present case, the first-order wave system requires fewer computational cells. The first-order system has the same range of length-scales as the higher-order system, but does not permit breaking, and the simplified condition is satisfied on a known boundary, $z = 0$.

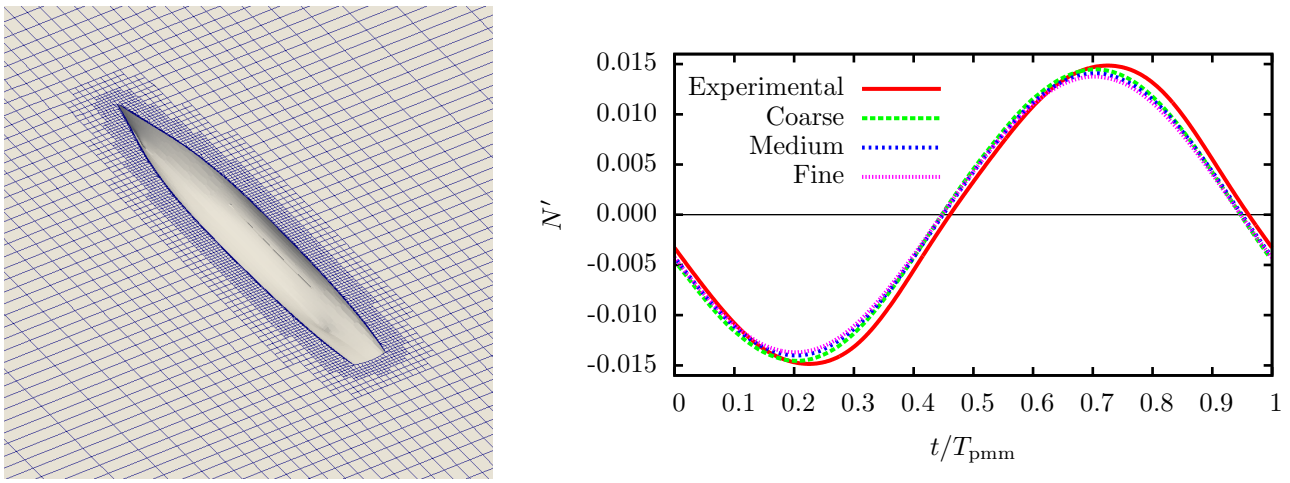

Figure 2: Coarse grid discretization (left), Yaw moment during pure yaw (right)

Also, any of the numerical results agree well with the experiment. Although not shown here, the present results are comparable to fully nonlinear URANS results [5]. Furthermore, the computational time required to perform a single PMM period ranges from 10 to 200 cpu-hours. This means that the coarse grid set-up is well-suited for desktop computing on a multi-core workstation.

Conclusions and future work

Linearized free-surface approximations provide an efficient alternative to fully nonlinear, multiphase CFD methods. While employing a simplified theory, they can produce suitably accurate results for a variety of engineering problems. Within the approach of a linearized free-surface, a URANS method is shown to be as computationally efficient as a field potential method. However, in addition to efficiency, the linearized URANS formulation benefits from the inclusion of viscous effects. Force and moment predictions are shown to compare well with experimental data. This technology has been expanded to include rotating propellers for prescribed motion simulations. Future work includes developing the technology for self-propelled, free-running model tests by solving for the motion of the ship in the horizontal directions.

Acknowledgments

The authors would like to gratefully acknowledge the U.S. Office of Naval Research program number N00014-13-1-0759 administered by Kelly Cooper. Additional acknowledgement goes to the Flux HPC Cluster provided by the University of Michigan Office of Research and operated by the High Performance Computing Group at the College of Engineering.

Bibliography

[1] Faltinsen, O. M., Rognebakke, O. F., and Timokha, A. N. Two-dimensional resonant piston-like sloshing in a moonpool. *Journal of Fluid Mechanics*, 575:359–397, 2007.

[2] Kristiansen, T. and Faltinsen, O. M. Gap resonances analyzed by a domain-decomposition method. In *26th International Workshop on Water Waves and Floating Bodies*, 2011.

[3] Kristiansen, T. and Faltinsen, O. M. Gap resonance analyzed by a new domain-decomposition method combining potential and viscous flow. *Applied Ocean Research*, 34:198–208, 2012.

[4] Longo, J., Y. H.-S. T. Y. and Stern, F. Phase-averaged 3dpiv/wave elevations and force/moment measurements for surface compatant in pmm maneuvers. In *Proc. 26th ONR Symposium on Naval Hydrodynamics*, Rome, Italy, 2006.

[5] Stern, F. and Agdrup, K., editors. *Proceedings SIMMAN 2008 Workshop*, Copenhagen, Denmark, 2008.

Oblique water entry of a wedge with vortex shedding

G.D. Xu[a]; G.X. Wu[a,b*]

[a]College of shipbuilding engineering, Harbin Engineering University, Harbin China (xuguodong@hrbeu.edu.cn)

[b]Permanent address: Department of Mechanical Engineering, University College London, Torrington Place, London WC1E 7JE, UK (author for correspondence: g.wu@ucl.ac.uk)

highlights:

- oblique water entry of a wedge with vortex wake is simulated
- the Kutta condition is imposed at the wedge apex and the local pressure jump is removed

1. Introduction

Wedge water entry is one of the most typical fluid/structure impact problems. For water entry of a symmetric wedge with only vertical motion, Howison et al. (1991), Mei et al. (1999), Korobkin & Iafrati (2005) presented the analytical solutions based on the Wagner theory; Dobrovol'skaya (1969) considered the fully nonlinear similarity solution; Zhao & Faltinsen (1993), Lu et al (1999), Wu et al (2004), Battistin & Iafrati (2003) simulated the nonlinear impact through the boundary element method (BEM). For water entry of an asymmetric wedge or oblique water entry, typical work include those by Iafrati & Semenov (2006) and Xu et al (2008, 2010). In their results pressure jump was observed at the wedge apex. As there is transverse flow passing the sharp corner, such discontinuity or singularity in the potential flow was not unexpected. In real flow there would be strong vortex shedding at a sharp corner. To simulate water entry of a wedge with transverse flow at its tip, flow separation due to vortex shedding needs to be treated properly. Riccardi & Iafrati (2004) investigated the vortex shedding of the water entry of an asymmetric wedge through conformal mapping, although the effect of the free surface elevation was ignored. Point vortex and Kutta condition were introduced to remove the velocity singularity at the apex.

The general problem of vortex shedding at a sharp corner of a marine structure has been receiving extensive attentions. Downie et al (1988) studied the vortex shedding of a rectangular barge in waves. Kristiansen & Faltinsen (2010) simulated the vortex shedding of a rectangular box in waves through BEM. The damping effects due to the shed vortices were accounted for properly. However, it seems that there is far less work in the context of water entry of a wedge, which is the focus of the present study. A Kutta condition for numerical simulation is imposed at the sharp edge. The pressure jump at the wedge apex is removed. Results for the free surface profile and pressure distribution are provided.

2. Mathematic equations

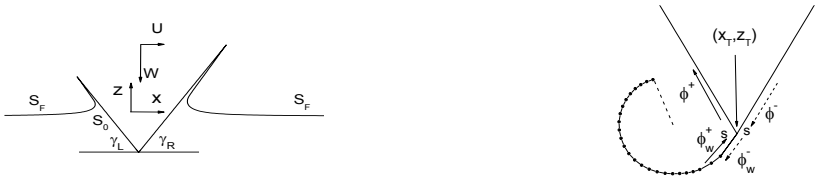

(a) (b)

Fig.1 illustration of (a) the wedge water entry with vortex shedding and (b) the local wake surface

The velocity potential theory is adopted to describe the flow field since the viscosity and compressibility effects are less important during high speed water entry over a short period of time. As shown in Fig.(1a), the origin of the space-fixed Cartesian coordinate system $x-O-z$ is located on the initially calm water

surface with z pointing upwards. The introduced velocity potential ϕ satisfies Laplace equation in the fluid domain

$$\nabla^2\phi = \frac{\partial^2\phi}{\partial x^2} + \frac{\partial^2\phi}{\partial z^2} = 0 \tag{1}$$

On the body surface S_0, the boundary condition can be written as

$$\frac{\partial\phi}{\partial n} = \vec{U}\cdot\vec{n} \tag{2}$$

where $\vec{U} = (U,W)$ is the translational constant velocity of the body and $\vec{n} = (n_x, n_z)$ is the unit normal vector pointing out of the fluid domain. In the Lagrangian framework, the free surface boundary conditions can be written as

$$\frac{d\phi}{dt} = \frac{1}{2}\nabla\phi\nabla\phi \tag{3}$$

$$\frac{dx}{dt} = \frac{\partial\phi}{\partial x}, \quad \frac{dz}{dt} = \frac{\partial\phi}{\partial z} \tag{4}$$

When there is transverse flow at the wedge apex, vortex wake will be shed into the fluid. On the wake surface S_w, the dipole strength can be written as

$$\mu = \phi_w^+ - \phi_w^- \tag{5}$$

while the normal velocity across S_w is continuous, or

$$\frac{\partial\phi_{w+}}{\partial n} = -\frac{\partial\phi_{w-}}{\partial n} \tag{6}$$

In Eq.(5) ϕ_w^+ and ϕ_w^- are the velocity potentials on the two sides of the wake surface, as shown in Fig.(1b). At the apex of the wedge, we impose the Kutta condition in the following form (Xu & Wu 2013)

$$\left.\frac{\partial\phi^+}{\partial l}\right|_{\bar{x}_{apex}} - \left.\frac{\partial\phi^-}{\partial l}\right|_{\bar{x}_{apex}} = \left.\frac{\partial\mu}{\partial l}\right|_{\bar{x}_{apex}} \tag{7}$$

where the tangential vector in $\left.\frac{\partial\mu}{\partial l}\right|_{\bar{x}_{apex}}$ has the same direction as $\left.\frac{\partial\phi^+}{\partial l}\right|_{\bar{x}_{apex}}$, as shown in Fig.(1b). The continuity of the pressure p across the wave surface gives

$$\frac{d\mu}{dt} = 0 \tag{8}$$

We notice that the wedge water entry problem usually starts from a contact point. An ideal approach is to use the stretched coordinate system (Wu et al 2004). It has the advantage that both the computational domain and the element size remain similar size in the stretched system as body continues to enter water in the physical domain. We define

$$s = Wt, \quad h = Ut \tag{9}$$

In the stretched coordinate system $\alpha - o - \beta$, we write

$$\phi(x,y,t) = s\varphi(\alpha,\beta,t), \quad x = s\alpha, \; y = s\beta \tag{10}$$

Laplace equation in the stretched system retains the same form, while the body surface boundary condition becomes

$$\frac{\partial\varphi}{\partial n} = Un_\alpha - Wn_\beta \tag{11}$$

and the free surface boundary conditions can be written as

$$\frac{d(s\alpha)}{dt}=\varphi_\alpha,\quad \frac{d(s\beta)}{dt}=\varphi_\beta \tag{12}$$

$$\frac{d(s\varphi)}{dt}=\frac{1}{2}(\varphi_\alpha^2+\varphi_\beta^2) \tag{13}$$

To solve the above equations, following the numerical procedure of Xu & Wu (2013), we have the boundary integral equation at $m+1$ time step

$$\Lambda(p)\varphi(p)=\int_{S_0+S_F}[\frac{\partial G(p,q)}{\partial n_q}\varphi(q)-G(p,q)\frac{\partial\varphi(q)}{\partial n_q}]dS$$
$$+\int_{S_{w1}}\frac{\partial G(p,q)}{\partial n_w}\mu'(q)\,dS+\mu'(\vec{\alpha}'_T)H(p,\vec{\alpha}'_T)+\sum_{j=1}^{m}k_jH(p,q)dS \tag{14}$$

where $H(p,q)=\arctan\frac{\alpha-\xi}{\beta-\eta}$, S_{w1} is the dipole element attached to the sharp edge, κ_j is the point vortex formed from vortex dipole element in the $(j-1)th$ time step.

3. Results and discussions

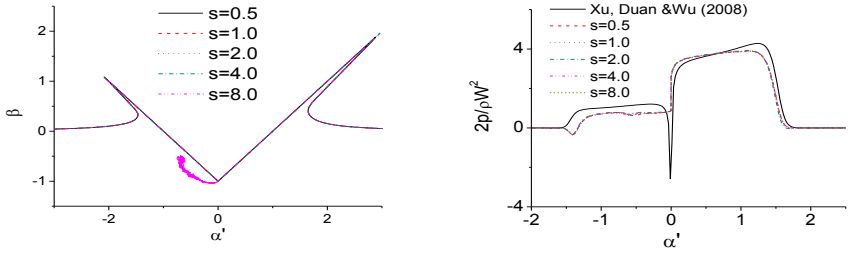

(a) (b)

Fig.2 oblique water entry of a wedge, (a) free surface profile and (b) the pressure distribution, $\alpha'=\alpha-\varepsilon$

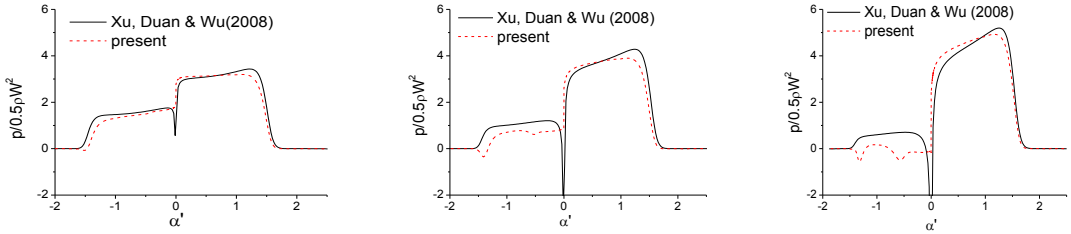

(a) (b) (c)

Fig.3 oblique wedge water entry with $\gamma_L=\gamma_R=\pi/4$, $s=1.0$, (a) $\varepsilon=0.3$(b) $\varepsilon=0.5$ (c) $\varepsilon=0.7$

The work is still on-going and only some preliminary results from the simulation are presented here. Oblique water entry of a symmetric wedge at constant velocity with left and right deadrise angles $\gamma_L=\gamma_R=\pi/4$, $\varepsilon=U/W=0.5$ is considered. The initial free surface profile and the velocity potential are prescribed at $s=0.001$ and are obtained from the similarity solution without vortex shedding. At this moment, there is just one vortex dipole of the same size of element as that on the wedge surface at its apex. The simulation is then carried out based on the procedure discussed in the previous section. The shed vortex wake is updated through Eq.(8). Figure 2 gives the obtained results. It can be seen that unlike the solution without the vortex wake, the pressure is continuous at the tip. Fig.2 also shows that the variations of the free surface profile and pressure distribution with S in the stretched system are hardly visible. We note that negative pressure exists near the jet root of the left hand side of the wedge. Air could be sucked into the fluid and air cavities could be formed.

Further simulations are carried out with different ε. Fig.3 gives the pressure distribution at $\varepsilon = 0.3,\ 0.5,\ 0.7$. Comparing with the similarity solution without vortex shedding (Xu, Duan & Wu 2008), the pressure jump at the wedge apex has been removed. This is a result of the imposed Kutta condition and vortex wake, through which the flow velocity becomes continuous. The pressure on the left hand side of the wedge is lower than the similarity solution, while the pressure on the right hand side has a lower peak and a smaller slope. We note that when $\varepsilon = 0.7$, the pressure on the left hand side of the wedge has two troughs, which may be due to the flow induced by the shed vortices. Further analysis and results will be provided at the Workshop.

Acknowledgement

The work is mainly supported by Lloyd's Register Foundation (LRF) through the joint centre involving University College London, Shanghai Jiaotong University and Harbin Engineering University, to which the authors are most grateful. LRF helps to protect life and property by supporting engineering-related education, public engagement and the application of research. The first author appreciates the support of NSFC (51479044), China Post-doctor research Fund (2014M560250) and Heilongjiang Post-doctor Research Fund (LBH-Z14057).

References

Battistin D., Iafrati A. 2003 Hydrodynamic loads during water entry of two-dimensional and axisymmetric bodies, Journal of Fluids and Structures 17, 643-664.

Dobrovol'skaya Z.N. 1969 Some problems of similarity flow of fluid with a free surface. Journal of Fluid Mechanics 36, 805-829.

Donwin M.J., Bearman P.W., Graham J.M.R. 1988 Effect of vortex shedding on the coupled roll response of bodies in waves. Journal of Fluid Mechanics 189, 243-264.

Howison S.D., Ockendon J.R., Wilson S.K. 1991 Incompressible water entry problems at small deadrise angles. Journal of Fluid Mechanics 222, 215-230.

Lu C.H., He Y.S., Wu G.X. 2000 Coupled analysis of nonlinear interaction between fluid and structure during impact. Journal of Fluids and Structures 14, 127-146.

Kristiansen T., Faltinsen O.M. 2010 A two-dimensional numerical and experimental study of resonant coupled ship and piston-mode motion. Applied Ocean Research 32, 158-176.

Riccardi G., Iafrati A., 2004 Water impact of an asymmetric floating wedge Journal of Engineering Mathematics 49, 19-39.

Mei X., Liu Y. & Yue D.K.P. 1999 On the water impact of general two-dimensional sections. Applied Ocean Research 21, 1-15.

Korobkin A.A., Iafrati A. 2005 Hydrodynamic loads during initial stage of floating body impact. Journal of Fluids and Structure 21, 413-427.

Semenov Y.A., Iafrati A. 2006 On the nonlinear water entry problem of asymmetric wedges. Journal of Fluid Mechanics 547, 231-256.

Wu G.X., Sun H., He Y.S. 2004 Numerical simulation and experimental study of water entry of a wedge in free fall motion. Journal of Fluids and Structures 19: 277-289.

Xu G.D., Wu G.X. 2013 Boundary element simulation of inviscid flow around an oscillatory foil with vortex sheet, Engineering Analysis with Boundary Elements 37, 825–835.

Xu G.D., Duan W.Y., Wu G.X. 2008 Numerical simulation of oblique water entry of an asymmetrical wedge. Ocean Engineering 35 1597-1603.

Xu G.D., Duan W.Y., Wu G.X. 2010 Simulation of water entry of a wedge through free fall in three degrees of freedom. Proceeding of Royal Society A, 466, 2219-2239.

Zhao R., Faltinsen O.M. 1993 Water entry of two-dimensional bodies. Journal of Fluid Mechanics 246, 593-612.

Fully nonlinear and dispersive of nearshore wave modeling: accuracy and efficiency of two methods of solving the potential flow problem

Marissa L. Yates[1,2], Michel Benoit[1,3], Cécile Raoult[1,3]
[1]Université Paris-Est, Saint-Venant Hydraulics Laboratory (ENPC, EDF R&D, Cerema), 78400 Chatou, France
[2]Cerema, [3]EDF R&D
marissa.yates-michelin@cerema.fr, michel.benoit@saint-venant-lab.fr, cecile.raoult@edf.fr

Highlights

- A finite difference approach and a spectral approach of resolving the velocity potential in the vertical are compared in a fully nonlinear potential flow model. The spectral approach shows improved accuracy and efficiency for two test cases.
- The resultant model simulates well the propagation and nonlinear interactions of irregular waves over a submerged bar in comparison to experimental data.

Introduction

To model waves in the nearshore region, it is necessary to have accurate, rapid models that can simulate the nonlinear and dispersive effects over large spatial domains. Models ranging from the mild slope equation to CFD (Computational Fluid Dynamics) approaches based on the Navier-Stokes equations are used for a variety of different applications, with varying degrees of accuracy and computational cost. Potential flow theory models, based on the assumption of irrotational flow, may be an ideal compromise between simplified linear wave models and CFD approaches modeling the fine scale processes.

Potential flow wave models require the resolution of the Laplace equation in the fluid domain with specification of the boundary conditions. Boundary integral methods are commonly used to develop highly accurate fully nonlinear models (e.g. [6]), but recent work also uses a finite difference approach (e.g. [7, 3, 5]). The relative simplicity of this approach, in comparison to more mathematically complex projection methods, may be ideal when studying nonlinear wave-body interactions [3].

Here, a fully nonlinear potential flow theory model resolving the Zakharov equations [12] is developed. The Zakharov equations express the temporal evolution of the free surface elevation η and velocity potential $\tilde{\phi}$, which require calculating the free surface vertical velocity $\tilde{w}$. The accuracy and efficiency of two methods of calculating $\tilde{w}$ as a function of $(\eta, \tilde{\phi})$ ("Dirichlet-to-Neumann" or DtN problem) is compared as a function of the horizontal and vertical resolution for two test cases. The optimal spectral approach is then validated with a comparison to experimental data.

Overview of the mathematical and numerical models

By assuming irrotational flow, the velocity potential $\phi(\underline{x}, z, t)$ satisfies the Laplace equation in the three dimensional $(\underline{x}, z)$ fluid domain:

$$\nabla^2\phi + \phi_{zz} = 0, \qquad -h(\underline{x}) \leq z \leq \eta(\underline{x}, t), \tag{1}$$

with free surface elevation $z = \eta(\underline{x}, t)$ and a bottom boundary $z = -h(\underline{x})$. By assuming continuity of the fluid from the bottom to the free surface (i.e. non-overturning free surface), setting the free surface atmospheric pressure equal to 0, and defining the free surface velocity potential as $\tilde{\phi}(\underline{x}, t) \equiv \phi(\underline{x}, \eta(\underline{x}, t), t)$, the kinematic and dynamic surface nonlinear boundary conditions are derived as a function of $\tilde{\phi}$, following Zakharov [12]:

$$\eta_t = -\nabla\eta \cdot \nabla\tilde{\phi} + \tilde{w}(1 + (\nabla\eta)^2), \tag{2}$$

$$\tilde{\phi}_t = -g\eta - \tfrac{1}{2}\left(\nabla\tilde{\phi}\right)^2 + \tfrac{1}{2}\tilde{w}^2(1 + (\nabla\eta)^2), \tag{3}$$

where $\tilde{w}(\underline{x}, t)$ is the vertical velocity at the free surface defined by:

$$\tilde{w}(\underline{x}, t) = \phi_z(\underline{x}, \eta(\underline{x}, t), t). \tag{4}$$

By specifying the lateral boundary conditions and solving the DtN problem to calculate the free surface velocity $\tilde{w}(\underline{x}, t)$ from $(\eta(\underline{x}, t), \tilde{\phi}(\underline{x}, t))$, (2) and (3) model the temporal evolution of the free surface quantities η and $\tilde{\phi}$.

Equations (2) and (3) are integrated in time using the classical explicit four-step, fourth-order Runge-Kutta scheme. Fourth-order finite difference schemes with regular or irregular point distribution are used to calculate horizontal gradients and Laplacian operators. Two methods of resolving the DtN problem are compared in one horizontal dimension, x, which is discretized by N_X points.

- *Model A.* Following [3], [5], and [4], the domain is discretized with N_Z points in the vertical ($N = N_Z - 1$ fluid layers), and fourth-order finite difference schemes are used to resolve the vertical spatial derivatives.
- *Model B.* The second method, based on the spectral approach of [9], expresses the vertical profile of ϕ as a linear combination of Chebyshev orthogonal polynomials of the first kind (N_T is the maximum order of the polynomial). (See [11] for more details).

For both methods, a system of $N_X(N + 1)$ linear equations must be solved at each time step, where $N = N_L$, the number of layers in the vertical for Model A, and $N = N_T$, the maximum order Chebyshev polynomial for Model B. The direct solver MUMPS ("MUltifrontal Massively Parallel Solver", v4.10.0) [1] is applied in the Fortran code using the default settings.

Test Cases: comparison of accuracy and efficiency

Propagation of a regular nonlinear wave

The first test case compares the resolution of the DtN problem and errors in propagating a regular, nonlinear wave of permanent form in a uniform depth periodic domain. The initial conditions are calculated using a highly accurate Fourier series approximation (20th order) of the stream function method [8] for a wave with wavelength $L = 64$ m and wave height $H = 6.4$ m in a water depth $h = 64$ m (domain length L). The wave steepness is $H/L = 0.1$ (or $ka = kH/2 = \pi/10$), and the relative water depth is $h/L = 1$ (or $kh = 2\pi$).

The normalized error of the free surface vertical velocity decreases with an increase in the vertical resolution N, and both models converge to the same minimum for large values of N (Figure 1). Model

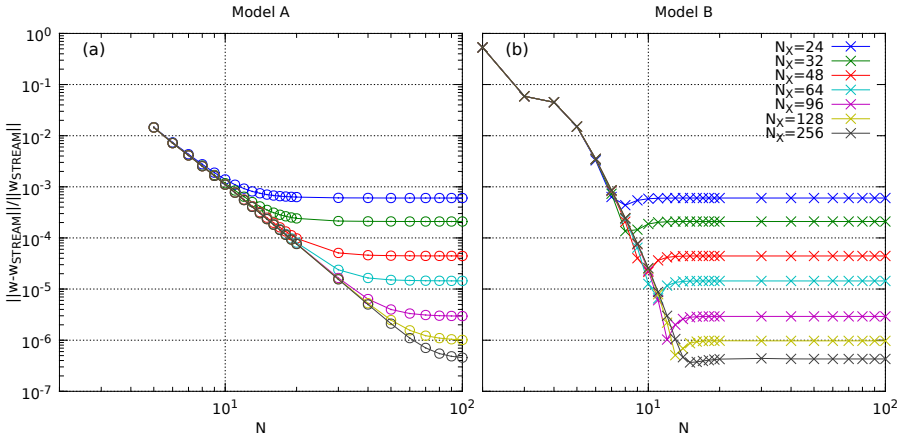

Figure 1: Convergence of the free surface vertical velocity $\tilde{w}$ for a regular nonlinear wave with wave steepness $H/L = 0.1$ ($ka = \pi/10$) and relative water depth $h/L = 1$ ($kh = 2\pi$) for (A) Model A and (b) Model B.

A converges algebraically with errors decreasing as N^{-k}, with $k \approx 3.8$, while Model B converges geometrically, with errors decreasing as $exp(-qN)$, with $q \approx 1.26$. Propagation errors in maximum free surface elevation and phase lag after 25 periods of wave propagation show a strong dependence on the horizontal and vertical resolution. Errors are similar in both model approaches, with expected increases in errors with decreases in resolution, and the optimal value of vertical resolution N for both models appears to be in the range $7 < N < 15$. Comparisons of the computational time required to obtain certain thresholds in total energy errors also shows improved efficiency using the Model B approach.

Motion of a nonlinear standing wave

The second test case compares the motion of a nonlinear standing wave in a domain with fully reflective lateral boundaries. After an integer number of wave periods, the wave characteristics should remain identical to those of the initial condition, calculated using the highly accurate (14th order) Fourier method of [10]. A wave with wavelength $L = 192$ m, relative water depth $kh = 3$, and wave steepness $ka = 0.42$ is calculated (with a corresponding water depth and wave height of $h \approx 91.6732$ m and $H \approx 25.6685$ m, respectively). The simulation is initiated with the displacement of the free surface η in a domain of length L, with no initial fluid velocity.

After 100 periods of wave motion, errors in the maximum free surface position primarily increase with increasing CFL number and decreasing horizontal resolution. Overall, Model B generally produces smaller free surface position errors than Model A, with the exception of the coarsest horizontal grid. Errors in the total energy also increase with increasing CFL number and decreasing horizontal resolution. For small CFL numbers, Model B has overall smaller errors than Model A. For large CFL numbers, the two methods converge to the same errors.

Validation case: propagation of irregular nonlinear waves over a bar

Finally, the selected approach, Model B is validated by simulating the propagation of irregular waves over a submerged bar, reproducing a non-breaking flume experiment of [2]. In the experiments, waves were generated using a piston-type random wave-maker with a JONSWAP spectrum with a peak enhancement factor of $\gamma = 3.3$, with a significant wave height of $H_{m0} = 0.34$ m and a peak period of $T_p = 2.39$ s ($f_p = 0.418$ Hz). The simulation results are compared to the free surface elevation measured at 16 wave probes throughout the domain. In the numerical model, waves are generated in a relaxation zone using the wave spectra calculated at the probe located at the base of the submerged bar, and absorbed in a relaxation zone at the end of the beach.

The simulated wave energy spectra (with $N_T = 7$, $\Delta x = 0.05$ m, and $\Delta t = 0.07$ s) agree well with the experimental data, showing the transfer of energy to super- and sub-harmonics (up to $5f_p$, e.g. Figure 2) as the waves shoal and pass over the trough behind the bar. The spatial variability

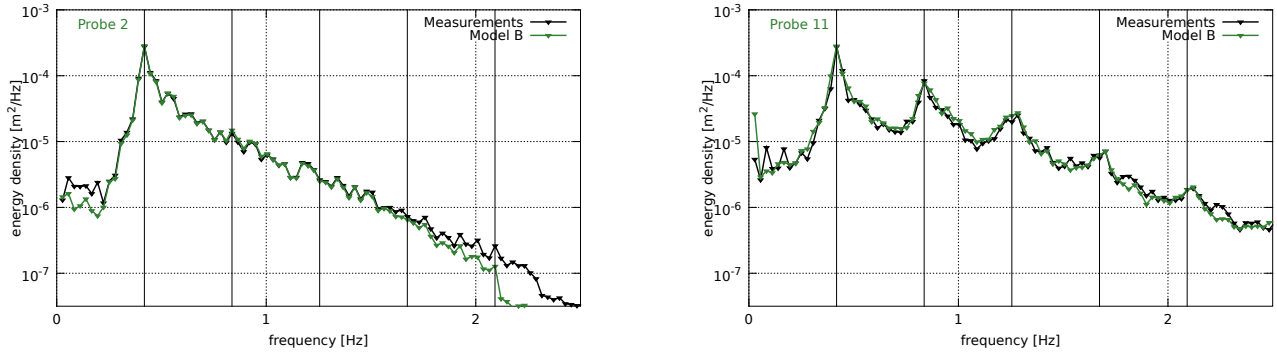

Figure 2: Simulated and measured wave energy density spectra at (left) the base of the bar and (right) the crest of the bar. Vertical black lines indicate the location of the peak frequency and the first four harmonics.

of the integral parameters (significant wave hight, mean period, kurtosis, horizontal and vertical asymmetry) also agrees well with the observations along the bathymetric profile.

Conclusions
Two test cases were used to compare the convergence properties, propagation errors, and CPU time of two approaches to solving the fully nonlinear potential flow problem in 1DH. The Model B spectral approach shows improved accuracy and efficiency in comparison with the Model A fourth-order finite difference schemes. Model B has an exponential convergence rate, while Model A has an algebraic convergence rate, as expected. Based on these tests, the Model B approach was selected and applied to a final validation test case where comparison with experimental data showed its ability to simulate the propagation of irregular nonlinear waves in a wave tank. The optimal value of the vertical resolution, which reduces model errors while limiting the computational time, is recommended in the range of $5 < N_T < 10$ for practical applications with this model. Ongoing work includes the optimization and extension of the Model B approach to 2DH domains.

References

[1] P. R. Amestoy, I. S. Duff, J. Koster, and J.-Y. L'Excellent. A fully synchronous multifrontal solver using distributes dynamic scheduling. *SIAM J. of Matrix Anal. and Appl.*, 23(1):15–41, 2001.

[2] F. Becq-Girard, P. Forget, and M. Benoit. Non-linear propagation of unidirectional wave fields over varying topography. *Coast. Eng.*, 38:91–113, 1999.

[3] H. B. Bingham and H. Zhang. On the accuracy of finite-difference solutions for nonlinear water waves. *J. Eng. Math*, 58:211–228, 2007.

[4] G. Ducrozet, H. B. Bingham, A. P. Engsig-Karup, F. Bonnefoy, and P. Ferrant. A comparative study of two fast nonlinear free-surface water wave models. *Int. J. Numer. Meth. Fluids*, 69(11): 1818–1834, 2012. doi: 10.1002/fld.2672.

[5] A. P. Engsig-Karup, H. B. Bingham, and O. Lindberg. An efficient flexible-order model for 3D nonlinear water waves. *J. Comp. Phys.*, 228:2100–2118, 2009.

[6] S. T. Grilli and J. Horrillo. Shoaling of periodic waves over barred-beaches in a fully nonlinear numerical wave tank. *Int. J. Offshore Polar Eng*, 9(4):257–263, 1999.

[7] B. Li and C. Fleming. A three dimensional multigrid model for fully nonlinear water waves. *Coast. Eng.*, 30:235–258, 1997.

[8] M. M. Rienecker and J. D. Fenton. A Fourier approximation method for steady water waves. *J. Fluid Mech.*, 104:119–137, 1981.

[9] Y. Tian and S. Sato. A numerical model on the interaction between nearshore nonlinear waves and strong currents. *Coast. Eng. Journal*, 50(4):369–395, 2008.

[10] C.-P. Tsai and D.-S. Jeng. Numerical Fourier solutions of standing waves in finite water depth. *Applied Ocean Res.*, 16:185–193, 1994.

[11] M. L. Yates and M. Benoit. Accuracy and efficiency of two numerical methods of solving the potential flow problem for highly nonlinear and dispersive water waves. *Int. J. Numer. Meth. Fluids*, 2015. doi: 10.1002/fld.3992, in press.

[12] V. E. Zakharov. Stability of periodic waves of finite amplitude on the surface of a deep fluid. *J. Appl. Mech. Tech. Phys.*, 9(2):190–194, 1968.

Hydro-elastoplastic analysis of floating plates in waves

Joo-Seong Yoon and Phill-Seung Lee

Division of Ocean Systems Engineering, KAIST, Daejeon 305-600, Korea
jooseong@kaist.ac.kr, phillseung@kaist.edu

Highlights:

- A formulation for hydro-elastoplastic analysis is provided to fully couple the time-dependent response of a floating plate with elastoplastic material.
- A numerical procedure based on the incremental finite element analysis is applied to analyze the elastoplastic material behavior.
- The effects of plastic deformations on the response of a floating plate in a regular wave are investigated by comparing the solutions of hydroelastic and hydro-elaistoplastic analyses.

1. Introduction

Hydroelasticity is concerned with interactions between the deformations of floating elastic structures and hydrodynamic responses. Since the deformation effect is more dominant to the dynamic responses as the size of floating structures is getting larger, hydroelastic analysis has been applied to the design of very large floating structures such as pontoon-type offshore structures and bridges, floating airports, and ice floes. In recent years, the analytical and numerical methods have been developed to solve the nonlinear problems of hydroelasticity. Many studies have focused on nonlinear effects related to hydrodynamic forces. However, studies on the nonlinear structural response have been rarely founded.

The recent review [1] mentions the hydroplastic analysis as a way toward future development in hydroelasticity of ships, which may be required to analyze the dynamic collapse response of ship's hull, propagation of crack and so on. In this context, a 2D hydro-elastoplasticity method was proposed by combining strip theory and simplified progressive collapse method for the nonlinear dynamic responses of a ship beam in extreme waves [2]. The aim of the present study is to provide a numerical method that can consider fully coupled behaviors between the deformations of floating elastoplastic plate and linear hydrodynamic loads in time domain.

In this abstract, firstly, the formulation for the 2D hydro-elastoplastic analysis of floating structures is briefly described. Then, the numerical procedure of hydroelastic analysis in time domain and elastoplastic analysis is presented based on finite element method. Finally, the present method is validated by comparing numerical results of previous studies. In addition, the plastic effects on the response of floating structures in a regular wave are investigated by comparing the results of hydroelastic and hydro-elastoplastic analyses.

2. Mathematical model

Let consider a floating plate on water surface under a constant water depth h. The fixed Cartesian coordinate system (x_1, x_2, x_3) is defined on the free surface of the calm water. It is assumed that the floating plate with homogeneous, isotropic and elastoplastic material is infinite in the x_3 direction and is sufficiently thin enough that the draft is ignorned. The motion and strain of the floating plate are assumed to be small. The equilibrium equations of the floating plate at time t are

$$\frac{\partial {}^t\sigma_{ij}}{\partial {}^t x_{ij}} - {}^t\rho_s g\delta_{i2} - {}^t\rho_s {}^t\ddot{u}_i \quad \text{in } {}^tV, \qquad {}^t\sigma_{ij}\,{}^t n_j = -{}^t p\,{}^t n_j \quad \text{on } {}^tS_B, \tag{1}$$

where σ_{ij} is the Cauchy stress tenor, u_i is the displacement vector, ρ_s is the density of the structure, p denotes the total water pressure. Note that ${}^t p = -\rho_w g x_2 + {}^t p_d$, in which p_d is the hydrodynamic pressure. Also, n_j is the unit normal vector outward from the structure to the fluid, and δ_{ij} is the Kronecker delta. The overdot means the material time derivative. V denotes the structural domain, and S_B means the wet body surface.

The principle of virtual work for the floating plate at time t can be written as

$$\int_{{}^tV} {}^t\rho_s\, {}^t\ddot{u}_i \delta u_i dV + \int_{{}^tV} {}^t\sigma_{ij}\delta e_{ij} dV = -\int_{{}^tV} {}^t\rho_s g \delta u_2 dV + \int_{{}^tS_B} \rho_w g\, {}^t x_2\, {}^t n_i \delta u_i dS - \int_{{}^tS_B} {}^t p_d\, {}^t n_i \delta u_i dS\,, \tag{2}$$

where δu_i and δe_{ij} refer to the virtual displacement vector and small strain tensor, respectively. Employing the materially-nonlinear-only formulation based on the incremental equilibrium equation [3], Eqs. (2) is linearized as

$$\int_V \rho_s\, {}^{t+\Delta t}\ddot{u}_i \delta u_i dV + \int_V {}^tC_{ijkl}^{EP}\, {}^{t+\Delta t}_{\ t}e_{ij}\delta e_{ij} dV - \int_{S_B} \rho_w g\, {}^{t+\Delta t}u_2 n_i \delta u_i dS = -\int_{S_B} {}^{t+\Delta t}p_d n_i \delta u_i dS - \int_V {}^t\sigma\, {}^t e_{ij}\delta e_{ij} dV\,, \tag{3}$$

where C_{ijkl}^{EP} is the elastoplastic stress-strain relation tensor. Note that the hydrostatic analysis is not performed in this problem since we assume that the static equilibrium state is known [4].

The incompressible, inviscid and irrotational fluid flow is assumed and surface tension is neglected. The incident wave is coming from right side to plate and its amplitude is small enough to use the linear wave theory. This implies that the hydrodynamic pressure can be described in form of the convolution integral of the arbitrary time-dependent motion with the radiation ϕ^R and diffraction ϕ^D potentials corresponding to the impulsive velocity of the plate or impulsive wave elevation, respectively [5].The hydrodynamic pressure is expressed by the linearized Bernoulli equation as follows

$$\begin{aligned} p_d &= -\rho_w \left[\int_{-\infty}^{\infty} \frac{\partial}{\partial t}\phi^R\left(x_1, x_2; t-\tau\right)\dot{u}(\tau)\, d\tau + \int_{-\infty}^{\infty} \frac{\partial}{\partial t}\phi^D\left(x_1, x_2; t-\tau\right)\eta(\tau)\, d\tau \right] \\ &= -\rho_w \left[\psi\left(x_1, x_2\right)\ddot{u} + \int_{-\infty}^{t} \frac{\partial}{\partial t}\varphi\left(x_1, x_2; t-\tau\right)\dot{u}(\tau)\, d\tau + \int_{-\infty}^{\infty} \frac{\partial}{\partial t}\phi^D\left(x_1, x_2; t-\tau\right)\eta(\tau)\, d\tau \right], \end{aligned} \tag{4}$$

where η is the incident wave elevation. Note that $\phi^R = \psi\left(x_1, x_2\right)\delta(t) + \varphi\left(x_1, x_2; t\right)h(t)$, in which $h(t)$ is the Heaviside function.

Substituting the Eqs. (4) into Eqs. (3), we finally obtain the equation coupled between an elastoplastic plate and fluid:

$$\begin{aligned} &\int_V \rho_s\, {}^{t+\Delta t}\ddot{u}_i \delta u_i dV - \int_{S_B} \rho_w \psi\, {}^{t+\Delta t}\ddot{u}_i n_i \delta u_i dS - \int_{-\infty}^{t+\Delta t}\int_{S_B} \rho_w \frac{\partial}{\partial t}\varphi \dot{u}_i n_i \delta u_i dS d\tau + \int_V {}^tC_{ijkl}^{EP}\, {}^{t+\Delta t}_{\ t}e_{ij}\delta e_{ij} dV - \int_{S_B} \rho_w g\, {}^{t+\Delta t}u_2 n_i \delta u_i dS \\ &\qquad = \int_{-\infty}^{\infty}\int_{S_B} \rho_w \frac{\partial}{\partial t}\phi^D \eta n_i \delta u_i dS d\tau - \int_V {}^t\sigma\, {}^t e_{ij}\delta e_{ij} dV\,. \end{aligned} \tag{5}$$

3. Numerical Procedure

The formulation in Eqs. (5) can be transformed into the matrix form using the standard finite element discretization as

$$\left(\mathbf{M}+\mathbf{A}\right){}^{t+\Delta t}\ddot{\mathbf{U}} + \int_{-\infty}^{t+\Delta t}\mathbf{B}\left(t+\Delta t-\tau\right)\dot{\mathbf{U}}(\tau)\, d\tau + \mathbf{C}\,{}^{t+\Delta t}\mathbf{U} + {}^t\mathbf{K}\mathbf{U} = \int_{-\infty}^{\infty}\mathbf{X}\left(t+\Delta t-\tau\right)\boldsymbol{\eta}(\tau)\, d\tau - {}^t\mathbf{F}\,, \tag{6}$$

in which the matrices and vectors are defined as follows:

$$\int_V \rho_s\, {}^{t+\Delta t}\ddot{u}_i \delta u_i dV = \delta\mathbf{U}^T\mathbf{M}\,{}^{t+\Delta t}\ddot{\mathbf{U}}\,,\ -\int_{S_B} \rho_w \psi\, {}^{t+\Delta t}\ddot{u}_i n_i \delta u_i dS = \delta\mathbf{U}^T\mathbf{A}\,{}^{t+\Delta t}\ddot{\mathbf{U}}\,,$$

$$-\int_{-\infty}^{t+\Delta t}\int_{S_B} \rho_w \frac{\partial}{\partial t}\varphi \dot{u}_i n_i \delta u_i dS d\tau = \delta\mathbf{U}^T\int_{-\infty}^{t+\Delta t}\mathbf{B}\left(t+\Delta t-\tau\right)\dot{\mathbf{U}}(\tau) d\tau\,,\ -\int_{S_B} \rho_w g\, {}^{t+\Delta t}u_2 n_i \delta u_i dS = \delta\mathbf{U}^T\mathbf{C}\,{}^{t+\Delta t}\mathbf{U}\,,$$

$$\int_V {}^tC_{ijkl}^{EP}\, {}^{t+\Delta t}_{\ t}e_{ij}\delta e_{ij} dV = \delta\mathbf{U}^T\,{}^t\mathbf{K}\mathbf{U}\,,\ \int_{-\infty}^{\infty}\int_{S_B} \rho_w \frac{\partial}{\partial t}\phi^D \eta n_i \delta u_i dS d\tau = \delta\mathbf{U}^T\int_{-\infty}^{\infty}\mathbf{X}\left(t+\Delta t-\tau\right)\boldsymbol{\eta}(\tau)\, d\tau\,,\ \int_V {}^t\sigma\, {}^t e_{ij}\delta e_{ij} dV = \delta\mathbf{U}^T\mathbf{F}\,. \tag{7}$$

We here employ the 2-node Euler-Bernoulli beam element for the finite element model of plate structures in 2D and the three-dimensional von Mises plasticity model with the associated flow rule and isotropic hardening for the elastoplastic material. At each integration point in beam cross-sections, the unknown stress and plastic strain are implicitly evaluated by solving a single nonlinear equation in accordance with the governing parameter method [6, 7]. In order to solve the nonlinear Eqs. (6), the full Newton-Raphson iterative scheme and Newmark method are employed.

Since the impulse response functions such as $\mathbf{A}$, $\mathbf{B}$ and $\mathbf{X}$ are related to the corresponding coefficients in the frequency domain by Fourier transformation, we evaluate the frequency domain results using the direct coupling analysis

of floating structures, in which we solve the coupled equations discretized by finite and boundary elements for structure and fluid, respectively [4, 8, 9]. A 2-node boundary element is used for fluid modeling.

4. Numerical Experiments

To validate the proposed formulation, the numerical results are compared with reference solutions. Since there are no available results for hydro-elastoplastic analysis of floating plates, we solve two basic problems. The first problem deals with the transient response of a floating elastic plate and the second problem considers the dynamic response of an elastoplastic beam.

Meylan and Sturova (2009) provided the benchmark solutions for the time-dependent motion of a floating elastic plate released from rest [10]. As shown in Fig. 1, our numerical solutions were in good agreement with the reference solutions for a symmetric initial displacement case ($h / L = 0.02$).

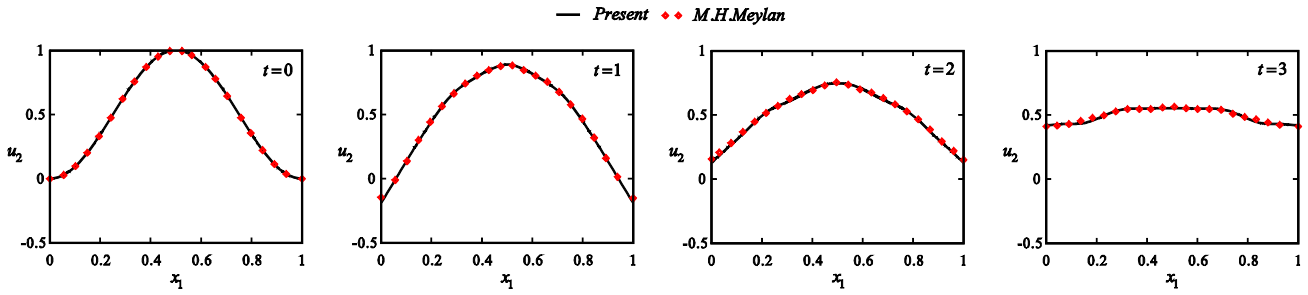

Fig. 1. Time history of the floating elastic plate deflection.

We consider a cantilever beam with bilinear elastoplastic material model subject to an impact load and compare the results with the reference solutions obtained using ADINA [11] as shown in Fig 2. The results show that the proposed formulation is suitable for hydro-elastoplastic analysis.

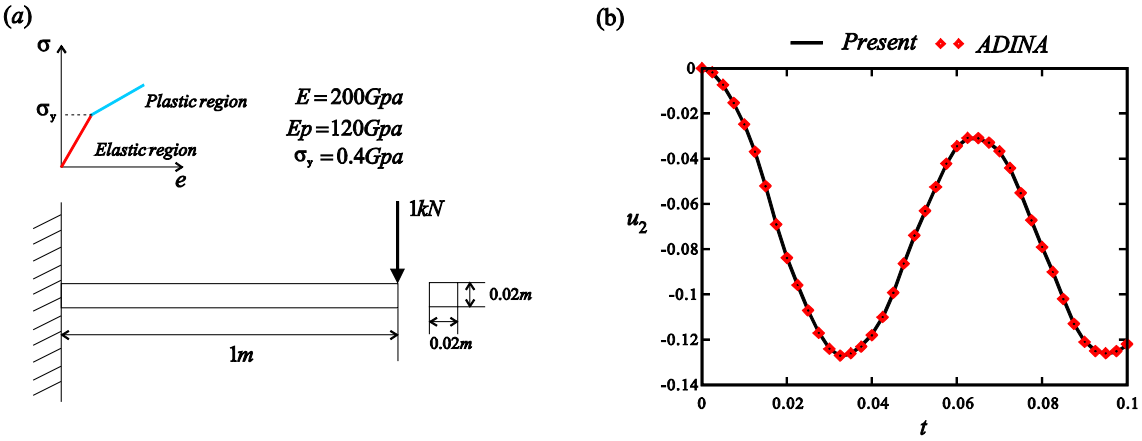

Fig. 2. (a) Elastoplastic cantilever beam problem and (b) deflection at the free tip.

To investigate the effect of plastic deformations on the response of floating plate in a regular wave, we consider a floating plate subjected to an impact load at the middle and compare the numerical results of hydroelastic and hydro-elastoplastic analyses. The structural properties are based on the weight-drop experiment carried out by Endo and Yago [12] and the regular wave length is $\lambda = 3.25m$. As shown in Fig. 3, the response of the floating plate is influenced by the plastic deformation. It is observed that the deflection of the elastoplastic plate is smaller than that of the elastic plate since the energy is dissipated due to plastic mechanism.

5. Conclusions

In this study, we proposed a formulation for hydro-elastoplastic analysis of a floating plate in regular waves and compared our solutions with available numerical results for hydroelastic and elastoplastic analyses. However, it is necessary to carry out related experimental tests and to validate the proposed formulation. In order to extend the research scope, we will investigate elastoplastic behaviors of floating structures under various conditions and extend to the formulation for 3D hydro-elastoplastic analysis.

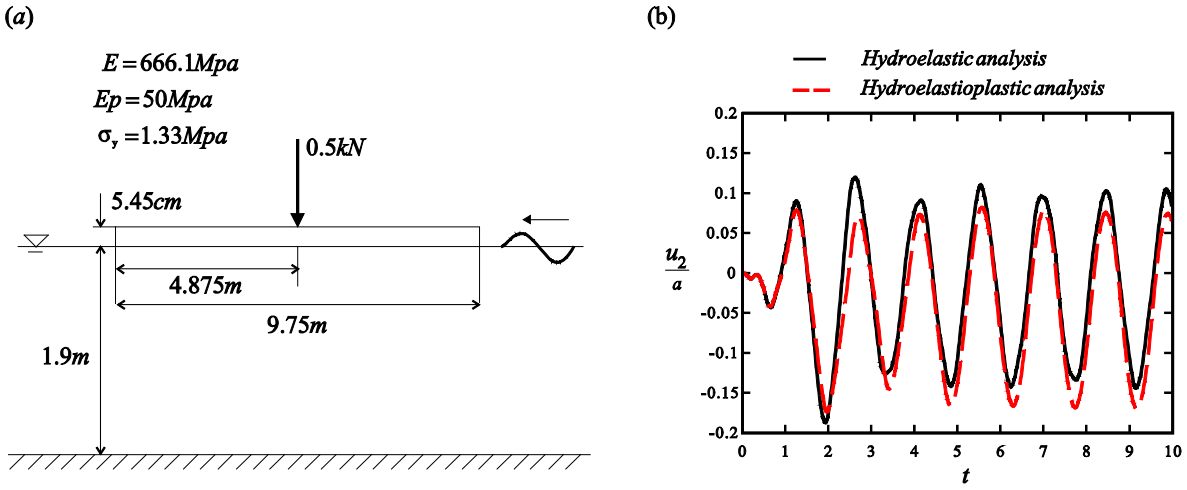

Fig. 3. (a) A floating plate subjected to an impact load in a regular wave and (b) deflections at the middle of plate calculated using hydroelastic and hydro-elastoplastic analyses.

REFERENCES

[1] Hirdaris, S.E. and Temarel, P., Hydroelasticity of ships: Recent advances and future trends, *Proc. IMechE part M*, J Eng Maritime Environ, 2009;223;305-30.

[2] Liu, W., Suzuki, K., Shibanuma, K. and Pei, Z., Nonlinear dynamic response and strength evaluation of a container ship in extreme waves based on hydroelastoplasticity method, *Proc. of the 24th Int Ocean and Polar Eng. Conf.*, Busan, Korea, IOSPE, 2014;652-57.

[3] Bathe, K.J., Finite element procedure, Prentice Hall. Englewood Cliffs, NJ, 1996.

[4] Kim, K.T., Lee, P.S. and Park, K.C., A direct coupling method for 3D hydroelastic analysis of floating structures, Int J Numer Meth Eng, 2013;96;842-66.

[5] Korsmeyer, F.T., Bingham, H.B. and Newma, J.N., TiMIT – a panel method for transient wave-body interactions, Research Laboratory of Electronis, MIT, 1999.

[6] Kojic, M. and Bathe, K.J., Inelastic analysis of solids and structures, Springer, Verlag Berlin Heidelberg, 2005.

[7] Yoon, K. and Lee, P.S., Nonlinear performance of continuum mechanics based beam elements focusing on large twisting behaviors, Comput Methods Appl Mech Engrg, 2014;281;106-30.

[8] Kim, J.G., Cho, S.P, Kim, K.T. and Lee, P.S., Hydroelastic design contour for the preliminary design of very large floating structures, Ocean Eng 2014;78l;112-23.

[9] Yoon, J.S., Cho, S.P., Jiwinangun, R.G. and Lee, P.S., Hydroelastic analysis of floating plates with multiple hinge connections in regular waves, Mar struct, 2014;36;65-87.

[10] Meylan, M.H. and Sturova, I.V., Time-dependent motion of a two-dimensional floating elastic plate, J Fluid Struct, 2009:25:445-60.

[11] ADINA R&D, ADINA theory and modeling guide, Watertown, MA: ADINA R&D, 2013.

[12] Endo, H. and Yago., Time history response of a large floating structure subjected to dynamic load, J Soc Nav Archit Jpn, 1999:186:36-76.

Double Doppler shift theory on water waves generated by a translating and oscillating source

Zhi-Ming Yuan, Atilla Incecik, Alexander Day, Laibing Jia

Dep. of Naval Architecture, Ocean & Marine Engineering, University of Strathclyde, Henry Dyer Building, G4 0LZ, Glasgow, UK

Highlights

- Development of double Doppler shift theory
- Application of double Doppler shift theory on the prediction of water waves generated by a translating and oscillating source

Introduction

The V-shaped wakes behind a translating source on calm water have been widely investigated by many researchers, and the wake half-angle $\psi = \arcsin(1/3) \approx 19.47°$. However, as the source point are advancing in waves, the scattered wave patterns become complicated. As indicated by Becker [1] and Noblesse [2], there exists three wave systems (shown in Figure 1 (a)) as the parameter $\tau < 0.25$ ($\tau = \omega_e u/g$, ω_e is the encounter frequency, u is the forward speed, and g is the gravity acceleration): one ring wave system, which are approximately elliptical in shape, and two Kelvin fan wave systems confined within two distinct wedges, which can be referred as 'outer and inner V waves'. At $\tau < 0.25$, as shown in Figure 1 (b), the upstream portion of the ring waves do not exist. The constant-phase curves depicted in Figure 1 can be obtained by the stationary phase method, which is based on the framework of Green function method.

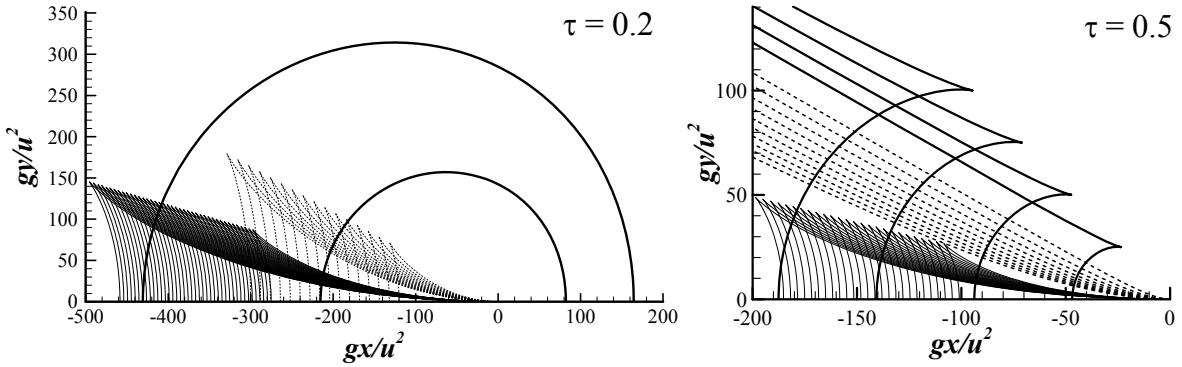

Figure 1 Far-field wave patterns for a translating and pulsating source point located at (0, 0, z), z > 0. (a) $\tau = 0.2$; (b) $\tau = 0.5$.

The present study attempts to establish a method based on physical propagation of the waves to investigate the far-field wave patterns, and this method is referred as double Doppler shift theory hereafter. It should be noticed that the present method was firstly used by Das and Cheung [3] to satisfy the radiation condition for the marine vessels advancing in waves, and Yuan et al. [4] verified this theory through a series of numerical simulation about a single or two ships advancing in waves.

Mathematical expression of double Doppler shift theory

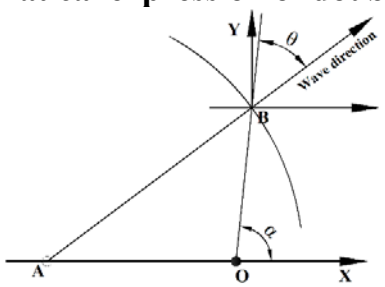

Figure 2 Sketch of the physical propagation of the waves.

Figure 2 shows the propagation of the scattered waves produced by a translating and oscillating source. Supposing there is source point travelling along x-axis from point A to point O with constant forward speed u_0. The traveling time should be $t = AO/u_0$. During this period of time, the translating and oscillating source produces scattered waves all along AO, and the scattered waves produced at point A is propagating to point B. Compared to waves produced at point O, the wave

direction has been rotated by an angle θ. Let's define the velocity of the scattered wave as c, then $AO/u_0 = AB/c$. According to the sine theorem, it can be easily transferred to

$$\frac{u_0}{c} = \frac{\sin\theta}{\sin\alpha} \tag{1}$$

The scattered wave velocity at B can be expressed as

$$c^2 = \frac{g}{k_s}\tanh k_s d \tag{2}$$

where ω_s is the angular frequency of the scattered waves from a fixed reference point given as

$$\omega_s = \omega_e + u_0 k_s \cos(\alpha - \theta) \tag{3}$$

The local dispersion relation for the scattered waves is

$$\omega_s^2 = g k_s \tanh k_s d \tag{4}$$

where k_s is the local wave number at any point on the free surface and d is the water depth. The dimensionless local wave length and local wave number can be defined as

$$\gamma = \frac{2\pi g}{k_s u_0^2}, \quad \kappa = \frac{k_s u_0^2}{g} \tag{5}$$

Combining Eqs. (1)-(5), the following governing equation can be obtained

$$A\kappa^2 + B\kappa + \tau^2 = 0 \tag{6}$$

The coefficient A and B are defined as

$$A = \cos^2\left[\alpha - \sin^{-1}\left(\sqrt{\kappa}\sin\alpha \Big/ \sqrt{\tanh\left(\kappa / F_h^2\right)}\right)\right] \tag{7}$$

$$B = 2\tau\cos\left[\alpha - \sin^{-1}\left(\sqrt{\kappa}\sin\alpha \Big/ \sqrt{\tanh\left(\kappa / F_h^2\right)}\right)\right] - \tanh\left(\kappa / F_h^2\right) \tag{8}$$

where F_h is the depth Froude number and can be written as

$$F_h = \frac{u_0}{\sqrt{gd}} \tag{9}$$

At infinite water depth, $d\to\infty$, Eq. (6) can be reduced to

$$\cos^2\left[\alpha - \sin^{-1}\left(\sqrt{\kappa}\sin\alpha\right)\right]\kappa^2 + \left\{2\tau\cos\left[\alpha - \sin^{-1}\left(\sqrt{\kappa}\sin\alpha\right)\right] - 1\right\}\kappa + \tau^2 = 0 \tag{10}$$

2D wave patterns

Let's firstly discuss the wave length on x-axis. At $\alpha \to 0$ or π, $\sin^{-1}(\kappa\sin\alpha) \to 0$ and Eq. (10) becomes

$$\cos^2(\alpha)\kappa^2 + \left[2\tau\cos(\alpha) - 1\right]\kappa + \tau^2 = 0 \tag{11}$$

The solutions for Eq. (11) can be written as

$$\kappa = \frac{1 - 2\tau\cos\alpha \pm \sqrt{1 - 4\tau\cos\alpha}}{2\cos^2\alpha} \tag{12}$$

In the positive x-axis ($\alpha \to 0$), $\cos\alpha \to 1$ and Eq. (12) can be expressed as

$$\kappa_{1,2} = \frac{1 - 2\tau \pm \sqrt{1 - 4\tau}}{2} \tag{13}$$

Substitute Eq. (13) into Eq.(5), we can obtain the dimensionless local wave length on positive x-axis as

$$\gamma_{1,2} = \frac{4\pi}{1 - 2\tau \mp \sqrt{1 - 4\tau}} \tag{14}$$

In the negative x-axis ($\alpha \to \pi$), $\cos\alpha \to -1$ and Eq. (12) can be expressed as

$$\kappa_{3,4} = \frac{1 + 2\tau \pm \sqrt{1 + 4\tau}}{2} \tag{15}$$

Substitute Eq. (15) into Eq.(5), we can obtain the dimensionless local wave length on negative x-axis as

$$\gamma_{3,4} = \frac{4\pi}{1 + 2\tau \mp \sqrt{1 + 4\tau}} \tag{16}$$

The dimensionless local wave length defined in Eq. (14) and (16) is depicted in Figure 3. The results in Figure 3 are consistent with the solutions provided by Becker[1]. At $\tau < 0.25$, there are four wave systems on the x-axis. At $\tau > 0.25$, the wave systems on positive x-axis vanish and only two wave systems exist on negative x-axis. At $\tau = 0$, the dimensionless local wave length γ_1 and γ_3 (corresponding to the ring wave system, which will be discussed further on) turn to be infinity, and γ_2 and γ_4 merge together as Kelvin wave with the dimensionless local wave length $\gamma = 2\pi$.

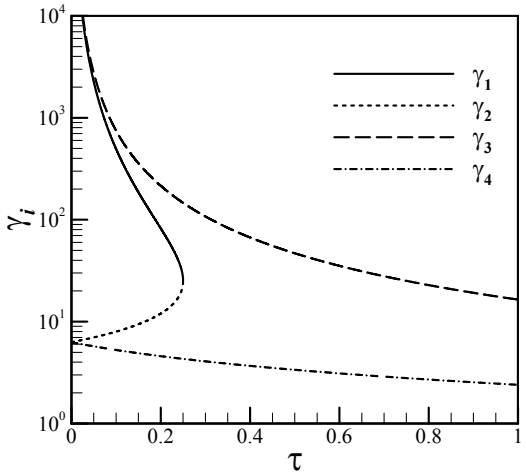

Figure 3 Dimensionless wavelength on x-axis.

It should also be noticed that at infinite water depth, as $\alpha \to \pi$,

$$\omega_s = -\frac{1}{2}\left(1+\sqrt{1+4\tau}\right) < 0 \tag{17}$$

The physical explanation of this negative local encounter frequency is similar to that of encounter frequency [5]. The apparent direction of the scattered wave propagation is obtained by observation. When $\omega_s < 0$, the ship outraces the waves and their crests actually appear to be moving from the ship's bow toward her stern. Therefore, γ_4 represents the wave length behind the ship propagating in the opposite direction.

3D wave patterns

From Eq. (6) we find the dimensionless local wave number is determined by three independent parameters: τ, F_h and α. For a given τ in infinite water depth, from Eq. (10) it can be found that the dimensionless local wave number is only determined by α. Based on the similar idea of stationary phase method, the curves of equal phase for the various systems of waves can be drawn as α varies from 0 to 2π. For a given α, the nonlinear equation in Eq. (10) can be solved by a numerical iterative scheme. Figure 4 shows the solutions of Eq. (10) for parameter $\tau = 0.25$ and $\tau = 0.5$ at infinite water depth. Typically, there are four solutions for Eq. (10), and these solutions can be only found at some limited range of α. For the case of $\tau = 0.25$, two sets of solution can be found in the entire range of α, and at $\alpha = 0$, these two sets of solution merge at $\kappa = 25.12$. The rest two sets of solution are limited at $\alpha > 162.12°$. For the case of $\tau = 0.5$, two sets of the solution only exist at $\alpha > 107.47°$, and the rest two sets of solution only exist at $\alpha > 163.26°$. As parameter increases, these four solutions become small and are close to each other, and they are limited to a very small range of α, which is approaching 180°.

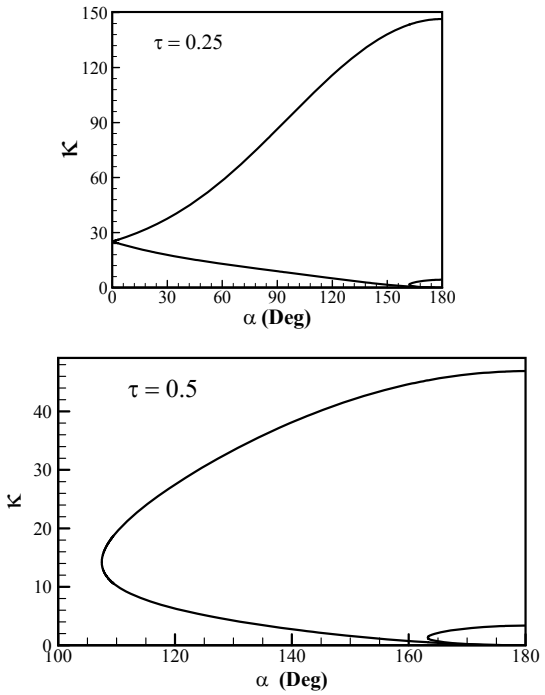

Figure 4 Typical solutions of Eq.(10)

Defining κ_i as the i-th solution for Eq.(10), and each solution corresponds to an independent wave system, then the corresponding points of stationary phase can be written as

$$\begin{cases} x = \dfrac{\psi}{\kappa_i}\cos\alpha \\ y = \dfrac{\psi}{\kappa_i}\sin\alpha \end{cases}, \quad i = 1,2,3,4 \tag{18}$$

Eq. (18) is parametric equation defining the curves (x, y) along which the phase Ψ remains constant. It can be found from Eq. (18) that the curves are symmetrical about x-axis. Therefore, only the plane of $y \geq 0$ will be displayed hereafter. The constant-phase curves defined by the parametric equation (18) are depicted in Figure 5 for a set of values of Ψ with increment equal to 2π, and for following six values of τ: 0.2, 0.25, 0.26, 0.5, 1 and 4. This figure shows that, for values of τ smaller than 0.25, three distinct wave systems can be identified. These wave systems consist of 'ring waves' which are approximately elliptical in shape, and two wave systems found in two distinct regions. The raindrop-shape wave system appeared downstream can be called 'raindrop waves', and the helical-shape wave system, which appears mainly upstream, can be called 'helical waves'. For value of $\tau = 0.25$, the helical waves merge with the ring waves in the positive x-axis. As $\tau \to 0.25^+$, there is no wave existing in the positive x-axis. For value of $\tau >$ 0.25, the helical waves merge with the ring waves, forming an integrated and closed wave system. And as the parameter τ increases, this integrated wave system shifts downstream, merging with the raindrop-shape wave system gradually.

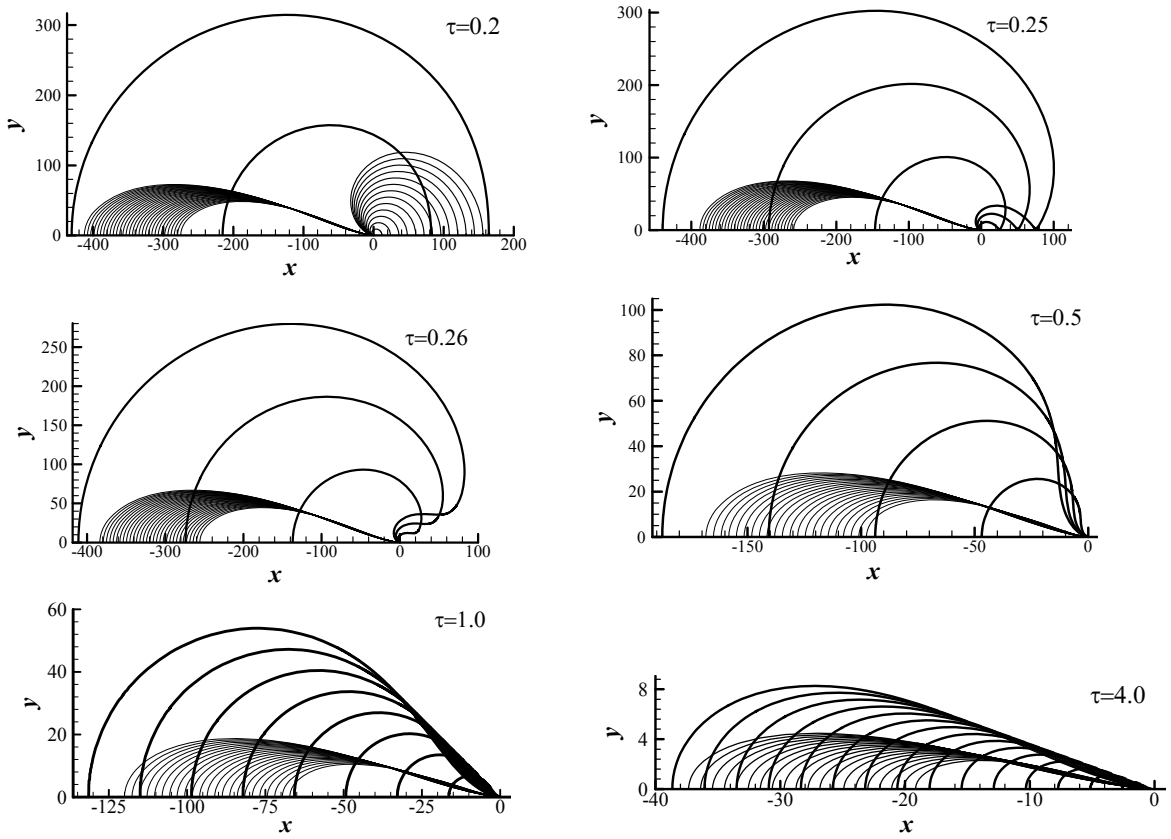

Figure 5 Far-field wave patterns for a translating and pulsating source point with six values of τ: 0.2, 0.25, 0.26, 0.5, 1 and 4.

Steady wave patterns

Particularly, as $\tau \to 0$, Eq. (10) can be reduced to

$$\cos^2\left[\alpha - \sin^{-1}\left(\sqrt{\kappa}\sin\alpha\right)\right]\kappa^2 - \kappa = 0 \tag{19}$$

The solutions for Eq. (19) can be written as

$$\left.\begin{array}{c} \kappa_1 = 1 \\ \kappa_{2,3} = \dfrac{4}{-1+3\cos 2\alpha \pm \sqrt{2\cos^2\alpha(9\cos 2\alpha - 7)}} \end{array}\right\} \tag{20}$$

Substituting Eq. (20) into Eq. (18), we can obtain the constant-phase wave patterns, as shown in Figure 6. κ_1 corresponds to the particular case $u = 0$ and $\omega_e \neq$, and the wave pattern represents the waves generated by a pulsating source. The other case which makes $\tau = 0$ is $u \neq 0$ and $\omega_e = 0$, and the wave pattern represents the waves generated by a translating source. κ_2 and κ_3 are the solutions corresponding to this case. It can be observed from Figure 6 that κ_2 and κ_3 merged into the raindrop waves as $\sqrt{2\cos^2\alpha(9\cos 2\alpha - 7)} \to 0$. The raindrop waves will confined within $\alpha = \frac{1}{2}\cos^{-1}\left(\frac{7}{9}\right) \approx 19.47^\circ$, which is exact the same as Kelvin angle.

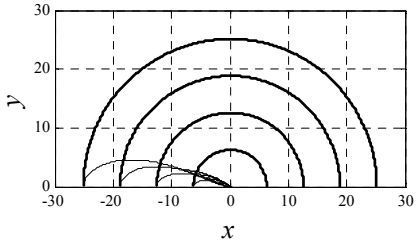

Figure 6 Far-field wave patterns for a translating and pulsating source point at $\tau = 0$.

References

1. Becker, E., *Das Wellenbild einer unter der Oberfläche eines Stromes schwerer Flüssigkeit pulsierenden Quelle.* Journal of Applied Mathematics and Mechanics, 1958. **38**(9-10): p. 391-399.
2. Noblesse, F. and D. Hendrix, *On the theory of potential flow about a ship advancing in waves.* Journal of Ship Research 1992. **36**(1): p. 17-30.
3. Das, S. and K.F. Cheung, *Scattered waves and motions of marine vessels advancing in a seaway.* Wave Motion, 2012. **49**(1): p. 181-197.
4. Yuan, Z.M., A. Incecik, and A. Day, *Verification of a new radiation condition for two ships advancing in waves.* Applied Ocean Research 48, 2014: p. 186-201.
5. Denis, M.S., Member, and W.J. Pierson, *On the motions of ships in confused seas.* Trans. NAME, 1953. **61**.

Liquid sloshing and impact in a closed container with high filling

H.J. Zekri[1], A.A. Korobkin[1], M.J. Cooker[1]
[1]School of Mathematics, University of East Anglia, Norwich, UK
E-mail: h.zekri@uea.ac.uk

1 Introduction

Violent liquid sloshing is of concern to cargo tank designers due to the problems of safety in extreme loadings. It is an interesting topic with still some disputable problems. For example Abramson, Bass, Faltinsen and Olsen [1] investigated the sloshing and resultant loads in liquid natural gas carriers for different tank geometries and liquid fill depths. Ibrahim [3] provided a comprehensive study with examples of free tank motions. Cooker [2] analysed with experiments a horizontal rectangular wave tank which swings at the lower end of a pendulum. Ten, Malenica and Korobkin [5], presented a semi-analytical approach for fluid-structure interactions inside tanks in different impact situations with high and low fillings. Our work is about the sloshing of standing waves inside a closed highly filled container. Unsteady two-dimensional (2-D), irrotational flow is treated. The liquid-roof interaction is discussed with and without the effect of gravity and a comparison is made. The short-time model of the liquid-roof impact is governed by a Mixed Boundary Value Problem (MBVP), which is solved numerically and using the asymptotic methods.

2 Mathematical formulation

In figure 1, a stationary highly filled rectangular tank, containing an inviscid incompressible liquid is shown. The flow is 2-D and irrotational and surface tension force is neglected. The container has height H and length $2L$ and lies in the region $\tilde{y} \geq 0$. Here $\tilde{y} = 0$ is the bottom and $\tilde{y} = H$ is the roof of the container, $\tilde{y} = H - h$ is the still water level, and $\tilde{x} = \pm L$ are the rigid impermeable walls. The lengths, time, velocity potential and pressure are scaled by H, $\sqrt{H/g}$, $h\sqrt{Hg}$ and $\rho g h$, respectively, where g is the gravitational acceleration and ρ is the constant density. The small parameter $\epsilon = h/H \ll 1$ is responsible for linearisation. In non-dimensional variables (without tilde), the initial shape of the free surface is given by the equation $y = f(x)$, $f(x) = 1 - \epsilon + \frac{2\epsilon}{\lambda} \sum_{n=1}^{\infty} a_n \cos(k_n x)$, a_n and k_n are known constants and $\lambda = \frac{L}{H}$.

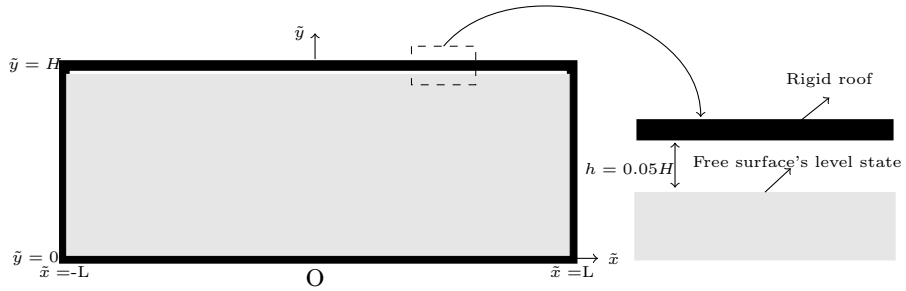

Figure 1: Container description with free surface at its level state.

Considering the container to be without the rigid roof, in non-dimensional linearised initial bound-

ary problem at the leading order the velocity potential $\phi_l(x, y, t)$ and the surface elevation $\eta_l(x, t)$ read

$$\phi_l(x, y, t) = \sum_{n=1}^{\infty} \bar{a}_n \cosh(k_n y) \cos(k_n x) \sin(w_n t), \tag{1}$$

$$\eta_l(x, t) = \frac{2}{\lambda} \sum_{n=1}^{\infty} a_n \cos(k_n x) \cos(w_n t), \qquad a_n = -\bar{a}_n \omega_n \cosh(k_n), \tag{2}$$

where the angular frequencies ω_n are related to the wave numbers $k_n = n\pi/\lambda$ by the dispersion relation $\omega_n = \sqrt{k_n \tanh(k_n)}$, for $n \in \mathbb{N}$. In the next section we introduce the rigid roof to the tank, we decompose the velocity potential $\phi(x, y, t)$ and the surface elevation $\eta(x, t)$ into two parts. This has been done by adding unknown functions: a so called correction velocity potential $\phi_c(x, y, t)$ and a correction surface elevation $\eta_c(x, t)$ resulting in $\phi = \phi_c + \phi_l$ and $\eta = \eta_l + \eta_c$ respectively.

3 Semi-analytical solution

At the leading order, we derive the linearised non-dimensional MBVP, with gravity and the rigid roof included. During the early stage of the impact, with some asymptotic analysis, we have found that gravity has a small influence. We define $\delta \ll 1$ to stretch the time $t = t^* + \delta\hat{t}$, $t = t^*$ instant of impact, consequently the other variables, $x = \delta^{1/2}\hat{x}$, $y = \delta^{1/2}\hat{y}$, $\phi_c(x, y, t) = \delta^{1/2}\hat{\phi}_c(\hat{x}, \hat{y}, \hat{t})$, $x_{c0}(t) = \delta^{1/2}\hat{x}_{c0}(\hat{t})$ and $\eta_l(x, t) = \delta\hat{\eta}_l(\hat{x}, \hat{t})$. By combining the dynamic and kinematic boundary conditions we arrive at (without hat)

$$\frac{\partial^2 \phi_c}{\partial t^2} + \delta^{\frac{3}{2}} \frac{\partial \phi_c}{\partial y} = 0 \qquad |x| > x_c(t), \qquad y = 0, \tag{3}$$

where $x = x_c(t)$ is where the free surface meets the roof. The corresponding limiting problem as $\delta \to 0$ is depicted in Figure 2. This problem does not account for gravity.

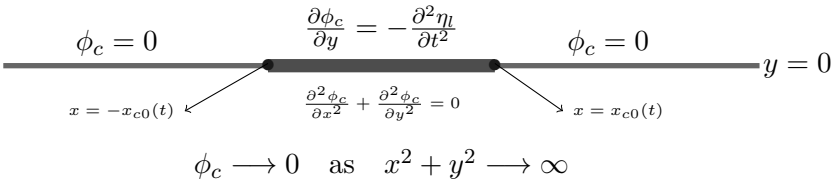

Figure 2: The MBVP at the leading order.

Working with stretched variables, we can approximately replace the wall and the bottom conditions with the far-field condition given in Figure 2. With the condition introduced by Wagner [6] at the contact points and the displacement potential $\Phi(x, y, t) = \int_0^t \phi_c(x, y, \tau)\mathrm{d}\tau$ introduced by Korobkin [4], we are able to calculate semi-analytically the leading order position of the contact point, $x = x_{c0}(t)$, during impact. Consequently the hydrodynamic pressure distribution can be found (see Figure 3).

4 Numerical solution

A collocation method was used for the symmetric flow considered in the original coordinates x and y. The unknowns, velocity potential $\phi(x, y, t)$, surface elevation $\eta(x, t)$ and the pressure on the roof $p(x, 0, t)$ are respectively presented by Fourier series. The domain is discretized into N regularly spaced nodes ($N = 350$ in our calculations).

The combined kinematic and dynamic boundary conditions (with gravity included) lead to a system of the form

$$\vec{\eta} = \vec{\eta}_l - A^{-1}B\vec{P} - A^{-1}\sum_{m=1}^{M-1} G^{t_m}\vec{p}^{\,t_m}, \tag{4}$$

where the initial pressure $\vec{p}^{\,t_1}$, found in the previous section, with respect to this algorithm is given. The tri-diagonal matrix A is associated with unknown and known surface elevation vectors, $\vec{\eta}$ and $\vec{\eta}_l$ respectively. The matrix G is calculated at every time step while the matrix B is independent of time and depends only on the time step length. The pressure $\vec{P}$ and surface elevation $\vec{\eta}$ are to be determined at the instant $t = t_M$. However, the fact that on the free surface, $x_{c0}(t_M) < x < 1$, we have $p(x, t_M) = 0$ and on the impact region, $0 < x < x_{c0}(t_M)$, we have $\eta(x, t_M) = 1$, with some rearrangements makes the system (4) solvable on its own. The free surface and the wetted region are distinguished and updated at each time step by calculating the position of $x = x_{c0}(t_M)$ as part of the solution. The pressure vector $\vec{p}^{\,t_m}$ is known from the previous time steps $t = t_m$, for $1 \leq m \leq M-1$.

Continuing with the stretched variables introduced from Section 3, we study the gravity influence on the length of the wetted region during the impact stage, that is $x_{c0}(t) + \delta \cdot x_{c1}(t)$. The correction due to gravity $x_{c1}(t)$ in Figure 4b, is found to be almost completely insignificant at the early stage of impact. As time goes on the effect of gravity is that it decreases the length of the wetted region and even at the very late period of this stage, its effect is found to be small. Figure 4a shows the wetted length with and without gravity. More results of the numerical simulation will be presented at the workshop.

5 Acknowledgements

H. Zekri gratefully acknowledges the financial support received from Kurdistan Regional Government-Iraq for his study.

References

[1] H. N. Abramson, R. Bass, O. Faltinsen, and H. Olsen. Liquid slosh in LNG carriers. In *Symposium on Naval Hydrodynamics, 10th, Proceedings, Pap and Discuss, Cambridge, Mass, June 24-28, 1974.*, number Proceeding, 1976.

[2] M. J. Cooker. Water waves in a suspended container. *Wave Motion*, 20(4):385–395, 1994.

[3] R. A. Ibrahim. *Liquid sloshing dynamics: theory and applications.* Cambridge University Press, 2005.

[4] A. Korobkin. Formulation of penetration problem as a variational inequality. *Din. Sploshnoi Sredy*, 58:73–79, 1982.

[5] I. Ten, Š. Malenica, and A. Korobkin. Semi-analytical models of hydroelastic sloshing impact in tanks of liquefied natural gas vessels. *Philosophical Transactions of the Royal Society A: Mathematical, Physical and Engineering Sciences*, 369(1947):2920–2941, 2011.

[6] H. Wagner. Phenomena associated with impacts and sliding on liquid surfaces. *Z. Angew. Math. Mech*, 12(4):193–215, 1932.

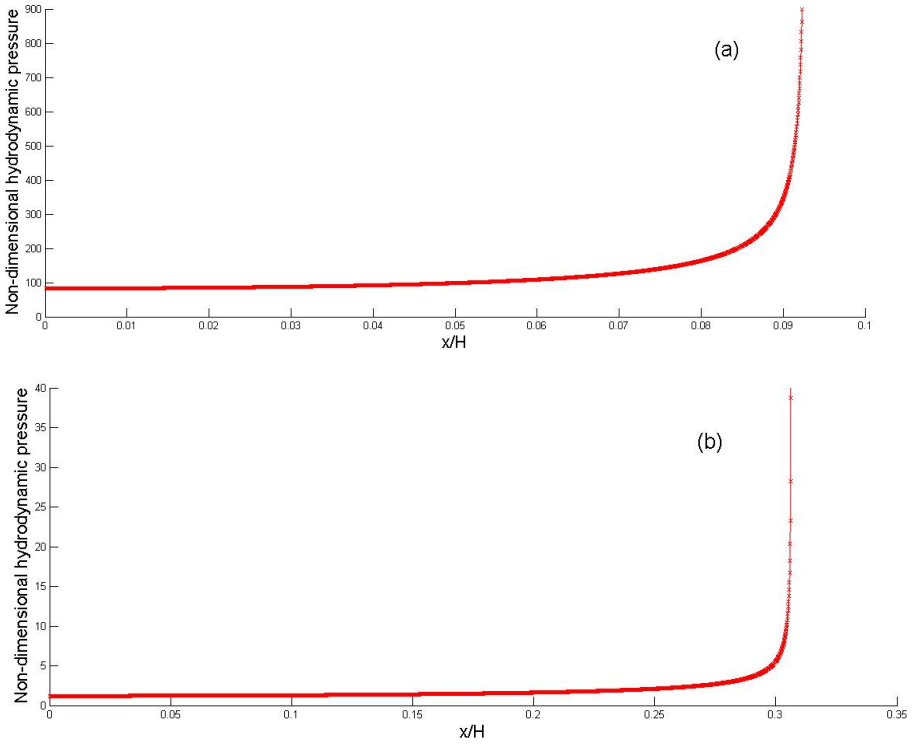

Figure 3: Semi-analytical pressure distribution without gravity at: (a) $t = 1.0790$; (b) $t = 1.5760$.

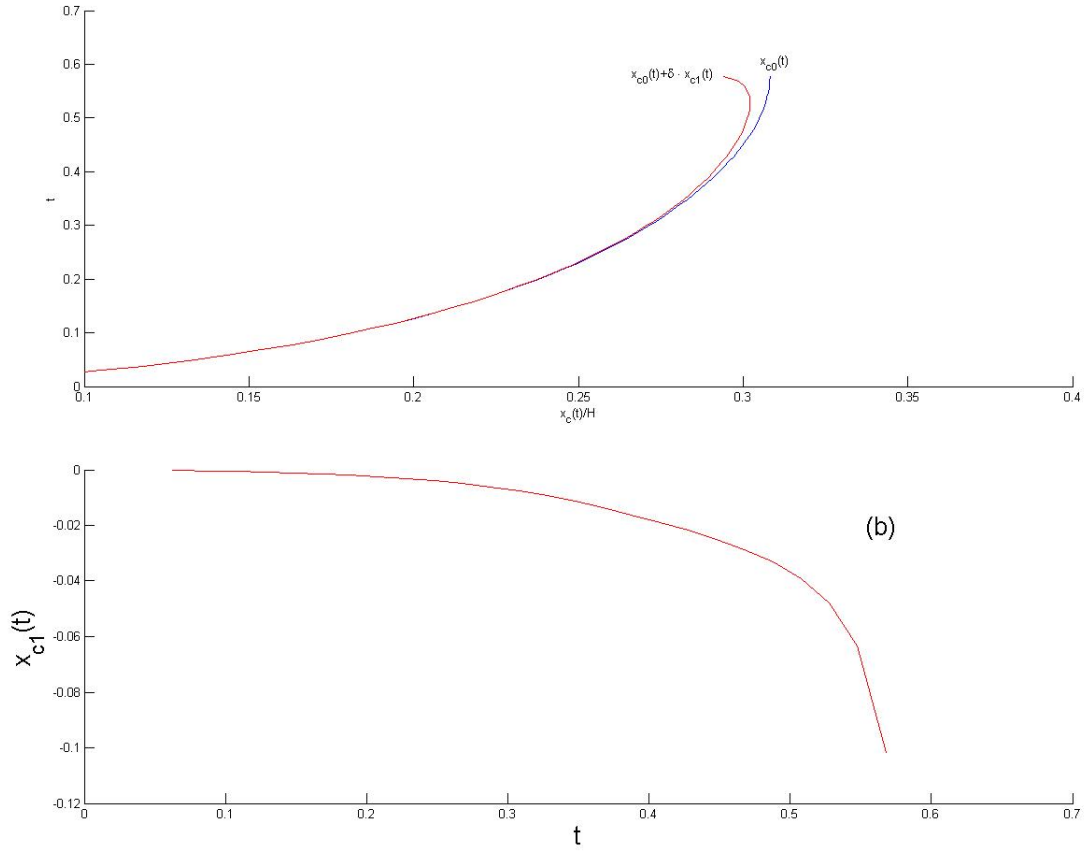

Figure 4: Contact point position with correction due to gravity, here $t = 0$ is the impact time: (a) The leading order contact point, blue line,and the contact point with correction due to gravity, red line; (b) details of correction $x_{c1}(t)$ due to gravity,for the contact point position.

(*30th International Workshop on Water Waves and Floating Bodies, Bristol, UK, 2015*)

Fully Nonlinear Computations of Wave Radiation Forces and Hydrodynamic Coefficients for a Ship with a Forward Speed

Xinshu Zhang[1]*, Robert F. Beck[2]

[1] School of Naval Architecture, Ocean & Civil Engineering, Shanghai Jiao Tong University, Shanghai, China

[2] Department of Naval Architecture & Marine Engineering, University of Michigan, Ann Arbor, USA

1 Introduction

The accurate prediction of nonlinear wave loads on a ship with a forward speed is critical to the evaluation of it's global motion performance and manoeuvring capabilities. The seakeeping performance is one of the key factors for hull form optimization. Traditionally, the seakeeping computation can be performed using the strip theory developed, for example, by Salvesen *et al.* (1970) or the one extended to the body-exact version in time-domain for large amplitude motion computations by Zhang *et al.* (2010*a*). Recently, with rapid development of computing hardware, three-dimensional time-domain approaches using Rankine sources or desingularized sources have been developed to accurately model and capture the forward speed effects. Due to the nonlinear properties of both the free surface kinematic and dynamic boundary conditions (FSBC) applied on the unknown free surface, the FSBC and body boundary condition (BBC) are often linearized with respect to the calm water surface at $z = 0$ (z is the vertical coordinate). Different forms of linearizations have been developed over the past several decades, including Neumann-Kelvin linearization (NKL) and double body linearization (DBL). The comparisons of those linearized approaches to a time-domain body exact strip theory and experiments have been extensively studied in a previous paper (Zhang *et al.*, 2010*b*).

However, due to the assumptions made upon deriving the linearized FSBC and BBC, both NKL and DBL may have limited validity depending on Froude number or slenderness of a hull. The details on the NKL and DBL models are presented in the next Section. Without any assumptions on small parameters, fully nonlinear computations may provide more reliable solutions and can be employed as a benchmark for the linearized or quasi-nonlinear models.

The primary focus of the present study is on identifying and quantifying the nonlinearities associated with wave-body interaction including forward speed and hull slenderness. We developed a fully nonlinear model to compute the wave radiation forces on vessels travelling with a forward speed. The final objective is to quantify validity of different linearized models.

2 Theory and Approach

2.1 Fully nonlinear model

We developed a fully nonlinear potential flow computational model to study the wave radiation problem for ships with a forward speed. Desingularized sources and Rankine panels are applied on the free surface and instantaneous wetted hull surface, respectively. On the free surface, a mixed Euler-Lagrange free surface tracking scheme is employed (Longuet-Higgins & Cokelet, 1976; Yeung, 1982; Zhang *et al.*, 2010*a*,*b*). The nonlinearities associated with both the body boundary condition and the free surface boundary conditions (except wave breaking) are automatically accounted for in the developed three-dimensional time-domain model.

The vessel is assumed to move with speed $\mathbf{U}(t) = (U_o(t), 0, 0)$, and may be undergoing unsteady oscillations in six degrees of freedom. The fluid is assumed to be ideal and the flow irrotational. Three coordinate systems are employed: the $\mathbf{x_o}$ system is fixed in space, the $\mathbf{x}$ system is fixed to the mean position of the ship (moving with forward speed $\mathbf{U}(t)$ along the straight track of the ship), and the $\overline{\mathbf{x}}$ system is fixed to the ship. The boundary value problem is solved in the right hand moving coordinate system (x, y, z), as illustrated in Figure 1. The x-axis points in the direction of travel and the z-axis points upward. The origin is on the calm water plane at midship.

In the $\mathbf{x}$ coordinate system, a velocity potential is introduced to describe the fluid motion by using the above assumptions such that the fluid velocity can be expressed as the gradient of a potential function,

$$\mathbf{V}(\mathbf{x}, t) = \nabla\Phi = \nabla(-U_o(t)x + \phi(x, y, z, t)) \tag{1}$$

*Presenting author. Email: xinshuz@sjtu.edu.cn

where ϕ is the disturbance velocity potential which may include the radiation and/or diffraction potential.

The velocity potential $\phi(x, y, z, t)$ satisfies the Laplace equation

$$\phi_{xx} + \phi_{yy} + \phi_{zz} = 0 \tag{2}$$

The exact nonlinear kinematic and dynamic free surface boundary conditions are

$$\frac{\partial \eta}{\partial t} = \frac{\partial \phi}{\partial z} - \nabla\phi \cdot \nabla\eta + U_o(t)\frac{\partial \eta}{\partial x} \qquad \text{on} \qquad z = \eta(x, y, t) \tag{3}$$

$$\frac{\partial \phi}{\partial t} = -g\eta - \frac{1}{2}\nabla\phi \cdot \nabla\phi + U_o(t)\frac{\partial \phi}{\partial x} \qquad \text{on} \qquad z = \eta(x, y, t) \tag{4}$$

where $\eta(x, y, t)$ represents the free surface elevation; g is the gravitational acceleration. All the velocity potentials satisfy the Laplace equation under the assumption of ideal potential flow.

The exact body boundary condition can be written as

$$\mathbf{n} \cdot \nabla\phi = U_o(t)n_1 + \mathbf{V_H} \cdot \mathbf{n} - \nabla\phi^I \cdot \mathbf{n} \qquad \text{on} \quad S_B \tag{5}$$

where S_B is the instantaneous wetted body surface; $U_o(t)$ is the time-dependent translating velocity of the body in the x direction; $\mathbf{n}$ is the inward unit normal on the body surface(out of fluid); n_1 is the component of the unit normal in the x direction; $\mathbf{V_H}$ is the motion velocity including rotational modes of a point on the ship's surface; ϕ^I is the velocity potential for an incident wave .

The initial conditions at $t = 0$ are

$$\Phi = \Phi_t = 0 \quad \text{in the fluid domain} \tag{6}$$

At each time step, a mixed boundary value problem must be solved; the potential is given on the free surface and the normal derivative of the potential is known on the body surface. In order to solve the initial boundary value problem, desingularized sources are distributed over the free surface and constant strength flat panels are utilized on the body surface. Given the strength of the desingularized sources above the free surface and sources distributed on the body surface, the potential at any point in the fluid domain can be obtained. The details on the application of desigularized sources and panels have been presented in previous papers (Zhang *et al.*, 2010*a*,*b*).

The free surface is time stepped through applying a mixed Euler-Lagrange scheme on the fully nonlinear free surface boundary conditions (3) and (4). The wetted hull surface is re-panelized at each time step by updating the instantaneous intersection curve between the wetted hull and dynamic wave surface. After solving the boundary value problem at each time step, the wave radiation force and moments, and the hydrodynamic coefficients can be computed.

2.2 Neumann-Kelvin linearization (NKL)

The nonlinear free surface boundary conditions are often linearized by introducing a basis flow Ψ. The total perturbation velocity potential can be written as

$$\phi = \Psi + \phi' \tag{7}$$

where $\Psi \sim O(1)$ and $\phi' \sim O(\epsilon)$ are assumed.

In Neumann-Kelvin linearization, it is assumed that the uniform flow $-U_0(t)x$ in translating coordinate system $\mathbf{x}$ is not disturbed due to the presence of a hull, which leads to $\Psi = 0$. Linearized FSBC and BBC can be obtained by substitute $\phi \sim O(\epsilon)$ and $\eta \sim O(\epsilon)$ into Eqns. (3), (4) and (5).

2.3 Double-body basis flow linearization (DBL)

In double-body linearization, the basis flow is computed by assuming an unbounded uniform flow passing a double-body. Hence we have the following:

$$\partial\Psi/\partial z = 0 \ \text{ at } \ z = 0 \tag{8}$$

$$\mathbf{n} \cdot \nabla\Psi = U_o(t)n_1 \quad \text{on} \quad S_{\bar{B}} \tag{9}$$

where $S_{\bar{B}}$ is the mean wetted body surface. A set of linearized FSBC and BBC can be derived through substituting Eqns. (7), (8) and (9) into Eqns. (3), (4) and (5) and keeping all the leading order terms. We remark the obtained linearized BBC contains so-called m-terms which represent the coupling effects between the steady flow and unsteady flow (see Zhang *et al.*, 2010*b*). For purpose of comparison, we also build up a

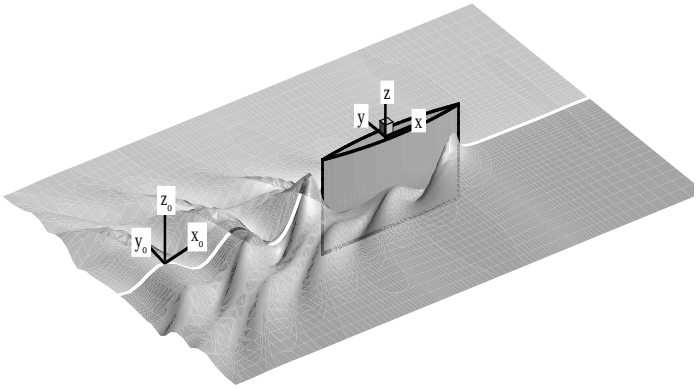

Figure 1: Definition of the problem and coordinate systems

model (called LFS DB m-terms) using the double-body m-terms in BBC while retaining the linearized free surface boundary conditions the same as the one in Neumann-Kelvin model.

It should be noted that wave breaking, which is a natural phenomenon, can occur in both wave radiation and diffraction problems for a ship travelling with a forward speed. The wave breaking normally can be observed near the bow, stern and in the wake. In the present study, we focus on non-wave breaking cases and keep the forward speed and the forced motion amplitude of hull relatively small to prevent the wave breaking in the simulations.

3 Results and Discussion

The developed fully nonlinear model is validated by comparing the obtained numerical solutions to experiments and other numerical results using different linearized models. The tested hull forms include Wigley I hull and a Series 60 hull with $C_B = 0.7$. The comparison of the diagonal/coupling added mass and damping coefficients due to a heave motion are illustrated in Fig.2. The forced motion frequencies $\omega\sqrt{L/g}$ vary from 2.2 to 4.5. The numerical solutions using fully nonlinear computations are compared with those using DBL, NKL, linearized FSBC with double-body m-terms, and experimental data reported by Journeé (1992). As can be seen from the figure, the present computations of added mass and damping agree quite well with experiments and show better agreement with measured data than other linearized models including NKL and linearized FSBC with double-body m-terms (LFS, DB m-terms). We remark here that the predictions using fully nonlinear simulations are very close to the solutions using DBL. This confirms that DBL is a valid linearized model for the Wigley I hull at $F_n = 0.3$. The computed hydrodynamic coefficients due to a forced pitch motion are illustrated in Fig.3. The same conclusion is found for the predicted hydrodynamic coefficients.

We are also investigating the dependence of the hydrodynamic coefficients on Froude number and the hull slenderness, for both a Wigley hull and a Series 60 hull. The additional results will be presented at the workshop.

References

Journeé, J. M. J 1992 Experiments and calculations on 4 wigley hull forms in head waves. Report 0909. DUT-SHL.

Longuet-Higgins, M. S. & Cokelet, C. D. 1976 The deformation of steep surface waves on water: I. a numerical method of computation. *Proc. of the Royal Society of London* **A350**, 1–26.

Salvesen, N., Tuck, E. O. & Faltinsen, O. 1970 Ship motions and sea loads. *Trans. SNAME* **78**, 250–287.

Yeung, R. W. 1982 Numerical methods in free-surface flows. *Annual Review of Fluid Mechanics* **14**, 395–442.

Zhang, X., Beck, R. F. & Bandyk, P. 2010*a* Time-domain simulations of radiation and diffraction forces. *Journal of Ship Research* **54** (2), 79–94.

Zhang, X., Beck, R. F. & Bandyk, P. 2010*b* Seakeeping computations using double body basis flows. *Applied Ocean Research* **32**, 471–481.

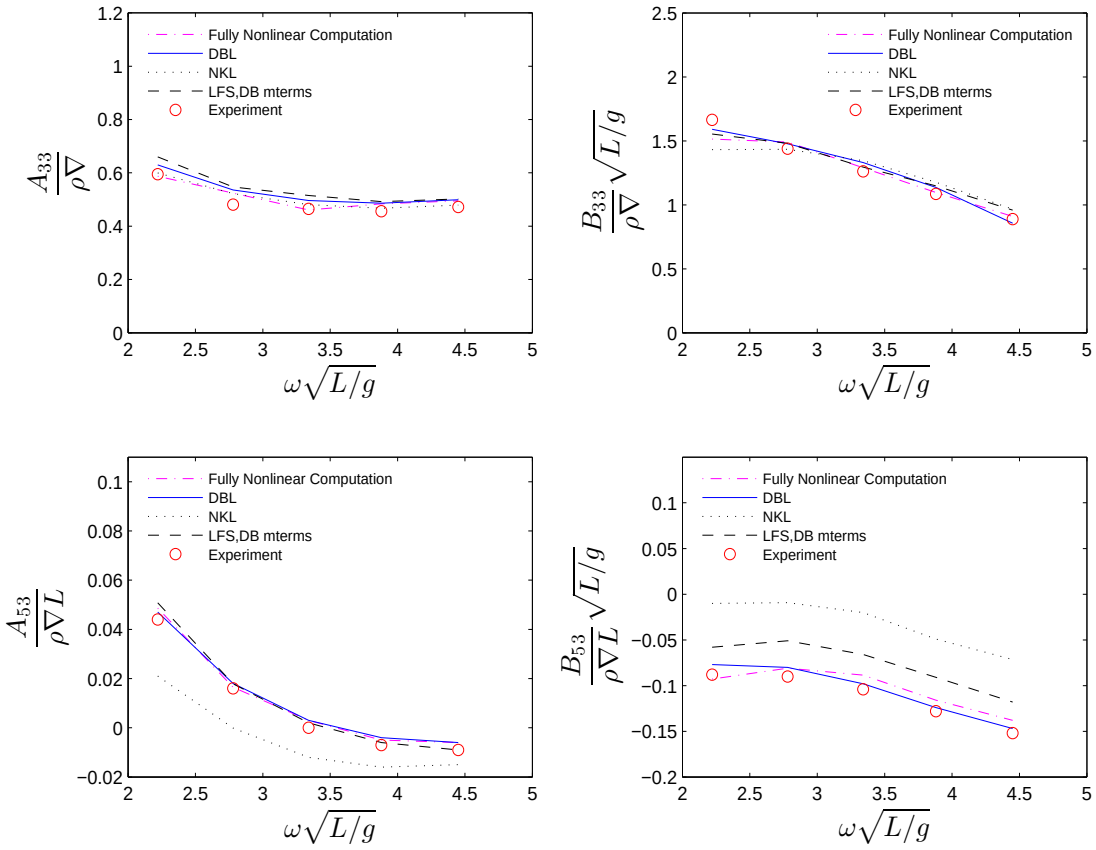

Figure 2: The hydrodynamic coefficients due to a forced heave motion for Wigey I hull, Froude number $F_n = 0.3$, heave motion amplitude $a/L = 0.01$, L is the length of the ship; ω is the forced motion frequency.

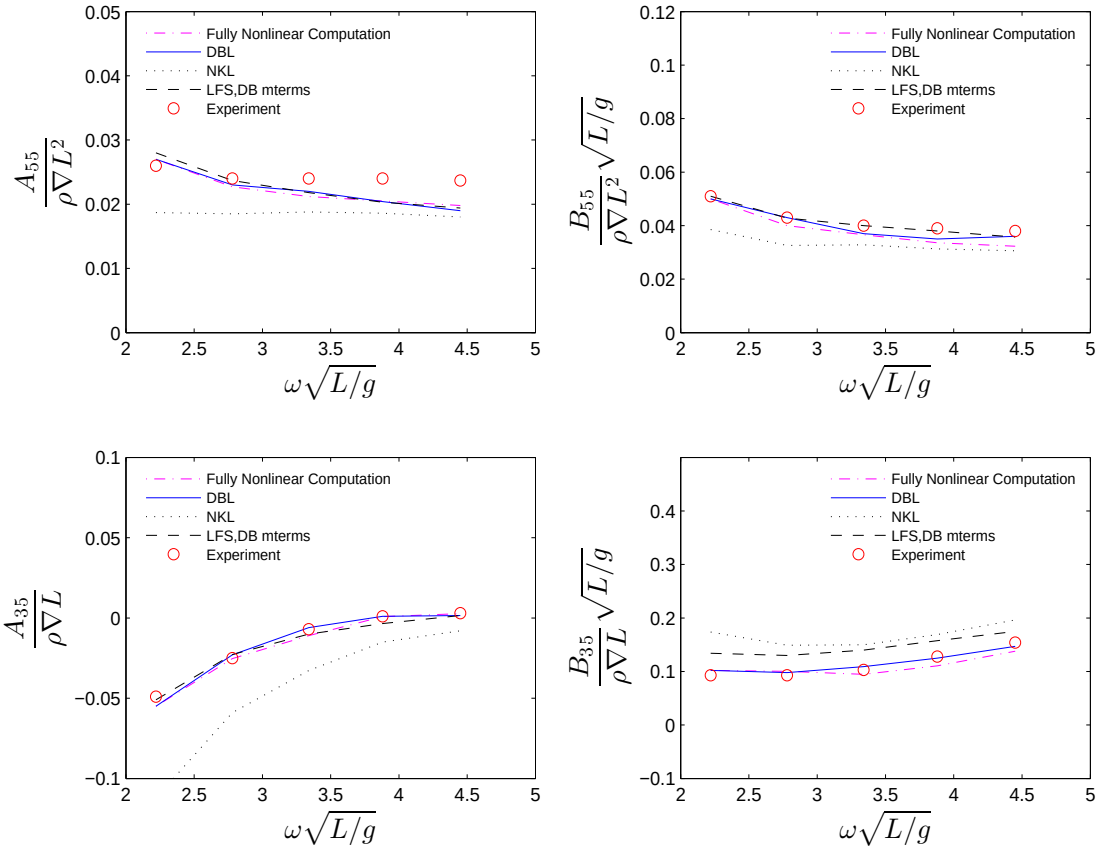

Figure 3: The hydrodynamic coefficients due to a forced pitch motion for Wigey I hull, Froude number $F_n = 0.3$, pitch motion amplitude $a = 0.05$ *rad* with $L = 10$ m.

A numerical study on prediction of ship maneuvering in waves

ZHANG Wei[1], ZOU Zaojian[1,2]

1. School of Naval Architecture, Ocean and Civil Engineering; 2. State Key Laboratory of Ocean Engineering,

Shanghai JiaoTong University, Shanghai 200240, China

(drwood@sjtu.edu.cn zjzou@sjtu.edu.cn)

Highlights:

- A numerical method is developed for predicting ship maneuvering in waves, based on the two-time scale model.
- The linear hydrodynamic forces on the maneuvering hull are evaluated based on the double body model with a trailing vortex sheet, and the effects of the trailing vortices on the wave forces are considered indirectly.
- The present method is validated by comparing the numerical results with the free running model test data.

1 Introduction

Prediction of ship maneuverability is typically carried out in clam water conditions. This gives valuable information at the ship design stage. However, an actual seagoing ship usually maneuvers in the presence of waves. From the viewpoint of ship safety, it is meaningful to understand the maneuvering behavior of a ship in waves.

To study the maneuverability of a ship in waves, combining the theories of maneuvering and seakeeping is needed. A practical combining approach is to use the two-time scale model, which separates the basic motion equations into two groups: the one for high frequency wave-induced motion and the other for the low frequency maneuvering motion. Typical works in this area have been reported by Skejic and Faltinsen [1], Yasukawa and Nakayama [2] and Seo and Kim [3].

In the present study, numerical simulations of the ship maneuvering in waves are carried out. The maneuvering motion is calculated using 4-DOF MMG model, whereas the wave-induced motions are determined by solving a linearized boundary value problem (BVP) in time domain. The maneuvering and seakeeping problem is integrated by a two-time scale model, following the approach of Seo and Kim [3]. Numerical results for the S-175 container ship turning in waves are presented and compared with experimental data to validate the numerical method.

2 Mathematical formulations

2.1 *Coordinate systems*

Two coordinate systems are adopted, as shown in Fig. 1. The first one $\vec{x} = (x, y, z)$ is body-fixed, with the positive x towards the bow and the positive z pointing upward. The xy plane is coincident with the calm water level and the origin of the frame is at the midship; the second one $\vec{X} = (X, Y, Z)$ is fixed in space.

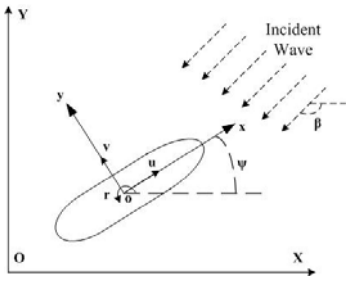

Fig. 1 Coordinate systems

2.2 *Basic motion equations*

The ship is assumed rigid and undergoing six degrees of freedom oscillations while translating with forward speed u, transverse speed v and rotating with yaw rate r in regular waves. Based on the two-time scale model, ship motion is assumed to be the sum of the high frequency wave-induced motion and the low frequency maneuvering motion.

The 6-DOF motion equations for high frequency problem are expressed as:

$$[M_{ij}]\{\ddot{\xi}_j(t)\} + [C_{ij}]\{\xi_j(t)\} = \{F_i\} \quad (i, j = 1,2\ldots6) \qquad (1)$$

where $\vec{\xi}_T = (\xi_1, \xi_2, \xi_3)$ and $\vec{\xi}_R = (\xi_4, \xi_5, \xi_6)$ represent the ship's translational and rotational displacements, respectively; $[M_{ij}]$ is the inertial matrix for the hull, $[C_{ij}]$ is the matrix of hydrostatic restoring coefficients and $\{F_i\} = (F_x, F_y, F_z, M_x, M_y, M_z)$ denotes the hydrodynamic force and moment for high frequency component. The ship displacement about the body-fixed frame is written as:

$$\vec{\xi} = (\xi_x, \xi_y, \xi_z) = \vec{\xi}_T + \vec{\xi}_R \times \vec{x} \qquad (2)$$

The equations of low frequency ship maneuvering motion

are expressed as:

$$\left.\begin{aligned} &m(\dot{u}-vr-x_G r^2+\dot{\phi}rz_G)=X_H+X_P+X_R+X_W\\ &m(\dot{v}+ur+x_G\dot{r}+\ddot{\phi}z_G)=Y_H+Y_R+Y_W\\ &I_{xx}\dot{p}-mz_G(\dot{v}+ur)=K_H+K_R+K_W\\ &I_{zz}\dot{r}+mx_G(\dot{v}+ur)=N_H+N_R+N_W \end{aligned}\right\} \quad (3)$$

where m is ship's mass, I_{xx} and I_{zz} are moments of inertia. x_G and z_G represent the coordinates of the center of gravity, the subscripts H, P, and R denote the hydrodynamic forces of low frequency motion on the hull, propeller and rudder, respectively; the subscript W denotes the wave drift forces. The hull force $\vec{F}_H=(X_H,Y_H,K_H,N_H)$ can be decomposed as

$$\begin{aligned} X_H&=-m_x\dot{u}+m_y v\dot{\psi}+X_{nonlinear}-R(u)\\ Y_H&=-m_y\dot{v}-m_x u\dot{\psi}+Y_v v+Y_r r+Y_{nonlinear}\\ K_H&=-mg\overline{GM}\sin\phi-K(\dot{\phi})-z_H Y_H\\ N_H&=-J_{zz}\dot{r}+N_v v+N_r r+N_{nonlinear} \end{aligned} \quad (4)$$

where m_x and m_y are the added masses, and J_{zz} and J_{xx} are the added moments of inertia in zero frequency.

In the present study, the linear force ($Y_v v, Y_r r, N_v v, N_r r$), the high frequency force $\{F_i\}$, and the wave drift forces are calculated by solving the BVPs. The rudder, propeller and nonlinear hull force components are obtained from the model test [4].

2.3 *Modeling of hydrodynamic forces*

In order to calculate the hydrodynamic forces in time domain, temporal discretizations must be introduced. Since the frequencies of maneuvering motion and wave-induced motion are very different, two different time scales, denoted by τ_L and τ_H, are used in the low frequency problem and the high frequency problem, respectively. The ratio between τ_L and τ_H is donated by N, which is generally much larger than 1.

During the interval of each maneuvering time step τ_L, the ship speed is assumed to be constant, and is defined as

$$\vec{W}=(u-ry)\vec{i}+(v+rx)\vec{j}+0\vec{k} \quad (5)$$

where $(\vec{i},\vec{j},\vec{k})$ are the unit vectors associated with the ship-fixed coordinates.

Under the assumption that the fluid is inviscid and incompressible, and the flow is irrotational, the fluid velocity potential can be introduced. The total disturbance potential $\Psi(\vec{x},t)$ satisfies the following BVP:

$$\left.\begin{aligned} &\nabla^2\Psi=0 \quad \text{in fluid domain}\\ &(\frac{\partial}{\partial t}-(\vec{W}-\nabla\Psi)\cdot\nabla)[z-\eta(x,y,t)]=0 \quad \text{on z=}\eta(x,y,t)\\ &\frac{\partial\Psi}{\partial t}-\vec{W}\cdot\nabla\Psi+\frac{1}{2}\nabla\Psi\cdot\nabla\Psi=-g\eta \quad \text{on z=}\eta(x,y,t)\\ &\frac{\partial\Psi(\vec{x},t)}{\partial n}=\vec{W}\cdot\vec{n}+\frac{\partial\vec{\xi}}{\partial t}\cdot\vec{n} \quad \text{on body surface} \end{aligned}\right\} \quad (6)$$

where $\vec{n}$ is the inward unit normal on the hull surface.

In addition, for the ship in oblique or turning motion, which can be regarded as a lifting body, a Kutta condition should be imposed at the trailing edge of the hull.

To linearize the free surface boundary conditions, the total disturbance potential Ψ is decomposed into a basis flow $\Phi(\vec{x})$ and a perturbation flow $\varphi_P(\vec{x},t)$:

$$\Psi(\vec{x},t)=\Phi(\vec{x})+\varphi_P(\vec{x},t) \quad (7)$$

The basis flow is assumed to be the main component with its order of $O(1)$ and is related to the double body flow, which includes the one induced by maneuvering motion. To account for the lifting effect associated with the maneuvering motion, trailing vortex sheets are introduced which are assumed shed from the hull at both the keel line and the trailing edge of the hull, as shown in Fig. 2. By referring the work of Matsui et al. [5], a linear trailing vortex sheet is adopted. In the numerical approach, the length of the vortex sheets are assumed to be six times of the ship length and the angle Θ between the x-axis and the free vortex line is determined by the following formula:

$$\Theta=0.5\arctan(v/u) \quad (8)$$

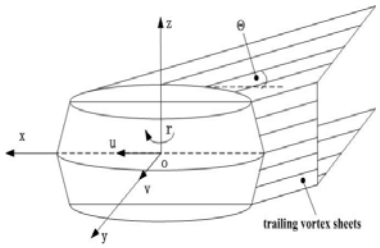

Fig. 2 The vortex model

The perturbation potential $\varphi_P(\vec{x},t)$ and the wave elevation η are assumed to be order of $O(\varepsilon)$. They are decomposed as:

$$\varphi_P(\vec{x},t)=\varphi(\vec{x},t)+\varphi_I(\vec{x},t) \quad (9)$$

$$\eta(x,y,t)=\zeta(x,y,t)+\zeta_I(x,y,t) \quad (10)$$

where $\varphi_I(\vec{x},t)$ represents the incident wave potential, $\zeta_I(x,y,t)$ is the incident wave elevation. $\varphi(\vec{x},t)$ and $\zeta(x,y,t)$ denote the remaining parts of the disturbance potential and wave elevation, respectively.

The linearized BVP for $\varphi(\vec{x},t)$ is written as follows:

$$\left.\begin{aligned} &[\frac{\partial}{\partial t}-(\vec{W}-\nabla\Phi)\cdot\nabla]\zeta=\frac{\partial^2\Phi}{\partial z^2}\eta+\frac{\partial\varphi}{\partial z}-\nabla\Phi\cdot\nabla\zeta_I \quad \text{on z=0}\\ &[\frac{\partial}{\partial t}-(\vec{W}-\nabla\Phi)\cdot\nabla]\varphi=-g\zeta-\nabla\Phi\cdot\nabla\varphi_I \quad \text{on z=0}\\ &\frac{\partial\varphi}{\partial n}=\sum_{j=1}^{6}(\frac{\partial\xi_j}{\partial t}n_j+\xi_j m_j)-\frac{\partial\varphi_I}{\partial n} \quad \text{on } \bar{S}_B \end{aligned}\right\} \quad (11)$$

where $(n_1,n_2,n_3)=\vec{n}$, $(n_4,n_5,n_6)=\vec{x}\times\vec{n}$ and m_j is the so-called m-terms, which are evaluated as

$$\begin{aligned} &(m_1,m_2,m_3)=(\vec{n}\cdot\nabla)(\vec{W}-\nabla\Phi),\\ &(m_4,m_5,m_6)=(\vec{n}\cdot\nabla)(\vec{x}\times(\vec{W}-\nabla\Phi)) \end{aligned} \quad (12)$$

Theoretically, an interaction exists between the trailing

vortices and the disturbance potential $\varphi(\vec{x},t)$. In the present study, however, the influence of the wave potential on the trailing vortices is neglected, because of the difficulty to determine the strength of the vortex in the presence of free surface and incident waves. The error introduced by this treatment is supposed to be small, since $\varphi(\vec{x},t)$ is smaller than $\Phi(\vec{x})$ by an order of magnitude. On the other hand, the effects of the trailing vortices on the wave potential $\varphi(\vec{x},t)$ are considered through the *m*-terms as well as the leading-order terms kept in the free surface boundary conditions.

Using Bernoulli's equation, the hydrodynamic pressure is obtained

$$p^{(0)} = -\rho(\vec{W}\cdot\nabla\Phi + \frac{1}{2}\nabla\Phi\cdot\nabla\Phi) \tag{13}$$

$$p^{(1)} = -\rho(\frac{\partial}{\partial t} - (\vec{U}-\nabla\Phi)\cdot\nabla)\varphi \tag{14}$$

where $p^{(0)}$ and $p^{(1)}$ denote the pressures from the base flow and the perturbation flow, respectively.

The linear forces for low frequency motion satisfy the following equations:

$$Y_v v + Y_r r = \iint_{\bar{S}_B} p^{(0)} n_2 \, ds \tag{15}$$

$$N_v v + N_r r = \iint_{\bar{S}_B} p^{(0)} n_6 \, ds \tag{16}$$

The generalized hydrodynamic force for high frequency motion can be determined by:

$$F_j = \iint_{\bar{S}_B} p^{(1)} n_j \, ds, \quad j = 1,2,\cdots,6 \tag{17}$$

The second-order hydrodynamic force $\vec{F}^{(2)}$ is evaluated by the following equation:

$$\begin{aligned}
\frac{1}{\rho}\vec{F}^{(2)} &= -\iint_{S_{\bar{B}}}[-\vec{W}\cdot\nabla\Phi + \frac{1}{2}\nabla\Phi\cdot\nabla\Phi + gz]\vec{n}_2 ds - \frac{1}{2}\iint_{S_{\bar{B}}}(\nabla\phi\cdot\nabla\phi)\vec{n} ds \\
&-\iint_{S_{\bar{B}}}\left\{\frac{\partial\phi}{\partial t} - (\vec{W}-\nabla\Phi)\cdot\nabla\phi + g\xi_Z + \nabla[-\vec{W}\cdot\nabla\Phi + \frac{1}{2}\nabla\Phi\cdot\nabla\Phi]\cdot\vec{\xi}\right\}\vec{n}_1 ds \\
&-\iint_{S_{\bar{B}}}\left\{\nabla[\frac{\partial\phi}{\partial t} - (\vec{W}-\nabla\Phi)\cdot\nabla\phi]\cdot\vec{\xi}\right\}\vec{n} ds + \frac{1}{2}\int_{WL} g(\eta-\xi_z)^2\vec{n} dl \\
&-\int_{WL}\left\{\nabla[-\vec{W}\cdot\nabla\Phi(0) + \frac{1}{2}\nabla\Phi\cdot\nabla\Phi(0)]\cdot\vec{\xi}\right\}(\eta-\xi_z)\vec{n} dl \\
&-\int_{WL}[-\vec{W}\cdot\nabla\Phi(0) + \frac{1}{2}\nabla\Phi\cdot\nabla\Phi(0)](\eta-\xi_z)\cdot\vec{n}_1 dl
\end{aligned} \tag{18}$$

where $\vec{n}_1$ and $\vec{n}_2$ mean the linear and second-order components of normal vector on the body surface, respectively. Details about Eq. (18) can be found in Joncquez [6]. The mean values of the *x* and *y* component of $\vec{F}^{(2)}$ equal to the wave drift forces X_W and Y_W, respectively. The wave drift moments K_W and N_W are neglected in the present study, because their magnitudes are generally small.

In this study, the linearized BVP (11) is solved by a time domain Rankine panel method, following the approach of Kring [7]; whereas the maneuvering motion equations (3) is solved by a 4th-order Runge-Kutta scheme. Referring to the study by Seo and Kim [3], a parallel time marching scheme is used (See Fig. 3). The linearized BVP (11) is firstly solved for *N* time steps to obtain the wave-induced ship motion as well as the linear forces (Eqs. (15) and (16)) and the wave drift forces. Then the maneuvering motions are simulated for one time step and the resulted ship speed and position are substituted back to update the BVP for the next time step. This cycle is continued until the end of time-marching procedure.

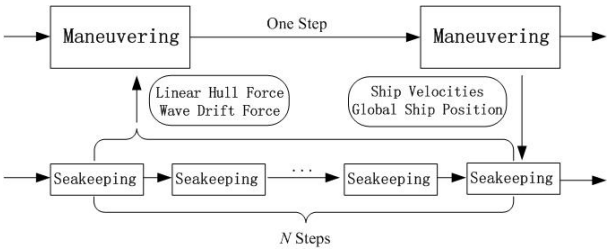

Fig. 3 Time marching scheme

3 Numerical results and discussion

Numerical simulations of the turning tests of the S-175 container ship are carried out, and the numerical results are compared with the data of model tests carried out at the Ocean Engineering Model Basin of Shanghai Jiao Tong University.

Fig. 4 illustrates the comparisons of the turning trajectory in clam water and in waves. It can be seen that the turning trajectories move both along and normal to the wave progress direction. The numerical results can generally give the drift tendency of the turning trajectories, but the predicted turning circles are smaller than those of the experiment. The reason for this difference may be due to the inaccurate evaluation of the mean drift forces.

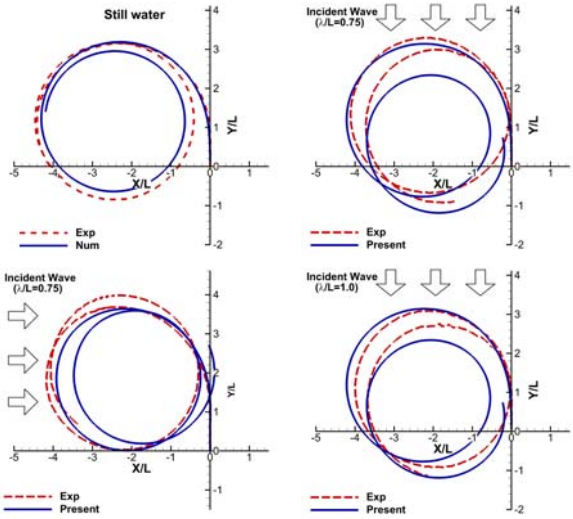

Fig. 4 Comparison of turning trajectories of S-175 model, rudder angle $\delta = 35°$ (port side), wave height $A = 0.01L$.

Fig. 5 illustrates the comparisons of roll and pitch motion when the wave direction $\beta = 180°$. Fig. 6 shows that of $\beta = 90°$. As seen in the figures, the predictions for roll and pitch motion roughly capture the increasing and decreasing of wave-induced motion amplitude associated with turning motion. But a time lag could be found between the predicted motions and the experimental measurements, especially for $t > 60s$. The reasons for this difference may be as follows: The turning period of the S-175 model is about 60*s*. For $t > 60s$, the discrepancies between the numerical prediction of the low frequency motion and the experiment become more remarkable. The poor predictions of the ship turning trajectory result in an error in the encounter frequency of the waves and therefore decrease the prediction accuracy of the wave-induced motions.

4 Concluding remarks

A numerical study on ship maneuvering in waves is carried out, based on the two-time scale model. In order to validate the present numerical method, the turning tests of S-175 model in the presence of waves are simulated. The numerical results are compared with the model test data, which shows that the present method can roughly capture the maneuvering performance of the ship in waves. A further study to improve the present method is still in process.

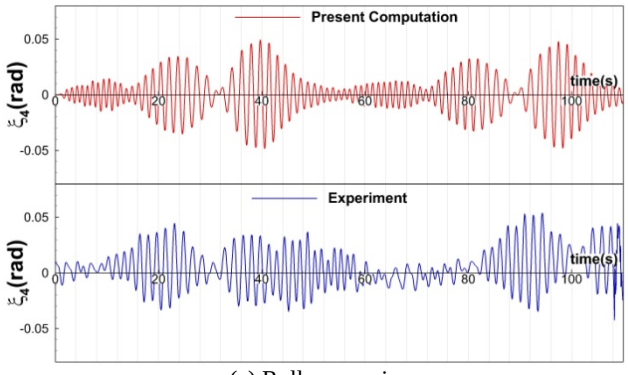

(a) Roll comparison

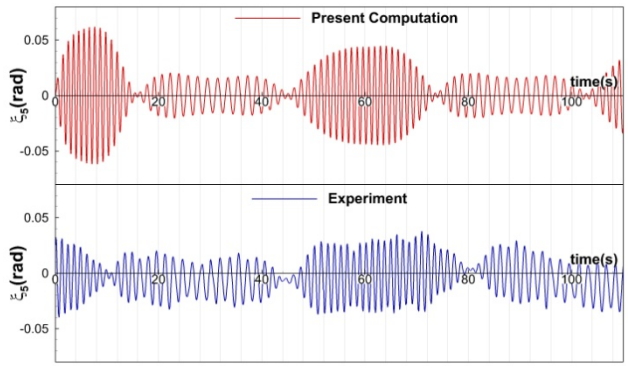

(b) Pitch comparison

Fig. 5 Time histories for S-175 model
($\lambda/L = 1.0,\ A = 0.01L,\ \beta = 180°$)

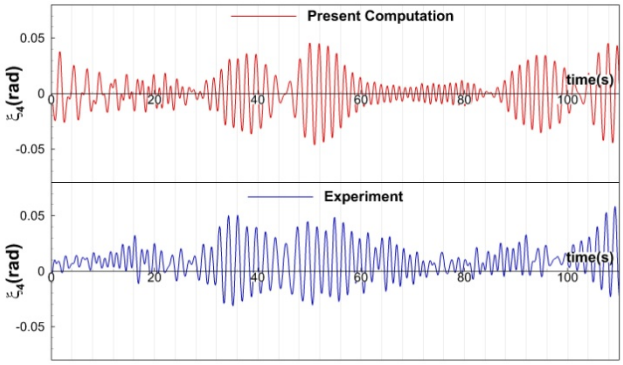

(a) Roll comparison

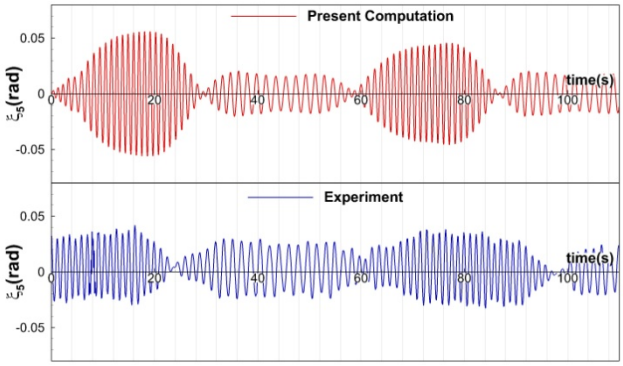

(b) Pitch comparison

Fig. 6 Time histories for S-175 model
($\lambda/L = 1.0,\ A = 0.01L,\ \beta = 90°$)

References

[1] Skejic, R., and Faltinsen, O. M. (2008). A unified seakeeping and maneuvering analysis of ships in regular waves. *J. Mar. Sci. Technol.*, **13**(4), 371-394.

[2] Yasukawa, H., and Nakayama, Y. (2009). 6-DOF motion simulations of a turning ship in regular waves. *Proceedings of MARSIM 2009*, Panama City, Panama.

[3] Seo, M. G., and Kim, Y. (2011). Numerical analysis on ship maneuvering coupled with ship motion in waves. *Ocean Eng.*, **38**(17), 1934-1945.

[4] Son, K. H., and Nomoto, K. (1982). On the coupled motion of steering and rolling of a high-speed container ship. *J. Soc. of Naval Arch. and Ocean Eng.*, **20**, 73-83.

[5] Matsui, S., Yang, J., Tamashima, M., and Yoshitake, A. (1994). Calculation of flow around a hull in turning motion and its hydrodynamic forces. *Trans. West-Japan Soc of Naval Arch*, **88**, 13-21.

[6] Joncquez, S. A. G. (2009). Second-order forces and moments acting on ships in waves. Ph.D. Thesis, DTU.

[7] Kring, D. C. (1994). Time domain ship motions by a three-dimensional Rankine panel method. Ph.D. Thesis, MIT.

A comparative study of the GN-3 and Boussinesq equations for nonlinear wave propagation

B.B. Zhao[1], W.Y. Duan[1,*], R.C. Ertekin[2], Z. Demirbilek[3] and W.C. Webster[4]

[1] College of Shipbuilding Engineering, Harbin Engineering University, 150001 Harbin, China
Email: duanwenyang@hrbeu.edu.cn

[2] Department of Ocean & Resources Engineering, University of Hawai'i 2540 Dole St., Holmes Hall 402, Honolulu, HI 96822, USA

[3] Coastal and Hydraulics Laboratory, U.S. Army Engineer Research and Development Center, Vicksburg, MS.

[4]Civil & Environmental Engineering, The University of California, Berkeley, California 94720, USA

Highlights:

- We set the level of the GN model to Level III, i.e., GN-3 model, and use it to compare the results with the results of a program we developed based on the theory of BOUSS-2D.
- For nonlinear shallow water waves, we increase the wave amplitude; both the GN-3 results and the Boussinesq results are presented and compared with the stream function theory.

1 Introduction

Nwogu's (1993, 1996) Boussinesq-type equations are widely used to study wave-current interaction, wave breaking, run-up (Nwogu and Demirbilek, 2001, 2010), among others. Nwogu's (1993) Boussinesq-type equations are based on the assumption that the wave heights are much smaller than the water depth. This may limit the ability of the equations to describe highly nonlinear waves in shallow water, and therefore this led Wei et al. (1995) to derive a fully nonlinear form of the equations. Wei et al. (1995) derived the equations from the dynamic free-surface boundary condition by retaining all nonlinear terms, up to the order of truncation of the dispersive terms. Nwogu (1996) derived a more compact form of the equations. The computer program BOUSS-2D is based on the Boussinesq-type equations derived by Nwogu (1993, 1996). The equations are depth-integrated equations for the conservation of mass and momentum for nonlinear waves propagating in shallow and intermediate water depths.

The Green-Naghdi approach (see e.g., Demirbilek and Webster, 1992) is fundamentally different from the perturbation method which is used in deriving the Boussinesq model. The GN model only introduces an assumption on the velocity variation in the vertical direction across the fluid layer or sheet. No restriction is placed on the wave amplitude. Following the development of different polynomial orders for the description of velocity in the vertical direction, the GN theory can be of different levels, such as I (GN-1), II (GN-2), III (GN-3), and so forth. Zhao et al. (2014) applied the GN-3, GN-5 and GN-7 models to some wave transformation problems, and they showed that high-level GN models can simulate strongly dispersive and strongly nonlinear waves.

In this study, we set the level of the GN model to Level III. And use the GN-3 model to compare the results with a computer program we developed based on the theory of the BOUSS-2D model to study nonlinear wave propagation for periodic and solitary waves.

2 The BOUSS-2D model

In the BOUSS-2D model, the vertical profile of the flow field is obtained by expanding the velocity potential, $\Phi(\boldsymbol{x}, z, t)$, in a Taylor series about an arbitrary elevation, z_α, in the water column. For waves of length, L, much longer than the water depth, h, the series is truncated at the second order resulting in a quadratic variation of the velocity potential over depth:

$$\begin{aligned}\Phi(\boldsymbol{x}, z, t) = \varphi_\alpha &+ \mu^2(z_\alpha - z)[\nabla\varphi_\alpha \cdot \nabla h] \\ &+ \tfrac{1}{2}\mu^2\left[(z_\alpha + h)^2 - (z + h)^2\right]\nabla^2\varphi_\alpha\end{aligned} \tag{1}$$

where $\varphi_\alpha = \Phi(\boldsymbol{x}, z_\alpha, t)$, $\nabla = (\partial/\partial x, \partial/\partial y)$, and $\mu = h/L$is a measure of frequency dispersion. The horizontal and vertical velocities are obtained from the velocity potential as:

$$\begin{array}{c} \boldsymbol{u}(\boldsymbol{x}, z, t) = \nabla\Phi = \boldsymbol{u}_\alpha + (z_\alpha - z)[\nabla(\boldsymbol{u}_\alpha \cdot \nabla h) + (\nabla \cdot \boldsymbol{u}_\alpha)\nabla h] \\ +\frac{1}{2}\left[(z_\alpha + h)^2 - (z + h)^2\right]\nabla(\nabla \cdot \boldsymbol{u}_\alpha) \end{array} \tag{2}$$

$$w(\boldsymbol{x}, z, t) = \frac{\partial\Phi}{\partial z} = -[\boldsymbol{u}_\alpha \cdot \nabla h + (z + h)\nabla \cdot \boldsymbol{u}_\alpha] \tag{3}$$

where $\boldsymbol{u}_\alpha = \nabla\Phi\big|_{z_\alpha}$is the horizontal velocity at $z = z_\alpha$. Given a vertical profile for the flow field, the continuity and Euler (momentum) equations can be integrated over depth, reducing the three-dimensional problem to two dimensions. Nwogu and Demirbilek (2001) gave the revised form of the fully nonlinear equations as

$$\eta_{,t} + \nabla \cdot \boldsymbol{u}_f = 0 \tag{4}$$

$$\begin{array}{l} \boldsymbol{u}_{\alpha,t} + g\nabla\eta + (\boldsymbol{u}_\eta \cdot \nabla)\boldsymbol{u}_\eta + w_\eta \nabla w_\eta + \\ (z_\alpha - \eta)[\nabla(\boldsymbol{u}_{\alpha,t} \cdot \nabla h) + (\nabla \cdot \boldsymbol{u}_{\alpha,t})\nabla h] \\ +\frac{1}{2}\left[(z_\alpha + h)^2 - (\eta + h)^2\right]\nabla(\nabla \cdot \boldsymbol{u}_{\alpha,t}) \\ -[\boldsymbol{u}_{\alpha,t} \cdot \nabla h + (\eta + h)\nabla \cdot \boldsymbol{u}_{\alpha,t}]\nabla\eta \\ +[\nabla(\boldsymbol{u}_\alpha \cdot \nabla h) + (\nabla \cdot \boldsymbol{u}_\alpha)\nabla h + (z_\alpha + h)\nabla(\nabla \cdot \boldsymbol{u}_\alpha)]z_{\alpha,t} = 0 \end{array} \tag{5}$$

where z_α is now a function of time and is given by $z_\alpha + h = 0.465(h + \eta)$. The volume flux density $\boldsymbol{u}_f$is given by:

$$\boldsymbol{u}_f = (h + \eta)\left\{ \begin{array}{c} \boldsymbol{u}_\alpha + \left[(z_\alpha + h) - \frac{(h+\eta)}{2}\right][\nabla(\boldsymbol{u}_\alpha \cdot \nabla h) + (\nabla \cdot \boldsymbol{u}_\alpha)\nabla h] \\ +\left[\frac{1}{2}(z_\alpha + h)^2 - \frac{1}{6}(h + \eta)^2\right]\nabla(\nabla \cdot \boldsymbol{u}_\alpha) \end{array} \right\} \tag{6}$$

3 The GN-3 model

In the GN-3 model, the horizontal velocity along the water column also changes as a quadratic polynomial. It is

$$u(x, z, t) = u_0(x, t) + u_1(x, t)z + u_2(x, t)z^2 \tag{7}$$

The GN-3 equations are as follows:

$$\frac{\partial\beta}{\partial t} = \sum_{n=0}^{K} \beta^n \left(w_n - \frac{\partial\beta}{\partial x}u_n\right) \tag{8}$$

$$\frac{\partial}{\partial x}\left(G_n + gS1_n\right) + nE_{n-1} - \alpha^n \frac{\partial}{\partial x}\left(G_0 + gS1_0\right) = 0 \quad \text{for} \quad n = 1, 2, 3, \cdots, K \tag{9}$$

where $K = 3$ in this work. For more details on the GN-3 model, the reader is referred to Demirbilek and Webster (1992), Webster et al. (2011) and Zhao et al. (2014).

4 Test cases

In this section, we simulate periodic nonlinear regular waves in shallow water generated through the stream function theory at the wavemaker through the computer programs we developed. The water depth is $h = 0.4$m and the wave period is $T = 2.02$s. We increase the wave height H from 0.16m to 0.20m, 0.24m and 0.28m. This means that the nonlinearity parameter, H/h, changes from 0.4 to 0.5, 0.6 and 0.7. The results of the Boussinesq equations are shown in Figure 1. The GN-3 results are shown in Figure 2.

For this case, the dimensionless depth is around $kh = 0.63$. Both the Boussinesq model and the GN-3 model should be able to simulate waves with this dispersive property. But we see that the results from Figures 1 and 2 show that neither of them can simulate successfully the largest-amplitude wave when $H/h = 0.7$. For waves when $H/h = 0.5$ and 0.6, we observe that the GN-3 results agree with the stream function wave theory better than the Boussinesq model.

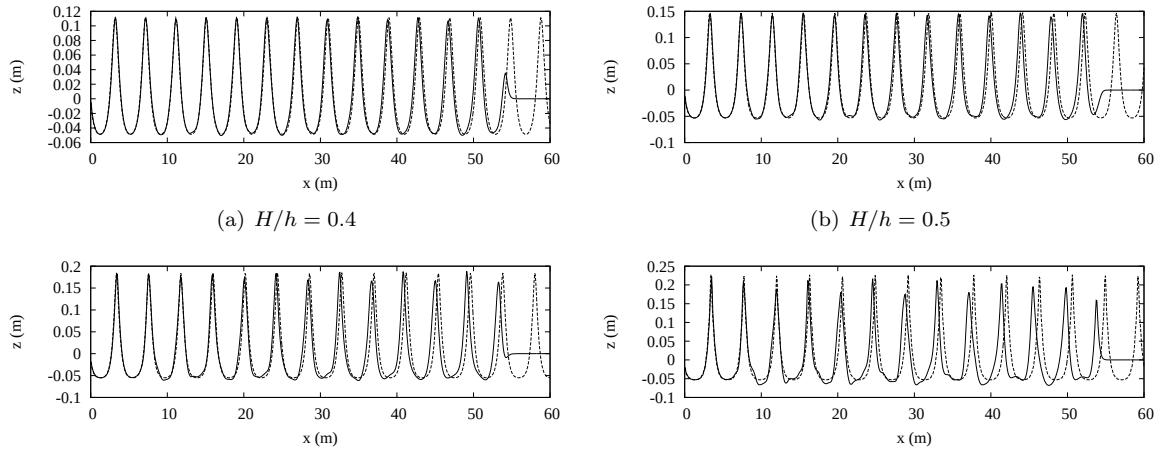

(a) $H/h = 0.4$ (b) $H/h = 0.5$

(c) $H/h = 0.6$ (d) $H/h = 0.7$

Figure 1: Snapshots at t=40s, solid line: Boussinesq model, dashed line: stream function wave theory.

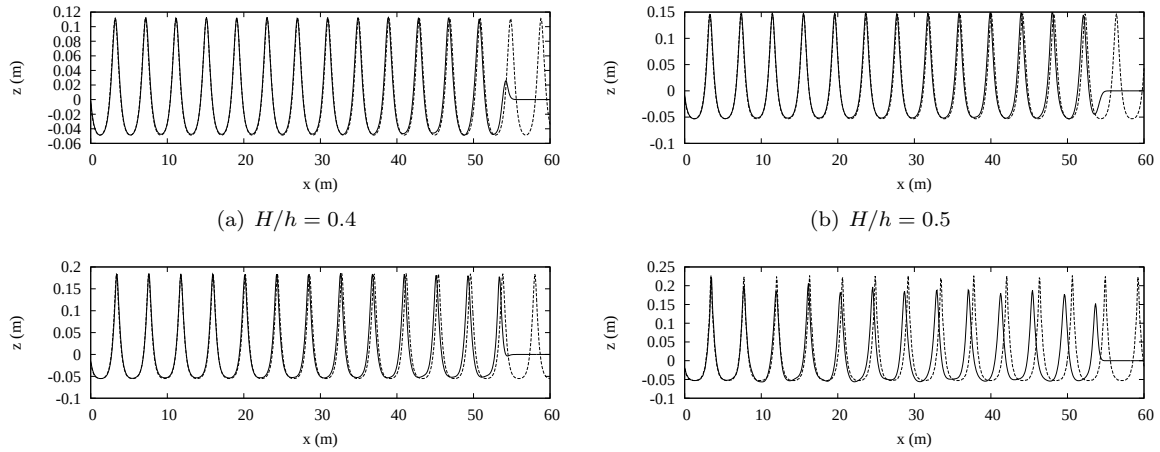

(a) $H/h = 0.4$ (b) $H/h = 0.5$

(c) $H/h = 0.6$ (d) $H/h = 0.7$

Figure 2: Snapshots at t=40s, solid line: GN-3 model, dashed line: stream function wave theory.

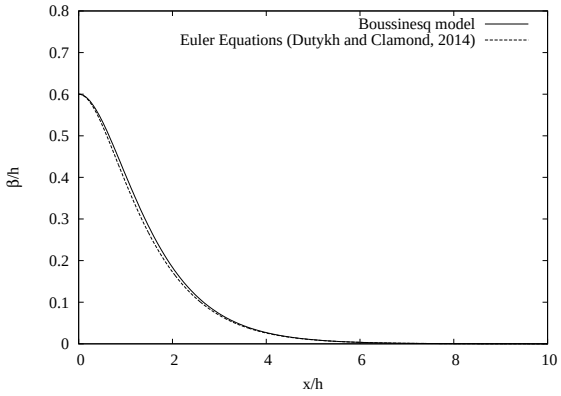

Figure 3: $H/h = 0.6$

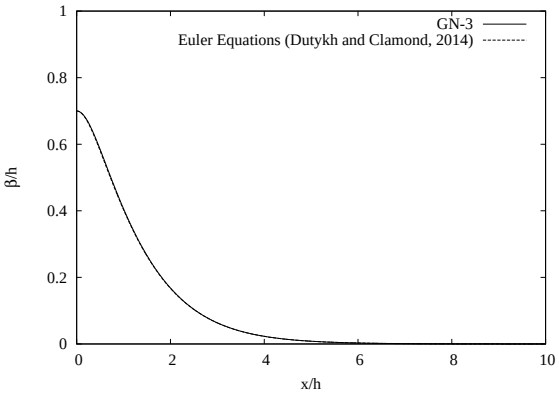

Figure 4: $H/h = 0.7$

We also studied the steady solitary wave solution from the GN-3 and Boussinesq models. Figure 3 shows that the Boussinesq model shows some differences compared with the Euler solution when $H/h = 0.6$. Figure 4 shows that the GN-3 model can simulate large amplitude solitary wave even when $H/h = 0.7$. More results will be presented at the workshop.

5 Conclusions

In this paper, we studied the GN-3 and Boussinesq models comparatively. We determined that the GN-3 model is more suitable to simulate strongly nonlinear solitary waves. For periodic waves, it appears that both models are incapable of simulating very large waves that are near breaking.

Acknowledgments

The work is supported by the National Natural Science Foundation of China (No. 11102049), National Ministry of Science and Technology (International Science and Technology Cooperation Project, No. 2012DFA70420), the Specialized Research Fund for the Doctoral Program of Higher Education of China (SRFDP, No. 20112304120021), the special Fund for Basic Scientific Research of Central Colleges (Harbin Engineering University) and High-tech Ship Research Projects Sponsored by the Ministry of Industry and Information Technology (MIIT) of China.

References

1. Dutykh, D. and Clamond, D. (2014). Efficient computation of steady solitary gravity waves, *Wave Motion*, Vol. 51, pp. 86-99.

2. Nwogu, O., & Demirbilek, Z. (2010). Infragravity wave motions and runup over shallow fringing reefs. *J. waterway, port, coastal, and ocean engineering*, 136(5), 295-305.

3. Nwogu, O. (1993). Alternative form of Boussinesq equations for nearshore wave propagation. *J. waterway, port, coastal, and ocean engineering*, 119(5), 618-638.

4. Nwogu, O., & Demirbilek, Z. (2001). BOUSS-2D: A Boussinesq wave model for coastal regions and harbors. *ERDC. CHL TR-01-25, US Army Engineer Research and Development Center, Vicksburg, MS.*

5. Wei, G., Kirby, J. T., Grilli, S. T., & Subramanya, R. (1995). A fully nonlinear Boussinesq model for surface waves. Part 1. Highly nonlinear unsteady waves. *J. Fluid Mech.*, 294, 71-92.

6. Webster, W. C., Duan, W.Y., & Zhao, B.B. (2011). Green-Naghdi theory, part A: Green-Naghdi (GN) equations for shallow water waves. *J. Marine Science and Application*, 10(3), 253-258.

7. Zhao, B. B., Duan, W. Y., & Ertekin, R. C. (2014). Application of higher-level GN theory to some wave transformation problems. *Coastal Engineering*, 83, 177-189.

8. Demirbilek, Z., & Webster, W. C. (1992). Application of the Green-Naghdi theory of fluid sheets to shallow-water wave problems. *US Army Corps. of Eng. Waterways Experiment Station, Rep. No. CERC-92-11, Vicksburg, MS.*

Wave-interference and wave-breaking effects on the Kelvin wakes of high-speed monohull ships and catamarans

Yi Zhu, Jiayi He, Chenliang Zhang, Li Wei, Decheng Wan, Francis Noblesse

State Key Laboratory of Ocean Engineering, School of Naval Architecture, Ocean & Civil Engineering, Shanghai Jiao Tong University, Shanghai, China; noblfranc@gmail.com

Highlight

Wave-interference and wave-breaking effects on the wave pattern of a ship that advances at constant speed along a straight path in calm water are considered. Realistic numerical computations, based on the Neumann-Michell theory or the related Hogner approximation, for seven ship hulls that correspond to broad ranges of main hull-shape parameters (beam/length, draft/length, beam/draft, waterline entrance angle), show that the apparent wake angle ψ_{max} where the largest waves created by a ship (monohull or catamaran) are found (at high Froude numbers) is only weakly influenced by the hull shape, and moreover can be well approximated by simple analytical relations. These relations provide useful relatively-accurate practical estimates (without computations) of the apparent wake angle ψ_{max} for *general* monohull ships and catamarans at any Froude number. Furthermore, elementary considerations suggest that wave-breaking effects are significant and result in a *lower* bound $\psi_{min} < |\psi|$. This lower bound complements Kelvin's classical upper bound $|\psi| \leq \psi_K \approx 19°28'$ and the more precise high-Froude-number upper bound $|\psi| \leq \psi_{max} \leq \psi_K$ related to interference between divergent waves.

1. Simple analytical models of far-field ship wave patterns

• 1.1 The 1-point wavemaker approximation and Kelvin's analysis

The simplest analysis of the wave pattern of a ship was given by Kelvin in 1887. A ship is approximated as a 1-point wavemaker in this classical analysis. Although particularly crude, the 1-point approximation is sufficient to determine essential features of the far-field waves created by a ship. In particular, Kelvin showed that ship waves can only be found inside a wedge $|\psi| \leq \psi_K$ with $\psi_K \approx 19°28'$. Kelvin's analysis also shows that the pattern of transverse and divergent waves created by a ship does not depend on the length L or the shape of the ship and only depends on the ship speed V, specifically on $(X, Y)g/V^2$.

• 1.2 Wave-interference effects

Within the context of a linear potential-flow analysis, considered by Kelvin and here, the flow around a ship hull can be represented by a continuous distribution of sources over the ship hull surface. The 1-point wavemaker approximation used in Kelvin's analysis evidently cannot account for interference effects that occur between the waves created by the sources distributed over a ship hull surface. However, wave-interference effects are very important. Indeed, interference between *transverve* waves is an essential element of the design of common displacement ships, and [1] shows that observations of narrow wave patterns at high Froude numbers are explained by interference effects between *divergent* waves.

• 1.3 The 2-point wavemaker approximation

[1] shows how interference effects can be approximately taken into account via a trivial refinement of Kelvin's analysis. Specifically, a monohull ship is approximated in [1] as a 2-point wavemaker, in accordance with the well-known property that a steadily-advancing ship creates two dominant waves that originate at the ship bow and stern (where the hull geometry varies most rapidly). The superposition of two basic Kelvin wakes with origins at the bow and the stern of a ship considered in [1] introduces an important additional parameter, the ship length L, that determines the occurrence of constructive or destructive interference between the basic Kelvin bow and stern wakes. Thus, the superposition of two Kelvin wakes associated with the dominant waves created by the bow and the stern of a monohull ship, or by the bows (or sterns) of the twin hulls of a catamaran, introduces the Froude numbers

$$F \equiv V/\sqrt{gL} \quad \text{or} \quad F_s \equiv V/\sqrt{gS} \equiv F\sqrt{L/S} \tag{1}$$

where S denotes the lateral separation distance between the two hulls of a catamaran. The elementary analysis of interference effects given in [1] does not involve the *amplitudes* of the dominant (bow and/or stern) waves created by a ship, and is then a particularly simple 'geometrical' analysis.

• 1.4 Longitudinal (x) interference effects for a 2-point wavemaker

[1] shows that longitudinal (x) interference between two basic Kelvin wakes associated with the dominant bow and stern waves created by a monohull ship yields largest waves along rays $\psi = \pm\psi^x_{max}$ that are inside the cusp lines $\psi = \pm\psi_K$ of the Kelvin wake for Froude numbers $F^x < F$. The apparent wake angle ψ^x_{max} and the related Froude number F^x are given by the analytical relations

$$\psi^x_{max} \approx \arctan\left(\frac{\sqrt{\pi^2F^4/\ell^2-1}}{2\,\pi^2F^4/\ell^2-1}\right) \approx \arctan\left(\frac{0.16\,\ell}{F^2}\right) \text{ and } F^x = \frac{\sqrt{\ell/\pi}}{(2/3)^{1/4}} \approx 0.62\sqrt{\ell} \qquad (2)$$

where ℓ denotes the nondimensional distance (related to the dimensional distance ℓL) between the effective origins of the bow and stern waves, assumed to be located slightly aft of the bow or slightly ahead of the stern. For lack of better knowledge, ℓ is taken as $\ell = 0.9$ in [1], as commonly used by naval architects in the analysis of interference between the transverse waves created by a ship bow and stern and the selection of a ship length L that avoids unfavorable interference effects (and related humps of the wave resistance curve). The choice $\ell = 0.9$ in (2) yields $\psi_{max} \approx \arctan(0.14/F^2)$ and $F^x \approx 0.59$.

• 1.5 Lateral (y) interference effects for a 2-point wavemaker

[1] also shows that lateral (y) interference between two Kelvin wakes associated with the dominant waves created by the twin bows (or the twin sterns) of the two hulls of a catamaran similarly yields largest waves along rays $\psi = \pm\psi^y_{max}$ that are inside the cusp lines $\psi = \pm\psi_K$ of the Kelvin wake for Froude numbers $F^y_s < F_s$ with F_s defined by (1). The wake angle ψ^y_{max} and the Froude number F^y_s are given by

$$\psi^y_{max} \approx \arctan\left(\sqrt{\frac{\sqrt{1+16\,\pi^2F_s^4}-1}{2\,(1+16\,\pi^2F_s^4)}}\right) \approx \arctan\left(\frac{0.2}{F_s}\right) \text{ and } F^y_s \equiv \frac{3^{1/4}}{2\sqrt{\pi}} \approx 0.37 \qquad (3)$$

The Froude numbers F that correspond to $F_s = 0.37$ are $F \approx 0.17,\ 0.26,\ 0.33$ for $S/L = 0.2,\ 0.5,\ 0.8$.

• 1.6 Merits and limitations of the 2-point wavemaker approximation

The basic relations (2) and (3) show that the apparent wake angle ψ_{max} decreases like $1/F^2$ for longitudinal (x) interference or like $1/F$ for lateral (y) interference. These relations are based on a highly-simplified analysis that essentially approximates a continuous distribution of sources over a ship hull surface by means of a point source and a point sink (for a monohull ship) or two point sources (for a catamaran), i.e. as a 2-point wavemaker. This relatively crude approximation has the merit of providing useful basic insight into wave interference effects, ignored in Kelvin's classical analysis. Another merit of the elementary analysis given in [1] is that it yields the simple analytical relations (2) and (3), which provide a realistic practical estimate of the apparent wake angle of a ship without computations. However, the analytical estimates (2) and (3) are based on a relatively crude 2-point wavemaker approximation, and therefore cannot be expected to be very accurate (obviously).

2. Numerical analysis of wave-interference effects

• 2.1 Practical numerical determination of apparent wake angle

A more precise estimate of the apparent wake angle ψ_{max} related to the largest waves created by a ship requires numerical computations. A realistic and practical method for determining ψ_{max} for arbitrary ship hulls (and/or distributions of pressure at the free surface) is used in [2]. The method, which closely follows [3], is based on the numerical determination of the highest peak of the amplitude function associated with the Fourier-Kochin representation of far-field ship waves [4]. The amplitude function in the Fourier-Kochin representation of far-field waves is evaluated in [2] via the classical Hogner approximation [4,5]. Numerical predictions (of the sinkage, trim, and drag experienced by several ship hulls, and of wave profiles along the hulls, for a range of Froude numbers) based on the Hogner approximation are found in [4,5] to be consistent with experimental measurements as well as numerical predictions given by the more accurate Neumann-Michell theory. The Hogner approximation is explicitly defined in terms of the speed and the length of a ship (the Froude number) and the hull shape via a distribution of sources with density n^x equal to the x-component of the unit vector $\mathbf{n} \equiv (n^x, n^y, n^z)$ normal to the hull surface. An important major consequence of this feature is that the *far-field waves* created by a ship (and the related wave drag of the ship) can be determined without having to compute the *near-field flow* around the ship hull, i.e. very simply, as is well known [4]. Indeed, the method considered in [2] can be applied to realistic ship hulls (including multihulls) of arbitrary shape (as well as general pressure distributions over the free surface), and moreover only involves elementary numerical computations that can be performed simply and very efficiently.

• 2.2 Apparent wake angle $\psi_{max}(F)$ for general monohull ships

The method considered in [2] is applied to seven simple (analytically-defined) hull forms at ten Froude numbers $F \approx 0.65,\ F = 0.7, 0.8, ..., 1.5$. The seven hull forms correspond to a broad range of main hull-form parameters; specifically, to beam/length ratio B/L, draft/length ratio D/L, beam/draft ratio B/D and waterline entrance angle $2\,\alpha$ within the ranges $0.1 \le B/L \le 0.25,\ 0.025 \le D/L \le 0.1,$

$1 \le B/D \le 10$, $33^\circ \le 2\,\alpha \le 90^\circ$. A notable interesting finding of the numerical computations reported in [2] is that the main parameters related to the shape of a ship hull only have a modest influence on the wake angle ψ_{max}. A useful practical consequence of this finding is that ψ_{max} can be estimated (without computations) for *general* monohulls (of any shape), specifically via the simple analytical relations

$$\psi_{max} \approx \psi_K \approx 19^\circ 28' \;\text{ for }\; F \le 0.573 \tag{4a}$$

$$\psi_{max} \approx \arctan(0.116/F^2) \;\text{ for }\; 0.573 \le F \le 0.85 \tag{4b}$$

$$\psi_{max} \approx \arctan[0.08\,(1+0.6/F)/F\,] \;\text{ for }\; 0.85 \le F \tag{4c}$$

These relations account for both *longitudinal* interference between the waves created by the fore and aft regions of a monohull ship and *lateral* interference between the waves created by the port and starboard sides of the hull, whereas the relation (2) only accounts for longitudinal interference between the dominant bow and stern waves. As expected, the relations (4) yield a practical estimate of the wake angle $\psi_{max}(F)$ of a general monohull ship that is more precise than the analytical estimate (2), although differences are not very large.

• 2.3 Apparent wake angle $\psi_{max}(F, s)$ for general catamarans

Interference effects are significantly more complicated for catamarans than for monohull ships because catamarans essentially are 4-point wavemakers and involve the additional parameter $s \equiv S/L$ that defines the lateral separation distance between the two hulls of the catamaran. Furthermore, interference effects between the divergent waves created by a monohull ship and a catamaran differ in a major way because a peak, called *outer peak* in [6], of the amplitude function in the Fourier-Kochin-Hogner representation of far-field waves [2] can occur for $\psi^y_{max} < |\psi| < \psi_K$ for catamarans (but not for monohulls). The method given in [2] is applied to catamarans in [6], where seven simple (analytically-defined) hulls are considered for lateral separation distances $s \equiv S/L$ and corresponding Froude numbers F_s within the ranges $0.2 \le s \le 0.8$ and $0.4 \le F_s \le 3.5$. The seven hulls correspond to a broad range of main hull-form parameters; specifically, to $0.05 \le B/L \le 0.1$, $0.0375 \le D/L \le 0.075$, $1 \le B/D \le 2$, $17^\circ \le 2\,\alpha \le 48^\circ$. The parametric study considered in [6] shows that the main parameters related to the shape of a ship hull only have a weak influence on the wake angle ψ_{max}, as also found in [2] for monohull ships. Moreover, the numerical computations considered in [6] show that the relation (3) that defines the *inner peak* of the amplitude function in the Fourier-Kochin-Hogner representation of far-field waves can be refined as

$$\psi_{max} \approx \psi_K \approx 19^\circ 28' \;\text{ for }\; F \le 0.46 - 0.02/s \tag{5a}$$

$$\psi_{max} \approx \psi^y_{max} + \frac{1.4}{s}\left(\frac{0.39 + 0.13\,s - \sqrt{s}\,F}{0.39 - 0.77\,s + 0.55\,s^2}\right)^2 \;\text{ for }\; 0.46 - \frac{0.02}{s} \le F \le \frac{0.39 + 0.13\,s}{\sqrt{s}} \tag{5b}$$

$$\psi_{max} \approx \psi^y_{max} \;\text{ for }\; (0.39 + 0.13\,s)/\sqrt{s} \le F \qquad \text{where } \; s \equiv S/L \tag{5c}$$

Here, ψ^y_{max} is given by (3) and the angles ψ_{max} and ψ^y_{max} are assumed to be expressed in degrees. The relation (5c) shows that the apparent wake angle ψ_{max} is equal to the angle ψ^y_{max} if F is large and/or if s is large, i.e. for fast and/or wide catamarans. The Froude number $F = (0.39 + 0.13\,s)/\sqrt{s}$ in (5c) varies between 0.93 and 0.55 for $0.2 \le s \le 0.8$. Thus, the systematic numerical study considered in [6] shows that *lateral* interference effects between the two hulls of a catamaran are dominant for fast and/or wide catamarans. However, *longitudinal* interference effects are important and cannot be ignored for slow narrow catamarans. Indeed, the outer peak can be higher than the inner peak in a region of the 'Froude-number and separation-distance plane' (F, s) that corresponds to small values of F and s. This relatively small region of the (F, s) plane where the outer peak is dominant and the relations (5a)-(5c) are not valid is given in [6].

• 2.4 Neumann-Michell computations of Kelvin wakes

The numerical results obtained in [2] for monohulls and in [6] for catamarans are based on the Hogner approximation, used to evaluate the amplitude function in the Fourier-Kochin representation of far-field ship waves. The relations (4) and (5) are further considered in [7] via the Neumann-Michell theory given in [4,5]. Specifically, computations of far-field waves are reported in [7] for seven monohull ships that correspond to broad ranges of main hull-shape parameters at four Froude numbers $F = 0.58$, 0.68, 0.86, 1.58, for which the relations (4b) and (4c) yield $\psi_{max} \approx 19^\circ$, 14°, 9°, 4°. These numerical computations confirm that the apparent wake angle ψ_{max} related to the largest waves created by a ship is only weakly influenced by the hull shape and thus mostly depends on the Froude number, in accordance with the relations (4). The Neumann-Michell theory is also used in [6] to supplement and confirm the 'Hogner-approximation-based' parametric study of interference effects for catamarans.

3. Wave-interference effects in shallow water

The elementary analysis of longitudinal (x) or lateral (y) interference between the dominant waves created by the bow and the stern of a monohull ship, or by the bows of the twin hulls of a catamaran, given in [1] for deep water is extended in [8,9] to the more general, and considerably more complicated, case of uniform finite water depth. This analysis shows that the largest waves due to constructive interference are found at an 'apparent wake angle' ψ_{max} that can differ greatly from the cusp or asymptote angles associated with the wave pattern of a ship when interference effects are ignored. Thus, wave-interference effects on the wave signature of a ship in shallow water are very large and cannot be ignored. The analysis given in [8,9] also yields practical relations that determine when water-depth effects on the apparent wake angle ψ_{max} are small and can be neglected.

4. Wave-breaking effects on the Kelvin wake

The foregoing linear potential-flow analysis of wave-interference effects ignores important effects related to wave-breaking, notably the breaking of bow waves. Indeed, ship bow waves typically are higher and shorter, and therefore steeper as well as far more influenced by nonlinear effects, than waves aft of the bow wave. Two main types of ship bow waves exist. Specifically, a slow ship with a blunt bow typically creates a highly unsteady and turbulent bow wave, whereas the bow wave created by a fast ship with a fine bow consists of a detached thin sheet of water that is mostly steady, until it hits the main free surface and undergoes turbulent breaking up and diffusion [10]. Both these two bow-wave regimes result in the dissipation of a portion of the wave energy of a ship bow wave, as well as the partial transformation of the wave drag of a ship into a wave-breaking drag component [11]. A reasonable *conjecture* is that the wave-breaking that commonly occurs at a ship bow destroys short waves more effectively than long waves. This *assumption* means that wave-breaking may result in the effective elimination of short waves with wavelengths $\lambda < \lambda^{min}$ from the spectrum of farfield ship waves. Moreover, the wavelength λ^{min} may be taken as a fraction ϵ of the longest wave $\lambda^{max} \equiv 2\pi F^2$ created by a ship, i.e. as

$$\lambda^{min} = \epsilon\, \lambda^{max} \equiv \epsilon\, 2\pi F^2 \tag{6}$$

The assumption that wavelengths $\lambda < \lambda^{min}$ are eliminated as a result of wavebreaking is mathematically equivalent to the restriction $\lambda^{min} < \lambda$, which is mathematically equivalent to the relation $\psi_{min} < |\psi|$ as shown in [12] if $\epsilon \leq 2/3$. Specifically, expression (15) in [12] yields the approximation

$$\psi_{min} \approx \arctan(\sqrt{\epsilon}/2) \quad \text{where} \quad 0 < \epsilon \equiv \lambda^{min}/\lambda^{max} \leq 2/3 \tag{7}$$

The special case $\epsilon = 2/3$ corresponds to $\psi_{min} = \psi_K \approx 19°28'$, and means that all divergent waves are eliminated. The relation (7) yields

$$\psi_{min} \approx 6°23' \approx \psi_K/3 \text{ for } \epsilon = 5\% \quad \text{and} \quad \psi_{min} \approx 12°32' \approx 2\,\psi_K/3 \text{ for } \epsilon = 20\% \tag{8}$$

Thus, the angle ψ_{min} of the 'no-divergent-wave wake' that is obtained if waves with wavelengths smaller than 5% or 20% of the dominant wavelength $\lambda^{\max} \equiv 2\pi F^2$ are assumed to be eliminated due to wave-breaking is approximately equal to $\psi_K/3$ or $2\,\psi_K/3$, i.e. is not small, and much larger than the angle ψ_{min} related to surface-tension effects [1]. The relations (8) suggest that wave-breaking, commonly found at a ship bow, may be assumed to have a very large influence on the Kelvin wake of a ship.

References

[1] Noblesse F, He J, Zhu Y, Hong L, Zhang C, Zhu R, Yang C 2014 Why can ship wakes appear narrower than Kelvin's angle?, European J Mech. B/Fluids 46:164-171

[2] Zhang C, He J, Zhu Y, Yang C-J, Li W, Zhu Y, Lin M, Noblesse F 2014 Interference effects on the Kelvin wake of a monohull ship represented via a continuous distribution of sources, submitted

[3] Barnell A, Noblesse F 1986 Far-field features of the Kelvin wake, Proc. 16th Symp. Naval Hydrodynamics, pp.18-36. National Academy Press

[4] Noblesse F, Huang F, Yang C 2013 The Neumann-Michell theory of ship waves, J Engineering Mathematics 79:51-71

[5] Huang F, Yang C, Noblesse F 2013 Numerical implementation and validation of the Neumann-Michell theory of ship waves. European J Mech. / B Fluids 42:47-68

[6] He J, Zhang C, Zhu Y, Wu H, Noblesse F, Wan D, Zou L, Li W 2014 Interference effects on the Kelvin wake of a catamaran, in preparation

[7] Zhang C, He J, Zhu Y, Yang C-J, Li W, Noblesse F 2014 Numerical illustrations of narrow Kelvin ship wakes, submitted

[8] Zhu Y, He J, Zhang C, Wu H, Wan D, Zhu R, Noblesse 2015 Farfield waves created by a monohull ship in shallow water, European J Mech. B/Fluids 49:226-234

[9] Zhu Y, Zhang C, He J, Ma C, Li W, Noblesse F 2015 Farfield waves created by a catamaran in shallow water, in preparation

[10] Noblesse F, Delhommeau G, Liu H, Wan D, Yang C 2013 Ship bow waves, J Hydrodynamics / B 25(4):491-501

[11] Baba E 1976 Wave Breaking Resistance of ships, Mitsubishi Techn. Bulletin No.110, ISSN 0540-469X

[12] He J, Zhang C, Zhu Y, Wu H, Yang CJ, Noblesse F, Gu X, Li W 2015 Comparison of three simple models of Kelvin's ship wake. European J. Mech. / B Fluids 49:12-19